The role of low-mass star clusters in the formation of massive stars

A thesis presented for the degree of Doctor of Astrophysics

Víctor M. Rivilla Rodríguez

Consejo Superior
de Investigaciones Científicas

Centro de Astrobiología
Departamento de Astrofísica

Universidad Autónoma
de Madrid

Facultad de Ciencias
Departamento de Física Teórica

SUPERVISOR:

Dr. Jesús Martín-Pintado Martín

TUTOR:

Dra. Ángeles Isabel Díaz Beltrán

Madrid, July 24, 2014

A mi tío Luis, la estrella más luminosa de mi cielo.

Contents

Abstract

Massive stars (M>8$M_{\odot}$) are the main source of energy and turbulence injection into the interstellar medium (ISM) of galaxies. Despite their importance, their formation process is still not well understood, being one of the most debated topic in modern Astrophysics.

Several theories have been proposed to explain the formation of the most massive stars: i) the monolithic gravitational collapse and core accretion; ii) the coalescence of low-mass stars in high density stellar clusters; and iii) the competitive accretion of material by low- and intermediate-mass stars in the cluster potential well.

While the classic theory of monolithic core accretion requires low levels of fragmentation of the parental gas condensation, coalescence and competitive accretion models require high levels of fragmentation resulting in a dense population of low-mass stars. Therefore, to distinguish between the different scenarios, it is crucial to establish how the parental condensation fragments by studying the distribution of low-mass stars in massive star cradles.

According to the scenario in which massive stars are born escorted by a dense population of low-mass stars, the turbulence injected by molecular outflows driven by young stars may affect the collapse and fragmentation processes as well as the accretion rates onto the potential well. Therefore, the outflow-driven feedback may play an important role in the formation of the cluster and the massive stars.

This thesis is focused on the role of stellar clusters of pre-main sequence (PMS) low-mass stars in the mechanisms leading to the formation of massive stars. We study the spatial distribution of the young low-mass stellar population in three nearby massive star-forming regions: Orion, DR21 and Monoceros R2. The characterization of this population is a challenge because it is usually still deeply embedded in the parental molecular cloud. Large amounts of dust and gas produce high extinctions that prevent their detection in the optical and even in the near-infrared (IR) wavelengths. Only X-ray, radio/(sub)millimeter and very deep IR observations are able to penetrate into the massive star cradles and reveal the low-mass stellar population. Thus, we use the X-ray catalogs provided by the space telescope *Chandra*, complementing them with deep IR surveys. We study the properties of the low-mass stellar population (such as the spatial distribution, the clustering, the stellar densities, the

extinction distribution or the evolutionary phase) and discuss which massive star formation scenario better agrees with our results.

Additionally, with the aim of better understanding both the properties of the members of these young clusters and the molecular environment of massive star cradles, we carry out new Very Large Array (VLA) radio continuum multi-epoch observations of Orion, and new Submillimeter Array (SMA) observations of the central region of Monoceros R2.

To assess the impact of outflow feedback, we study the role of the outflow-driven turbulence in two clusters of outflows embedded in massive star-forming regions, such as the Orion OMC1-S region and the central region of Monoceros R2.

The main findings and conclusions of this thesis are:

• **Massive stars born within dense low-mass star subclusters**: The results derived from the analysis of Orion, DR21 and Monoceros R2 show that the young low-mass stellar population is clustered towards the regions related to massive stars, where it reaches very high stellar densities (up to 10^6 stars pc^{-3}). This indicates that massive stars usually are born in high-clustered environments, escorted by a dense population of low mass stars. This suggests that the parental molecular clumps have suffered high levels of fragmentation.

Our results point out that the formation of massive objects is favored not only by the presence of dense gas, but also by the presence of a subcluster of low-mass stars, consistently with the competitive accretion scenario. The regions with high stellar densities create local gravitational wells which are able to attract the available gas which remains after the fragmentation process. Then, the material can be funnelled towards these dense subclusters through infalling accretion filaments. The stars located in the central regions of the potential well will *win* the competition for the surrounding gas. As a consequence, they can accrete more material and become more massive. This scenario successfully explains the overall centrally peaked structure of the extinction observed in the clusters studied in this thesis, whose stellar density is also centrally peaked. Moreover, the overall mass segregation reported in the Orion Trapezium Cluster and in the DR21 populations, and the fact that massive stars in Monoceros R2 are all located in the central region, also support competitive accretion as the mechanism leading to the formation of the more massive stars in these clusters.

• **Short- and long-term radio variability of young stars in Orion**: With

the aim of studying the radio properties of this young cluster, we use the Very Large Array (VLA) to carry out multi-epoch radio continuum monitoring of the Orion Nebula Cluster (ONC) and the background Orion Molecular Cloud (OMC). We detect 19 radio sources, mainly concentrated in the Trapezium Cluster and the Orion Hot Core massive-star forming regions. All the sources show clear variability on timescales of months, with the exception of the massive Becklin-Neugebauer (BN) object and the source C. We find tentative evidence of variability in the emission from the massive source I. Our observations also confirm radio flux density variations of a factor >2 on timescales of hours to days in 5 sources. One of these flaring sources, OHC-E, has been detected for the first time.

The radio emission can be attributed to two different components: i) a highly-variable (flaring) non-thermal radio gyrosynchrotron emission produced by electrons accelerated in the magnetospheres of PMS low-mass stars; ii) a thermal emission due to free-free radiation from ionized gas and/or heated dust around embedded massive objects and proplyds.

Based on the detections of radio flares, we suggest that they are more common events during the first stages of stellar evolution than previously thought.

A comparison between the radio and X-ray populations in Orion shows that the radio detections so far have been strongly biased to the brighter X-ray stars. This supports the link between the X-ray activity and the mechanisms responsible for the radio variability. The improved sensitivity of the new VLA and ALMA facilities have the potential to dramatically increase the number of low-mass stars in young clusters detected at radio wavelengths. This will allow to: i) measure the low-mass stellar densities in embedded massive star cradles through its emission at radio wavelengths; and ii) improve our understanding of the origin and nature of this radio emission.

• **Massive stars, hot molecular cores and outflows in Monoceros R2**: Our continuum SMA observations of the central region of Monoceros R2 have revealed thermal emission towards the massive objects IRS1, IRS2, IRS3 and IRS5. The emission from IRS1 and IRS2 is dominated by free-free radiation, while that from IRS3 and IRS5 appears to be dominated by dust emission. Our ^{12}CO(2-1) images reveal 11 previously unknown molecular outflows. In addition, our images of molecular emission from species such as CH_3CN, CH_3OH or SO_2 show that, besides IRS3 (a well-known molecular hot core), IRS5 is the most chemically active source in the region. The analysis of the properties of the molecular gas derived from the CH_3CN lines towards IRS5 reveals two different physical components: i) a dense and hot (T=230 K) core,

which suggests the presence of a deeply embedded protostar at the hot-core stage of its evolution; and ii) a less dense and colder (T=25 K) envelope. The fit of the Spectral Energy Distribution (SED) of IRS5 gives a mass for the central source of ∼7 $M_\odot$ and a luminosity of ∼300 $L_\odot$. The detection of a large number of CO outflows in the central region confirms the presence of very young objects and argues in favor of the competitive accretion scenario as origin of this stellar cluster.

• **The role of outflow-driven turbulence:** The study of the spatial distribution of young low-mass stars emitting X-rays in Orion reveals that the multiple outflows detected in the OMC1-S region are driven by an embedded young stellar subcluster. The injection of turbulence due to outflows could explain the observed velocity dispersion of the gas and hence the observed linewidths of dense molecular tracers. If the outflow feedback is maintained throughout the lifetime of the clump, it could potentially disrupt it. However, a significant fraction of the material would be already accreted by the forming subcluster before suffering ejection by outflows.

In the Monoceros R2 region, the previously known highly-energetic large-scale CO outflow may contribute to the gas velocity dispersion of the clump and may be able to expel a significant fraction of material outside the central region. However, the smaller-scale molecular outflows newly discovered by SMA are not supposed to be relevant contributors to the gas velocity dispersion in the central region, with no impact on the clump disruption.

The presence of outflows in massive star cradles can induce fragmentation of the parental region, favoring the formation of low-mass objects and preventing the formation of massive stars directly from monolithic collapse. The outflow-driven turbulence produced by the stellar subclusters can contribute to the turbulent support of the region, preventing its collapse in the very short free-fall time and allowing the formation of stars during a longer period. As a result, a subcluster of low-mass stars can be formed, as observed in OMC1-S and in the central region of Monoceros R2.

• **Violent stellar encounters producing highly-energetic and large-scale outflows**: the Orion Hot Core region and the central regions of DR21 and Monoceros R2 harbor large-scale and high energetic outflows whose origin is still uncertain. Since we have found very high stellar densities in these regions ($>10^5-10^6$ stars pc^{-3}), we evaluate the possibility of a close encounter of stars as the origin of the highly-energetic outflows. This scenario would be consistent with previously reported evidences of violent events occurred in the past. We consider likely that a single stellar

collision may occur in these high-dense stellar subclusters, favored by the presence of circumstellar disks, stellar binaries, and gas accretion during the lifetime of cluster formation. This suggests that, although coalescence does not seem to be the general mechanism able to build up massive stars, these violent events might be more frequent during the earliest phases of formation of a dense stellar subcluster than previously thought.

Resumen

Las estrellas masivas ($M>8M_{\odot}$) suponen la principal fuente de inyección de energía y turbulencia en el medio interestelar de las galaxias. Sin embargo, a pesar de su importancia, los procesos que conducen a su formación están todavía lejos de estar bien entendidos, siendo uno de los temas más debatidos de la Astrofísica moderna.

Se han propuesto varias teorías para intentar explicar la formación de las estrellas masivas: i) colapso gravitacional monolítico; ii) coalescencia de estrellas de masa baja en cúmulos estelares muy densos; y iii) acreción competitiva de material por parte de estrellas de masas bajas e intermedias en el seno del pozo del potencial gravitacional del cúmulo estelar. Mientras que la teoría clásica de colapso monolítico requiere bajos niveles de fragmentación de la condensación de gas natal, los modelos de coalescencia y de acreción competitiva requieren altos niveles de fragmentación, dando lugar a una población densa de estrellas de baja masa. Por lo tanto, para distinguir entre las distintas teorías, es crucial establecer el grado de fragmentación de la condensación natal mediante el estudio de la distribución de estrellas de baja masa en las regiones de formación de estrellas masivas.

Si las estrellas masivas nacen rodeadas de una población muy densa de estrellas de baja masa, la turbulencia debida a *outflows* moleculares generados por las estrellas puede afectar a los procesos de colapso y fragmentación de la condensación natal, así como a las tasas de acreción de material. Por tanto, el impacto de la energía inyectada por múltiples *outflows* puede tener una influencia importante en la formación del cúmulo estelar y de las estrellas masivas.

Esta tesis se centra en el papel que juegan los cúmulos de estrellas jóvenes de baja masa en los mecanismos que desembocan en la formación de estrellas masivas. Hemos estudiado la distribución espacial de la población joven de estrellas de baja masa en tres regiones de formación estelar masiva cercanas: Orión, DR21 y Monoceros R2. Detectar esta población estelar supone todo un desafío porque parte de ella se encuentra profundamente embebida en la nube molecular natal. Grandes cantidades de gas y polvo interestelar producen altas extinciones, impidiendo la detección de las estrellas mediante observaciones ópticas o incluso infrarrojas. Sólo observaciones de rayos X, (sub)milimétricas u observaciones infrarrojas muy profundas son capaces de penetrar en las cunas de las estrellas masivas y revelar la población de estrellas

de baja masa que se aloja en ellas. Por tanto, en esta tesis utilizamos catálogos estelares proporcionados por el telescopio espacial de rayos X *Chandra*, complementados con catálogos obtenidos con observaciones infrarrojas profundas. Estudiamos las propiedades de la población estelar de baja masa (tales como su distribución espacial, densidades, estructura de la extinción o estado evolutivo), y discutimos qué escenario de los propuestos para explicar la formación de estellas masivas se ajusta mejor a nuestros resultados.

Además, con el objeto de entender mejor las propiedades de los miembros de estos cúmulos estelares asociados con estrellas masivas y del entorno molecular donde nacen, hemos llevado a cabo nuevas observaciones de Orión y de Monoceros R2 con los interferómetros *Very Large Array* (longitudes de onda radio) y *Submillimeter Array* (longitudes de onda (sub)milimétricas), respectivamente.

Para evaluar el impacto de los *outflows* moleculares en la formación de estrellas masivas, estudiamos los cúmulos de *outflows* que se encuentran embebidos en la región de Orión OMC1-S y en la región central de Monoceros R2.

Los principales resultados y conclusiones de esta tesis son:

• **Las estrellas masivas nacen en el seno de subcúmulos de estrellas de masa baja**: Nuestro análisis de Orión, DR21 y Monoceros R2 muestra que la población joven de estrellas de baja masa es más densa precisamente en las regiones relacionadas con estrellas masivas (hasta 10^6 estrellas pc^{-3}). Esto indica que las estrellas masivas suelen nacer en entornos con alta densidad estelar de estrellas de menor masa. Este resultado sugiere que la condensacion molecular natal a partir del cual se forma el cúmulo estelar ha experimentado altos niveles de fragmentación.

De nuestros resultados se extrae que la formación de estrellas masivas viene favorecida no sólo por la presencia de gas denso, sino también por la existencia de un subcúmulo de estrellas de masa baja, de acuerdo con la teoría de acreción competitiva. Aquellas regiones con densidades estelares más altas crean pozos de potencial gravitacional locales que son capaces de atraer el gas circundante que ha quedado disponible tras el proceso de fragmentación. El material puede ser canalizado hacia los subcúmulos estelares más densos mediante filamentos de acreción que caen hacia los pozos de potencial. Las estrellas localizadas en las regiones centrales de los pozos son favorecidas en la "competición" por el gas, y como consecuencia pueden acretar mayores cantidades de material y convertirse en estrellas masivas. Este escenario explica satisfactoriamente y de manera natural el perfil radial, con máximo en el cen-

tro, de la extinción en los cúmulos estelares estudiados en esta tesis, cuya densidad de estrellas es también es radial con su máximo valor en el centro. La segregación en masa observada en el Trapecio de la Nebulosa de Orión y en la parte central del cúmulo de DR21, y el hecho que las estrellas masivas de Monoceros R2 estén situadas en la parte central del cluster, son otros apoyos al modelo de acreción competitiva como mecanismo que gobierna la formación de las estrellas masivas en estos cúmulos estelares.

• **Radio variabilidad de estrellas jóvenes de Orión en distintas escalas de tiempo**: Hemos utilizado el radio interferómetro *Very Large Array* para realizar un seguimiento a lo largo de dintintas épocas de la emisión de radio-ondas emitidas por estrellas de la Nebulosa de Orión (ONC) y de la Nube Molecular de Orión (OMC) situada detrás. Hemos detectado 19 fuentes, principalmente concentradas en el cúmulo de estrellas masivas del Trapecio y en la región del *Hot Core* de Orión. Con la excepción de la estrella masiva Becklin-Neugebauer (BN) y de la fuente C, todas las fuentes muestran clara variabilidad en escalas de tiempo de meses. Asímismo, hemos encontrado evidencias de variabilidad en la emisión de la fuente masiva I. Nuestras observaciones también confirman variaciones en la densidad de flujo de un factor >2 en escalas de tiempo de horas a días en 5 de las fuentes. Una de ellas, OHC-E, ha sido detectada por primera vez.

La emisión de radio puede atribuirse a 2 componentes distintas: i) emisión muy variable (incluyendo fulguraciones) de carácter no térmico debida a radiación girosincrotrón producida por electrones acelerados en la magnetosfera de estrellas de masa baja en fase pre-secuencia principal; ii) emisón térmica debida a radiación libre-libre del gas ionizado y/o a polvo calentado en torno a objetos masivos embebidos o *proplyds*.

En base a nuestras detecciones de fulguraciones, proponemos que durante las primeras fases de evolución estelar estos eventos son más comunes de lo que se pensaba anteriormente.

La comparación entre la población que emite radio-ondas y rayos X muestra que las detecciones en radio se han limitado hasta ahora a las estrellas más brillantes en rayos X. Esto confirma que existe una relación ente la actividad en rayos X y los mecanismos responsables de la variabilidad en radio-ondas. La mejoradas sensibilidades del nuevo *Very Large Array* y del *Atacama Large Millimeter Array* tienen el potencial de incrementar significativamente el número de estrellas de masa baja que se podrán observar con radio-ondas. Esto permitirá: i) revelar una mayor fracción de

los miembros de baja masa embebidos en las cunas de estrellas masivas; y ii) mejorar nuestro entendimiento actual del origen de la emisión de radio-ondas.

• **Estrellas masivas, "hot molecular cores" y "outflows" en Monoceros R2**: Nuestras observaciones del *Submillimeter Array* de la zona central de Monoceros R2 revelan emisión térmica procedente de los objetos masivos IRS1, IRS2, IRS3 and IRS5. La emisión de IRS1 y IRS2 está dominada por radiación libre-libre, mientras que en IRS3 y IRS5 parece estar dominada por emisión del polvo. Nuestras imágenes de la emisión de ^{12}CO(2-1) revelan 11 *outflows* moleculares hasta ahora desconocidos. Por otro lado, las imágenes de la emisión molecular de especies como CH_3CN, CH_3OH o SO_2 muestran que, además de IRS3 (un bien conocido *hot core* molecular), IRS5 es la fuente con una química más activa. El análisis de las propiedades del gas molecular derivadas de las líneas de CH_3CN procedentes de IRS5 revelan dos componentes físicas distintas: i) un núcleo denso y caliente (T=230 K), que sugiere la presencia de una protoestrella muy embebida en la fase de evolución de *hot core*; ii) una envoltura menos densa y más fría (T=25 K). El ajuste de la distribución espectral de energía de IRS5 indica que la estrella central tiene una masa de $\sim$7 $M_\odot$ y una luminosidad de $\sim$300 $L_\odot$. La detección de un gran número de *outflows* moleculares en la región central confirma la presencia de estrellas muy jóvenes y es compatible con el escenario de acreción competitiva como origen de este cúmulo estelar.

• **El papel de la turbulencia producida por "outflows":** nuestro estudio de la distribución espacial de estrellas jóvenes de masa baja en Orión revela que los múltiples *outflows* detectados en OMC1-S están producidos por un joven subcúmulo muy embebido. La turbulencia producida por los *outflows* podría explicar la dispersión de velocidad del gas y por tanto las anchuras de las líneas moleculares de gas denso. Si la inyección de energía se mantuviera durante todo el tiempo de vida de la condensacion natal, ésta podría llegar a disgregarse. Sin embargo, una fracción importante de material habría sido ya acretada por el subcúmulo antes de ser eyectada por los *outflows*.

En la región de Monoceros R2, el muy energético y extenso outflow de CO observado en la región podría contribuir a la dispersión de velocidad del gas y podría ser capaz de explulsar una fracción importante de material fuera de la región natal. Sin embargo, no se espera que los *outflows* moleculares de menor tamaño que hemos descubierto tengan una contrinución apreciable a la dispersión de velocidades del gas de la region central. Tampoco parece que tengan impacto alguno en una posible

disgregacioń futura de la condensación natal.

La presencia de *outflows* en las regiones de formación de estrellas masivas puede inducir la fragmentación de la región natal, favoreciendo la formación de objetos de masa baja e impidiendo la formación de estrellas masivas directamente mediante un colapso monolítico. La turbulencia proporcionada por los *outflows* puede contribuir al soporte de la región, impidiendo su colapso en el corto tiempo de caída libre y permitiendo así la formación de estrellas durante un periodo más largo. Como consecuencia, un subcúmulo de estrellas de masa baja puede formarse, como el observado en OMC1-S y en la región central de Monoceros R2.

• **Violentas interacciones estelares podrían producir "outflows" muy grandes y energéticos**: la región del *Hot Core* de Orión y las regiones centrales de DR21 y de Monoceros R2 albergan outflows de gran tamaño muy energéticos. Puesto que hemos encontrado densidades estelares muy altas en esas regiones ($>10^5-10^6$ estrellas pc^{-3}), hemos evaluado la posibilidad de que interacciones muy cercanas entre estrellas puedan ser el origen de estos outflows. Este escenario sería compatible con otras evidencias encontradas anteriormente acerca de eventos violentos ocurridos en el pasado. Consideramos que es probable que una colisión entre estrellas haya tenido lugar en estos subcúmulos tan densos, favorecida por la presencia de discos circunestelares, binarias, y acreción de gas durante el periodo de formación del cúmulo. Esto sugiere que, aunque la coalescencia de estrellas no parece el mecanismo general para formar estrellas masivas, estos eventos son quizá más frecuentes de lo que se ha pensado anteriormente durante las fases más tempranas de la formación de densos subcúmulos de estrellas.

CHAPTER 1

Introduction

1.1 The formation of stars

The interstellar medium (ISM), the material out of which the stars are formed, includes gas (atoms, ions and molecules), dust grains, magnetic fields and cosmic rays. Stars form by the gravitational collapse of large structures of the ISM. The ISM is known to be highly inhomogeneous and presents a hierarchical structure: from large entities known as molecular clouds, which harbors thousand of stars, to the smaller and denser cores where single stars are born. The processes leading to star formation involve changes of 20 orders of magnitude in density (from molecular clouds densities of 10^{-20} g cm^{-3} to stars with densities $\sim$1 g cm^{-3}), of $\sim$6 orders of magnitude in temperature and $\sim$7 orders of magnitude in size. This wide range of scales makes necessary a classification of different objects characterized by their size, mass, density and temperature. In Tab. 1.1 the classification scheme suggested by Williams et al. (2000) is presented. Throughout this thesis we will use this nomenclature whenever possible.

Given that the mass of a typical molecular cloud (10^3–10^4 M$_\odot$) is much larger than the mass of a single star, and its the density is much lower, it is evident that a fragmentation process followed by collapse is needed to form stars. The classical view of star formation from the ISM is based on gravitational fragmentation, originally formulated by Larson (1969, 1972) and Shu (1977). The initial structure of the parental molecular cloud makes gravitationally unstable some subregions or *clumps*,

Table 1.1: Typical properties of molecular clouds, clumps and cores.

	Molecular cloud	Clump	Core
Size (pc)	2-15	0.2-3	0.02-0.2
Mass (M$_\odot$)	10^3–10^4	50–500	0.5–5
Density (cm^{-3})	50–500	10^3–10^4	$>10^4$

with a centrally peaked density structure, masses of 50−500 $M_\odot$ and sizes of 0.2−3 pc. These clumps will fragment to even smaller condensations (0.02−0.2 pc) called *cores* (e.g. Saito et al. 2008). The cores, which have a distinct gravitational potential from their environment, do not contain any smaller scale structure. They are already gravitationally bound and lead to the formation of single stars. The masses of these cores are expected to reach values around the $M_{\rm Jeans}$, defined as the minimum mass whose gravitational attraction is able to counteract the gas thermal support:

$$M_{\rm Jeans}(r) \simeq 1.1 \left[\frac{T(r)}{10\ K}\right]^{3/2} \left[\frac{\rho(r)}{10^{-19}\ g\ cm^{-3}}\right]^{-1/2} [M_\odot] \tag{1.1}$$

where $T(r)$ and $\rho(r)$ are the temperature and density profiles, respectively. When the mass of the core is higher than the Jeans mass, the core is gravitationally bound and (in the absence of internal turbulence) it will collapse. The Jeans radius ($R_{\rm Jeans}$) is the associated minimum radius for an object to be gravitationally bound:

$$R_{\rm Jeans}(r) \simeq 0.057 \left[\frac{T(r)}{10\ K}\right]^{1/2} \left[\frac{\rho(r)}{10^{-19}\ g\ cm^{-3}}\right]^{-1/2} [pc] \tag{1.2}$$

In absence of other forces, the gas of the cores will collapse ideally in the free-fall time, which is usually used to characterize the typical timescale for collapse:

$$t_{\rm ff} \simeq 2.1 \times 10^5 \left[\frac{\rho}{10^{-19}\ g\ cm^{-3}}\right]^{-1/2} [yr] \tag{1.3}$$

The gas will fall towards the center of the core in a $t_{\rm ff}$. For the typical densities found in the molecular cores ($\rho \geq 10^{-19}$ g cm^{-3} or $n > 3\times10^4$ cm^{-3}), this timescale is $\leq 2\times10^5$ yr. Since $t_{\rm ff}$ depends on the gas density ρ, the collapse is faster in the central denser regions. In this scenario, the densest and innermost parts collapse rapidly and the more diffuse envelopes fall later (*inside-out* collapse).

This collapse is initially isothermal, because the gravitational energy released in the infall can be released in the far IR (the medium is optically thin at these wavelengths). When the central density reaches $\sim 10^{-13}$ g cm^{-3}, the medium becomes optically thick, and the energy cannot be radiated away. Then, the temperature and the pressure increase, forming a nuclear core in hydrostatic equilibrium, known as a *protostar*. In the meantime, the outer material is still being accreted by the central object, radiating away the gravitational potential energy. At this stage, the luminosity of the object is mainly due to accretion. The protostar then increases its mass by accreting material from its natal environment. Shu (1977) found that a low-mass

star has an accretion rate of:

$$\dot{m} = 4.36 \times 10^{-6} \left(\frac{T}{20\ K} \right)^{3/2} [M_\odot\ yr^{-1}] \tag{1.4}$$

where T is the temperature of the gas, which ranges typical values of 10−20 K. Then, the typical accretion rate for a low-mass star resulting from this simple expression is $\sim 10^{-5}$−10^{-6} $M_\odot$ yr^{-1}, in agreement with simulations (McKee and Tan 2003; Bate 2012).

When the central temperature reaches $\geq 10^6$ K, the fusion of deuterium[1], which needs lower temperatures that the main isotope of hydrogen, can start. The deuterium burning process maintains nearly constant the central temperature of the protostar, acting as a thermostat. During this phase the star is still accreting mass, allowing the formation of stars up to $\sim$3 $M_\odot$. When the deuterium is exhausted in the core, the temperature increases and the hydrogen fusion starts. We consider that the star is born at this point, and enters the Zero Age Main Sequence (ZAMS). Previous stages are usually known as pre-main sequence (PMS), while the main sequence (MS) phase encompass the full period when the star is burning hydrogen in its center. The timescale in which the pre-hydrogen burning evolution takes place, known as the Kelvin-Helmholtz time[2] ($t_{\rm KH}$), can be estimated as the ratio between the gravitational potential energy of the protostar and the rate the energy is radiated away (i.e., the luminosity):

$$t_{\rm KH} = \frac{G\,m^2}{R\,L} \simeq 3 \times 10^7 \left(\frac{m}{1\ M_\odot} \right)^2 \left(\frac{R}{1\ R_\odot} \right)^{-1} \left(\frac{L}{1\ L_\odot} \right)^{-1} [yr] \tag{1.5}$$

where G is the gravitational constant and m, R and L are the mass, radius and luminosity of the star, respectively. For a star $\sim$ 1 $M_\odot$ this time is longer ($\sim 10^7$ yr) that the typical accretion timescale $t_{\rm ff}$ (about several 10^5 yr), and therefore the star enters the MS when the accretion is already finished. However, in the case of massive stars, $t_{\rm KH}$ $\sim 10^4$ yr, and therefore $t_{\rm KH} < t_{\rm ff}$. As a result, the star enters in the MS when it is still accreting. This, among other factors, makes massive star formation a process much poorly understood than low-mass star formation (see Sect. 1.2).

[1] Deuterium in one of the two stable isotopes of hydrogen, and contains one proton and one neutron in its nucleus.

[2] This time was originally proposed in the late 19th century to estimate the age of the Sun. As nuclear reactions were unknown, the main candidate for the source of energy was the gravitational contraction. However, soon later Eddinggton noted the the age obtained, $\sim$20 Myr, contradicted longer ages inferred from geological and biological evidence. Some decades later it was discovered that the true source of the Sun's energy was the nuclear fusion.

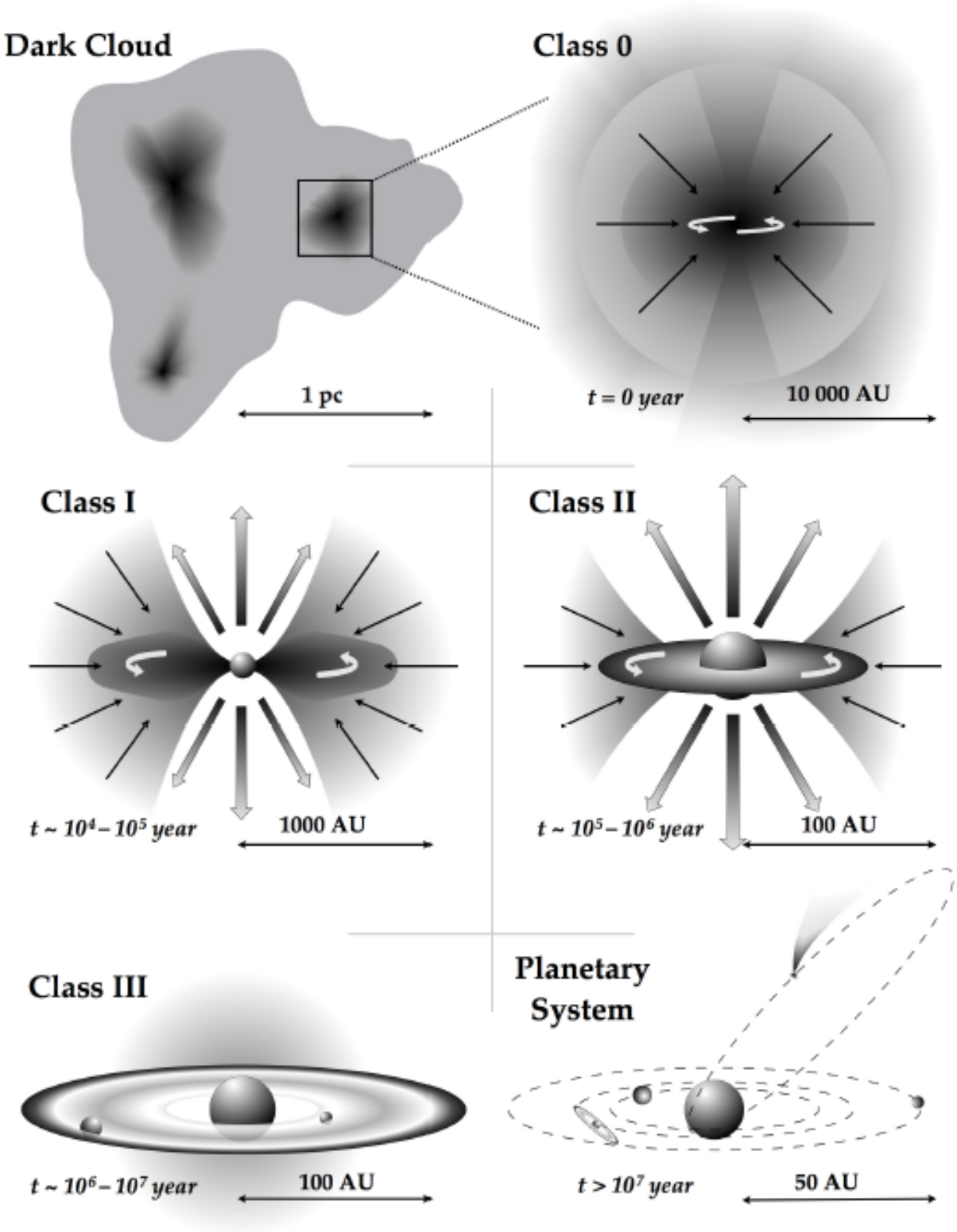

Figure 1.1: Evolutionary stages for the formation of low-mass stars, adapted from Frieswijk (2008).

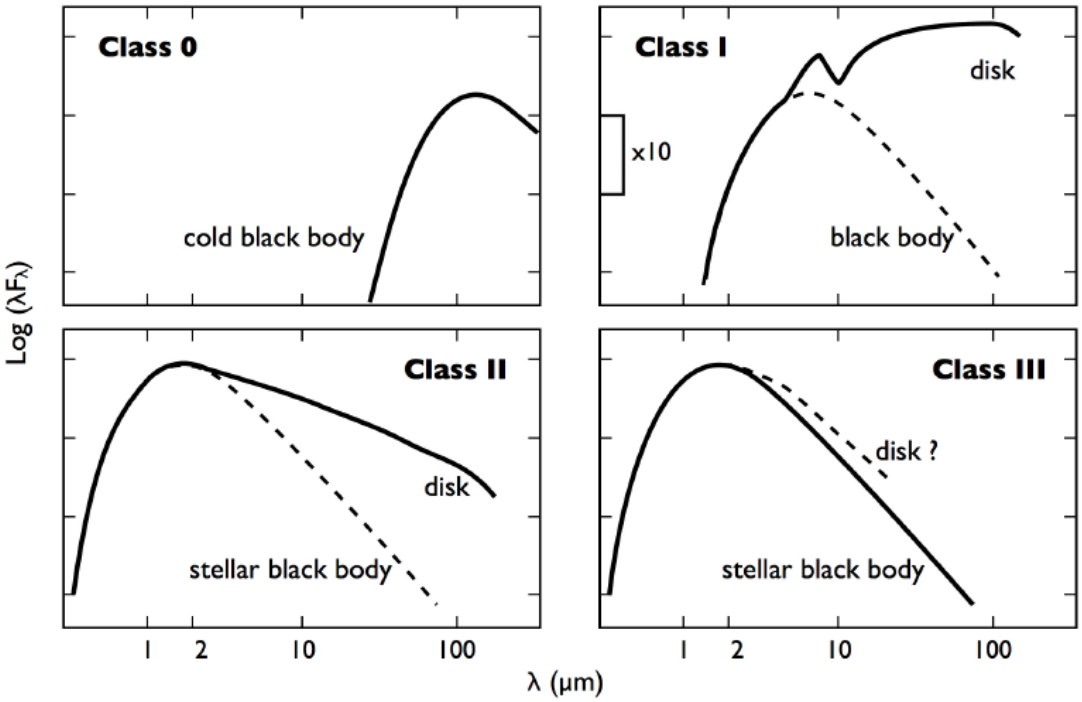

Figure 1.2: Spectral energy distributions (SED) of the different evolutionary stages of low-mass stars. Adapted from Frieswijk (2008).

1.1.1 Evolutionary phases in the formation of low-mass stars

From a theoretical point of view, the formation of low-mass stars ($m < 3\mathrm{M}_{\odot}$) is considered to be fairly well understood. Low-mass young stellar objects are classified along their evolutionary phases into Classes 0, I, II and III (Lada 1987; Andre et al. 1993; André 1994). A schematic picture of low-mass stellar evolution is shown in Fig. 1.1. Low-mass PMS stars emits significantly at infrared (IR) wavelengths due to the hot dust from the disk and/or envelope that absorbs and reemits the energy from the central object.

Fig. 1.2 shows the typical spectral energy distribution (SED) that characterizes the different classes. As the protostar evolves, it becomes warmer, and the peak of its spectral energy distribution shifts to shorter wavelengths. The objects are progressively less embedded, and the importance of the emission from the circumstellar envelope/disk diminishes. An observational parameter used to distinguish these evolutionary stages is the IR spectral index α (usually defined in the range 2−100 μm):

$$\alpha = -\frac{d}{d\,log\nu}(\nu F_{\nu}) \tag{1.6}$$

where ν is the frequency of the radiation and F_ν is the flux emitted at this frequency.

Class 0: these are the youngest low-mass stellar objects known. The SED is fitted by a black body[3] with low temperature peaking at sub-mm wavelengths ($\geq$100 μm). This emission arises from the infalling cold envelope and not from the central object, which is heavily embedded. In this phase the accretion is strong, and there is a huge amount of circumstellar dust.

Class I: these objects are low-mass stars characterized by a SED broader than that of a cold black body, because of the presence of a warm circumstellar envelope that produces an excess of emission in the near- and mid-IR. Its spectral index is positive ($0< \alpha <3$) as a consequence of the presence of large amounts of dust (see upper right panel in Fig. 1.2). Class I protostars have accreted most of their final mass but they are still deeply embedded. Their luminosity is dominated by accretion, and thus they are systematically more luminous than the more evolved classes II and III.

Class II: these objects show a broad SED, characterized by the presence of a circumstellar disk, which also produces an excess at IR wavelengths. These objects exhibit less circumstellar dust than Class I objects, and hence the spectral index becomes negative ($-2 < \alpha < 0$). Class II objects correspond roughly to the objects known as "classical T Tauri stars" (CTTSs).

Class III: the SED of these objects is similar to a black body, consistent with a redded photosphere (and therefore their colors can be confused with extincted foreground/background stars). They do not show significant excesses at IR wavelengths, because they have lost almost all their circumstellar dust. Its spectral index is in the range $-3 < \alpha < -2$. Class III objects correspond roughly to "weak-lines T-Tauri stars" (WTTSs). During this stage planet formation occurs (Fig. 1.1).

1.2 The formation of massive stars

Massive stars are a key ingredient in the formation and evolution of galaxies. The term *massive star* refers to stars with masses $m > 8$ M$_\odot$ and MS spectral types[4] from

[3] A black body is an idealized physical object that absorbs all incident electromagnetic radiation and reemits it regardless of frequency. Its emission is known as black-body radiation, and follows the Planck's law, i.e, is a function of the frequency ν and the temperature T.

[4] The spectral type is used to classify the stars according with their spectral features. Different letters (O, B, A, F, G, K and M) are used to characterize stars according to their mass and temperature, from the more massive and hotter to the less massive and colder.

B3 to O2 (usually called OB stars), which have enough mass to evolve to type II supernovae. Massive stars are the main source of mechanical energy injection into the ISM through several phenomena such as UV radiation, stellar winds, outflows, expanding HII regions, or supernova explosions. They are also responsible for the generation of the heavy chemical elements and it is also believed that they regulate the rate of star formation in galaxies. However, despite their importance, their formation process is still not well understood (Zinnecker and Yorke 2007) and today is one of the challenges in the field of star formation.

1.2.1 Phases of massive star formation

Since massive stars evolve much faster than low-mass stars, there is not a equivalent classification scheme like that described for low-mass stars in Sect. 1.1.1. The earliest evolutionary stages of massive stars, when the protostar is still embedded in the natal molecular material, only last around 15% of their lifetime (Churchwell 2002). Therefore these objects only exist during a very short timescale. This rapid evolution can be divided in several phases (Zinnecker and Yorke 2007), summarized in Fig. 1.3:

- **Infrared dark clouds (IRDC's)** : fragmentation, local collapse and infall in the molecular cloud produce starless cold, dense and turbulent massive clumps gravitationally bound. These objects are in a phase immediately before the collapse or during the collapse. They do not emit strongly in the IR (hence their name), and are usually observed in absorption against the bright background and by its emission at (sub)millimeter wavelengths.

- **Molecular hot cores**: very compact ($\sim$0.05 pc) condensations where one or more intermediate-high mass protostars have formed, heating up the environment from the initial temperature of $\leq$ 20 K up to a few 100 K (see Kurtz et al. 2000). At these temperatures the icy grain mantles are evaporated from the dust, producing a very rich chemistry in gas phase (van Dishoeck and Blake 1998). In this phase collimated jets and molecular outflows from the stars might appear.

- **Hypercompact, ultracompact, compact and diffuse HII regions**: when the hydrogen burning starts, the generated UV radiation destroys complex molecules in the closer vicinity of MS stars and ionizes the neighboring hydrogen, forming a hypercompact HII region, which emits broad hydrogen re-

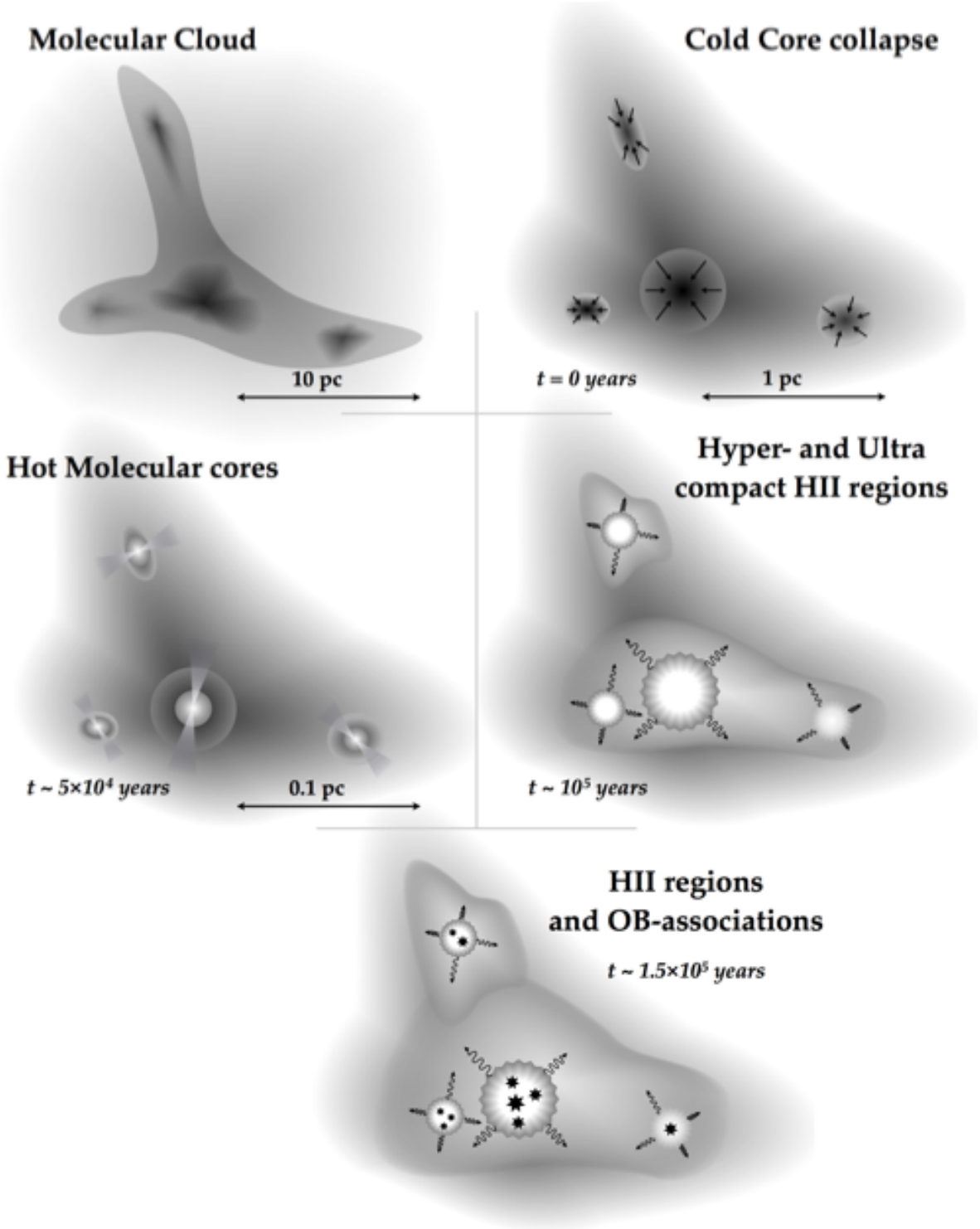

Figure 1.3: Schematic picture of the phases of massive star formation, from Frieswijk (2008).

combination lines[5]. The initial scales for the ionized regions are less than ∼0.01 pc. The increase of pressure due to the heating produced by the ionization radiation is no longer quenched by accretion and the HII regions expand, forming ultracompact (UC) HII regions, which will further evolve to compact and finally to a diffuse optically visible HII region dominated by OB massive stars, like the Orion Nebula.

1.2.2 The challenge of understanding massive star formation

The study of massive star formation has been challenging because of the large distances to the massive star-forming regions (from $d > 400$ pc up to several kpc within the galaxy) compared with low-mass star-forming regions (few tens of pc), their short time-scales for evolution, the complexity of their birth regions and the large extinction they suffer. As remarked by Zinnecker and Yorke (2007) massive star formation is not merely a scaled-up version of low-mass star formation. The environmental conditions of the formation of massive stars are significantly different that those in low-mass star-forming regions. In general, massive star-forming regions are more massive, denser and hotter, which may affect the phenomena involved in the collapse and the accretion. Moreover, they are usually found in more clustered environments, which is expected to affect the star formation process.

As already mentioned, the Kelvin-Helmholtz timescales for massive stars ($\sim 10^4$ yr) is shorter than the accretion timescale ($t_{\rm ff}$), and hence massive stars are still accreting when they enter the main sequence and the hydrogen burning starts. This could hinder the subsequent accretion to form more massive objects, because the radiation pressure arising from the star could halt the infall of the accreting material (Wolfire and Cassinelli 1987).

In the last decade several works have shown that it is possible to overcome the radiation pressure problem and gather enough mass to build up a massive star. One option is subsequent non-spherical mass accretion through the equatorial disk, which is favored by the fact that the radiation from the star is beamed in the pole direction. This is known as the "flashlight effect" (Yorke and Sonnhalter 2002, Cesaroni et al. 2006). Other processes, like Rayleigh-Taylor instabilities between gas and radiation, have been also proposed to allow the infall of gas avoiding the radiation pressure

[5] Hydrogen radio recombination lines (RRL) are produced by electronic transitions between energy levels of the atomic hydrogen. They are usually detected in HII regions, where the neutral hydrogen gas is ionized by a nearby massive star. The ultraviolet (UV) photons emitted by the star ionize the atoms, and the electrons recombine and cascade downward towards the ground state.

(Krumholz et al. 2009).

However, even considering that the radiation pressure problem has been solved, the very short timescale for the formation of massive objects (several 10^5 yr) requires higher accretion rates than that observed in low-mass star formation (e.g., Keto 2003). According to the picture from low-mass star formation, high accretion rates imply high temperatures (see Eq. 1.4). To significantly increase the temperature an already formed star should heat the environment. However, the argument is circular, because a massive star would be needed to allow the formation of a massive star. Therefore, other alternatives are required to explain the formation of massive stars.

1.2.3 Massive star formation theories

The three main theories proposed to explain massive star formation are: i) monolithic gravitational collapse and core accretion (Yorke and Sonnhalter 2002, McKee and Tan 2002, Krumholz et al. 2009); ii) competitive accretion of low- and intermediate-mass stars in the cluster potential well (Bonnell and Bate 2006); and iii) coalescence of low-mass stars in high stellar density clusters (Bonnell et al. 1998, Bally and Zinnecker 2005, Stahler et al. 2000). The first two scenarios are mainly based on accretion, differing on *when* and *how* the mass that forms the massive stars is gathered. The third one proposes a completely different scenario, based on dynamical mergers occurring during the first stages of the formation of stellar clusters.

In what follows the three scenarios are described in detail.

Monolithic core accretion

This theory has been proposed by McKee and Tan (2002, 2003). It is esentially a "scale-up" version of low-mass star formation characterized with higher accretion rates. According to this scenario, massive stars form from massive cores supported against self-gravity by their internal turbulence and magnetic fields. These turbulent cores[6] allow enough material to be available for high mass star formation, and accretion rates can be high enough to overcome the radiation pressure problem. As shown Fig. 1.4, the massive condensation collapses monolithically and produces a single massive object (or at most a few massive stars), rather than many low-mass

[6] The typical size and mass of the objects they call *cores* is ∼0.2 pc and 100 $M_\odot$ (see Fig. 1.4). According with the nomenclature adopted in Tab. 1.1 these objects would be classified as clumps rather than cores. Therefore, we note that although the nomenclature of this theory refers to the term *core*, their initial condensations are indeed *clumps* using the nomenclature defined in Tab. 1.1.

stars (Krumholz 2006; Krumholz et al. 2007; see Fig. 1.4).

According to this theory, the mass accretion rate is (McKee and Tan 2002, Krumholz et al. 2012):

$$\dot{m} = 1.2 \times 10^{-3} \left(\frac{m_{\rm f}}{30\ m_{\odot}} \right)^{3/4} \Sigma^{3/4} \left(\frac{m}{m_{\rm f}} \right)^{1/2} \ [M_{\odot}\ yr^{-1}] \tag{1.7}$$

where $m_{\rm f}$ is the final mass of the star, and Σ is the gas surface density in g cm^{-2}. Using typical conditions from massive star-forming regions, the accretion rates can reach values of 10^{-3}–10^{-4} M$_{\odot}$ yr^{-1}, high enough to build up a massive star in the relevant timescale. Integrating the accretion rate over the time one can obtain the accretion time needed to form a massive star with final mass m$_f$:

$$t = 5.0 \times 10^{-4} \left(\frac{m_f}{30 M_{\odot}} \right)^{1/4} \Sigma^{-3/4} \ [yr] \tag{1.8}$$

This *clump-to-star* formation mechanism is successful overcoming the radiation pressure and forming massive stars (Krumholz et al. 2009). Furthermore, it can explain the relation found between the parent clump and the stellar mass functions (Motte et al. 1998, Testi and Sargent 1998). If the stars are directly formed from the clumps without additional fragmentation, the mass spectrum of stars should be the same (or very similar) of the spectrum of clumps. However, this issue is not fully settled and it is under debate, because other observations did not find a direct correlation between clump and stellar masses (e.g., Pillai et al. 2011).

Although this scenario presents a feasible explanation for the formation of isolated massive stars, it has been questioned by other authors. The theory assumes the existence of turbulent massive cores/clumps that have prevented fragmentation during their formation. However, several observations (Motte et al. 2007; Longmore et al. 2011; Pillai et al. 2011; Duarte-Cabral et al. 2013) and simulations (e.g. Smith et al. 2009a) did not find such turbulent massive condensations, but smaller and lower mass fragmented objects. The monolithic collapse claims that the radiative feedback from the star halts the fragmentation of the condensation (Krumholz 2006; Krumholz et al. 2007), allowing the formation of a single massive (or a few) massive objects. Krumholz et al. (2007) suggested that the equation of state that describes the gas deviates from the isothermal condition (typically considered in the Jeans fragmentation) at high column densities since the gas becomes optically thick. As a result, the radiative heating can stop the fragmentation, and the final cores would have masses significantly

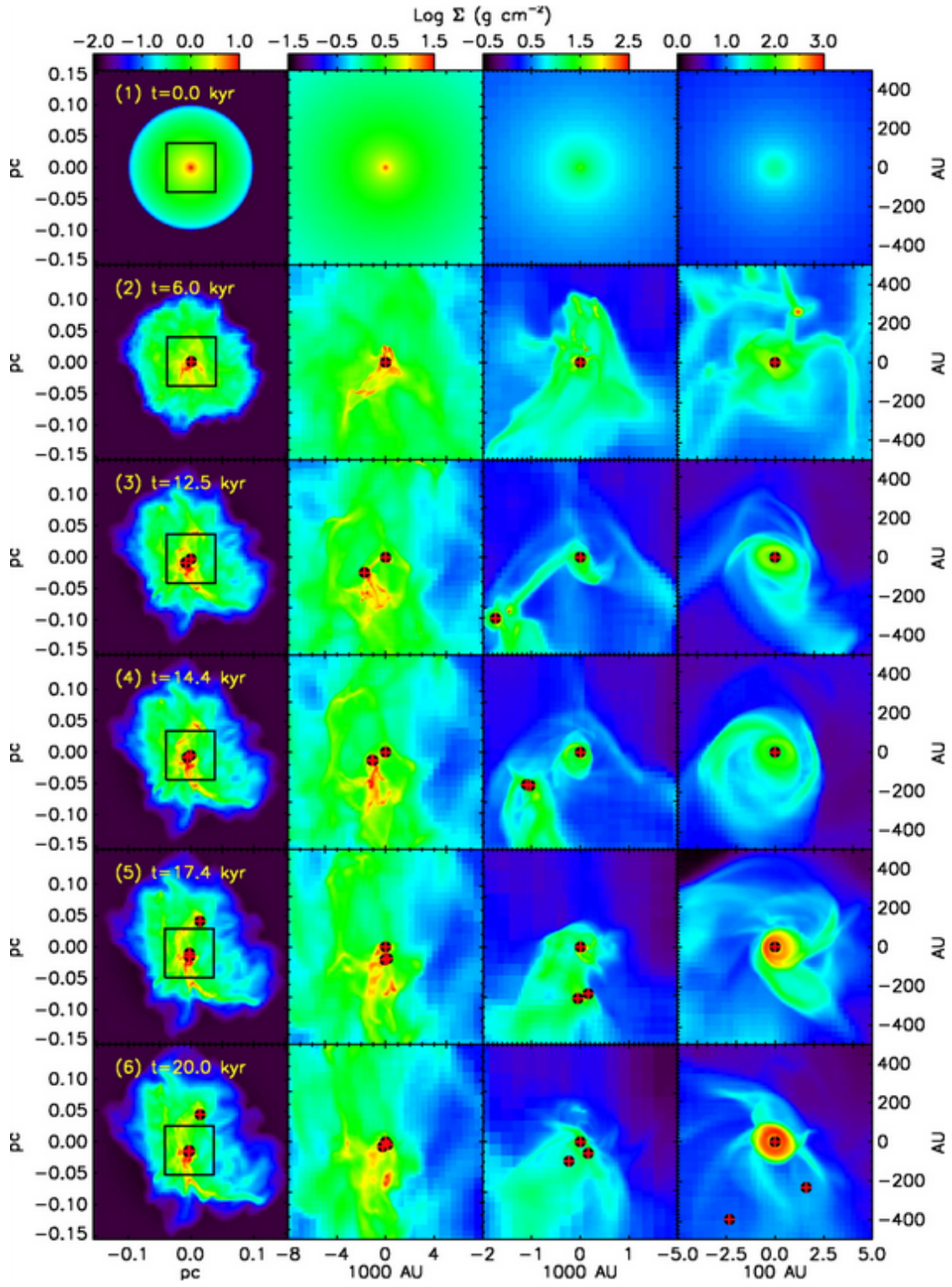

Figure 1.4: Monolithic collapse simulations of the column density of gas of an initial massive turbulent condensation with diameter 0.2 pc and 100 $M_\odot$ (Fig. from Krumholz et al. 2007). From top to bottom, the rows show the evolution at increasing time. From left to right, the size of the region shown decreases by a factor of 4, from a 0.31 pc region in the left column to a 1000 AU region in the right column. The black square in the first column represents the field shown in the second column. The formed stars are indicated with red plus signs inside black dots.

higher than the typical $M_{\rm Jeans}$ ($\sim$1 $M_\odot$). However, many other works (Dobbs et al. 2005, Clark and Bonnell 2006, Bonnell and Bate 2006, Smith et al. 2009a,b, Federrath et al. 2010, Peters et al. 2010, Pillai et al. 2011, Palau et al. 2013) have suggested that a massive clump, even with the presence of turbulence, very likely fragments to form many stars, especially if stellar outflows are present, since they could favor fragmentation (Cunningham et al. 2011).

Also magnetic fields have been invoked to prevent fragmentation of such a massive clumps. Some works proposed that magnetic fields are able to reduce or inhibit the fragmentation through magnetic braking (eg., Hosking and Whitworth 2004). This mechanism produces a significant loss of the initial angular momentum of the rotating clump due to material getting captured by the magnetic field lines and throwing outwards. This yields to a rather steep density profile, which seems highly resistant to fragmentation (Boss 1987; Palau et al. 2014). Palau et al. (2013) ran magneto-hydrodynamic simulations (Commerçon et al. 2011) finding that the different levels of fragmentation observed in their sample of clumps may be explained by different initial magnetic field strengths, with the clumps with higher magnetic fields exhibiting less fragmentation. However, other works (Dobbs et al. 2005; Bonnell et al. 2007) suggested that magnetic fields should not prevent the fragmentation process because they are intrinsically non-isotropic, or even that magnetic tension prevents the formation of a central density singularity, increasing hence the fragmentation (Boss 2000).

Competitive accretion

This theory relies on the well known fact that nearly all massive stars are formed in clusters together with low- and intermediate-mass stars (Clarke et al. 2000, Lada and Lada 2003b). According to observations, $\sim$ 96% of massive O stars are surrounded by a cluster of low-mass stars or are runaway stars (de Wit et al. 2004, 2005). In this context, the stellar clusters where massive stars are born may influence the massive star formation process.

The competitive accretion theory assumes that the parental molecular cloud fragments until reaching the minimum mass on which fragmentation can occur (i.e., the Jeans mass, M_{Jeans}). This is in agreement with the previously mentioned works which suggested that a massive clump, even if supported by turbulence and by the presence of radiative feedback, can fragment to form many cores with lower masses. For typical conditions of massive star-forming regions, the M_{Jeans} corresponds to 1 $M_\odot$ (Garay and Lizano 1999, Palau et al. 2013). Indeed, numerical simulations have shown that

gravitational fragmentation of a molecular cloud produces fragments of gas and dust around $M_{Jeans} \leq 1\ M_{\odot}$ (Klessen et al. 1998, Bate and Bonnell 2004, Bonnell et al. 2004) that collapse forming a low-mass star cluster. During the evolution of the cluster, high density subclusters (with up to several tens of stars) are formed (Bonnell et al. 2003). The number of stars in the subclusters increases as the star formation occurs in the vicinities, since newly formed stars fall into the existing potential wells.

For the formation of massive stars, an additional mechanism is needed. It has been proposed that this is the subsequent accretion of the remnant gas. Indeed, during the fragmentation of a cloud, a fraction of the total available mass is converted into clumps, a fraction of the clumps is converted into cores, and a fraction of the cores is converted into stars. The observations have shown that this process is inefficient, and that only less than 40% of the initial mass of the cloud is converted into stars (Lada and Lada 2003b). Then, since the star formation efficiency (SFE) seems to be low, there is a gas reservoir that potentially can be accreted (Bonnell et al. 2003; Krumholz and Bonnell 2007). This fact has been confirmed by observations of massive star-forming clumps (Longmore et al. 2011; Pillai et al. 2011). The overall potential well created by the low-mass star cluster funnels gas from this reservoir down to the potential center, producing a global infall of material. Evidence of these infall motions have been suggested by observations in massive star-forming clumps (André et al. 2007; Peretto et al. 2007; Schneider et al. 2010; Pillai et al. 2011; Longmore et al. 2011). Therefore, infall can feed stellar formation from clump-scales to smaller spatial scales (Galván-Madrid et al. 2009).

As indicated by Bonnell et al. (2001b), when the gas falls onto the cluster it passes through two different regimes:

- *Gas-dominated phase:* initially the gas dominates the potential well and the accretion is regulated by the tidal lobes of each star. The gas inside the tidal lobe is attracted to the star, while outside the lobe the acceleration is dominated by the cluster potential. During this stage, the low-mass stars accumulate the majority of their masses.

- *Stellar-dominated phase:* the formed low-mass stars fall into local potential wells forming dense subclusters. The following mass accretion onto an individual star decreases its kinetic energy, which forces them to sink deeper into the cluster potential (Bonnell et al. 2001b). At this stage, the stellar cluster is virialized and dominates the potential. In this context, only the gas within a radius where the escape velocity is less than the velocity of the star relative to the gas can be

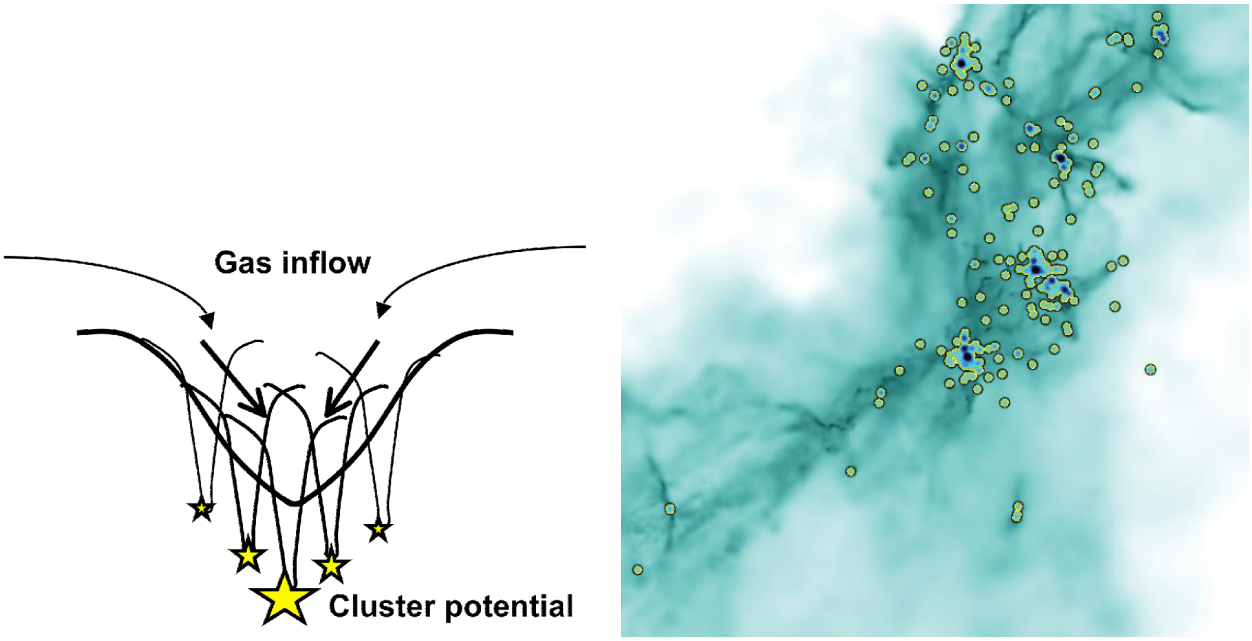

Figure 1.5: *Left:* schematic representation of the competitive accretion scenario. The stars located in the center of the cluster gravitational potential well accrete more gas and became massive (from Bonnell et al. 2007). *Right:* Spatial distribution of stars from Bonnell et al. (2004) simulations, adapted from Zinnecker and Yorke (2007). The field shown in the image is $\sim$ 0.6 pc $\times$ 0.6 pc. The dark blue circles shows the positions of massive stars, which are preferrentially located in the center of low-mass subclusters (light circles) because of competitive accretion.

accreted. This is known as Bondi-Hoyle accretion, whose rate $\dot{m}_{\rm BH}$ is defined as (Bonnell and Bate 2006):

$$\dot{m}_{\rm BH} = 4\pi\rho\frac{(Gm)^2}{\sigma^3} \ [M_\odot \ yr^{-1}] \tag{1.9}$$

where ρ is the volume gas density, m is the mass of the star, G the gravitational constant and σ the velocity dispersion of the accreted gas.

In the simulations from Smith et al. (2009b) the most massive star is formed in the clumps which are dominated by the mass in stars, and not by the mass in gas. This suggests that the accretion that forms massive stars is dominated by the cluster of low-mass stars. The stars that will become massive accumulate the majority of their masses during the stellar-dominated phase. The simulations from Bonnell et al. (2004) indicated that even though the most massive stars form from the most massive envelopes, this envelope only represents $\sim$10% of the final stellar mass. The rest of the material will be accreted in the stellar-dominated phase of subsequent accretion. Therefore, the final mass of the star is determined by the Bondi-Hoyle accretion, and not by the initial collapse.

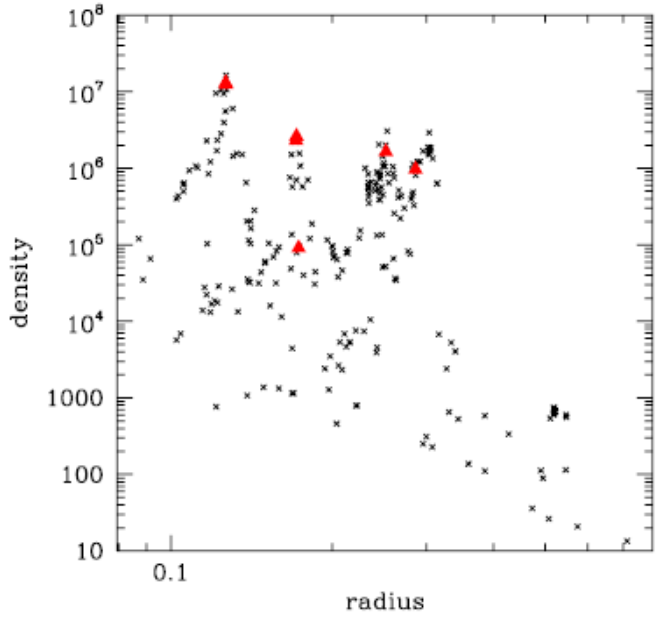

Figure 1.6: Stellar density (in stars pc^{-3}, calculated considering the volume that contains the first 10 neighbors) as a function of the distance to the cluster center (in pc), from the competitive accretion simulations from Bonnell et al. (2004). The red triangles denote massive star with more than 5 $M_\odot$, which are located in the center of dense subclusters of low-mass stars. Adapted from Bonnell et al. (2004).

Once the material distributed throughout the clump is funneled by the action of the full potential well, the accretion will not be uniformly distributed. The stars located closer to the center of the cluster are favored by their "privileged" position, because the material is transferred towards the center (see Fig. 1.5). Therefore, it is expected that the massive stars are found within dense subclusters of low-mass stars (Fig. 1.6). Moreover, the stars with higher initial masses are favored in the competition for accretion. They have a larger gravitational radius and hence higher accretion rates, $\dot{m}_{\rm BH}$ (Eq. 1.9). These stars then increase their masses and become massive.

Assuming the Bondi-Hoyle accretion rate, the time needed to build up a massive star (assuming a density profile $\rho \sim r^{-2}$) is (Bonnell and Bate 2006):

$$t = t_{\rm i} + \frac{\sigma^3}{2\pi\rho\, m_i^{3/2} G^2}(m^{1/2} - m_i^{1/2}) \ [yr] \tag{1.10}$$

where m is the mass of the star, m_i is the initial mass of the stellar "stellar seed", σ the velocity dispersion of the gas accreted, ρ is the volume gas density, and $t_{\rm i}$ is the

time needed to form the initial mass with mass m_i.

This theory naturally produces a whole cluster of stars with different masses, which seems to be compatible with the observations. Bonnell et al. (2007) showed that the competitive accretion is able to reproduce the stellar initial mass function (IMF) of stellar clusters. Furthermore, this theory successes to explain the correlation found observationally between the number of stars in a cluster (or the total stellar mass) and the mass of the most massive star (Testi et al. 1997; Bonnell et al. 2004). This suggests a potential relationship between the cluster properties and the mass of the most massive star, as implied by this theory.

Krumholz et al. (2005) expressed some concerns about the efficiency of competitive accretion forming massive stars. The Bondi-Hoyle accretion (see Eq. 1.9) is very sensitive to the gas density ρ and very particularly to the velocity dispersion σ of the gas, so that slightly variations of these parameters can give accretion rates which are different by orders of magnitude. Bonnell and Bate (2006) demonstrated that using the typical values observed from the regions where massive stars forms, competitive accretion can build up a massive star in timescales of 10^5 yr. Pillai et al. (2011) showed that a dense core in steady contact with a large mass reservoir can collect mass at a rate high enough to form massive stars. The mass received by the star can be continuously replenished by the accretion from the clump onto the cores. Namely, the mass reservoir from which stars form is not limited to the cores. The simulations of a full cluster by Smith et al. (2009a) showed that the gas of the clump, initially unbounded, is subsequently accreted by the stars formed within the cores after only 6 $\times 10^4$ yr. In the same line, Wang et al. (2013) claimed that subsequent competitive accretion can sustain infall rates that are sufficient to sustain high-mass star formation.

Coalescence of low and intermediate-mass stars

One of the scenarios that were initially proposed to circumvent the radiation pressure problem was the coalescence of low- and intermediate-mass stars in dense clusters (Bonnell et al. 1998; Bonnell and Bate 2002, 2005). In the last years, this mechanism has been considered exotic since it requires higher stellar densities (10^6–10^9 stars pc^{-3}) than that generally found in stellar clusters. Furthermore, this theory lost momentum when several works based on accretion (a much less dramatic process) showed that it was possible to overcome the radiation pressure without invoking coalescence.

However, given that very high stellar densities are expected during a short period at the earliest stages of cluster formation (Bonnell et al. 1998; Stahler et al. 2000), close stellar encounters or even mergers may occur, which might affect the mechanisms related to the formation of the more massive stars.

1.3 The role of low-mass star clusters in the formation of massive stars

The monolithic collapse theory predicts the formation of massive stars almost in isolation, and not within a highly clustered population of lower mass stars. The turbulent clumps that give rise to the massive stars barely interact with the surroundings during and after the collapse. On the other hand, in the competitive and coalescence scenarios the interaction with the environment is crucial and a dense population of low- and intermediate-mass stars is required. In these cases, the formation of massive stars is directly linked to the global evolution of the cluster and the surrounding gas.

Therefore, to distinguish between different theories and fully understand the processes which play a relevant role in the early phases of massive star formation, we need a detailed knowledge of the census and the properties of the stellar population embedded in massive star cradles.

1.3.1 Revealing the population of low-mass stars in massive star cradles

Detecting the population of low-mass stars in massive star-forming regions has been extremely difficult due to large extinction produced by the huge amount of dust. This completely prevents their detection in the optical range, and observations at other wavelengths are needed.

In the last two decades, the study of the population of newly formed stars embedded in molecular clouds improved with the advent of large and efficient IR detectors (Carpenter et al. 1997; Hillenbrand and Hartmann 1998; Lada et al. 1991). The IR observations are less affected by extinction than the optical ones.

The idea of massive star formation as an event occurring in isolation (Shu et al. 1987) has dramatically changed. A new emerging view of star formation relies on a group activity, where clusters of stars formed in small volumes (Clarke et al. 2000, Lada and Lada 2003b). These works showed that massive stars are usually born in

young stellar clusters. However, a complete census of the stellar population (and hence an accurate determination of stellar densities) was not possible using near-IR or even at mid-IR wavelengths, because of the extreme extinction. The environment where massive stars form suffers visual extinctions of A_V >25 mag, and thus only the brightest objects in the IR (the more massive ones) were detected using IR instruments, but the low- and intermediate-mass population remained elusive. Therefore, if we want to know if the surroundings where massive stars form contain a dense population of low- and intermediated-mass stars (which is key to understand how they form) we need an alternative way to detect these populations of stars.

Therefore, in order to characterize the distribution of the low-mass stellar population embedded in massive star-forming regions, observations at other wavelengths are needed. In what follows, we describe radio and (sub)millimeter and X-ray observations, which are able to penetrate into the massive star cradles and reveal their low-mass stellar content.

★ Radio and (sub)millimeter observations

Traditionally, long wavelengths (radio and (sub)millimeter) have been used to study star formation since they are barely affected by extinction. Thus, they are able to detect emission from very embedded objects. This emission arises from dust and molecular gas, as well as from the stellar population. The dusty envelopes and ionized gas around massive stars emit thermal continuum emission[7], which is detectable at radio and (sub)millimeter wavelengths.

Furthermore, the acceleration of electrons in magnetic events in the corona of PMS low-mass stars produces variable non-thermal radio emission (Drake and Linsky 1989; see also the review by Güdel 2002). These events could explain the observed long-term radio variability (in timescales of weeks to years) observed in the radio population of young stellar clusters (see e.g. Felli et al. 1993; Zapata et al. 2004a). Moreover, in the last years a few cases of powerful short-term radio flares have been also detected from young low-mass stars (Bower et al. 2003, Gómez et al. 2008, Forbrich et al. 2008), some of them very embedded in the molecular cloud. These findings open an interesting possibility of revealing the low-mass stellar population in these regions using radio wavelengths.

However, our knowledge about this radio emission (origin, flaring rate or relation

[7] The ionized gas in HII regions around young massive stars emits free-free emission (also known as thermal *bremsstrahlung*) produced by free electrons scattering off ions without being captured.

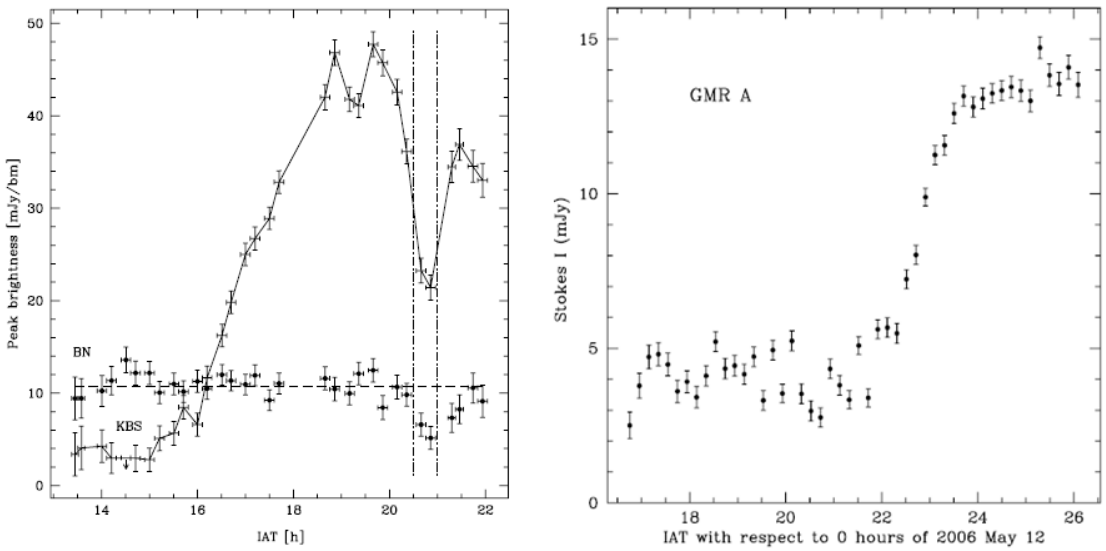

Figure 1.7: *Left:* Light flux curve of the radio flare observed on 1991 July 5 at 22 GHz towards the ORBS source by Forbrich et al. (2008) (solid line) compared with the curve from BN (circles). *Right:* Light flux curve of the radio flare observed on 2006 May 12 at 8.3 GHz towards the source GMR A by Gómez et al. (2008).

with magnetic fields) is still limited. Although the low number of observed events could indicate that radio flares are a rare phenomenon (Andre 1996), recent works (Forbrich and Wolk 2013) have indicated that this is likely due to the limited sensitivity of the radio continuum observations carried out so far.

It is still unclear if flares from young low-mass stars can be produced at higher frequencies (i.e., in the millimeter range), as occurred for instance in the Sun, where millimeter gyrosyncrhotron flares have been observed (Kundu et al. 2000). New observations at higher frequencies could detect emission from highly-energetic electrons, helping us to answer this question.

Therefore, deep radio and (sub)millimeter observations open an unprecedented opportunity to detect the low-mass star population of young and embedded stellar clusters. Given the high radiovariability observed towards young low-mass stars, multi-epoch monitoring with different time spans between observations will increase the chance of detecting flares and hence the young low-mass stellar population. Moreover, they will allow to better constrain the nature of the mechanisms responsible for the radiovariability.

★ X-ray observations

In the last years a new opportunity have emerged from the other side of the electromagnetic spectrum. It came as a surprise in star-formation research when it was discovered that the earliest evolutionary stages of protostars are associated with high-energy processes emitting in X-rays (e.g., Feigelson and Montmerle 1999). Massive stars emit X-ray emission arising from shocks produced in their winds (Favata and Micela 2003; Stelzer et al. 2005). But the most interesting finding was that also the PMS low-mass stars strongly emit in the X-ray range. This emission arises from plasma heated to high temperatures (∼100 MK) by violent reconnection events in magnetic loops in the corona. This X-ray emission is orders of magnitude ($10-10^4$) more luminous than that found in MS stars. The X-ray emission is a superposition of many flares of different amplitude: weak flares are very frequent, and strong flares occur rarely at rates of about one per week (Getman et al. 2008).

X-ray observations are extremely useful to study high-mass star-forming regions. The high-energy X-ray photons (>3 keV) can penetrate into the cloud despite of high extinctions. For example, the Chandra Orion Ultradeep Project (COUP, Getman et al. 2005c) have been able to detect stars with extreme visual extinctions (A_V >500 mag; Grosso et al. 2005). Moreover, the high spatial resolution of the X-ray space telescope *Chandra* (<1") allows the detection of single stars in nearby dense clusters. In addition, X-ray observations are less affected by from foreground and background galactic contamination than optical and IR studies. Therefore, deep X-ray images can peer into the low-mass stellar population in embedded regions where only the more massive stars have been studied so far.

1.3.2 Testing predictions with observations

If a theory seeks to fully explain massive star formation, it should be able to predict all of the observed properties found in the massive star cradles. In what follows we introduce some key observational parameters: level of fragmentation of the parental condensation and low-mass stellar distribution, mass segregation and distribution of the extinction.

★ Level of fragmentation: stellar distribution, clustering and densities

When studying the initial conditions for massive star formation, the level of fragmentation is one of the key aspects to distinguish between different theories. The

monolithic core accretion model predicts the formation of mainly massive companions in small multiple systems (Krumholz 2006) from turbulent-supported clumps that evade fragmentation. On the other hand, the coalescence and competitive accretion models require a high level of fragmentation, which gives rise to a dense population of low-mass stars (Bonnell et al. 1998, 2003, 2004).

The spatial scales affected by the fragmentation process range from pc-scale clouds to compact (∼0.05 pc) cores. To resolve fragmentation at the smallest scales high spatial resolution (<1") observations are needed. The technique commonly used to study the fragmentation is through observations of the dust emission at (sub)millimeter wavelengths. To characterize the most compact scales, the high resolution provided by interferometers is needed (e.g., Longmore et al. 2011; Palau et al. 2013). However, this technique presents two fundamental problems inherent to interferometry: missing flux and dynamic range limitations. Due to spatial filtering, interferometers are only sensitive to a limited range of spatial scales and to density contrasts, so it is possible that the observations are missing a population of uniformly distributed and weaker low-mass stars.

Offner et al. (2012) simulated interferometric dust (sub)millimeter observations of a fragmenting clump, showing that the spatial filtering from interferometry significantly underestimate the clump substructure. Consistently, Smith et al. (2009b) simulations showed that only the more dense and warm condensations in the central region of the clump are detectable. During their simulations the collapse feeds massive star formation at the center of the clump, which heats the surrounding gas. The emission then become dominated by one or two sources which are hotter/denser than the surrounding cores. In real observations this may lead to dynamic range[8] problems because typical (sub)millimeter interferometer images are limited to dynamic ranges of few hundred at best. Therefore, interferometric studies are strongly biased to detect relatively bright and compact structures, mostly massive envelopes associated with massive stars (Takahashi et al. 2013).

Alternatively to dust continuum observations, the level of fragmentation could also be studied directly detecting the emission from the very young stellar population, which is the final product of the fragmentation process. Deep X-ray observations, which are able to detect the lower mass stellar content of the PMS cluster, are a very well suited tool to determine the spatial distribution, clustering and stellar densities for the whole cloud, and particularly of the close vicinity of massive stars that are

[8] Dynamic range is the ratio between the maximum intensity in an image to the minimum believable intensity.

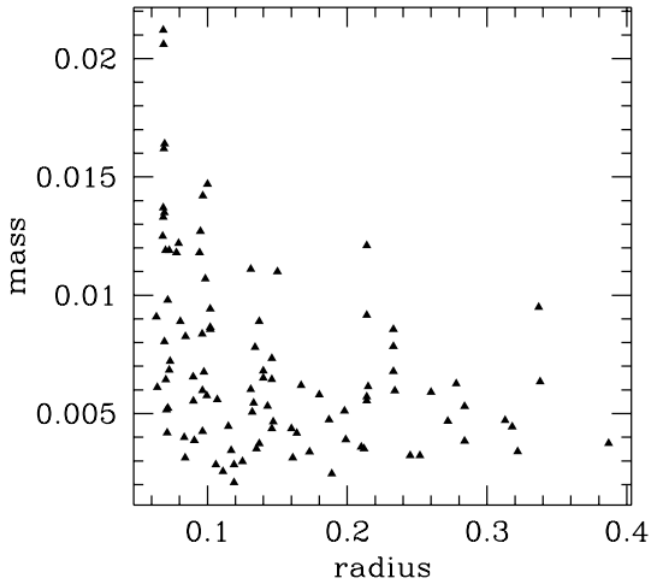

Figure 1.8: Stellar masses (in units of the total cluster mass) as a function to the cluster center (in pc) after a free-fall time of evolution (from simulations by Bonnell et al. 2001a). It is evident a mass segregation, with more massive stars in the cluster center, although there are also a significant number of low-mass stars.

strongly embedded in dense gas and dust.

★ Mass segregation

Another observational fact that can be used to study how the molecular cloud has evolved to its current morphology is the spatial distribution of the stellar masses. Whether stars with a particular range of masses are predominantly concentrated in a region, we consider that there is a *mass segregation*. Although the concentration of more massive stars in stellar clusters could be consequence of dynamical evolution (massive stars will sink to the center of the gravitational potential), this is unlikely in young clusters with on-going massive star formation (≤ 1 Myr) because the dynamical time needed would be larger than the cluster age. Therefore, the mass segregation can be considered as a birthmark, clearly indicating that the massive stars formed at its current positions.

Although the monolithic collapse theory does not address how the natal massive turbulent-supported clumps were formed, their location within the cloud depends on the early structure produced by the initial turbulence, and there is not a clear preference to form massive cores in a particular region. Therefore, no clear mass segregation is expected in this scenario. On the other hand, the competitive accretion scenario predicts naturally an overall mass segregation, with the more massive stars

located in the central regions of the cluster (see Fig. 1.8). This as a consequence of the more efficient accretion towards the center of the gravitational potential well. Therefore, the study of mass segregation in massive star-forming clouds can be useful to distinguish between different theories.

★ Extinction distribution

According to the competitive accretion theory, the global collapse and gas funneling towards the bottom of the gravitational potential well predicts a larger concentration of gas and dust in the central parts, with secondary concentrations associated with subclusters of low-mass stars. As a result, the extinction is supposed to show an overall centrally peaked distribution, with some secondary peaks. Observationally, we can estimate the extinction using several different methods:

- From IR colors indexes ($J-H$ or $H-K$): we can derive the dust extinction towards each star (Lada et al. 1994, Lombardi and Alves 2001). Using the extinction law by Rieke and Lebofsky (1985), the color index (in absence of significant near-IR emission from disk or envelopes) is related to the visual absorption $A_{\rm V}$ following the expression:

$$A_{\rm V} = \frac{(H-K)-0.2}{0.063} \quad [mag] \tag{1.11}$$

- From the X-ray spectra: fitting the X-ray spectra of stars, the hydrogen column density ($N_{\rm H}$) can be derived, independently of the commonly used optical and infrared dust extinction laws. This value can be related to the visual absorption extinction through the relation:

$$\frac{N_{\rm H}\ [cm^{-2}]}{A_{\rm V}\ [mag]} \simeq 2 \times 10^{21}, \tag{1.12}$$

  which is an intermediate value between the relations found by Ryter (1996), Vuong et al. (2003) and Feigelson et al. (2005).

- From the column density (N) derived from (sub)millimeter and radio observations of molecular lines. In Appendix B the rotational diagram method used to obtain the column density of a molecule like CH_3CN using several rotational lines is explained. The column density can also be derived from observations of

the CO(2−1) transition, considering that the emission is optically thin, according to the expression (Garden et al. 1991 and Scoville et al. 1986):

$$N_{\rm CO} = 1.08 \times 10^{13}(T_{ex} + 0.92) \exp\left(\frac{16.6}{T_{ex}}\right) \int T_B \ dv \quad [cm^{-2}], \tag{1.13}$$

where dv is the velocity interval of the line in km s^{-1}, T_{ex}[9] and T_B[10] are the excitation and brightness temperatures, respectively. Assuming a typical CO to H_2 abundance of 10^{-4} we can estimate the molecular hydrogen column density ($N_{\rm H_2}$).

1.3.3 The impact of outflow-driven turbulence on massive star formation

During their first stages of evolution, young stars accrete material from the circumstellar disk along the equatorial plane, and eject mass in the perpendicular direction forming bipolar outflows (Arce et al. 2007). Therefore, the detection of molecular outflows indicates a very early phase in star formation, and hence can be used to identify the distribution of very young stars (Class 0/I). Since the emission of rotational transitions of molecules, such as CO, emitted at (sub)millimeter and radio wavelengths barely suffer from extinction, it can indirectly reveal the very young population of embedded stars in massive star cradles.

The ubiquitous presence of outflows from low- and intermediate-mass stars may have important implications in star formation (Stanke and Williams 2007), especially in the crowded clusters where massive stars are born (Lada and Lada 2003a). Outflows from young stars are very energetic phenomena and inject momentum and energy into the ISM, which may have several consequences in: i) favoring the fragmentation of the parental clump (Knee and Sandell 2000, Li and Nakamura 2006, Shimajiri et al. 2009, Cunningham et al. 2011); ii) generating turbulence (Li and Nakamura 2006; Nakamura and Li 2007), which could affect the accretion rates onto the stars (Krumholz et al. 2005), the initial fragmentation (Fontani et al. 2012) and can give support against rapid collapse; iii) reducing the efficiency of radiation feedback in preventing accretion

[9] The excitation temperature T_{ex} is the temperature (see Eq. B.1 in Appendix B) that reproduces the populations of the two levels involved in the molecular transition, according to the Boltzmann law.

[10] The velocity-integrated brightness temperature of the lines ($\int T_B dv$) can be obtained from the areas of the observed lines (see Eq. B.4 Appendix B).

(Hansen et al. 2012); iv) triggering further star formation through the compression of gas due to shock waves.

1.4 Thesis project

The mechanisms leading to the formation of massive stars are still not well known. In this introduction we have shown the relevance of studying the enviroment where massive stars are born since it can have important implications on their formation mechanisms. Several theories have been proposed to explain the formation of the most massive stars: i) monolithic gravitational collapse and core accretion; ii) coalescence of low-mass stars in high density stellar clusters; and iii) competitive accretion of material by low- and intermediate-mass stars in the cluster potential well. They mainly differ on the level of fragmentation of the parental condensation, and hence they predict very different populations of low-mass stars. Therefore, to distinguish between the different scenarios, the role of stellar clusters of pre-main sequence (PMS) low-mass stars in the formation of massive stars has been studied in this thesis. In particular, we analyze in detail the young low-mass stellar population in 3 nearby ($d \leq$1.5 kpc) massive star-forming regions using multi-wavelength data (from radio to X-rays):

- *Orion*: it is the nearest massive star-forming region, located at d=414 pc. It has been observed in X-rays by *Chandra* with an unprecedented very long exposure ($\sim$ 10 days), allowing a very complete census of the low-mass stellar population, even in the very extincted regions where massive stars are formed. Orion contains three sites harboring massive stars. Two of them are still embedded in the Orion Molecular Cloud (OMC): the Orion Hot Core (OHC), prototype object for studying the earliest stages of massive stars, and OMC1-S. Besides, the optically visible Orion Nebula Cluster (ONC) harbors the Trapezium Cluster (TC) formed by 4 MS massive stars.

- *DR 21*: this filamentary region is embedded in the Cygnus-X molecular cloud at a distance of 1.5 kpc. It exhibits three main regions with massive star formation, which include hot molecular cores, ultracompact HII regions and massive (sub)millimeter dust clumps.

- *Monoceros R2*: this cluster is located at a distance of $\sim$ 830 pc, and it shows clear evidence of on-going massive star formation such as bright and massive IR

sources, (sub)millimeter sources, a shell-like complex IR nebula and HII regions.

Furthermore, the three studied massive star-forming regions harbor large-scale very energetic outflows (i.e., Orion: Nissen et al. 2007, Zapata et al. 2009; DR 21: Garden et al. 1991, Zapata et al. (2013); Monoceros R2: Wolf et al. 1990, Tafalla et al. 1997). The origin of these poweful outflows remains very intriguing and it is still under debate. It has been suggested that they are possibly powered by extremely luminous massive stars or, alternatively, by violent explosive events.

The main goals of this thesis are summarized as follows:

i) To study in detail the low-mass stellar population of PMS low-mass stars in 3 nearby young clusters with on-going massive star formation (Orion, DR 21 and Monoceros R2). We use different methods (spatial gridding and close neighbors) to analyze X-ray and deep IR stellar catalogs. We derive the stellar distribution and densities, the distribution of the extinction and several other properties of the low-mass stellar population such as evolutionary phase. We discuss the implications of our results on the models proposed to explain massive star formation.

ii) To evaluate the role of outflow-driven turbulence on massive star formation. We study in detail the impact of clusters of outflows in the massive star cradles such as those located in the Orion OMC1-S and the central region of Monoceros R2.

iii) To study the radio emission in the young clusters located in the Orion Nebula (ONC) and Orion Molecular Cloud (OMC) using a new multi-epoch monitoring carried out with the Karl Janky Very Large Array (VLA) interferometer.

iv) To analyze the (sub)millimeter radio continuum and molecular environment of the central region of the Monoceros R2 stellar cluster. With this aim we present new Submillimeter Array (SMA) observations.

v) To find out the origin of the highly-energetic large-scale outflows arising from the three aforementioned young stellar clusters.

This thesis is organized as follows:

- In chapter 1 we give a general overview on star formation, in particular on the main issues directly related to massive star formation, and presents the motivations of this thesis.

- In chapters 2, 3 and 4 we present our study of the role of PMS low-mass star clusters in forming the massive stars in Orion, DR 21 and Monoceros R2, respectively.

  These works have been published respectively as Rivilla et al. (2013a) (A&A), Rivilla et al. (2013c) (MNRAS) and Rivilla et al. (2014c, in preparation to be submitted to MNRAS), respectively.

- In chapter 5 we present our new VLA multi-epoch radio continuum monitoring study of Orion. We study the origin and properties of the radiocontinuum emission arising from young stars, and characterize their short- and long-term radiovariability.

  The work contained in this chapter has been submitted to the ApJ (Rivilla et al., 2014b).

- In chapter 6 we focus on the low-mass stellar cluster embedded in the southern massive star-forming region in Orion, OMC1-S. We provide the identification of the embedded stars which drives the molecular outflows in the region and we study their properties.

  This chapter has been published in MNRAS as Rivilla et al. (2013b).

- In chapter 7 we present new SMA (sub)millimeter observations of the Monoceros R2 central region to study the continuum emission from young massive stars and the molecular enviroment.

  This chapter has been submitted to the ApJ (Dierickx, Jiménez-Serra, Rivilla and Zhang, 2014).

- In chapter 8 we evaluate how the outflow-driven turbulence can influence the star formation processes and the formation of massive stars. In particular, we study the turbulence injected by the members of the dense stellar clusters embedded in the massive star-forming regions located in OMC1-S and Monoceros R2.

  Part of the work presented in this chapter has been published in MNRAS as Rivilla et al. (2013b). Other part of this chapter has been submitted to the ApJ (Dierickx, Jiménez-Serra, Rivilla and Zhang, 2014).

- Finally, the main conclusions of this thesis are summarized.

Two appendices are presented at the end of these chapters to complement the analysis previously described. In Appendix A we derive some expressions to describe the physics of stellar collisions in dense stellar clusters. In Appendix B we describe the rotational diagram method to derive excitation temperatures and column densities from CH_3CN rotational lines.

CHAPTER 2

The role of low-mass stellar clusters in forming massive stars in Orion

Abstract

In this chapter, we analyze deep X-ray observations of the Orion massive star-forming region using the Chandra Orion Ultradeep Project (COUP) catalog, with the aim of revealing the distribution and clustering of the population of PMS low-mass stars, and of studying their possible role in massive star formation. We study the distribution of PMS low-mass stars as a function of extinction with two different methods: a spatial gridding and a close-neighbors method, with cells of $\sim$0.03$\times$0.03 pc^2, the typical size of protostellar cores. We derive density maps of the stellar population and calculated cluster stellar densities. Consistent with previous studies, we find that PMS low-mass stars cluster towards the three massive star-forming regions: the Trapezium Cluster (TC), the Orion Hot Core (OHC), and the OMC1-S region. We derived PMS low-mass stellar densities of $>10^5$ stars pc^{-3} in the TC and OMC1-S, and of $>10^6$ stars pc^{-3} in the OHC. The close association between the low-mass star clusters with massive star cradles supports the role of these clusters in the formation of massive stars. The X-ray observations show for the first time in the TC that low-mass stars with intermediate extinction are clustered towards the position of the most massive star θ^1 *Ori C*, which is surrounded by an envelope of non-extincted PMS low-mass stars. This 'envelope-core' structure is also supported by infrared and optical observations. Our analysis suggests that at least two basic ingredients are needed for massive star formation in clusters: the presence of dense gas and a cluster of low-mass stars. The sequence of events that better explains our findings is: i) high levels of fragmentation in the parental clump forming smaller and denser cores; ii) collapse of the cores into a low-mass stellar cluster, and iii) subsequent competitive accretion that form the more massive stars in the cluster. Finally, although coalescence does not seem a common mechanism for building up massive stars, we show

that a single stellar merger may have occurred in the evolution of the OHC cluster, favored by the presence of disks, binaries, and gas accretion.

2.1 Introduction

Orion is the nearest (d∼414 pc) region of high-mass star formation, where three sites of massive star formation have been identified: the Trapezium Cluster (TC), the Orion Hot Core (OHC), and OMC1-S. The TC contains the well-known four main-sequence (MS) massive Trapezium stars and is located in the central region of the optically visible Orion Nebula Cluster (ONC). The ONC has a size of ∼3 pc (Hillenbrand and Hartmann 1998) and an age of about 10^6 yr (Hillenbrand 1997).

The Orion Hot Core (OHC), located within the Orion KL nebula (Zuckerman et al. 1981, Shuping et al. 2004) embedded in the Orion Molecular Cloud (OMC) is a very compact (size of ∼ 0.03 pc), hot (T>200K), and dense molecular condensation (mean density of n[H_2]=5×10^7 cm^{-3}, Morris et al. 1980), with a total luminosity of few 10^5 $L_\odot$ (de Vicente et al. 2002). The OHC is the prototype object for studying the formation of massive stars. Three massive objects with masses around 10 $M_\odot$ have been identified in this region: the Becklin-Neugebauer Object (BN), and sources *I* and *n*.

The OMC1-S region (∼10^4 $L_\odot$; Mezger et al. 1990, Rodríguez-Franco et al. 1999a), located ∼ 90" south of the OHC, is the other young massive star-forming region embedded in the OMC. OMC1-S is a very active star forming region, harboring several outflows (Ziurys et al. 1990, Rodríguez-Franco et al. 1999a, Rodríguez-Franco et al. 1999b, Zapata et al. 2005, Zapata et al. 2006).

The Chandra Orion Ultradeep Project (COUP, Getman et al. 2005b), based on a ∼10-day Chandra X-ray observation centered on the ONC, provided a unique data base of X-ray PMS stars. In this chapter, we extend previous works based on the COUP database to study the spatial distribution and estimate the densities of low-mass PMS stars. We find low-mass PMS stars clusters towards the three regions where massive star formation has recently occurred (TC), or it is currently taking place (OHC and OMC1-S). This fact and the high densities of PMS stars in these regions suggest that low-mass stars could play a role in the formation of massive stars.

2.2 Data analysis

We have analyzed the distribution and stellar densities of PMS low-mass stars with X-ray emission in Orion as a function of extinction. We have used the Chandra COUP database provided by Getman et al. (2005b). We have applied two different methods: i) spatial gridding, and ii) a close-neighbors method. This section is structured as follows: we present the two methods in 2.2.1. Sects. 2.2.2, 4.2.3, 2.2.4, and 2.2.5 are devoted to the effects introduced in our analysis by the cell size, the selected extinction ranges, the background/foreground contamination, and incompleteness, respectively.

2.2.1 Methods

★ Spatial gridding

We have integrated the spatial distribution of the X-ray stars into a grid of square cells (see Sect. 2.2.2 about the cell size), counting the number of stars contained in each cell. This method is very adequate to obtain maps of the stellar density, because it samples the entire region. However, spatial gridding can underestimate the real values of the stellar density peaks.

★ Close-neighbors method

The clustering of low-mass PMS stars may be affected by the spatial gridding used to compute the density of X-rays sources across the Orion region. For instance, depending on the grid origin, a stellar density peak could be within a single cell, or could be divided into two or more adjacent cells, leading to different values of the peak stellar densities. To estimate this effect we also analyzed of the distribution of close neighbors centered on every COUP source, which is independent of the grid origin. This method allows us to calculate the real stellar density peaks, but it is unable to generate density maps because it undersamples the field.

2.2.2 Cell size

From IR observations, Lada et al. (2004) found several dense and compact stellar clusters in Orion, some of them with sizes of < 0.05 pc. We are interested in detecting these compact clusters, and in particular those connected with massive star formation. Massive stars are born in dense and hot condensations of gas, with typical sizes in

the range 0.01 pc - 0.1 pc (Kurtz et al. 2000), with a mean size of 0.03 pc (Saito et al. 2008). This size also matches the size of the OHC (Wright et al. 1996). Therefore, we selected a cell size of 15" × 15" (0.03 pc×0.03 pc) to match the mean size of the molecular cores where massive stars form as well as the sizes of dense stellar clusters. To evaluate the effect introduced by the cell size, we have also repeated our analysis using a larger cell of 24" × 24" (∼0.05 pc×0.05 pc). We compare the results obtained with these two different cell sizes in Sect. 2.3.2.

2.2.3 Selected extinction ranges

Because the extinction across the Orion central region changes by several orders of magnitude (from 10^{21} to 10^{24} cm^{-2}), we have analyzed the X-ray population as a function of three X-ray extinction ranges. The selection of the extinction bins are based on physical arguments. The first extinction range, log$N_{\rm H}$ < 22.0 cm^{-2} ($A_{\rm V}$ <5 mag), corresponds to the regions with low extinction that are mainly affected by the foreground gas in front of the optically visible ONC. With the bin log$N_{\rm H}$ >22.5 cm^{-2}, corresponding to $A_{\rm V}$ >15 mag, we expect to find sources that are embedded in the OMC. The condition log$N_{\rm H}$ > 22.5 cm^{-2} has also been used by Wang et al. (2007) to identify the heavily embedded population obscured by molecular material in the massive star-forming region NGC 6357. The population with 22.0 cm^{-2} <log$N_{\rm H}$ <22.5 cm^{-2} (5< $A_{\rm V}$ <15 mag) corresponds to slightly extincted sources. In our analysis we considered COUP sources with high enough X-ray counts to allow one to determine the value of log$N_{\rm H}$ with an error of <0.5 dex.

2.2.4 Background/foreground contamination

One of the advantages of using X-rays to study massive star-forming regions is that they suffer less foreground- and background contamination than optical and infrared observations. Galactic contamination has very little impact on X-ray studies, but extragalactic sources can still be confused with embedded PMS stars. However, as Getman et al. (2005a) showed, the three regions studied in detail in this chapter (i.e., the TC, OHC, and OMC1-S) are nearly free from contamination, so the detected sources reflect the actual cluster-member population. Despite this, we have estimated a non-zero background/foreground level to provide a reasonable upper limit to the error of the stellar densities calculated in this chapter. A very conservative upper limit for the contamination would be to consider a uniform distribution of all COUP

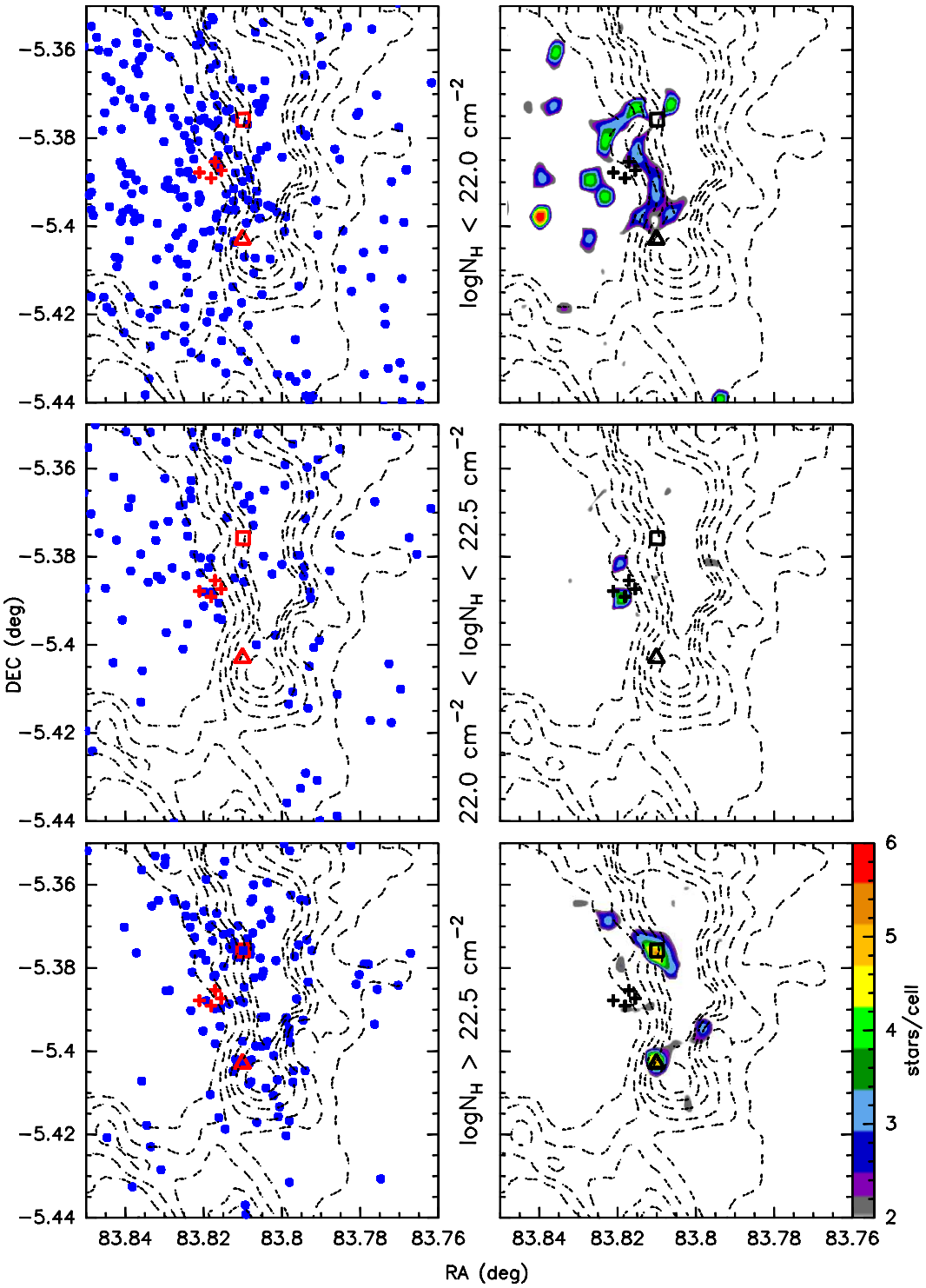

Figure 2.1: Spatial distribution of low-mass stars for three different extinction ranges: log$N_{\rm H}$ <22.0 cm^{-2} (upper panels), 22.0 cm^{-2} <log$N_{\rm H}$ <22.5 cm^{-2} (middle panels), and log$N_{\rm H}$ >22.5 cm^{-2} (lower panels). Dashed contours represent dense gas traced by the integrated intensity emission of CN (N=1-0) (Rodriguez-Franco et al. 1998). The first contour level corresponds to 7 K km s^{-1}, the interval between contours is 4 K km s^{-1}. The left panels show the position of the X-ray stars as blue dots. Four crosses, the open square, and the open triangle show the location of the four main sequence massive Trapezium stars, the OHC, and the OMC1-S. The right panels report the stellar surface density for the same extinction ranges, derived by counting the number of COUP sources using a cell size of 15" × 15" (0.03 pc × 0.03 pc) (right color scale), superimposed on the CN emission. The color contours have been smoothed for display purposes.

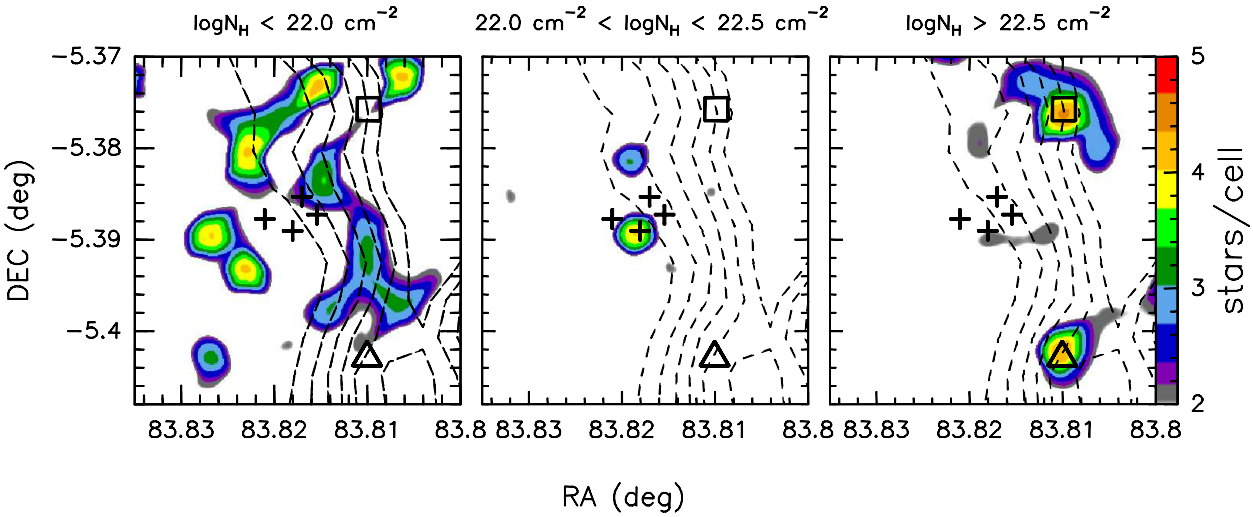

Figure 2.2: Zoom of the central region from Fig. 2.1. The color contours represent the stellar surface density (number of COUP sources using a cell box of 0.03 pc×0.03 pc, right color scale) for the three extinction ranges (log$N_{\rm H}$ <22.0 cm^{-2} in the left panel; 22.0 cm^{-2} <log$N_{\rm H}$ <22.5 cm^{-2} in the middle panel; and log$N_{\rm H}$ <22.5 cm^{-2} in the right panel). The color contours have been smoothed for display purposes. As in Fig. 2.1, the dashed contours represent the CN emission, and the four crosses, the open square, and the open triangle show the location of the four main-sequence massive Trapezium stars, the OHC, and the OMC1-S.

sources (∼1600) in the field observed by Chandra (17' × 17'). This gives an error of ±0.35 stars cell^{-1}, considering 0.03 pc×0.03 pc cells. Getman et al. (2005a) claimed that only 217 COUP sources do not belong either to the ONC or the molecular cloud. Considering these sources, we obtain a lower limit for the background/foreground contamination of only 0.05 stars cell^{-1}. In our density analysis we will consider a contamination level between the two values of 0.2 stars cell^{-1}, which is equivalent to 3×10^2 star pc^{-2} in surface density and 2×10^4 stars pc^{-3} in volume density.

2.2.5 Completeness

Although the COUP observations are quite deep and hence very sensitive, there is still a missing population of sources due to obscuration, especially in regions with high extinction, like the OHC and OMC1-S massive star cradles. By comparing the X-ray luminosity functions of the incomplete OHC and OMC1-S populations with the more complete ONC population, Grosso et al. (2005) estimated that only about 48% of the low-mass stars have been detected in the OHC, and 63% in the OMC1-S region. The TC is not as strongly obscured, and therefore its population is considered to be nearly complete.

2.3 Results

2.3.1 Distribution of the low-mass stellar population

We have used spatial gridding to obtain maps of the stellar density as a function of extinction. Fig. 2.1 shows the spatial distribution of X-ray low-mass stars for three different extinction ranges superimposed on the total column density of dense molecular gas traced by the emission of CN (N=1-0) (dashed contours; Rodriguez-Franco et al. 1998). The left panels show the location of the X-ray stars as blue filled circles. Four crosses, an open square, and an open triangle indicate the location of the four TC stars, the OHC region, and the OMC1-S region. The right panels present the stellar surface density in terms of the number of COUP sources contained in cells of 15" × 15" (0.03 pc×0.03 pc). A zoom of the central part of the field is presented in Fig. 2.2. Consistent with Grosso et al. (2005), we find that PMS low-mass stars cluster towards the three regions related to massive stars: the TC, the OHC and the OMC1-S region.

The less extincted population, with $\log N_{\rm H} < 22.0$ cm^{-2} (upper panels in Fig. 2.1, left panel in Fig. 2.2), shows a ring-like structure around the TC. The slightly extincted stellar population, with 22.0 cm^{-2} $<\log N_{\rm H} <$22.5 cm^{-2} (middle panels in Fig. 2.1 and 2.2), is clustered towards the position of the most massive star in the Trapezium, θ^1 *Ori C*. Remarkably, this population partially fills the hole found in the non-embedded population. The most extincted X-ray sources ($\log N_{\rm H} >$22.5 cm^{-2}; lower panels in Fig. 2.1 , right panel in Fig. 2.2), clearly associated with the molecular cloud traced by the CN emission, are clustered towards the OHC and the OMC1-S regions (open square and triangle, respectively, in Fig. 2.1 and 2.2), which host the ongoing massive star formation activity.

The selected extinction ranges have major implications on the outcome of this type of studies. Previous studies by Feigelson et al. (2005) and Grosso et al. (2005) only considered two extinction ranges with $\log N_{\rm H} >$22.0 cm^{-2} and $\log N_{\rm H} <$22.0 cm^{-2}. Although these authors already reported the clustering towards the TC, OHC, and OMC1-S, their classification criteria did not allow them to clearly separate a non-extincted PMS population in the ring around the TC from the slightly extincted PMS stars towards the TC core, around the most MS massive star θ^1 *Ori C*.

In addition, instead of the condition of $\log N_{\rm H} >$22.0 cm^{-2} used by Feigelson et al. (2005) and Grosso et al. (2005), we propose that the condition $\log N_{\rm H} >$ 22.5 cm^{-2} is more appropriate to isolate the embedded population of low-mass PMS sources in

Table 2.1: Number of COUP stars in 15" × 15" (0.03 pc×0.03 pc) cells centered on COUP sources (close-neighbors method), and derived stellar densities (surface and volume) for the density peaks seen at different extinctions.

Region	Column density range (cm^{-2})	# Sources	Surface stellar density Σ_* (stars pc^{-2})	Volume stellar density ρ_* (stars pc^{-3})
TC envelope	<22.0	5	$(5.5\pm 0.3)\cdot 10^3$	$(3.5\pm 0.2)\cdot 10^5$
TC core	22.0-22.5	4	$(4.4\pm 0.3)\cdot 10^3$	$(2.8\pm 0.2)\cdot 10^5$
OMC1-S	>22.5	6	$(6.6\pm 0.3)\cdot 10^3$	$(4.2\pm 0.2)\cdot 10^5$
OMC1-S (corrected)[a]	>22.5	10	$(1.10\pm 0.03)\cdot 10^4$	$(7.0\pm 0.2)\cdot 10^5$
OHC	>22.5	9	$(1.10\pm 0.03)\cdot 10^4$	$(7.0\pm 0.2)\cdot 10^5$
OHC (corrected)[a]	>22.5	19	$(2.10\pm 0.03)\cdot 10^4$	$(1.30\pm 0.02)\cdot 10^6$

[a] Stellar densities corrected from incompleteness (see Sect. 4.2.5).

the OMC. Fig. 2.2 shows that the populations of sources with $\log N_{\rm H}$ <22.5 cm^{-2} (upper and middle panels) are distributed throughout the field, including the regions without molecular emission. However, the sources with $\log N_{\rm H}$ >22.5 cm^{-2} (lower panels) are predominantly concentrated in the region with CN molecular emission, suggesting their physical association with the molecular cloud.

2.3.2 Stellar densities

From spatial gridding we can derive the stellar densities in terms of the number of stars per cell. However, as explained in Sect. 2.2.1, this method may underestimate the values of the density peaks. For that reason, we used the close-neighbors method to calculate the densities in the low-mass PMS star clusters. In Fig. 2.3 we report the histograms of the number of 0.03 pc × 0.03 pc cells centered on COUP stars as a function of the number of stars found within each cell. The different colors and line types indicate the extinction ranges considered in our study. Consistently with our results from Fig. 2.1 and 2.2 (from spatial gridding), Fig. 2.3 (from the close-neighbors method) shows that the cells with the largest number of neighbors correspond to the X-ray sources detected towards the TC, the OHC, and the OMC1-S region independently of the spatial gridding. The densities obtained using cells centered on COUP stars are slightly higher than those calculated using the spatial gridding, and reflect the real value for the density peaks more reliably.

The surface and volume stellar densities derived for the three extinction ranges towards the main density peaks (OHC, OMC1-S, the TC envelope, and the TC core) are summarized in Table 1. The surface densities were calculated by using 0.03 pc × 0.03 pc cells, and the volume densities using spheres with radius of 0.015 pc, in both

cases centered on COUP sources. The errors were estimated by considering ±0.2 star cell^{-1} as background/foreground contamination (Sect. 4.2.4).

The highest stellar density, with nine stars in the 0.03 pc cell in the range $\log N_{\rm H} > 22.5$ cm^{-2}, is found in two cells located within the OHC; one centered on COUP 621, likely a low-mass companion of the infrared source *n* (Lonsdale et al. 1982), and the other on COUP 622, located only 3.3" south of source *n*.

These densities must be considered as lower limits since they do not consider the unseen population behind very high extinctions. This is particularly critical for the extinction range $\log N_{\rm H} > 22.5$ cm^{-2} (see Sect. 4.2.5). Considering the incompleteness due to obscuration, the surface and volume stellar densities in the OHC and OMC1-S could be as high as (7.0± 0.2)×10^5 stars pc^{-3} and (1.30± 0.02)×10^6 for OMC1-S and the OHC, respectively. These densities may be even higher due to the presence of unresolved binaries. These values, along with the one found by Martín-Pintado et al. (2005) in Cep A HW2 (1.6×10^8 stars pc^{-3}), are the highest found in all observed star clusters (Bally and Zinnecker 2005).

In Fig. 2.4 we show the derived stellar surface density[1] of PMS stars for the three extinction ranges versus the distance to the X-ray cluster centers. Left panel shows that the TC is dominated by slightly embedded sources concentrated in the central ∼ 0.03 pc, where the four MS massive stars of the Trapezium are located. The TC envelope formed by moderately extincted sources is located at a radius of ∼ 0.05 pc from the cluster center. The middle and right panels show that the embedded populations in the OHC and the OMC1-S PMS clusters are very compact with sizes ∼ 0.03 pc.

★ Effect of the cell size

Table 2 compares the number of sources found in the main stellar density peaks (TC envelope, TC core, OMC1-S, and OHC) using the close neighbors method with different cells sizes (0.03 pc×0.03 pc and 0.05 pc×0.05 pc). We defined a *clustering parameter* (α) as the ratio between the number of sources found in the 0.03 pc×0.03 pc cell and the number found in the 0.05 pc × 0.05 pc cell. A value of α closer to 0 would mean that there is no central concentration of stars and hence that the distribution is not clustered. A value of α=0.39 would correspond to a uniform stellar distribution. A value α=1 would mean that all stars are concentrated in the smaller

[1] We calculated the stellar densities counting the numbers of stars contained in rings with widths of ∼0.016 pc, centered on the cluster centers.

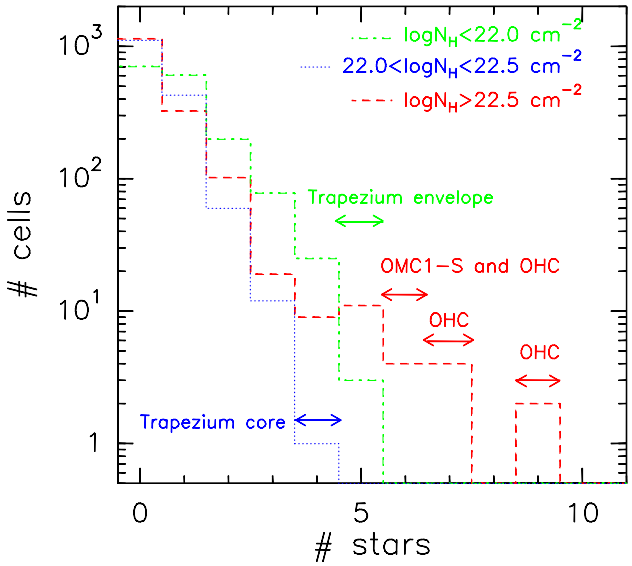

Figure 2.3: Number of cells versus the number of stars located inside the cell, considering 15" ×15" (0.03 pc×0.03 pc) cells centered on each COUP X-ray star. Different colors and dashed lines show different extinction ranges. The densest cells (i.e., cells with the highest number of X-ray stars) are located in the OHC, OMC1-S, the TC core and the TC envelope (see text).

cell. Our results show that the clustering parameter α is between 0.7 and 0.8 in the clusters of PMS low-mass stars found in Orion (Table 2), which means that 70-80% of the stars in those clusters are concentrated in the inner cell of 0.03 pc. If we assume a Gaussian distribution for the stellar density $\rho_* \propto e^{-(2r/\gamma)^2}$ (where r is the distance to the center of the cluster and γ is defined as the cluster size), α=0.7-0.8 corresponds to $\gamma \sim$ 0.024-0.028 pc. This size range is very similar to the size of our smaller cell. Consequently, our choice of the cell size (0.03 pc) is appropriate for sampling these clusters and for studying its stellar densities.

We note that the cell size is a key parameter for calculating stellar densities. The last column in Table 2 shows that the volume stellar densities calculated using 0.03 pc cells are ∼3 times higher than those calculated using larger cells of 0.05 pc. This is because the stellar density peaks are very concentrated ($\leq$0.03 pc). Therefore, the choice of an adequate cell size is the key in studying the stellar densities, in particular in the very young clusters of PMS low-mass stars, which are expected to be very compact.

Table 2.2: Comparison between the density analysis using the close-neighbors method, with cells centered on COUP sources with areas of 15" × 15" (0.03 pc×0.03 pc) and 24" × 24" (0.05pc×0.05pc).

Region	Column density range (cm^{-2})	# Sources 15" × 15" 0.03 pc ×0.03 pc	# Sources 24" × 24" 0.05 pc×0.05 pc	Clustering parameter α	Volume stellar density ratio $\rho_{*[0.03pc]}$ / $\rho_{*[0.05pc]}$
TC envelope	<22.0	5	7	0.7	2.9
TC core	22.0-22.5	4	5	0.8	3.3
OMC1-S	>22.5	6	8	0.8	3.1
OHC	>22.5	9	13	0.7	2.8

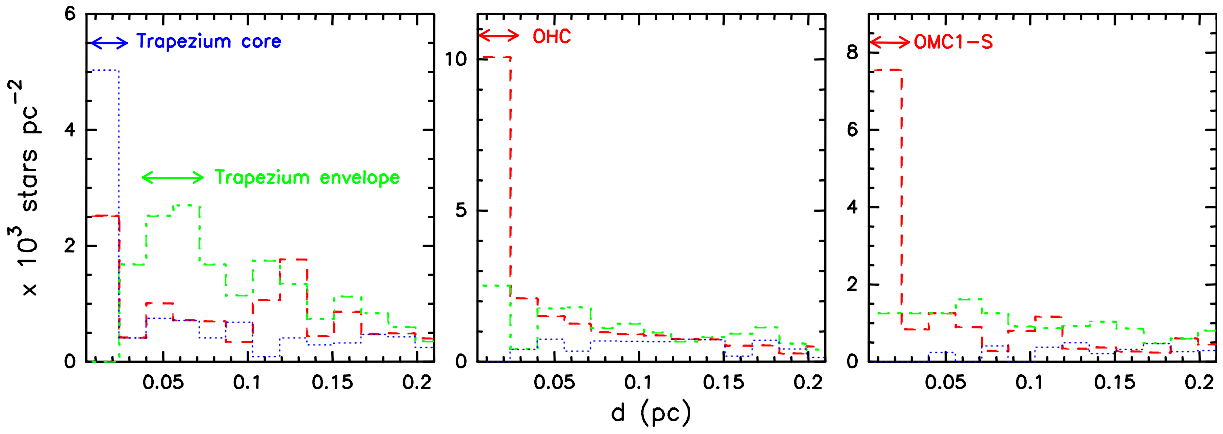

Figure 2.4: Surface stellar density versus the distance to the PMS cluster center for the TC (left), the OHC (middle), and OMC1-S (right). The different colors and dashed lines show different extinction ranges: green corresponds to $\log N_{\rm H} < 22.0$ cm^{-2}, blue indicates an extinction range of 22.0 cm^{-2} $< \log N_{\rm H} <$ 22.5 cm^{-2}, and red corresponds to $\log N_{\rm H} >$ 22.5 cm^{-2}.

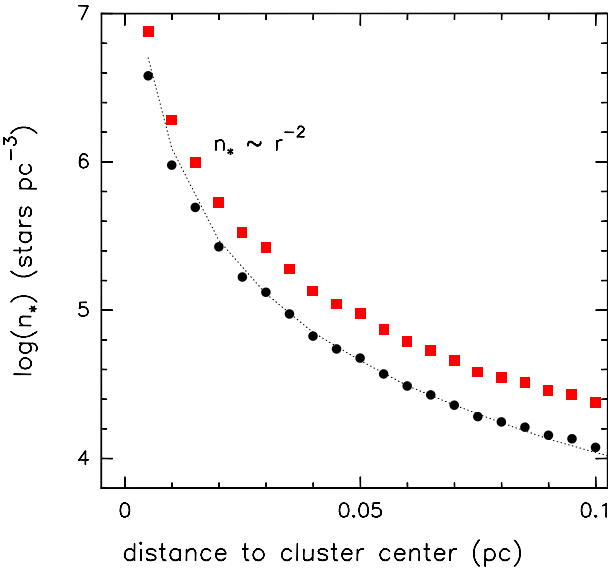

Figure 2.5: Cumulative stellar density radial profile in the OHC computing the stars with log$N_{\rm H}$ >22.5 cm^2 in concentric circles with 0.05 pc steps (black dots). The stellar densities corrected by completeness (factor of 2) are indicated with red squares. The dotted line indicates a r^{-2} profile.

★ Cumulative stellar density radial profile in the OHC

The OHC is the prototype region to study massive star formation. The deep Chandra observations offer for the first time the opportunity to study the low-mass stellar density of an embedded cluster harboring massive star formation. In this section we derive the radial stellar density profile of the OHC cluster by calculating the cumulative stellar density with respect to the cluster center. We consider that the center of the cluster coincides with the location of the stellar density peak seen in the 0.03 pc × 0.03 pc grid. We count the number of COUP embedded stars (log$N_{\rm H}$ >22.5 cm^2) within concentric circles with radius increasing in 0.005 pc steps. We considered as the innermost concentric circle the one containing at least 2 stars. The results are presented in Fig. 4.9. According with the completeness discussion in Sect. 4.2.5 we also present the stellar densities corrected by a factor of 2. The cluster follows an approximate radial profile $\sim r^{-2}$ with the exception of the very inner region, where the cumulative density is slightly lower. This is likely due to the high extinction in the very central region. The cumulative profile shows that in the inner region r <0.015 pc the stellar density is >10^6 pc^3, consistently with our previous analysis.

2.3.3 Comparison with other wavelengths

We compared surveys of the stellar population in Orion carried out at different wavelengths with our analysis in X-rays. The different catalogs used for the comparison are presented in Table 3: one at optical (Hillenbrand 1997), and three at IR wavelengths (Hillenbrand and Carpenter 2000, Muench et al. 2002, Lada et al. 2004). For the comparison we applied the same spatial gridding as for the X-rays, integrating the stellar population in cells of 0.03 pc × 0.03 pc. Fig. 2.6 shows the spatial distribution of the stars for the different surveys. Note that the color scale representing the number of sources per cell is different from that in Figs. 1 and 2.

★ Qualitative comparison with optical and IR observations

We have shown in Sect. 2.3.1 the importance of considering the population of stars in different extinction ranges, to distinguish members from the optically visible ONC and from the stellar population embedded in the molecular cloud located behind. In this subsection, however, we consider *all* stars observed at different wavelengths (Fig. 4.9), without applying any criteria to separate population at different extinctions. This prevents a reliable quantitative stellar density analysis study, because we are taking into account stars along the same line of sight that belong to different physical regions. However, this comparison between different wavelengths can give us interesting additional information.

The optical observation (upper panel in Fig. 2.6) reveals the ONC population, and presents a morphology consistent with the non- extincted X-ray sources ($\log N_{\rm H}$ <22.0 cm^{-2}; upper panel in Fig. 2.1), with the main density peaks in the TC envelope (NE, NW and SE of the Trapezium stars), and without a significant population in the TC core. This gap in the radial distribution of low-mass stars surrounding the most massive star, θ^1 *Ori C*, was already remarked by Hillenbrand (1997).

The three infrared observations show basically the same result. Unlike the optical population, the IR population is clustered in the TC core, around the most massive of the four Trapezium stars (θ^1 *Ori C*) and in the OHC region. However, IR surveys do not detect the cluster found in X-rays towards OMC1-S. This is probably caused by a very high extinction towards this region.

The clustering in the TC core resembles the morphology presented by slightly extincted COUP sources (22.0 cm^{-2} <$\log N_{\rm H}$ <22.5 cm^{-2}; middle panels in Fig. 2.1). This, along with the fact that this clustering is observed at IR but not at optical

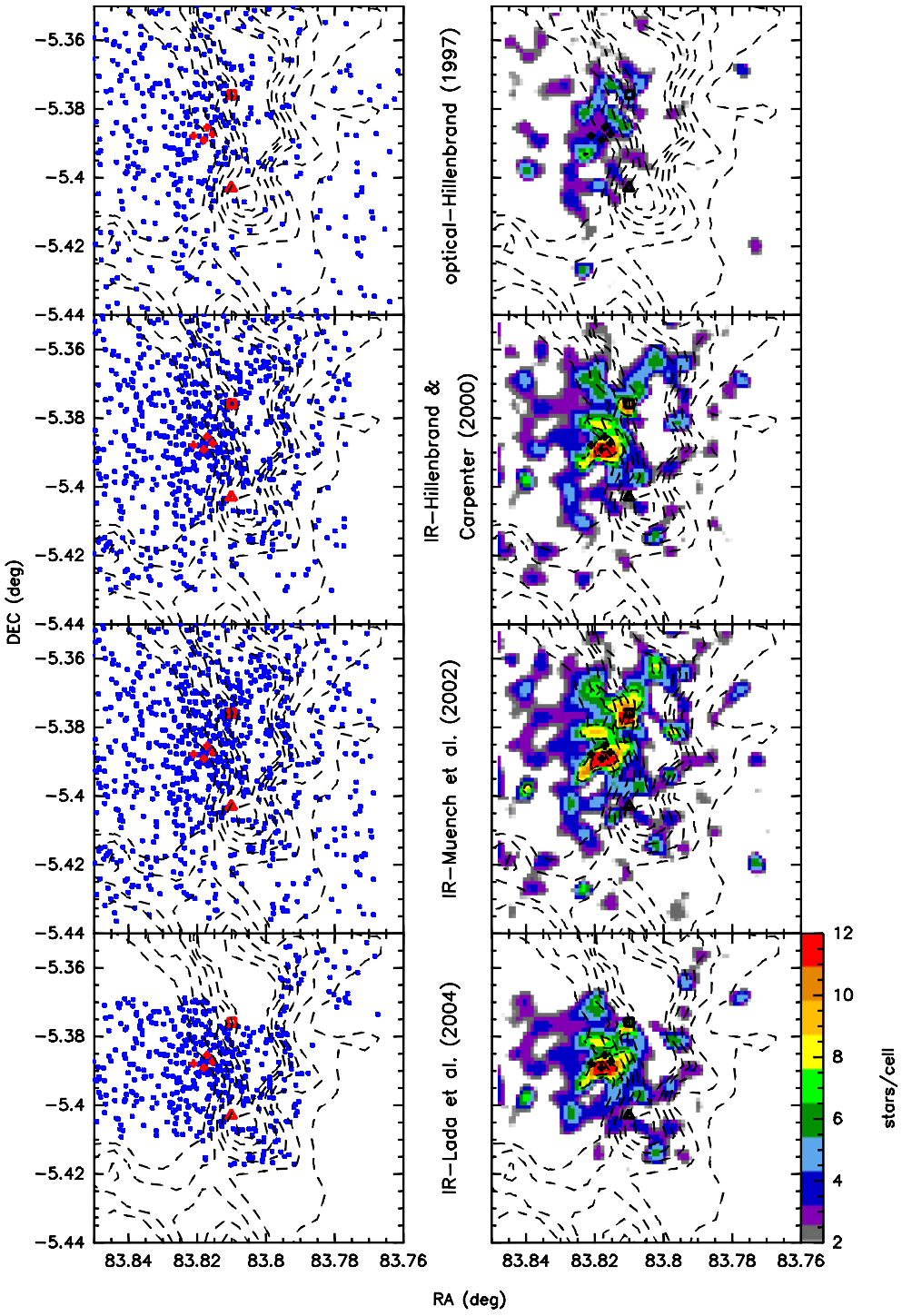

Figure 2.6: Spatial distribution of stars from four different surveys. From upper to lower panels: optical catalog (V and I_C bands) from Hillenbrand (1997), IR catalog (H and K bands) from Hillenbrand and Carpenter (2000), IR catalog (J, H and K_S bands) from Muench et al. (2002)), and IR catalog (L' band) from Lada et al. (2004). As in Fig 1., dashed contours represent dense gas traced by the integrated intensity emission of CN (N=1-0) (Rodriguez-Franco et al. 1998). The left panels show the position of the X-ray stars as blue dots. Four crosses, an open square and an open triangle show the location of the four main-sequence massive Trapezium stars, the OHC, and OMC1-S. The right panels report the stellar surface density for the same extinction ranges, derived by counting the number of COUP sources using a kernel box of 15" (0.03 pc)(right color scale), superimposed on the CN emission.

wavelengths, suggests that the TC core contains more dust than its surroundings in the TC envelope, consistent with the X-ray results. This might yield some clues about the formation mechanism of the massive stars in the Trapezium (see the discussion in Sect. 2.4.3).

It would be expected that the L' band observations (Lada et al. 2004; lower panel in Fig. 2.6), more sensitive to the presence of dust than IR observations at shorter wavelengths, show a clear clustering in the OHC. However, the peak in the OHC region is not as prominent as the peaks found in the other two surveys. This is because this region is located at the border of the Lada et al. (2004) observation (Fig. 2.6).

★ Quantitative comparison with IR observations

Similar to the procedure used to study the X-ray population in different extinction ranges, Lada et al. (2004) used the condition $J-H$ <1.5 mag to select partially extincted and non-extincted sources ($A_{\rm V}$ < 8 mag). These authors found that the main peak in the TC region (they called it Trapezium Core, but it is equivalent to the region containing our TC envelope and TC core) has a surface stellar density of 7.2×10^3 stars pc^{-2}, a value of the same order (although slightly higher) as the average density of the TC envelope and TC core obtained from the X-ray data ($\sim5\times10^3$ stars pc^{-2}).

Lada et al. (2004) also used the condition $K-L$ >1.5 mag (roughly corresponding to $A_{\rm V}$ >15-26, and approximately equivalent to our condition log$N_{\rm H}$ >22.5 cm^{-2}) to select sources deeply embedded in molecular gas and dust. They found that the main peak in the embedded population is located in the OHC region, with a stellar density of 3.2×10^3 stars pc^{-2}. This value is a factor 7 below the density we have calculated here (2.0×10^4 stars pc^{-2}). This is because the most deeply embedded population remains unseen at IR wavelengths. Therefore, our work confirms the potential of X-ray observations to detect the population of heavily extincted low-mass stars in massive star cradles.

2.3.4 The Trapezium Cluster: intermediate extincted core and non-extincted envelope

Our analysis has revealed for the first time a dense cluster of X-ray low-mass stars with intermediate extinction (22.0 cm^{-2} < log$N_{\rm H}$ < 22.5 cm^{-2}) around the most

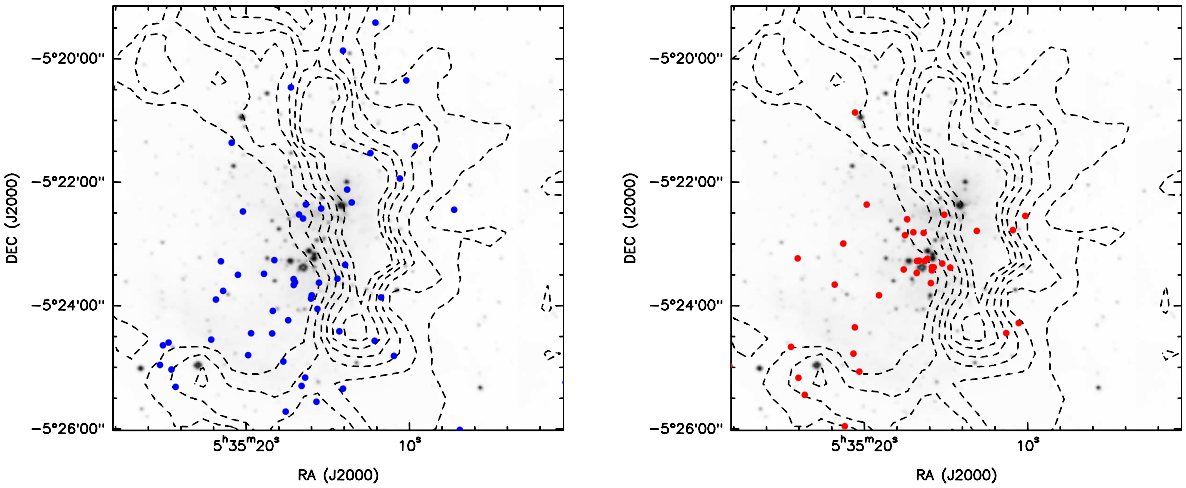

Figure 2.7: Proplyds from the Kastner et al. (2005)) catalog with X-ray counterparts. The gray scale is the 2MASS image at K band, and the dashed contours denote the CN N=1-0 emission from the OMC (Rodriguez-Franco et al. 1998) *Left*: stars with measured values of the hydrogen column density of $\log N_{\rm H} < 22.0$ cm^{-2}. *Right:* stars with measured values of the hydrogen column density of $\log N_{\rm H} > 22.0$ cm^{-2}.

massive star in the Trapezium, θ^1 *Ori C*, surrounded by a non-extincted envelope of stars. Most of these stars in the TC core were not detected in the optical survey from Hillenbrand (1997), consistently with their intermediate extinction. We have shown that the gap found in the radial distribution in the optical survey disappears when considering intermediate extincted X-ray stars or IR stars.

To test whether the COUP stars clustered around θ^1 *Ori C* are ONC members with extinctions higher than that usually found in the optical visible nebula, or whether they are simply slightly extincted members of the background OMC cloud, we crossed-checked the COUP catalog with optical HST observations of ONC proplyds from Kastner et al. (2005), which can detect stars more obscured than the optical Hillenbrand (1997) observations. In Fig. 2.7 we have plotted the spatial distribution of the proplyds with COUP counterparts, distinguishing those with $\log N_{\rm H}$ <22.0 cm^{-2} (blue dots in left panel) and $\log N_{\rm H}$ >22.0 cm^{-2} (red dots in right panel). We found that in the close vicinity (20" × 20", ∼0.04 pc × 0.04 pc) of θ^1 *Ori C* there is an absence of stars with low extinction, and a cluster of ten X-ray stars with $\log N_{\rm H}$ >22.0 cm^{-2}, eight of which are proplyds in Kastner et al. (2005). This clearly confirms that these stars with intermediate extinction are ONC members.

With the aim of testing the significance of this intermediate-extincted population of low-mass PMS stars around θ^1 *Ori C*, we have compared the spatial distribution of the sources with $\log N_{\rm H}$ <22.0 cm^{-2} and $\log N_{\rm H}$ >22.0 cm^{-2} in the TC core and

Table 2.3: Surveys of Orion at different wavelengths.

Wavelength	Telescope	Reference
optical (bands V and I_C)	KPNO 0.9 m + data from previous literature	Hillenbrand (1997)
IR (H and K bands)	Keck I 10m	Hillenbrand and Carpenter (2000)
IR (J, H and K_s bands)	1.2 m telescope at FLWO & 3.5 m NTT in La Silla	Muench et al. (2002)
IR (L')	VLT UT1	Lada et al. (2004))

Table 2.4: Number of extincted/non-extincted ONC stars observed in the TC core and envelope, compared with those expected from an uniform distribution of stars.

Region	$\log N_{\rm H}$ ($\rm cm^{-2}$)	# stars observed	# stars expected from uniform distribution
TC core	<22.0	2	3
TC core	>22.0	10	2
TC envelope	<22.0	41	40
TC envelope	>22.0	17	25

envelope with those expected for an uniform distribution of stars. We have considered a 60" × 60" region around the TC. The 20" × 20" region around θ^1 *Ori C* is considered as the TC core, being the TC envelope the remaining area. We have only considered ONC members, i.e., we have not considered COUP stars that are expected to be embedded in the OMC[2]. The results are summarized in Table 2.4. It is clear that the extincted population in the TC core (10 sources) is significantly higher than that expected from a uniform distribution (∼2 sources). However, the non-extincted population (2 sources) is very similar to that expected (∼3 sources) for an uniform distribution. On the other hand, in the TC envelope the non-extincted population is distributed uniformly (41 sources observed and ∼40 sources expected), while there is a deficit in the extincted population (17 stars observed while the expectation from an uniform distribution is ∼25 stars). Therefore, this analysis confirms our finding of a core-envelope structure with intermediate extincted stars concentrated in the core and non-extincted stars distributed in the envelope.

2.3.5 Comparison with molecular/dusty filaments

The very deep X-ray COUP observation allows to compare the morphology of the stellar population with the dense molecular filaments (MF) found in the region by

[2] The OMC members fulfill that: i) $\log N_{\rm H}$ >22.5 cm; ii) they are located within the CN emission from Rodriguez-Franco et al. (1998); and iii) they do not have optical counterpart in Hillenbrand (1997) or in the sample of proplyds from Kastner et al. (2005).

Martin-Pintado et al. (1990) and Rodriguez-Franco et al. (1992). Their maps of the dense gas tracer HC_3N revealed several long (up to 0.8 pc) and thin MF's (Fig. 2.8). These MF's are coincident with the dusty elongated structures at the western border of the OMC observed by SCUBA at 850 *mu*m (right panel of Fig. 2.8; see also Johnstone and Bally 1999). In Table 2.5 we show the physical parameters for the MF's derived by Rodriguez-Franco et al. (1992). The morphology of the MF's (shown in Fig. 2.8) shows an interesting spiral-like structure pointing towards the TC/OHC/OMC1-S region.

The comparison with the stellar population revealed by COUP allows us to determine whether star-formation has occurred within the MF's. As shown in Table 2.5, their average column densities are $N_{\rm H_2}$ $\geq$2.7$\times$10^{22} cm^{-2}, which is equivalent to logN_H $\geq$22.7 cm^{-2}. As we have already shown, the COUP observation was able to detect stars with extinctions higher than this value, and it has revealed the population embedded in regions even with column densites one order of magnitude higher, such as the OHC (see Table 3 from Rodriguez-Franco et al. 1992). Fig. 2.8 shows that there are only a few embedded stars (we have plotted those with logN_H $>$22.5 cm^{-2}) in the MF's. Therefore, it seems unlikely that significant star formation is occurring within the filaments.

Instead, the MF's could be accretion channels that are transferring gas from the external region to the center of the cluster. Their aspect ratio (length/width) around 10 and the linewidths detected in the filaments (0.5$-$ 2 km s^{-1}) are very similar to collapsing filaments observed in other massive star-forming regions (see e.g, Peretto et al. 2014). Along the filaments there are velocity gradients of 1$-$2 km s^{-1} pc^{-1}. The smooth velocity structure observed shows that they are dynamically coherent. In Fig. 2.9 we show the radial velocities of the longer filaments, MF3 and MF4 (from Rodriguez-Franco et al. 1992), which increase as one moves away from the central region. This structure might be due to infalling motions of the gas along the filaments (Peretto et al. 2014). The gravitational potential well created by the stellar cluster can naturally explain the the observed velocity gradients as the gas moves towards the centre of the system, the TC/OHC/OMC1-S region, where all the MF's (with the only exception of MF 7) are pointing. In this context, the spiral-like structure could be reminiscent of the inital rotation of the parental cloud.

We can estimate the accretion timescale for the MF's using the collapse time of

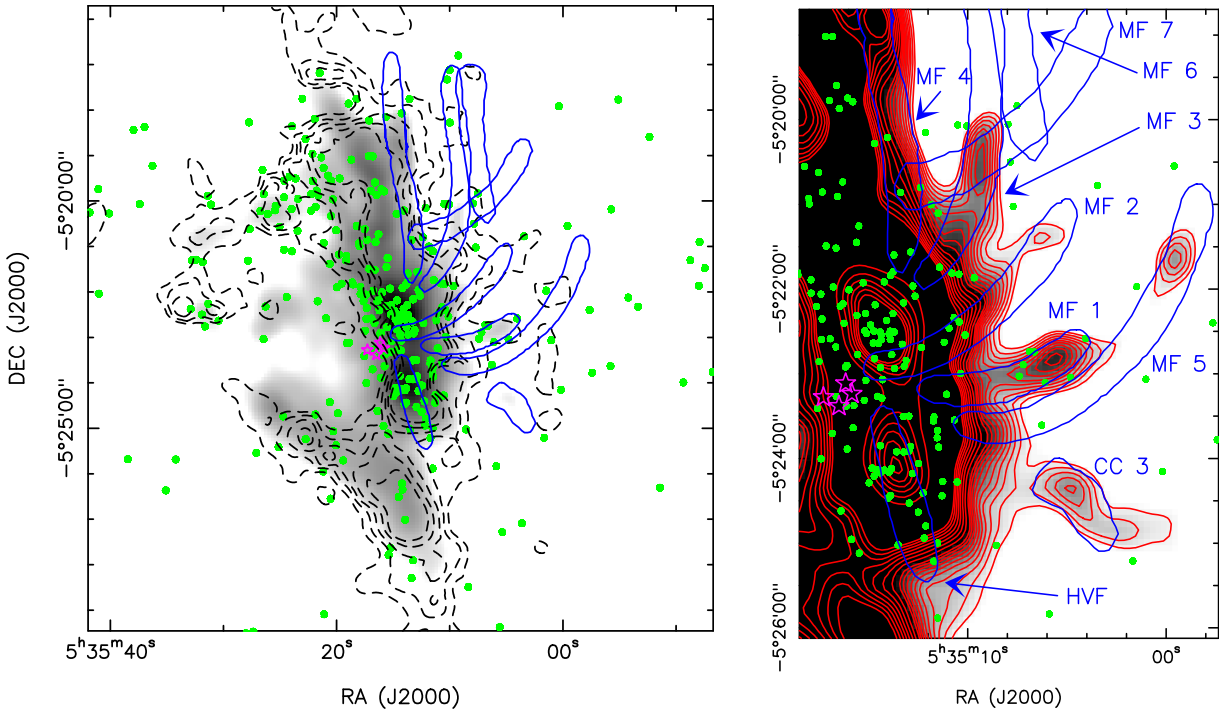

Figure 2.8: *Left*: comparison between the spatial distribution of COUP stars with log$N_{\rm H}$ >22.5 cm^{-3} (green dots) and the location of the HC_3N molecular filaments (MF; blue contours) detected by Martin-Pintado et al. (1990) and Rodriguez-Franco et al. (1992). Dashed contours represent dense gas traced by the integrated intensity emission of CN (Rodriguez-Franco et al. 1998) and the grey scale is 850 μm emission from SCUBA observations. The position of the four Trapezium stars are indicated with magenta star symbols. *Right:* Zoom-in view of the central region, with the different MF's labelled. Note that the grayscale (SCUBA emission at 850 μm) is different than that in the left panel. Red contours also correspond to SCUBA emission, which peaks at the OHC and the OMC1-S regions.

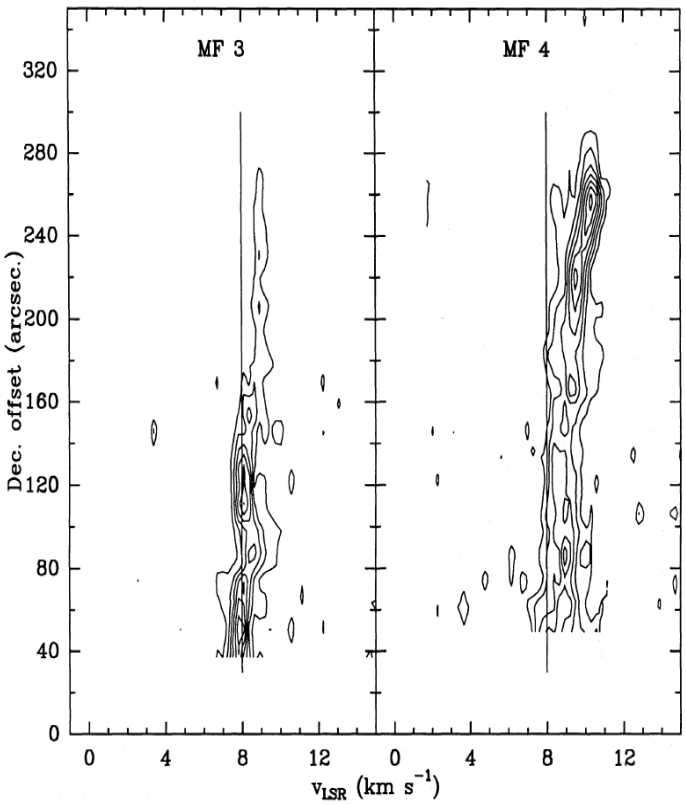

Figure 2.9: Radial velocity along the length of the two longest molecular filaments, MF3 and MF4, from Rodriguez-Franco et al. (1992). The offsets are measured in declination are relative to the declination DEC=-05d 22m 30.15s.

free-falling fillaments derived by Pon et al. (2012)[3] (see also Peretto et al. 2014):

$$t_{ff}^{1D} = 2A\sqrt{\frac{\pi}{16\,G\rho}} = 2\sqrt{\frac{2}{3}}\,A\,t_{ff}^{3D}, \tag{2.1}$$

where A is the aspect ratio (lenth/width of the filament), ρ is the density of the filament, and t_{ff}^{3D} is the spherical free-fall time for the same density.

The Eq. 2.1 shows that the collapsing time of a filament can be significantly longer than the time for a equal-density spherical condensation. Therefore, these filaments may play a main role once the first generation of stars is formed, allowing the continuous replenishment of material to be accreted. The funneling of new material towards the center of the gravitational potential well created by the stellar cluster allows to form new stars and/or feed already formed stars, which is crucial to build-up the more massive objects.

In the last column of Table 2.5 we show the calculated collapsing time for each filament. We obtain that t_{ff}^{1D} range between $2{\times}10^5$ yr and $2{\times}10^6$ yr, which is consistent with the expected young stellar ages of the stars embedded in the OMC. We can approximate the mass accretion rate of these filaments as $\dot{M} \simeq M/t_{ff}^{1D}$. We find that $\dot{M}$=0.9−2.7 $M_\odot$ yr^{-1} (Table 2.5).

We will show in Chapter 8 that the expected time that the OMC1-S cluster has been forming stars is $2{-}8{\times}10^5$ yr, in agreement with the expected age of young Class I objects (Evans et al. 2009). Assuming that the accretion rate $\dot{M}$ has been constant and that the MF's are replenished from the available gas in the parental cloud, the derived accretion rates would allow the MF's to transfer 20−80 $M_\odot$ towards the center of the cluster during a period of $2{-}8{\times}10^5$ yr. This can have important implications for massive star formation, as we will discuss in Sect. 2.4.

2.4 Scenarios for massive star formation

One of the first theories proposed to resolve the radiation pressure problem (see chapter 1) was the coalescence of low- and intermediate-mass stars in a dense stellar cluster (Bonnell et al. 1998; Bonnell and Bate 2002, 2005). The observational evidence suggesting that a violent event occurred in the OHC region around 500 yr ago (Zapata et al. 2009, Gómez et al. 2008, Goddi et al. 2011b), along with the high stellar density reported in our work ($\sim 10^6$ stars pc^{-3}) would make coalescence possible in this region.

[3] The factor 2 is included to take into account that the filaments are collapsing towards one of their ends.

Table 2.5: Orion Molecular Filaments (MF) physical parameters.

Filament	size	A	N_{H_2}	M	t_{ff}^{1D}	$\dot{M}$
	(pc×pc)	(aspect ratio)	(cm^{-2})	($M_\odot$)	(10^5 yr)	(10^{-5} $M_\odot$ yr^{-1})
MF 1	0.298×0.0412	7.2	4.9	14	5	2.7
MF 2	0.482×0.0461	10.5	2.7	9	13	0.7
MF 3	0.725×0.0557	13.0	2.7	16	18	0.9
MF 4	0.770×0.0703	11.0	4.4	35	13	2.6
MF 5	0.604×0.0630	9.6	3.5	19	13	1.5
CC 3	0.109×0.0969	1.1	4.2	4	2	1.9

In Sect. 2.5 we will discuss the possibility of a stellar collision in the high dense cluster revealed by Chandra in the OHC region, and conclude that a stellar interaction could have occurred in the cluster although it is uncertain whether this event has finally led to the formation of a massive star.

A general picture for massive star formation should likely be based on the two theories based on accretion: monolithic core accretion and competitive accretion. The main difference between these two theories is how and when the stars accrete the mass needed to become massive.

According to the monolithic core accretion theory (McKee and Tan 2002, 2003), massive stars form from massive clumps[4] supported against self-gravity by its internal turbulence and magnetic field support, with accretion rates high enough to overcome the radiation pressure. The massive clump collapses monolithically and produces a single massive object or a few massive stars, rather than many low-mass stars (Krumholz 2006; Krumholz et al. 2009).

On the other hand, the competitive accretion theory relies on the fact that nearly all massive stars are formed in stellar clusters with low-mass stars (Clarke et al. 2000; Lada and Lada 2003b). This theory assumes that the parental molecular cloud fragments into several condensations with masses around the Jeans mass[5]. Numerical simulations have shown that gravitational fragmentation of a molecular cloud produces condensations with masses of about $M_{Jeans} \leq 1$ $M_\odot$ (Klessen et al. 1998, Bate and Bonnell 2004, Bonnell et al. 2004) that collapse and form a low-mass star cluster. An additional mechanism is then needed to explain the formation of massive

[4] As we mention in chapter 1, although the nomenclature of this theory refers to the term *core*, their initial condensations are indeed *clumps* using the nomenclature defined in chapter 1.

[5] The Jeans mass, M_{Jeans}, is the mass necessary for an object to be gravitationally bound against its thermal support.

stars. It has been proposed that this mechanism is continuous gas accretion. Because fragmentation is inefficient in accumulating gas onto stars, there is a common gas reservoir in the clump that can potentially be accreted (Bonnell et al. 2003). Observations of pre-stellar structures and young clusters indeed show that most of the total mass (Krumholz and Bonnell 2007) is in a distributed gaseous form, so that it can potentially be accreted. Then, after low-mass stars are formed, they fall into local gravitational potential wells forming small-N clusters. This overall cluster potential well funnels gas down to the potential center, where it is captured via Bondi-Hoyle accretion by the "privileged" stars located at the potential center, progressively increasing their masses.

Clearly, core accretion and competitive accretion are rather different ways to explain massive star formation. However, it is not unreasonable to think of a scenario that involves a combination of the two theories, whenever the physical conditions allow them to work. Some authors have already suggested mixed scenarios for massive star formation (Peretto et al. 2006, Wang et al. 2010).

In this section we present and discuss three possible scenarios for massive star formation, where in principle both accretion theories could work. In practice, we show that the dominant mode of star formation is determined by the level of fragmentation in the clump. While some works claim that radiation feedback from the stars can stop fragmentation (Krumholz 2006), and allows monolithic collapse to work, others claim that the clump inevitably fragments into smaller condensations to form many stars (Clark and Bonnell 2006, Dobbs et al. 2005, Bonnell and Bate 2006, Peters et al. 2010, Federrath et al. 2010). In this context, our scenarios consider different levels of fragmentation: i) low fragmentation and monolithic collapse of the clump; ii) intermediate fragmentation of the clump and collapse of cores forming a cluster; iii) high fragmentation, collapse forming stellar seeds and subsequent competitive accretion. We compare the predictions from each scenario with the results of our analysis presented in Sect. 2.3.

2.4.1 Low fragmentation: Monolithic collapse of the clump

In this scenario the accretion luminosity[6] from the newly formed stars, increases the gas temperature, halting the fragmentation of the parental clump (Krumholz et al. 2007). Then, the clump collapses monolithically forming a single massive star (or

[6] The accretion luminosity produces a radiative feedback produced by the gravitational energy released by the accreting material when falling onto the central object.

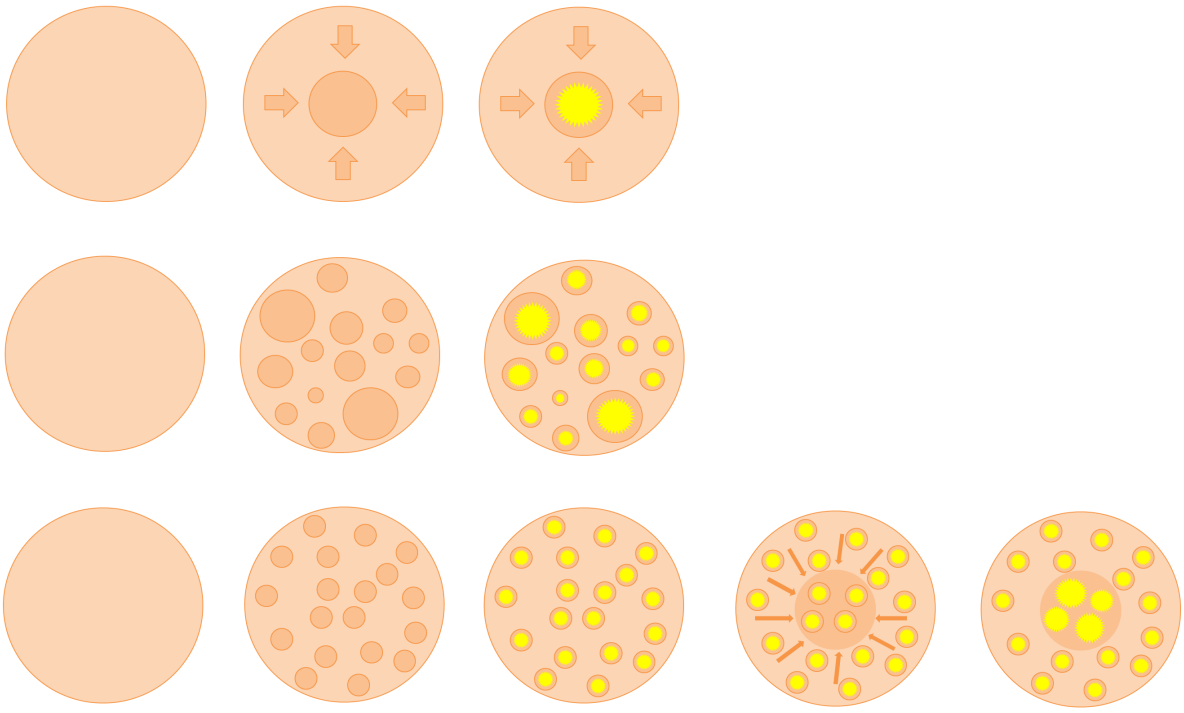

Figure 2.10: Scenarios for massive star formation based on the two accretion theories. The dominant role of each theory is mainly determined by the level of fragmentation in the clump (see text). *Upper panels:* low fragmentation and monolithic collapse. *Middle panel:* intermediate fragmentation. *Lower panel:* high fragmentation and competitive accretion.

a few massive stars). The rapid collapse consumes the available gas, so subsequent Bondi-Hoyle accretion of the remnant gas is negligible. A simple schematic picture of this scenario is presented in the upper row in Fig. 2.10.

According to this scenario, massive stars should be born in isolation or be accompanied by other massive stars, rather than by a low-mass star cluster. Therefore, although monolithic collapse could explain the small fraction of the massive stars found in isolation (de Wit et al. 2004), it would not explain our results in Orion, which have shown that massive star cradles (TC, the OHC and OMC1-S; see Sect. 2.3) harbor dense low-mass star clusters.

In Fig. 2.11 we compare monolithic collapse simulations (Krumholz et al. 2007) with the embedded low-mass stellar population observed by *Chandra* in the OHC region. It is clear that the parental clump in the OHC region has been fragmented much more than what it is expected from a pure monolithic collapse. This suggests that radiative feedback did not play a significant role in the fragmentation of the parental clump in the OHC region.

Indeed, Krumholz (2006) simulations showed that the radiative feedback should be only relevant when it is able to heat the gas at temperatures T >20 K, which

ocurrs at distances r <1000 AU (i.e., $r < 0.005$ pc). In the case of the OHC region shown in the lower right panel of Fig. 2.11, the fraction of volume affected by radiative feedback would be only a ∼2%. Furthermore, since the minimum separation[7] between stars in the OHC region is ≥0.005 pc, it is not expected that the radiative heating could stop the fragmentation, as observed.

The presence of dense low-mass star clusters in the Orion massive star cradles indicates that neither radiative feedback nor other mechanisms such as magnetic fields (e.g., Hosking and Whitworth 2004) were able to inhibit the fragmentation of the initial clump. This clearly rules out the monolithic collapse scenario and suggests that clumps producing massive stars suffer higher levels of fragmentation.

2.4.2 Intermediate fragmentation and collapse forming a cluster

One could think of an scenario based on monolithic collapse, but acting at smaller scales. In this scenario, the clump would suffer fragmentation, generating several cores with different masses and sizes. The cores with lower masses would produce low-mass stars, while those with higher masses could potentially form massive stars, in both cases via core accretion. A schematic picture explaining this scenario is presented in the middle row in Fig. 2.10. In principle, massive stars could be formed in isolation or be accompanied by low-mass stars, depending on how the clump initially fragments into cores.

Once the stellar cluster is born, subsequent Bondi-Hoyle accretion from the gas reservoir still available would be possible. However, it is difficult for competitive accretion to work in this context because there is no overall well-defined central cluster potential well, but a collection of local potential wells around each formed star. Therefore, there is no efficient funneling of gas to the center of the stellar cluster.

This scenario is very similar to the results presented by the simulations by Krumholz et al. (2011, 2012) and it is able to produce stars with different masses. These works implement the theory of core accretion in the general collapse of a cloud instead of the single massive clump considered in previous simulations (Krumholz 2006; Krumholz et al. 2009). The outcome of their simulations includes some massive stars formed nearly in isolation (consistently with their previous works) and also others located in low-mass stellar clusters, which would be more compatible with our

[7] This is a lower limit because we are considering a projected distance.

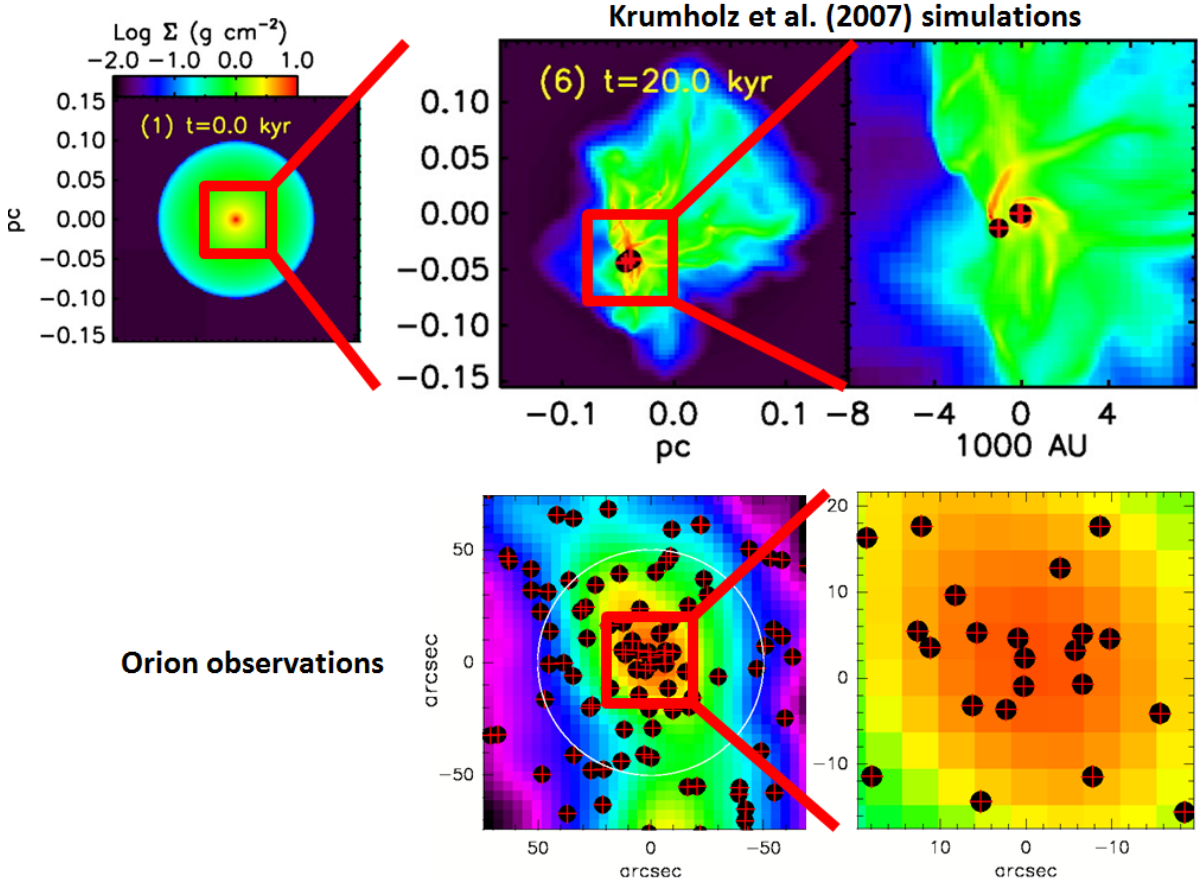

Figure 2.11: Comparison between simulations of the monolithic collapse model from Krumholz et al. (2007) (upper panels) and the observations of the OHC region (lower panels). *Upper panels*: The leftmost panel shows the initial parental clump of diameter 0.2 pc and 100 $M_{\odot}$ used in the simulations. The color scale indicates the gas column density. The middle panel shows the central region of the clump at the end of the simulation. The stars formed are indicated with red plus signs within black dots. The righmost panel is a zoom-in view of the middle panel. *Lower panels:* COUP embedded ($\log N_{\rm H}$ >22.5 cm^{-2}) stars are also denoted with red plus signs within black dots. The color scale correspond to emission at 850 μm observed by SCUBA. The white circle in the left panel indicates the size (diameter=0.2 pc) of the initial parental clump used in the Krumholz et al. (2007) simulations (upper left panel). The size scales of the panels are the same than the size scales of the two rightmost upper panels.

results in Orion.

However, this scenario presents several problems. Krumholz et al. (2011, 2012) argued that radiative feedback from the stars stops further fragmentation, explaining why not all cores reach low-masses ~ 1 $M_\odot$ during the collapse phase. However, as we have discussed in Sect. 2.4.1, it is not clear that radiative feedback from the newly stars could be so efficient to stop fragmentation. Several works claimed that the clumps should fragment into many stars (Dobbs et al. 2005, Clark and Bonnell 2006, Bonnell and Bate 2006, Federrath et al. 2010, Peters et al. 2010), especially with the presence of outflows that could favor the fragmentation (Cunningham et al. 2011).

In addition, there is other evidence indicating that this scenario does not fully explain, at least, the massive star formation that occurred in Orion. In this scenario fragmentation does not always produce more massive cores at the center of the initial clump (see Krumholz et al. 2011, 2012). Therefore, one would not expect a trend for massive stars to form at the center of the clump, as seen in the TC (see discussion in Sect. 2.4.3).

2.4.3 High fragmentation, collapse forming stellar seeds and subsequent competitive accretion

We assume now that the clump fragments into cores, which collapse producing a cluster of low-mass stars. Only a fraction of the gas is directly incorporated into the low-mass stars, while the rest is distributed throughout the clump. In this context, the stars compete to accrete this material. The stars located near the center of the potential well created by the whole cluster benefit from the higher gravitational attraction and gather matter via Bondi-Hoyle accretion at much higher rates, becoming higher mass stars. The stars that are not at the center of the potential well do not accrete significant amounts of gas, and remain low- and intermediate-mass stars. This scenario with high fragmentation (lower row in Fig. 2.10) is essentially coincident with competitive accretion, and naturally produces a *whole* cluster of stars with different masses.

Bonnell et al. (2004) simulated the evolution of a turbulent molecular cloud with properties similar to those in Orion, where fragmentation and competitive accretion play the main role in the formation of massive stars. The result of their simulation (see Fig. 1.5 of this thesis) shows a ~ 0.6 pc $\times$ 0.6 pc region where the massive stars are formed in the center of low-mass star clusters. The similarity between the

morphology of the whole cluster with the Orion observations presented in this chapter is remarkable (Fig. 2.1). Moreover, there is a trend in the TC for higher mass stars to be found at closer distances to the most massive star θ^1 *Ori C*. Fig.2.12 shows the mass of the stars in the TC versus the distance to θ^1 *Ori C* (data from the optical observations by Hillenbrand 1997). This mass segregation have been confirmed by the minimum spanning tree[8] analysis by Allison et al. (2009). The mass segregation in the ONC is primordial, i.e., the massive stars were initially born in the cluster center without migration (Bonnell et al. 2007, Reggiani et al. 2011). Therefore, this suggests a preference for the most massive stars to be born in the densest and central parts of the low-mass star cluster, as expected in the competitive accretion theory.

This scenario can also naturally explains the structure of extincted and non-extincted low-mass stars found in the TC (Fig. 2.1, 2.2 and 2.7, and Sect. 2.3.4). The non-extincted stars in the envelope of the TC could have lost the battle of competitive accretion - keeping their low-mass - against the four Trapezium stars in the core, which would have grown until they reached their current high masses. The non-extincted PMS stars in the envelope of the TC are therefore devoid of gas while those in the core are still partially embedded in gas and dust.

The molecular filaments (MF's) discussed in Sect. 2.3.5 are also in good agreement with this scenario. The simulations from Smith et al. (2009b) showed that massive stars form in the center of star-forming clumps, fed not only by the material located in their closer vicinity but also by material located at larger distances. The gravitational potential well is able to funnel material to the center through narrow accretion filaments. We have shown in Sect. 2.3.5 that the MF's detected in the region are able to transfer large amounts of material in short-timescales to the central region, where massive star formation has recently occurred (TC) or is on-going (OHC and OMC1-S). This continuous replenishment of material is able to produce dense reservoirs that favors the build-up of more massive objects.

Given that this scenario provides the best explanation for our results, we evaluated whether Bondi-Hoyle accretion can indeed gather enough mass to produce a massive star in the Orion environment. The accretion rate $\dot{m}$ is given by equation 1.9 (Bonnell and Bate 2006). Considering that the relative gas velocity follows the turbulent velocity size-scale relation $v \sim R^{1/2}$ (Larson 1981, Heyer and Brunt 2004), and assuming that the gas density ρ is centrally condensed with $\rho \sim R^{-1}$ (as found in other massive star-forming regions like Monoceros R2, Choi et al. 2000) the relation

[8]The minimum spanning tree (MST) is the path connecting all points in a sample with the shortest possible pathlength, which contains no closed loops (see, e.g., Prim 1957).

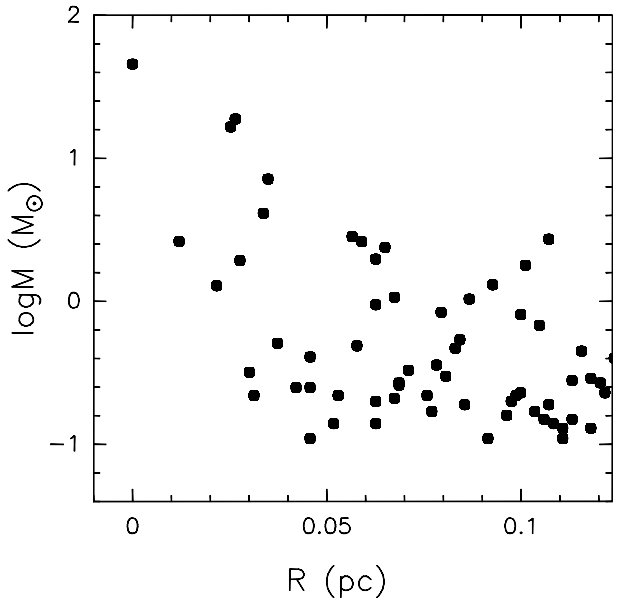

Figure 2.12: Mass of the stars in the TC versus the distance to the most massive star θ^1 *Ori C* (data from the optical observation presented by Hillenbrand (1997).

between the velocity and the mass of the clump is $v \sim m^{1/4}$. Combining this with Eq. 1.9 and integrating, one can obtain the time needed to build up a massive star:

$$t = t_{\rm mi} + \frac{v^3}{\pi\rho\, G^2 m_i^{3/4}} \left(\frac{1}{m_i^{1/4}} - \frac{1}{m^{1/4}} \right), \tag{2.2}$$

where m is the mass of the star and m_i is the initial mass of the "stellar seed", and $t_{\rm i}$ is the time needed to form the stellar seed with initial mass m_i.

The relative velocity of the gas v is a key parameter to determine whether competitive accretion is efficient or not (Krumholz et al. 2005, Bonnell and Bate 2006). It has been suggested that turbulence injected by winds, protostellar outflows, or ionized regions could increase the relative velocity of the gas, preventing competitive accretion from being the dominant process in the massive star formation (Krumholz et al. 2005). However, the results presented in this work have shown that massive stars in Orion have formed in small-N clusters (tens of stars, see Table 1), where the gas velocity dispersion is expected to be lower (Bonnell et al. 2003, Bonnell and Bate 2006).

Assuming a Maxwellian distribution of velocities, we used the root mean square of the gas velocity, v_{RMS}, as a good estimate of the relative velocity v. The value of

v_{RMS} is related to the linewidth of the molecular lines, Δv, with the expression

$$v_{\rm RMS} = \frac{1}{2}\left(\sqrt{\frac{3}{2\,Ln2}}\right)\Delta v, \tag{2.3}$$

We use here the linewidth of vibrationally excited HC_3N (HC_3N*, hereafter) because this molecule is particularly well suited to study the kinematics of the dense gas close to very young massive stars (Wyrowski et al. 1999, de Vicente et al. 2000, 2002). The OHC observations by de Vicente et al. (2002) show that $\Delta v \sim 7$ km s^{-1}. This value is consistent with those observed with other dense molecular tracers as NH_3 ($\sim$5 km $^{-1}$, Goddi et al. 2011a) or CH_3OH (4$-$6 km s^{-1}, Peng et al. 2012). Using Eq. 2.3, the HC_3N* linewidth is equivalent to $v_{\rm RMS}$=5.2 km s^{-1}.

Fig. 2.13 shows the time needed to form a massive star from stellar seeds with M_i=1 $M_\odot$ by competitive accretion. The blue line indicates the accretion time from the expressions from Krumholz et al. (2012) and McKee and Tan (2003) to form the stellar seed. The red line corresponds to the Bondy-Hoyle accretion time using Eq. 2.2, with $v = v_{\rm RMS}$=5.2 km s^{-1}. The volume- and surface densities used are ρ=1.95$\times$10^{-16} g cm^{-3} and Σ=12 g cm^{-2}, calculated from the average gas density in the OHC of $N[H_2]$=5$\times$10^7 cm^{-3} (Morris et al. 1980). According to Fig. 2.13, a 10 $M_\odot$ star (approximately the mass estimated for the massive objects found in this region) can be formed in the OHC by accretion of gas in $<$ 4$\times$10^5 years. We note that this accretion time estimate does not demonstrate by itself that massive stars are formed by competitive accretion in the OHC, but it shows that it could be possible.

In the OMC1-S region, where the gas density is lower but on the order of the OHC region (see CN contours in Fig. 2.1 and 2.2), and where a similar (or lower) turbulence may be expected, massive stars could form in the same way.

In the case of the TC, the current gas density is $\sim$10^{-17} g cm^{-3} (Hillenbrand and Hartmann 1998, Bonnell and Bate 2006), one order of magnitude lower than that in the OHC ($\sim$1.95$\times$10^{-16} g cm^{-3}). This implies that competitive accretion could be less important according to Eq. 1.9. However, as indicated by Krumholz et al. (2011), this density must have been higher by an order of magnitude at the moment where the stars were formed, because the cluster has likely expanded due to gas ejection (Kroupa 2001, Tan et al. 2006). Then, competitive accretion could still have been responsible for the formation of the massive stars in the Trapezium.

In summary, from our combined data (CN molecular emission and X-ray PMS stars), it seems that at least two basic ingredients are needed to form massive stars:

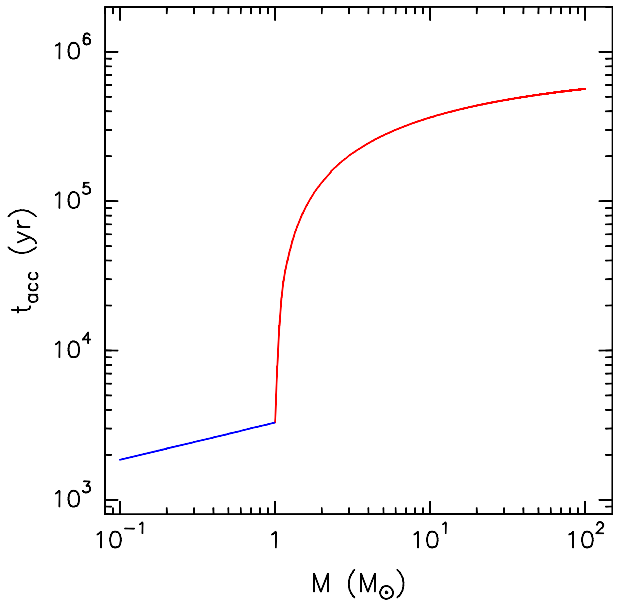

Figure 2.13: Accretion time necessary to form a massive star in the OHC in the high fragmentation scenario. The blue line corresponds to the time needed to form the stellar seeds of 1 $M_\odot$ via core accretion. We have used the expressions from Krumholz et al. (2012) for the accretion rate. The red line corresponds to the accretion time needed to reach the final mass M, using Eq. 2.2. The volume and surface densities used are ρ=1.95×10^{-16} g cm^{-3} and Σ=12 g cm^{-2}.

i) dense gas, and ii) a cluster of low-mass stars. It is remarkable that the low-mass star clusters appear only at certain positions of the north-south elongated ridge of dense molecular material (Fig. 2.1), suggesting that dense molecular material only does not necessarily form massive stars. This idea has also been suggested by Krumholz et al. (2012). Along with dense gas, our results suggest that the presence of low-mass star clusters is also a necessary but not sufficient condition for massive star formation. This is supported by the existence of dense low-mass star clusters, like the one at ∼[83.84, -5.395] (see Fig. 2.1), which does not present any massive star. This low-mass star cluster is seen in the non-extincted column density range ($\log N_{\rm H}$ <22.0 cm^{-2}) in the X-ray observations (upper panel in Fig. 2.1), and also in the IR surveys and in the optical observation by Hillenbrand (1997) (see upper panel in Fig. 2.6), confirming that it belongs to the ONC. In this region, the lack of dense molecular gas suggests that this low-mass star cluster was unable to accrete additional material to increase its mass to form more massive objects.

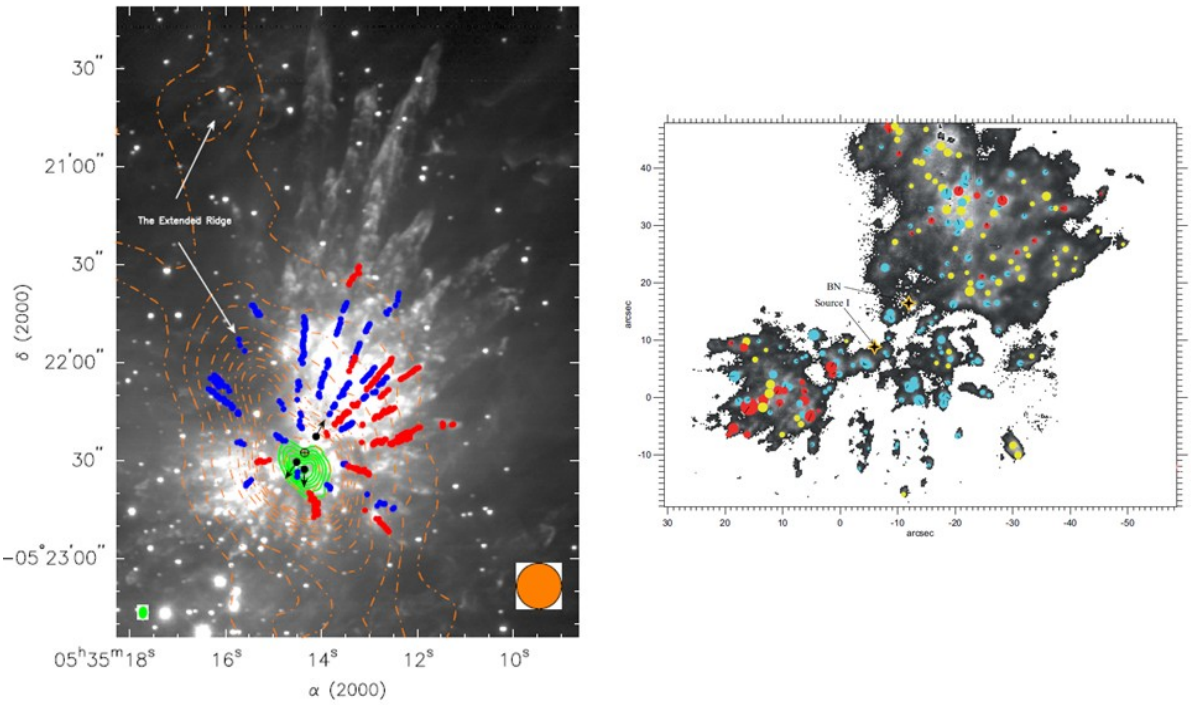

Figure 2.14: Images of the large-scale Orion outflow. *Left*: image adapted from Zapata et al. (2011). The gray scale is correspond to H_2 emission, overlaid with CH_3CN emission from the OHC (green contours), SCUBA dust continuum at 850 μm, and positions of blueshifted and redshifted CO(2-1) fingers (blue and red dots, respectively). The black dots with vectors indicate the positions and orientations of the proper motions of the radio sources BN, I and *n*. *Right*: H_2 emission in grey scale and 193 kinematic features identified by Nissen et al. (2007): blue, red and yellow dots indicate features blueshifted, redshifted and with no clear velocity pattern.

2.5 A stellar collision caused the large-scale outflow?

A large-scale and poorly collimated CO outflow have been observed in the OHC region (Kwan and Scoville 1976, Nissen et al. 2007; see Fig. 2.14). The origin of this powerful outflow, whose morphology and properties are very different than that observed towards typical outflows originated by single young stars, is still unclear. Bally and Zinnecker (2005) speculated that this outflow may be caused by a stellar collision. This interpretation is supported by some observational evidence that suggests that a violent event occurred in the OHC in the past: H_2 fingers (Taylor et al. 1984, Allen and Burton 1993), the CO filaments (Zapata et al. 2009), and proper motions measured for the massive objects BN, I and *n* (Rodríguez et al. 2005, Gómez et al. 2008, Goddi et al. 2011b), all of them pointing towards approximately the same central position within the OHC region (see left panel of Fig. 2.14). Rodríguez et al. (2005) and Zapata et al. (2009) suggested that this violent event could have been triggered by an interaction among several stars in the protostellar cluster. We have reported in Sect. 3.3.4 the presence of a very high stellar density in the OHC region, $>10^6$

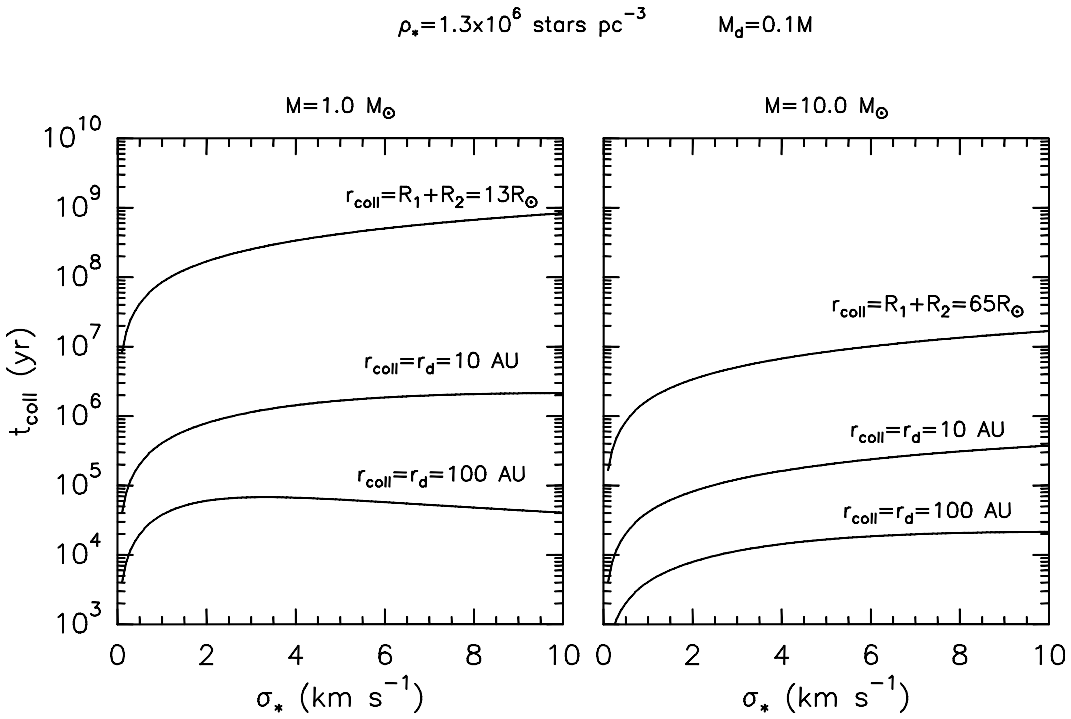

Figure 2.15: Stellar collision time t_{coll} versus stellar velocity dispersion σ_*. We have used the lower limit for the stellar density we have determined for the OHC of 1.30×10^6 stars pc^{-3}. We have considered collisions between 1 $M_\odot$ stars (left panel), and 10 $M_\odot$ stars (right panel). We have included the case of a direct collision between 'naked' stars (Eq. A.1) and the case with the likely presence of circumstellar disks (Eq. A.2) with radii 10 and 100 AU (see text).

stars pc^{-3}, which makes likely this violent interaction between members of this dense stellar cluster. In this section we evaluate if a coalescence of stars could occur in the OHC cluster, and whether this could have implications in the formation of massive stars.

In Appendix A we derive the expressions for the time needed for a stellar collision to occur in a stellar cluster, $t_{\rm coll}$. Fig. 2.15 shows the collision time $t_{\rm coll}$ as a function of the stellar velocity dispersion σ_* in a cluster of low-mass stars with a stellar density equal to that found in the OHC of 1.30×10^6 stars pc^{-3}. We considered collisions between 1 M$_\odot$ stars (left panel), and 10 M$_\odot$ stars (right panel). We included the case of a direct collision between 'naked' stars (Eq. A.1) and the case with the likely presence of circumstellar disks (Eq. A.2). In the direct 'naked' star collision, the collision distance $r_{\rm coll}$ is the sum of the radii of the stars. We considered that the radii of the stars are those of stars with 1 M$_\odot$ and 10 M$_\odot$ at 10^5 yr (left and right panels, respectively), the typical timescale for massive star formation. In the case including disks, the collision distance can be as high as the size of the disk (Bally and Zinnecker 2005). We considered disks with a mass of 0.1 times the mass of the star and reasonable radii of 10 and 100 AU, which can significantly reduce the collision time via disk-captures (Zinnecker and Yorke 2007, Davies et al. 2006, Bonnell and Bate 2005). Moreover, binaries and/or multiple stellar systems are commonly found in Orion (Kraus et al. 2009) and could additionally decrease $t_{\rm coll}$, favoring coalescence.

There are no direct measurements of the stellar velocity dispersion of the OHC cluster σ_*. However, lower and upper limits can be estimated. As indicated by Bonnell and Bate (2006), one might expect that the stars forming part of a small-N young cluster like that in the OHC have a low-velocity dispersion. These authors proposed to use values as low as 0.4 km s^{-1}. Gómez et al. (2008) claimed that typical random motions of recently formed stars have a velocity dispersion of 1-2 km s^{-1}. The ONC has a measured velocity dispersion of $\sim$2.3 km s^{-1} (van Altena et al. 1988). On the other hand, we can use the gas velocity dispersion of the OHC as a conservative upper limit to the stellar velocity dispersion, because stars are expected to be much less affected by turbulence than gas. The gas velocity dispersion in the OHC, using HC$_3$N* (see Sect. 2.4) is $\sigma = \Delta v/(2\sqrt{2\,Ln2}) \sim 3$ km s^{-1} (de Vicente et al. 2002). This upper limit for σ_* is very consistent with the values presented before.

According to Fig. 2.15, a stellar cluster as dense as the OHC with a stellar velocity dispersion of $\sigma_* \sim 3$ km s^{-1} could experience one stellar collision of two 1 M$_\odot$ stars with circumstellar disks with radius 10-100 AU (left panel) in a collision time of about

$\sim 10^5$ yr, making it plausible that the OHC cluster has suffered an encounter of low-mass stars. If a 10 $M_\odot$ star (which can be formed by competitive accretion in the low-mass star cluster, see Sect. 2.4.3) is involved, the collision time is even shorter. Therefore, this analysis suggests that the violent event that has been proposed for the OHC could be a collision between two members of the dense cluster revealed by X-rays studied in our work.

At this point, one may wonder if this close encounter may lead to a direct star-star merger. This is a necessary condition (although it may not be sufficient) to build up a more massive star. Of course, a rigorous characterization of the evolution of this system would need complex simulations that are out of the scope of this thesis. However, we can make some assumptions and simple calculations to determine if this is, at least, viable.

After one star has impacted the disk of a neighboring star, it can be captured to form a binary if its energy is lower than the potential energy created by the star+disk system (Bally and Zinnecker 2005; see also Sect. A.3). This condition sets a maximum collision distance at which the star can be captured, r_{max}. According to Eq. A.6 this maximum distance in a cluster with stellar velocity dispersion of 3 km s^{-1} and disk mass M_d=0.1 M_{star}, is $\sim$250 AU for a 10 $M_\odot$ star and $\sim$2500 AU for a 1 $M_\odot$ star. Therefore, the encounters we considered in this work with $r_{coll} \leq$100 AU can potentially form a binary system as a consequence of the disk capture.

Once the binary system is formed, subsequent accretion of the parental molecular core will harden the binary, triggering an orbital decay (Bate et al. 2002). Bonnell and Bate (2005) proposed that competitive accretion in a dense cluster naturally forms more massive and closer binaries. If we consider stars with 1 $M_\odot$ with disks of reasonable radii of $\sim$100 AU, collisions with r_{coll}=r_{disk} are expected to occur in 7×10^4 yr for a stellar velocity dispersion of $\sigma_* \sim 3$ km s^{-1} (Fig. A.1). Fig. 2.13 shows that the binary system, if located at the center of the OHC low-mass star cluster, can gather a mass of 5 $M_\odot$ via competitive accretion in $\sim$2-3$\times10^5$ yr. Therefore, in several 10^5 yr the final individual masses of the binary would be $\sim$6 $M_\odot$. Then, from Eq. A.8 we find that the continuous accretion onto the binary could reduce the semi-major axis of the orbit in a factor 0.005. Considering an initial semi-major axis a_i=100$-$1000 AU, a_f would then be 0.5-5 AU. These simple calculations are roughly consistent with the results from numerical simulations of Bonnell and Bate (2005) (see their Fig. 2), where the binaries forming in this way typically have very eccentric orbits with periastron separations comparable to the stellar radii, allowing mergers

in clusters with stellar densities of 10^6 stars pc^{-3}. The stellar density in the OHC is similar to this value, and the final semi-axis binary separation we estimated can be as low as tens of solar radii, which is slightly higher but on the order of the sum of the radius of two 6 $M_\odot$ stars with $\sim 10^5$ yr (Siess et al. 2000). This implies that a collision due to orbital decay in a binary system induced by accretion could occur in the OHC.

Whether such a merger leads to a more massive object is difficult to asses. However, we can compare our analysis with other works where stellar coalescence play a role in massive star formation (Davies et al. 2006 and Moeckel and Clarke 2011). The first work suggests that very high stellar densities (10^9 $M_\odot$ pc^3) are needed to form a 50 $M_\odot$ star through mergers in the adequate timescale. This is three orders of magnitude higher than what we found in OHC. However, as Davies et al. (2006) recognized in their work, this stellar density can decrease significantly if circumstellar disks or primordial binaries are considered. Indeed, Davies et al. (2006) showed that including circumstellar disks decreases the collision time (and the stellar density needed) by a factor up of 3-10, and that the presence of primordial binaries additionally decreases the stellar density by a factor of 3. In addition, these authors considered the formation of a 50 $M_\odot$-star by coalescence, while the most massive objects in the OHC region have masses of only $\sim$10 $M_\odot$. According to Fig. 5 in Davies et al. (2006), a star with 10 $M_\odot$ is formed in a time $\sim$2.5 shorter than a star with 50 $M_\odot$. Then, the stellar density presented in Davies et al. (2006) could be reduced by nearly 2 orders of magnitude, resulting in 10^7 $M_\odot$ pc^3. This density is still higher than what we found in the OHC, suggesting that coalescence cannot be considered a general process for building up massive stars. This is because to be effective it needs multiple stellar collisions (Davies et al. 2006). According to our analysis, a single merger could occur in the cluster evolution, but not many.

This also agrees very well with the recent work by Moeckel and Clarke (2011). They simulated an Orion-like cluster, assuming a stellar density of 2.5×10^4 stars pc^{-3}, and followed its evolution until 3 Myr, the approximate age of the cluster. Even with this relatively low stellar density, in two of their five runs they observed two stellar collisions involving binaries at the central and dense regions of the cluster. However, they concluded that an Orion-like cluster can be explained without many collisions. This is evidence against the need for collision to explain massive star formation. Furthermore, even when a collision is involved, Moeckel and Clarke (2011) found that the final mass is mainly determined by accretion growth. Bonnell and Bate (2005)

also showed that in collisions the mass accreted by accretion is generally higher than the mass directly gathered by the mergers.

In conclusion, coalescence certainly does not seem a common mechanism for building up massive stars. However, this does not directly rule out the possibility that it may work under certain circumstances, or that a stellar collision may occur in a massive star cradle, especially in regions with high stellar densities. In particular, there is enough evidence to make a stellar collision possible in the OHC. This is supported by the very high stellar density we found in our work ($\sim 10^6$ stars pc^{-3}). Whether this collision produced a massive star as a result of a stellar merger still remains unclear, and the current observations do not allow to resolve this controversial question. Moreover, given that other mechanisms such as competitive accretion (see Sect. 2.4.3) can explain massive star formation in the OHC, there is no need to invoke coalescence to build up massive stars.

2.6 Summary and conclusions

We have analyzed the distribution of PMS low-mass stars with X-ray emission in Orion observed by Chandra as a function of extinction, and calculated their stellar densities. Our results show that PMS low-mass stars cluster towards the three regions connected to massive stars: the Trapezium Cluster (TC), the Orion Hot Core (OHC), and the OMC1-S region. We derived PMS low-mass stellar densities of 10^5 stars pc^{-3} in the TC and OMC1-S, and 10^6 stars pc^{-3} in the OHC. These very high stellar densities and the close association between the low-mass star clusters with the regions where massive star formation has recently occurred (TC) or it is currently taking place (OHC and OMC1-S) suggest that not only dense gas is needed to form massive objects, but also a cluster of low-mass stars.

The X-ray observations show for the first time in the TC that low-mass stars with intermediate extinction are clustered towards the position of the most massive star θ^1 *Ori C*, which is surrounded by an envelope of non-extincted PMS low-mass stars. This 'envelope-core' structure is also supported from infrared and optical observations.

We proposed several scenarios for massive star formation in which the theories based on accretion (core accretion and competitive accretion) play different roles and the parental core presents different levels of fragmentation: i) low fragmentation and monolithic collapse; ii) intermediate fragmentation forming a cluster with stars with different masses; iii) high fragmentation, formation of a low-mass star cluster

and subsequent competitive accretion. We compared the predictions of each scenario with the findings of our analysis of the X-ray observations by COUP.

The first scenario, based on the classic core accretion theory does not explain the formation of a significant population of low-mass stars, contradicting the results presented in this chapter.

We showed that the second scenario (intermediate fragmentation) is not fully appropriate to explain our results. In this scenario fragmentation does not always produce more massive cores at the center of the parental clump. Therefore, we would not expect the trend for massive stars to form at the center of the clump that we observe in the TC. Moreover, the presence of a significant low-mass stellar population revealed by X-rays in the massive star cradles suggests that the level of fragmentation of the initial clump is high.

This led us to a third scenario, with higher fragmentation forming a low-mass stellar cluster. These ″stellar seeds″ can gather enough mass by competitive accretion, forming more massive stars at the cluster center. Therefore, the outcome of this scenario predicts our findings. Furthermore, we showed that the formation of massive stars in a region with the physical conditions measured in the OHC can be explained in terms of competitive accretion. Competitive accretion could also work in OMC1-S, with similar gas properties, and in the TC, which was denser at the moment when the stars were formed.

Finally, given that the stellar density in the OHC is one of the highest reported in the galaxy (1.30×10^6 stars pc^{-3}) and because there is much observational evidence that a violent process occurred in the region, we discuss the possibility of a coalescence event in the OHC stellar cluster. We conclude that although coalescence does not seem a common mechanism for building up massive stars, a single stellar merger may occur in the evolution of the cluster of the OHC, favored for the presence of disks, binaries, and accretion.

CHAPTER 3

The role of low-mass star clusters in forming massive stars in DR21

Abstract

In this chapter, we study the young low-mass PMS stellar population associated with the massive star-forming region DR21 by using archival X-ray Chandra observations and by complementing them with existing optical and IR surveys. The Chandra observations have revealed for the first time a new highly extincted population of PMS low-mass stars previously missed in observations at other wavelengths. The X-ray population exhibits three main stellar density peaks, coincident with the massive star-forming regions, being the DR21 clump the main peak. The cross-correlated X-ray/IR sample exhibits a radial "Spokes-like" stellar filamentary structure that extends from the DR21 clump towards the northeast. The near-IR data reveal a centrally peaked structure for the extinction, which exhibits its maximum in the DR21 clump and gradually decreases with the distance to the N-S ridge axis and to the cluster center. We find evidence of a global mass segregation in the low-mass stellar cluster, together with a stellar age segregation. While the youngest stars are still embedded in the N-S ridge, the more evolved stars spatially more distributed. The results are consistent with the scenario where an elongated overall potential well created by the whole low-mass stellar cluster funnels gas through filaments feeding stellar formation. In addition to the global gravitational well due to by the low-mass stellar cluster, smaller-scale local potential wells created by dense stellar subclusters of low-mass stars are privileged in the competition for the gas of the common reservoir, allowing the formation of more massive stars. We also discuss the possibility that a stellar collision in the very dense stellar cluster revealed by Chandra in the DR21 clump is the origin of the large-scale and highly-energetic outflow arising from this region.

3.1 Introduction

The DR21 massive star-forming region is located at 1.50 kpc (Rygl et al. 2012) and belongs to the Cygnus X molecular cloud. It harbors a massive and dense filament-shaped ridge (Chandler et al. 1993; Davis et al. 2007), forming part of a large-scale network of filamentary structures (Schneider et al. 2010). DR21 exhibits three main regions of massive star formation: i) the DR21 clump , where several ultra-compact (UC) HII regions are detected (Cyganowski et al. 2003); ii) the DR21(OH) hot molecular core (Chandler et al. 1993); and iii) the FIR 1/2/3 region (Chandler et al. 1993; Kumar et al. 2007).

A high energetic outflow has been detected in the DR21 clump (Garden et al. 1991; Smith et al. 2006; Davis et al. 2007), whose origin is still unclear. The outflow has been suggested to be powered by a massive protostar with a luminosity $\sim 10^{5-6}$ $L_{\odot}$ (Garden et al. 1991), which corresponds to a zero age main sequence (ZAMS) star with spectral types O7−O4 (Panagia 1973). However, such a massive star has not been detected so far (Cruz-González et al. 2007). Moreover, the luminosity of this object would exceed the total luminosity of the DR21 region of 10^5 $L_{\odot}$ (Harvey et al. 1977). Recently, Zapata et al. (2013) claimed that the outflow appears to have been produced by an explosive event.

In this chapter we present the results of X-ray Chandra observations of the massive star-forming region DR21. We complement these data with publicly available optical and near-IR and mid-IR observations. The chapter is organized as follow. In Sect. 3.2 we describe the data selection. We present the Chandra X-ray source catalog of the DR21 cluster obtained from the Chandra XAssist Source List archive, and discuss the source membership to the cluster, possible contamination and completeness. We also present the optical and IR catalogs used to complement the X-ray survey. In Sect. 3.3 we show the results of the cross-correlation between the Chandra catalog with the optical and IR catalogs, and study the spatial distribution, density, evolutionary stages and extinction of the stellar cluster. In Sect. 3.4 we discuss the implications of our results in the formation of the cluster and of the massive stars in the region. In view of the stellar population revealed by Chandra, in Sect. 3.5 we evaluate the possibility of a stellar merger as origin of the large-scale and highly-energetic outflow found in the DR21 clump. Finally, in Sect. 3.6 we summarize our findings.

Table 3.1: Chandra observing runs in the DR21 region.

Observing run	Date	Time exposure (ks)
07444	2007-08-22	48
08598	2007-11-27	20
09770	2007-11-29	19
09771	2007-12-02	9

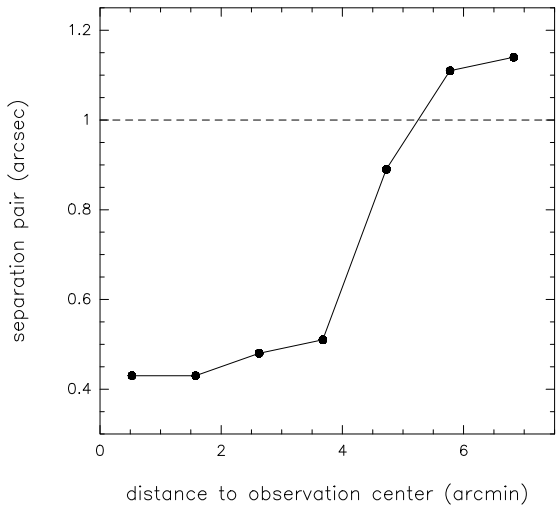

Figure 3.1: Average position separation of pair of counterparts when cross-correlating the 4 Chandra observing run samples two by two, as a function of the distance to the pointing center of the observation. The number of sources in each bin is 27, 41, 53, 11, 21 and 28, from lower to higher distances.

3.2 Data analysis

In our analysis we used archival stellar catalogs in X-rays, optical and IR wavelengths. We also made use of the Spitzer 4.6 μm and 8 μm images (Cygnus-X Legacy Project), and the SCUBA 850 μm data (Matthews et al. 2009).

3.2.1 Stellar catalogs

★ X-rays source catalog (Chandra)

Table 3.2: DR21 Chandra source catalog.

DR21-X number	RA (J2000)	DEC (J2000)	Counts	log L_X^a (erg s^{-1})	SDSS	UKIDSS	Spitzer SSTCYGX
1	20 39 0.04	42 19 36.8	36	30.89		J203900.04+421936.6	
2	20 39 0.60	42 19 36.9	9	30.27			
3	20 39 0.35	42 19 31.0	9	30.28		J203900.35+421931.7	
4	20 38 59.95	42 19 44.6	8	29.87			
5	20 39 0.92	42 19 41.4	8	30.22			
6	20 38 59.55	42 19 33.3	9	30.61			
7	20 39 1.30	42 19 36.5	12	30.43			
8	20 39 1.11	42 19 44.5	45	30.98		J203901.11+421944.3	
9	20 38 59.09	42 19 39.5	12	30.03		J203859.08+421939.5	
10	20 39 0.12	42 19 51.6	24	30.31			
11	20 38 59.60	42 19 53.4	13	30.45		J203859.61+421953.2	J203859.65+421952.9
12	20 39 1.02	42 19 54.3	5	30.10		J203901.01+421954.4	
13	20 39 0.45	42 19 59.0	20	30.63			
14	20 39 1.19	42 19 18.9	7	30.21			
15	20 39 1.21	42 19 18.6	84	30.85			
16	20 39 1.68	42 19 54.9	7	30.53			
17	20 39 1.37	42 19 59.1	9	30.64			
18	20 39 2.39	42 19 53.6	10	30.36		J203902.39+421953.0	
19	20 39 1.80	42 19 13.6	4	30.32			
20	20 39 2.59	42 19 25.0	11	29.98			
21	20 38 58.01	42 19 54.8	6	30.10		J203858.02+421954.1	
22	20 39 1.67	42 19 9.2	14	30.08			
23	20 38 59.36	42 20 11.6	19	30.22		J203859.34+422011.9	
24	20 38 58.36	42 20 9.3	22	31.00		J203858.40+422009.7	
25	20 39 0.19	42 20 16.2	8	29.84			
26	20 38 59.81	42 18 58.3	32	30.83		J203859.82+421858.2	J203859.82+421858.2
27	20 38 59.15	42 18 59.5	24	31.02		J203859.18+421859.5	
28	20 39 3.65	42 19 23.5	9	30.27		J203903.68+421923.0	J203903.68+421923.0
29	20 38 59.97	42 20 18.0	10	30.35		J203859.94+422018.1	
30	20 39 4.04	42 19 35.7	7	30.16		J203904.08+421935.6	J203904.08+421935.6
31	20 39 0.11	42 18 54.8	28	30.38			

Continues on next page

Table 3.2 – Continued from previous page

DR21-X number	RA (J2000)	DEC (J2000)	Counts	log L_X^a (erg s^{-1})	SDSS	UKIDSS	Spitzer SSTCYGX
32	20 39 2.03	42 20 21.4	10	30.30		J203901.99+422021.4	J203902.00+422021.4
33	20 39 4.22	42 19 58.9	47	30.84		J203904.23+421958.8	J203904.24+421958.5
34	20 39 3.43	42 20 11.6	21	30.31		J203903.40+422011.8	
35	20 39 1.78	42 20 29.0	15	30.52	J203901.78+422028.9	J203901.77+422028.9	J203903.40+422011.7
36	20 39 1.77	42 18 40.2	10	29.93		J203901.78+421840.2	J203901.77+421840.0
37	20 39 5.51	42 19 50.7	6	30.14		J203905.53+421950.2	
38	20 39 2.79	42 18 42.7	9	30.51			
39	20 39 3.24	42 18 44.1	7	30.44			J203903.24+421843.9
40	20 38 59.04	42 20 40.4	167	31.14		J203859.03+422040.5	J203859.05+422040.5
41	20 39 6.14	42 19 19.3	6	30.11		J203906.12+421919.4	
42	20 39 4.70	42 18 49.0	6	29.70			
43	20 39 5.48	42 20 15.5	5	30.41			
44	20 38 58.61	42 20 48.3	7	29.80		J203858.65+422048.4	J203858.67+422048.4
45	20 39 0.83	42 20 50.7	5	30.05		J203900.81+422050.6	J203900.82+422050.5
46	20 39 4.87	42 20 33.1	7	29.81		J203904.85+422033.4	J203904.85+422033.5
47	20 39 5.41	42 20 27.0	4	30.00			
48	20 38 58.26	42 20 51.5	11	29.97			
49	20 38 55.43	42 20 37.5	5	30.41	J203855.42+422037.5	J203855.42+422037.6	J203855.44+422037.5
50	20 38 57.96	42 18 20.9	3	30.01	J203858.00+421820.6	J203858.02+421820.8	J203858.01+421820.7
51	20 38 55.11	42 18 36.4	10	30.32		J203855.10+421836.1	J203855.11+421836.2
52	20 39 7.91	42 19 59.8	39	30.93		J203907.90+421959.6	J203907.91+421959.5
53	20 39 1.66	42 18 5.0	12	30.51			
54	20 39 5.77	42 20 55.9	19	30.63		J203905.80+422055.6	
55	20 38 52.29	42 18 43.9	5	30.06	J203852.26+421843.5	J203852.26+421843.6	J203852.29+421843.5
56	20 38 58.13	42 17 56.3	13	30.11		J203858.09+421756.1	J203858.10+421756.2
57	20 38 50.53	42 19 22.4	11	30.37		J203850.53+421922.3	J203850.54+421922.5
58	20 39 2.23	42 17 50.5	38	30.51		J203902.26+421750.5	J203902.26+421750.6
59	20 39 6.76	42 21 1.7	7	29.80		J203906.75+422101.8	J203906.78+422101.8
60	20 39 7.40	42 20 55.7	13	30.78		J203907.39+422055.3	J203907.41+422055.2
61	20 38 59.11	42 21 28.7	7	29.81			
62	20 39 10.25	42 19 2.8	9	29.91	J203910.26+421902.7	J203910.26+421902.8	J203910.27+421902.9
63	20 39 11.06	42 19 55.0	3	30.25			

Continues on next page

Table 3.2 – Continued from previous page

DR21-X number	RA (J2000)	DEC (J2000)	Counts	log L_X^a (erg s^{-1})	SDSS	UKIDSS	Spitzer SSTCYGX
64	20 39 9.64	42 20 42.7	26	30.40		J203909.64+422043.0	J203909.66+422043.0
65	20 39 5.56	42 17 46.8	17	30.16		J203905.56+421746.7	J203905.55+421746.7
66	20 38 54.18	42 21 25.9	4	30.02	J203854.13+422125.4	J203854.13+422125.5	J203854.16+422125.3
67	20 39 8.17	42 21 11.7	10	29.94		J203908.17+422112.1	J203908.20+422112.1
68	20 38 50.03	42 18 34.4	3	30.23		J203849.98+421833.9	J203849.99+421833.7
69	20 39 11.76	42 19 4.4	23	30.69		J203911.76+421904.1	J203911.76+421904.0
70	20 38 55.39	42 17 35.0	6	29.77			
71	20 39 7.87	42 17 52.7	9	29.91			J203907.88+421752.6
72	20 38 55.94	42 21 47.2	26	30.73		J203855.95+422147.0	J203855.94+422147.2
73	20 38 50.48	42 18 9.7	17	30.15	J203850.46+421809.9	J203850.46+421809.7	J203850.49+421810.0
74	20 39 1.89	42 21 57.2	15	30.13		J203901.93+422157.2	
75	20 38 59.97	42 21 59.4	3	30.27			J203859.95+422159.7
76	20 39 2.34	42 21 58.7	33	30.47			
77	20 39 2.16	42 22 0.0	5	30.08		J203902.16+422159.1	
78	20 39 2.91	42 21 59.4	15	30.18		J203902.85+422200.1	J203902.87+422200.2
79	20 38 50.20	42 18 2.8	7	29.77			
80	20 38 55.35	42 21 54.0	21	30.28	J203855.29+422154.4	J203855.30+422154.4	J203855.30+422154.4
81	20 38 57.35	42 17 10.8	19	30.22	J203857.35+421710.9	J203857.35+421710.9	J203857.36+421711.1
82	20 39 1.02	42 22 7.6	4	30.39			J203901.01+422207.6
83	20 38 54.42	42 21 54.0	2	00.00	J203854.40+422153.7	J203854.42+422153.7	J203854.44+422153.5
84	20 38 46.73	42 19 6.6	4	30.35	J203846.72+421906.5	J203846.72+421906.5	J203846.75+421906.2
85	20 39 13.88	42 19 9.1	15	30.52	J203913.87+421909.1	J203913.87+421909.1	J203913.86+421909.3
86	20 39 8.03	42 17 27.8	8	30.26		J203908.05+421727.7	J203908.07+421727.6
87	20 39 14.33	42 19 56.1	6	29.71			
88	20 38 53.69	42 22 2.1	16	30.89	J203853.66+422201.6	J203853.66+422201.7	J203853.67+422201.6
89	20 39 3.82	42 16 58.2	154	31.12		J203903.81+421658.2	J203903.82+421658.3
90	20 39 13.22	42 18 17.9	21	30.30	J203913.20+421817.9	J203913.20+421818.0	J203913.19+421817.9
91	20 38 52.33	42 21 57.0	12	30.46	J203852.32+422156.9	J203852.33+422157.0	J203852.35+422157.1
92	20 39 10.50	42 21 39.3	9	29.90		J203910.54+422139.0	J203910.57+422138.8
93	20 39 4.90	42 22 16.5	5	30.43		J203904.90+422216.8	J203904.89+422216.7
94	20 39 7.03	42 22 8.1	31	30.42	J203907.03+422208.2	J203907.03+422208.2	J203907.02+422208.4
95	20 38 46.38	42 18 26.8	6	30.12		J203846.33+421826.7	J203846.33+421826.7

Continues on next page

Table 3.2 – Continued from previous page

DR21-X number	RA (J2000)	DEC (J2000)	Counts	log L_X^a (erg s^{-1})	SDSS	UKIDSS	Spitzer SSTCYGX
96	20 39 15.67	42 19 48.1	9	29.89			
97	20 38 50.79	42 17 21.6	16	30.55	J203850.79+421721.5	J203850.78+421721.5	J203850.81+421721.6
98	20 38 59.34	42 22 29.2	12	30.44			J203859.31+422229.1
99	20 39 0.94	42 22 31.8	9	29.92			J203900.90+422231.9
100	20 38 52.37	42 22 14.6	3	30.24			
101	20 39 13.72	42 21 19.0	23	30.33		J203913.72+422119.5	J203913.70+422119.5
102	20 39 10.43	42 22 5.7	9	30.29		J203910.43+422205.6	J203910.44+422205.6
103	20 38 53.04	42 22 20.1	9	29.92			
104	20 39 12.13	42 21 42.2	11	29.99		J203912.12+422142.5	J203912.10+422142.7
105	20 39 9.62	42 17 8.6	5	30.07	J203909.62+421708.7	J203909.63+421709.0	
106	20 38 53.07	42 22 21.6	3	00.00	J203853.07+422221.6	J203853.06+422221.5	J203853.07+422221.5
107	20 38 59.61	42 22 40.0	20	30.24			J203859.64+422239.9
108	20 38 54.83	42 22 30.8	4	30.35		J203854.85+422230.7	J203854.82+422230.7
109	20 39 16.77	42 19 19.2	36	30.49	J203916.74+421919.5	J203916.74+421919.4	J203916.76+421919.6
110	20 39 3.33	42 22 38.3	7	30.19		J203903.35+422238.1	J203903.37+422238.3
111	20 38 58.65	42 22 42.3	14	30.83		J203858.66+422241.7	J203858.69+422241.7
112	20 38 57.18	42 22 40.5	33	30.46	J203857.17+422241.0	J203857.17+422241.0	J203857.22+422240.9
113	20 39 0.90	42 22 43.6	320	31.18	J203900.90+422243.7	J203900.90+422243.7	J203900.90+422243.8
114	20 39 10.43	42 22 5.7	18	30.93			J203910.44+422205.6
115	20 38 55.66	42 22 37.2	14	30.48		J203855.63+422236.9	J203855.65+422236.8
116	20 38 52.78	42 22 25.2	8	30.27	J203852.79+422224.8	J203852.78+422224.8	J203852.80+422225.0
117	20 39 2.45	42 16 29.8	19	30.98	J203902.47+421629.7	J203902.47+421629.7	J203902.48+421629.9
118	20 38 42.95	42 19 42.8	16	30.14	J203843.01+421942.6	J203843.02+421942.6	J203843.02+421942.5
119	20 38 58.60	42 22 50.6	18	30.20		J203858.60+422250.6	J203858.63+422250.8
120	20 38 56.85	42 22 47.9	66	30.76	J203856.84+422248.1	J203856.84+422248.3	J203856.85+422248.3
121	20 39 0.42	42 22 52.3	20	30.24			
122	20 38 50.96	42 22 25.0	3	30.25			
123	20 39 8.87	42 16 45.5	5	30.04			
124	20 39 13.76	42 21 47.2	13	30.06		J203913.75+422146.8	J203913.78+422146.9
125	20 39 3.99	42 22 55.9	7	29.84		J203903.96+422256.3	J203903.96+422256.4
126	20 39 2.42	42 23 0.0	13	30.06		J203902.44+422259.7	J203902.46+422259.9
127	20 38 59.82	42 23 6.2	10	30.38			

Continues on next page

Table 3.2 – Continued from previous page

DR21-X number	RA (J2000)	DEC (J2000)	Counts	log L_X^a (erg s^{-1})	SDSS	UKIDSS	Spitzer SSTCYGX
128	20 38 50.05	42 16 40.4	9	30.65	J203850.02+421640.1	J203850.02+421640.0	J203850.03+421640.1
129	20 38 41.95	42 18 42.0	11	30.36			
130	20 39 14.52	42 21 57.2	7	29.81		J203914.51+422157.7	J203914.51+422157.6
131	20 39 11.67	42 16 46.1	6	29.73			
132	20 38 41.06	42 19 52.7	26	30.73	J203841.03+421952.5	J203841.05+421952.5	J203841.06+421952.5
133	20 38 53.47	42 22 58.6	5	30.11			
134	20 39 2.69	42 16 4.2	15	30.91	J203902.71+421604.0	J203902.71+421603.9	J203902.70+421604.1
135	20 39 15.77	42 17 28.2	8	29.84			
136	20 38 42.35	42 21 3.8	10	29.95	J203842.30+422104.3	J203842.32+422104.5	J203842.32+422104.6
137	20 38 54.91	42 23 6.2	19	30.28		J203854.91+422306.8	J203854.92+422306.9
138	20 38 42.29	42 21 4.7	13	30.47	J203842.31+422104.5	J203842.32+422104.5	J203842.32+422104.6
139	20 39 1.89	42 23 14.9	7	29.81	J203901.92+422315.5	J203901.91+422315.6	J203901.92+422315.8
140	20 38 53.83	42 23 4.2	6	30.17	J203853.78+422304.0	J203853.77+422304.0	J203853.75+422303.9
141	20 39 20.00	42 19 13.0	180	31.19		J203919.97+421913.1	J203920.01+421913.2
142	20 38 57.82	42 15 58.4	14	30.49		J203857.80+421557.9	J203857.83+421557.9
143	20 38 54.01	42 23 7.3	15	30.12	J203854.03+422307.7	J203854.02+422307.8	J203854.04+422307.9
144	20 39 19.08	42 20 52.4	7	29.09		J203919.09+422052.7	
145	20 38 40.66	42 18 53.1	3	00.00			
146	20 39 6.70	42 16 7.5	8	29.86			
147	20 39 11.95	42 16 35.8	75	30.82	J203911.95+421636.0	J203911.94+421636.0	J203911.93+421636.1
148	20 39 19.54	42 20 42.5	6	29.77		J203919.52+422042.7	J203919.52+422043.0
149	20 39 15.58	42 17 11.1	193	31.13	J203915.58+421711.1	J203915.58+421711.1	J203915.60+421711.5
150	20 39 15.96	42 17 12.0	179	31.66		J203915.96+421711.7	
151	20 38 41.23	42 20 56.8	9	29.90			
152	20 39 14.17	42 16 51.9	31	30.43	J203914.15+421652.0	J203914.16+421652.1	J203914.17+421652.1
153	20 39 10.67	42 16 19.3	19	30.22	J203910.65+421619.9	J203910.65+421619.5	J203910.66+421619.5
154	20 38 44.56	42 22 9.9	24	30.36		J203844.55+422209.3	
155	20 39 13.30	42 22 50.0	7	29.82			
156	20 39 12.98	42 16 21.9	7	29.83		J203913.02+421621.4	J203913.05+421621.7
157	20 39 21.79	42 20 39.5	21	30.27	J203921.77+422039.6	J203921.77+422039.6	J203921.77+422039.9
158	20 39 5.62	42 15 36.0	22	30.69	J203905.64+421535.6	J203905.63+421535.5	J203905.62+421535.4
159	20 39 7.42	42 23 35.2	28	30.78		J203907.42+422334.8	J203907.43+422334.9

Continues on next page

Table 3.2 – Continued from previous page

DR21-X number	RA (J2000)	DEC (J2000)	Counts	log L_X^a (erg s^{-1})	SDSS	UKIDSS	Spitzer SSTCYGX
160	20 38 37.57	42 19 13.9	13	30.49	J203837.56+421913.9	J203837.57+421913.8	J203837.57+421913.9
161	20 38 40.61	42 17 26.2	14	30.49			
162	20 38 37.22	42 19 27.4	7	29.82			
163	20 38 39.64	42 17 41.2	20	30.66	J203839.63+421741.2	J203839.62+421741.1	J203839.64+421741.0
164	20 39 0.90	42 23 54.3	14	30.11	J203900.85+422353.7	J203900.85+422353.6	J203900.90+422353.9
165	20 38 57.34	42 15 21.7	2	30.12			
166	20 39 21.53	42 17 51.1	5	30.09		J203921.54+421751.3	J203921.52+421751.4
167	20 39 4.71	42 15 21.1	9	29.93		J203904.68+421520.8	J203904.69+421520.7
168	20 38 41.12	42 16 57.8	7	29.83			
169	20 39 16.31	42 22 56.6	32	30.45		J203916.30+422256.5	J203916.30+422256.2
170	20 39 4.86	42 15 13.5	140	31.44	J203904.86+421513.4	J203904.86+421513.4	J203904.85+421513.5
171	20 39 17.83	42 22 43.5	12	30.05		J203917.76+422243.1	J203917.76+422243.3
172	20 39 6.56	42 23 58.9	4	30.40			
173	20 39 21.36	42 22 0.1	5	30.10	J203921.40+422159.7	J203921.40+422159.6	J203921.40+422159.7
174	20 39 24.77	42 18 58.9	120	31.02		J203924.76+421859.1	J203924.77+421858.9
175	20 38 38.91	42 21 58.8	8	29.88	J203838.91+422157.9	J203838.89+422157.9	
176	20 39 2.92	42 24 14.8	22	30.29		J203902.89+422414.9	
177	20 39 17.51	42 23 0.4	7	30.23	J203917.53+422300.1	J203917.54+422300.0	J203917.55+422300.1
178	20 39 18.79	42 22 48.1	7	30.23		J203918.72+422248.1	J203918.72+422248.1
179	20 39 12.32	42 15 28.1	3	30.25		J203912.31+421527.2	
180	20 39 24.97	42 18 21.1	4	30.01			
181	20 38 36.45	42 21 25.9	8	29.91	J203836.50+422125.8	J203836.51+422125.9	J203836.49+422125.9
182	20 39 0.51	42 24 22.9	9	29.96			
183	20 39 23.96	42 17 46.0	7	29.84			
184	20 39 26.00	42 18 50.2	15	30.14		J203926.00+421850.1	J203926.01+421850.1
185	20 39 8.02	42 15 0.2	8	30.28	J203907.98+421459.5	J203907.98+421459.5	J203908.00+421459.5
186	20 39 6.37	42 24 21.4	6	29.74			
187	20 38 54.97	42 24 25.7	8	29.86			
188	20 39 25.80	42 20 56.5	24	30.32	J203925.81+422056.8	J203925.79+422056.9	J203925.78+422057.0
189	20 38 40.30	42 22 51.5	7	29.83			
190	20 38 45.73	42 23 44.4	8	30.28			
191	20 38 33.70	42 20 19.1	6	30.53			

Continues on next page

Table 3.2 – Continued from previous page

DR21-X number	RA (J2000)	DEC (J2000)	Counts	log L_X^a (erg s^{-1})	SDSS	UKIDSS	Spitzer SSTCYGX
192	20 39 0.55	42 24 35.0	26	30.79			
193	20 39 0.26	42 24 36.8	17	30.58			
194	20 38 57.84	42 14 37.6	29	30.45	J203857.84+421437.7	J203857.83+421437.6	J203857.80+421437.5
195	20 38 33.78	42 18 30.5	8	29.87	J203833.86+421830.8		J203833.85+421831.0
196	20 39 15.56	42 15 28.2	6	30.16			J203915.57+421529.0
197	20 38 51.45	42 24 24.4	8	29.89			
198	20 38 41.13	42 15 56.0	18	30.24			
199	20 38 47.72	42 15 0.5	9	29.94			
200	20 39 19.86	42 23 23.2	6	30.16			
201	20 38 46.61	42 24 16.2	7	29.80			
202	20 39 2.07	42 24 54.1	2	30.11		J203902.13+422454.0	
203	20 39 22.10	42 16 10.0	6	29.79	J203922.12+421610.9		
204	20 39 2.95	42 24 55.4	13	30.10			
205	20 39 23.92	42 16 34.5	29	30.46		J203923.95+421634.8	J203923.94+421635.0
206	20 39 28.30	42 20 53.4	9	29.94	J203928.31+422054.3	J203928.30+422054.3	J203928.31+422054.3
207	20 38 32.94	42 17 52.0	7	29.88			
208	20 39 2.16	42 24 59.3	7	30.24			
209	20 39 13.67	42 24 26.6	7	29.84			
210	20 38 58.55	42 25 2.5	6	30.20			
211	20 39 29.60	42 19 6.8	6	29.79			
212	20 39 8.66	42 24 51.0	23	30.72		J203908.67+422450.1	J203908.68+422450.1
213	20 38 44.18	42 24 12.4	19	30.96	J203844.09+422412.6		J203844.10+422412.6
214	20 38 36.45	42 22 52.2	7	29.80			
215	20 39 21.36	42 23 28.7	14	30.10		J203921.33+422328.7	J203921.33+422328.9
216	20 39 24.84	42 16 32.6	6	29.78			
217	20 38 41.10	42 15 24.3	8	29.87			
218	20 39 24.25	42 16 21.3	12	30.07		J203924.25+421621.1	J203924.24+421621.2
219	20 39 16.95	42 24 15.8	5	30.09			
220	20 38 31.34	42 21 13.3	8	30.27			
221	20 38 31.19	42 18 1.6	24	30.72	J203831.17+421801.7	J203831.17+421801.7	J203831.17+421801.8
222	20 39 1.52	42 25 25.9	10	29.99		J203901.51+422526.2	J203901.52+422526.3
223	20 38 54.25	42 25 21.6	9	29.93	J203854.26+422521.4	J203854.26+422521.5	

Continues on next page

Table 3.2 – Continued from previous page

DR21-X number	RA (J2000)	DEC (J2000)	Counts	log L_X^a (erg s^{-1})	SDSS	UKIDSS	Spitzer SSTCYGX
224	20 39 18.17	42 14 48.4	8	29.87			
225	20 38 54.75	42 13 48.1	53	30.78	J203854.76+421348.2	J203854.77+421348.2	J203854.78+421348.3
226	20 39 3.64	42 25 29.6	67	30.78		J203903.72+422529.6	J203903.72+422529.7
227	20 39 3.48	42 25 30.4	7	30.27			
228	20 38 39.14	42 15 7.3	6	29.80			
229	20 38 30.40	42 21 53.4	5	30.07			
230	20 38 40.03	42 24 17.1	170	31.57	J203839.97+422416.9	J203839.96+422416.9	J203839.98+422417.0
231	20 38 29.45	42 21 28.1	7	30.53			
232	20 38 29.37	42 21 29.9	26	30.76	J203829.37+422129.6	J203829.37+422129.6	J203829.37+422129.5
233	20 38 44.09	42 14 21.6	20	30.67	J203844.08+421421.8	J203844.08+421421.8	J203844.07+421421.7
234	20 38 33.84	42 16 0.1	6	29.82	J203833.79+421600.1	J203833.80+421600.4	J203833.80+421600.5
235	20 39 4.02	42 25 40.1	22	30.32		J203904.05+422540.4	
236	20 38 40.01	42 14 46.0	7	29.80			
237	20 38 54.96	42 25 41.3	17	30.21			
238	20 38 27.25	42 20 22.9	22	30.32			
239	20 39 5.40	42 25 42.4	55	30.70			
240	20 38 44.74	42 25 8.2	9	30.36			
241	20 39 21.83	42 24 29.4	10	30.01			
242	20 38 32.82	42 23 22.9	13	30.47	J203832.85+422322.6	J203832.85+422322.7	J203832.84+422322.6
243	20 39 34.13	42 20 26.2	11	30.01		J203934.13+422026.2	J203934.15+422026.4
244	20 38 25.99	42 20 11.2	9	30.30			
245	20 39 33.88	42 20 58.6	8	29.91			
246	20 39 12.97	42 13 42.8	105	31.24	J203912.96+421342.7	J203912.97+421342.6	J203912.98+421342.7
247	20 39 27.61	42 15 43.3	38	30.94		J203927.57+421543.3	J203927.59+421543.1
248	20 38 48.69	42 13 34.6	8	29.93			
249	20 39 34.24	42 18 14.2	15	30.15	J203934.21+421813.7	J203934.20+421813.7	J203934.23+421813.6
250	20 38 39.51	42 24 48.8	8	30.31			
251	20 39 11.01	42 25 47.4	16	30.57			
252	20 39 23.36	42 14 45.3	5	30.11			
253	20 38 41.92	42 25 11.8	6	30.18			
254	20 38 28.65	42 22 35.7	9	29.96	J203828.64+422235.2	J203828.65+422235.3	J203828.66+422235.2
255	20 38 48.24	42 25 53.1	27	30.40			

Continues on next page

Table 3.2 – Continued from previous page

DR21-X number	RA (J2000)	DEC (J2000)	Counts	log L_X^a (erg s^{-1})	SDSS	UKIDSS	Spitzer SSTCYGX
256	20 38 26.00	42 21 46.8	3	29.90			
257	20 39 27.22	42 24 6.8	6	29.78			
258	20 38 43.64	42 13 37.7	9	30.31	J203843.64+421337.3	J203843.64+421337.2	J203843.64+421337.4
259	20 38 30.16	42 15 46.5	5	30.10			
260	20 39 24.04	42 24 51.4	26	30.39	J203924.05+422451.4	J203924.05+422451.4	J203924.06+422451.4
261	20 39 24.18	42 24 50.5	6	30.19			
262	20 39 17.49	42 13 33.9	4	30.17			
263	20 39 7.66	42 26 20.1	5	30.11			
264	20 38 31.42	42 15 17.0	12	30.07			J203831.41+421517.8
265	20 38 31.24	42 15 17.3	9	30.35			
266	20 39 25.48	42 14 28.3	51	30.73		J203925.51+421428.7	J203925.51+421428.7
267	20 39 36.23	42 17 14.9	45	30.62		J203936.27+421715.2	J203936.27+421715.1
268	20 39 10.20	42 12 42.2	9	29.95			
269	20 39 27.33	42 14 30.3	8	30.27		J203927.32+421430.9	
270	20 39 27.22	42 14 28.2	20	30.28	J203927.22+421428.2	J203927.22+421428.2	J203927.22+421428.4
271	20 39 38.24	42 18 4.9	7	30.25		J203938.26+421804.6	
272	20 39 2.31	42 26 48.6	12	30.46		J203902.32+422648.3	J203902.31+422648.4
273	20 39 16.56	42 26 10.2	9	30.34	J203916.53+422609.4	J203916.52+422609.7	J203916.55+422609.5
274	20 39 27.35	42 24 48.7	5	30.13			
275	20 38 38.97	42 25 40.2	8	29.88			
276	20 39 23.55	42 13 48.4	10	29.98			
277	20 38 25.78	42 16 5.9	28	30.43	J203825.81+421605.6	J203825.81+421605.5	J203825.82+421605.6
278	20 38 31.40	42 14 28.2	14	30.17	J203831.42+421428.8	J203831.42+421428.8	J203831.44+421428.8
279	20 39 15.95	42 12 47.5	15	30.16			
280	20 38 53.52	42 12 17.4	9	29.96			
281	20 39 23.68	42 13 32.5	154	31.17	J203923.71+421331.8	J203923.72+421331.8	J203923.73+421331.9

[a] X-ray luminosity not corrected from extinction.

We used the catalog of X-ray sources presented in the Chandra XAssist Source List archive (CXOXASSIST[1], Ptak and Griffiths 2003). This database provides Chandra data that have been automatically reduced for sources with sufficient counts. The DR21 region was monitored in four observing runs between August and December 2007, with net exposure times between 48 and 9 ks (Table 3.1), with the Advanced CCD Imaging Spectrometer (ACIS) onboard the Chandra X-ray Observatory. The ACIS-I array, consisting of four X-ray CCDs, covered a full region of 17.4' × 17.4', which comprises the full region of DR21. The telescope position of the field target was $\mathrm{RA}_{J2000} = 20^h\ 39^m\ 0.70^s$ and $\mathrm{DEC}_{J2000} = 42^\circ\ 18'\ 56.8''$. The Chandra point-spread function at the on-axis position is ∼0.5". For source detection, the CXOXASSIST catalog used a wavelet transform detection algorithm implemented as the WAVDETECT program within the Chandra Interactive Analysis of Observations (CIAO) package version 4.3.0. with a threshold significance of 10^{-6}. Due to intrinsic X-ray variability of PMS stars (expected to be the vast majority of the X-ray sample, see Getman et al. 2005a), not all sources were detected in the 4 observing runs. Therefore, to obtain a complete catalog, we have cross-correlated the samples from the 4 different runs. We have estimated the relative positional error of the sources cross-correlating the runs two by two, and calculating the separation between pair of counterparts within separations from 0" to 4". In Fig. 3.1 we plot the average separation as a function of the distance to the center of the observation. As expected, the positional error increases with the off-axis distance: remains below 1" for distances < 5', and below 1.2" in the outer parts of the region studied in this chapter. Therefore, we have considered the same object those sources from different runs that falls within 1" for distances < 5' and within 1.5" for distances >5'[2]. In the case of objects observed in several runs, since some X-ray variability is present between epochs, we selected the observation with better signal-to-noise ratio[3].

In this chapter we focus our analysis on a region with a radius of 7.5' around the center of DR21, obtaining a final catalog with 281 X-ray sources. The spatial distribution of the full X-ray sample is shown in Fig. 3.2. We present the list of sources in Table 3.2, with their coordinates, number of counts and luminosities (not

[1] http://heasarc.gsfc.nasa.gov/W3Browse/chandra/cxoxassist.html

[2] We note that this cross-correlation provides properly the positions of the Chandra X-ray source catalog of the region, which is the interest for this work. However, for a rigorous derivation of the physical X-ray parameters of the sources (which is not the focus of this work), a deeper image resulting for sum of the 4 observations runs would be more appropriate.

[3] The values for signal-to-noise ratio have been determined in terms of the equivalent number of background fluctuations, defined as the net counts in the source over the square root of the background counts.

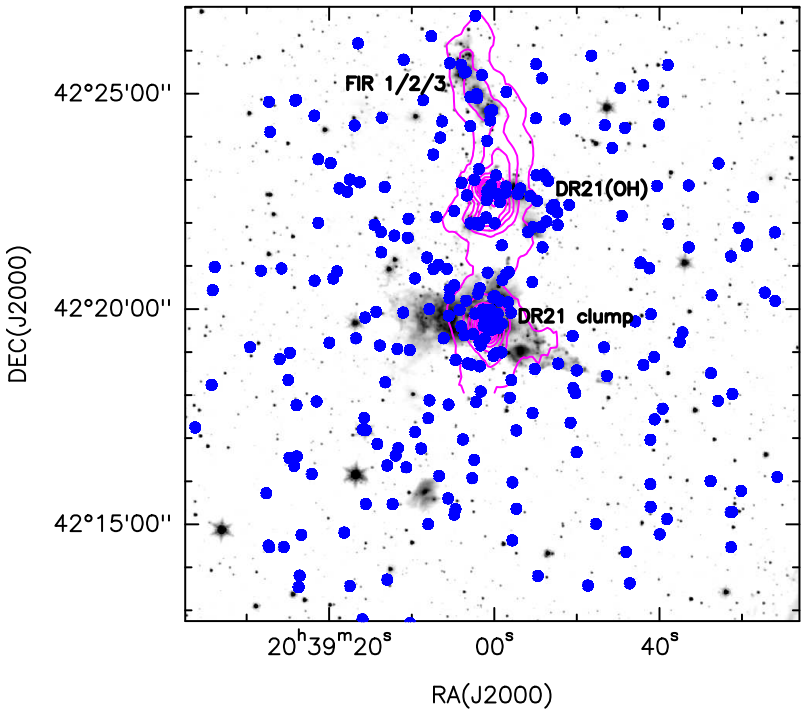

Figure 3.2: Spatial distribution of the X-ray Chandra catalog of the DR21 cluster (blue dots). The background image is the 4.6 μm Spitzer image, and magenta contours correspond to dust emission detected by SCUBA at 850 μm (Matthews et al. 2009). The approximate size of the region shown is 6 pc $\times$ 6 pc.

corrected by extinction). The luminosities in the 0.3 to 8 keV energy range have been calculated by using $L_X = 4\pi\ d^2\ F_X$, where d is the distance to the region and F_X has been obtained from CXOXASSIST[4].

★ Optical source catalog (SDSS) and IR source catalogs (UKIDSS and Spitzer)

We complemented the X-ray source catalog with the optical catalog provided by the Sloan Digital Sky Survey (SDSS, data release 9[5]), and with two archival infrared (IR) surveys: i) the UKIDSS (UKIRT Infrared Deep Sky Survey, Lawrence et al. 2007) Galactic Plane Survey (GPS, data release 6, Ukidss 2012), and ii) Spitzer Space telescope catalog provided by the Cygnus-X Legacy survey [6,7]. The UKIDSS survey observed the region at J (1.25 μm), H (1.65 μm) and K (2.2 μm) bands with the Wide Field Camera (WFCAM) on the United Kingdom Infrared Telescope (UKIRT), with typical 90% completeness limits in uncrowded fields of K=18.0, H=18.75 and J=19.5. The Infrared Array Camera (IRAC) onboard the Spitzer telescope observed in band 1 (3.6 μm), band 2 (4.5 μm), band 3 (5.8 μm) and band 4 (8.0 μm), with 90% completeness limits in uncrowded fields of 14.98, 14.87, 13.82, and 12.60, respectively (Beerer et al. 2010). We cross-checked the DR21 X-ray catalog with these catalogs, searching counterparts for the X-ray sources within a radius of 1". In the case that two sources fall within this radius, we selected the best match. In Table 3.2 we also present the association between X-ray and SDSS, UKIDSS and Spitzer sources. In Fig. 3.3 we show an scheme summarizing the subsamples resulting from the cross-correlation with the different catalogs.

3.2.2 Foreground/background contamination

While foreground and background galactic sources produce significant contamination in the IR studies of young clusters, X-ray surveys have the advantage of presenting very little galactic contamination, because PMS stars emit X-rays at levels 10-10^4 times higher than foreground/background main-sequence stars (Preibisch and Feigel-

[4] The values for the X-ray luminosities presented in CXOXASSIST are calculated from a power-law model with a default slope of 1.8. Although little changes are expected, we note that for a more rigorous derivation of the luminosities of the stars (which is out of the scope of this work), a two-temperatures plasma model would be more adequate (see Getman et al. 2005c).

[5] http://www.sdss.org/

[6] http://irsa.ipac.caltech.edu/cgi-bin/Gator/nph-scan?projshort=SPITZER

[7] http://www.cfa.harvard.edu/cygnusX/

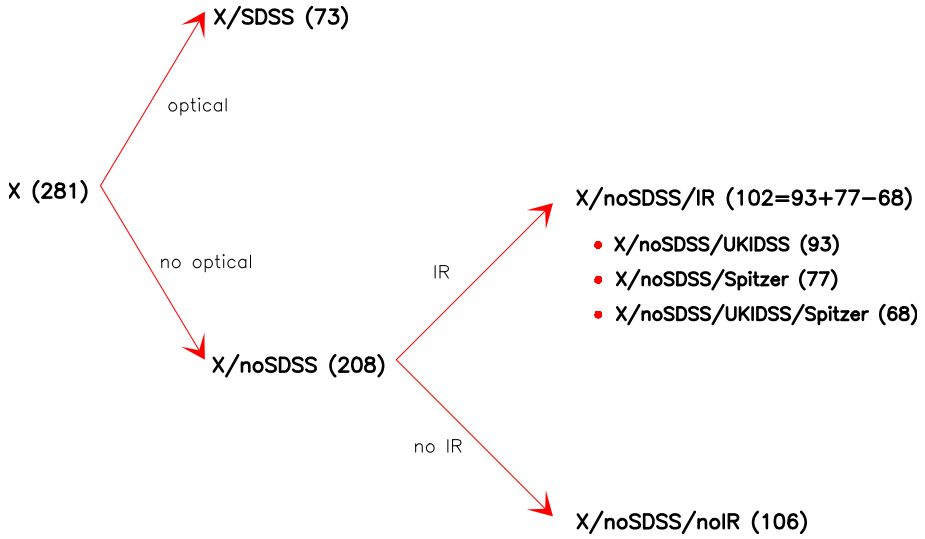

Figure 3.3: Scheme of the different samples and subsamples we used in this chapter, along with the number of sources in each group.

son 2005). Several works (Getman et al. 2005c; Townsley et al. 2011; Mucciarelli et al. 2011) have shown that X-ray studies are very effective in revealing the embedded young stellar population in clusters, discriminating the PMS cluster members from unrelated older stars. Besides the effect of the sensitivity limit, which will be discussed in Sect. 3.2.3, this is mainly because IR surveys are affected by a much higher foreground/background contamination. However, X-ray sources could still be confused with extragalactic (EG) sources. In that case, other criteria, like spatial distribution, must be used to distinguish between cloud members and unrelated sources.

To discriminate the embedded young stellar population from foreground stars, we cross-checked the X-ray source catalog with the SDSS optical survey. We found that 73 out of the 281 X-ray sources (26%) have SDSS counterpart (X/SDSS sample). Most of these sources have visual extinctions $A_V < 5$ mag[8], confirming that they are likely galactic foreground stars unrelated to the cluster. This percentage is the same that was found by Mucciarelli et al. (2011) in the S255-IR cluster. The remaining 208 sources (X/noSDSS sample) are candidates to DR21 cluster members. We cross-checked this non-optical X-ray sample with the UKIDSS and Spitzer source catalogs finding that 102 X-ray sources have UKIDSS and/or Spitzer counterparts (X/noSDSS/IR sample). The spatial distribution of these very likely cluster members is shown in left panel of Fig. 3.4.

[8] We have estimated their extinction from their location in a $J-H$ vs. $H-K$ diagram (not shown), using the colors of their UKIDSS counterparts.

The remaining X-ray sources without UKIDSS/Spitzer counterpart (106 sources, X/noSDSS/noIR sample) can be new cluster members which are not detected at IR wavelengths (likely because they suffer high extinction) or EG contamination, whose infrared emission is usually too faint to be detected in the IR catalogs. To estimate the expected number of EG sources we used the contamination detected in the more sensitive Chandra observations of the Orion Nebula Cluster (Chandra Orion Ultra Deep Project, COUP, Getman et al. 2005c, ∼850 ks) and the Carina Nebula (Chandra Carina Complex Project, CCCP, Townsley et al. 2011, ∼80 ks). The COUP analysis classified 10% of the total detected sources as EG contaminants. In DR21 this would be ∼28 sources. The CCCP observation exhibits ∼1.5 EG contaminants per deg^2. Scaling these numbers to the field-of-view of DR21, we obtain ∼20 sources. Taking into account that these observations are deeper, and then more EG contamination is expected (especially in the very deep COUP), we set an upper limit of ∼20 EG contaminants in the X/noSDSS/noIR sample. Namely, more than 80% of these sources are likely new cluster members detected by Chandra for the first time. We can also use the spatial distribution as a criteria to discriminate between heavily embedded cluster members and background EG sources[9]. The former are expected to be located preferentially in the more extincted region, which is the N-S ridge traced by the 850 μm SCUBA dust emission, while the latter are expected to be distributed throughout the whole field. The right panel of Fig. 3.4 clearly shows that a significant fraction (∼30%) of the X/noSDDS/noIR sample are distributed along the ridge, with a maximum at the DR21 clump. We conclude thus that these sources are heavily obscured cluster members. The classification of the other sources (∼80) is less clear. According to the estimates of the EG contamination, up to ∼20 could be contaminants, while the remaining would be cluster members.

3.2.3 Completeness

We can estimate the sensitivity limits of the X-ray source catalog of DR21 from the distribution of X-ray luminosities of the detected sources. In Fig. 3.5 we show the histogram of the X-ray luminosities (not corrected from extinction) of the DR21 population. The minimum value of log$L_{\rm X}$ is 29.70 erg s^{-1}. Using the correlation between $L_{\rm X}$ and the stellar mass found by Preibisch and Feigelson (2005) in the Orion

[9] The presence of X-ray flare events has been also used in previous works (see Getman et al. 2005a) to identify cluster members from EG contaminants. However, we can not use this criteria because X-ray light curves for the DR21 sources are not available.

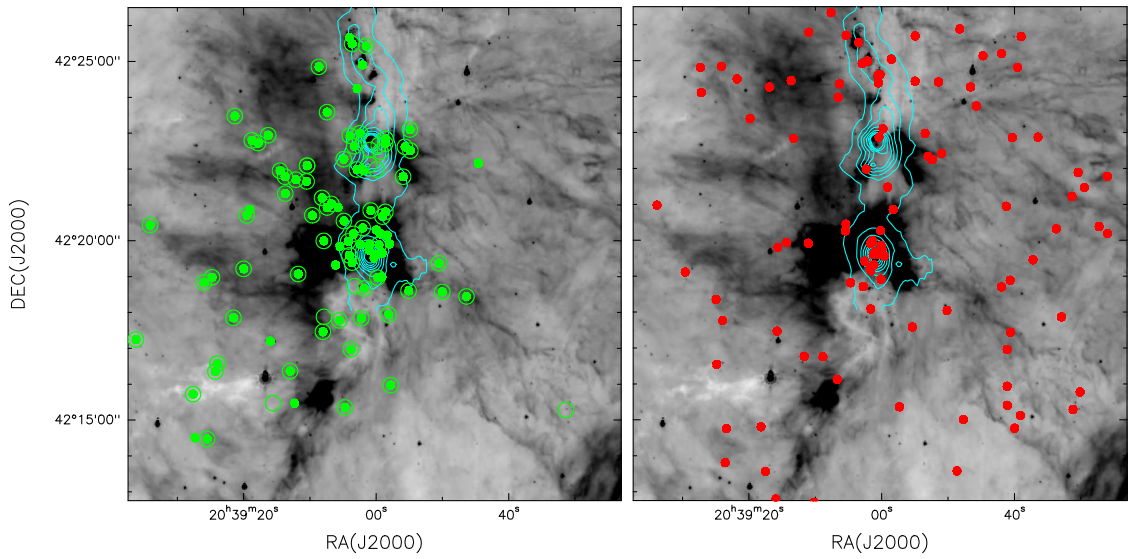

Figure 3.4: Spatial distribution of the X/noSDSS/UKIDSS source sample (green dots, left panel) and X/noSDSS/Spitzer source sample (open green circles, left panel), and X/noSDSS/noIR source sample (red dots, right panel). The background image is the 8.0 μm Spitzer image, which traces warm dust emission (Beerer et al. 2010). The light blue contours indicate cold dust emission detected by SCUBA at 850 μm (Matthews et al. 2009).

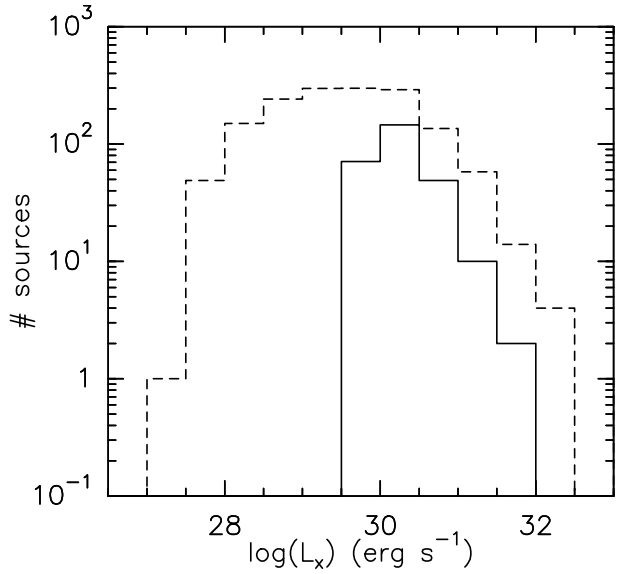

Figure 3.5: Distribution of X-ray luminosities (not corrected from extinction) of the full Chandra sample, compared with that of the COUP sample (dashed line).

Nebula Cluster, this is equivalent to a lower mass limit of ∼0.34 $M_{\odot}$. Considering the typical initial mass function (IMF) of young clusters (Chabrier 2003), and a range of masses in the cluster between 0.02 and 10 $M_{\odot}$, the population detected would represent ∼54% of the total cluster population.

An alternative method to estimate the fraction of stars that Chandra observations has detected towards DR21 is to calculate the fraction of stars that COUP detected with luminosities above the DR21 limit of log $L_{\rm X}$ = 29.70 erg s^{-1}. Fig. 3.5 shows the histogram of X-ray luminosities (also without extinction correction) of the Orion Nebula Cluster (COUP, Getman et al. 2005c), whose census can be considered nearly complete[10]. It is clear that the Chandra DR21 observation is biased to detect the brighter X-ray sources. The fraction of COUP sources with log$L_{\rm X}$ > 29.70 erg s^{-1} is 45%. This is a value similar to the one obtained previously, indicating that the Chandra observation of DR21 detected around half of the total cluster population in the absence of extinction.

This fraction is obviously even lower in the obscured regions, like the N-S ridge traced by the 850 μm dust emission. Grosso et al. (2005) estimated that in the obscured regions in Orion like the Orion Hot Core and OMC1-S regions (which suffers $A_{\rm V}$ > 25 mag) the X-ray observation detected ∼48-63% of the sources due to obscuration. Therefore, in regions with such high extinctions, like the DR21 clump (see Sect. 3.3.1), it is expected that the X-ray observations only detect a half of the population due to extinction. Furthermore, we need to take into account the likely presence of unresolved binaries that the spatial resolution of Chandra is unable to discern.

To summarize, the Chandra observations of DR21 have detected a new population of deeply embedded stars. Our analysis indicates that we underestimate the population of stars by a factor of 2 for the regions with low extinction and by a factor of >4 for the highly extincted regions ($A_{\rm V}$ > 25 mag.).

[10] With the exception of the population heavily embedded in the Orion Molecular Cloud, see chapter 2 and Grosso et al. (2005).

3.3 Results: The new X-ray PMS stellar population in DR21

3.3.1 X-ray sources with UKIDSS counterparts

The cross-correlation with the UKIDSS catalog shows that 162 X-ray sources within the sample have UKIDSS counterpart (58%). For comparison, in the S255-IR star-forming region, the embedded cluster observed with Chandra (Mucciarelli et al. 2011) has a similar IR counterpart fraction of 63%. Considering the X/noSDSS sample, 93 of the 208 sources (45%) have UKIDSS counterparts (X/noSDSS/UKIDSS sample). The spatial distribution of this sample is shown in the left panel of Fig. 3.4. It shows a centrally peaked distribution of the stars, with the DR21 clump as the main feature. The morphology of this population shows a filament-like feature towards the NE, with origin in the DR21 clump. In Sect. 3.4 we will discuss the possible implications for star formation inferred from this observed structure.

In Fig. 3.6 we show the $J-H$ vs. $H-K$ color-color diagram of the X/noSDSS/UKIDSS sample. Stars without strong emission from a disk have colors typical of extincted zero-age main sequence (ZAMS) stars and populate the confined region between the two leftmost black dotted lines. Stars with the presence of accretion disks, populate the region between the two rightmost dotted lines, while those with additional IR excess dominated by infalling envelopes should be found in the rightmost region of the diagram. Besides the sources detected in J, H and K bands, there is a significant fraction of X/noSDSS/UKIDSS stars detected in H and K bands, but not in the J band due to extinction. For those sources, we have considered lower limits for the color $J-H$, using the UKIDSS detection limit for the J band ($m_{\rm J}$=19.5 mag, Lawrence et al. 2007; Ukidss 2012).

From the color-color diagram we estimate the extinction suffered by the stars.[11] Using the extinction law by Rieke and Lebofsky (1985), the color index (in absence of significant near-IR emission from disk or envelopes) is related to the visual absorption $A_{\rm V}$ with the expression: $A_{\rm V}$= $(H-K\text{-}0.2)/0.063$[12]. We used this expression to calculate the extinction of sources without near-IR excesses. According to Fig. 3.6

[11] The extinction could also be derived from the values for the hydrogen column density $N_{\rm H}$ from the fitting of the X-ray spectra of the sources. However, CXOXASSIST only provides $N_{\rm H}$ values for sources with >100 counts (less than 10 sources). A more detailed spectroscopy study of the X-ray spectra for the full sample would be needed to calculate $N_{\rm H}$.

[12] We adopted $H-K$=0.2 as the typical intrinsic color of most stars (Siess et al. 2000).

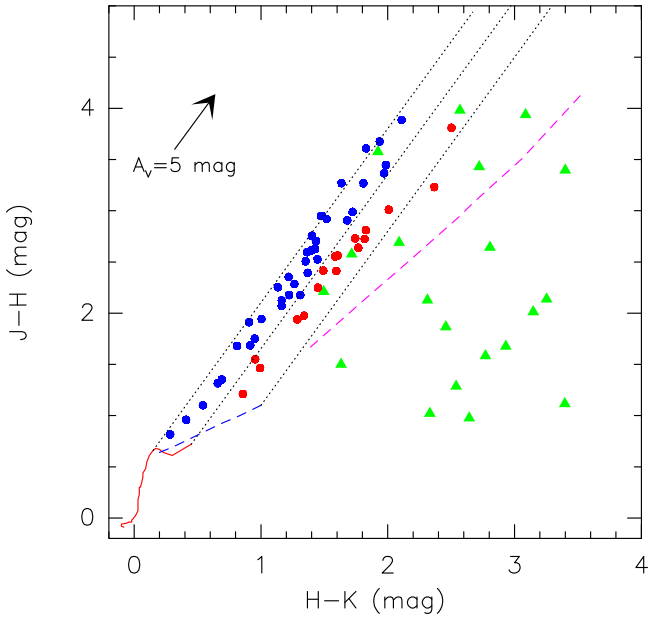

Figure 3.6: $J-H$ vs. $H-K$ color-color diagram of the X/noSDSS/UKIDSS source sample. Stars with/without near-IR excesses are denoted by blue/red dots, respectively. The green triangles are lower limits for those sources detected in H and K bands, but not in the J band. The solid red line indicates the IR colors of ZAMS stars with masses from 0.1 to 7 $M_{\odot}$ from the theoretical evolutionary tracks of Siess et al. (2000). The dashed blue line denotes the unreddened locus of intrinsic near-IR excesses due to presence of disks from Meyer et al. (1997). The black dotted lines are reddening vectors using the extinction law from Rieke and Lebofsky (1985), extended from the ZAMS colors and the from unreddened locus. The magenta line denotes the minimum value of $J-H$ that stars with masses 0.1−4 $M_{\odot}$ and an age of 1 Myr (approximated mean age for the cluster, Beerer et al. 2010) must have to be detected in the H band and not in the J band.

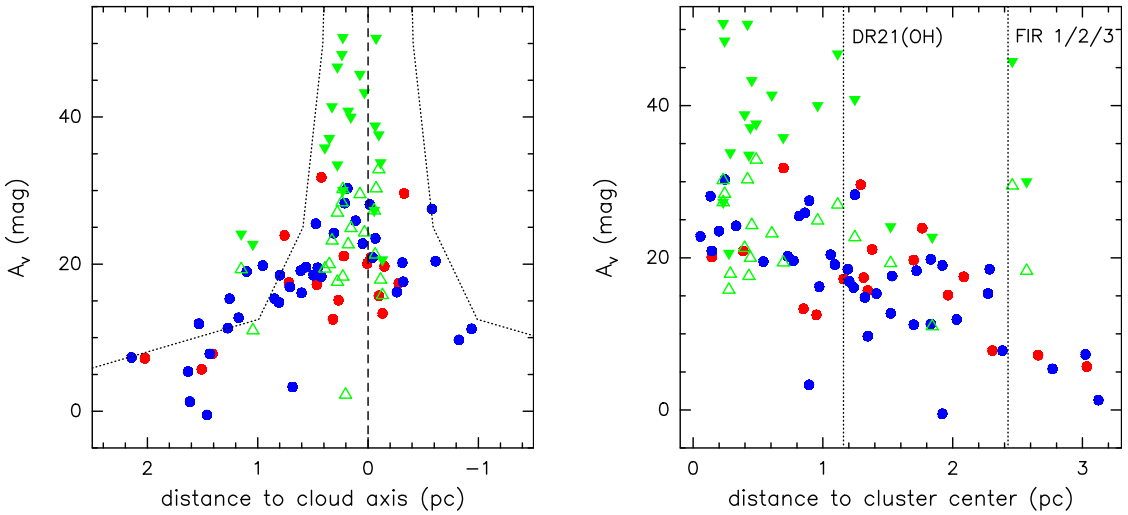

Figure 3.7: *Left panel:* Values of the extinction of the X/noSDSS/UKIDSS sample derived from the $H-K$ colors of the stellar population versus the distance to the approximate axis of the ridge detected at 850 μm by Matthews et al. (2009) (vertical dashed line). Blue and red dots correspond to stars without/with near-IR excesses, respectively. Open and filled green triangles indicate the lower and upper limits, respectively, for the stars not detected in the J band. The dotted curve indicates the column density profile obtained by Hennemann et al. (2012) using *Herschel* data. Distances to the east are defined as positive. *Right panel:* Values of the extinction towards the stellar population versus the distance to the cluster center, located in the DR21 clump. The colors and symbols are the same as in the left panel. The dotted vertical lines indicate the location of the DR21(OH) and FIR 1/2/3 regions.

the presence circumstellar disks produce an average excess in the $H-K$ color of $\sim$0.3 mag. We estimate then the extinction suffered for the stars with color excesses subtracting this contribution to the measured value of $H-K$. For those sources not detected in J we calculate lower an upper limits for the extinction. For the upper limits we consider that the star do not show a near-IR excess, i.e., the $H-K$ is only due to extinction (without contribution from disk/envelope). For the lower limits we consider a maximum disk/envelope contribution, assuming that the $J-H$ values are those corresponding to the limit for detection in J band (magenta dashed line in Fig. 3.7), and subtracting the $H-K$ excess due to disk/envelope material. We show in Fig. 3.8 the spatial distribution of the X/noSDSS/UKIDSS sources as a function of extinction: stars with $A_{\rm V} < 15$ mag (blue dots), stars with 15 mag $< A_{\rm V} <$ 20 mag (green dots), and stars with $A_{\rm V} > 20$ mag (red dots). We also include (red triangles) the sources not detected in the J band, expected to be highly embedded. This analysis shows that the X/noSDSS/UKIDSS sources with higher extinction follow the N-S ridge, those with intermediate extinction are concentrated along the NE stellar filament, and those with lower extinction are more distributed and located at larger distances from the ridge. The sources not detected in J are concentrated along the ridge, mainly surrounding the DR21 clump, DR21(OH) and the FIR 3 source, confirming that they are more embedded objects.

In Fig. 3.7 (left panel) we show the extinction versus the distance to a N-S axis following the 850 μm emission from the ridge. It is clear that the extinction increases when the distance to the ridge axis decreases. The X/noSDSS/UKIDSS sources detected in all three near-IR bands show extinctions up to $A_{\rm V}$=30 mag, peaking in the inner part. This extinction peak is similar to the one found in the low resolution extinction map from Schneider et al. (2006) from the Two Micron All Sky Survey (2MASS). However, the *Herschel* observations from Hennemann et al. (2012) showed that the extinction is even higher in the inner region of the ridge (dashed black curve in Fig. 3.7)[13]. Since the UKIDSS survey is deeper than the 2MASS survey, we expect to detect stars more embedded in the ridge. Actually, as indicated Fig. 3.7, the X/noSDSS/UKIDSS sources not detected in J band are located in the inner region of the ridge, and show extinctions between $A_{\rm V}$=20 mag and $A_{\rm V}$=50 mag, consistently with the column density profile from Hennemann et al. 2012. In Sect. 3.3.5 we will show that in the very inner region there are stars even more extincted, which have only been detected by Chandra.

[13] We have used the relation $N_{\rm H}/A_{\rm V}=2\times10^{21}$, which is an intermediate value between the relations found by Ryter (1996) and Vuong et al. (2003).

In the right panel of Fig. 3.7 we show the value of the extinction with respect to the center of the cluster, located in the DR21 clump. With the only exception of some high-extincted stars around DR21(OH) (∼1 pc) and the FIR 1/2/3 region (∼2.2 pc), there is also a clear overall trend in the extinction, gradually decreasing with increasing distance to the cluster center.

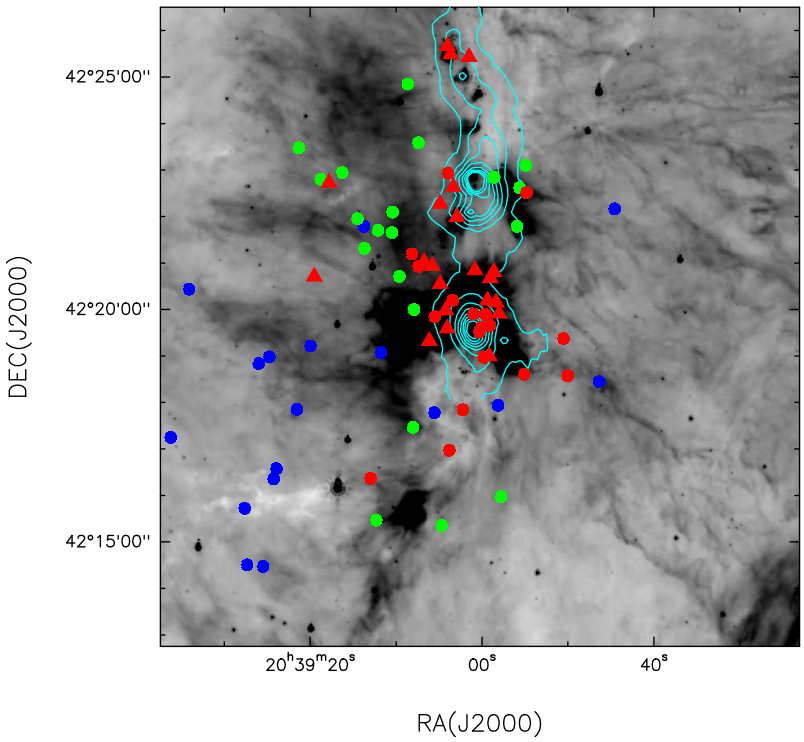

Figure 3.8: Spatial distribution of the X/noSDSS/UKIDSS source sample as a function of extinction: stars with A_V <15 mag (blue dots), stars with 15 mag < A_V < 20 mag (green dots), and stars with A_V >20 mag (red dots). We also include (red triangles) the sources not detected in the J band, expected to be more embedded (see Fig. 3.7). The background image is the 8.0 μm Spitzer image and the light blue contours indicate the emission detected by SCUBA at 850 μm (Matthews et al. 2009).

3.3.2 X-ray sources with Spitzer counterparts

The cross-correlation between the Chandra and the Spitzer-IRAC source catalogs shows that 145 X-ray sources have UKIDSS counterparts (52%). Considering only the X/noSDSS sample, 77 of the 208 sources (37%) have Spitzer counterparts (X/noSDSS/Spitzer sample), of which 68 have UKIDSS counterpart (X/noSDSS/UKIDSS/Spitzer sample). Many works have shown that the IRAC data are very efficient identifying young stellar objects, because it detects excess emission

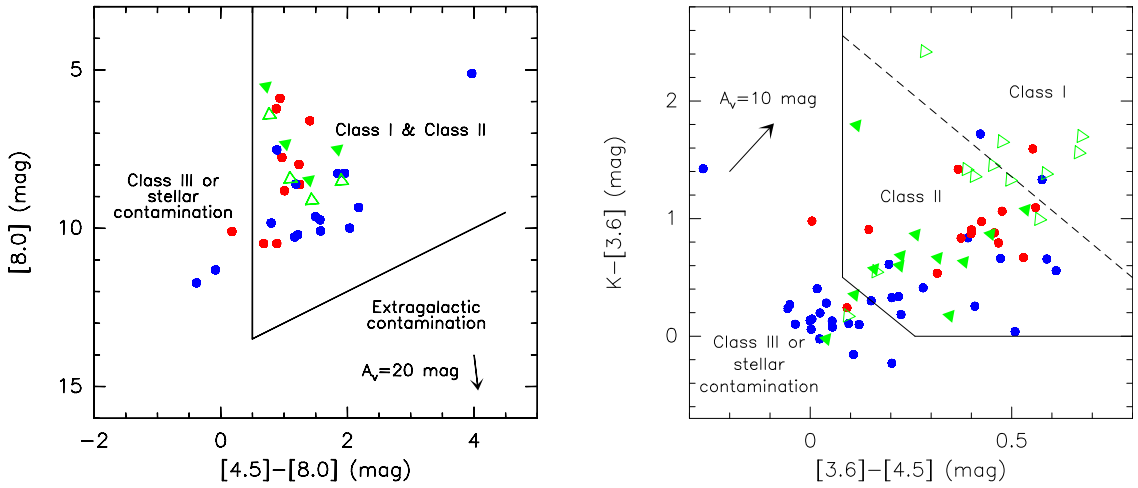

Figure 3.9: *Left panel:* Extinction-corrected magnitude-color diagram of the X/noSDSS/UKIDSS/Spitzer sample source sample. Blue and red dots correspond to stars without/with near-IR excesses, respectively. Open and filled green triangles indicate the fluxes corrected with lower and upper limits of the extinction, respectively, for the stars not detected in the J band. The regions corresponding to different classes of objects are indicated (Jørgensen et al. 2006), along with and extinction vector from the Flaherty et al. (2007) extinction law. *Right panel:* Extinction-corrected color-color diagram of the Chandra/Spitzer source sample. The symbols are the same as in the left panel. The regions correspond to the different classes and the extinction vector are indicated.

well above that expected from reddened stellar photospheres that originates from the dusty circumstellar disks and envelopes surrounding young stars (Allen et al. 2004; Harvey et al. 2006; Jørgensen et al. 2006).

In the right panel of Fig. 3.2 we presented the spatial distribution of the X/noSDSS/Spitzer sample. Similarly to the X/noSDSS/UKIDSS sample, the morphology of this population shows the NE filament-like feature. Compared with UKIDSS, Spitzer detected less sources in the inner DR21 clump. Besides the higher extinction in the DR21 central region (which also affect UKIDSS), this is likely due to two other factors: i) the lower Spitzer spatial resolution prevents a complete census of crowded dense clusters (Mucciarelli et al. 2011) like the one found in the DR21 clump; ii) the extended emission from the large outflow (detected in all 4 IRAC bands) decreases the sensitivity to detect point-like stellar sources[14].

From the IRAC colors, it is possible to classify the stars as Class I, Class II and Class III (according to the classification from Wilking and Lada 1983), which

[14] The decrease of sensitivity due to extended emission from the large outflow can also affect the UKIDSS observations in the K band, but barely in the H and J bands, where the outflow is not detected.

indicates their evolutionary stage, from earlier to more evolved. Since extragalactic sources may also be misidentified as young stars or protostars, we use a magnitude-color diagram ([8.0] vs. [4.5]-[8.0], Whitney et al. 2003; **?**; Harvey et al. 2006) that allows the discrimination of EG contamination. The left panel of Fig. 3.9 shows the extinction-corrected [8.0] vs. [4.5]-[8.0] diagram of the X/noSDSS/Spitzer sample. It is remarkable that none of the sources fall in the region expected for extragalactic objects, in agreement with the low extragalactic contamination discussed in Sect. 3.2.2.

Although the [8.0] vs. [4.5]-[8.0] diagram effectively discriminate EG contaminants, the relatively poor sensitivity and spatial resolution of the longer wavelength IRAC 8.0 μm band (see Ukidss 2012) prevents the classification of many stars. For this reason, to classify the sources in their evolutionary stages we use the K-[3.6] vs [3.6]-[4.5] diagram, which in the DR21 region is able to classify a number of stars twice than the [8.0] vs. [4.5]-[8.0] diagram. The right panel of Fig. 3.9 shows the K-[3.6] vs [3.6]-[4.5] extinction-corrected diagram of the X/noSDSS/Spitzer sample. Since background planetary nebulae and asymptotic giant branch (AGB) stars may also be misidentified as young stars, some of the stars in the Class III region could be stellar contamination unrelated to the cluster. However, the cross-correlation between the Spitzer and Chandra samples makes unlikely this possibility, because X-ray emission from PMS stars is significantly higher than that from main sequence or post-main sequence stars.

The diagram shows that most of the stars with near-IR excesses (Sect. 3.3.1) are Class II objects, while those without excesses are Class III objects. This is expected because Class II objects are younger PMS stars that still exhibit optically thick circumstellar disks, while Class III objects are more evolved PMS stars with colors more similar to naked stellar photospheres[15].

The spatial distribution of the different evolutionary classes from the K-[3.6] vs [3.6]-[4.5] diagram is shown in Fig. 3.10. The youngest objects (Class I[16]) are found along the N-S ridge, while the subsequent evolutionary stages are more distributed. The NE stellar filament is composed by mainly Class II/III stars, suggesting that this stellar population is more evolved than that embedded in the ridge.

[15] Although we note that it is well known that longer IR wavelengths (L-band or Spitzer bands) are much more effective (and hence more reliable) to detect excesses from the disk and envelopes (Lada et al. 2000).

[16] We have included as Class I candidates those stars not detected in the J band whose flux corrected with the lower extinction fall in the Class I region.

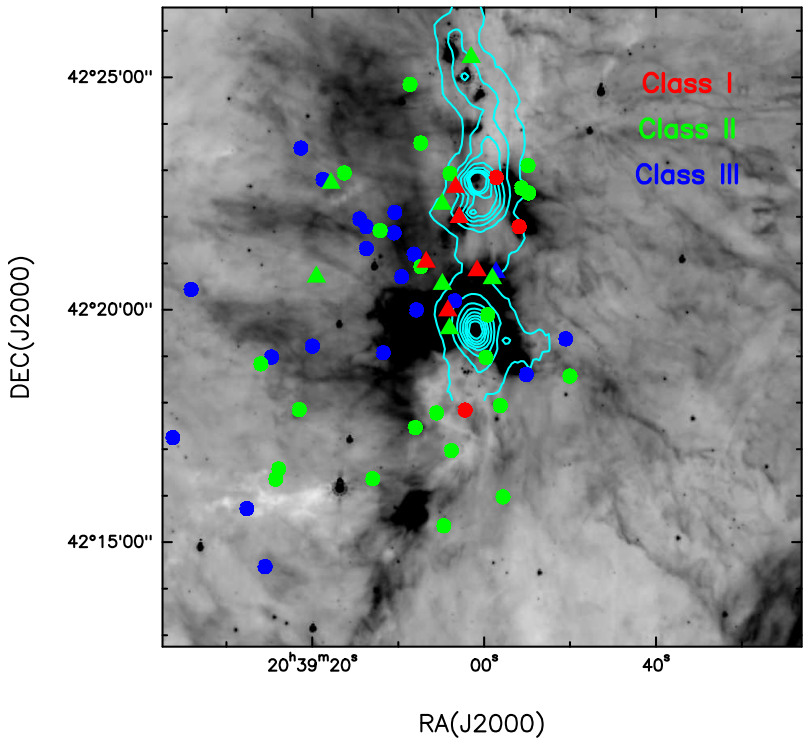

Figure 3.10: Spatial distribution of the X/noSDSS/UKIDSS/Spitzer sample, classified by evolutionary PMS star stages using the Spitzer K-[3.6] vs. [3.6]-[4.5] diagram. The dots denotes stars detected in all 3 near-IR bands (JHK) and triangles stars not detected in J band. Different colors correspond to different evolutionary stages: Class I (red), Class II (green), and Class III (blue). We consider Class I candidates (red triangles) those stars not detected in J band whose flux corrected with the lower extinction fall in the Class I region of the color-color diagram. The background image is the 8.0 μm Spitzer image and the light blue contours indicate the emission detected by SCUBA at 850 μm (Matthews et al. 2009).

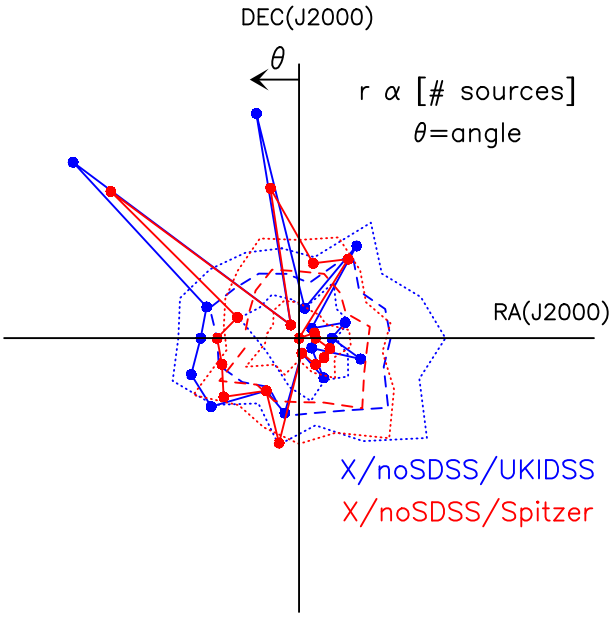

Figure 3.11: Angular distribution of the X/noSDSS/UKIDSS (solid blue line) and X/noSDSS/Spitzer (solid red line) stellar populations. The angle θ runs east from north as indicated. The radial distance to the center is proportional to the number of sources detected in angular bins of 20 deg. The dashed and dotted lines indicate average and $\pm 1\sigma$ standard deviation value for each angular bin, respectively, considering randomly distributed stellar distributions from 10 Monte Carlo simulations.

3.3.3 Angular distribution of the stellar population: the NE filament

We showed in Sect. 3.3 that the X/noSDSS/UKIDSS and X/noSDSS/Spitzer samples exhibit in DR21 an elongated structure from the DR21 clump towards the NE that resemble these radial filaments. In Fig. 3.11 we plot the angular distribution of the two stellar samples, in angular bins of 20 deg. The presence of the NE stellar filament is evident at ∼50 degrees. There is also other peak in the angular distribution, at ∼10 degrees, caused by the subclusters around DR21(OH) and FIR 1/2/3 (see Sect. 3.3.4) rather than by an additional stellar filament. To confirm that the NE feature is real and not caused by a random fluctuation in the stellar spatial distribution, we carried out a Monte Carlo analysis. For each sample, we generate artificial clusters with random distributions. We show in Fig. 3.11 the average value and 1σ standard deviation values of the set of 10 Monte Carlo runs for each angular bin. While the simulations show an approximately isotropic distribution, the observed distribution in DR21 clearly peaks in the two directions previously mentioned. Therefore, it is clear that the NE filament is well above the noise level, clearly showing that it is not

due to a chance alignment of sources.

3.3.4 Stellar densities: subclusters of PMS stars

★ Stellar density maps

We have shown that the distribution of the Chandra sample (Fig. 3.2) are not homogeneously distributed over the DR21 region, but centrally clustered towards the DR21 clump. Following the procedure used in chapter 2, we compute the stellar density of the X/noSDSS sample (208 sources) using a spatial gridding method. We count the number of stars in square cells with three different sizes: 120" ×120" (0.87 pc×0.87 pc), 60" ×60" (0.44 pc×0.44 pc) and 30" ×30" (0.22 pc×0.22 pc). We have chosen the cell sizes to match the range of clump sizes resulting from the fragmentation of molecular clouds (Williams et al. 2000; Saito et al. 2007) where massive star formation is expected to occur. The results are presented in Fig. 3.12. We remark that, according to our completeness estimates, almost $\sim 50\%$ of the cluster members still remain undetected in the regions without extinction due to sensitivity limits and only $< 25\%$ of the sources were detected in the regions affected by extinction (Sect. 3.2.3). This means that the stellar densities that we obtained should be increased by factors of 2 or > 4, respectively. Moreover, even these completeness-corrected stellar densities must be considered as lower limits due to the likely presence of binary and multiple systems which are not resolved by the Chandra spatial resolution.

Our lowest resolution spatial gridding (120" ×120" cell) reveals the large-scale structures of the cluster. The NE stellar filament is also evident in the stellar density contours. The overall elongated N-S morphology of the X-ray population, peaking in the DR21 clump, agrees with the distribution of the ridge traced by its dust emission at 850 μm measured with SCUBA.

The spatial gridding with the 60" ×60" cell reveals the more compact clustering of stars, with three well defined peaks along the cloud. The main peak is located in the central region of DR21, coincident with the location of the young massive stars exciting the UC HII regions (Cyganowski et al. 2003). A secondary density peak is located at the molecular hot core DR21(OH) (Chandler et al. 1993), and a third peak is located around the FIR 1/2/3 young massive stars.

The morphology of the stellar density from the 30" ×30" grid also peaks clearly in the three massive star-forming regions, following the N-S ridge seen at 850 μm (see right panel in Fig. 3.12). With this higher resolution grid the DR21(OH) population

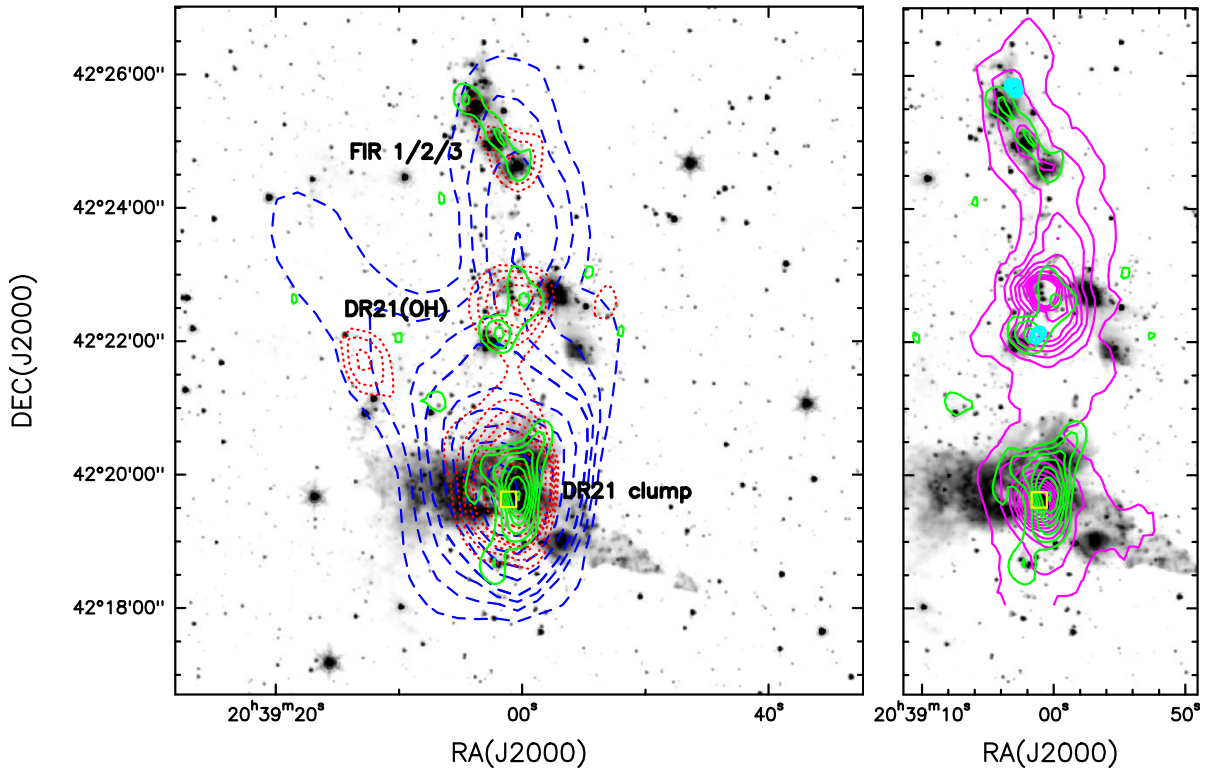

Figure 3.12: *Left panel*: Stellar density map of the X/noSDSS sample, computed with the 120" × 120" grid (0.87 pc × 0.87 pc, blue dashed contours), the 60" × 60" grid (0.44 pc × 0.44 pc, red dotted contours) and the 30" × 30" grid (0.22 pc × 0.22 pc, green solid contours). The contours are 6, 8, 10, 12, 17, 22, 27, 32, and 37 stars cell^{-1} for the 120" grid; 4, 5, 6, 7, 8, 11, 14 and 17 stars cell^{-1} for the 60" grid; and 2, 3, 4, 5, 6, 7, and 8 stars cell^{-1} for the 30" grid. The background image is the 4.6 μm Spitzer image. The positions of the massive star-forming regions (DR21 clump, DR21(OH) and FIR 1/2/3) are labeled. The open yellow square indicates the position of the explosion center proposed by Zapata et al. 2013 to explain the large CO outflow (seen in the 4.6 μm Spitzer image). *Right panel:* Zoom-in view of the N-S ridge, comparing the stellar density obtained with the 30" ×30" grid (green contours) and the dust emission detected by SCUBA at 850 μm (magenta contours). The light blue circles indicate the positions of millimeter sources detected by Bontemps et al. (2010) that are candidates to form massive stars.

splits into two subclusters, with the more dense located SE of the DR21(OH) main peak. This subcluster is coincident with a secondary peak in the 850 μm map (also detected at 1200 μm, see Chandler et al. 1993), and located close to the center of the massive (>8 $M_{\odot}$) dense cores CygX-N48 MM1 and MM2 (Bontemps et al. 2010), that are candidates to form massive stars. The stellar subcluster revealed by Chandra is embedded in the ridge, with $A_V > 20$ mag[17], and may represent the outer part of the more obscured CygX-N48 cluster of cores ($\log N_H \sim 23$ cm^{-2}, from Bontemps et al. (2010), i.e., $A_V \sim 50$ mag). Similarly, the massive dense cores CygX-N53 MM1 and MM2 are located very near the FIR 3 stellar density peak, suggesting that they could be related.

The DR21 clump shows a clear centrally peaked distribution. To provide quantitatively a value for the cluster size we use the *clustering parameter* (α) defined in chapter 2 as the ratio between the number of sources found in the 0.22 pc ×0.22 pc cell and the number found in the 0.44 pc × 0.44 pc cell. Our results show that the clustering parameter in the DR21 clump of α=0.47. If we assume a Gaussian distribution for the stellar density $\rho_* \propto e^{-(2r/\gamma)^2}$ (where r is the distance to the center of the cluster and γ is defined as the cluster diameter), α=0.47 corresponds to $\gamma \sim$ 0.6 pc. This cluster size is in the typical range for molecular clumps − regions of enhanced density within a molecular cloud − which will typically form stellar clusters (Williams et al. 2000; Smith et al. 2009b).

3.3.5 Cumulative stellar density radial profile

We have shown in previous sections that the DR21 low-mass stellar cluster is centrally condensed, with its density peak towards the DR21 clump. In this section we derive the radial stellar density profile of the DR21 clump cluster by calculating the cumulative stellar density with respect to the cluster center. We considered that the center of the cluster coincides with the location of the stellar density peak seen in the 0.22 pc × 0.22 pc grid (see Fig. 3.12). We count the number of stars of the X/noSDSS sample within concentric circles with radius increasing in 0.01 pc steps. We considered as the innermost concentric circle the one containing at least 2 stars. The results are presented in Fig. 3.13. According with the completeness discussion in Sect. 3.2.3 we also present the stellar densities corrected by a factor of 2, which

[17] One of their members is detected in H and K bands, but not in J band, show extinction $A_V >$ 20 mag (Sect. 3.3.1) and it is classified as Class I candidate (Sect. 3.3.2). Two other members are only detected in the K band, and other is not detected by UKIDSS, suggesting that they are all more embedded in the ridge.

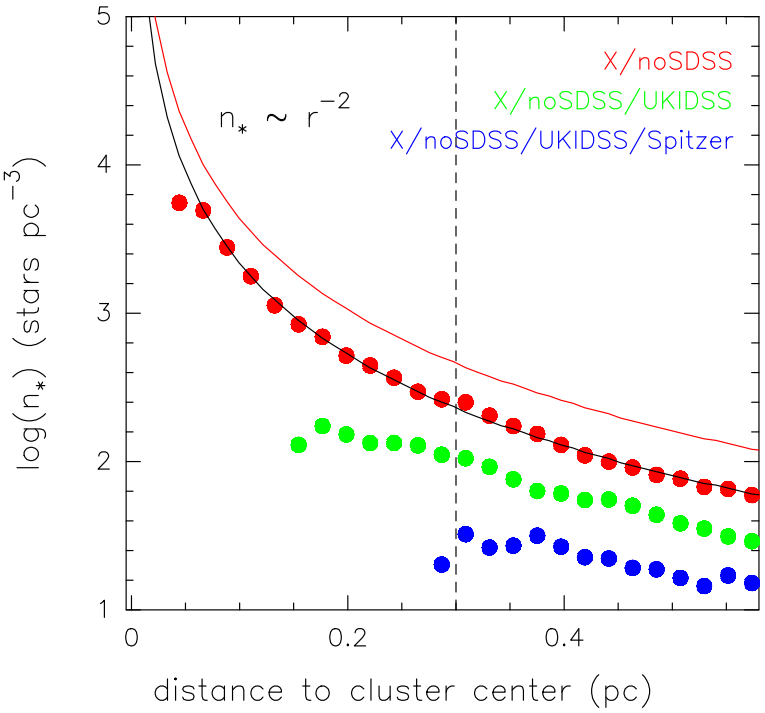

Figure 3.13: Cumulative stellar density of the X/noSDSS sample (red dots), compared with the X/noSDSS/UKIDSS (green dots) and X/noSDSS/UKIDSS/Spitzer (blue dots) samples. We considered as inner distance that one at which at least 2 sources were detected. The fit of the only Chandra sample points follows a r^{-2} profile (black curve). The red curve corresponds to the stellar density profile corrected by a factor of 2, due to the incompleteness of the Chandra observation (see Sect. 3.2.3). The dashed vertical line indicate the radius of the DR21 clump cluster calculated in section 3.3.4.

accounts for the limited sensitivity of the DR21 Chandra observation. The cluster follows an approximate radial profile $\sim r^{-2}$ with the exception of the very inner region, as occurred in the OHC region (see chapter 2). This is likely due to the higher extinction in the central part of the clump, that prevents the detection of stars with weaker X-ray emission.

We compare the cumulative radial density profile of the X/noSDSS sample with the X/noSDSS/UKIDSS and X/noSDSS/UKIDSS/Spitzer samples. Obviously the stellar density of the X/IR samples are lower because they are subsamples of the Chandra sample. The plot shows that Spitzer is not effective detecting cluster members in the inner < 0.25 pc, because as already mentioned, it likely suffers from source crowding and from extended emission from the large outflow. The X/noSDSS/UKIDSS sample, less affected by extended emission, detect sources until 0.15 pc, but only Chandra has revealed the stellar population for smaller distances. The high extinction in the very inner region of the core (Sect. 3.3.1) prevents the detection of the stellar population at IR wavelengths. However, the X-ray observations are able to detect sources more deeply embedded (see chapter 2 and also Mucciarelli et al. 2011). Note that even the derived X-ray stellar densities seem to be heavily affected in the very inner region of the cluster, where the extinction is extremely high, and where the stellar density profile also deviates from the r^{-2} profile.

The different profiles for the samples also reflect the centrally peaked structure of the extinction. The profiles gradually deviate one from another for smaller distances to the cluster center. While the density of the X/noSDSS sample increases following the $\sim r^{-2}$ profile, the densities of the X/noSDSS/UKIDSS and X/noSDSS//UKIDSS/Spitzer exhibit less steep profiles. We interpret this as a consequence of the extinction in the cluster (Fig. 3.7).

3.4 Competitive accretion scenario for cluster and massive star formation

One of the main results of this work is that the density of PMS low-mass stars peaks at the massive star cradles: DR21 clump, DR21(OH) and FIR/1/2/3 region. Beerer et al. (2010) also found that young stars tend to cluster around massive B stars in the Cygnus X region from their Spitzer data. This close association between the low-mass star clusters and the massive star cradles was also reported towards the ONC and OMC (see chapter 2 and Grosso et al. 2005). This suggests that not only dense gas

plays a role to form massive objects, but also a cluster of low-mass stars, in agreement with the "competitive accretion" theory of massive star formation (Bonnell et al. 2004; Bonnell and Bate 2006; Smith et al. 2009b). According to this theory, stars located in the densest regions of a stellar cluster benefit from the local potential wells created by the stellar population, and can gather enough mass to become massive.

This scenario predicts three main features: i) massive stars are born in the low-mass stellar density peaks; ii) an overall centrally condensed structure of the extinction, because the potential well funnels gas and dust towards the cluster center; and iii) an overall mass segregation, with the more massive stars expected to be found in the central regions of the cluster.

These 3 conditions are well fulfilled in the ONC/OMC region (see chapter 2 and Hillenbrand and Hartmann 1998; Allison et al. 2009). As we have shown in Sects. 3.3.1 and 3.3.4, the first and second conditions are also met in DR21 region. With the aim of studying the third condition, i.e., the level of mass segregation in the DR21 region, we use the IR fluxes corrected by extinction (M_λ) of the X/noSDSS/UKIDSS sample without IR excesses. Whether the IR emission of the sources is not affected by the presence of disks or envelopes, the value of the corrected IR emission is a good proxy for the stellar masses (Siess et al. 2000). Fig. 3.14 shows that the fluxes in the J and H bands gradually decrease with increasing distance to the cluster center. Obviously, the central structure of the extinction (right panel of Fig. 3.7) bias the detection of fainter objects in the inner region where the extinction is higher. However, the important point here is that there is not a population of bright (more massive) stars at larger distances where the extinction is expected to be lower. This pattern is very similar to the result obtained from the competitive accretion simulations from Bonnell et al. (2001b) (see Fig. 1.8 in chapter 1), and shows that the mass segregation in the DR21 complex could be explained by the competitive accretion scenario.

Supporting this idea, several works (Kumar et al. 2007, Schneider et al. 2010, Hennemann et al. 2012) have found several dusty and molecular filaments falling into the DR21 N-S ridge (see Fig. 3.15). Hennemann et al. (2012) suggested that the mass accretion through these filaments is driven by the gravitational potential of the full ridge. These infalling filaments provide a continuous mass inflow into the ridge and replenish the available mass reservoir. Kumar et al. (2007) suggested that this morphology of filaments compare well with simulations relying on the competitive accretion scenario (Bate et al. 2003). Actually, the results of the Smith et al. (2009b) simulations (see their Fig. 1), based on competitive accretion, shows a morphology

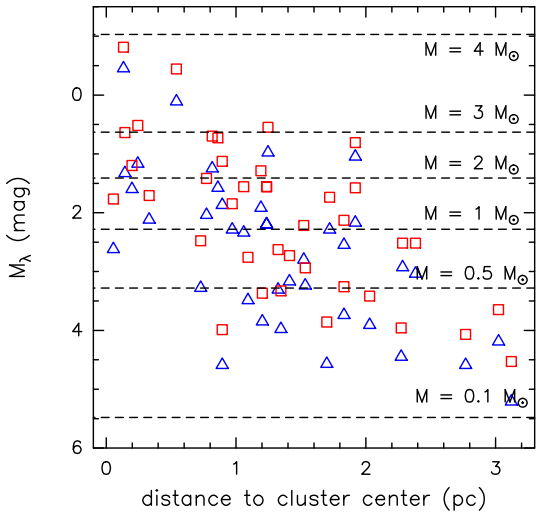

Figure 3.14: IR absolute magnitudes M_λ of the X/noSDSS/UKIDSS sample without near-IR excesses versus the distance to the cluster center. The blue triangles correspond to the J filter and the red squares to the H filter. The extinction correction was applied using the values of A_V obtained from the color index $H-K$, which is a good estimation of the absorption (see Sect. 3.3.1). The horizontal dashed lines indicate the J absolute magnitudes for 1 Myr stars for different masses, from the Siess et al. (2000) PMS models.

very similar to the one found in DR21, with gas filaments feeding the star formation in narrow filament-like structures.

Since the filaments are gravitationally unstable (Hennemann et al. 2012), the inflowing material can fragment (Csengeri et al. 2011) and form stars. As a result, a stellar filament is formed. Since the filaments point towards the accretion center, these filaments can exhibit a radial structure that resembles the spokes of a wheel. Teixeira et al. (2006) detected this "Spokes−like" structure in the stellar cluster NGC 2264, with the more massive stars located towards the center. The morphology of the stellar population in radial filaments is thought to represent primordial structures in the formation of stellar clusters (Bate et al. 2003; Kurosawa et al. 2004; Teixeira et al. 2006). We have detected in DR21 a similar structure. In Sects. 3.3 and 3.3.3 we showed that the X/noSDSS/IR samples exhibit an stellar filament from the DR21 clump towards the NE.

Once the gas falls towards the ridge, it can feed further stellar formation. The overall gravitational well will funnel a significant fraction of gas and dust to the central DR21 clump (explaining the observed overall centrally peaked structure of the extinction), and favoring the formation of a dense low-mass stellar cluster and massive stars at the center, as observed in the DR21 clump. However, this do not rule out

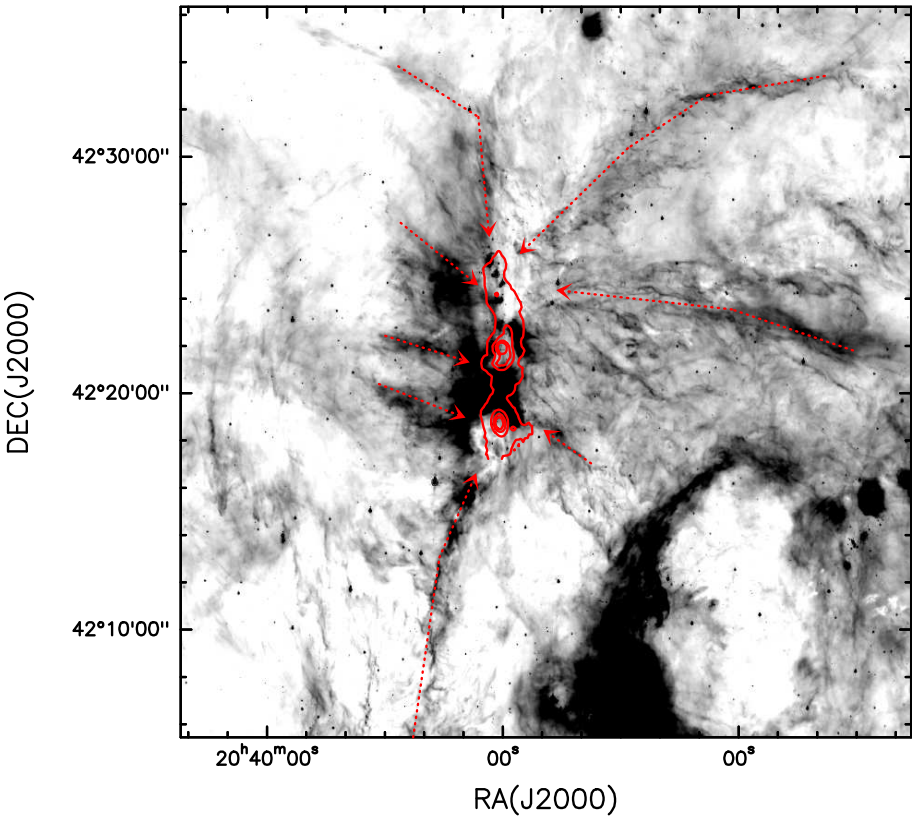

Figure 3.15: Accretion filaments (dashed arrows) falling onto the DR21 ridge, feeding star formation. The SCUBA 850 μm emission (red solid contours) is overplotted on the 8 μm IRAC Spitzer image (gray scale).

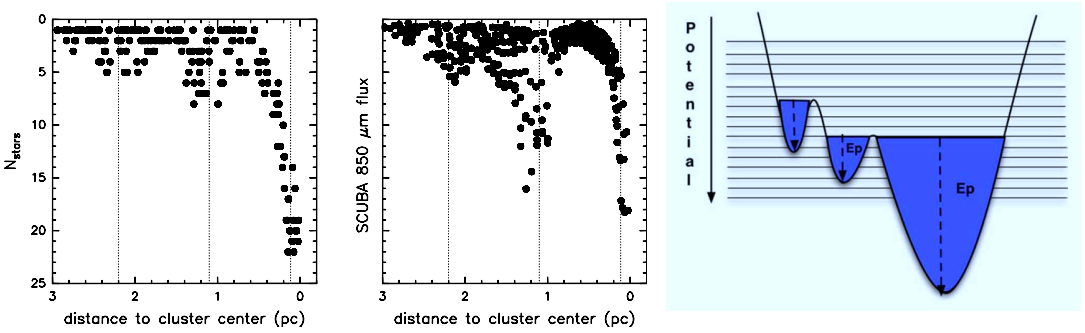

Figure 3.16: *Left panel:* number of stars of the X/noSDSS sample contained within a radius of 0.2 pc around each star, as a function of the distance to the cluster center (considered as the peak density of the 30" ×30" grid). The three densest regions (FIR 1/2/3, DR21(OH) and DR21 clump, from left to right) are indicated with dotted lines. *Middle panel:* SCUBA 850 μm flux (from Matthews et al. 2009) as a function to the cluster center. *Right panel:* Schematic representation of the gravitational potential wells created in a cluster by dense stellar concentrations in subclusters, adapted from Smith et al. (2009a).

that massive stars can also born in outer parts of the cluster. The denser subclusters of low-mass stars can also benefit from their own small-scale gravitational potential wells, winning the competition from the surrounding mass reservoir and allowing the formation of massive stars. We propose that this mechanism could explain the massive star formation in the DR21(OH) and FIR 1/2/3 regions (which show secondary peaks in the extinction, see right panel of Fig. 3.7). In the two leftmost panels of Fig. 3.16 we show that the stellar density in the DR21 cluster is well correlated with the flux at 850 μm (which is a combination of the dust temperature and density), being both centrally peaked with two secondary peaks coindicent with massive star cradles. This is the expected outcome of the competitive accretion process: the potential wells created by the dense subclusters of stars (see schematic picture in the right panel of Fig. 3.7) attract gas from the enviroment to feed more stellar formation, and allowing to the central stars to become massive by subsequent accretion.

In agreement with this scenario, the millimeter interferometric observations from Bontemps et al. (2010) showed that the dense condensations of gas that are expected to be the earliest stages of massive star evolution in the DR21 ridge (CygX-N48 and CygX-N53, in the DR21(OH) and FIR 1/2/3 regions, respectively) appears fragmented, forming subclusters. Csengeri et al. (2011) proposed that significant amount of competitive accretion may be present in these condensations. In this direction, we pointed out in chapter 2 that the low-mass stellar population found in the massive star-forming regions in Orion strongly indicates that the natal condensations suffers

high levels of fragmentation, forming subclusters of low-mass stars rather than single massive objects.

A consequence of the proposed scenario for the DR21 cluster formation is that one would also expect that the younger stars of the cluster are located along the overall potential gravitational well, where the material from the natal cloud is funneled via the filaments. We discuss here some aspects about the estimated ages of the DR21 stellar population.

Prisinzano et al. (2008) and Ybarra et al. (2013), combining Chandra and Spitzer data, found a relation between the extinction of the stars and their evolutionary phase: the more extincted the star appears, the younger the star is. Given that the extinction is significantly higher along the N-S ridge than in the rest of the field, this would imply an analogous distribution of stellar ages. Kumar et al. (2007) already pointed out that the Spitzer sources with higher IRAC spectral indexes (indicative of youth) are distributed along the dense ridge and also coincident with signposts of massive star formation. Beerer et al. (2010) also find that the younger Class I objects follow the ridge, while the Class II object are more distributed. Our classification of the X/noSDSS/UKIDSS/Spitzer sample also shows that the youngest sources are located within the ridge (Sect. 3.3.2).

Using the relation between the extinction and the age found by Ybarra et al. (2013) in the Rossete Nebula, the visual extinction suffered by the stars more deeply embedded in the ridge (A_V >15 mag, left panel of Fig. 3.7) implies that their expected age is $\sim 10^5$ yr, in agreement with the estimated age for Class I objects (André 1994; Evans et al. 2009).

To check this we have estimated quantitatively the age of one of the embedded stars in the clump, DR21-D[18]. This source is located in the core of DR21, believe to ionize the UC HII region D (Cyganowski et al. 2003). We fitted the spectral energy distribution of the source with the Robitaille et al. (2006) stellar models, using the K-band flux from UKIDSS, the Spitzer fluxes, and the SCUBA 850 μm flux. In Fig. 3.17 we show the results of the best 100 models. We obtained that this object is a $\sim 10-11$ $M_\odot$ star with a luminosity of $\sim 10^4$ $L_\odot$, heavily obscured by A_V >100, with a very massive circumstellar envelope and with an estimated stellar age of $\leq 10^5$ yr. This is fully consistent with our previous estimate of the age of the stars deeply embedded within the N-S ridge. On the other hand, Fig. 3.10 shows that more evolved (but

[18] We note that this source is not included in the general analysis of this chapter because Chandra did not detect emission, very likely due to the very high absorption produced by the dense circumstellar material.

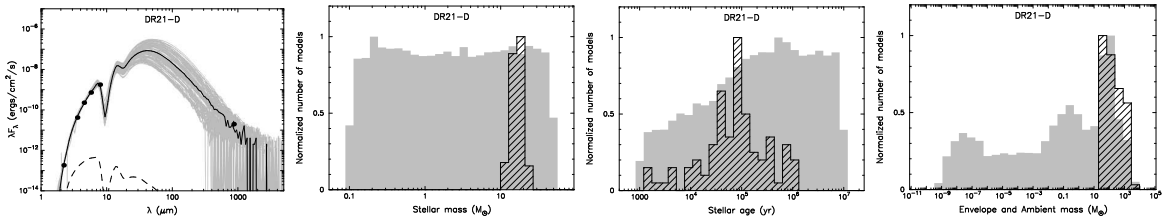

Figure 3.17: Results of the best 100 fits for the DR21-D source obtaining by using the Robitaille et al. (2006) stellar models. From left to right: SED, stellar mass, stellar age and circumstellar envelope mass. In the SED panel, the filled circles show the input fluxes, the black line shows the best fit, and the gray lines show subsequent 99 best fits. The dashed line shows the stellar photosphere corresponding to the central source of the best fitting model, as it would be seen in the absence of circumstellar dust (but including interstellar extinction). In the 3 rightmost panels, the gray histogram shows the distribution of models in the model grid, and the hashed histogram shows the distribution of the 100 best models.

still young) stars (Class II), with an estimated age of 10^6 yr, exhibit a more spatially distributed configuration. The NE stellar filament has a population of Class II and Class III objects, indicating that they a more evolved than the sources detected in the ridge (Fig. 3.10). This would imply that the stellar filament has already consumed a significant fraction of the initial gas, in agreement with the lower extinction we have found (Sect. 3.3.1 and Fig. 3.8). This also explain why the filament is not clearly detected at 8 μm, far-IR (Hennemann et al. 2012), 850 μm or by molecular observations. We note that the absence of the Class II/III objects along the N-S ridge could be caused by the higher extinction in this region. However, the non detection of Class I sources in the outer parts of the field clearly indicates that the youngest objects are concentrated in the ridge. This age segregation is consistent with the competitive accretion formation of the cluster, although it needs to be confirmed by higher sensitivity observations at mid-IR, far-IR and submillimeter wavelengths of the individual stars.

In summary, all the findings of this work and previous observations agree with the predictions from the scenario where massive star formation is directly linked to the formation and early evolution of the low-mass stellar clusters, and where competitive accretion plays a crucial role.

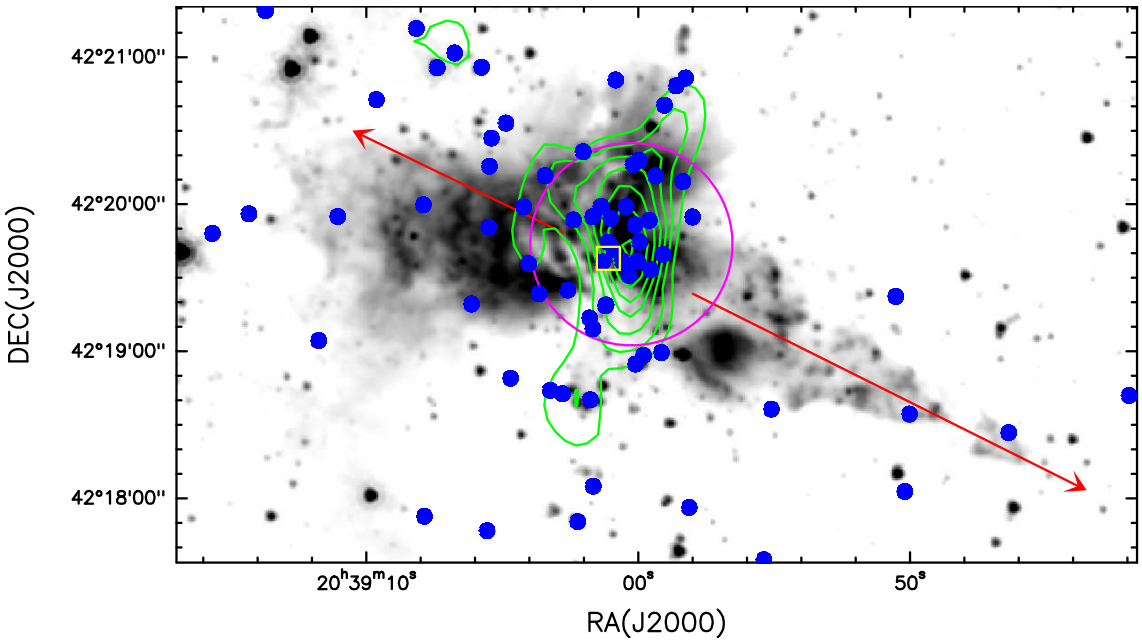

Figure 3.18: Zoom-in view of the DR21 clump and the large high-energetic outflow. The sources from the X/noSDSS sample are denoted with blue dots. The open yellow square indicates the position of the explosion center proposed by Zapata et al. (2013), and the red arrows follow the H_2 outflow lobes observed by Davis et al. (2007) (see their Fig. 2). The magenta circle indicate the DR21 clump cluster diameter (0.6 pc) calculated in Sect. 3.3.4. The green contours are the stellar density obtained with the 0.22 pc × 0.22 pc grid, as in Fig 3.12. The background gray scale image is the Spitzer 4.6 μm image, where the outflow is also detected.

3.5 A stellar collision as the origin of the large-scale outflow?

The Chandra detection of a dense stellar cluster of young stars in the DR21 clump, within the expected region of the explosive event proposed by Zapata et al. (2013) (see Fig. 3.18), leads us to consider the possibility of a coalescence of stars as the origin of the highly-energetic outflow, as we did in chapter 2 for the OHC region.

Although the stellar density of the DR21 region is about one order of magnitude lower than that found in the OHC region region, one may wonder whether a collision can also have occurred in the DR21 clump. A collision event in a dense cluster is favored by the presence of circumstellar disks via disk-captures, which enhance the probability of an encounter (Zinnecker and Yorke 2007; Davies et al. 2006; Bonnell and Bate 2005). This opens the possibility of having stellar mergers that may generate powerful outflows.

We study in Appendix A (see also Sect. 2.4.3 in chapter 2) a collision involving disks and obtained an expression for the expected time of collision between two stars, $t_{\rm coll}$ (Eq. A.4). In Fig. 3.19 we show $t_{\rm coll}$ versus the stellar velocity (σ_*). We used similar stellar parameters to those derived for DR21 D (Sect. 3.4), i.e., masses of M_*=10 $M_\odot$ with disks of 0.1 M_* and a radius of 100 AU. We considered the stellar density estimated in the region in Sect. 3.3.4.

For the expected values of σ_* in young stellar clusters (0.4−2 km s^{-1}, see chapter 2 and Bonnell and Bate 2006 and Gómez et al. 2008), Fig. 3.19 shows that a single collision in the system can occur in $\sim$1−2 $\times$ 10^5 yr. Given that the expected age of the stellar cluster embedded in the DR21 clump is around this value, we propose that a collision may have occurred in the center of this dense cluster, which could have led to the explosive event described in Zapata et al. (2013) and possible origin of the large-scale DR21 outflow.

The energy produced during the collision between the disks of two stars can lead to the decay of the system, producing at the end a direct collision between the two stars. In that case, the energy released would be $E = GM_*M_*/r$ (Bally and Zinnecker 2005), where G is the gravitational constant, M_* is the stellar mass, and r is the radius of the collision. At that moment the radius of the collision corresponds to twice the value of the stellar radius. Considering then two 10 $M_\odot$ stars with and r = 2 R_* $\sim$ 80 $R_\odot$[19], the energy produced by the collision would be $\sim$5 $\times$ 10^{48} ergs, which is of

[19] We considered the radius of a 10 $M_\odot$ star with an age of 10^5 yr, extrapolating from the PMS

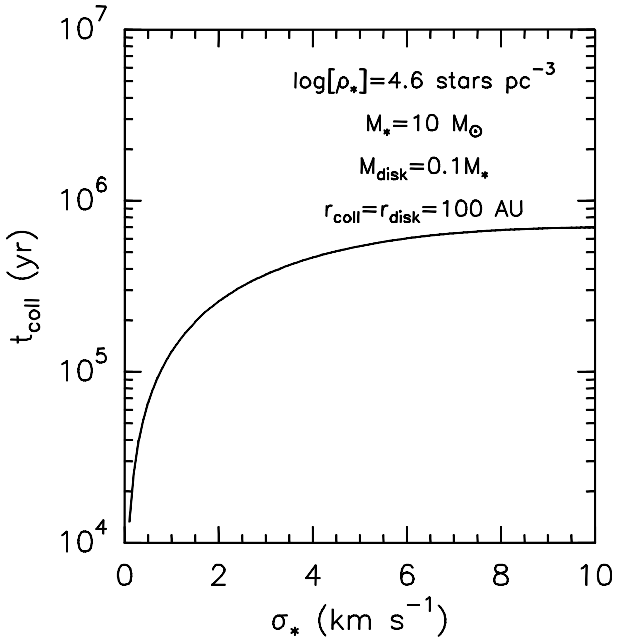

Figure 3.19: Time expected to produce a collision in the DR21 dense stellar cluster, as a function of the stellar velocity dispersion σ_*. We used the stellar density found in the DR21 inner region (log ρ_* ~4.6 stars pc^{-3}), and assume a collision between two stars with M_*=10 $M_\odot$ stars with disk with masses 0.1 M_* and radius of 100 AU.

the same order as that observed in the DR21 clump (Zapata et al. 2013). Therefore, such a violent event produced by the coalescence of two massive objects of the dense DR21 stellar cluster could occur, explaining the highly-energetic outflow observed in the region.

3.6 Summary and conclusions

We presented the results of the analysis of X-ray Chandra observations towards the massive star-forming region DR21, which are summarized as follows:

- The X-rays observations have revealed a new highly embedded population of PMS low-mass stars previously missed in observations at other wavelengths.
- The spatial distribution of the young low-mass PMS stars emitting X-rays shows a central concentration around the DR21 clump. The densest subclusters of low-mass stars coincide with the regions of massive star formation: the DR21 clump, DR21(OH) and the FIR 1/2/3 region.

models of Siess et al. (2000).

- The X/noSDSS/IR sample of stars shows a stellar filament from the DR21 clump towards the NE, resembling a "Spokes-like" structure.

- We obtained the spatial profile of the extinction, which decreases when the distance to the axis of the N-S ridge increases, in agreement with dust observations. Moreover, we found that the extinction also globally decreases with respect to the distance to the cluster center located in the DR21 clump.

- We classified the X/noSDSS/UKIDSS/Spitzer PMS stars in different evolutionary phases. Consistently with previous works, we find evidence for an age segregation, with the younger population (Class I) embedded in the N-S ridge, and more evolved sources (Class II/III) more distributed along the NE stellar filament and the rest of the field.

- We found that the low-mass stellar population of the whole cluster appears globally mass-segregated, with a trend of more massive stars to be located at the center of the DR21 clump.

- The high stellar density found in the cluster embedded in the DR21 clump may have induced the coalescence of two massive stars. We propose that this event could be the origin of the large-scale and highly-energetic DR21 outflow detected in the region.

Our findings are consistent with a picture where the evolution of the stellar cluster and massive star formation are regulated by competitive accretion. The gravitational potential well of the cluster accretes large amounts of gas through dusty/molecular filaments. These infalling filaments can also fragment and form stars, producing stellar filaments like the one observed in DR21. Since the stellar density (and hence the gravitational potential) is centrally peaked towards the DR21 clump, a significant fraction of the material is funneled towards the center, where the densest low-mass stellar cluster is detected. This would explain the observed spatial profile of the extinction, that increases when the distance to the DR21 clump center decreases. However, this does not mean that massive stars can not be formed outside the DR21 clump. In addition to the global large-scale potential well, the dense subclusters of low-mass stars can act at smaller scales. Their own local gravitational potential wells contribute to *win* the competition for the surrounding gas reservoir, allowing the formation of massive stars in the DR21(OH) and FIR 1/2/3 regions.

CHAPTER 4

The role of low-mass star clusters in forming massive stars: Monoceros R2

Abstract

In this chapter, we study the low-mass PMS stellar population in the massive star-forming region Monoceros R2 (MonR2) using archival X-ray and near-IR data. We apply two different methods (spatial gridding and close-neighbors method). To reveal the structure of the extinction of the cluster we have differentiated in our study 3 extinction ranges. The stellar density maps derived from the spatial gridding show that the PMS low-mass population is centrally peaked, with its maximum ($>10^{5.5}$ stars pc^{-3}) in the inner region where the more massive objects (IRS1, IRS2, IRS3 and IRS5) are located. The cumulative stellar density shows a steep radial profile following r^{-2}, as observed in the OHC and DR21 stellar clusters. The close-neighbors method shows that the 0.04 pc $\times$ 0.04 pc vicinity of the more massive objects is populated by subclusters of lower mass stars, with >6 stars in all cases ($>10^{5.25}$ stars pc^{-3}). Using HST-NICMOS near-IR photometry we have analysed in detail the properties the stars in these subclusters, obtaining rough estimates of their masses and extinctions.

From the hydrogen column density derived towards the PMS stars, we have obtained that the structure of the extinction is also centrally peaked, in agreement with molecular line and dust observations. In the central region (r <0.15 pc) we have revealed that the sources with lower extinction forms a ring-like structure surrounding an inner region with more extincted stars, similarly to that found also in the Trapezium Cluster in Orion (chapter 2).

Our analysis shows that the parental clump of MonR2 (r ~0.4 pc) has suffered high levels of fragmentation compatible with a typical Jeans fragmentation, forming the low-mass stellar cluster Fragmentation seems to have been acting even at small scales ($\sim$ 0.04 pc $\times$ 0.04 pc), producing subclusters and multiple low-mass stars

instead of single massive stars formed by direct monolithic collapse of a massive core. These findings favor a competitive accretion scenario for cluster and massive star formation. The central overall gravitational potential well of the cluster transfers gas to the center, where some of the stars can accrete additional material and become massive.

Finally, the high stellar density peak found in the central region of the MonR2 cluster may have favored the collision of two cluster members, especially in the presence of massive stars, circumstellar disks, binaries and accretion of gas. This violent event may be the origin of the highly-energetic large-scale outflow detected in this region, similarly to the ones detected in Orion and DR21.

4.1 Introduction

The massive-star forming region Monoceros R2 (hereafter, MonR2), located at a distance of $\sim$ 830 pc (Racine 1968), is an excelent region to study the first stages of evolution of stellar clusters because the young stellar population (average age of $\sim$1 Myr; Carpenter et al. 1997; Andersen et al. 2006; Kohno et al. 2002; Nakajima et al. 2003) is still significantly embedded in its natal clump (Choi et al. 2000). Ridge et al. (2003) estimated a mass of $\sim$1800 $M_\odot$ for the MonR2 clump within a radius of $\sim$0.7 pc, and Walker et al. (1990) found that the inner $\sim$0.22 pc of the clump contains $\sim$180 $M_\odot$. These masses are consistent the density stellar profile of r^{-1} found in the region by Choi et al. (2000). The central region of the cluster contains all signposts of recent massive star formation like bright IR sources (Beckwith et al. 1976), submillimeter sources (Henning et al. 1992), a shell-like complex infrared nebula (de Wit et al. 2009), HII regions (Massi et al. 1985; Jiménez-Serra et al. 2013), and H_2O and OH masers (Smits et al. 1998), and molecular hot cores (see chapter 7).

By using near-IR 2.12 μm H_2 observations, Hodapp (2007) reported the detection of H_2 jets likely associated with young Class 0/I sources at their main accretion phase. These jets were not found in the central region of the cluster but towards the periphery of the MonR2 clump, which was interpreted as a signature of *inside − out* star formation (Hodapp, 2007; Carpenter and Hodapp, 2008) triggered by the action og the large-scale CO outflow. This region also harbors a highly-energetic and large-scale CO outflow (one of the largest ($\sim$0.6-7 pc) and most massive (275 $M_\odot$) reported so far; Loren, 1981; Wolf et al., 1990; Tafalla et al., 1997), whose origin is still unknown.

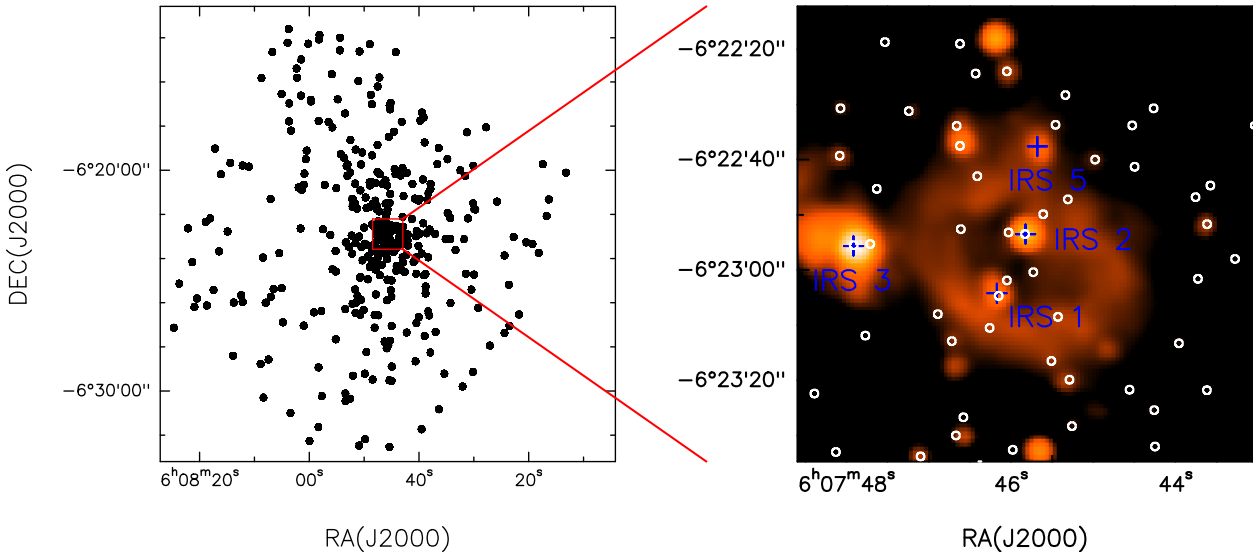

Figure 4.1: *Left:* X-ray observations of MonR2 region from Nakajima et al. (2003). *Right:* Zoom-in of the central region. The color scale is the K-band image from 2MASS, white dots are X-ray stars from Nakajima et al. (2003). The IR bright sources IRS1, IRS2, IRS3 and IRS5 are labeled.

In this chapter, we study the distribution of the PMS low-mass stellar population in this massive star-forming region combining different stellar surveys in X-rays and IR. We focus on the stellar population located in the close vicinity of the more massive objects IRS1, IRS2, IRS3 and IRS5. In view of our results, we discuss the possible implications for clustered and massive star formation. The chapter is written as follows. In Sect. 4.2 we analyze the stellar content of the MonR2 stellar cluster, using several X-rays and IR catalogs. We study the spatial distribution of the stars with a spatial gridding with different bin sizes, and we differentiate 3 extinction ranges to find out the morphology of the extinction produced by dust and gas. We also apply a close-neighbors method to detect the main stellar density peaks. We derive the radial profile for the extinction from X-ray data, and for the cumulative stellar density using IR and X-ray surveys. In Sect. 4.3 we present the results of our stellar density analysis, and analyze in detail the stellar subclusters found around the massive objects IRS1, IRS2, IRS3 and IRS5. In Sect. 4.4 we discuss the implications of this work in the current knowledge about massive star formation in stellar clusters. Finally, in Sect. 4.5 we summarize our results and conclusions.

Table 4.1: Stellar catalogs of MonR2 stellar cluster at different wavelengths.

Reference	Wavelength	sources	Telescope	Instrument	FoV	Spatial resolution (")	Completeness limits
Nakajima et al. (2003)	X-rays	368	Chandra	ACIS	17.4'×17.4' (4.2 pc×4.2 pc)	∼0.5	-
Kohno et al. (2002)	X-rays	155	Chandra	ACIS	3.2'×3.2' (0.77 pc×0.77 pc)	∼0.5	-
Carpenter et al. (1997)	IR	390	UKIRT	IRCAM3	3.2'×3.2' (0.77 pc×0.77 pc)	∼1	[J,H,K]>[18.2,17.6,16.6[a]]
Andersen et al. (2006)	IR	181	HST	NICMOS2	1'×1' (0.24 pc×0.24 pc)	∼0.12-0.2	[J,H,K]>[20.6,20.3,17.7]

[a] The completeness limits are slightly brighter along the ring of nebulosity of the HII region at the center of the cluster (see Fig. 4.1).

4.2 Data analysis

4.2.1 Stellar catalogs

The MonR2 stellar cluster has been observed in X-rays (Kohno et al. 2002, [K02, hereafter]; and Nakajima et al. 2003, [N03, hereafter]) and in the near-IR (Carpenter et al. 1997, [C97, hereafter]; and Andersen et al. 2006, [A06, hereafter]) surveys. The details of these observations are shown in Table 4.1.

The X-ray catalogs provided by K02 and N03 were obtained from the same *Chandra* observations. While K02 focused on the central 0.77 pc × 0.77 pc region, N03 studied the full ACIS (Advanced CCD Imaging Spectrometer) FoV, which is 4.2 pc × 4.2 pc[1]. In the left panel of Fig 4.1 we plot with black dots the population of the cluster observed with Chandra (from N03) in a region of ∼5×5 pc. In the right panel we zoom-in the inner ∼0.3 pc × 0.3 pc region, containing the massive objects and the HII region (Massi et al. 1985) and the shell-like IR nebula (color scale in Fig 4.1; see also de Wit et al. 2009).

Regarding the IR catalogs, C97 observed the same FoV than K02 with UKIRT, while A06 observed with the Hubble Space Telescope (HST) a smaller area of 0.24 pc× 0.24 pc region, reaching a better sensitivity and resolution (<0.2") (see Table 4.1)

[1] In the inner region studied by both works, K02 detected some more sources than N03. This discrepancy arises from the use of a different source detection algorithm. Moreover, N03 only considered sources detected in both energy bands (0.5−2.0 and 2.0−10 keV), and hence sources detected only in one of the bands (for example, sources deeply embedded detected only in the high energy band) are not included in their catalog.

4.2.2 Stellar density study

★ Spatial griding

To study the morphology of the stellar content of MonR2 we have integrated the spatial distribution of the stars in different grids of square cells, counting the number of stars contained in each cell. With the purpose of studying the stellar distribution at different scales, we use different bin sizes: 90" (∼0.35 pc) for large scales, and 15" and 7.5" (∼0.06 pc and ∼0.03 pc, respectively) for smaller scales.

★ Close-neighbors method

We have also applied a close-neighbors method similar to the analysis we carried out in chapter 2. We have counted the number of stars in square cells centered on each star. We chose a bin size of 10" (∼0.04 pc). This is because this will allow us to compare with the regions harboring the natal cores of the massive stars formed in the simulations by Krumholz et al. (2012). We have applied this method to the more sensitive NICMOS stellar catalog from A06.

4.2.3 Selected extinction ranges

The presence of extinction, produced by gas and dust, is characteristic of young stellar clusters with on-going massive star formation. It is a key parameter when studying these regions because: i) it is responsible − along the instrumental sensitivity− of the completeness, which affects the calculation of stellar densities; and ii) the morphology of the extinction can provide clues about how the cluster was established and how the massive stars could accrete mass (see previous chapters).

The X-ray observations from K02 and N03 provided individual values for the hydrogen column density $N_{\rm H}$ towards each star. This parameter is related to the visual extinction $A_{\rm V}$ through the Eq. 1.12, and is a good estimate of how the young stars are embedded within the natal molecular clump. With the aim of studying the morphology of the extinction in the cluster, we have used in this work the same 3 different extinction ranges as those from chapter 2: non-extincted stars with $\log N_{\rm H}$ <22.0 cm^{-2} ($A_{\rm V}$ <5 mag); intermediate-extincted stars with 22.0 cm^{-2} <$\log N_{\rm H}$ <22.5 cm^{-2} (5 mag< $A_{\rm V}$ <15 mag); and high-extincted stars with $\log N_{\rm H}$ >22.0 cm^{-2} ($A_{\rm V}$ >15 mag).

In the case of IR observations, we will use the index $H-K$ as a proxy for the

extinction and for the presence of circumstellar material in a disk or an envelope. The observed $H-K$ color index of a star can be due to different effects: i) intrinsic photospheric stellar emission, which depends on the stellar mass and age; ii) intrinsic emission from an envelope or disk; iii) local circumstellar extinction ; and iv) global interstellar extinction. In the MonR2 stellar cluster, still embedded in the parental clump, the variation of $H-K$ due to photosphere emission arising from stars with different masses (if we consider the cluster with the same age ∼1 Myr; see C97 and A06) is nearly negligible compared with the effects related to interstellar/circumstellar extinction or intrinsic disk/envelope emission. The PMS evolutionary tracks from Siess et al. (2000) indicates that the $H-K$ colors vary from 0.4 to −0.09 for stars in the range 0.1−7 $M_{\odot}$. The IR catalogs from C97 and A06 showed that the $H-K$ values of the MonR2 cluster members are usually in the range between 0.8−4. This indicates that this contribution is negligible compared to other effects, such as interstellar/circumstellar extinction or emission from an envelope/disk.

Using equations 1.11 and 1.12 , and similarly to the 3 extinction ranges of $N_{\rm H}$ used with the X-ray catalogs, with the IR catalogs we will use the corresponding ranges $H-K$ <0.5 mag, 0.5< $H-K$ <1.2 mag and $H-K$ >1.2 mag. As we have seen in chapter 3, in the case of stars without presence of IR excesses due to circumstellar material, the $H-K$ index is a good estimate for the extinction. In the case of sources with IR excesses (∼40% and ∼55% of the sources in the C97 and A06 catalogs, respectively), the extinction calculated from $H-K$ using Eq. 1.11 is clearly an upper limit[2]. In any case, for the purpose of this chapter, we use the $N_{\rm H}$ value from X-ray as a good proxy for the extinction (interstellar+circumstellar), and high values of $H-K$ to denote the presence of large amounts of dust along the line of sight towards the stars.

4.2.4 Contamination

As we have seen in previous chapters, X-ray observations suffer in general lower foreground contamination than IR studies, because the PMS low-mass stars in X-rays are 10-10^4 times brighter than field main sequence stars. However, extragalactic sources (EG) could be confused with very embedded PMS stars. A comparison with near IR observations (from C97 and 2MASS surveys; see details in K02 and N03) shows that most of the X-ray sources detected by K02 (∼85%) and N03 (∼80%) have

[2] For the sources showing IR excesses, the contribution of intrinsic emission from circumstellar material should be substracted, as we did in chapter 3, to obtain a better estimation of the extinction.

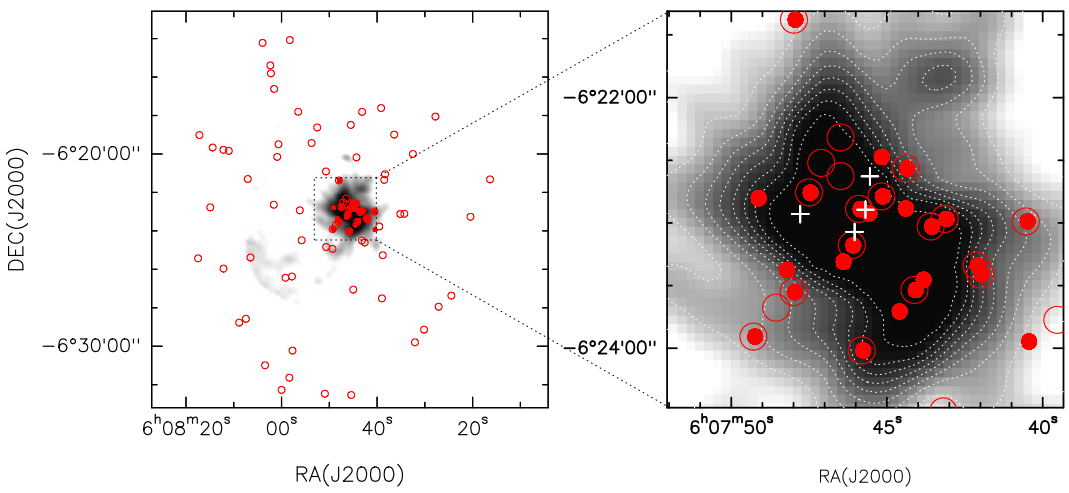

Figure 4.2: Spatial distribution of X-ray sources from K02 and N03 without IR counterparts. *Left:* Open red circles indicate X-ray sources from N03 without IR counterparts in the C97 and 2MASS catalogs (see text). Red dots denote X-ray sources from K02 without C97 counterpart. The gray scale is the emission at 850 μm detected by SCUBA (Di Francesco et al. 2008). *Right:* Zoom-in view of the 0.77 pc × 0.77 pc central region. The symbols and gray scale are the same than in the left panels. The dotted contours indicate the 850 μm SCUBA emission. The four white plus signs indicate the position of IRS1, IRS2, IRS3 and IRS5.

near IR counterpart in C07, clearly indicating they are not EG sources, much less brighter in IR. In Fig. 4.2 we show the X-ray sources from K02 and N03 without IR counterparts. As found for DR21, in MonR2 the sources are not uniformly distributed (see Fig. 4.2), as expected if they were EG sources, but concentrated in the central region, and coincident with the emission at 850 μm of the MonR2 clump detected by SCUBA (gray contours in Fig. 4.2). This strongly suggests that the sources located within the SCUBA contours are very likely embedded cluster members which have been missed by C97 observations and only revealed by X-ray observations, which are less affected by extinction.

In the case of the IR surveys, as C97 claimed, foreground stars to the MonR2 molecular cloud should have $H - K \leq 0.36$. In C97 and A06 catalogs only 9 sources and 2 sources, respectively, have these colors. We can also estimate the contamination expected using the galactic model by Robin et al. (2003). Considering the mean extinction of the cluster in the central region (∼3' ×3') of A_V=30 mag (see C97) , and the sensitivity limit in H band of 17.6 and 20.5 mag from C97 and A06, respectively, we expect only 8.4/1.6 foreground/background contaminants in the C97 survey and 1.2/1.3 in the A06 survey. Therefore, we can conclude that the majority of the stars detected in IR are embedded cluster members.

4.2.5 Completeness

The two IR surveys we use in this work have their own sensitivity limits (Table 4.1), allowing the detection of stars down to different lower mass limits. This is specially critical for the most obscured regions, where dust and gas can even block the IR radiation, preventing the detection of a fraction of the stellar population. While C07 detected all stars with stellar masses $\geq$0.1 $M_{\odot}$ with extinctions $A_V \leq$11.3 mag, the deeper observations by A06 reached a value of $A_V \leq$19 mag. However, the central region of MonR2 exhibits extinctions above these values: average extinction of $A_V \sim$30 mag in the inner 0.7 pc region, and $A_V \sim$50 mag in the inner 0.06 pc region (see C97). Therefore, it is clear that the IR observations are detecting only a fraction of the stellar population embedded in the central region.

Regarding the X-ray observations, we have shown in chapters 2 and 3 that they are very sensitive to reveal members deeply embedded in massive star forming regions, because they suffer less from extinction effects. As shown in Sect. 4.2.4, *Chandra* has revealed new sources in the central region of MonR2 missed by C97 or 2MASS observations. However, we note that the X-ray observations of MonR2 did not detect all the stars detected by the IR surveys. As an illustrative example, in the FoV from A06 (0.24 pc $\times$ 0.24 pc), they detected 181 sources, while C07 and K02 detected 122 and 50 sources, respectively.

4.3 Results

4.3.1 Spatial distribution of the PMS low-mass stellar population

★ Spatial griding method: stellar density maps

In this section we present maps of the stellar density derived for the X-ray and IR surveys. In the case of X-ray observations, we will study the population as a function of the extinction (measured by the hydrogen column density N_H). For the IR surveys, we will study the population as a function of the $H-K$ color index, which is indicative of extinction and circumstellar material (Sect. 4.2.3).

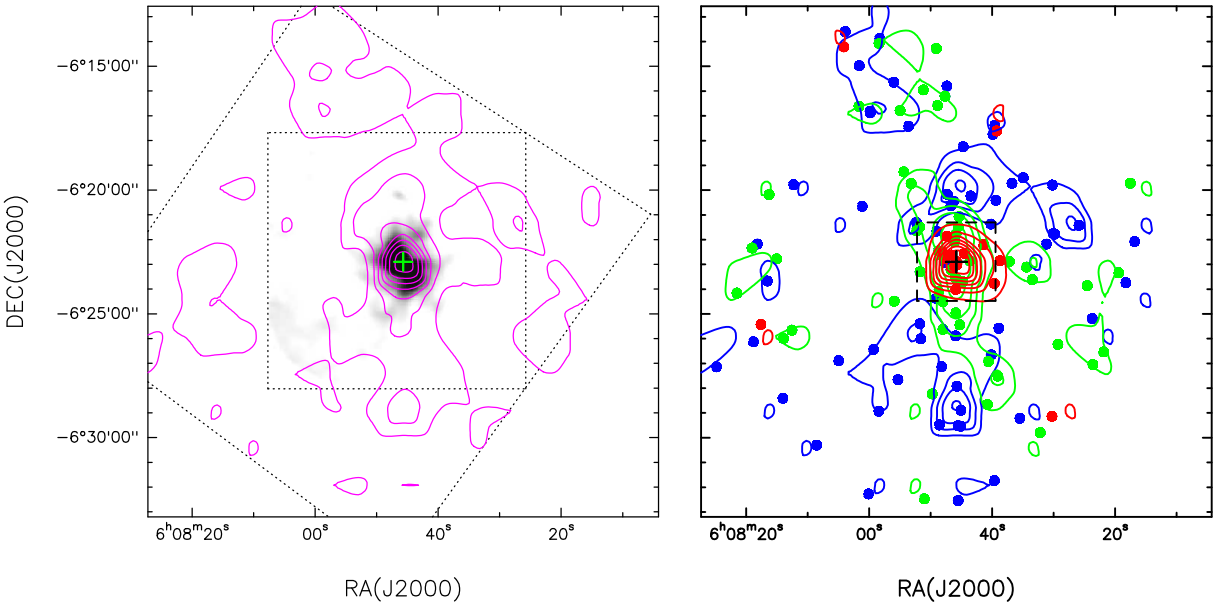

Figure 4.3: Stellar density maps of the MonR2 stellar cluster, from the X-ray catalog from N03, and using a bin size of 90" (0.35 pc). *Left:* the magenta contours show the number of stars per cell, starting from 1 star, in steps of 1 star. The background gray scale corresponds to the emission at 850 μm detected by *SCUBA*. The plus signs denotes the positions of the massive object IRS2, and the larger dotted box indicates the FoV of the Chandra observation from N03 and the smaller dotted box the FoV of the *SCUBA* image. *Right*: stellar population in 3 different $N_{\rm H}$ ranges (Sect. 4.2.3): log$N_{\rm H}$ <22.0 cm^{-2} (blue); 22.0 cm^{-2} <log$N_{\rm H}$ <22.5 cm^{-2} (green); and log$N_{\rm H}$ >22.0 cm^{-2} (red). The colored dots indicate the position of the stars and the contours the number of stars per cell, starting from 1 star in steps of 1 star. The dashed box indicates the FoV of the observations from K02 and C97.

- Large scale

To study the distribution of stars at large scale, we used the wide-field observation from N03 (FoV of 17.4' ×17.4', equivalent to 4.2 pc×4.2 pc, left panel of 4.1). Using a spatial griding method with a cell size of 90" (∼0.35 pc) we have computed the stellar spatial distribution. The results of this density analysis is shown in the left panel of Fig. 4.3. It is clear that the stellar cluster is centrally condensed, with a morphology oriented in the north-south (N-S) direction.

The right panel show the distribution of the population as a function of the extinction. The extinction exhibits a clear dependence with the distance to the cluster center: i) the non-extincted stars ($\log N_{\rm H}$ <22.0 cm^{-2}) are located in the outer part of the stellar cluster; ii) the intermediate-extincted stars appear more centrally concentrated, with an N-S elongated structure; iii) the high-extincted sources ($\log N_{\rm H}$ >22.5 cm^{-2}) are clustered in the inner region, coincident with the dusty clump detected by *SCUBA* at 850 *m*m (see gray scale in the left panel of Fig. 4.3). This central region, indicated with a dashed box in the right panel of Fig. 4.3 , will be studied in more detail in Sect. 4.3.1.

- Small scale

In this section we focus our analysis in the central region (∼ 0.77 pc × 0.77 pc), where both the stellar density and the extinction are higher. We use the X-ray observations from K02, and the IR observations from C97 and A06. Since our aim is to resolve the structure of the cluster distribution with higher spatial resolution, we use a smaller cell size of 15" (0.06 pc). In the case of the more sensitive IR observations from A06, with an even smaller FoV (Table 4.1), we also used a cell size of 7.5" (0.03 pc). The sizescales are in the range of typical dense stellar subclusters (see chapter 2 and Lada et al. 2004) and natal molecular condensations where massive stars are born (Kurtz et al. 2000; Saito et al. 2008).

The stellar distribution of the X-ray population is shown in Fig. 4.4. The left panel shows that the higher stellar density is located in the inner region of the MonR2 central clump (see comparison with SCUBA emission, dotted contours), where the massive stars (white plus signs) are located. The main density peak is found around the massive IRS2 star, which has an estimated mass of ∼13 M$_\odot$ (Jiménez-Serra et al. 2013). The right panel of Fig. 4.4 shows the spatial distribution as a function of extinction. It is remarkable that most stars exhibit intermediate or high extinction (i.e., $\log N_{\rm H}$ >22.0 cm^{-2}, $A_{\rm V}$ >5 mag), confirming that the central region of the

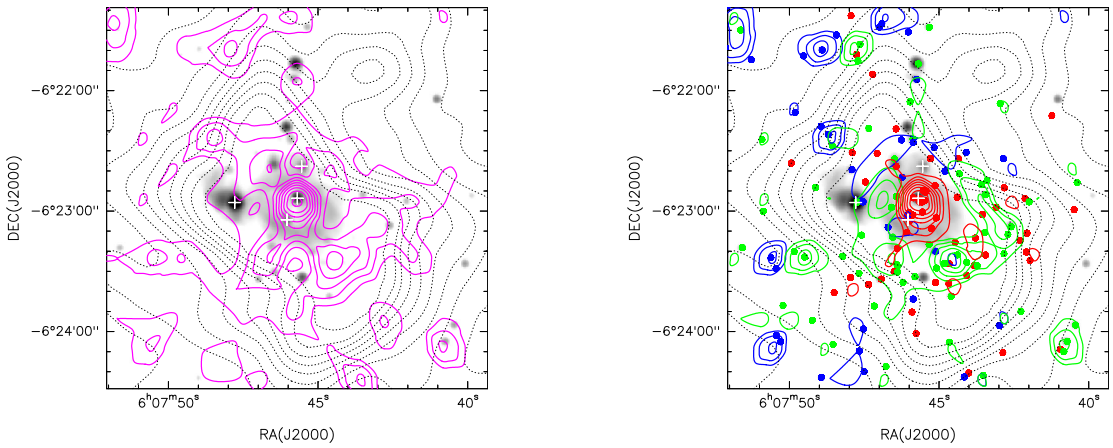

Figure 4.4: Stellar density maps of the central region of MonR2 stellar cluster, from the X-ray catalog from K02, using a bin size of 15" (0.06 pc). *Left:* the magenta contours present the number of stars per cell, starting from 1 star in steps of 1 star. The four white plus signs indicate the position of IRS1, IRS2, IRS3 and IRS5. The dotted contours correspond to the 850 μm emission detected by *SCUBA* (Di Francesco et al. 2008) and the gray scale is the IR K-band image from 2MASS. *Right:* stellar population in 3 different $N_{\rm H}$ ranges (Sect. 4.2.3): log$N_{\rm H}$ <22.0 cm^{-2} (blue contours); 22.0 cm^{-2} <log$N_{\rm H}$ <22.5 cm^{-2} (green); and log$N_{\rm H}$ >22.5 cm^{-2} (red). The colored dots indicate the position of the stars and the contours the stellar density: from 1 star in steps of 0.5 stars (blue and green contours), and from 2 stars in steps of 1 star (red contours).

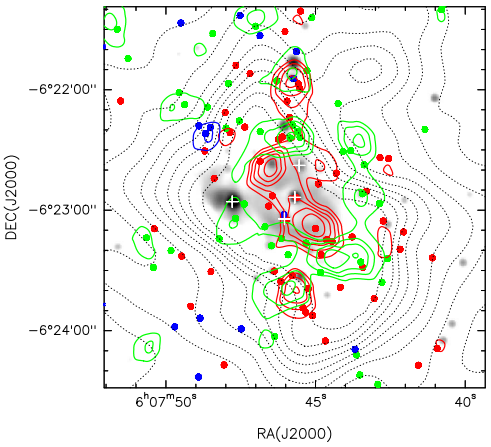

Figure 4.5: Stellar density maps of the central region of MonR2 stellar cluster, using the IR catalog from C97, using a bin size of 15" (0.06 pc), as a function of the $H-K$ color index. The blue and green contours show the number of stars per cell with $H-K$ <0.5 mag and 0.5< $H-K$ <1.2 mag, respectively, starting from 2 stars in steps of 0.5 stars. The red contours show the number of stars per cell with $H-K$ >1.2 mag, starting from 3 stars in steps of 1 star. The colored dots indicate the position of the stars in the different $H-K$ ranges. The four white plus signs indicate the position of IRS1, IRS2, IRS3 and IRS5. The dotted contours correspond to the 850 μm emission detected by *SCUBA* (Di Francesco et al. 2008) and the gray scale is the IR K-band image from 2MASS.

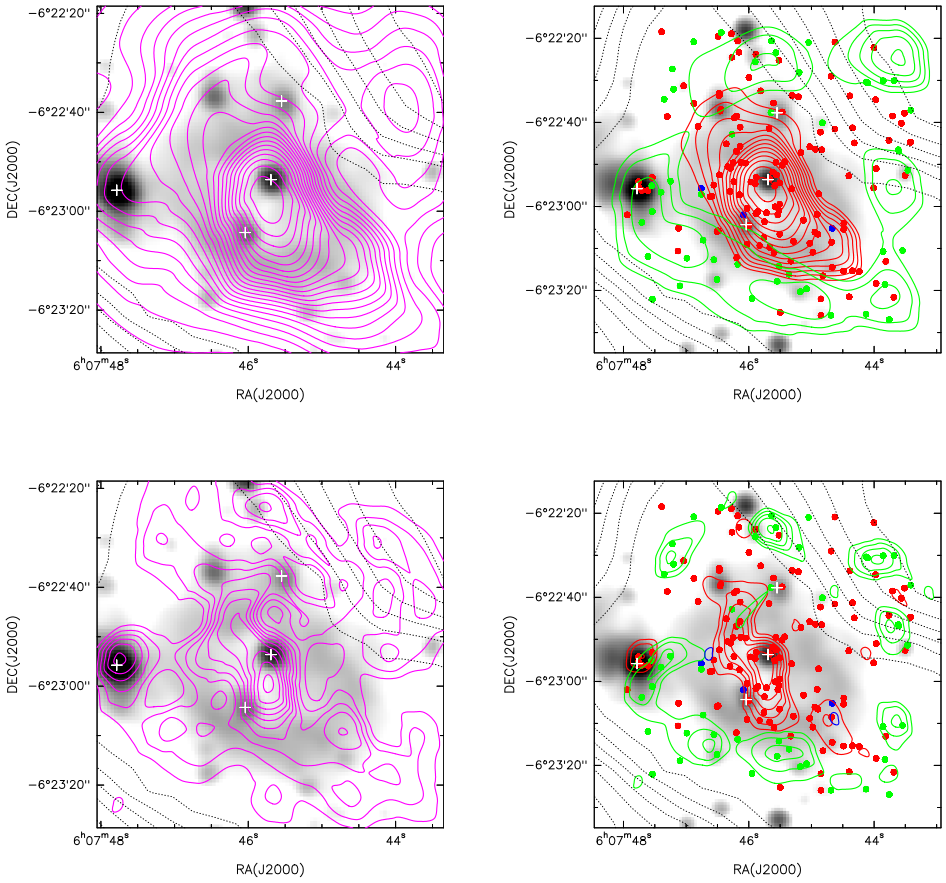

Figure 4.6: Stellar density maps of the very central region of MonR2 stellar cluster, using the IR catalog from A06, using a bin size of 15" (0.06 pc; upper panels), and a bin size of 7.5" (0.03 pc; lower panels). *Left:* the magenta contours present the number of stars per cell, starting from 1 star in steps of 1 star. The four white plus signs indicate the position of IRS1, IRS2, IRS3 and IRS5. The dotted contours correspond to the 850 μm emission detected by *SCUBA* (Di Francesco et al. 2008) and the gray scale is the IR K-band image from 2*MASS*. *Right:* The blue and green contours show the number of stars per cell with $H-K$ <0.5 mag and 0.5< $H-K$ <1.2 mag, respectively, starting from 2 stars in steps of 0.5 stars (upper right panel) and starting from 1 star in steps of 0.5 stars (lower right panel). The red contours show the number of stars per cell with $H-K$ >1.2 mag, starting from 7 stars in steps of 1 star (upper right panel) and starting from 3 stars in steps of 0.5 stars (lower right panel). The colored dots indicate the position of the stars in the different $H-K$ ranges.

cluster is still very embedded in the parental clump. The non-extincted population ($\log N_{\rm H}$ <22.0 cm^{-2}) is uniformly distributed throughout the field, without evidence of clustering. In contrast, the intermediate extincted stars (22.0 cm^{-2} <$\log N_{\rm H}$ <22.5 cm^{-2}) are distributed around a central region populated by the more extincted sources ($\log N_{\rm H}$ >22.5 cm^{-2}).

The spatial distribution of the IR observations from C97 as a function of the $H-K$ color index is shown in Fig. 4.5. A similar structure to the one observed using the $N_{\rm H}$ ranges as derived from X-rays is observed also using $H-K$ ranges. Only a few sources shows values of $H-K$ <0.5 mag (which using Eq. 1.11 would be equivalent to <5 mag), confirming that the stellar population in the central region of the cluster is embedded. The sources with 1.2< $H-K$ <0.5 mag are mainly located in a ring-like structure surrounding a central region − where massive stars are located − populated by the stars with higher values of $H-K$.

The more sensitive IR observations by A06 are focused in the very inner region of the cluster (0.24 pc × 0.24 pc). The stellar density analysis, using two cell sizes of 15" and 7.5", is shown in Fig. 4.6. The structure of the stellar density considering all stars (left panel) is centrally condensed, with the main peak around the position of IRS2. The higher resolution grid (7.5") evidences that there is a secondary peak in the position of IRS3.[3] The populations as a function of $H-K$ ranges show the same structure observed in the C97 survey, with the sources with higher $H-K$ index clustered in the center around IRS2, being surrounded by the stars with intermediate $H-K$ index. The high resolution grid (7.5") shows that the sources in the IRS3 peak have high values of $H-K$.

In Sect. 4.4 we will discuss the implication of these results in the process of star cluster and massive star formation.

★ Close neighbors method: subclusters around massive stars

In Fig. 4.7 we show the result of the close neighbors method. We have used different colors to show the location of stars with different numbers of neighbors within their associated 0.04 pc × 0.04 pc cell.

The close neighbors method confirms that the stars with higher numbers of neighbors (more than 9 stars per cell) are located in the central region of the cluster, in the region harboring the massive stars IRS1 and IRS2. The IRS3 region also harbors

[3]This stellar subcluster has been already studied by Preibisch et al. (2002) with sensitive and high resolution IR interferometric observations.

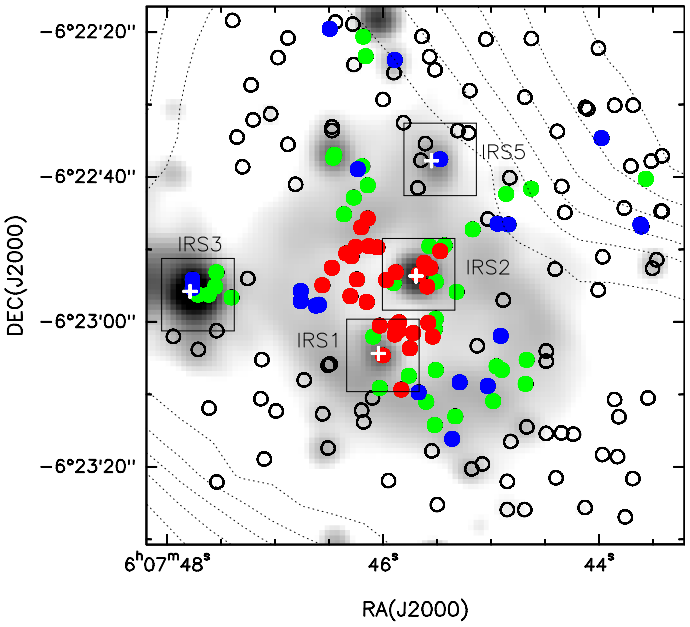

Figure 4.7: Result of the close-neighbors analysis applied to the NICMOS catalog. The blue, green and red dots are stars located at the center of cells (0.04 pc × 0.04 pc) with 6, 7-8 and >9 stars, respectively. The open circles denote stars located at the center of cells with lower number of stars. We have indicated with boxes the 0.04 pc × 0.04 pc cells around the most massive objects in the region (IRS1, IRS2, IRS3 and IRS5). The gray scale is the IR K-band image from 2*MASS*.

a dense subcluster (7 star per cell), as already showed by the higher resolution stellar density map obtained from NICMOS data (Fig. 4.6). This embedded subcluster was studied in detail by Preibisch et al. (2002), who found that it is formed by 3 massive stars and 3 lower mass stars. The IRS5 region shows a slightly lower concentration of stars (6 stars per cell), although we will see in chapter 7 that the NICMOS observations may have missed other 3 young stars located very close to IRS5.

Therefore, we have confirmed that the massive stars in the MonR2 region (IRS1, IRS2, IRS3 and IRS5) do not appear as isolated objects, but escorted by other lower mass stars in their close vicinity (0.04 pc × 0.04 pc). In Sect. 4.3.4 we will study in detail the stellar population within the cells indicated with boxes in Fig. 4.7 surrounding these massive stars.

4.3.2 Structure of the extinction: a centrally condensed clump

C97 obtained a map of the visual extinction A_V through the region from molecular ^{13}CO (1-0) data (Xie and Goldsmith 1994)[4]. They showed that the extinction has a

[4] They assumed a $^{13}CO/H_2$ abundance ratio of 1.5×10^{-6} and $N_{H2}=10^{21}$ A_V (cm^{-2}).

peaked radial profile (see their Fig. 3), with a maximum value around $A_{\rm V}$=50 mag in the inner ∼0.18 pc. Alternatively, we can also calculate a value for the expected extinction in the central region of the cluster from the mass derived by Walker et al. (1990) ($M_{\rm gas}$=180 $M_{\odot}$) in the inner 0.22 pc. This implies an average gas density in the clump, n ∼2.7 ×10^{-19} g cm^{-3}. Integrating in the line of sight from the center of the cluster to a radius of r=0.22 pc, we obtain that the maximum hydrogen column density is log$N_{\rm H}$=23 cm^{-2}, which is equivalent to A_v ∼55 mag, in agreement with the peak value from the C97 extinction map.

A centrally condensed structure has also been revealed by Gutermuth et al. (2009) using $H-K_s$ color index of a near-IR survey. The molecular observations of the dense gas tracer CS presented by Choi et al. (2000) also revealed a centrally condensed structure (see their Fig. 9), with a radial profile ∼ r^{-1} in the central 0.5 pc region.

Our approach here is an alternative study of the extinction structure using the values of $N_{\rm H}$ provided by the X-ray observations. Using the Eq. 1.12, we obtain the value for $A_{\rm V}$. As we have already discussed in Sect. 4.2.1, the N03 catalog contains less sources than K02 due to the use of a different source selection criteria.[5] This is particularly important for the center of the cluster, where the extinction is the highest. Therefore, to study the extinction up to distances of d =3 pc from the cluster center, we used the N03 catalog, while we use the K02 catalog to better characterize the inner 0.5 pc region of the cluster.

To compute the radial profile of the extinction, we have calculated the distance of each cluster member to the cluster center (considered to be the position of IRS2). Then, we have considered distance bins and calculated the median value ($A_{\rm V}^{\rm med}$) of the extinctions of the stars in each bin. The errors of $A_{\rm V}^{\rm med}$ have been computed with the median absolute error, defined as:

$$\Delta A_{\rm V}^{\rm med} = median(|A_{\rm V}^{\rm i} - A_{\rm V}^{\rm med}|) \tag{4.1}$$

where $A_{\rm V}^{\rm i}$ are the values of the extinctions considered in each distance bin. We have used bins of 0.2 pc and 0.03 pc for the N03 and K02 catalogs, respectively. The results are shown in Fig. 4.8. The upper panel of Fig. 4.8 shows that the extinction radial profile is approximately constant for distances d >0.5 pc with $A_{\rm V}$ ∼5 mag, and clearly increases in the inner region. The lower panel shows in more detail the profile

[5] Since they only considered sources detected in the soft and high energy bands, their catalog does not contain sources deeply embedded in the clump material, which are usually only observed in the hard band due to heavy absorption of softer photons.

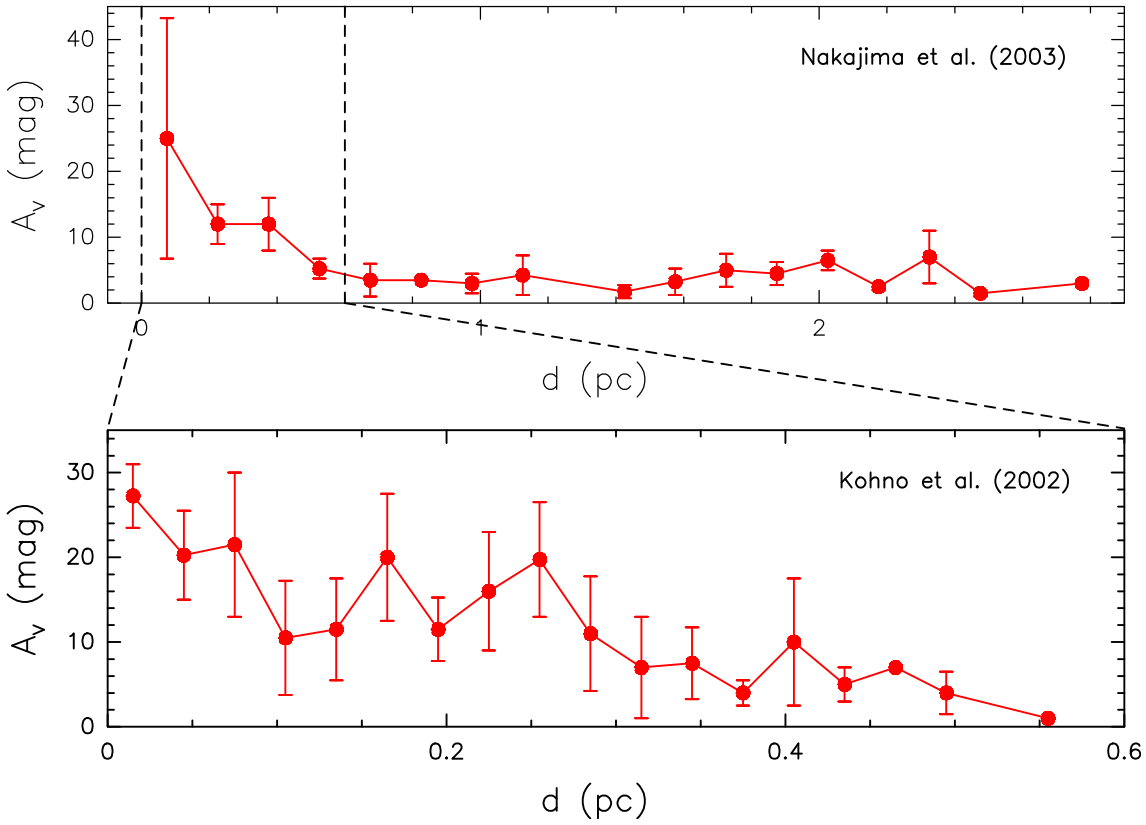

Figure 4.8: Radial profile of the extinction in the cluster, obtained from the $N_{\rm H}$ values of the stellar population provided by the Chandra catalogs N03 (upper panel) and K02 (lower panel). The distance bins used in each panel are 0.2 and 0.03, respectively. For each bin, we have calculated the median value $A_{\rm V}^{\rm med}$ of the extinction of the stars within each bin. To compute the uncertainties we have used the median absolute error (see definition in the text).

for d <0.5 pc using the K02 data, and confirms that the centrally dense radial profile, with a maximum value ∼30 mag in the vicinities of the cluster center.

4.3.3 Radial cumulative stellar density: a centrally condensed cluster

Since the stellar cluster shows a centrally condensed distribution, in this section we study the radial profile of the stellar density. As suggested by the stellar density maps shown in Sect. 4.3.1, we define as cluster center the location of the massive star IRS2.

Similarly to chapters 2 and 3, we have defined the cumulative radial stellar density (n_*) counting the number of stars located in concentric circles of increasing radius R in the plane of the sky divided by the volume of the spheres with radius R.

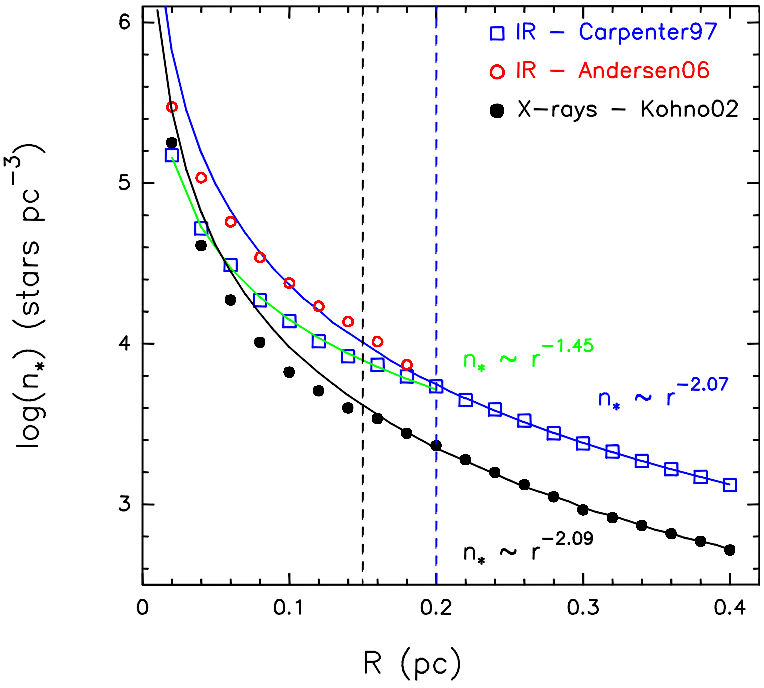

Figure 4.9: Radial profiles of the cumulative stellar density. The black dots correspond to the radial profile obtained from the X-ray observation from K02. The black line is the best fit for the radial profile for distances r >0.15 pc, which is $r^{-2.09}$. The open blue squares and open red circles are the radial profile from the IR catalogs from C97 and A06, respectively. The blue and green lines are the best fits for the outer ($r > 0.2$ pc) and inner ($r < 0.2$ pc) regions for the C97 profile, which follows $r^{-2.07}$ and $r^{-1.44}$, respectively.

In Fig. 4.9 we plot the value of the cumulative stellar density n_* versus the distance to the IRS2 position for the surveys from the X-ray catalog from K02, and the IR catalogs from C97 and A06. As shown in Fig. 4.9 the radial distribution of the population detected by C97 can be reproduced by two different radial profiles: $n_* \sim r^{-2.07}$ (blue fit) in the outer region (r >0.2 pc) and a less steep profile ($r^{-1.45}$) in the inner region 0.2 pc region. As we discussed in chapter 3 for the central region of DR21 cluster, the fact that the profile becomes less steep in the central region is an indirect evidence of the centrally peaked structure of the extinction, which prevents the detection of the more embedded objects in the very central region. Indeed, the profile of the more sensitive IR observation by A06 follows well the r^{-2} profile even for distances r <0.2 pc (see Fig. 4.9), because this observation was able to detect sources more deeply embedded (see Sect. 4.2.5). However, in the very central region, the stellar density (r <0.05 pc) observed by A06 is slightly lower than the expected from a pure r^{-2} profile, likely due to extreme extinction in the most central region.

On the other hand, since the X-rays are less affected by extinction than IR surveys,

it is expected that the radial stellar density profile follows more closely to the r^{-2} profile. The radial cumulative stellar density of the X-ray population indeed follows this profile for distances r >0.15 pc. In the inner region the observed density is slightly lower than the r^{-2} profile, but it does not exhibit the abrupt change in the radial dependence observed in the C97 observations. In fact, although the stellar density of the X-ray catalog is ∼2.5 times lower than the one from C97 in the outer part, the difference gradually decreases as the distance to cluster center decreases, to the extent that in the central region both have similar values. This clearly shows that the X-ray observations are less affected by the extinction of the clump.

The mean stellar density in the region harbored by massive stars (r <0.13 pc) is >10^4 stars pc^{-3}, with a peak value of ∼5.5×10^5 stars pc^{-3}. These densities must be considered as lower limits since they do not account for the unseen population behind very high extinctions due to sensitivity limits, nor the presence of unresolved binaries.

4.3.4 Properties of the stellar subclusters around massive stars

Our stellar density analysis have shown that the most massive objects in the MonR2 cluster (IRS1, IRS2, IRS3 and IRS5) are not isolated objects but members of dense subclusters of low-mass stars (see Fig. 4.7). Preibisch et al. (2002) already studied the embedded IRS3 subcluster using the NICMOS data also used by A06, showing that it is formed by stars with different masses from ∼1 $M_\odot$ to ∼15 $M_\odot$. However, the subclusters around IRS2, IRS1 and IRS5 have not been studied in detail so far. In this section we study the stellar population in regions of 0.04 pc × 0.04 pc around these massive stars (see Fig. 4.10). We use the NICMOS photometry from A06. They identified the sources using DAOFINF in IRAF (Image Reduction and Analysis Facility) with a 5σ threshold. The aperture photometry was performed with the APPHOTT package in IRAF. They used an aperture of radius of 0.263" around each source and the background emission was measured in an annulus from 0.75" to 1.125" (see more details in their Sect. 2.2.). We present in Table 4.2 the J, H and K fluxes obtained from the NICMOS photometry using their Eq. 1-3[6]. From this photometry we have derived the extinctions (A_V) and rough estimates for the stellar masses of

[6] The conversion was done by comparing with the photometry of 41 sources in common with C97 with 0.4≤ $m_{F160W} - m_{F160W}$ ≤ 3.2, where m_{F160W} and m_{F207M} are the magnitudes in the NICMOS bands F160W and F207M. In this work, we have applied the flux conversion to 30 sources, of which most have colors in this range . In the case of the only 4 exceptions (IRS2 A, B, D and E), the photometry should be taken with caution.

the members of the subclusters surrounding IRS1, IRS2, IRS3 and IRS5[7].

We obtain a first estimate for the extinction using a color-color (C-C) diagram (left panel of Fig. 4.11). We follow the same procedure that we applied in chapter 3. We also give an alternative second estimate of the extinction using the J vs. $J-H$ diagram (M-C, right panel of Fig. 4.11). The stellar mass can be obtained by dereddening the stars in this diagram until reaching a theoretical PMS isochrone. Since the expected median stellar age is ∼1 Myr (C97 and A06), we have used this isochrone[8]. For sources with m ≤2 $M_\odot$, there is a degeneracy because the reddening path crosses the isochrone twice, and hence two solutions are possible, one with lower mass and less extinction and other with higher mass and higher extinction.

We have used the models of Baraffe et al. (1998) (m=0.02−0.1 $M_\odot$), Siess et al. (2000) (m=0.1-7 $M_\odot$) and Palla and Stahler (1999) (m=15 $M_\odot$). Although this diagram is less affected by IR excesses, the presence of circumstellar material can still introduce systematic errors and may cause the masses to be overestimated. We show the results in Table 4.2. Since some of the stars have been also detected by Chandra, we also show the extinction resulting from the X-ray data[9]. The extinctions estimated from the color-color and magnitude-color diagrams are very similar, and they are also in agreement with the estimates from X-ray data.

★ IRS1 embedded subcluster

The star IRS1-A (also known as IRS1-SW) is the ionizing source of the HII region. It is expected to be a B0-type star in the ZAMS (Massi et al. 1985), in agreement with our mass estimate. We obtain that it is highly embedded, with A_V ∼32-33 mag. The source IRS1-B is not extincted, and also coincident with an optical star from the USNO-B1.0 catalog (Monet et al. 2003). This is the already known object IRS1-NE, a foreground optical B massive star in the main sequence (Howard et al. 1994), and hence it is not related to this subcluster. The other sources shown in the upper left panel of Fig. 4.10 are embedded lower mass stars with A_V >18 mag. The absence of stars towards the SE of IRS1 is likely due to an effect of the poorer sensitivity of

[7] As already mentioned the NICMOS data of the IRS3 subcluster was already studied by Preibisch et al. (2002). We note that specially in case of the IRS3 and IRS5 regions (see Fig. 4.10) the photometry can be partially affected by strong diffuse background emission likely related with nebulosity from dusty walls of outflow cavities (see below).

[8] It seems that some stars are even younger that 1 Myr. For instance, in chapter 7 we will derive a younger age for the dominant star in the IRS5 region. In these cases, the masses derived from the M-C diagram considering the 1 Myr isochrone should be considered as upper limits.

[9] We obtain A_V from the N_H values presented by K02 using the Eq. 1.12 of chapter 1.

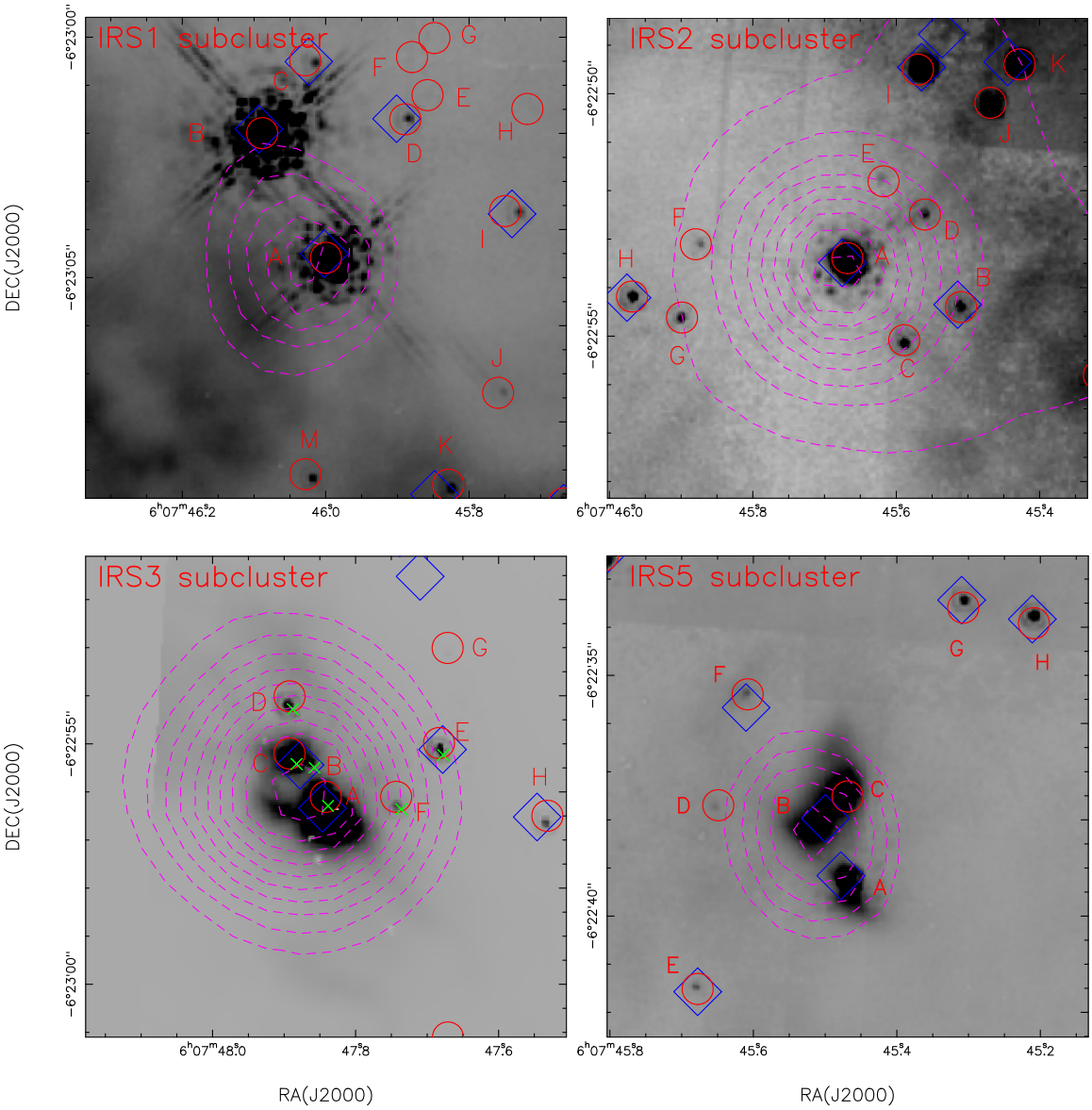

Figure 4.10: Zoom-in NICMOS F165M images of 0.04 pc × 0.04 pc regions around IRS1, IRS2, IRS3 and IRS5. The red open circles indicate the position of the stars reported by A06, and the open blue squares the stars reported by C97. In the case of the IRS3 subcluster (lower left panel) we have also added with green crosses the postions of the stars identified with high-resolution speckle near-IR interferometry by Preibisch et al. (2002). The different stars studied in Sect. 4.3.4 are labelled. The dotted magenta contours indicate the K-band emission from 2MASS.

Table 4.2: Positions and near IR magnitudes for the individual members of the IRS1, IRS2, IRS3 and IRS5 subclusters derived from the NICMOS observations (A06). We also show the estimates for the extinction and mass.

Star	near IR fluxes			IR	A_V (mag)			mass
	J	H	K	excess	C-C	M-C	X-rays	($M_\odot$)
IRS1-A	15.99±0.14	12.20±0.11	9.94±0.13	n	33	32	24	∼15
IRS1-B	11.56±0.08	11.50±0.08	11.43±0.11	n	0	0	0	
IRS1-C	21.12±0.51	18.00±0.16	15.09±0.16	y	25	22	-	0.1
IRS1-D	-	-	-	-	-	-	37	-
IRS1-E	20.56±0.33	19.98±0.32	17.04±0.25	y	∼0	<8	-	<0.02
IRS1-F	-	-	-	-	-	-	-	-
IRS1-G	-	-	-	-	-	-	-	-
IRS1-H	23.7±3.9	20.72±0.46	17.43±0.31	y	23	22	-	0.03
IRS1-I	21.62±0.50	18.00±0.11	15.00±0.13	y	29	28	-	0.2
IRS1-J	21.45±0.25	18.90±0.10	16.88±0.12	y	19	18	-	0.055
IRS1-K	20.16±0.24	17.15±0.10	14.80±0.11	y	23	23	-	0.2
IRS1-M	-	-	-	-	-	-		-
IRS2-A	17.79±0.19	13.23±0.11	8.08±0.12	y	38	39	46	∼15
IRS2-B	21.64±0.44	17.90±0.12	14.17±0.14	y	30	29	27	0.2
IRS2-C	23.01±0.78	17.71±0.11	14.99±0.13	n	40	45/50	28	3/7
IRS2-D	21.46±0.44	17.82±0.12	14.17±0.12	y	29	27	-	0.2
IRS2-E	20.88±0.38	19.75±0.33	15.15±0.22	y	6	<9	-	<0.02
IRS2-F	21.90±0.49	19.06±0.18	15.88±0.16	y	22	21	31	0.07
IRS2-G	23.91±2.9	18.56±0.18	15.53±0.17	n	45	58	-	1.3
IRS2-H[a]	-	17.31±0.12	13.89±0.04	-	-	-	-	-
IRS2-I	20.49±0.19	16.51±0.09	14.28±0.12	n	32	31	20	1.3
IRS2-J	20.79±0.2	17.11±0.09	14.86±0.12	y	30	28	25	0.5
IRS2-K	21.31±0.31	16.74±0.12	13.94±0.15	y	38	37/42	24	2.5/7
IRS3-A	13.00±0.14	9.75±0.11	7.32±0.14	y	26	-	-	∼15
IRS3-B[b]	18.1±0.2	13.5±0.2	9.1±0.2	y	39	-	-	∼15
IRS3-C	14.03±0.14	11.25±0.11	8.85±0.13	y	22	25	8	∼15
IRS3-D	16.01±0.13	13.38±0.11	11.77±0.15	y	20	19/25	-	2.5/7
IRS3-E	14.74±0.11	13.34±0.09	12.30±0.12	y	8	6	3	0.5
IRS3-F	16.76±0.14	14.21±0.19	12.30±0.13	y	19	19	-	1.5
IRS3-G	19.67±0.20	17.41±0.19	15.22±0.19	y	17	15	-	0.09
IRS5-A[c]	17.24±0.05	14.48±0.03	11.97±0.03	y	31	20/28	-	1.5/5
IRS5-B[d,e]	-	-	11.05±0.02	-	-	-	-	-
IRS5-C[e]	16.35±0.13	12.58±0.10	10.13±0.12	y	30	33	-	-
IRS5-D	16.96±0.10	15.16±0.08	13.99±0.10	y	12	11	-	0.2
IRS5-E	23.7±2.0	18.30±0.12	15.54±0.13	n	41	44	-	1.7
IRS5-F	21.41±0.29	17.44±0.08	14.53±0.10	y	32	30	-	0.5
IRS5-G	20.72±0.22	16.51±0.12	13.60±0.14	y	35	34	22	1.7
IRS5-H	19.31±0.14	16.69±0.11	14.82±0.14	y	20	20	-	0.2

[a] This star is not detected neither in the shorter wavelength NICMOS filter (F110W) nor in the J band in the C97 observations (their source 205). We present here the fluxes at H and K bands from C97.

[b] Since A06 did not report this source, we use the fluxes from Preibisch et al. (2002).

[c] Since A06 did not report this source, we use the fluxes from C97 (their source 151). As we will show in chapter 7, this source dominates the emission at longer wavelengths: IRAC 1-4 (3.6−8.0μm) and (sub)millimeter. We will study in more detail the full Spectral Energy Distribution (SED) of this source, obtaining that it is a embedded young star with a mass of ∼7 $M_\odot$, which is roughly consistent with the higher mass estimated here from the M−C diagram.

[d] Since A06 did not report this source, we use the fluxes from C97 (their source 156).

[e] As we will discuss in chapter 7, the sources IRS5-B and IRS5-C are likely reflected light arising from the dusty walls of an outflow cavity, rather than young stars.

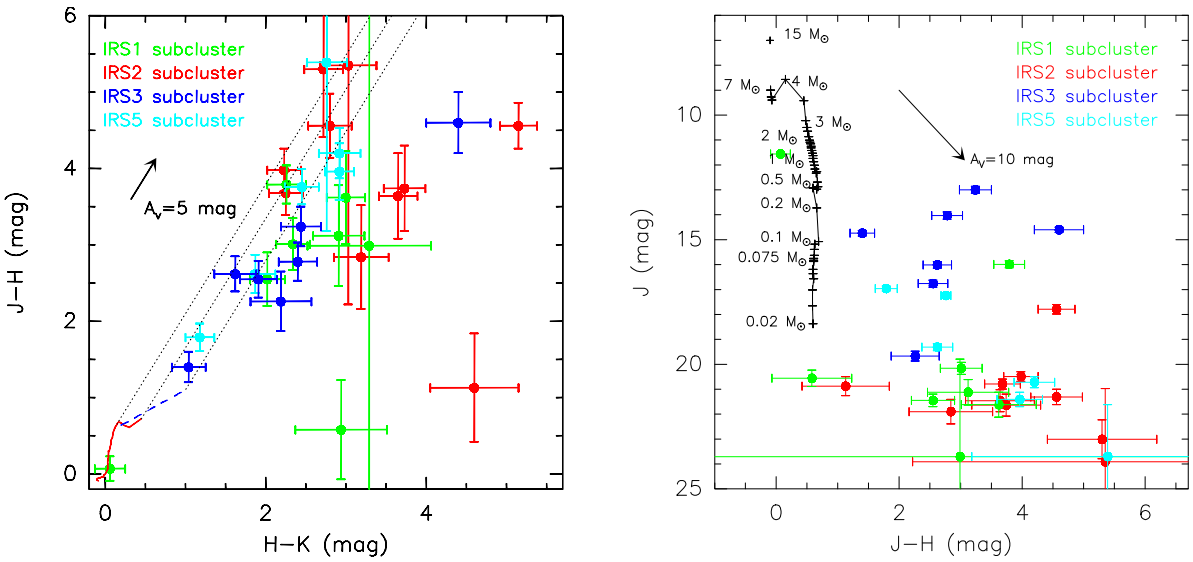

Figure 4.11: *Left:* $J-H$ vs. $H-K$ color-color diagram of the stellar population within regions of 0.04 pc × 0.04 pc around the most massive stars IRS1, IRS2, IRS3 and IRS5. The solid red line indicates the IR colors of ZAMS stars with masses from 0.1 to 7 $M_\odot$ from the theoretical evolutionary tracks of Siess et al. (2000). The dashed blue line denotes the unreddened locus of intrinsic near-IR excesses due to presence of disks from Meyer et al. (1997). The black dotted lines are reddening vector using the extinction law from Rieke and Lebofsky (1985), extended from the ZAMS colors and the unreddened locus. *Right:* J vs $J-H$ diagram of the stellar population within regions of 0.04 pc × 0.04 pc around the massive stars IRS1, IRS2, IRS3 and IRS5. The plus signs and solid line in the left part of the diagram shows theoretical colors and magnitudes based on the PMS models from Baraffe et al. (1998) (m=0.02-0.1 $M_\odot$), Siess et al. (2000) (m=0.1-7 $M_\odot$) and Palla and Stahler (1999) (m=15 $M_\odot$) for an age of 1 Myr. The arrow shows the reddening vector for A_V = 10 mag, using the extinction law from Rieke and Lebofsky (1985).

the IR NICMOS observations due to strong extended emission from the IR ring-like nebula (see right panel of 4.1).

★ IRS2 embedded subcluster

The extinction obtained towards this subcluster (upper right panel of Fig. 4.10) confirms that it is deeply embedded, with extinctions up to A_V ∼50 mag, in agreement with the extinction peak from C97 and the value obtained by Henning et al. (1992) from millimeter emission. Our results show that the IRS2 subcluster is more embedded than the other subclusters in MonR2. This is in agreement with the overall centrally condensed structure of the extinction of the MonR2 cluster (Sect. 4.3.2), where the main peak in IRS2 is located towards IRS2. This was also noted by Henning et al. (1992), who found that IRS2 is more extincted than IRS1 and IRS3 using low resolution millimeter observations.

As expected, we obtain that IRS2-A is a massive star. This estimate is consistent with the total luminosity of the source (5000-6000 $L_\odot$, Henning et al. 1992), which implies a B1 star on the zero-age main sequence with a mass of ∼13 $M_\odot$ (see also Jiménez-Serra et al. 2013). This source has been detected in the high resolution observations at 0.85 mm and 1.3 mm that we discuss in chapter 7 (see also Fig. 4.10).

Our analysis of the cluster clearly shows that the other members of this compact subcluster are lower mass stars. The stars IRS2-C and IRS2-K are intermediate-mass stars (2-7 $M_\odot$), and the remaining sources are low-mass stars (<1.3 $M_\odot$).

★ IRS3 embedded subcluster

We have obtained JHK fluxes (following the procedure from A06) slightly different from the ones derived by Preibisch et al. (2002) from the same NICMOS data (∼1 mag at J band and ∼0.6 mag in H and K bands). This discrepancy likely arises from the different photometry measure analysis between A06 and Preibisch et al. (2002) (they used different apertures, software packages and flux conversions between NICMOS and JHK filters[10]).

In any case, the results for extinctions and stellar masses are in good agreement (∼15% discrepancies in extinction and ∼45% in mass, compare our Table 4.2 with

[10] Preibisch et al. (2002) used DAOPHOT in IRAF (Image Reduction and Analysis Facility) to measure the fluxes in apertures of radius 0.188" for sources IRS3 A, B, C, D and F, and 0.5" for source E. The background flux was determined from a circular point-source free area between B and E. The JHK fluxes were determined according to the recipe in the NICMOS handbook.

their Table 2), having in mind that they are rough estimates. As commented before, we note that the accuracy of the IR fluxes is limited by the strong diffuse background emission in this region.

We also obtain that IRS3-A, IRS3-B[11] and IRS3-C are massive stars. IRS3-D is an intermediate-mass star and IRS3-E and IRS3-F are low-mass stars. Furthermore, in our analysis we have also included the source IRS3-G, which is an embedded star with a mass even lower.

All the stars of this subcluster have A_V >15 mag, with the exception of IRS3-E. We have obtained for this source A_V >6−8 using the IR diagrams. Moreover, IRS3-E is coincident with an optical star in the Monet et al. (2003) catalog, confirming that it is not deeply embedded. Given that it shows a significant IR excess, it seems unlikely that it is a foreground field star. Therefore, it seems a young MonR2 star located in the foreground region of the cluster.

★ IRS5 embedded subcluster

The NICMOS observations reveal up to 8 IR sources that the vicinity of IRS5 (lower right panel of Fig. 4.10). The more massive object is IRS5A. In chapter 7 we will show that the source IRS5A is very young stellar object enshrouded by a dense circumstellar envelope (as shown by Spitzer and SMA observations). This star is not reported in the NICMOS catalog from A06, but it was detected by C97 (blue square in lower right panel of Fig. 4.10) and Spitzer-images (Gutermuth et al. 2009). In chapter 7 we will study its spectral energy distribution (SED) in detail, showing that it is a very young star with a mass of ∼7 $M_\odot$, in agreement with the upper mass estimated from the near-IR M-C diagram. As we will discuss in chapter 7, this source is a very early evolution and likely in the way to become massive.

We will also show in chapter 7 that the sources labeled as IRS5B and IRS5C in Fig. 4.10 are likely due to IR nebulosity related to an outflow driven by IRS5A, rather than stellar objects.

The HST-NICMOS observations reveal the presence of five low-mass stars (IRS5D-IRS5H) with extinctions from ∼10 to 40 mag, indicating that they are embedded members of the subcluster. Besides these stars, the SMA millimeter observations we present in chapter 7 also show that IRS5A is resolved into binary (IRS5A-1 and IRS5A-2, see Fig. 7.3), and that other source (IRS5A-3) is located towards the west of IRS5A. Therefore, it is clear that the close vicinity of IRS5 region is populated by

[11] We will see in chapter 7 than IRS3-B is likely driving a compact molecular CO outflow.

up to 8 young embedded stars.

4.4 Discussion

4.4.1 Scenario for massive star formation: high fragmentation and competitive acretion

We discuss in the following points the implications of our analysis in the formation of massive stars in MonR2.

• *High levels of fragmentation, from clump to cores:* The combined IR and X-ray surveys show that the MonR2 central clump (∼0.4 pc) has formed a crowded low-mass star cluster, which implies that it has suffered high fragmentation. This is also supported by observations of gas and dust (Richardson et al. 1988; Walker et al. 1990; Choi et al. 2000), which found that the volume filling factor − ratio between the effective volume of the emitting sources and the total volume of the region − is <<1, indicating that the parental clump has fragmented into smaller cores. Otherwise, the high central densities observed in the inner 0.2 pc ($10^{6.5-7}$ cm^{-3}, see Fig. 9 from Choi et al. 2000) would produce column densities of log$N_{\rm H}$ ∼24.3-24.8 cm^{-2}, which are two orders of magnitude higher than the observed towards the stars. Therefore, it is clear that the dense gas is concentrated in smaller cores. Indeed, the higher angular resolution interferometric observations from Gonatas et al. (1992) showed that the clump (see their Fig. 2) fragments into condensations with sizes down to 0.036 pc. This high level of fragmentation has been also reported in other massive star-forming clumps that split into denser and compact cores with sizes around 0.03−0.05 pc (Saito et al. 2008).

Our cumulative density analysis (Sect. 4.3.3) indicates that there are ∼ 200 stars in the inner 0.22 pc region. Assuming a typical SFE efficiency for young clusters of 0.3 (Lada and Lada 2003b) and the mass of the clump in this region ($M_{\rm gas}$ ∼180 M$_\odot$, Walker et al. 1990), we obtain that the total stellar mass would be M_* ∼80 M$_\odot$. This would imply a mean star mass of ∼0.4 M$_\odot$. We compare this value with the mass expected from Jeans fragmentation (see chapter 1), $M_{\rm Jeans}$. The simulations by Bonnell and Bate (2005) showed that the characteristic stellar mass of the final stellar population is around the $M_{\rm Jeans}$ of the parental clump. We consider that the central part (r <0.22 pc) of the initial parental clump had a total mass of $M_{\rm tot} = M_{\rm gas} + M_*$ =260 M$_\odot$. Assuming a spherical clump with uniform density this

implies an average gas density of $\sim 4 \times 10^{-19}$ g cm^{-3}. Using the Eq. 1.1, and a typical temperature of 10 K at the moment of fragmentation, we obtain that $M_{\rm Jeans} \sim 0.5$ M$_{\odot}$, which is very similar to the mean stellar mass we have previously calculated. This implies that the observed number of stars in the inner 0.22 pc, where the massive stars are born, is consistent with Jeans fragmentation. However, Jeans fragmentation does not produce massive stars in the regions with denser gas, as observed in MonR2. Therefore, other mechanism is needed to account for the formation of massive stars. We propose that this is competitive accretion (see below).

• *Massive stars are located in the region with higher low-mass stellar density:* As occurred in Orion and DR21, the spatial distribution of PMS low mass-stars shows that massive stars are located in the regions with the highest stellar density, which in the case of MonR2 is at the center of the cluster. Although an overall mass segregation in the cluster is not compelling (C97), it is clear that the most massive stars are located in the inner part of the cluster (r <0.13 pc), while the cluster extends more than 3.5 pc.

The detailed analysis of the close vicinity of the massive stars within a region 0.04 pc×0.04 pc, shows that they contain stellar populations with >6 stars in all cases (>10^5 stars pc^{-3}). This clearly indicates that fragmentation has also been acting at these small scales, producing subclustering instead of single massive stars formed by monolithic collapse of the natal core (Krumholz et al. 2007). In their simulations Krumholz et al. (2012) found that the massive stars formed in distinct and non-subfragmented massive cores without the presence of low-mass stars in their 0.04 pc×0.04 pc vicinity (see their Fig. 10). However, our analysis of the regions of the same size around the most massive objects in MonR2 have revealed that they are escorted by low-mass stars, in agreement with competitive accretion simulations (e.g. Smith et al. 2009b).

• *A centrally condensed structure for the extinction:* Our study of the stellar population as a function of the extinction, from large scales to small scales shows a clear centrally condensed structure of the extinction (in agreement with molecular observations; see C97 and Choi et al. 2000). The low resolution grid (cells of 0.35 pc size) shows that the PMS stars emitting X-rays with higher extinctions (log$N_{\rm H}$ >22.5 cm^{-3} or $A_{\rm V}$ >15 mag) are concentrated in the central region (right panel of Fig. 4.3), while the population with lower extinction appears gradually at larger distances to the cluster center (right panel of Fig. 4.3). Our high resolution grids (cells of 0.06 pc and 0.03 pc size) have revealed an structure of PMS stars with intermediate extinction

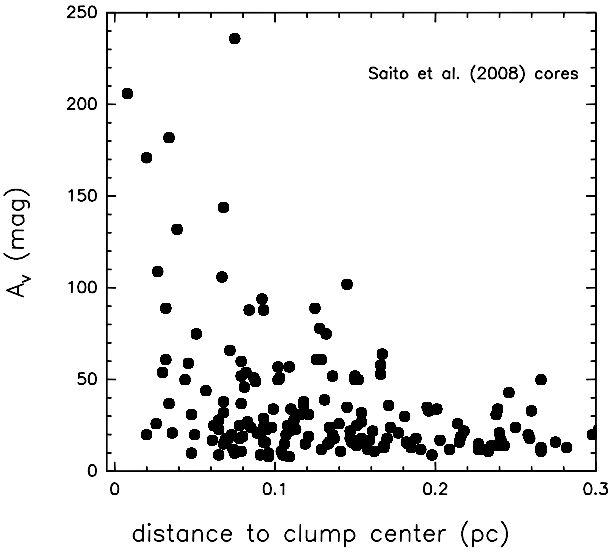

Figure 4.12: Hydrogen column density of the cores detected by Saito et al. (2008) towards different massive star forming clumps versus the distance to the clump center.

in a ring-like geometry surrounding a central region populated by stars more deeply extincted. This central region harbors the massive stars (Fig. 4.4, 4.5 and 4.6). This structure is similar to that found in chapter 2 around the massive star $^1\theta$ *Ori C* in the Trapezium Cluster, and can be explained as the outcome of the competitive accretion from the surrounding gas in a clustered environment. In this scenario, the central overall gravitational potential well of the cluster transfers gas to the center, where the stars can accrete additional material. Then, while the outer region is less extincted, the inner region appears more extincted. Those stars located in the central region or those favoured by the local gravitational potential wells created by dense subclusters *win* the competition from the gas and are able to become massive.

A centrally condensed structure of the extinction have been also observed towards other massive star-forming regions (Saito et al. 2008). In Fig. 4.12 we have plotted the extinction of the cores resulting from the fragmentation of the clumps detected by Saito et al. (2008) as a function to the distance to the cluster center[12]. It is clear that the more extincted cores are located in the more central regions, in agreement with the centrally condensed structure of the extinction found in MonR2.

• *The r^{-2} profile for the cumulative stellar density:* The MonR2 cluster shows a clear centrally condensed structure in the low-mass stellar content (Sect. 4.3.3). The cumulative stellar density follows a r^{-2} radial profile, as occurred in the clusters in

[12] We have converted the N_{H_2} values provided by Saito et al. (2008) to visual extinction A using the relation $N_{H_2}(\mathrm{cm}^{-2})=10^{21}\ A_V(\mathrm{mag})$

OHC and DR21. This may indicate that this profile is a common feature of embedded clusters. These clusters are in their first evolutionary stages and hence they are not expected to have suffered significant dynamical evolution. Therefore, if this profile is confirmed in a more complete sample of young massive star-forming regions, it could provide important clues about how the clusters have been formed. Only X-ray (like in the cases of OHC and DR21, chapters 2 and 3) and deep IR observations like the ones shown here (HST-NICMOS data from A06) are able to penetrate into the high extincted regions located in the center of the clusters and reveal their radial profile.

• *On-going star formation in the center of the cluster:* The massive stars (expected to be in a early evolutionary stage) and the detection of a cluster of CO outflows expected to be driven by very young objects (see chapter 7) towards the very inner region of the cluster (r <0.15 pc) evidence active on-going star formation. This is supported by the large concentration of dust in the central region traced by SCUBA (Fig. 4.2). Furthermore, the youngest objects (Class I) are confined in the region with SCUBA dust emission, while Class II are more distributed (Fig. 4.13). Therefore, it seems that there is an age segregation across the cluster. This is supported by the observed structure of the extinction, because there is a correlation between the extinction of the stars and their evolutionary phase: the more extincted the younger (Prisinzano et al. 2008 and Ybarra et al. 2013). Therefore, an scenario of $inside-out$ sequential star formation, previously suggested (Hodapp 2007), can be ruled out.

Our interpretation in terms of a competitive accretion scenario can naturally explain the on-going star formation activity in the center of the cluster. The potential gravitational well created by the whole cluster funnels gas to the central region, where new star formation can be fed and some stars can grow to become massive. This can explain the apparent age gradient observed in MonR2 and the ones reported in other clusters like Orion or NGC 2024 (Reggiani et al. 2011; Getman et al. 2014).

.

• *Large-scale accretion filaments feeding cluster and massive star formation:* We have discussed in previous chapters that the central regions of the clusters can be fed by through dusty/molecular filaments that tranfer mass from the outer regions. In the case of MonR2, large-scale *Spitzer*-IRAC images have revealed a network of bright filament-like features located in the northern region of the stellar cluster (Fig. 4.14). As proposed by Hodapp (2007), these long (up to 2 pc) filaments are likely due to H_2 and polycyclic aromatic hydrocarbons (PAH) emission excited by the illumination

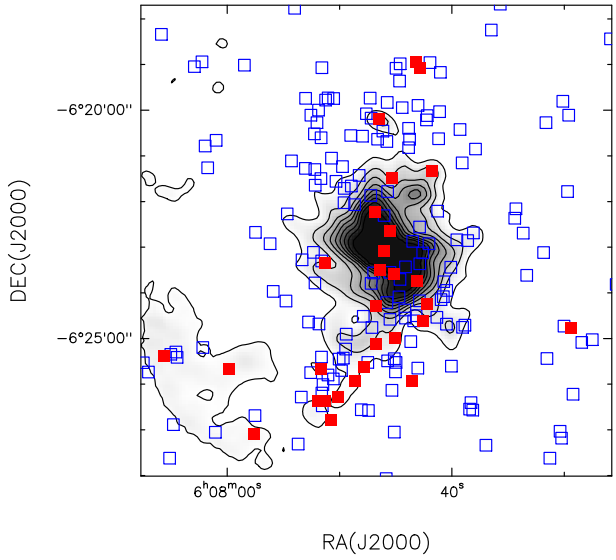

Figure 4.13: Spatial distribution of young stars classified from their mid-IR Spitzer colors as Class I (protostars with infalling envelopes or deeply embedded sources; red squares) and Class II (PMS stars with circumstellar disks; open blue squares) by Gutermuth et al. (2009). The gray scale and black contours contours correspond to the 850 μm emission detected by *SCUBA* (Di Francesco et al. 2008). The FoV of the image is 2.3 pc × 2.3 pc.

of the background MS star related with the optically reflection nebula vdB 68 (Fig. 4.15). These dusty filaments seem to converge towards the central part of the stellar cluster (Fig. 4.14), and therefore they might be infalling towards the gravitational potential well. The low spatial resolution CO maps (beam of 2.6', i.e., 0.6 pc) from Loren (1977) revealed that there is also molecular material in the region where these dusty filaments appear. However, new observations with higher spatial resolution are needed to identify the molecular counterparts of the filaments detected in the IR, and to better study their properties.

• *Clues about initial conditions of cluster formation:* Since it is expected that the cluster has suffered a global collapse (see for instance simulations by Bate 2012), the current r^{-1} profile of the gas (Choi et al. 2000, and confirmed by other observations) suggests that the initial gas density profile of the clump was shallower. This agrees with the simulation by Smith et al. (2009b), who showed that the initial clump evolves from a diffuse distribution to a centrally condensed distribution, by a combination of global collapse and competitive accretion. As opposed from a rapid collapse of a strongly centrally peaked natal clump, a more uniform initial density profile would allow the initial turbulence to develop multiple overdensities in the clump. The evolution of these overdensities would give birth to a stellar cluster of low-mass stars,

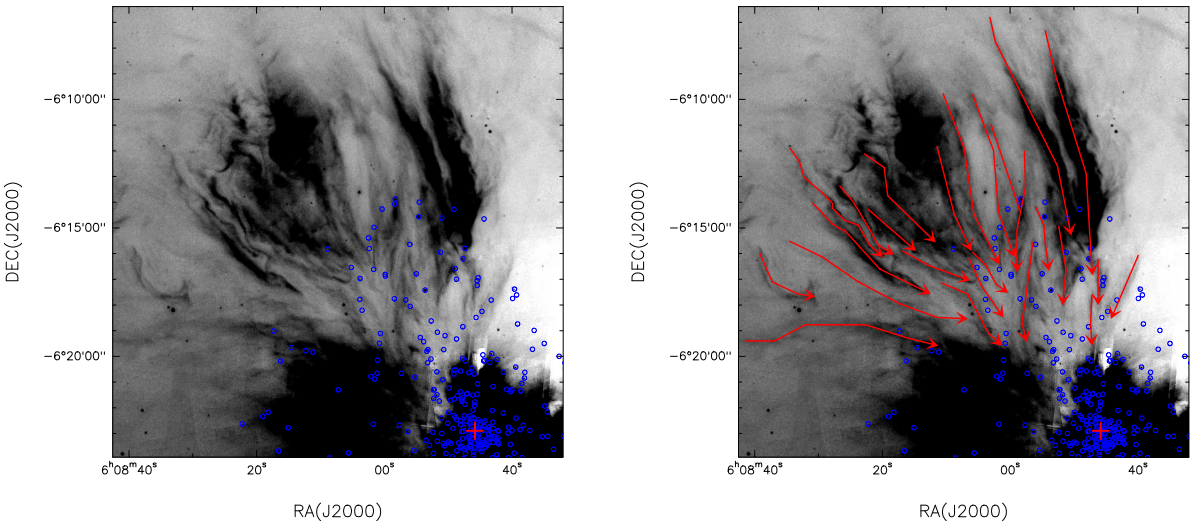

Figure 4.14: *Left:* Spitzer IRAC 4 (8 μm) large-scale image (∼4.2 pc × 4.2 pc) of the region located towards the north of the MonR2 star-forming clump analysed in this chapter. The blue open circles are X-ray sources detected by Chandra (from K02 and N03). The red plus sign indicate the position of IRS2. The bright emission from the region located towards the east of the MonR2 clump is the reflexion nebula vdB 69, which also appears in optical images (see Fig. 4.15). *Right:* Same image than in the left panel, with the main filament-like features indicated with red arrows.

as observed in MonR2, instead of a single massive object (Girichidis et al. 2011).

• *Impact of outflow turbulence:* The coincidence in the central region of a dense cluster of low-mass stars and a group of compact CO outflows (see chapter 7) suggests that the turbulence injected by outflows is not providing support against fragmentation down to Jeans masses, as suggested by Fontani et al. (2012). Conversely, the outflow feedback could favor fragmentation and the formation of subclusters (further discussion about implications of outflow feedback in chapter 8).

4.4.2 The origin of the large-scale outflow

The stellar density found in the central region of the MonR2 cluster (>$10^{5.5}$ stars pc^{-3}) is higher than the one we reported in the central DR21 cluster (chapter 3) and close to the one found in the Orion Hot Core clusters (chapter 2). These three regions present large-scale and highly-energetic outflows whose origin is still under debate (see also chapters 2 and 3). In the upper panel of Fig. 4.15 we show the large-scale CO outflow arising from the MonR2 clump (Loren 1981). For comparison, in the lower panel we show the same FoV with the positions of the Chandra X-ray PMS stars overplotted (from K02 and N03).

As we have already discussed from Fig. 2.15 of chapter 2 and Fig. 3.19 of chapter 3, a direct stellar collision in these dense low-mass star clusters associated with massive stars is likely, especially if massive stars are involved. Moreover, this is favored by the presence of circumstellar disks, binaries and accretion of gas, which are all expected in young star forming clusters. The presence of highly embedded and dense stellar clusters in these 3 massive star-forming regions supports the hypothesis that the large-scale outflows may have been triggered by violent interaction between some of the members of the young stellar clusters.

4.5 Summary and conclusions

In this chapter we have studied the spatial distribution of the low-mass star population in the Monoceros R2 star-forming region, using a spatial gridding and a close neighbors method. The stellar density maps from the spatial gridding at large scales (4.2 pc $\times$ 4.2 pc, cells of 0.35 pc size) and smaller scales (0.77 pc $\times$ 0.77 pc, cells of 0.06 pc size; and 0.24 pc $\times$ 0.24 pc, cells of 0.03 pc size) show a centrally peaked low-mass population, with its maximum found in the inner region where the more massive stars (IRS1, IRS2, IRS3 and IRS5) are located. The cumulative stellar density shows a steep radial profile following r^{-2}, as observed in the clusters of OHC and DR21, which suggests that this profile is a birthmark of young embedded stellar clusters.

The close-neighbors method shows that the very close vicinity (0.04 pc $\times$ 0.04 pc) of the more massive stars is populated by subclusters of lower mass stars, with >6 stars in all cases (>$10^{5.25}$ stars pc^{-3}). Using HST-NICMOS near-IR photometry we have analysed in detail the properties of these subclusters, obtaining rough estimates of their masses and extinctions. We have confirmed that these compact subclusters are highly embedded ($A_{\rm V}$ >20 mag) and that they host stars from low to high masses.

We have derived the radial structure of the extinction from the hydrogen column density derived towards the PMS stars, finding that it is centrally peaked, in agreement with other molecular and dust observations. In the very central region (r <0.15 pc) the stars with lower extinctions show a ring-like structure surrounding an inner region with more extincted stars, similarly to the structure observed in the Trapezium Cluster in Orion (chapter 2).

Our analysis of the spatial distribution of the cluster is compatible with Jeans fragmentation, which breaks the parental clump in smaller and dense cores with

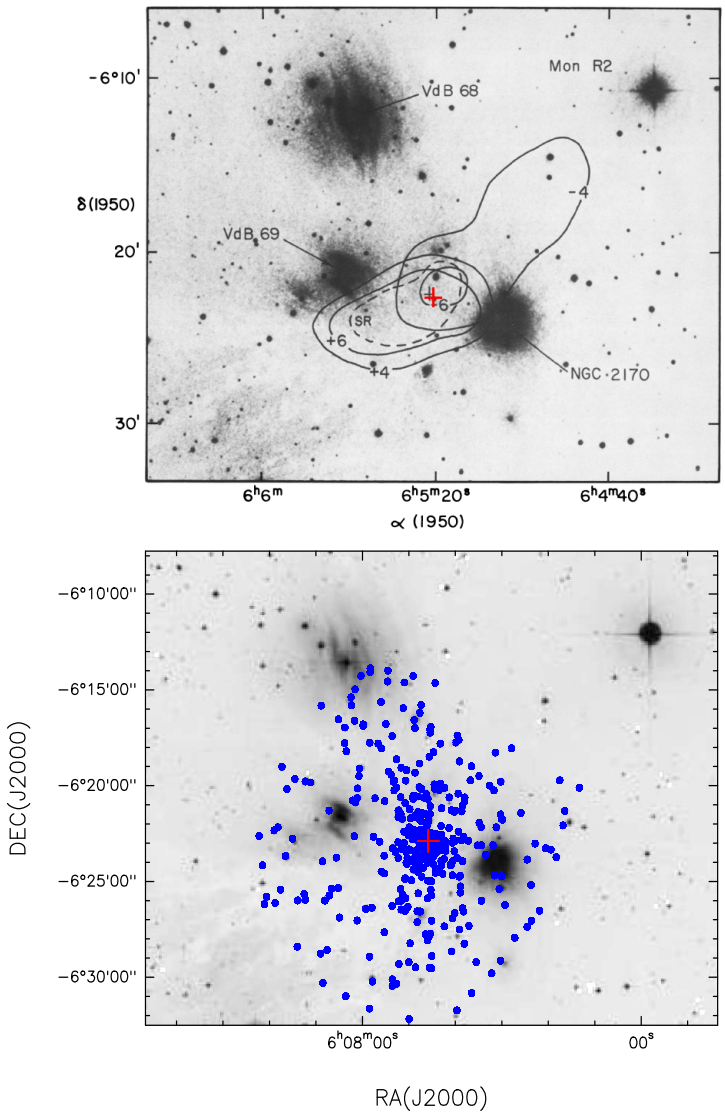

Figure 4.15: *Upper panel:* Large-scale CO outflow lobes (redshifted and blueshifted lobes at ±4 and ±6 km s^{-1}; solid lines), adapted from Loren (1981). The background image is from the optical red print of the Palomar Sky Survey, and the red plus sign denotes the position of the IRS2 star. *Lower panel:* For comparison we show a similar optical image (from Digital Sky Survey (DSS) at 0.468 μm) of the same FoV, with the positions of the Chandra X-ray PMS stars overplotted (from K02 and N03). As in the upper panel, the red plus sign denotes the position of the IRS2 star.

masses $\sim M_{\rm Jeans}$ and forming the low-mass stellar cluster. The overall potential gravitational well of the cluster funnels gas through accretion filaments to the central region, where some stars win the competition for the gas and can become massive. This competitive accretion scenario is also in agreement with the evidence for active on-going star formation in the center of the cluster (large concentration of gas and dust, presence of molecular outflows and Class 0/I stars), and seems to rule out the the *inside − out* sequential star formation previously suggested for this cluster.

Finally, we propose that the origin of the highly-energetic large-scale outflow detected in the region may be due to the collision of two stars in the high dense cluster (stellar density peak of $>10^{5.5}$ stars pc^{-3}), as ocurred in OHC and DR21 (see chapters 2 and 3).

CHAPTER 5

Short- and long-term radio variability of young stars in the Orion Nebula Cluster and Molecular Cloud

Abstract

In this chapter, we present new Karl G. Jansky Very Large Array (VLA) multi-epoch radio continuum monitoring of the Orion Nebula Cluster (ONC) and the background Orion Molecular Cloud (OMC). Our observations reveal the presence of 19 radio sources, mainly concentrated in the Trapezium Cluster and the Orion Hot Core regions. With the exception of the Becklin-Neugebauer (BN) object and the source C (which we here identify as dust emission associated with a proplyd) the sources all show variability on timescales of months. We find tentative evidence of variability in the emission from the massive protostar Orion source I. Our observations also confirm radio flux density variations of a factor >2 on timescales of hours to days in 5 sources. One of these flaring sources, OHC-E, has been detected for the first time. Combining our sample with other radio and X-ray catalogs, we have studied the properties of the entire sample of radio/X-ray stars in the ONC/OMC region (55 sources). We have classified the sources as visible stars of the ONC (42 sources, $\sim$ 76%), younger stars still embedded in the OMC (11 sources, $\sim$ 20%), one confirmed extragalactic source (2%), and source which may be either extragalactic or an OMC member (2%). Among the ONC stars, 60% of the radio sources are associated with proplyds. We conclude that the radio emission can be attributed to two different components: i) highly-variable (flaring) non-thermal radio gyrosynchrotron emission produced by electrons accelerated in the magnetospheres of pre-main sequence low-mass stars; ii) thermal emission due to free-free radiation from ionized gas and/or heated dust around embedded massive objects and proplyds. Based on our detections of radio flares, we have estimated a radio flaring rate of $\sim$0.14 flares day^{-1} in the dense stellar cluster

embedded in the Orion Hot Core region. This suggests that radio flares are more common events during the first stages of stellar evolution than previously thought. A comparison between the radio and X-ray population in Orion shows that the radio detections have been limited mainly to the brighter X-ray stars, supporting the link between the X-ray activity and the mechanisms responsible for the radio variability. The advent of improved sensitivity with the new VLA and ALMA will dramatically increase the number of low-mass stars in young clusters detected at radio wavelengths, improving our understanding of the origin and nature of this radio emission.

5.1 Introduction

High energy processes during the first evolutionary stages of star formation are responsible for both radio and X-ray emission (Feigelson and Montmerle 1999). Low-mass pre-main sequence (PMS) stars are well known strong X-ray emitters. Their enhanced magnetic activity with respect to more evolved stars produces violent reconnection events in the corona of the stars, where the plasma heated to high temperatures strongly emits variable X-ray emission. Massive stars also emit X-ray radiation, usually related to wind shocks.

Our understanding of the X-ray emission from young stars has dramatically increased in the recent years due to *Chandra* and *XMM-Newton* (Getman et al. 2008, Arzner et al. 2007). X-ray observations have revealed thousands of PMS stars in tens of stellar clusters, resulting in good constraints on their X-ray properties such as plasma temperatures, levels of variability, luminosities and X-ray flare rate (see, e.g., Wolk et al. 2005).

In contrast, the physics associated with the radio events (nature and origin of the emission, variability, timescales, flaring rate) are still poorly constrained. Drake and Linsky (1989) proposed that radio flares might be produced by the same coronal activity that is responsible for bright X-ray emission (see review by Güdel 2002). It would be expected then that electrons spiraling in the magnetic field of the corona produce non-thermal and highly variable gyrosynchrotron radiation. Moreover, ionized material in the vicinity of stars, in circumstellar disks or envelopes or at the base of bipolar outflows, also produce thermal free-free (*bremsstrahlung*) radiation.

Although long-term radio variability on timescales of months to years has been observed in star-forming regions (Felli et al. 1993; Zapata et al. 2004a; Forbrich et al. 2007), it is still not clear whether these variations are caused by long-term mech-

anisms, or they are indeed produced by a continuous sequence of events occurring on shorter timescales. Systematic observations looking for short-term variability are required to answer this question.

Recently, Liu et al. (2014) detected radiovariability on hour timescales in the young stellar cluster R Coronae Australis. The most powerful radio flares[1] have been serendipitously reported so far towards the Orion Nebula Cluster (ONC) and the background Orion Molecular Cloud (OMC). Bower et al. (2003) reported a strong radio flare at 86 GHz arising from a PMS star in the ONC, and Forbrich et al. (2008) presented an even stronger radio flare at 22 GHz, originating from a young star deeply embedded in the OMC previously detected through its X-ray emission. The low number of observed events could indicate that radio flares are a rare phenomenon (Andre 1996), but at the same time prevents a proper statistical analysis of short-term variability phenomena.

Since the typical timescales of radio variability are poorly known, we have carried out a monitoring program comprising various cadences ranging from 3 hours to several months. The new capabilities of the Karl G. Jansky VLA now allows the scheduling of multiple, short snapshots with good sensitivity in a reasonable amount of observing time. The only two examples of powerful radio flares are located in Orion, and this region also harbors a rich cluster of low-mass stars (chapter 2); hence, this region is an excellent target for the detection of many sources in a single pointing. Our data allow us to study for the first time both the short (hours to days) and long (months) timescale variability of the radio sources in Orion at high frequencies (33-45 GHz).

The chapter is laid out as follows. In Sect. 5.2 we present the details of the observations. In Sect. 5.3 we show the results of the monitoring. In Sect. 5.4 we classify the full sample of radio sources in Orion as ONC or OMC members, and then examine their X-ray properties with the aim of better understanding the nature of the radio emission. In Sect. 5.5 we discuss in more detail the new radio flaring source detected by our monitoring, OHC-E. In Sect. 5.6 we analyze whether the radio variability observed in the binary system θ^1 *Ori A* might be caused by its orbital motion. In Sect. 5.7 we estimate the rate of radio flaring activity of young stars in the Orion Hot Core (OHC) based on our findings. Finally, in Sect. 5.8 we summarize the conclusions of our work.

[1] In this work we will use the term *flare* to refer to flux density variations of a factor of >2 on timescales from hours to days.

Table 5.1: Multi-epoch VLA radio continuum observations.

Config.	Project ID	Band name	Freq. (GHz)	BW (MHz)	Epoch	JD	Pointing center RA_{J2000} $5h\ 35m$	Pointing center DEC_{J2000} -5° 22'	Obs. length (min)	beam (" × ")	RMS (mJy)	Primary flux density calibrator	Gain calibrator flux density (Jy) (J0541-0541)
B	AJ356	Q	45.6	25	2009 Mar 9	2454900	$14.60s$	30.0"	120	0.23×0.15	0.45	J0137+3309	0.63
B	AJ356	Q	45.6	25	2009 Mar 19	2454910	$14.60s$	30.0"	240	0.22×0.15	0.37	J0137+3309	0.63
D	AR712	Q	43.3	100	2009 Dec 22	2455188	$14.50s$	31.0"	60	1.9×1.4	0.54	J0137+3309	0.46
C	10B-175	Ka	33.6	256	2010 Oct 24	2455494	$14.50s$	30.0"	30	1.3×0.65	0.36	J0542+4951	0.68
C	10B-175	Ka	33.6	256	2010 Nov 23	2455523.76	$14.50s$	30.0"	30	0.92×0.60	0.40	J0542+4951	0.68
C	10B-175	Ka	33.6	256	2010 Nov 23	2455523.89	$14.50s$	30.0"	30	0.75×0.56	0.44	J0137+3309	0.69
C	10B-175	Ka	33.6	256	2011 Jan 8	2455569	$14.50s$	30.0"	30	0.86×0.56	0.39	J0137+3309	0.62
CnB-B	10B-175	Ka	33.6	256	2011 Feb 8	2455601	$14.50s$	30.0"	30	0.30×0.24	0.32	J0137+3309	0.58
B	10B-175	Ka	33.6	256	2011 Mar 28	2455649	$14.50s$	30.0"	30	0.28×0.22	0.22	J0542+4951	0.50
BnA	10B-175	Ka	33.6	256	2011 May 27	2455709	$14.50s$	30.0"	30	0.62×0.077	0.22	J0542+4951	0.54
BnA-A	10B-175	Ka	37.5	128	2011 Jun 4	2455717	$14.50s$	30.0"	120	0.096×0.073	0.13	J0542+4951	0.50
BnA-A	10B-175	Ka	30.5	128	2011 Jun 4	2455717	$14.50s$	30.0"	120	0.13×0.083	0.10	J0542+4951	0.52
A	10B-175	Ka	33.6	256	2011 Jun 11	2455724	$14.50s$	30.0"	30	0.14×0.062	0.16	J0137+3309	0.54
A	10B-175	Ka	33.6	256	2011 Jul 09	2455752	$14.50s$	30.0"	30	0.091×0.060	0.14	J0542+4951	0.48

5.2 Observations and data reduction

The radio observations of the ONC/OMC region were made with the VLA in the A, B, C and D configurations at Q-band (3 epochs) and Ka-band (11 epochs) from 2009 to 2011. Table 5.1 summarizes the observational details for each of the epochs (array configuration, project ID, band name, frequency, observing bandwidth, date, pointing center, observation length (including all calibrations), synthesized beam, RMS noise at the center of the primary beam, primary flux density calibrator used, and the flux density of the complex gain calibrator). The first two observations at Q-band were made in spectral line mode using the old VLA correlator, single polarization. The third Q-band observation (AR712) used the standard dual polarization continuum set-up with the old correlator (100 MHz total bandwidth). For the data taken under observing code VLA/10B-175 the new WIDAR correlator was used, with two 128 MHz sub-bands placed contiguously in frequency for all observations except those of 2011 Jun 4, for which the sub-bands were separated by 7 GHz as noted in Table 5.1. The observations at Q-band were reduced using the Astronomical Image Processing System (AIPS) package. The observations at Ka-band were reduced using the VLA Calibration Pipeline[2], which uses the Common Astronomy Software Applications (CASA) package[3].

Phase self-calibration was performed where possible. However, the tropospheric phase stability of the observations on 2011 Jun 4 was poor, and the data were of insufficient signal-to-noise ratio to enable phase self-calibration on short enough timescales

[2]https://science.nrao.edu/facilities/vla/data-processing/pipeline
[3]http://casa.nrao.edu

to correct for the resulting decorrelation. While the typical uncertainty in the absolute flux density scale is 10% at these frequencies, the uncertainty in the absolute flux density scale for the 2011 Jun 4 data is increased to 20%. Images were made using CASA, applying an inner uv-cutoff to filter the extended emission from the foreground HII region ionized by the Trapezium cluster, and natural weighting to maximize sensitivity. The images are corrected for the response of the primary beam before being used for photometry.

5.3 Results: radio stellar population detected at high frequency

The large fields of view (FoVs) covered by the images made here, especially in the VLA's B and A configurations (the A-configuration images are 22,000 pixels on a side), requires a rigorous criterion for the detection of sources. We calculate that we would expect fewer than 0.3 sources above 5σ for a Gaussian noise distribution in the worst case, and therefore report only those detections that are at least 5 times the local RMS noise in our images; the RMS is a function of position across the field, due to the effect of the primary beam. In Sect. 5.4 we cross-correlate our radio sample with optical, near-IR, radio and X-ray samples, confirming that all our radio sources detected above 5σ have a counterpart at other wavelengths.

We detect a total of 19 sources (Table 5.2), 18 of which have been previously detected by the radio monitoring at lower frequencies of Felli et al. (1993) (5 and 15 GHz) and Zapata et al. (2004a) (8.3 GHz). Our observations have revealed the presence of a new radio source, hereafter OHC-E, detected in the OHC region in two different epochs. We will discuss in detail this new source in Sect. 5.5. In Fig. 5.1 we show the positions of all the detected sources, overplotted on the R-band Advanced Camera for Surveys/Wide Field Channel (ACS/WFC) Hubble Space Telescope (HST) image and on the infrared K-band image from the 2 Micron All Sky Survey (2MASS). The sources are mainly concentrated in the OHC region and the Trapezium Cluster.

To measure the flux densities of the sources, we use the AIPS task JMFIT. We also add an absolute uncertainty of 10% in quadrature (20% for the 2011 Jun 4 observations due to the poorer phase stability of those data; see Sect. 5.2). Table 5.3 summarizes the results. Only the sources BN and source I are detected in all epochs, showing nearly constant flux densities, and verifying the reproduceability of the flux density scale. Source C is consistent with a constant flux density, although is not

Table 5.2: Positions of the radio sources detected in our Ka-band and Q-band monitoring.

Source	RA_{J2000} 5 35	DEC_{J2000} -5
BN	14.11	22 22.69
I	14.51	22 30.58
OHC-E	14.73	22 29.83
D	14.90	22 25.38
n[a]	14.35	22 32.89
H	14.50	22 38.76
A	11.80	21 49.29
C	14.16	23 01.04
F	18.37	22 37.43
G	17.95	22 45.42
E	16.96	22 48.78
15	16.07	23 07.12
6	16.75	23 16.44
7	16.28	23 16.58
25	15.77	23 09.86
12	15.82	23 14.00
11	15.84	23 22.40
16	16.33	23 22.54
5	16.85	23 26.31

[a] This source was called *L* by Garay (1987), but its more common name is *n* (Menten and Reid 1995).

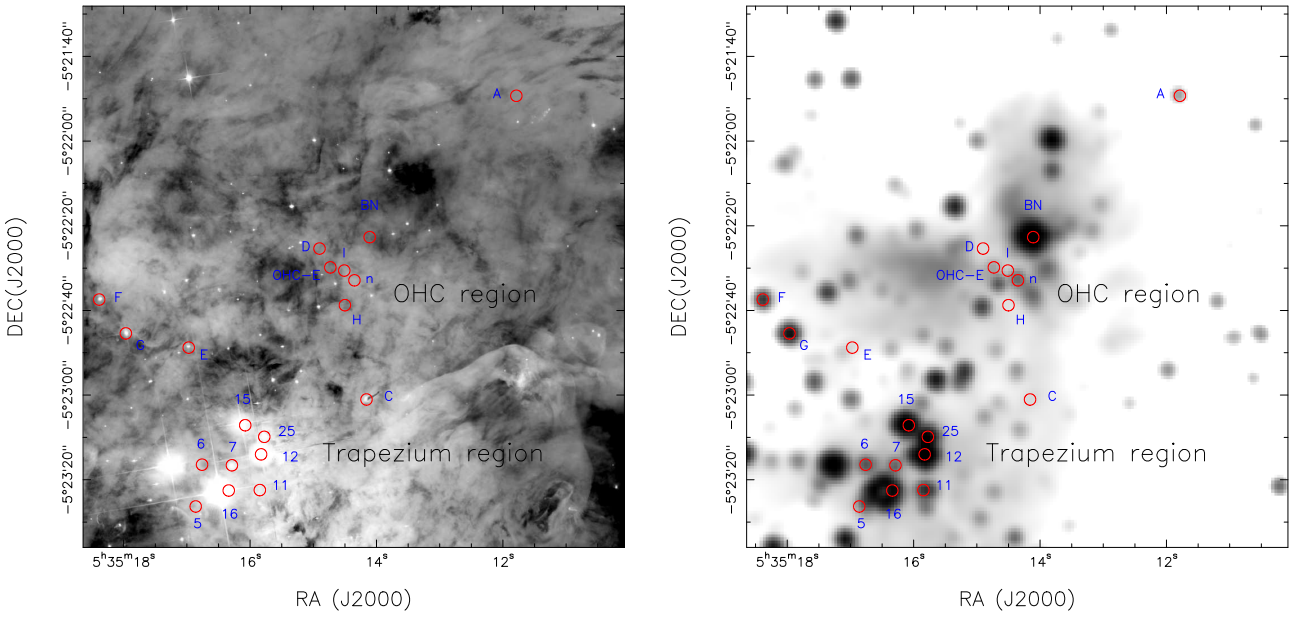

Figure 5.1: Positions of the 19 radio sources detected in our monitoring program, overplotted on the R-band ACS/WFC HST image (left panel) and on the K-band 2 Micron All Sky Survey (2MASS) image (right panel).

detected in all epochs (see Sect. 5.3.1). The other sources exhibit clear flux density variation between epochs. In the case of non-detections, we quote 3σ upper limits. We show in Fig. 5.2 the radio emission of all 19 sources as contours overlaid on the R-band HST image. We have selected the highest resolution image available for each source (with a good detection) for the overlay, and note the epoch in each panel.

5.3.1 Long-term variability: month timescales

The time separation between the monitoring epochs ranges from 3 hours to several months, allowing us to study radio variability at different timescales. In Figs 5.3 and 5.4 we show the measured integrated flux densities of all sources during the different epochs of our monitoring for the Q-band and Ka-band, respectively. We note that in the figures the observation on JD 2455188 (2009 Dec 22) at Q-band corresponds to a slightly different frequency (43.3 GHz) from the first two epochs (45.6 GHz). Also, the flux density from the observation on JD 2455717 (2011 June 4) at Ka-band (shown in Fig. 5.4) corresponds to 37.5 GHz, and not to 33.6 GHz as for the others.

With the aim of quantitatively studying the radio variability through the different epochs we follow Felli et al. (1993) by defining the radio variability parameter β as the ratio of the standard deviation of the flux densities and the average flux density:

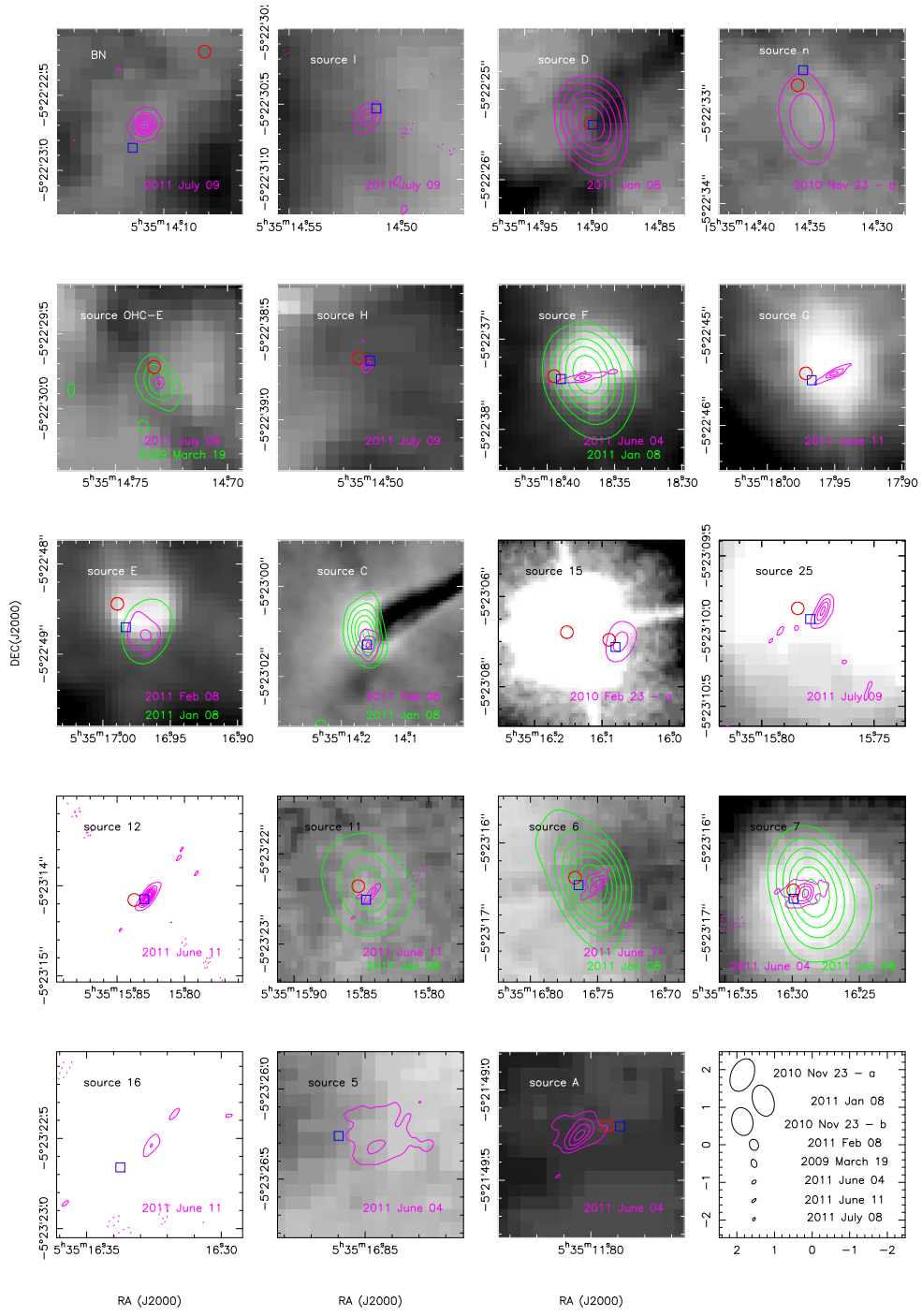

Figure 5.2: Images of the 19 radio sources detected in our radio monitoring. The name of the source is indicated in the top left corner of each panel. In the lower right corners we indicate the epoch of the observation (we have selected the epochs with the best spatial resolution and good detections, and in some cases we show the detections in two different epochs with different colors). The first contour level is 3σ and the step between successive contours is 2σ, with the exception of BN, I, 25 and 12 (which have steps of 10σ), and the 2009 March 19 epoch for OHC-E (steps of 5σ). The open blue squares indicate the position of known radio sources detected by Zapata et al. (2004a) at 8.3 GHz, and the red circles denote the position of X-ray stars detected by Chandra (COUP Project). The background greyscale image is the ACS/WFC HST image at R-band, from the Hubble Legacy Archive. In the lower right panel we show the synthesized beams of the different images used.

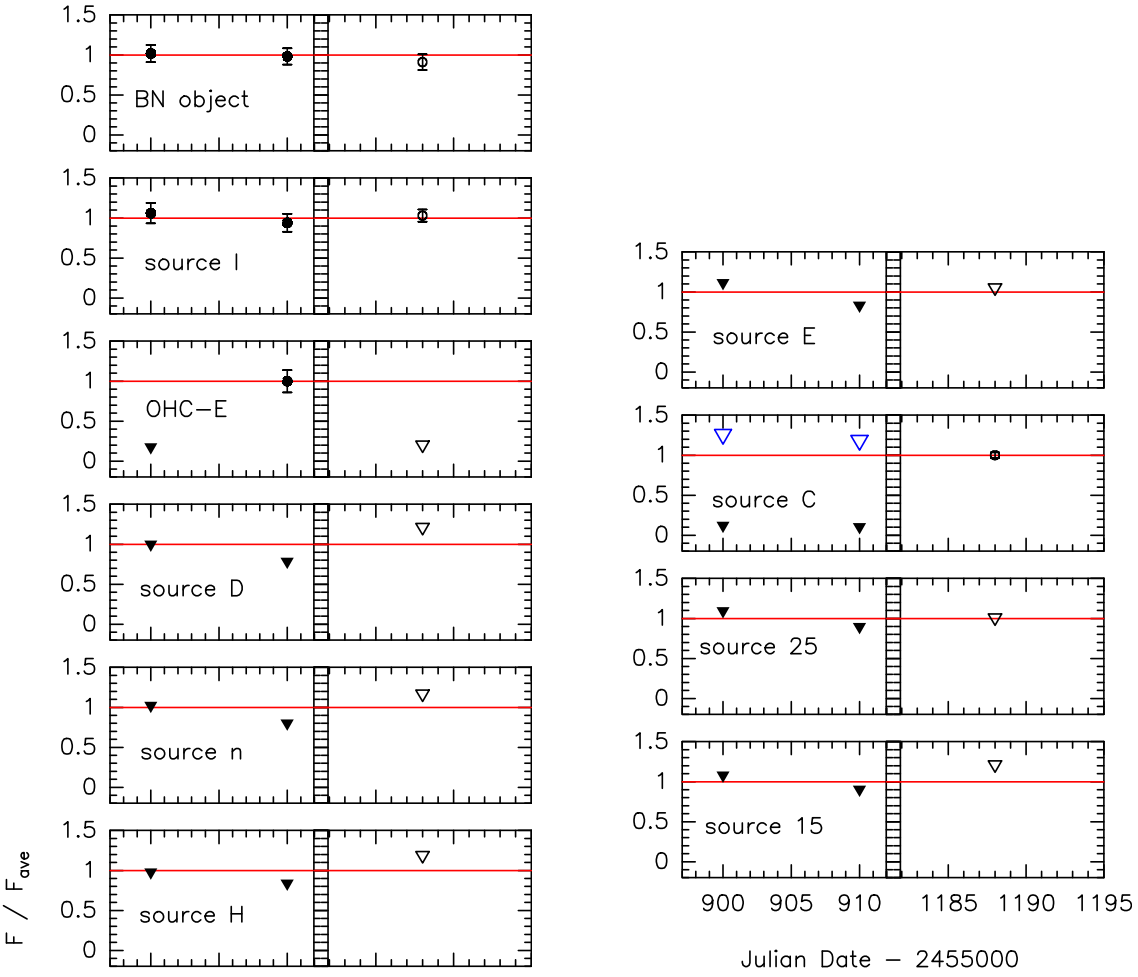

Figure 5.3: Q-band light curves for those sources that fall within the Q-band primary beam. In the case of non-detections, 3σ upper limits are indicated with triangles. The flux densities have been normalized by the average value ($F_{\rm av}$) calculated with the positive detections (or the average value of the upper limits if the source is not detected). The error bars indicate the flux density uncertainties. The red horizontal line indicates the value at which the flux density is equal to the average. The first two observations were carried out at 45.6 GHz (black filled symbols), while the last one was carried out at 43.3 GHz (black open symbols). For source C, the blue open triangles indicate upper limits for extended emission derived from smoothed images (see Sect. 5.3.1).

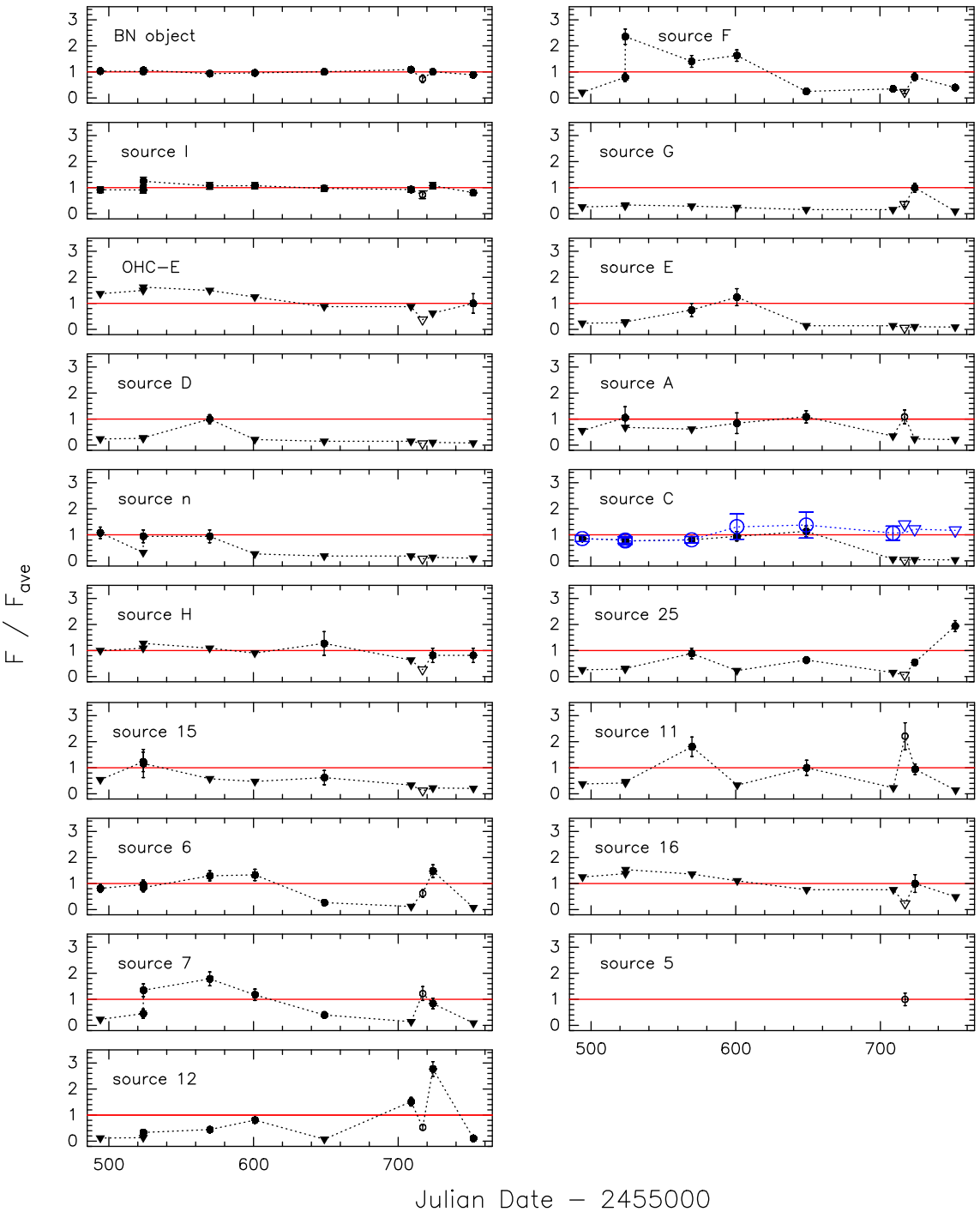

Figure 5.4: Ka-band light curves of all the 19 sources detected throughout the Ka-band monitoring. In the case of non-detections, 3σ upper limits are indicated with triangles. The flux densities have been normalized by the average value ($F_{\rm av}$) calculated with the positive detections (or the average value of the upper limits if the source is not detected). The error bars indicate the flux density uncertainties. The red horizontal line indicates the value at which the flux density is equal to the average flux density. The dotted line merely joins the flux densities at different epochs, and is not indicative of the evolution of the flux density between epochs. The frequency of the observations plotted is 33.6 GHz (black symbols), with the exception of the 2011 June 4 observation, which corresponds to a frequency of 30.5 GHz (indicated with open symbols). The second and third epoch on 2010 November 23 are only separated by ∼3 hours. We discuss this short-term variability in detail in Sect. 5.3.2. For source C, the blue open symbols indicate values for extended emission derived from smoothed images (see Sect. 5.3.1).

Table 5.3: Multi-epoch radio continuum flux densities[a]. The values in parenthesis correspond to 3σ upper limits.

	Epoch: 2454000 + (JD)														
Source	900	910	1188	1494	1523.76	1523.89	1569	1601	1649	1709	1717		1724	1752	
	Q-band (GHz)			Ka-band (GHz)											
	45.6	45.6	43.3	33.6	33.6	33.6	33.6	33.6	33.6	33.6	37.5	30.5	33.6	33.6	
BN	31.2±3.3	30.1±3.1	27.9±3.0	26.4±2.7	25.9±2.7	27.2±2.8	23.9±2.5	24.6±2.5	25.7±2.6	27.8±2.8	20.5±4.1	18.8±3.8	25.7±2.6	22.7±2.3	
I	14.1±1.7	12.5±1.5	13.7±1.7	9.2±1.1	9.1±1.2	12.5±1.5	10.7±1.3	10.8±1.2	9.7±1.1	9.3±1.0	9.1±1.9	7.3±1.5	10.8±1.2	8.1±0.9	
OHC-E	(1.4)	7.9±1.1	(1.6)	(1.1)	(1.3)	(1.2)	(1.3)	(1.0)	(0.7)	(0.7)	(0.4)	(0.3)	(0.5)	0.8±0.3	
D	(1.4)	(1.1)	(1.7)	(1.1)	(1.2)	(1.3)	4.6±0.8	(1.0)	(0.7)	(0.7)	(0.4)	(0.3)	(0.5)	(0.4)	
n	(1.4)	(1.1)	(1.6)	4.0±0.8	(1.2)	3.5±0.9	3.5±0.9	(1.0)	(0.7)	(0.7)	(0.4)	(0.3)	(0.5)	(0.4)	
H	(1.4)	(1.2)	(1.7)	(1.1)	(1.2)	(1.4)	(1.2)	(1.0)	1.4± 0.5	(0.7)	(0.4)	(0.3)	0.9±0.3	0.9±0.3	
A	-	-	-	(5.1)	9.6±3.8	(6.2)	(5.6)	7.7±3.6	9.9±2.1	(3.2)	-	9.9±2.4	(2.2)	(2.0)	
C	(35)	(33)	27.8±3.7	12.7±1.7	11.9±1.9	11.3±1.9	12.0±1.8	19.5±7.2	20.4±7.4	15.8±4.0	(20.8)	(16.0)	(18.0)	(17.4)	
F	-	-	-	(5.4)	19.5±4.1	57.9±7.2	34.6±5.5	40.1±5.4	6.2±2.6	8.6±2.5	-	5.5±1.5	20.0±3.6	9.9±2.6	
G	-	-	-	(4.1)	(4.6)	(5.2)	(4.5)	(3.7)	(2.5)	(2.5)	(2.2)	5.7±1.4	15.5±2.7	(1.6)	
E	(7.1)	(5.3)	(6.7)	(2.3)	(2.5)	(2.8)	7.1±2.4	11.8±3.1	(1.4)	(1.4)	(1.0)	(0.5)	(1.0)	(0.9)	
15	(8.5)	(7.1)	(8.0)	(2.6)	5.9±1.8	5.6±2.6	(2.8)	(2.3)	3.0±1.3	(1.6)	(1.2)	(0.6)	(1.1)	(1.0)	
6	-	-	-	20.9±3.9	24.5±4.6	21.7±4.1	33.2±4.9	34.1±5.6	7.0±2.4	(3.2)	-	16.0± 3.6	37.9±6.2	(2.0)	
7	-	-	-	(4.1)	8.0±3.1	23.8±4.3	31.4±4.7	20.7±3.8	7.1±2.2	(2.6)	11.9±3.5	21.5±4.7	14.8± 3.6	(1.6)	
25	(8.9)	(7.3)	(8.2)	(2.6)	(2.9)	(3.1)	8.8±2.0	(2.3)	6.3±1.3	(1.6)	(1.2)	(0.6)	5.4±1.2	19.2±2.1	
12	-	-	-	(3.1)	(3.5)	8.5±2.9	11.2±2.6	20.4±2.7	(1.9)	38.3±4.2	18.4±4.3	13.4±2.7	69.9 ±7.1	2.8±0.9	
11	-	-	-	(4.8)	(5.3)	(5.9)	22.8±4.7	(4.2)	12.6±3.7	(2.9)	-	27.9± 6.5	11.9±2.5	(1.8)	
16	-	-	-	(5.9)	(6.5)	(7.2)	(6.4)	(5.2)	(3.6)	(3.6)	-	(1.1)	4.7±1.6	(2.3)	
5[b]	-	-	-	-	-	-	-	-	-	-	-	30.9±7.5	-	-	

[a] Integrated flux densities are presented in mJy.

[b] Source 5 is outside the FoV for all but the 2011 Jun 4 at 30.5 GHz, whose FoV is larger.

$\beta = \Delta F/F_{\rm av}$. Given that some sources remain undetected in some epochs, and hence have flux densities below the sensitivity limit, we consider in the calculation of β positive detections as well as the lowest upper limit. In Table 5.4 we show the radio variability parameter defined at 33.6 GHz for the detected sources. We consider sources with β <0.2 to be constant, and sources with β >0.2 to be variable, with those sources with higher β being more variable.

The sources BN and I are associated with young massive stars (Reid et al. 2007, Goddi et al. 2011b), and are expected to emit mainly thermal (and constant) emission arising from ionized gas surrounding the central object. Our monitoring at Q-band and Ka-band (Figs 5.3 and 5.4) shows indeed that the flux density of BN is nearly constant, with a very low month-timescale radio variability parameter at 33.6 GHz of β=0.06.

In the case of source I the radio variability is higher, β=0.13, but is still below the threshold we define for "variable" sources. However, Zapata et al. (2004a) reported some variability towards this source, with flux density variations of a factor ∼2. Furthermore, Plambeck et al. (2013), using observations separated by 15 yr also found evidence of a gradual flux density increase from source I with respect the more steady

Table 5.4: Full radio sample of sources in the ONC/OMC region.

ID		Radio sources 33.6 GHz				X-ray sources									Optical[b]		IR[c]	Mem.[d]
Source	Z04[a]	F_{av} (mJy)	n_{det}	β	$\beta_{8.3GHz}$	COUP ID	Med$E$ (keV)	HR_1	logN_H (cm^{-2})	logP_{KS}	BB Num	X-ray flare?[e]	logL_X (erg s^{-1})		H97	K05 (proplyd)	HC00	
BN	12	25.5±1.6	1.0	0.06	0.07	599b[f]	-	-	-	-	-	-	-		-	-	y	OMC
I	19	10.0±1.3	1.0	0.13	0.36	-[g]	-	-	-	-	-	-	-		-	-	-	OMC
OHC-E	-	0.8±0	0.11	-	-	655	3.58	0.89	22.85±0.01	-4.00	9	y	31.37		-	-	-	OMC
D	21	4.6±0	0.11	>1.19	0.65	662	4.50	0.98	23.22±0.03	-4.00	13	y	31.29		-	-	-	OMC
n	17	3.7±0.3	0.33	>0.58	0.33	621	3.57	0.84	22.74±0.01	-4.00	13	y	30.97		-	-	y	OMC
H	18	1.1±0.3	0.33	>0.29	0.75	639	3.99	0.96	23.06±0.04	-4.00	8	y	30.90		-	-	-	OMC
A	6	9.1±3.0	0.33	>0.50	1.58	450	3.32	0.64	22.34±0.03	-4.00	12	y	32.27		-	-	y	ONC[h]
C[j]	14	14.8±3.8	0.78	0.26	0.32	-	-	-	-	-	-	-	-		y	y	y	ONC
F	76	24.6±18.2	0.89	>0.44	0.81	965	1.31	-0.63	21.25±0.10	-4.00	2	n	31.89		y	-	y	ONC
G	73	15.5±0	0.11	>1.15	0.84	932	1.29	-0.64	21.17±0.09	-4.00	12	y	32.18		y	-	y	ONC
E	63	9.5±3.3	0.22	>0.83	0.23	844	1.63	-0.50	22.01±0.14	-0.96	1	y	29.22		y	y	y	ONC
15	49	4.8±1.6	0.33	>0.60	0.19	766	1.58	-0.32	21.54±0.03	-4.00	20	y	30.71		y	-	y	ONC
6	59	25.6±10.5	0.78	>0.57	0.01	826	2.31	0.16	22.06±0.04	-4.00	11	y	30.35		y	y	y	ONC
7	52	17.6±9.5	0.67	>0.69	0.09	787	2.43	0.29	22.40±0.04	-4.00	5	y	30.22		y	y	y	ONC
25	38	9.9±6.3	0.44	>0.80	0.12	732	1.33	-0.60	20.99±1.99	-4.00	23	y	32.35		y	-	y	ONC
12	41	25.2±25.2	0.67	>1.13	0.65	745	1.33	-0.59	20.79±0.08	-4.00	20	y	32.33		y	-	y	ONC
11	42	12.6±8.1	0.44	>0.82	0.02	746	2.23	0.19	22.10±0.55	-3.40	2	n	28.79		y	y	y	ONC
16	53	4.7±0	0.11	>0.48	0.14	-	-	-	-	-	-	-	-		-	-	-	OMC or EG
5	61	-	-	-	0.02	-	-	-	-	-	-	-	-		y	y	y	ONC
RBS	-	-	-	-	-	647	5.20	1.00	23.51±0.03	-4.00	8	y	30.93		-	-	-	OMC
-	1	-	-	-	0.04	229	4.05	0.98	22.96±0.19	-0.05	1	n	29.28		-	-	-	EG
-	2	-	-	-	>1.43	342	1.98	-0.01	22.21± 0.01	-4.00	31	y	31.32		y	-	y	ONC
-	7	-	-	-	>0.63	510	4.75	1.00	23.54± 0.06	-2.59	3	y	31.26		-	-	-	OMC
-	9	-	-	-	>0.62	530	5.23	0.98	23.50±0.03	-4.00	2	(y)	30.75		-	-	-	OMC
-	16	-	-	-	0.56	625	4.81	0.98	23.42±0.05	-4.00	4	y	30.95		-	-	-	OMC
-	31	-	-	-	0.42	699	1.51	-0.50	21.61±0.11	-4.00	4	y	29.54		y	y	y	ONC
-	33	-	-	-	0.62	708	1.54	-0.36	21.46±0.05	-4.00	10	y	30.19		y	-	y	ONC
-	34	-	-	-	0.10	717	1.55	-0.54	20.98±0.70	-0.44	1	(y)	28.53		y	y	y	ONC
-	37	-	-	-	0.03	733	2.49	0.19	22.54±0.23	-2.33	2	n	29.40		-	y	y	ONC
-	43	-	-	-	0.11	747	3.47	0.33	22.25±0.35	-1.06	1	y	28.88		y	y	y	ONC
-	44	-	-	-	0.36	757	1.89	-0.17	22.45±0.21	-0.64	1	(y)	29.01		-	y	y	ONC
-	45	-	-	-	0.10	758	1.66	-0.29	21.73±0.02	-4.00	29	y	31.05		y	y	y	ONC
-	46	-	-	-	0.49	768	1.63	-0.33	21.52±0.04	-4.00	4	y	30.27		y	y	y	ONC
-	54	-	-	-	0.60	800	1.93	-0.14	22.36±0.21	-0.85	2	y	28.86		y	y	y	ONC
-	56	-	-	-	0.69	807	1.37	-0.60	21.43±0.10	-4.00	7	y	29.73		y	y	y	ONC
-	58	-	-	-	0.10	820	3.64	0.95	22.86±0.13	-4.00	3	y	30.07		-	y	y	ONC
-	60	-	-	-	0.13	827	1.63	-0.41	22.24±0.03	-4.00	2	n	30.46		y	y	y	ONC
-	64	-	-	-	0.06	847	1.35	-0.64	21.62±0.35	-2.00	1	(y)	29.22		y	y	y	ONC
-	65	-	-	-	0.05	855	1.96	-0.01	21.69±0.09	-4.00	8	y	31.79		y	y	y	ONC
-	69	-	-	-	0.19	876	3.22	0.70	22.69±0.06	-2.60	3	y	29.81		y	y	y	ONC
-	71	-	-	-	0.10	900	4.04	0.46	23.54±0.46	-4.00	2	y	30.44		y	y	y	ONC
-	75	-	-	-	>0.38	955	1.70	-0.31	21.46±0.19	-0.36	2	y	28.78		y	y	y	ONC
-	77	-	-	-	0.61	1130	1.23	-0.71	21.28±0.14	-4.00	7	(y)	31.67		y	-	y	ONC
-	3	-	-	-	-	378	1.23	-0.66	21.11±0.07	-4.00	5	y	30.20		y	-	y	ONC
-	4	-	-	-	-	394	1.20	-0.72	20.00±1.65	-4.00	6	y	31.32		y	-	y	ONC
-	5	-	-	-	-	443	2.42	0.35	21.76±0.39	-0.51	1	n	28.25		y	y	y	ONC
-	8	-	-	-	-	524	3.31	0.52	22.37±0.31	-4.00	2	y	28.51		y	y	y	ONC
-	13	-	-	-	-	607	4.37	0.22	-	-0.05	1	n	-		-	-	-	OMC
-	20	-	-	-	-	658	2.37	0.23	22.23±2.62	-4.00	9	y	30.41		y	y	y	ONC
-	23	-	-	-	-	671	1.50	-0.52	21.83±0.14	-2.20	3	y	29.21		y	-	y	ONC
-	28	-	-	-	-	690	3.72	0.82	22.70±0.15	-4.00	2	y	29.31		-	-	-	ONC
-	29	-	-	-	-	689	1.32	-0.61	20.85±0.15	-4.00	22	y	31.82		y	-	y	ONC
-	51	-	-	-	-	780	3.60	0.92	22.83±0.03	-4.00	6	y	30.95		-	-	y	ONC[i]
-	66	-	-	-	-	856	1.47	-0.47	21.65±0.02	-4.00	9	y	30.34		y	y	y	ONC
-	70	-	-	-	-	885	1.44	-0.50	21.61±0.02	-4.00	7	y	30.33		y	-	y	ONC

[a] Source ID from Zapata et al. (2004a).

[b] Optical association from the work of H97 (Hillenbrand 1997) and K05 (Kastner et al. 2005).

[c] Infrared association from the work of HC00 (Hillenbrand and Carpenter 2000).

[d] Source membership: OMC=Orion Molecular Cloud, ONC=Orion Nebula Cluster, EG=extragalactic.

[e] From visual inspection of the X-ray light curves published by Getman et al. (2005c). The parentheses denote that the detection is uncertain.

[f] The massive BN object has an X-ray counterpart, COUP 599b, much fainter than a low mass companion located 0.9" from BN, COUP 599a (Grosso et al. 2005).

[g] Although X-ray emission from wind shocks would be expected from the massive star associated with source I, the non-detection by Chandra is likely due to the presence of a nearly edge-on disk (Matthews et al. 2010) that absorbs the X-ray emission.

[h] The star associated with source A has intermediate extinction ($A_V \sim 11$ mag), and therefore is likely an ONC member rather than a star embedded in the background OMC, as also noted by Bower et al. (2003) and Forbrich et al. (2008).

[i] COUP 780 does not have optical counterpart and exhibits high extinction (log N_H=22.83 cm^{-2}). Given its location, we propose that it is a particularly embedded ONC star that belongs to the Trapezium cluster surrounding the massive star θ^1 *Ori C* (chapter 2), rather than an OMC member.

[j] As discussed in Sect. 5.3.1, the source C is filtered out by the more extended VLA configuration observations. To compute the average flux, the variability parameter and the number of detections at 33.6 GHz, we have considered the images after smoothing to a C-configuration resolution of 0.8" ∼0.8".

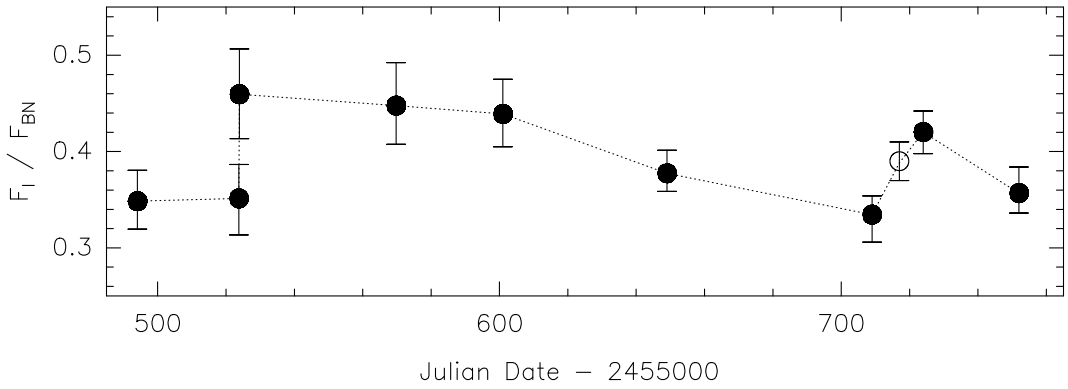

Figure 5.5: Ratio between the flux densities of sources I and BN versus time at 33.6 GHz (filled circles) and at 30.5 GHz (open circle).

flux density of BN (see their Fig. 5). From our Ka-band monitoring, we have studied the month-timescale evolution of the ratio between the flux densities of sources I and BN. Fig. 5.5 shows that this ratio exhibits variations larger than the statistical uncertainties (we do not include the uncertainty in the absolute flux density scale in calculating the error in these ratios), suggesting that real variability is present. The origin of this confirmed long-term variability towards source I could be due to ionization of infalling accretion flows onto the massive star (Galván-Madrid et al. 2011; De Pree et al. 2014). We discuss the shorter timescale variability of source I further below.

Source C is only detected in the epochs for which the VLA was in its most compact configurations. This strongly suggests that the radio emission from source C is extended, and hence is filtered out in by the most extended array configurations (B and A). To evaluate these resolution effects we have smoothed the B-configuration images at Q-band to the resolution of the D-configuration image (1.9" ×1.4"). For the Ka-band monitoring, we have smoothed the higher resolution images (from 2011 Feb 8 to 2011 Jul 09) to a C-configutration resolution of 0.8" ×0.8". We have inspected the smoothed images, and measured the flux density (or 3σ upper limit) at the location of source C. The resulting light curves (Figs 5.3 and 5.4) show that this source is consistent with being approximately constant during the monitoring. source is associated with one of the proplyds revealed by the HST (see Fig. 5.2). Using the flux densities detected at 33.6 GHz and 43.3 GHz, we obtain a spectral index ($F \sim \nu^{\alpha}$) of $\alpha \sim 3$, consistent with optically-thin dust emission from the proplyd.

The other sources detected show clear variations at Ka-band between epochs ($\beta > 0.29$). There is no clear trend or pattern in the variability, which appears to

be stochastic for many of the sources.

It is not possible to determine whether flux density variation between two epochs separated by ∼1 month is smooth during this period, or whether it happens in shorter timescales, based on these data. We address this issue in Sect. 5.3.2.

5.3.2 Short-term variability

★ Day timescales

The first two Q-band observations are only separated by 10 days (2009 March 9 and 19). The main result obtained by comparing these observations is the discovery of the new radio source OHC-E, which exhibits a clear radio flare. Fig. 5.6 shows the comparison of the two images. The source is detected at 3.3" northeast of source I. The flux density variation between the two epochs is >5.6 (using the 3σ upper limit as the flux density in the 2009 March 9 image). Source OHC-E shows a constant flux density during the 4 hours of the 2009 March 19 observation, indicating that we have detected a fraction of the flare event. later (2009 December 22). This is consistent with the duration reported on other radio flares observed in Orion (source A and RBS), which have timescales of hours to days.

★ Hour timescales

Two of the Ka-band observations are separated by only ∼3 hours (2010 Nov 23), enabling the study of flux density variations on even shorter timescales. Fig. 5.7 shows the flux density variation of the 10 sources detected in these two epochs, normalized by the flux density of BN. In Table 5.5 we show the ratio between the flux densities of the two epochs ($F_{523.89}/F_{523.76}$, where the subscript is the JD date minus 2455000), and the variability parameter defined between these two epochs is $\beta_{\rm hours}$. The sources BN, C, 15, 6 are constant within the flux density uncertainties, with variations within a factor 0.95−1.17 and $\beta_{\rm hours} < 0.11$. The latter 2 sources, however, exhibit clear variations at other epochs (see Fig. 5.4). The fact that we did not detect variation in 2010 Nov 23 does not rule out the possibility that short-term variability at other epochs may be present, producing the flux densities observed.

The sources n, 7, F and 12 show clear radio flares (see Fig. 5.7), with flux density increases by factors >2.4 and variability parameters $\beta_{\rm hours}$ >0.59 (Table 5.5). The source A, a well known radio flaring source (Bower et al. 2003; Zapata et al. 2004a; Gómez et al. 2008), suffers a decrease of its flux density with $\beta_{\rm hours}$ >0.3, being

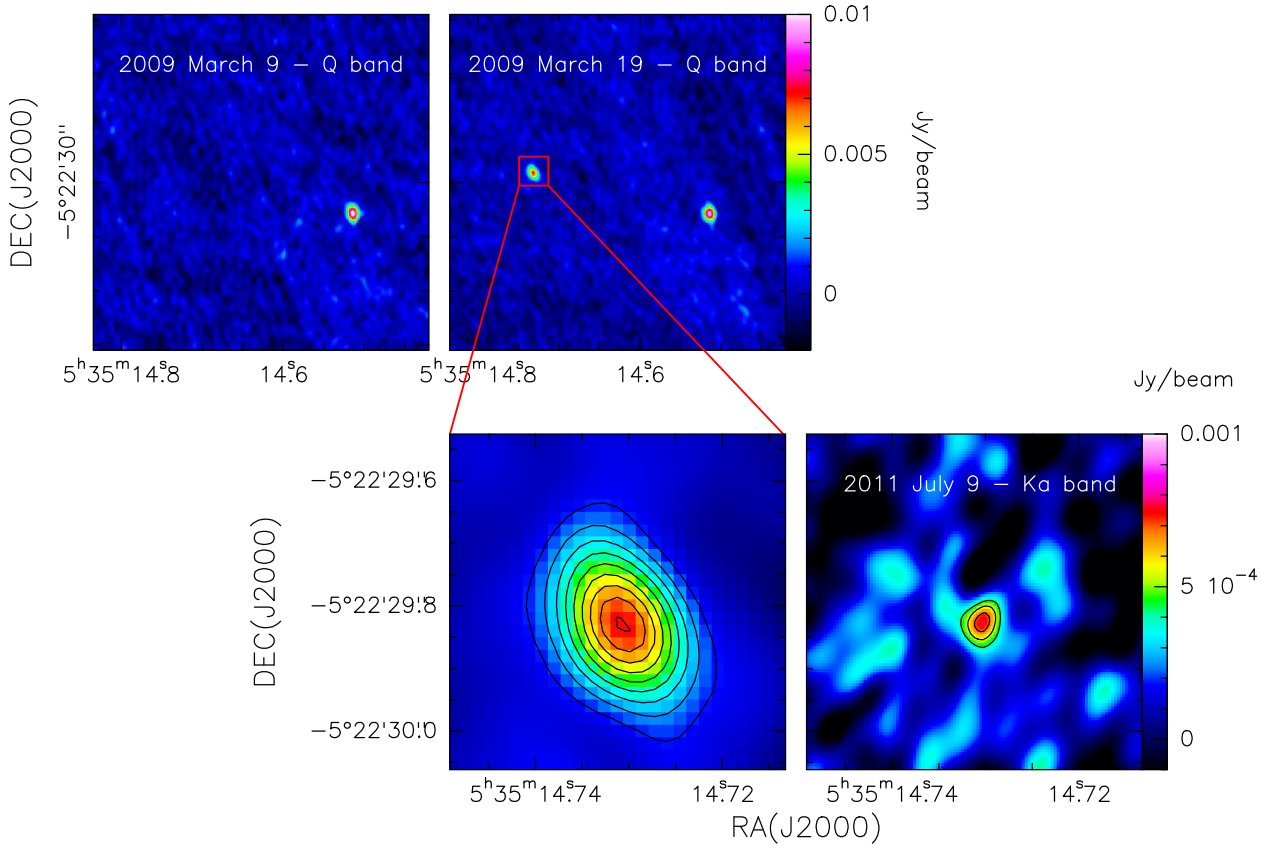

Figure 5.6: *Upper panels:* VLA observations of the OHC region at 45.6 GHz from 2009 March 9 (left) and 2009 March 19 (right). The source I is detected in both images, while the new radio flaring source OHC-E appeared 3.3" towards the northeast on 2009 March 19. *Lower left panel:* Zoom-in view of the detection of the source OHC-E from the 2009 March 19 observation. The flux density scale is the same as in upper panels. The contours indicate emission from 3σ to 19σ in steps of 2σ. *Lower right panel:* Second detection of OHC-E in the 2011 July 9 observation. The countours indicate emission at 3σ, 4σ and 5σ.

Table 5.5: Radio variability on hour timescales between the two observations on 2010 Nov 23.

Source	$F_{523.89}/F_{523.76}$	$\beta_{\rm hours}$
BN	1.05	0.03
I	1.4	0.22
n	>2.9	>0.69
F	3.0	0.70
7	3.0	0.70
A	<0.7	>0.30
C	0.95	0.04
15	0.95	0.04
6	1.17	0.11
12	>2.4	>0.59

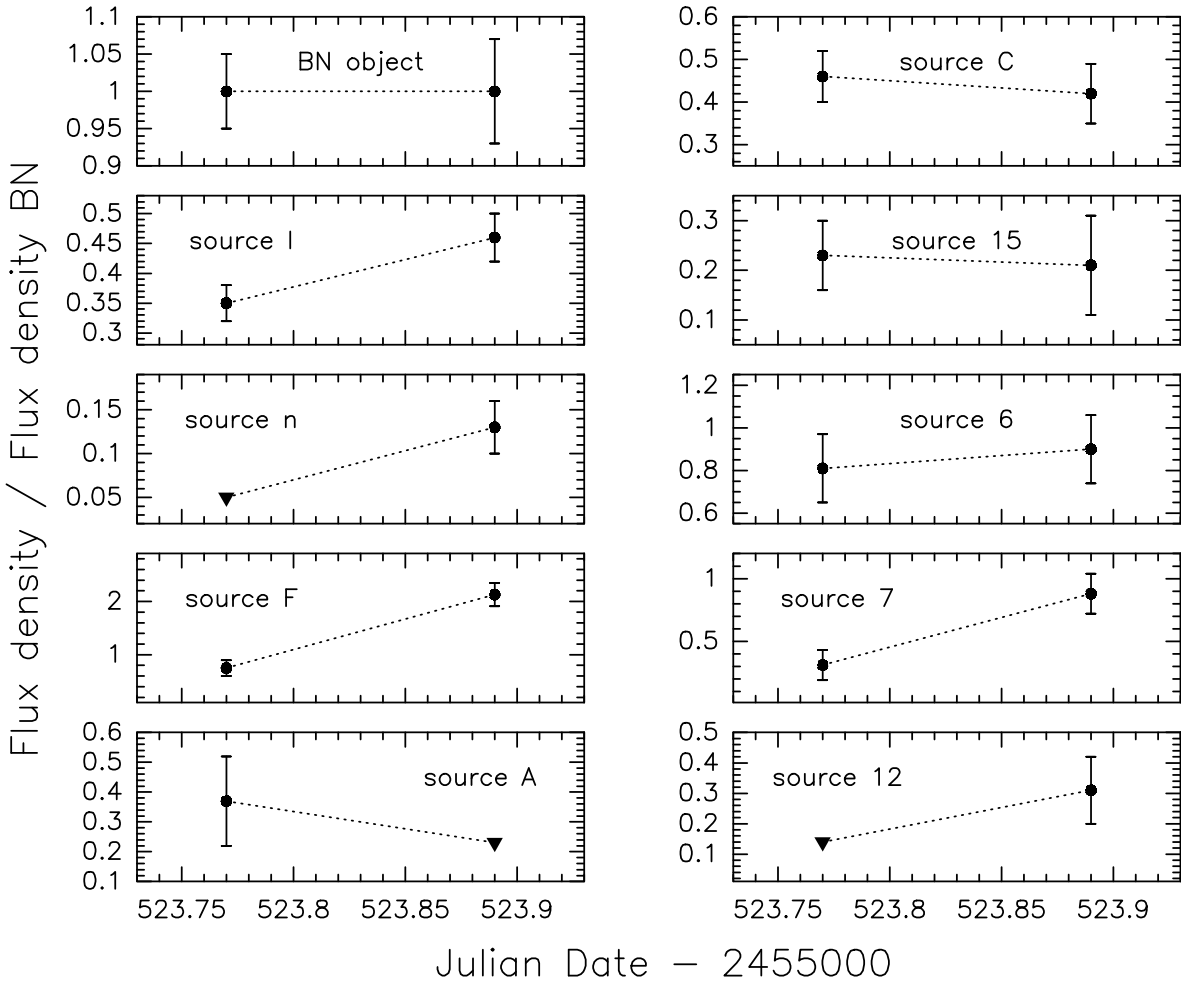

Figure 5.7: Flux density variation (normalized by the flux density of BN) on hour timescales for sources detected in the two runs observed on 2010 November 23.

undetectable in the second image.

There is a tentative detection of variability in Source I the two epochs. The flux densities measured are not within the flux density uncertainty limits (see Fig. 5.7 and Table 5.3), the variability parameter ($\beta_{\rm hours}$=0.22) is slightly above the threshold value we have set for defining variable sources, and the variation factor is 1.37 (while in the case of the BN source is only 1.05). We conclude that this short-term variation of source I is not due to calibration uncertainties, and might be real. This, along with the evidence of variations of the flux density of source I on month timescales (see Fig. 5.5), suggests that source I may also produce variable radio emission. As already commented, ionized gas of infalling accretion flows onto this massive star (Galván-Madrid et al. 2011; De Pree et al. 2014) might be responsible for the long-term variability observed (Fig. 5.5). However, other mechanism would be needed to explain the variability observed in hours-timescales. This could be the consequence of stochastic shocks due to instabilities in the radiative wind of the massive star (Stelzer et al. 2005), or of the presence of an unseen low-mass companion emitting non-thermal gyrosynchrotron radiation. Indeed, Goddi et al. (2011b) present arguments for source I harboring a binary system based on the kinematic history of the region, and the interaction of a companion with the wind from a massive primary could explain the variability observed here.

5.3.3 Detection rate

Given the variable nature of the radio emission of many of the sources, and the lack of knowledge about the timescale of the radio variability, it is not possible to predict whether a source will be detected in any particular epoch. However, one would expect a relationship between the mean flux density ($F_{\rm av}$) of a source and its detectability for a given sensitivity. We define $n_{\rm det}$ as the number of detections of a source normalized by the total number of observations. Considering only the 9 observations at 33.6 GHz, we obtain the values of $n_{\rm det}$ shown in Table 5.4. Only BN and source I have been detected in all epochs, i.e., $n_{\rm det} = 1$ Fig. 5.8 confirms that there is a correlation between the normalized number of detections and the mean flux density ($F_{\rm av}$) at 33.6 GHz, with the expected scattering due to the intrinsic radio variability.

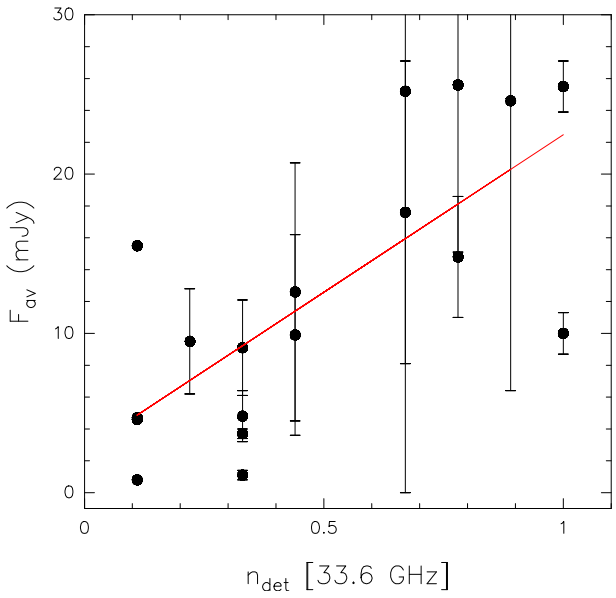

Figure 5.8: Mean flux densities ($F_{\rm av}$) versus the number of detections for the radio sources detected in the 33.6 GHz monitoring. The standard deviations from the mean are indicated with vertical bars. The red line corresponds to the best linear fit.

5.3.4 Comparison with the radio sample at 8.3 GHz

We have cross-correlated our sample of radio sources emitting at 33.6 GHz (18 sources total[4]) with the catalog of radio sources from Zapata et al. (2004a), who analyzed VLA observations at 8.3 GHz in 4 different epochs within a larger FoV and cadence ∼1 year. We have searched for counterparts within 0.5". All our sources, with the exception of the new radio flaring source OHC-E, were also detected at 8.3 GHz. Moreover, within the FoV of our 33.6 GHz monitoring, Zapata et al. (2004a) detected another 15 sources in at least one epoch and 10 sources in their deep average image.

To investigate why we have detected at higher frequency only some of the 8.3 GHz sources, we have compared the average flux densities at both frequencies. We note that the observations at 8.3 and 33.6 GHz are not simultaneous, and hence a direct estimate of the spectral index cannot be drawn. For those sources that fall within the FoV of our 33.6 GHz observations but are only detected at 8.3 GHz, we have considered 3σ upper limits measured in our image with best sensitivity, 2011 July 09.

Fig. 5.9 shows that, with only one exception,[5] the radio sources detected at Ka-

[4]Source 16 was detected only in the 30.5 GHz image, because of its larger FoV.

[5]The exception is source A, which has a large $F_{\rm av}^{8.3GHz}$ because a powerful radio flare was detected in one of the 8.3 GHz epochs. Considering the flux density of the other 3 epochs at 8.3 GHz, the source would also fall in the region with α >-0.1

band fall in the region with spectral indices $\alpha \geq$-0.1. However, if the stars would only emit variable non-thermal emission, one would expect also some sources in the region $\alpha <$-0.1. Therefore, Fig. 5.9 suggests that a thermal component is present in most stars, being responsible for a "quiescent" flux that increase with frequency. This emission can arise from ionized gas or heated dust surroundinf the stars. However, these sources also exhibit high levels of variability at both frequencies (Fig. 5.10), which is a hint of non-thermal radio emission. Later, in Sect. 5.4, we will find additional evidence to suggest that the radio emission from these sources arises from two different components, one thermal and nearly constant and other non-thermal and highly variable.

Fig. 5.9 shows that the sources detected by our monitoring in general exhibit higher 8.3 GHz flux densities than those that remained undetected. The latter are concentrated in the region of lower flux densities at both frequencies[6] (<2.5 mJy). Moreover, none of the fainter sources detected by Zapata et al. (2004a) in their deep average image is detected in our monitoring. This suggests that the non-detection at high frequency is simply a matter of sensitivity.

In Fig. 5.10 we compare the level of variability at 8.3 and 33.6 GHz. Most sources (12 of 17) detected at both frequencies exhibit higher variability at higher frequencies, while only 5 sources (including source C and the massive objects BN and source I) show the same or lower variability than at lower frequency. This may indicate that the radio variability might increase with frequency, although new observations of a more statistically representative sample of sources are needed to confirm this behavior.

5.4 Full sample of radio/X-ray low-mass stars in ONC/OMC

The earliest evolutionary stages of PMS stars are associated with high-energy processes observed at X-ray and radio wavelengths (Feigelson and Montmerle 1999). The very deep Chandra Orion Ultra Deep Project (COUP, Getman et al. 2005c) has provided a complete catalog of X-ray stars in the ONC/OMC region, with well-defined X-ray properties. While the magnetic nature of the X-ray emission in PMS low-mass stars is generally well established (Getman et al. 2005c), the origin of their radio emission, and its possible relationship to the processes that produce X-rays, are not

[6]With the exception of sources 40, 43, and 48 from Zapata et al. (2004a) (indicated in Fig. 5.9 with blue solid squares), which are located at the edge of our FoV where our sensitivity is worse.

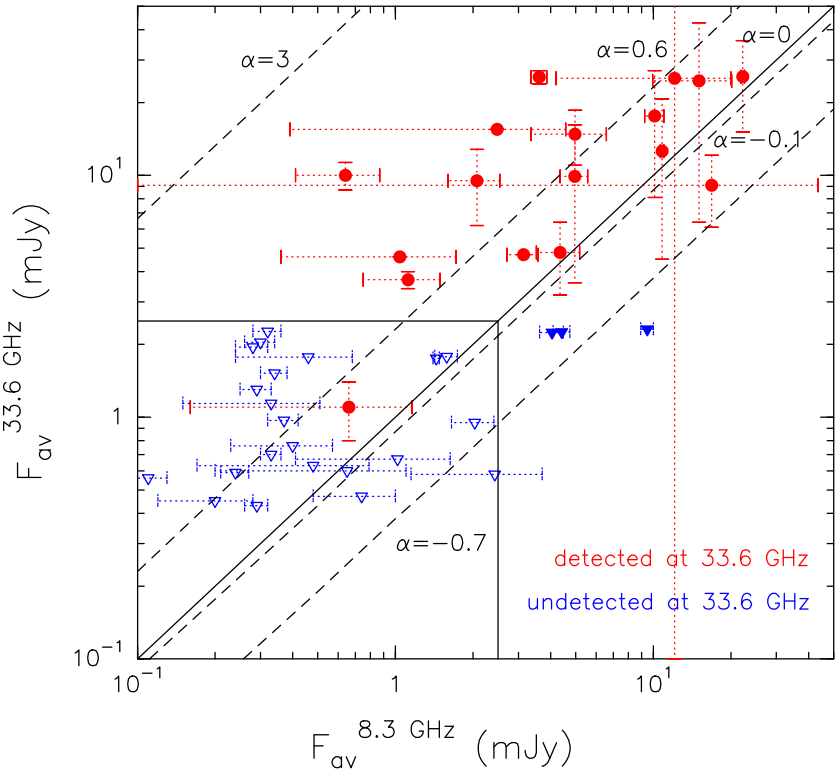

Figure 5.9: Mean flux density at 33.6 GHz versus the mean flux density at 8.3 GHz. The red dots indicate sources detected in our monitoring at 33.6 GHz. For those sources that fall within the FoV of our 33.6 GHz observations but are only detected at 8.3 GHz, we have included 3σ upper limits measured in our image with best sensitivity, 2011 July 09. The blue solid triangles correspond to 3 sources located at the edge of our Ka-band FoV. The dashed lines show the relation expected for different types of emission: optically-thin thermal dust (spectral index $\alpha \sim 3$); optically-thick, ionized, stellar wind ($\alpha = 0.6$); optically-thin free-free ($\alpha = -0.1$); and non-thermal synchrotron ($\alpha = -0.7$). We also indicate with a solid line the case of a flat spectrum ($\alpha = 0$). In the lower left corner, the box indicates the region of lower flux densities (<2.5 mJy), where the sources not detected by our Ka-band monitoring are located (see text).

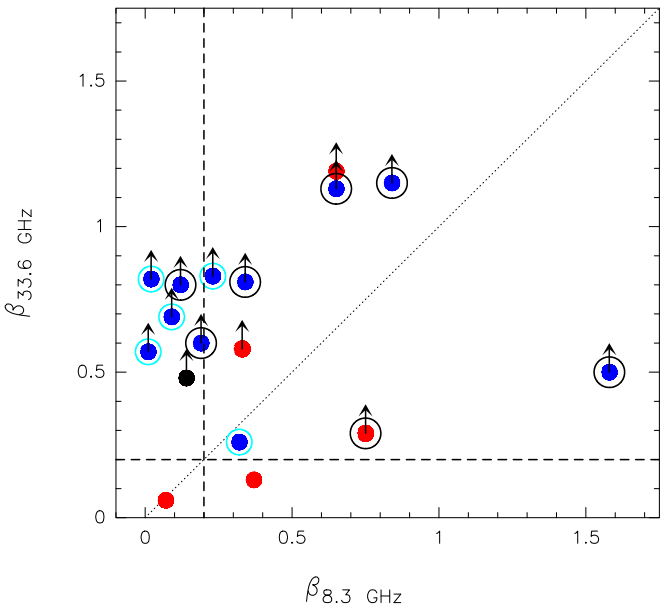

Figure 5.10: Comparison between the variability parameters at 8.3 GHz and 33.6 GHz. The stars classified as ONC and OMC members are indicated by blue and red dots, respectively. The light blue open circles show the proplyds from the Kastner et al. (2005) catalog, and large black open circles indicate radio sources classified as radio variables by Felli et al. (1993). The black dot corresponds to the radio source 16, whose classification is uncertain (OMC or EG). The dashed lines indicate the threshold for radio variability and the dotted line indicates the correlation 1-1.

fully understood. With the aim of better understanding possible connections between the radio and X-ray emission, we have compiled a sample of sources for which both radio and X-ray emission is detected. The full radio sample is presented in Table 5.4 and contains the sources detected by our monitoring program, the flaring radio source RBS detected by Forbrich et al. (2008), and the radio sources from Zapata et al. (2004a). We have searched for COUP X-ray counterparts within 0.5" of the radio sources.

5.4.1 Source membership

Since our aim is to study the PMS young stars emitting at radio wavelengths, the first step is to evaluate the presence of extragalactic (EG) contaminants in our sample. To derive the number of expected EG sources within our FoV we follow Fomalont et al. (2002), who estimated the expected number of EG contaminants at 8.4 GHz. Zapata et al. (2004a) inferred ∼1 EG source within their FoV at 8.3 GHz. In our case, for the most sensitive of our observations, and our detection criterion of 5σ, we find that within the smaller FoV of the 33.6 GHz observations we would expect very low EG contamination (∼0.01 sources) at 8.4 GHz. These extragalactic sources generally comprise non-thermal emission of the type $F \propto \nu^{\alpha}$ with $\alpha < 0$ between 1−100 GHz (Condon 1992), so the contamination at 33.6 GHz is expected to be even lower. We therefore conclude that almost all the radio sources detected by our monitoring are likely members of the ONC/OMC region.

Since EG contamination is ruled out, we classify the stars into two different populations: i) members of the optically visible foreground ONC; and ii) younger sources still embedded in the background OMC. This classification into these two groups can help to disentangle the nature of the radio emission. A fraction of the ONC members have been previously identified as *proplyds*, which are objects for which circumstellar material is being ionized by the ultraviolet (UV) radiation from the Trapezium stars, and they are expected to emit non-variable bremsstrahlung or dust emission. In the case of stars in the OMC, the molecular cloud shields the UV radiation and hence external ionization from the Trapezium is not expected. However, internal ionization from the central star could be present, producing weak free-free emission, or emission from heated dust. We also expect variable, non-thermal, emission associated with magnetic coronal activity.

To classify the sources as ONC or OMC members we use three criteria:

- The value of the hydrogen column density $N_{\rm H}$ derived from X-rays. In chap-

ter 2 we proposed the general condition of $\log N_{\rm H} > 22.5$ cm^{-2} to be adequate to distinguish the stars that are embedded in the OMC from those that are foreground ONC members.

- Spatial distribution of the sources with respect to the location of the OMC, traced by the CN N=1−0 emission from Rodriguez-Franco et al. (1998).

- We have cross-correlated the radio sample with optical (Hillenbrand 1997) and IR (Hillenbrand and Carpenter 2000) stellar catalogs, and with the catalog of optical proplyds presented by Kastner et al. 2005, using a search radius of 0.5". The presence of optical counterparts indicates that the star is a ONC member, while we expect that OMC members show only IR counterparts or no counterparts.

In Fig. 5.11 we plot the values of $\log N_{\rm H}$ obtained from the full X-ray population in a 60" ×60" region around the OHC and Trapezium regions. We differentiate sources with optical/IR counterparts, sources with only IR counterparts, and sources without any optical/IR counterparts. We find a clear trend: the stars with higher extinctions ($\log N_{\rm H} > 23.0$ cm^{-2}) do not show optical/IR counterparts, while the stars with only IR counterparts appear predominantly in the range $\log N_{\rm H}$=22.5−23.0 cm^{-2}. Most of the stars with low extinction ($\log N_{\rm H} < 22.5$ cm^{-2}) have optical/IR counterparts. The resulting membership classification for the full radio sample is shown in the last column of Table 5.4: 42 ONC members (∼76%), 11 OMC members (20%), 1 EG source (2%), and 1 source (2%) with an uncertain classification (OMC or EG). Among the ONC members, 60% of the sources are associated with proplyds.

Fig. 5.12 shows, as expected, that the stars without IR and/or optical counterparts are located in the OMC, while the ONC stars are predominantly found to the east of the OMC border.

Summarizing, we consider as OMC members those sources that: i) have values of $\log N_{\rm H} > 22.5$ cm^{-2}; ii) do not have an optical counterpart; and iii) fall within the boundaries of the molecular emission of the OMC. The rest of the sources are classified as ONC members. Additionally, we have also checked our sample with the list of EG sources compiled by Getman et al. (2005a), finding that only one source (source 1 from Zapata et al. 2004a) is classified as an EG source. This is consistent with the Zapata et al. (2004a) prediction of ∼1 EG source within the 8.3 GHz FoV.

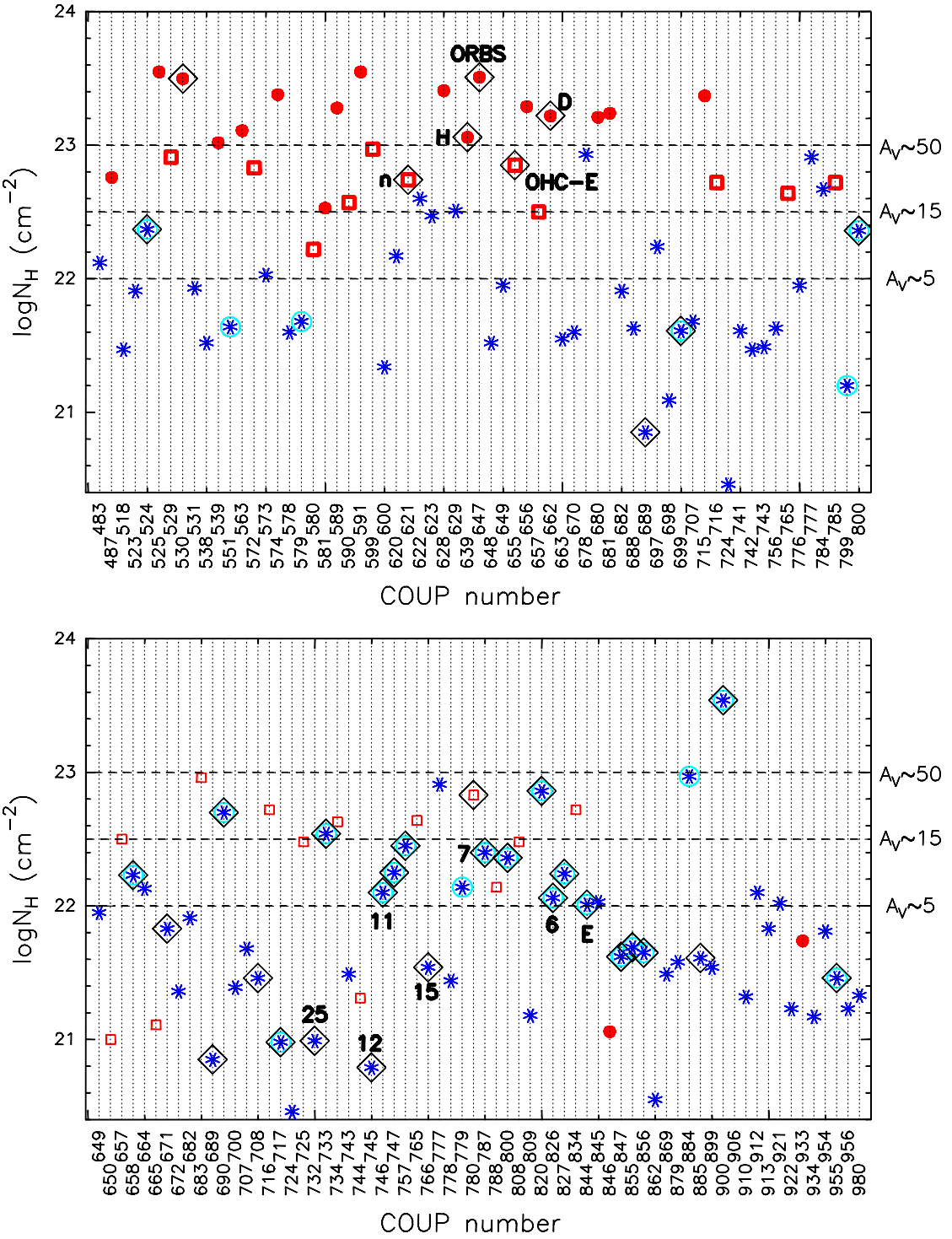

Figure 5.11: Hydrogen column density of the X-ray population in a 60" ×60" region around the OHC cluster (upper panel) and the Trapezium (lower panel). The red dots are stars without optical/IR counterparts; the red open squares are stars without optical counterpart but with an IR counterpart; and the blue asterisks are stars with both counterparts. The open dark blue circles denote sources identified as proplyds by Kastner et al. (2005). The open black diamonds indicate sources that are also detected at radio wavelengths. The radio sources detected in our monitoring are labeled.

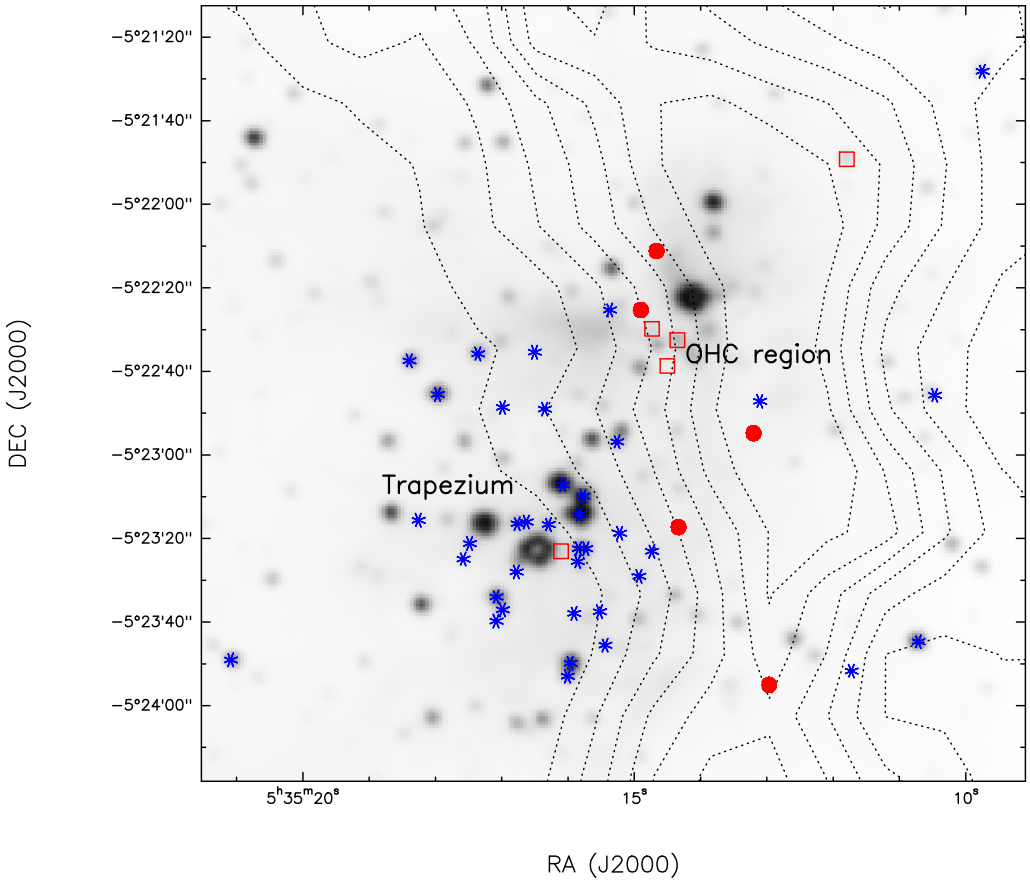

Figure 5.12: Spatial distribution of the full radio/X-ray sample of sources. The contours trace the dense gas from the OMC (CN N=1−0 emission from Rodriguez-Franco et al. 1998). The blue asterisks denote radio sources with optical/IR counterparts; open red squares are radio stars with IR but no optical counterparts; and red dots indicate radio sources without optical/IR counterparts. The radio source classified as EG falls outside the region shown.

5.4.2 Radio variability in ONC and OMC samples: clues to the nature of the radio emission

We now study whether the ONC and OMC members show differences in their radio variability. The left panel of Fig. 5.13 shows the radio variability parameter at 8.3 GHz as a function of the hydrogen column density. Most of the ONC stars are associated with radio emission from proplyds, which are expected to show constant thermal emission from ionized gas in their disks. However, Fig. 5.13 shows that although some ONC sources associated with proplyds (indicated with light blue circles) show $\beta_{8.3\mathrm{GHz}} < 0.2$, there is also a significant fraction (35%) that exhibits significant radio variability with values $\beta_{8.3\mathrm{GHz}} > 0.2$. Furthermore, some were also reported as highly radio variable sources by Felli et al. (1993) at 5 and 15 GHz (black circles). In the right panel of Fig. 5.13 we see that the stars associated with proplyds also show high levels of variability at high frequency. Therefore, the radio emission from proplyds cannot be explained only by the presence of non-variable thermal emission from the ionized gas or dust; a second mechanism is also needed. Moreover, some of the ONC sources not associated with proplyds (like sources G or 12) also show high radio variability at both frequencies, also pointing towards non-thermal emission. One possibility is gyrosynchrotron emission produced by the acceleration of electrons in magnetic field reconnection events in the corona of the PMS low-mass stars detected in X-rays (Andre 1996).

Low-mass stars embedded in the OMC show high radio variability, with values $\beta > 0.3$ both at 8.3 and 33.6 GHz, suggesting non-thermal emission associated with the magnetospheres of PMS low-mass stars. Whether there is also an underlying constant emission component from circumstellar material centrally ionized by the low-mass star is still unclear based on the present data. These low-mass stars are able to ionize less material than massive stars, producing as a result a weaker radio emission. This emission is difficult to disentangle from the observed variable emission, and may be below our sensitivity limit.

We conclude that the radio emission can be attributed to two different mechanisms: i) highly-variable (flaring) non-thermal radio gyrosynchrotron emission produced by accelerated electrons in the magnetospheres of low-mass PMS stellar members of both the ONC and OMC; and ii) non-variable thermal emission from the ionized gas and heated dust of the ONC proplyds illuminated by the Trapezium Cluster, or from the ionized gas in the envelopes surrounding massive stars, as in the case of the BN object.

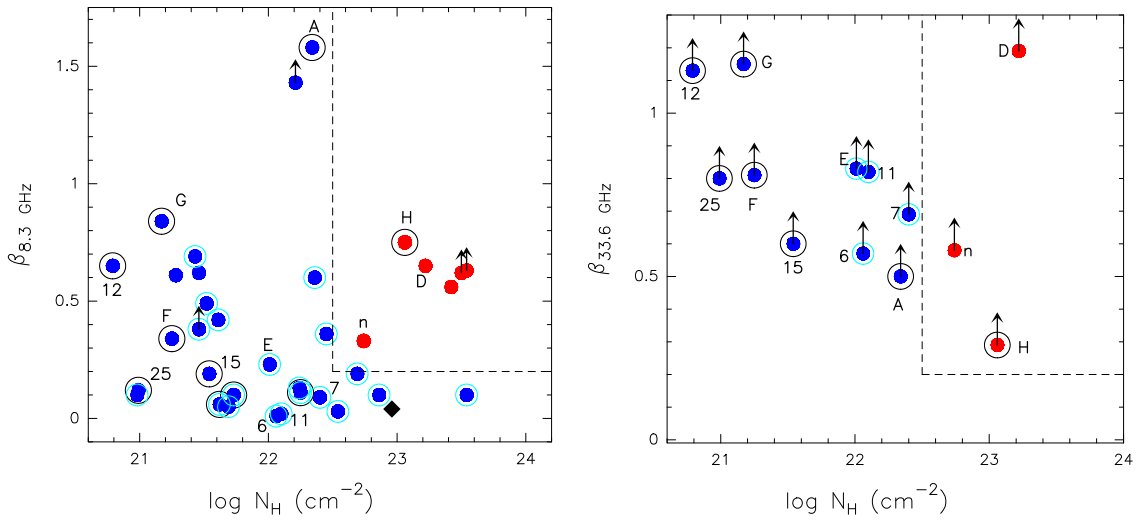

Figure 5.13: *Left:* Variability parameter at 8.3 GHz ($\beta_{8.3\mathrm{GHz}}$) of the radio/X-ray sample, versus the hydrogen column density ($\log N_{\mathrm{H}}$) of the X-ray counterparts. The stars classified as ONC and OMC members are indicated by blue and red dots, respectively. The light blue open circles show the proplyds from the Kastner et al. (2005) catalog, and large black open circles indicate radio sources classified as radio variables by Felli et al. (1993). The EG source is indicated with a black diamond. The arrows denote lower limits. The box delimited by the dashed line distinguishes OMC and ONC members. *Right:* The same as in the left panel, but for the variability parameter at 33.6 GHz ($\beta_{8.3\mathrm{GHz}}$).

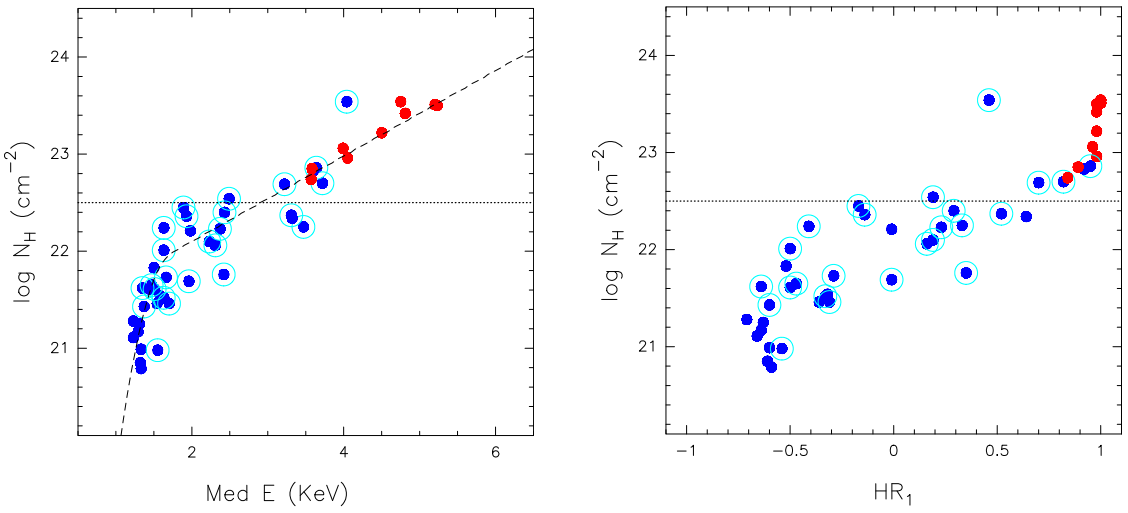

Figure 5.14: *Left*: Relationship between the hydrogen column density $N_{\rm H}$ and the median energy of X-ray photons ($MedE$) of the members of the radio/X-ray sample. The dashed line is the empirical fit found by Feigelson et al. (2005). The stars classified as ONC and OMC members are indicated by blue and red dots, respectively. The light blue open circles show the proplyds from the Kastner et al. (2005) catalog. *Right*: Relationship between the hydrogen column density $N_{\rm H}$ and the hardness ratio (HR_1). We use the same symbols as in the left panel.

5.4.3 Comparison with X-ray properties

★ Hardness ratio (HR_1) and median energy ($MedE$)

Table 5.4 and Fig. 5.14 show the values of median energies ($MedE$) of X-ray photons and the hardness ratio (HR_1) of the full radio/X-ray sample[7]. It is clear that the stars embedded in the OMC have higher values ($MedE$ >3.5 keV and HR_1 >0.84) than ONC stars. Feigelson et al. (2005) found a relationship between the median energy of the X-ray photons arising from the stars and the hydrogen column density $N_{\rm H}$ (left panel in Fig. 5.14). This trend is due to an absorption effect: in the embedded sources, only the harder photons are able to escape through the molecular gas and then be detectable, while softer ones (with lower energy) are absorbed. As a consequence, the embedded stars appear as harder sources. The high values of $MedE$ and HR_1 are consistent with our previous classification as OMC members (Sect. 5.4.1). On the other hand, the sources classified as ONC members exhibit generally lower values, as expected for sources with less extinction.

[7]Hardness ratio $HR_1 = (h-s)/(h+s)$, where h and s refer to the counts detected in the hard (2.0−8.0 keV) and soft (0.5−2.0 keV) bands, respectively. Values closer to 1.0 indicate a hard X-ray source, and −1.0 a soft X-ray source.

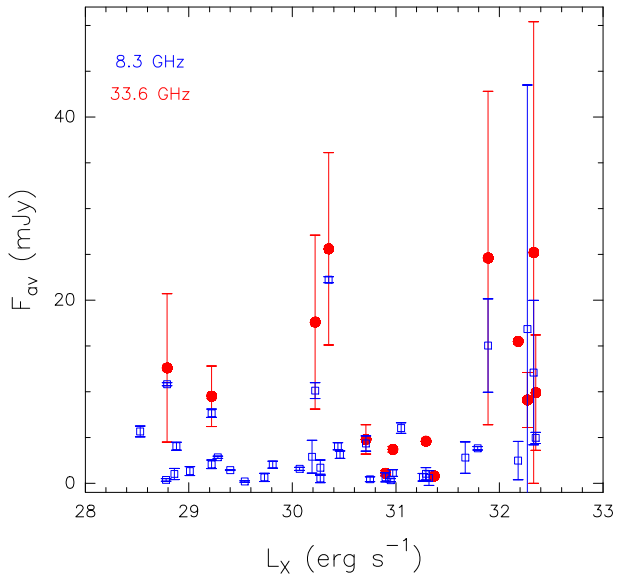

Figure 5.15: Plot of the average radio flux density $F_{\rm av}$ vs. the X-ray luminosity of the radio/X-ray sample. Red dots indicate the values of the sources detected at 33.6 GHz by our monitoring, while open blue squares are detections at 8.3 GHz from Zapata et al. (2004a). The error bars indicate the standard deviation of the flux densities with respect the average value $F_{\rm av}$.

★ X-ray luminosities

Here we investigate whether there is a relationship between the radio flux density and the X-ray luminosity. Forbrich and Wolk (2013) already remarked that there is no clear correlation between the radio flux densities measured by Zapata et al. (2004a) at 8.3 GHz and the COUP X-ray luminosities (Fig. 5.15). Similarly, we do not see a trend in our sample at 33.6 GHz.

We have also studied the fraction of X-ray sources detected at radio wavelengths as a function of the X-ray luminosity (Fig. 5.16) for our monitoring and that of Zapata et al. (2004a). In each case, we have considered the COUP sources that fall within the FoV of each observation with enough counts so that the X-ray luminosity corrected for extinction could be reported. We find 159 X-ray sources within our FoV and 595 sources within the 8.3 GHz FoV. Both samples show a very similar behavior. The weaker X-ray sources with $\log L_{\rm X} < 28.5$ erg s^{-1} (200 sources, i.e., 13% of the full COUP sample) were not detected by our radio monitoring, while Zapata et al. (2004a) only detected 1 source. Fig. 5.16 shows that the fraction of X-ray sources detected in the radio increases with X-ray luminosity. This indicates that, although individually there is not a direct correlation between radio flux density and X-ray luminosity (Fig.

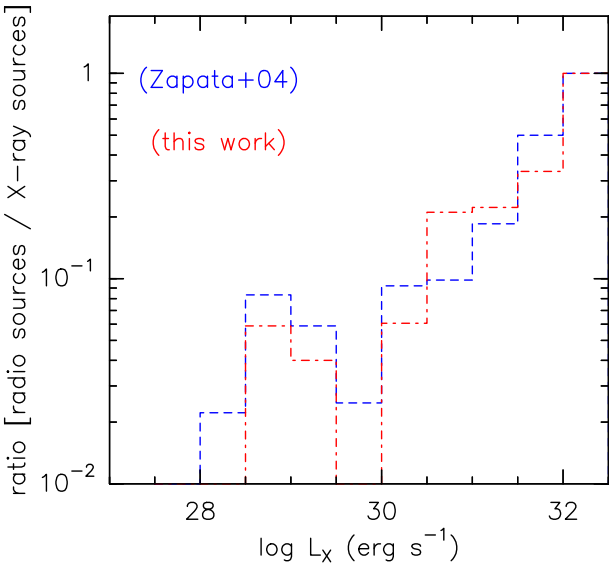

Figure 5.16: Fraction of X-ray COUP sources detected by our radio monitoring at 33.6 GHz (red line) and Zapata et al. (2004a) monitoring at 8.3 GHz (blue line) as a function of the absorption-corrected total X-ray luminosity L_X. In each case, we have considered the COUP sources that fall within the FoV and with enough counts so that the X-ray luminosity corrected for extinction could be reported: 159 for our monitoring and 595 for the 8.3 GHz monitoring (see Forbrich and Wolk 2013).

5.15), the radio observations have statistically detected the most luminous X-ray sources. This suggests then that: i) the underlying mechanisms responsible for X-ray and radio emission are somehow related; and ii) radio monitorings have been limited in the past due to sensitivity, confirming the conclusion of Forbrich and Wolk (2013).

★ X-ray variability

We study now whether there is a correlation between the radio variability and the X-ray variability. Following Getman et al. (2005c) we consider 3 signposts of X-ray radio variability: i) the significance of a Kolmogorov-Smirnov test (P_{KS}), which establishes whether variations are above those expected from Poisson noise associated with a constant source; ii) the number of segments of the Bayesian block parametric model ($BBNum$) of source variability developed by Scargle (1998); iii) visual inspection of the X-ray light curves. We consider that a source is X-ray variable when $P_{KS} < -2.0$ and/or $BBNum \geq 2$ and/or it exhibits X-ray flares in the light curves. For the latter, we have visually examined the light curves presented by Getman et al. (2005c). The values of P_{KS} and $BBNum$ (also from Getman et al. 2005c) are shown in Table 5.4.

Only one radio source (E) of the 14 radio/X-ray sample from our monitoring does

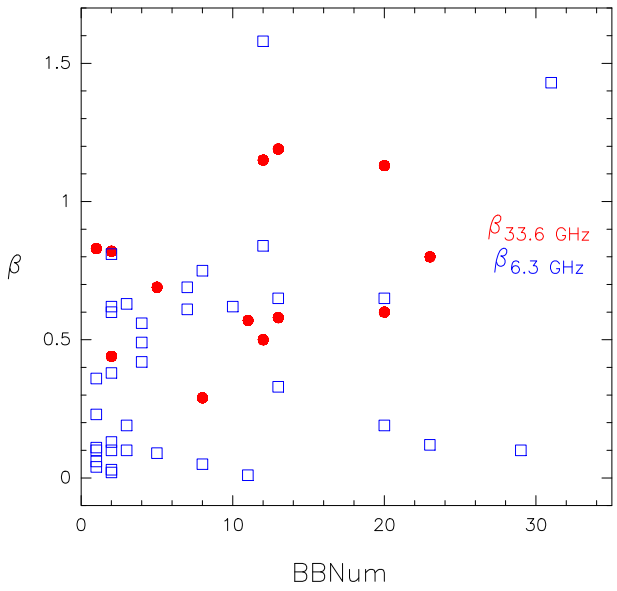

Figure 5.17: Radio variability parameter (β) at 33.6 GHz (red dots) and 8.3 GHz (open blue squares) versus the number of segments of the Bayesian block parametric model ($BBNum$), which indicates X-ray variability.

not exhibit X-ray variability. Namely, 93% of the stars of this sample are X-ray variable. Regarding the full radio/X-ray sample, 85% of the stars are X-ray variable. These fractions are higher than the fraction of X-ray variable sources of the full COUP sample, which is ∼60% (Getman et al. 2005c). Therefore, the radio sources are mostly associated with those X-ray variable stars. This suggest that radio emission might be related to magnetic events in the coronae of low-mass stars that give rise to the X-ray emission.

In Fig. 5.17 we compare the level of radio variability (at 8.3 and 33.6 GHz) with the level of X-ray variability, quantified by $BBNum$. While $\beta_{33.6\mathrm{GHz}}$ seems to show a weak trend with $BBNum$, $\beta_{8.3\mathrm{GHz}}$ does not show any correlation. However, given that the X-ray and radio observations were carried out at different epochs and different sensitivities, no firm conclusions can be drawn. Unlike the very deep COUP observation, which continuously observed the region during ∼10 days, the radio monitoring runs are much shorter and more spaced in time, yielding a lower probability to detect large flux density variation such as flares. To better understand if radio and X-ray variability are directly related, simultaneous observations of this population in both energy bands will be needed.

5.5 The new radio source embedded in the Orion Hot Core: OHC-E

Our observations have detected twice a new radio source, OHC-E (2009 March 19 and 2011 July 09, see Fig. 5.6). Neither Felli et al. (1993) nor Zapata et al. (2004a), who performed observations covering 7 months and 4 years at 5 and 15 GHz and 8.3 GHz,respectively, nor Goddi et al. (2011b), who observed the same region at 45 GHz two months before our detection (2009 January 12), detected emission towards this new source.

The source is not resolved by the beam of our observations in any of our two detections (~ 0.2" and ~ 0.075"). We can set upper limits to the deconvolved size of the emission of < 0.1" (< 40 AU) for the Q-band emission and of < 0.04" (< 10 AU) for the Ka-band emission. Unfortunately, it is not possible to determine the spectral index of the emission, because observations at several radio wavelengths were not carried out simultaneously. We derived lower limits to the brightness temperature of ~ 460 K and ~ 615 K from the source flux density at 45.6 GHz and 33.6 GHz, respectively, and the upper limits to the source sizes. Although these temperatures are consistent with both thermal and non-thermal emission, our monitoring shows that the emission is highly variable, suggesting a non-thermal origin.

The position of the radio flare coincides with an embedded X-ray low-mass pre-main sequence (PMS) star COUP 655 (Fig. 5.18). The source OHC-E is also located very close to the southest member of a binary stellar system (CB4, Fig. 5.18) observed with high angular resolution by the Near Infrared Camera and Multi-Object Spectrometer (NICMOS) onboard the Hubble Space telescope (HST) (see also Stolovy et al. 1998; Simpson et al. 2006). Therefore it seems that both the radio and the X-ray emission are related to this star. We can give a rough estimate for the mass of this star using the canonical relation for X-ray young stars, $\log[L_{\rm X}/L_{\rm bol}]=-3.0$ (Pallavicini et al. 1981). Assuming an stellar age typical for a massive star forming region of 5×10^5 yr, OHC-E would have a mass of $\sim$1 $M_\odot$ (using the Siess et al. 2000 stellar models), supporting that it is a low-mass star. Hence, the variability observed both in radio and X-rays wavelengths can be related with magnetic activity in the corona of this PMS low-mass star.

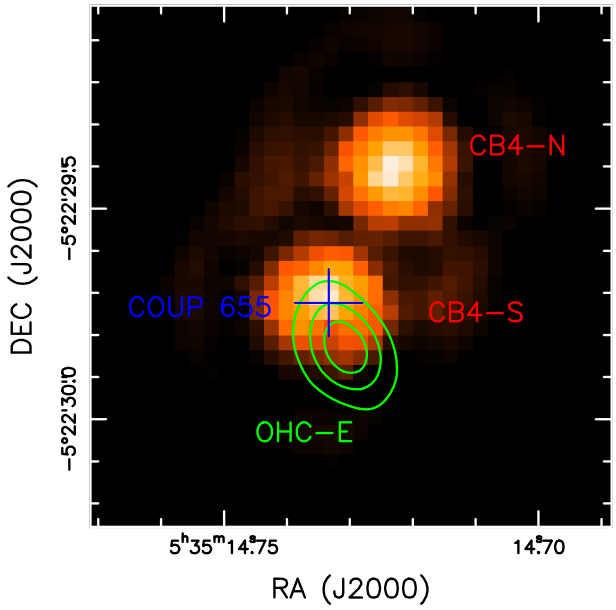

Figure 5.18: 2.15 μm HST-NICMOS image (color scale) of the region where OHC-E was detected, from the Hubble Legacy Archive (HLA). An IR binary is detected towards this region, CB4 (see also Stolovy et al. 1998; Simpson et al. 2006). The green contours correspond to the radio emission at 45.6 GHz detected on our 2009 March 19 image (5σ, 10σ and 15σ). The positions of the X-ray star COUP 655 is indicated with the blue plus sign.

5.6 Source 12: the binary θ^1 *Ori A*

θ^1 *Ori A* is a well known binary system, with a B0.5 primary and a low-mass companion (e.g., Close et al. 2013). As observed in the binary WR140 (Williams et al. 1990), the binarity can produce a smooth periodic variation of the radio emission caused by the combination of two geometrical effects: i) variation of the free-free opacity due to the ionized envelope of the primary star as the companion orbits; ii) variation of the stellar activity (and hence the non-thermal emission) inversely proportional to the separation between components.

Felli et al. (1991, 1993) monitored the radio emission from this binary at 5 and 15 GHz. We plot in Fig. 5.19 their flux densities and those of our monitoring as a function of the orbital phase ϕ. We have used the orbital parameters P=65.4325 and T_0=JD 2446811.95 (Bossi et al. 1989). The flux density at 5 and 15 GHz peaks near periastron (ϕ ∼0.15), with lower levels at ϕ ∼0.1 and ϕ =0.6 to 0.9. Our higher frequency flux densities are consistent with those at lower frequencies, with a peak after periastron at ϕ ∼0.2. As Felli et al. (1993) noted and our data at higher frequency confirm, the orbital modulation model may make the main peak be detected always at the same

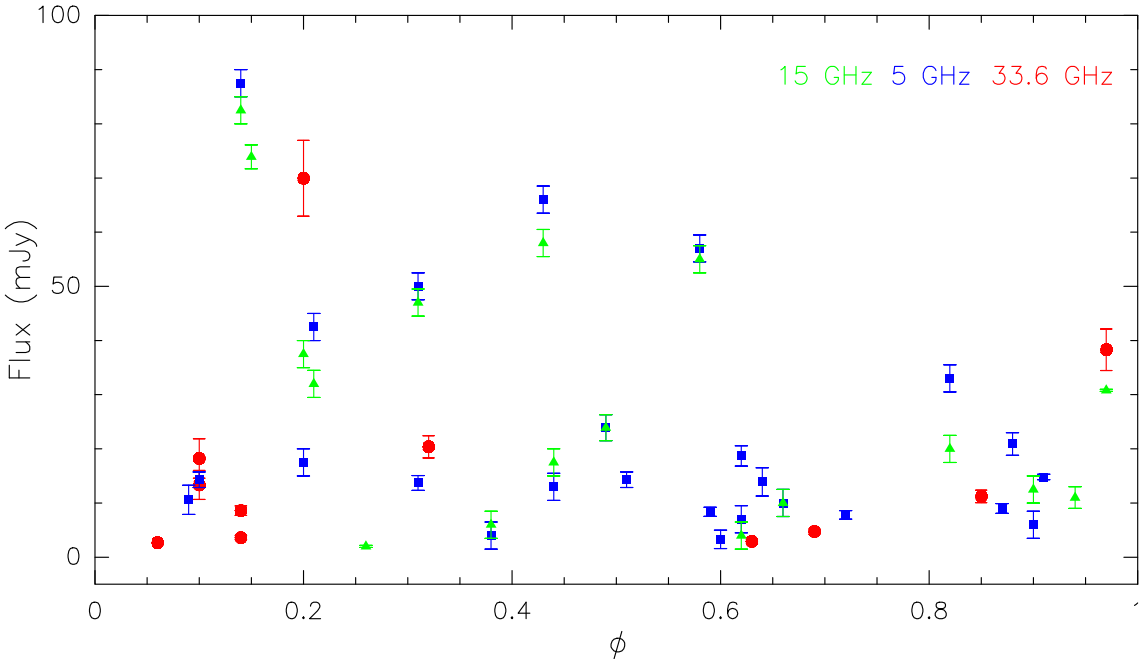

Figure 5.19: Flux densities of source 12 as a function of the orbital period at 33.6 GHz (red dots, this thesis), 5 and 15 GHz (blue squares and green triangles, respectively, from Felli et al. 1991, 1993).

position ϕ ∼0.15−0.2. However, the presence of large scatter in the radio emission cannot be explained with this model. Felli et al. (1993) set an upper limit for the variability timescale of 10 to 20 days. Our monitoring has revealed variability at shorter timescales of hours (Sect. 5.3.2). This is in agreement with non-thermal emission due to stellar activity, perhaps in addition to orbital modulation. Therefore, we conclude that although certain orbital modulation may be present, producing the observed flux density peak, there is also a non-thermal emission component arising likely from the low-mass companion that varies independently of the orbital phase.

5.7 Rate of radio flaring activity

There are only a few radio flares detected from young stellar objects. This could indicate that these phenomena are rare events, or alternatively, that the sensitivity of the observations carried out so far has limited their detection. Our monitoring allows us to evaluate which is the most likely scenario. We have detected flares in sources OHC-E, n, F, A, 12 and 7. Other sources (D, E, 25, 6, 12, 11, G...) that exhibit high levels of variability through different epochs (β >0.5) separated by longer timescales, might be also flaring sources, but with our present data we are not able to confirm

short-term variability.

Bower et al. (2003) parametrized the rate of radio flares (flares day^{-1}) in the entire ONC/OMC region based on their data and the previous observations of variable sources by Felli et al. (1993). Since the number of flares depends on the field of view (FoV) of a particular observation, and of the stellar density of the observed region, we reformulate the expression for the rate of radio flares, $N_{\rm RF}$, to:

$$N_{\rm RF} = \gamma \left(\frac{F_{3\sigma}}{100\, mJy} \right)^{\alpha} \left(\frac{A_{\rm FoV}}{A_{\rm tot}} \right) \left(\frac{\Sigma_{\rm FoV}}{\overline{\Sigma}} \right), \tag{5.1}$$

where $F_{3\sigma}$ is the threshold detection limit (considered as 3 times the RMS of the observation); α is the spectral index of the emission; $A_{\rm FoV}$ and $A_{\rm tot}$ are the areas of the observed region and the full ONC/OMC region, respectively; and $\Sigma_{\rm FoV}$ and $\overline{\Sigma}$ are the surface stellar density in the observed region and the mean stellar density of the entire ONC/OMC, respectively. The parameter γ is a constant that Bower et al. (2003) estimated to be between 0.01 and 0.1.

Since the flare rate is a function of the stellar density, it is convenient to observe the more crowded region of a cluster to enhance the chances of detecting radio flares. The region with highest stellar density in Orion is the OHC (chapter 2). Considering a ∼25" ×25" region centered in the stellar density peak, using the typical power-law index of non-thermal emission of $\alpha = -1$, the mean RMS noise of our monitoring (0.3 mJy), the approximated size of the ONC/OMC cluster of 15 pc×15 pc, and the census of stars in the region provided by COUP, we obtained that $N_{\rm RF}$ ∼0.017-0.17 flare day^{-1}.

We have detected 2 clear flares (OHC-E and source n[8].) in this area in 14 observations, so a rough estimate of the flaring rate is ∼0.14 flare observation^{-1}. Assuming that the typical duration of the radio flares is several hours to days (Andre 1996; Bower et al. 2003; Forbrich et al. 2008), this would be approximately equivalent to 0.14 flare day^{-1}, which is similar to the upper value from Eq. 5.1. Therefore, our results suggest that γ is closer to 0.1 rather than to 0.01, and consequently that the number of detectable flares is significant. Therefore, our multi-epoch monitoring confirms that the presence of radio flares is not a rare phenomenon in crowded young stellar clusters.

Obviously, the detection of radio flares in the OHC is favored by its high density of embedded low-mass stars. But, according to Eq. 5.1, even in less dense regions

[8]The detections of sources H and D in the OHC region show also tentative evidences of flaring emission towards these stars (see Sect. 5.3.4)

the number of detectable flares would be significant, especially if the sensitivity is enhanced. The improved capabilities of the VLA and ALMA may be expected to reveal many more radio flares arising from young low-mass star clusters. A single polarization ALMA observation at 90 GHz (band 3) with a full bandwidth of 7.5 GHz and 50 antennas, can reach a 8 μJy sensitivity limit in only 2.3 hours of on-source observing time[9] Considering a FoV of $\sim$25" $\times$25", this ALMA observation may find $\sim$ 6 radio flares day^{-1}, which represents $\sim$ 25% of the X-ray sources detected by Chandra in the region. This would confirm that radio flares are common events, similarly to the X-ray flares detected by Chandra.

Future observations are clearly needed to derive a better estimate of this radio flaring rate, through the detection of many more radio flares. The flaring information for tens or even hundreds of PMS stars will provide a complete statistical description of radio short-term variability. Beyond the purely scientific interest, this would have important technical implications for interferometric imaging (Bower et al. 2003). The classical interferometric imaging techniques assume a constant sky in image reconstruction. However, this assumption would be violated by the presence of many variable sources in the field. This would lead to a reduced dynamic range of the image (Stewart et al. 2011). Also, it would become difficult to concatenate multiple observations of the same region to obtain deeper images. Therefore, a more accurate determination of the radio flare rate would help to understand to what extent this may affect deeper VLA and ALMA observations of young stellar clusters.

5.8 Summary and conclusions

In this work we have presented a multi-epoch radio monitoring of the ONC/OMC region carried out with the VLA at high frequency (33 and 45 GHz). We have detected 19 radio sources, mainly concentrated in the Orion Hot Core and Trapezium regions. Two of them are related with young massive stars: sources BN and I. The BN source and source C flux density is nearly constant, while source I shows tentative evidences of radio variability at both short- and long-term timescales. The remaining 16 sources show long-term (month-timescale) variability, but it is not yet clear whether these comprise multiple short-term events on timescales not covered by our monitoring cadence. Indeed, we have confirmed radio flares (i.e., short-term radio variability on timescales of hours to days) in 5 sources: F, 7, n, 12 and the new source OHC-E,

[9]According to the ALMA sensitivity calculator available in the ALMA Observing Tool.

previously undetected at radio wavelengths. Other sources (A, H, D, E and G) also show tentative evidence of a flaring nature.

We have supplemented our radio sample with other radio detections from the literature. We have compared the radio variability from our monitoring at 33.6 GHz with that of Zapata et al. (2004a) at 8.3 GHz. Most of the sources (13 sources, ie., 76% of the sources detected at both frequencies) exhibit higher variability at higher frequencies, while the others (4 sources) show equal or lower variability than at lower frequency. We have also compared the radio variability with the X-ray variability, without finding a clear trend. However, given that the different radio and X-ray observations were carried out at different epochs and sensitivities, no firm conclusions can be drawn without further, simultaneous, observations.

Based on the comparison with optical, IR and X-ray surveys, the values of the hydrogen column density $N_{\rm H}$, and the spatial distribution with respect to the molecular emission of the OMC, we have classified the members of the entire radio sample as visible stars of the ONC ($\sim$ 76%) or even younger stars still embedded in the OMC ($\sim$ 20%). Of the ONC stars, the 60% of the radio sources are associated with proplyds.

Our analysis of the sample of emitting radio/X-ray stars in the ONC/OMC region suggests that radio emission from young stars can be explained by a combination of 2 different mechanisms: i) variable (flaring) non-thermal radio emission due to gyrosynchrotron emitted by accelerated electrons in the stellar corona of PMS low mass members of ONC and OMC; and ii) non-variable thermal emission from the ionized gas and/or heated dust of the proplyds around low mass ONC stars illuminated by the Trapezium, and from the ionized gas from the envelopes around the massive objects BN and I embedded in the OMC.

Based on our detection of radio flares we have derived a rough estimate of the radio flaring rate in the densest cluster in the region, which is embedded in the Orion Hot Core. We have obtained $\sim$0.15 flares day^{-1}, consistent with other empirical estimates. This confirms that radio flares are not rare phenomena during the earliest stages of star formation as previously thought, but relatively common events similarly to the well-known X-rays flares.

The comparison of the radio sample with the X-ray sample by COUP have shown that the radio monitoring to date has been strongly limited by sensitivity, detecting mail those sources with higher X-ray luminosity. On one hand, this suggests a link between the X-ray activity and the mechanisms responsible for the radio emission.

On the other hand, it impliess that the new capabilities of the VLA and ALMA offer a unique opportunity to detect a much larger population of radio sources in young stellar clusters. New observations with improved sensitivity and better angular resolution will provide crucial information about the origin and nature of the radio emission, and they will reveal whether radio and X-ray phenomena are indeed connected.

Furthermore, the presence of multiple variable radio sources would have important implications for interferometric imaging, since the classical techniques assume a constant sky. A more accurate determination of the radio flare rate would help to understand how this variability can affect the upcoming VLA and ALMA observations in young stellar clusters.

CHAPTER 6

X-ray embedded stars as driving sources of molecular outflows in OMC1-S

Abstract

Multiple molecular outflows and Herbig-Haro (HH) objects have been observed in Orion, many of them originating from the embedded massive star-forming region known as OMC1-S. The detection of the outflow driving sources is usually very difficult because they are hidden behind large extinctions, preventing their direct observation at optical and even near and mid-IR wavelengths. With the aim of improving our knowledge of the driving sources of the multiple outflows detected in OMC1-S, in this chapter we use the catalog provided by deep X-ray observations, which have unveiled the very embedded population of pre-main sequence stars. We compare the position of stars observed by the Chandra Orion Ultra Deep project (COUP) in OMC1-S with the morphology of the molecular outflows and the directions of measured proper motions of HH optical objects. We find that 6 out of 7 molecular outflows reported in OMC1-S (detection rate of 86%) have an extincted X-ray COUP star located at the expected position of the driving source. In several cases, X-rays observations detected the possible driving sources for the first time. This clustered embedded population revealed by Chandra is very young, with an estimated average age of few 10^5 yr. These X-ray stars are also likely responsible for the multiple observed HH objects, which are the optical counterparts of shocked gas by outflows flows arising from the Orion molecular cloud.

6.1 Introduction

During their first stages of evolution, young stars accrete material along the equatorial plane to grow up, and spell mass in the direction perpendicular to their circumstellar disk forming bipolar outflows (Arce et al. 2007). The ubiquitous presence of outflows

from low and intermediate mass stars has important implications in the formation of stars (Stanke and Williams 2007), especially in the crowded clusters where massive stars are born (Lada and Lada 2003a; see also chapters 2, 3 and 4). The outflows inject momentum and energy into the interstellar medium, favoring the fragmentation of the parental core (Knee and Sandell 2000; Li and Nakamura 2006; Cunningham et al. 2011), and producing turbulence (Li and Nakamura 2006; Nakamura and Li 2007), which could affect the accretion rates onto the stars (Krumholz et al. 2005). This is particularly important in the case of massive stars, that need high accretion rates to form.

These outflows can be observed through its emission over a wide range of the electromagnetic spectrum. At optical wavelengths, the features produced when the ejected material from the stars collide with the surrounding gas and dust are known as Herbig-Haro (HH) objects. At longer wavelengths, the outflows are traced by the emission from different molecules (Arce et al. 2007; Beuther et al. 2007; Zapata et al. 2010; Beltrán et al. 2012).

While outflows are often easily detected, it is much more difficult to unambiguously associate them with their driving sources. This is because the objects powering these outflows are very young stars, often hidden behind large extinction that commonly prevents their observation at optical and even near and mid-IR observations. However, as we have seen in previous chapters, X-rays can penetrate deeply into the molecular cloud, and therefore sensitive X-ray observations with high spatial resolution are a unique tool to detect most of the embedded driving sources of molecular outflows and HH objects arising from crowded stellar clusters.

We focus this chapter on identifying the driving sources of the numerous outflows detected in the massive star-forming region OMC1-S. This region, located at d$\sim$414 pc, is related the Orion Molecular Cloud (OMC) and the optically visible Orion Nebula Cluster (ONC) ionized by the four main sequence massive Trapezium stars[1]. The OMC1-S region contains a very dense and obscured molecular condensation with a mass $\sim$100 $M_\odot$ (Mezger et al. 1990) and a density of $n \sim 10^6$ cm^{-3} (Mundy et al. 1986). It exhibits several evidences of massive star formation: warm and dense gas (Ziurys et al. 1981, Batrla et al. 1983, Rodriguez-Franco et al. 1998), large dust column densities (Keene et al. 1982), and presence of H_2O masers (Gaume et al. 1998).

The OMC1-S region shows very intense outflow activity. Three large optical flows

[1] O'Dell et al. (2009) proposed that the OMC1-S core is detached from the background OMC, approximately at the same depth as the Trapezium stars.

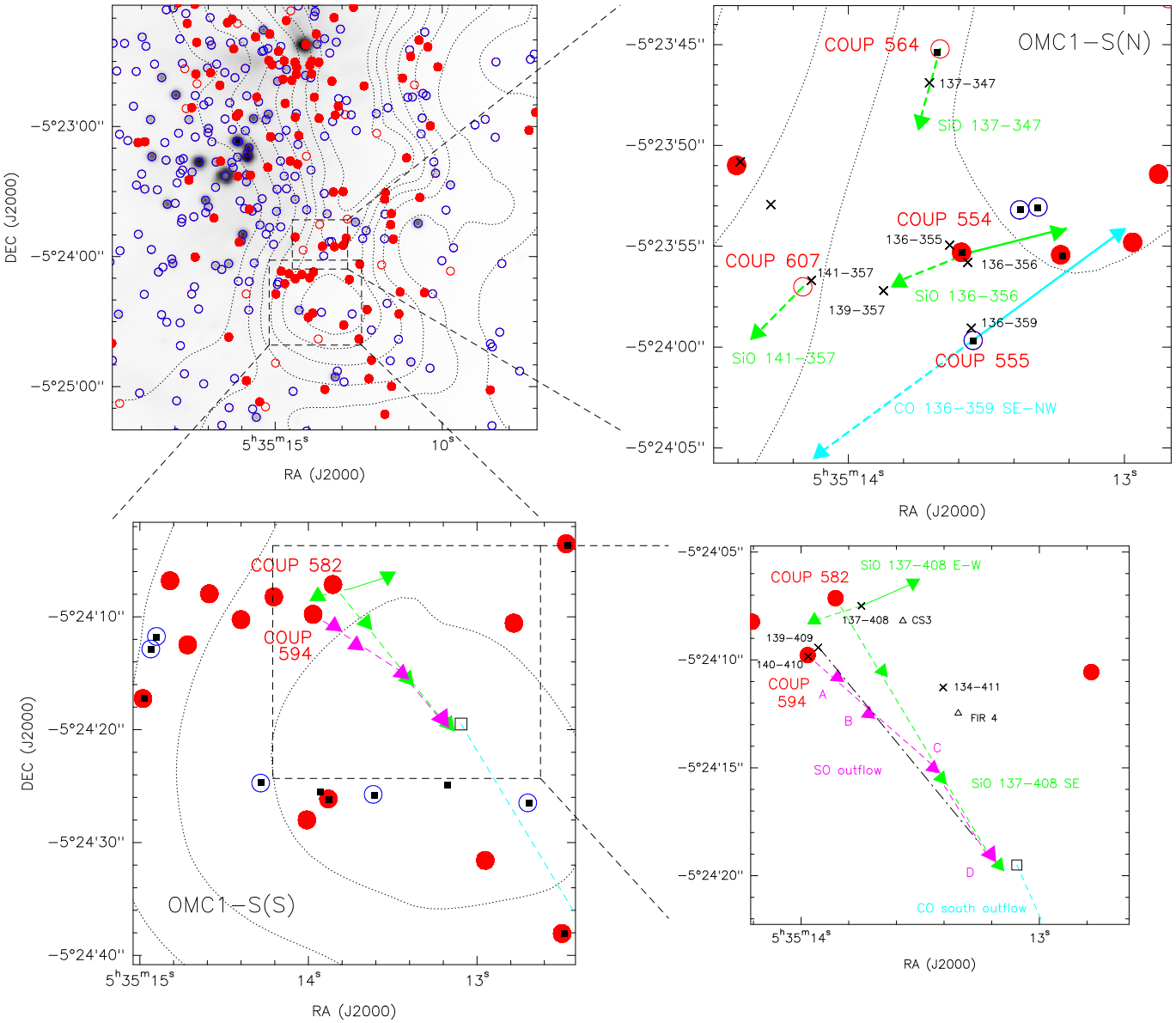

Figure 6.1: *Upper Left Panel*: Spatial distribution of COUP stars in the ONC/OMC region. Open blue circles are stars with $\log N_{\rm H}$ <22.5 cm^{-2} (expected to be ONC members); red dots are stars with measured values of $\log N_{\rm H}$ >22.5 cm^{-2} (expected to be embedded members of the OMC); and open red circles are stars without measured value for $\log N_{\rm H}$ (likely also embedded objects). The gray scale is the K-band 2MASS image. The dotted contours are the emission from the OMC traced by the CN (1-0) emission, from Rodriguez-Franco et al. (1998). The first contour level corresponds to 7 K km s^{-1} and the interval between contours is 4 K km s^{-1}. The dashed boxes indicate the location of the OMC1-S(N) and OMC1-S(S) regions where several molecular outflows have been detected. *Upper Right Panel:* Zoom-in of the OMC1-S(N) region. The CO and SiO molecular outflows from Zapata et al. (2005, 2006) are indicated with arrows. The redshifted lobes are marked with dashed strokes. The COUP stars driving the molecular outflows are labeled, with the same symbols as in the upper left panel. We have also added IR stars (black filled squares; Hillenbrand and Carpenter 2000) and cm/mm sources (black crosses; Zapata et al. (2004b, 2006). *Lower Panels:* Zoom-in of OMC1-S(S). The SiO and SO molecular outflows from Zapata et al. (2005, 2006) are indicated with arrows (redshifted lobes with dashed strokes). The COUP stars have the same symbols as in the upper panels. We have also added IR stars and cm/mm sources with same notation. The triangle symbols indicate the position of FIR 4 (Mezger et al. 1990) and CS3 (Mundy et al. 1986); and the open square indicates the position from where the CO south outflow propagates in a straight line (Zapata et al. 2010).

have been detected in [OIII] (Smith et al. 2004), along with multiple HH objects (Bally et al. 2000; O'Dell and Doi 2003), and several molecular outflows (Ziurys et al. 1990; Schmid-Burgk et al. 1990; Rodríguez-Franco et al. 1999a; Zapata et al. 2005, 2006, 2010).

Several works (Smith et al. 2004; Zapata et al. 2004b; Robberto et al. 2005; Henney et al. 2007) have proposed embedded mid-IR or cm/mm sources as possible candidates for the driving sources of both HH objects and molecular outflows. However, none of these studies have considered the population of X-ray stars detected by the Chandra Orion Ultra-Deep Project (COUP). We have shown in chapter 2 that OMC1-S harbors a dense population of very embedded X-ray stars, some of them revealed by Chandra for the first time.

In this chapter, we compared the position of COUP stars in OMC1-S with the morphology of the molecular outflows and the directions of measured proper motions of HH optical objects. The chapter is written as follows. In Section 6.2 we discuss the searching procedure for the driving sources of the outflows, and study their physical properties. In Section 6.3 we summarize our results and conclusions.

6.2 Analysis and results: X-ray embedded stars as outflow driving sources

We have used the catalog of PMS X-ray stars provided by the COUP Project (Getman et al. 2005c) to compare the positions of the stars with the morphology of the molecular and optical outflows and HH objects arising from OMC1-S. In Fig. 6.1 we show the location of the COUP stars together with a sketch of the molecular outflows and the spatial distribution of the dense gas in the OMC.

6.2.1 Membership of the COUP stellar population

As we have seen in previous chapters, one of the advantages of using X-rays to study young stellar clusters is that they suffer less foreground and background contamination than optical/IR observations. In the OMC1-S region, we expect low extragalactic contamination (Getman et al. 2005a), and low galactic contamination, because PMS stars exhibit much larger X-rays emission than older foreground stars unrelated to the cluster. Therefore, the COUP census reflect the very young stellar population of the cluster, both extremely young stars still embedded in the OMC together with

more evolved (but still young) members of the optically visible ONC. To discriminate between these two populations, we follow the criteria used in chapter 2 based on the hydrogen column densities ($N_{\rm H}$) obtained from the X-ray spectra: stars with $\log N_{\rm H} < 22.5$ cm^{-2} are expected to be ONC members, and stars with $\log N_{\rm H} > 22.5$ cm^{-2} are expected to be still embedded in dense gas.

Additionally, following the procedure used in chapter 5, we compare here in detail the COUP census of the OMC1-S region with optical (Hillenbrand, 1997) and near IR (Hillenbrand and Carpenter, 2000) surveys. For our study we used a region of 60" $\times$ 60" around the stellar density peak found in chapter 2. In Fig. 6.2 we plot the results of our comparison between the objects detected in these surveys and the value of $N_{\rm H}$. As observed in the OHC and the TC (see chapter 5), there is a clear trend between the presence (or not) of optical and IR counterparts as a function of $\log N_{\rm H}$. Since the optical stars and values of $\log N_{\rm H} < 22.5$ cm^{-2} are associated with ONC members, we will consider that the sources with $\log N_H > 22.5$ cm^{-2} and no optical counterpart are stars embedded in the OMC1-S core[2].

Since O'Dell et al. (2009) proposed that the OMC1-S core is detached from the OMC at roughly the same depth into the ONC as the Trapezium stars, it would be possible that stars considered members of the core are actually more evolved ONC members located between the core and the background OMC. If we assume that these COUP stars are ONC members distributed spherically, one would expect the same number of stars in front and behind the core. However, the region zoomed-in in Fig. 6.1 presents $\sim$77% of extincted stars as opposed to only $\sim$23% of non-extincted stars. This deficit of non-extincted objects suggests that the extincted population is indeed located within the OMC1-S core. In fact, in a dense molecular core such as OMC1-S, with ongoing star formation and cm/mm sources and molecular outflows, one expects the presence of a stellar cluster. As found in the OHC (see chapter 2), the most likely scenario is that the extincted COUP stars are embedded in the core rather than being ONC members. Furthermore, the fact that several of the extincted COUP stars are located at the expected positions of the driving sources of the molecular outflows (Figure 6.1 and Section 6.2.2) strongly suggests that these extincted stars are indeed embedded in the core[3].

[2] With the exception of COUP 555 ($\log N_{\rm H}$=22.44 cm^{-2}), that we also considered as a OMC1-S member because it drives one of the molecular outflows detected in the core (see Section 6.2.2) and exhibits X-ray properties typical of an embedded star (see Section 6.2.2).

[3] Although we cannot completely rule out that some of the embedded objects are ONC members located between the OMC1-S core and the background OMC or a star embedded in the OMC.

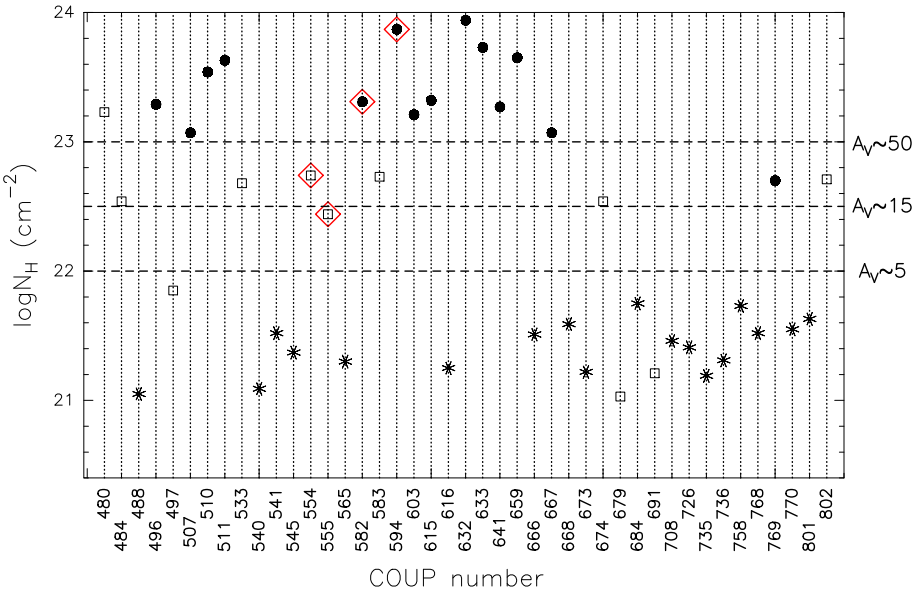

Figure 6.2: Hydrogen column density of COUP sources located in a 60" × 60" region around the OMC1-S region. The plot only include those COUP stars for which $N_{\rm H}$ can be derived from the X-ray spectra. The dots are stars without optical/IR counterparts; the open squares are stars without optical counterpart but IR counterpart; and the asterisks correspond to stars with optical and IR counterparts. With red diamonds we indicate outflow-driving stars candidates.

6.2.2 Molecular outflows

In the last two decades up to seven[4] different molecular outflows have been detected in the OMC1-S region, traced by their emission in CO (Schmid-Burgk et al. 1990; Rodríguez-Franco et al. 1999a; Zapata et al. 2005), SiO (Ziurys et al. 1990; Zapata et al. 2006) and SO (Zapata et al. 2010). These outflows are in general highly collimated, which allow to estimate the expected location of the driving source.

We compared the morphology of the molecular outflows with the stellar positions provided by the high angular resolution (∼ 0.5") COUP observations. In Fig. 6.1 we zoom-in in the two regions [OMC1-S(N) and OMC1-S(S)] where the molecular outflows have been detected. We found X-ray stars at the expected positions of the driving sources of 6 out of the 7 molecular outflows. In Table 1 we summarize the association between the outflows and the proposed COUP driving sources.

Given that the OMC1-S region exhibits a very dense population of COUP stars (see chapter 2), we evaluate the possibility that stars with a random distribution

[4] We do not count the CO south outflow (see lower panels in Fig. 6.1 and Table 6.1) as a separate outflow because, as we discuss in Section 8.4.2, it seems the result of a collision of two other outflows.

Table 6.1: COUP driving sources of the outflows detected in OMC1-S, with their coordinates, counterparts at other wavelengths, and other proposed candidates to drive the outflows from the literature.

Outflow	COUP driving source	RA(J2000) DEC(J2000)	Counterparts[a] IR[b]							cm/mm[c]	Other candidates[d]
			HC00	L00	M02	L04	S04	R05	G98		
CO 136-359	555	5 35 13.55 -5 23 59.67	178	16	263	138	5	42	C	-	136-359
SiO 136-356	554	5 35 13.59 -5 23 55.29	192	46	276	139	4	43	B	-	136-356
SiO 137-408 SE	582	5 35 13.86 -5 24 07.13	-	-	-	-	-	-	-	-	137-408
SiO 137-347	564	5 35 13.67 -5 23 45.20	222	-	313	141	-	-	-	-	137-347
SiO 141-357	607	5 35 14.16 -5 23 57.01	-	-	-	-	-	-	-	-	141-357
SiO 137-408 E-W	-	- -	-	-	-	-	-	-	-	137-408	-
SO	594	5 35 13.97 -5 24 09.78	-	-	-	-	-	-	-	140-410	139-409
CO south	594	5 35 13.97 -5 24 09.78	-	-	-	-	-	-	-	140-410	139-409
HH 529	632	5 35 14.41 -5 23 50.98	-	1	293	162	2	61	-	144-351	-

[a] We consider as counterparts those sources with separations lower than the "counterpart radius" $r_{\rm counter}$ (see Section 6.2.2).

[b] HC00 (Hillenbrand and Carpenter 2000); L00 (Lada et al. 2000); M02 (Muench et al. 2002); L04 (Lada et al. 2004); S04 (Smith et al. 2004); R05 (Robberto et al. 2005); G98 (Gaume et al. 1998).

[c] 1.3 cm sources from (Zapata et al., 2004b); and 1.3 mm sources from (Zapata et al., 2005).

[d] From Zapata et al. (2004b) and Zapata et al. (2005). These cm/mm sources are located near the COUP stars, but at separations larger than the "counterpart radius" $r_{\rm counter}$ (see Section 6.2.2).

are located at the driving positions of the molecular outflows. The probability that members of a random distribution of n stars fall within an area of size θ around the expected position of the driving source of l outflows in a region with size L is:

$$P = \frac{C_{m-l,m-n}}{C_{m,n}}, \tag{6.1}$$

where

$$C_{m,n} = \frac{m!}{n!\,(m-n)!}, \tag{6.2}$$

and $m = (L/\theta)^2$. Considering the population of embedded stars in OMC1-S in the two zoomed-in regions of Fig. 6.1, we obtained n =22. The size θ is defined as a combination of the Chandra spatial resolution (∼0.5”), uncertainties in the X-ray star positions[5] (< 0.2”), and the intrinsic uncertainty in the expected location of the outflow driving source. To estimate the latter, we use the maximum distance between the COUP outflow-driving candidates and other cm/mm sources candidates (Zapata et al. 2004b, 2005). Table 6.2 shows that the maximum distance is ∼1.8”[6].

[5] Getman et al. (2005c) shows that the positions of COUP sources is very well determined, with values generally < 0.2” (see Table 6.2 for some examples).

[6] For those outflows in which the position of the driving source is not defined with accuracy, the positional uncertainty could be somewhat larger. However, this will not change our result, i.e., that

Adding quadratically the three contributions, we found a value of θ=2". Assuming an approximate size for the total region of L ∼40" (0.08 pc) and 6 outflows (l =6) we find that the probability to find a random COUP source at the driving position of an outflow is extremely low (P ∼10^{-8}). Although we favor that X-ray stars are the driving sources (see discussion in Sections 6.2.2 and 6.2.4), other candidates to drive some of the molecular outflows have been proposed. We repeated the calculation taking into account the worst possible case in which only 3 COUP stars are driving sources. Then, l =3 and the random probability is still very low (P ∼10^{-4}). As a consequence, we conclude that the X-ray stars are very likely related to the molecular outflows.

★ X-ray sources vs. IR and cm/mm sources

We found COUP stars in the expected positions of the driving sources of 6 of 7 molecular outflows in the region. In this Section we compare these X-ray stars with the IR and cm/mm population detected in this region, with the aim of determining if they are counterparts of the X-ray sources, and also discuss what candidates are the most likely driving sources of the outflows.

Both cm/mm and X-rays observations are able to penetrate into the core, despite of the high extinction, which is an important advantage with respect to IR observations, which suffer much more absorption. Table 6.1 shows that only half (3 of 6) of the X-ray candidates have been detected at IR wavelengths.

The comparison between the position of COUP and cm/mm sources (Zapata et al. 2004b, 2005) provides a good opportunity to determine whether the cm/mm sources are COUP star counterparts. We compared their positions with those from the IR stars (position accuracy of 0.1"; Hillenbrand and Carpenter 2000). We consider that two sources are counterparts (i.e., their emission arises from the same object) when the separation between the sources is less than the "counterpart radius" ($r_{\rm counter}$), which is defined as the sum of the half value of their respective angular resolutions.

We present in Table 6.2 the results of this comparison for the candidates for driving sources of the outflows. We find that the COUP stars exhibit separations smaller than 0.24" with respect to the IR stars. The cross-correlation of the full samples show that 95% of the sources observed in X-rays and IR have separations < 0.30". This is less than the "counterpart radius", $r_{\rm counter}$[7], clearly confirming that the X-ray emission

the probability of a chance alignment of all outflows with X-ray sources is very small.

[7] Calculated from the angular resolution of COUP and IR observations from Hillenbrand and Carpenter (2000), which in both cases is ∼0.5" in the inner region of the field of view of the

arise from stars.

However, the cm sources from Zapata et al. (2004b) located close to IR sources (136-359, 136-356, 136-355 and 137-347, Fig. 6.1) exhibit larger separations to the IR stars (0.6" −1.6", Table 6.2). The centimeter sources without close IR stars (141-357, 137-408 and 139-409) also present large separations (0.6−1.8") to the closer COUP stars. Given that these separations are larger than the "counterpart radius", $r_{\rm counter}$[8]=0.4", it seems that these cm sources do not directly trace the position of the stars observed at X-ray and IR wavelengths. An exception is the source 140-410, located at only 0.07" from COUP 594, and that clearly is a counterpart of the X-ray star. This is confirmed by the detection of large circular polarization in this source (Zapata et al. 2004b), which is indicative of gyrosynchrotron emission from the magnetosphere of a PMS low mass star.

In Section 6.2.4 we will discuss in detail each molecular outflow and their more likely driving sources, considering the X-ray/IR and cm/mm candidates. We conclude that the COUP stars provides very good candidates for outflow drivers. X-ray emission probes efficiently the position of young PMS stars[9] , while the cm/mm continuum could also trace shocks or ionized gas from close circumstellar disks and jets (Hofner et al. 2007, Araya et al. 2009). Furthermore, unlike the COUP observations, the sensitivity of current cm/mm observations are strongly limited detecting low-mass stars (see chapter 5 and and Forbrich and Wolk 2013). Moreover, it is known that bright cm/mm emission from some stars is produced during flares (Bower et al. 2003, Forbrich et al. 2008 and chapter 5), which makes difficult the detection outside a flare event in a single-epoch observation.

Therefore, deep X-ray observations are a very good tool, complementary to cm/mm observations, to unveil the heavily obscured young stellar population, and hence to detect the driving sources of the molecular outflows embedded in stellar clusters.

★ X-ray properties of the outflow-driving stars

We discuss here more extensively the general X-ray properties of the outflow-driving stars, compared to the population of stars with no outflows (but also extincted)

observations, where the OMC1-S region is located.

[8] Using the value of angular resolution of the centimeter observations of 0.3" (Zapata et al. 2004b).

[9] In the COUP sample, Getman et al. (2005a) find that 1406 of the 1616 sources (87%) are young stars associated with the stellar cluster, while only 10% are extragalactic sources and 0.1% (2 sources) are outflows emitting in X-rays.

Table 6.2: X-ray position uncertainties and separations between the COUP outflow-driving stars and the nearest cm/mm and IR sources.

COUP	pos. unc. (")[a]	$d_{\rm X-IR}$	cm/mm	$d_{\rm cm/mm-IR}$ [b]	$d_{\rm cm/mm-X}$
555	0.04	0.05	136-359	0.65	0.61
554	0.01	0.05	136-356	0.58	0.61
			136-355	0.78	0.73
607	0.07	-	141-357	-	0.55
564	0.11	0.24	137-347	1.55	1.78
582	0.12	-	137-408	-	1.66
594	0.05	-	140-410	-	0.07
		-	139-409	-	0.76
632	0.13	0.20	144-351	0.09	0.28

[a] Source's positional uncertainty of COUP sources calculated as 68% (1σ) confidence intervals using the Student's T-distribution (see Getman et al. 2005c).

[b] Sources from Zapata et al. (2004b) and Zapata et al. (2005). The positions have been obtained from Zapata et al. (2004b) observations at 1.3 cm, whose angular resolution is ∼0.3".

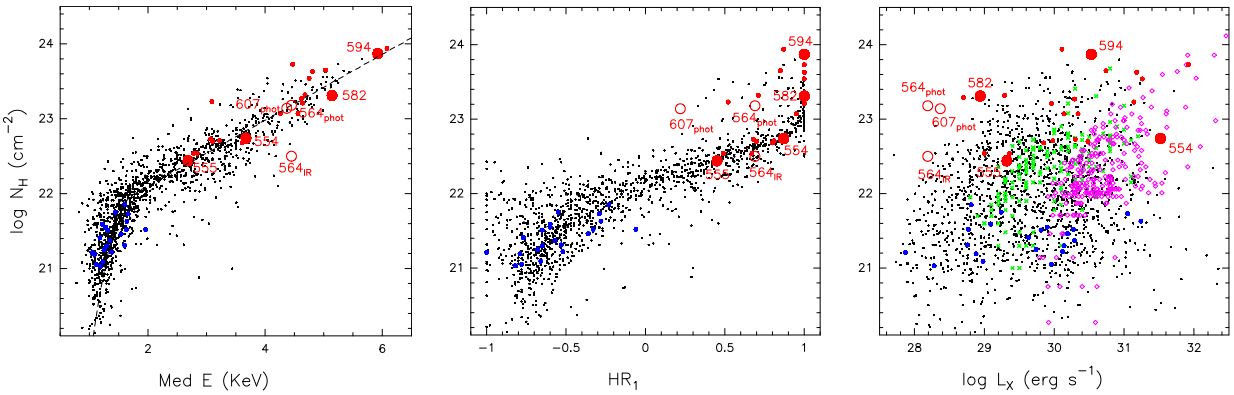

Figure 6.3: X-ray properties of COUP stars. We plot the hydrogen column density $\log N_{\rm H}$ versus: i) the mean energy of the stellar photons (left panel); ii) the hardness ratio (middle panel); and iii) the extinction-corrected X-ray luminosities (right panel). The large red circles correspond to the outflow-driving stars with values of $N_{\rm H}$ measured fitting the X-ray spectra. The large open red circles denote the COUP outflow-driving stars with $N_{\rm H}$ measured from photometry (labeled with the subscript *phot*) or from the IR counterpart (labeled with the subscript *IR*). The small red dots are the non-outflowing (but also embedded) sources of the 60" ×60" OMC1-S region considered, while the small blue dots correspond to the non-embedded ONC members. In the *left* panel we also plot with a dashed line the empirical fit found by Feigelson et al. (2005). In the *right* panel we add X-ray sources from Monoceros R2 (green crosses) and S255 (magenta diamonds), for comparison.

Table 6.3: X-ray properties of the outflow-driving stars in OMC1-S.

COUP	net counts[a]	SNR[b]	log$N_{\rm H}$	log$L_{\rm X}$	log$P_{\rm KS}$ [c]	$BBNum$[d]	flare[e]	$MedE$	HR$_1$[f]
555	151	49	22.44±0.09	29.32	-1.82	2	(yes)	2.68	$0.45^{+0.08}_{-0.08}$
554	14045	4445	22.74±0.01	31.52	-4.0	31	yes	3.67	$0.87^{+0.00}_{-0.00}$
582	18	9.0	23.31±0.48	28.94	-2.32	1	(yes)	5.14	$1.0^{+0.00}$
564	5	5.7	23.18[h] / 22.5[i]	28.19[g]	-0.07	1	-	4.45	$0.69^{+0.38}$
607	10	9.1	23.14[h]	28.37[g]	-0.05	1	-	4.37	$0.22^{+0.41}_{-0.36}$
594	125	45.0	23.87±0.06	30.53	-4.0	2	yes	5.92	$1.0^{+0.00}$

[a] Net source counts after background subtraction.

[b] The signal to noise is defined as $SNR = source\ counts/(background\ counts)^{1/2}$

[c] $P_{\rm KS}$ is the significance of a Kolmogorov-Smirnov (KS) test to establish whether variations are present above those expected from Poisson noise associated with a constant source (from Getman et al. 2005c). A source is considered variable if log$P_{\rm KS} < -2.0$. The values have been truncated at -4.0.

[d] $BBNum$ is the number of segments of the Bayesian block (BB) parametric model of source variability developed by Scargle (1998). A source is variable when $BBNum \geq 2$. The values shown here are from Getman et al. (2005c).

[e] From visual inspection of the X-ray light curves available at Getman et al. (2005c). The parenthesis denote that the identification is uncertain.

[f] Hardness ratio $HR_1 = (counts_h - counts_s)/(counts_h + counts_s)$, where subscripts h and s refer to the hard (2.0−8.0 keV) and soft (0.5−2.0 keV) bands, respectively.

[g] Estimated luminosity in hard band corrected for absorption, instead of luminosity in total band corrected for absorption, not available for this star.

[h] The $N_{\rm H}$ have been obtained photometrically, i.e., from the relation between the mean energy of the photons ($MedE$) and $N_{\rm H}$ found by Feigelson et al. (2005).

[i] The $N_{\rm H}$ have been obtained with the relation between the color index H-K of the IR counterpart and $N_{\rm H}$, found by Kohno et al. (2002).

sources, and non-extincted ONC stars. We also considered the stellar population contained in the same region of 60" × 60" used in Section 6.2.1. In Table 6.3 we show the properties of the outflow-driving population.

In Section 6.2.1 we established a general criterion to differentiate stars embedded in the OMC1-S core from the ONC members: no optical identification and values of log $N_{\rm H}$ >22.5 cm^{-2}. None of the COUP outflow-driving stars have optical counterparts. Regarding the values of $N_{\rm H}$, the fit of the X-ray spectra of COUP 554, COUP 582 and COUP 594 provides values of log $N_{\rm H}$ >22.5 cm^{-2} (Table 6.3). In the case of COUP 555, its hydrogen column density is slightly lower, log $N_{\rm H}$=22.44 cm^{-2}, but we also consider that this star is embedded because it clearly drives one of the molecular outflows, and its properties (see further discussion) are similar to those of the other embedded members. For COUP 564 and COUP 607 an spectral analysis was not possible given the low number of detected counts. In that case we have estimated $N_{\rm H}$ by using two alternative methods: i) from photometry, using the relation found by Feigelson et al. (2005) between $N_{\rm H}$ and the mean energy of the photons, $MedE$; and ii) from the correlation between the color index H-K of the IR counterpart and

$N_{\rm H}$ found by Kohno et al. (2002). The obtained values are log$N_{\rm H}$ >22.5 cm^{-2} (Table 6.3) and therefore all these stars are likely embedded within the OMC1-S core.

The X-ray properties of the outflow-driving stars are seriously affected by the high extinction, as we discussed in chapter 5. As a consequence of the relation between the median energy of background-substracted photons from the stars ($MedE$) and the hydrogen column density $N_{\rm H}$ (left panel in Fig. 6.3), the embedded stars should appear as harder sources. In the middle panel of Fig. 6.3 we show the values of the hardness ratio HR_1, defined as in chapter 5. It is clear that the embedded sources (shown in red) have much higher values than that of the foreground ONC members (blue). The high HR_1 of the sources without $N_{\rm H}$ measured from the X-ray spectra (COUP 564 and COUP 607) confirms that they are also embedded objects.

In the right panel of Fig. 6.3 we show the values of the extinction-corrected X-ray luminosities $L_{\rm X}$. These luminosities depend on the stellar mass (Preibisch et al. 2005), and at the age range of the stars in the region, slightly on the stellar age (Preibisch and Feigelson 2005). We compare the entire COUP sample (black dots) with surveys of other massive star-forming regions: Monoceros R2 (magenta diamonds, Kohno et al. 2002) and S255 (green crosses, Mucciarelli et al. 2011). In these two regions (with less sensitive Chandra observations) there is a clear trend of more luminous sources to have higher extinctions. This effect is simply due to absorption of the soft photons of sources hidden behind high extinction. In the deeper COUP sample this effect (although still present, see the absence of COUP sources in the top-left region of the right panel of Fig. 6.3) is less clear.

The luminosities of the outflow-driving stars show a wide range (log$L_{\rm X}$=28−31 erg s^{-1}), similar to the values exhibited by the non-outflow-driving (but also embedded) stars and the non-embedded stars. This suggests that the differences between the luminosities are not due to the evolutionary phase of the star, but likely to the different masses of the stars.

We have also studied the X-ray variability. It is expected that PMS low mass stars are high variable, due to flares produced by emission from plasma heated to high temperatures by violent reconnection events in magnetic loops in the corona. Following the procedure used in chapter 5, we use 3 criteria to determine the variability: i) Kolmogorov-Smirnov (KS) test to establish whether variations are present above those expected from Poisson noise associated with a constant source; ii) a Bayesian block (BB) parametric model of source variability developed by Scargle (1998); and iii) direct visual inspection of the X-ray light curves. The results (from Getman et al.

2005c) are shown in Table 6.3. The stars COUP 555, COUP 554, COUP 582 and COUP 594 fulfill at least one of this criteria, i.e., we confirm variability in a ∼66% of the outflow-driving stars. In the two other cases (COUP 564 and COUP 607), it is possible that the non-detection of variability is due to the low number of counts detected from these sources. Although we note that the statistic significance of this limited sample is very low, this fraction of variable stars is similar to the one shown by the non-outflowing but also embedded sample (∼75%) and the non-embedded sample (∼80%).

We conclude that there are not significant differences in the X-ray properties between the outflowing and non-outflowing (also extincted) population. The X-ray embedded sources without outflows are also very young stars in the prestellar phase. This reveals a population of PMS low-mass stars that cm/mm observations have missed so far.

6.2.3 Optical outflows and HH objects

The OMC1-S region is also the source of multiple HH objects (Bally et al. 2000, O'Dell and Doi 2003, Henney et al. 2007), and three large optical outflows observed in [OIII] (Smith et al. 2004). Unlike molecular outflows, whose origin can be generally well determined, in the case of HH objects it is more difficult to associate them to their driving source, because they are usually observed as the final part of a flow in the form of bow-shocks, and they are located at larger distances of their driving sources.

Although some of the HH objects might be produced by stars of the ionized nebula ONC seen at optical wavelengths, it is expected that most of them are powered by stars still embedded in the dense molecular core in OMC1-S. It is thought that the HH objects are the optical correspondence of flows which break out towards the ionized nebula ONC from the stellar population embedded in OMC1-S, where the molecular outflows are observed. Then it is worth to compare the proper motions of the HH objects (Bally et al. 2000; O'Dell and Doi 2003) with the embedded population revealed for the first time by Chandra.

We show schematically in Fig. 6.4 the distribution of embedded COUP stars, the orientations of the main HH objects (Bally et al. 2000 and O'Dell and Doi 2003), and the large optical outflows observed in [O III] (Smith et al. 2004). It is clear that the [O III] outflows and most of the HH objects point towards the same region: OMC1-S (indicated with a red ellipse in Fig. 6.4).

In particular, the embedded star COUP 632 (labeled in Fig. 6.4) is the X-ray

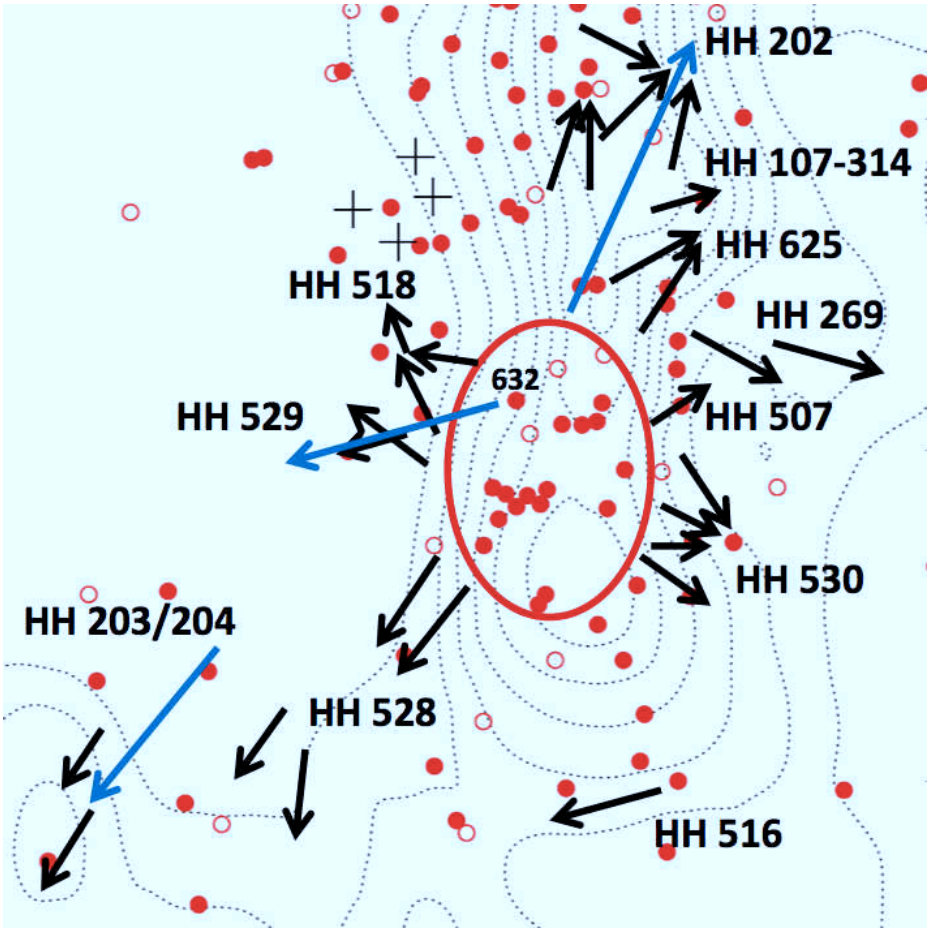

Figure 6.4: Distribution of the population of COUP stars embedded in the OMC. The red dots correspond to sources with $\log N_{\rm H}$ >22.5 cm^{-2}, and the open red circles denote sources without measured value for $N_{\rm H}$ (likely also embedded objects). The orientations of the [OIII] optical outflows (Smith et al. 2004) and the main HH objects detected in the region (Bally et al. 2000 and O'Dell and Doi 2003) are indicated with blue and black arrows, respectively. We have labeled the star COUP 632 (see text). The positions of the massive Trapezium stars are indicated with 4 black crosses. The dotted contours are the emission from the OMC traced by the CN (1-0) emission, from Rodriguez-Franco et al. (1998). The first contour level corresponds to 7 K km s^{-1} and the interval between contours is 4 K km s^{-1}.

Table 6.4: Physical parameters obtained from the fit of the SEDs of COUP 555, COUP 554 and COUP 632 (driving sources of the molecular outflows CO 136-359 and SiO 136-355, and the HH 529 optical flow, respectively).

COUP star	A_V^1 (mag)	SED results						
		M ($M_\odot$)	L_{bol} ($L_\odot$)	Stellar age ($\times 10^5$ yr)	A_V (mag)	$\log[L_X/L_{bol}]$	M_{disk} ($M_\odot$)	$M_{envelope}$ ($M_\odot$)
555	14	0.3−2	3−10	0.5−4	15−25	[-4.7,-5.3]	0.01−0.05	0.02−2
554	28	0.9−2.5	8−30	1.5−4	25−30	[-3.0,-3.5]	0.03−0.1	0.004−3
632	>400	0.5−1.5	7−50	nwc[2]	40−60	[-4.3,-5.2]	0.0002−0.002	0.01−0.5

[1] From the value of $\log N_H$ obtained fitting the X-ray spectra, and using the Vuong et al. (2003) relation.

[2] Parameter not well constrained.

counterpart of the known driving source of the large optical outflow detected in [OIII] by Smith et al. (2004), which is associated with multiple HH objects known as HH 529 (see Section 6.2.4 for a more detailed description).

We remark the presence of the compact and dense (>10^5 stars pc^{-3}, see chapter 2) stellar cluster (see the region located towards the SE within the red ellipse in Fig. 6.4; see also the lower left panel in Fig. 6.1). This cluster, which seems to drive the two molecular outflows detected in OMC1-S(S) (Section 6.2.2), represents a population of very young stars deeply embedded ($\log N_H$ >23 cm^{-2}, i.e., A_V >50) that was previously undetected at other wavelengths.

In conclusion, X-rays have detected, for the first time, numerous embedded stars that are excelent candidates to be the driving sources of the multiple HH objects found in this region.

6.2.4 Individual comments on outflows and driving sources

In this section we discuss the details of the different molecular outflows located in OMC1-S, along with their proposed driving sources. We also include the large optical flow associated with HH 529, whose driving source has also been observed in X-rays (COUP 632).

For the stars COUP 554, COUP 555 and COUP 632 (with detections at IR wavelengths) we fitted its spectral energy distribution (SED) with the models from Robitaille et al. (2006, 2007). These stars are presumably very young, and thus they likely have a gas envelope responsible for the SED in the mid-IR to millimeter range. Unfortunately, there are not available mid/far-IR measurements at wavelengths >20

μm. In the millimeter range, to constrain the envelope contribution we used the fluxes of the 1.3 mm sources 136-356, 136-359 and 144-351 detected by Zapata et al. (2005) (see Table 6.2). The results of the 100 best fits are shown in Fig. 6.5. Although the SED is not well characterized in the mid/far-IR range due to the lack of observational data, we can derive a range for the physical parameters (stellar mass, total luminosity, stellar age, extinction, fractional luminosity [$L_{\rm X}/L_{\rm bol}$], disk mass and envelope mass; Table 6.4). In all cases, we selected the parameter range shared by more than 50% of the best models (see Fig. 6.6, where we show for illustrative purposes the results for the bolometric luminosity of COUP 554 obtained considering the best 100 models).

In the case of COUP stars in which we cannot fit the SED, we used indicators as the X-ray variability, flaring activity and fractional luminosity ($L_{\rm X}/L_{\rm bol}$) to distinguish qualitatively between low mass (M<1.3 $M_{\odot}$), intermediate mass (1.3 $M_{\odot}$ < M <8 $M_{\odot}$), and high mass (M>8 $M_{\odot}$) stars. While high X-ray variability and X-ray flares attributed to plasma trapped in closed magnetic structures and violently heated by magnetic reconnection events are common in lower mass objects, they are not expected in more massive stars. We determined the variability using the same criteria as in Section 6.2.2.

The fractional luminosity $L_{\rm X}/L_{\rm bol}$ indicates the efficiency of the star in converting luminous energy into magnetic activity. It is expected that PMS stars with lower masses can reach the "saturation limit" for coronally active stars (emitting up to log [$L_{\rm X}/L_{\rm bol}$]=−3.0; Pallavicini et al. 1981; Fleming et al. 1995; Flaccomio et al. 2003; Güdel and Nazé 2009). In the case of low/intermediate (M< 3 $M_{\odot}$) mass accreting stars, Preibisch et al. (2005) found that this value is slightly lower, log [$L_{\rm X}/L_{\rm bol}$]=−3.7. This value is significantly different in stars with higher masses, more inefficient converting bolometric luminosity in magnetic energy, where log [$L_{\rm X}/L_{\rm bol}$] reaches values down to −7.0 (Pallavicini et al. 1981). In Table 6.5 we show the masses of COUP stars without SED, obtained applying the canonical relations log [$L_{\rm X}/L_{\rm bol}$]=−3.7 and log [$L_{\rm X}/L_{\rm bol}$]=−7.0. In the next subsections we will discuss that these sources without SED are likely low/intermediate mass objects.

★ The 136-359 SE-NW CO outflow (COUP 555)

This outflow was first detected by Rodríguez-Franco et al. (1999a,b), and subsequently resolved with higher angular resolution by Zapata et al. (2005) (Fig. 6.1). The position of the driving source coincides with the X-ray star COUP 555, located at 0.6" of the cm/mm source 136-359 (Zapata et al. 2005). Based on the large mechanical

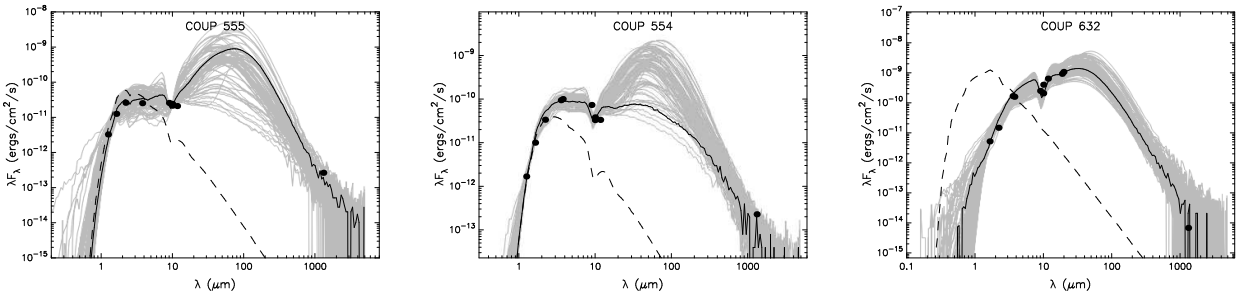

Figure 6.5: SEDs of COUP 555 (left), COUP 554 (middle) and COUP 632 (right) obtained from Robitaille et al. (2006, 2007) models. The filled circles show the input fluxes. The black lines show the best fit, the gray lines show the 100 best fits, and the dashed lines show the stellar photosphere corresponding to the central source of the best fitting model, as it would look in the absence of circumstellar dust (but including interstellar extinction).

luminosity of the outflow, Zapata et al. (2005) suggested that the driving source of this outflow could be an embedded high luminosity ($L_{\rm bol}$ $\sim$10^4 L$_\odot$) and massive object. They used in their calculation a correlation between the mechanical luminosity of the outflow and the luminosity of the driving star (Beuther et al. 2002). However, this correlation was established from single-dish data (which considerably underestimates the luminosity due to beam dilution), and therefore it can not be used with the mechanical luminosity obtained from the interferometric data from Zapata et al. (2005). Using the mass of the outflow calculated from the single-dish data from Rodríguez-Franco et al. (1999b), $m_{\rm outflow}$ $\sim$ 0.04 M$_\odot$, we have used the single-dish correlation presented by Wu et al. (2004) between the outflow mass and the bolometric luminosity of the driving source, obtaining that the luminosity of the driving star must be $\sim$1 L$_\odot$, which implies a low mass star. We note that this is a rough estimate with high uncertainty, because the outflow mass considers only the very high velocity gas and the Wu et al. (2004) relation exhibits a large dispersion.

Other arguments can be made to show that a low/intermediate luminosity source could drive the outflow: i) there are indications that the outflow is very young (low dynamical age, very high collimation, very high CO velocities), and it is well known that younger outflows have higher luminosity for a given driving source luminosity (e.g., Bontemps et al. 1996); and ii) the outflow is traced out to exceptionally high velocities, which will artificially boost the outflow luminosity, and mimic an outflow driven by a much higher luminosity source than it actually is.

With the aim of better constraining the mass of this outflow-driving star, we fitted their SED using the fluxes provided by several IR observations (see Table 6.1; Gaume et al. 1998; Hillenbrand and Carpenter 2000; Lada et al. 2000; Muench et al. 2002;

Lada et al. 2004; Smith et al. 2004; Robberto et al. 2005) with the Robitaille et al. (2006, 2007) models. The 100 best fits are shown in the left panel of Fig. 6.5, and the physical parameters derived are presented in Table 6.4. From the models, we obtain a range for the extinction of A_V=15−25 mag, consistent with that obtained from X-rays (A_V ∼14 mag). We obtain a stellar mass of M=0.3−2 $M_\odot$, a bolometric luminosity of L_{bol} = 3−10 $L_\odot$, and a young stellar age of (0.5−4)×10^5 yr, as expected. The star exhibits a moderate X-ray variability (Table 6.3), and it may show a flare, although the large error bars in the light curve prevent from a clear confirmation. The log [L_X/L_{bol}] ratio ranges between -4.7 and -5.3, which are more consistent with an intermediate-mass star than a low-mass star. Thus we favor the case of a mass in the higher part of the range mass resulted from the SED fit, i.e., ∼2 $M_\odot$.

★ The 136-356 bipolar SiO outflow (COUP 554)

This is the main SiO outflow detected by Zapata et al. (2006), produced by the embedded star COUP 554, which has an IR counterpart (Gaume et al. 1998; Hillenbrand and Carpenter 2000; Muench et al. 2002). Hashimoto et al. (2007) detected infrared polarization signatures typical of inner cavities of stellar outflows towards this position, confirming that this object is the driving source.

Gaume et al. (1998) called this object source B, and estimated the mass of the star from its IR K-band flux, finding that if it were a zero age main sequence (ZAMS) star, it would be a B2 star (with a mass ∼ 10 $M_\odot$ and a luminosity of 3×10^3 $L_\odot$). Using the fluxes measured from different works (see Table 6.1) we fitted the SED of COUP 554 with the Robitaille et al. (2006) models to better contrain the properties of this outflow-driving star. The right panel of Fig. 6.5 and Table 6.4 show the results. We obtained a value for the extinction of A_V=25−30 mag, consistent with that obtained from X-rays, A_V ∼28 mag. The models give a mass of M=0.9−2.5 $M_\odot$, a luminosity of L_{bol} =8−30 $L_\odot$ (Fig. 6.6), and a young stellar age of (1.5−4)×10^5 yr. The presence of X-rays flares in its light curve, and the high X-ray variability (Table 6.3) also allow us to rule out the massive nature of this star. The ratio between the X-ray luminosity and the bolometric luminosity log [L_X/L_{bol}] range between -3.0 and -3.5, consistently with a star with masses lower than 3 $M_\odot$, in agreement with the mass calculated from the SED.

The cm/mm continuum sources 136-356 and 136-355 are located at separations of 0.61” and 0.73”, respectively, outside the "counterpart radius" $r_{counter}$ (Section

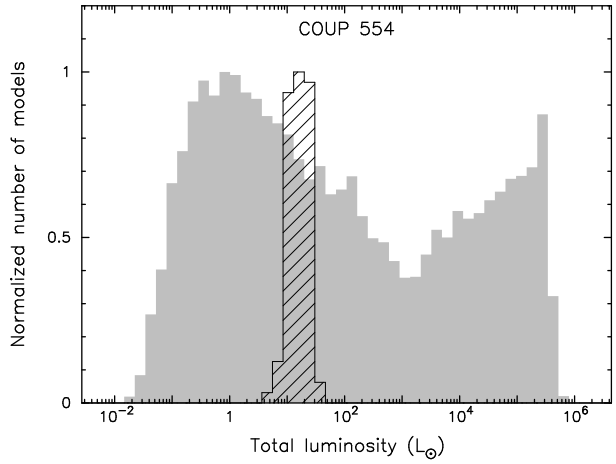

Figure 6.6: Results for the bolometric luminosity of COUP 554. The gray histogram shows the distribution of models in the model grid, and the hashed histogram shows the distribution of the 100 best selected models.

Table 6.5: Fractional luminosities of the COUP driving sources of OMC1-S outflows without SED fitting.

COUP star	M ($M_\odot$)	
	$\log[L_X/L_{bol}]=-3.7$	$\log[L_X/L_{bol}]=-7.0$
564	<0.1	3.5
607	<0.1	4
582	0.1	5-6
594	0.6	>7

6.2.2), suggesting that the emission does not directly arise from the star[10]. The position of the cm/mm sources, approximately perpendicular to the SiO outflow axis, may indicate that they are tracing ionized gas or shocks produced in a circumstellar disk. The cm source 139-357 (Fig. 6.1) is located in the outflow redshifted lobe axis of the SiO outflow, suggesting that it is tracing shocks related to the flow.

★ 137-347 Monopolar Outflow (COUP 564)

This is the northernmost outflow detected by Zapata et al. (2006) (upper right panel in Fig. 6.1). These authors claimed that it arises from the cm/mm compact source 137-347. This source is unresolved at 1.3 cm by the beam of the observations (0.3"), so we can set an upper limit for their size of 0.15". Given that the separation with the X-ray star is significantively larger (∼1.8") than this size and than the *counterpart*

[10] The possibility that COUP 554 is the combined counterpart to the cm sources is ruled out because the angular resolution of Chandra in the OMC1-S region (∼0.5") would resolve these sources, which are separated by 1.3".

radius (see Section 6.2.2), we conclude that these two sources are not counterparts. Zapata et al. (2005) detected 137-347 also at 1.3 cm, but in this case with an elongated shape of size ∼2.5" along the same direction (SE-NW) of the outflow lobe (Zapata et al. 2006). We interpret that the star COUP 564 (also detected in IR) is the driving source of the outflow, whose innemost part is traced by the shocks that produce the continuum emission of 137-347, and outermost part is traced by the SiO lobe.

The X-ray variability of COUP 564 is not confirmed (Table 6.3), although this might be due to the few counts detected from this source. Using the canonical relations for stars with lower and higher masses, we obtain masses of <0.1 $M_\odot$ and 3.5 $M_\odot$, respectively (assuming the estimated average age of the cluster of 2.5×10^5 yr and the Siess et al. (2000) PMS stellar models).

★ 141-357 Outflow (COUP 607)

This outflow is located to the east of the 136-356 main bipolar SiO outflow (see upper right panel of Fig. 6.1). Zapata et al. (2006) noted that this outflow does not belong to the 136-356 bipolar outflow, because: i) it is located ∼10" away from the driving source; ii) it shows much lower velocity gas; and iii) if powered by the same object as the bipolar outflow, its dynamical age would be much older. Zapata et al. (2006) proposed that this outflow is likely powered by their radio compact source 141-357. The X-ray observations reveal the presence of a star, COUP 607, so far undetected in near or mid-IR, located at ∼0.55" (Fig. 6.1 and Table 6.2). Therefore, we support the outflow nature of this molecular component, powered by this star. As we discussed in Section 6.2.2 the separation between the X-ray and cm sources is slightly larger than the "counterpart radius" $r_{\rm counter}$ ∼0.5". Given its relative location with respect to COUP 607 and the outflow axis (Fig 6.1), 141-357 may trace a close jet of the blueshifted counterlobe of the observed SiO flow.

The presence of a flare in the X-ray light curve is uncertain due to poor signal-to-noise ratio, and no clear variability is detected. Using the relation for higher mass stars, we obtain a mass 4 $M_\odot$; although a low mass star with ≤0.1 $M_\odot$ cannot be ruled out.

★ The 137-408 SE SiO outflow (COUP 582)

This redshifted SiO outflow was found by Zapata et al. (2006) in OMC1-S(S) (lower right panel in Fig. 6.1). It has a clumpy structure along the outflow axis, with "knots" at different velocities. Unlike most of molecular outflows (such as e.g. L1448-mm;

Guilloteau et al. 1992), this outflow is slowing down as it moves away from its origin, with moderate velocities (29−56 km s^{-1}) with respect to the ambient cloud velocity for the inner part, and low velocities (0−27 km s^{-1}) for the outer one.

Zapata et al. (2006) claimed that the outflow appears to be driven by the millimeter source 137-408 (labeled in the lower right panel of Fig. 6.1). If this is the case, this would indicate the presence of a close binary, because 137-408 is very likely the driving source of the 137-408 E-W outflow (Section 6.2.4). However, given that the well defined outflow axis (green dashed line) passes south (∼1.5") of the millimeter position, we think that the very embedded X-ray star COUP 582 is a more natural candidate, because it is perfectly aligned with the outflow axis, and consequently there is no need to invoke a bending trajectory. This star is one of the members of the densest stellar cluster detected in OMC1-S(S) (see chapter 2), with log $N_{\rm H}$=23.3 cm^{-2} (equivalent to $A_{\rm V} \sim 100$ mag). It does not have cm/mm, optical or IR counterparts, being detected for the first time in X-rays. It seems to exhibit a flare (although the large error bars in the light curve prevent a clear confirmation) and a moderate X-ray variability, suggesting that it is a low mass star. Using the relation log $[L_{\rm X}/L_{\rm bol}] \sim -3.7$, we obtain a mass of ~ 0.1 M$_\odot$. However, a star with higher mass cannot be completely ruled out. Using the relation log $[L_{\rm X}/L_{\rm bol}] \sim -7$, the mass would be ∼5−6 M$_\odot$.

★ The SO outflow (COUP 594)

This redshifted outflow traced by SO (Zapata et al. 2010) is located very close to the SiO 137-408 SE outflow (see lower panels in Fig. 6.1). This SO outflow exhibits four differentiated knots (A, B, C and D). Regarding the origin of the SO outflow, Zapata et al. (2010) suggested that the cm/mm source 139-409, a circumbinary ring (Zapata et al. 2007), could be the driving source. In the lower right panel of Fig. 6.1 we have plotted with a black dashed line the hypothetical outflow axis, with P.A.=48°. It seems that the SO knots are not well aligned. Actually, it is difficult to explain the SO outflow from the 139-409 position with a straight flow. Zapata et al. (2010) already recognized that a bending trajectory can not be excluded for this outflow. However, in order to produce the four knots from the 139-409 origin, it would be needed at least two bends, which although posssible, seems unlikely. Furthermore, Zapata et al. (2010) noted that the identification of the driving source still remained open because the orientation and sense of rotation of the 139-409 circumbinary ring does not coincide with those detected in the outflow. Furthermore, another circumbinary ring

detected in the region, 134-411, with similar characteristics to 139-409 (Zapata et al. 2007) and expected to be in the same evolutionary stage, do not drive a molecular outflow (see Fig. 6.1).

We consider that the X-ray star COUP 594 is a more plausible driving source. It is located at ∼0.7" from 139-409, and coincident with the 1.3 cm source 139-409 (Zapata et al. 2004b). As discussed in Section 6.2.2 this cm source is very likely produced by gyrosynchrotron emission from the magnetosphere of the star revealed by X-rays.

As shown in Fig. 6.1, the SO outflow could be originated from COUP 594, with a P.A.∼57° (magenta dashed line) until the knot C, where the outflow deviates to P.A.∼40°. The change in orientation occurs at the knot C, which is coincident with a SiO knot of the 137-408 SE SiO outflow. It is striking that both SO and SiO outflows share the same path from this point, and suggests that these two outflows may be interacting, as discussed in Section 8.4.2.

Based on its high X-ray variability and the presence of a flare in its light curve, we conclude that COUP 594, is very likely a low mass star. Using the relation log $[L_{\rm X}/L_{\rm bol}]$=−3.7, we obtain a mass of ∼ 0.6 $M_\odot$ (Table 6.5).

★ The CO south outflow (COUP 594 + COUP 582)

Schmid-Burgk et al. (1989) detected a large-scale CO outflow towards OMC1-S(S), that was re-observed by Zapata et al. (2010) with better spatial resolution. The powering source of this outflow is still not clear. From Zapata et al. (2010) it is difficult to determine exactly its origin, although they established a position from where it propagates in a straight line (white square in the lower right panel of Fig. 6.1). The X-ray observations did not detect any source along the outflow axis.

Zapata et al. (2010) speculated that this CO outflow is originated at a position towards the NE, where the redshifted SO outflow is detected. They found evidence for rotation in both outflows, which may indicate that they are related. They claimed that the CO outflow could be the extension of the SO outflow. Both outflows have a similar velocity range between 8 and 25 km s^{-1}, and additional observations showed that SO also extends to the SW (see Fig. 4 from Zapata et al. 2010), coincident with the orientation of the CO outflow. In addition, the SO clump D is nearly coincident with a CO clump, which suggests a link between both flows. As we have discussed in Section 8.4.2 and Section 6.2.4, the SO outflow seems to collide with the SiO 137-408 SE outflow, which provides energy to the SO flow and produces its deviation.

Therefore, and given that Zapata et al. (2010) did not find CO emission at the inner part of the SO outflow (before the encounter), we interpret that the CO outflow is the continuation of the encounter of the SO and SiO outflows powered by COUP 594 and COUP 582, respectively.

★ 137-408 E-W Outflow

This SiO emission exhibits two lobes, one blueshifted (between −30 and −80 km s^{-1}) and the other redshifted (between 30 and 80 km s^{-1}). Zapata et al. (2006) suggested that the strong millimeter source 137-408 could be the driving source. Zapata et al. (2006) already noted that the presence of two outflows around this position (this one and SiO 137-408 SE) may indicate the presence of more than one embedded driving source. The closest X-ray star is COUP 582, shifted ∼1.7" with respect to the origin of the 137-408 E-W lobes. As shown in Section 6.2.4, this X-ray star might drive the SiO SE 137-408 outflow. Given that the millimeter source 137-408 is located more symmetrically with respect to the lobes of the 137-408 E-W outflow, this source is the most likely driving source.

★ The optical outflow HH 529 (COUP 632)

This large optical outflow detected in [OIII] (Smith et al. 2004) is associated with the multiple HH objects known as HH 529. Its driving source is detected in X-rays (COUP 632), near-IR (Lada et al. 2000; Muench et al. 2002; Lada et al. 2004), mid-IR (source 2 from Smith et al. 2004), and also at 1.3 cm (source 144-351 of Zapata et al. 2004b) and 1.3 mm (Zapata et al. 2005). As indicated by Zapata et al. (2004b), the radio emission migth emanates from the magnetosphere (gyrosynchrotron emission) or the ionized outflow (free-free emission) of a low/intermediate mass star.

Hashimoto et al. (2007) found polarization signatures around this star, characteristic of cavities along the inner parts of outflows, and Robberto et al. (2005) detected an IR elongated filament immediately to the west of the star with the same orientation as the HH 529, supporting that it is the driving source of the optical outflow and the HH objects.

This star is one of the three reddest stars of the entire L-band (3.5 μm) survey from Lada et al. (2000), and its K-L excess suggests a visual extinction of A_V >100. The high extinction is supported by the X-ray observations, because COUP 632 has the highest hydrogen column density measured in the entire COUP sample, $\log N_H$=23.94 cm^{-3}. This extremely high value may also indicate the presence of an edge-on circum-

stellar disk. The extinction estimated from X-rays (which corresponds to A_V >400 mag) is even larger than the obtained from IR. This could indicate that there is a "gas excess" around this star, may be because it is still forming and accreting material. The X-ray source does not exhibit X-ray variability, although this can be due to the low number of detected net counts (16). We fitted the SED of this star using the measured fluxes from the literature (right panel in Fig. 6.6). The results confirm the high extinction suffered by this object and indicates a stellar mass in the range 0.5−1.5 $M_\odot$. We favor the higher mass limit, because the obtained fractional luminosity L_X/L_{bol} range is more consistent with an intermediate-mass star than a low-mass star (Table 6.4).

6.3 Summary and conclusions

In this chapter we correlated the OMC1-S census of stars observed in X-rays by Chandra with the expected positions of the sources driving the molecular outflows and measured proper motions of HH optical objects. Deep X-rays observations penetrating into the core and tracing the positions of very obscured stars are a very good tool to detect the driving sources of embedded molecular outflows. We find that X-ray stars are very good candidates for the driving sources of 6 out of 7 molecular outflows detected in OMC1-S (identification rate of $\sim$ 86%). The driving sources of these outflows are very young ($\sim 10^5$ yr) low/intermediate mass stars deeply embedded in the OMC1-S core, with visual extinctions of $A_V > 15$ mag. Moreover, X-rays observations revealed for the first time numerous embedded stars in the core that likely contribute to drive the HH objects produced when the flows break out into the ionized ONC.

CHAPTER 7

Massive stars, molecular outflows and hot cores in Monoceros R2

Abstract

We present a high-angular resolution study carried out with the Submillimeter Array (SMA) of the MonR2 star-forming cluster at (sub)millimeter wavelengths. We imaged both the continuum and molecular line emission towards the center of the cluster at 0.85 mm (348 GHz) and 1.3 mm (225 GHz), with resolutions ranging from 0.5" to $\sim$ 3". The SMA observations show that the continuum emission from IRS1 and IRS2 is dominated by free-free radiation, while that from IRS3 and IRS5 appears to be dominated by dust thermal emission, with estimated masses of $\sim$0.3-6 $M_{\odot}$. The SMA images towards IRS5 at sub-arcsecond scales reveal for the first time that this source splits into, at least, two compact sources – IRS5A1 and IRS5A2 – where IRS5A1 is the most massive source of the two. We have not detected (sub)millimeter emission from any of the low-mass stars of the cluster. The SMA ^{12}CO(2-1) images reveal 11 previously unknown molecular outflows in the MonR2 molecular core. The comparison of the ^{12}CO(2-1) outflows with known IR sources in the IRS5 and IRS3 subclusters allows for tentative identification of the driving stars. In addition, our SMA line images of molecular species such as CH_3CN, CH_3OH or SO_2 show that, besides IRS3 (a well-known hot molecular core), IRS5 is the most chemically active source in the MonR2 cluster region. The analysis of the gas derived from the CH_3CN lines towards IRS5 reveals two different physical components: i) dense and hot ($T_{\rm rot}$=230 K) component, which suggests the presence of a deeply embedded protostar at the hot-core stage of its evolution; and ii) less dense and colder ($T_{\rm rot}$=25 K) component. The derived SED of IRS5 gives a mass for the central source of $\sim$7 $M_{\odot}$ and a luminosity of 700 $L_{\odot}$. The detection of a large number of CO outflows widespread across the MonR2 region argues in favor of the competitive accretion scenario as origin of the MonR2 star cluster.

7.1 Introduction

Molecular outflows appear early in the star formation process as a mechanism to remove the excess angular momentum in the star/circumstellar disk system produced by accretion. Molecular outflows thus represent an additional tool to probe the population of Class 0 low-mass stars in clusters. Since molecular outflows inject momentum and energy into the surrounding medium, they are expected to increase the level of turbulence and even disrupt the parental molecular cloud, potentially impacting any subsequent star formation within the cluster (see Stanke and Williams, 2007).

By using near-IR 2.12 μm H_2 observations, Hodapp (2007) reported the detection of 15 new H_2 jets in the MonR2 cluster that are likely associated with young Class 0 and I sources still in the main accretion phase. These jets were mainly found towards the edges of the MonR2 molecular cloud core, which was interpreted as a signature of triggered star formation (Hodapp, 2007; Carpenter and Hodapp, 2008). However, near-IR observations may provide a biased view of the global population of molecular outflows in deeply embedded star-forming clusters such as MonR2, because of the large extinction found in these regions. Alternatively, the rotational transitions of carbon monoxide (CO) in the millimeter and sub-millimeter wavelength range are known to be excellent probes of the material swept-up by the propagation of the jet into the surrounding molecular envelope (e.g. Gueth and Guilloteau, 1999; Lee et al., 2007). Interferometric observations of the rotational transitions of CO at sub-millimeter/millimeter wavelengths are thus tools to unveil the most embedded (and the youngest) population of molecular outflows driven by Class 0 and Class I low-mass stars, at the cluster centers of high-mass star-forming regions.

In this chapter, we report the first interferometric images of the thermal continuum and molecular line emission carried out with the Submillimeter Array (SMA; Ho et al., 2004)[1] towards the MonR2 high-mass star-forming cluster at angular resolutions ranging from 0.5" to ∼3" (i.e. of ∼0.012 pc at a distance of 830 pc)[2]. Our SMA ^{12}CO images of the ^{12}CO J=2→1 line emission reveal the presence of 11 new CO outflows towards the innermost ∼1′-region in the cluster. This population of outflows is widely distributed across the MonR2 core, which contradicts the previously proposed scenario of $inside-out$ triggering for the stelar cluster. The chapter is organized as follows.

[1]The Submillimeter Array is a joint project between the Smithsonian Astrophysical Observatory and the Academia Sinica Institute of Astronomy and Astrophysics and is funded by the Smithsonian Institution and the Academia Sinica.

[2]MonR2 has only been imaged once before in HCO+ J=1→0 by using the Hat Creek interferometer and at an angular resolution of ∼9" (Gonatas et al., 1992).

Table 7.1: Instrumental parameters of the SMA observations.

Date	Conf.	L.O. freq. (GHz)	Synthesized Beam	τ_{225GHz}	T_{sys} (K)	BP Cal.	Flux Cal.	Gain Cal
Feb 13, 2010	VEX	224.611	$0.68'' \times 0.45''$, P.A.=-43°	0.05	200-240	3C273	Titan	0607-085/0730-116
Feb 20, 2010	VEX	224.611	$0.68'' \times 0.45''$, P.A.=-43°	0.03	200-240	3C273	Titan	0607-085/0730-116
Nov 15, 2011	COM	226.227	$2.75'' \times 2.73''$, P.A.=-77°	0.07	200-240	BLLAC	Ganymede	0607-085/0530+135
Nov 15, 2011	COM	348.324	$2.29'' \times 1.50''$, P.A.=-39°	0.07	400-500	BLLAC	Ganymede	0607-085/0530+135

In Sect. 7.2, we report the details about the SMA observations. The results of the dust continuum and ^{12}CO line emission are presented in Sects. 7.3.1and 7.3.2, respectively. In Sect. 7.3.3 we analyze the line emission from other molecular tracers such as CH_3CN, CH_3OH or SO_2 detected towards the IRS3 and IRS5 sources, and in Sect. 7.3 we discuss our results. The conclusions are summarized in Sect. 7.5.

7.2 Observations and data reduction

Observations of the MonR2 star-forming region were carried out with the SMA in very extended configuration (VEX) in February 2010 for two tracks, and in compact configuration (COM) in November 2011 for one track. The observations were phase-centered on IRS2 at coordinates α(J2000) = $06^h07^m45.83^s$ and δ(J2000) = $-06°22'53.5''$ (Carpenter et al., 1997), and the central radial velocity of the source was set at 10 km s^{-1} (Torrelles et al., 1983). Instrumental and calibration parameters for the VEX and COM observations are summarized in Table 7.1. The VEX observations at 1.3 mm were obtained in single-receiver mode with a total bandwidth of 4 GHz per sideband. The resulting frequency coverage was 216.64−220.60 GHz and 228.60−232.58 GHz. The receivers for the COM observations were configured in dual receiver mode, which allowed to simultaneously imaged MonR2 at 1.3 and 0.85 mm, with a total bandwidth of 2 GHz per sideband. As a result the frequency coverage was in 2 GHz windows, as follows: 220.24−222.23 GHz and 230.24−232.23 GHz for the 230 GHz receiver, and 342.67−344.66 GHz and 352.67−354.66 GHz for the 345 GHz receiver. The correlator provided a uniform channel spacing of 0.8 MHz, yielding a velocity resolution of $\sim$ 1.1 km s^{-1} at 1.3 mm and $\sim$0.7 km s^{-1} at 0.85 mm. Calibration of the raw data was done with the IDL MIR software package, while continuum subtraction, imaging and deconvolution were carried out with MIRIAD. We note that for the COM data, the quasar BLLAC was used as bandpass calibrator (see Table 7.1). Since BLLAC's spectrum shows a prominent ^{12}CO absorption feature, the bandpass calibration of the corresponding upper sideband was performed

Table 7.2: Properties of the dust continuum emission in COM configuration.

Source	Receiver (GHz)	Wavelength (mm)	α (J2000)	δ (J2000)	Size ("×")	P.A. (°)	F_{peak} [a] (Jy/beam)	F_{int} (Jy)
IRS2	230	1.3	$06^h07^m45.802^s$	$-06°22'53.50''$	3.05×2.78	106	0.157±0.004	1.0
IRS2	353	0.85	$06^h07^m45.804^s$	$-06°22'53.55''$	2.82×2.75	99.8	0.141±0.008	0.5
IRS5	230	1.3	$06^h07^m45.591^s$	$-06°22'39.46''$	2.97×2.77	61.9	0.111±0.004	0.6
IRS5	353	0.85	$06^h07^m45.611^s$	$-06°22'39.43''$	2.95×2.83	79.7	0.391±0.008	2.5
IRS3	230	1.3	$06^h07^m47.824^s$	$-06°22'56.11''$	3.03×2.90	84.2	0.061±0.004	0.3

[a] The error in the peak flux corresponds to the 1σ noise level in the corresponding image.

Table 7.3: Envelope mass estimates from COM data.

Source	Mass ($M_\odot$)	
	T_{dust}=25 K	T_{dust}=230 K
IRS5	5.9	0.52
IRS3[a]	3.2	0.29

[a] For IRS3, no emission is detected at 0.85 mm (353 GHz), so the mass is derived using the same dust opacity index as for IRS5.

by phase-conjugating the lower sideband SMA BLLAC data.

7.3 Results: massive stars, molecular outflows and hot cores

7.3.1 Dust Continuum Emission from young massive stars

★ Compact SMA Observations

In Fig. 7.1, we present the continuum emission seen in COM configuration at 1.3 mm (left panel) and at 0.85 mm (right panel) towards MonR2. For comparison, Fig. 7.1 includes the 1.3 cm Very Large Array continuum image from the dataset of Zapata et al. (2009), where the MonR2 central HII region is clearly visible. Our SMA image at 1.3 mm shows extended structure towards IRS1 coincident with the brightest emission seen at centimeter wavelengths. However, in the 0.85 mm map of Fig. 1 this source is not detected. This could be due to: i) IRS1 is located at the edge of the primary beam of the 0.85 mm observations; and ii) the continuum

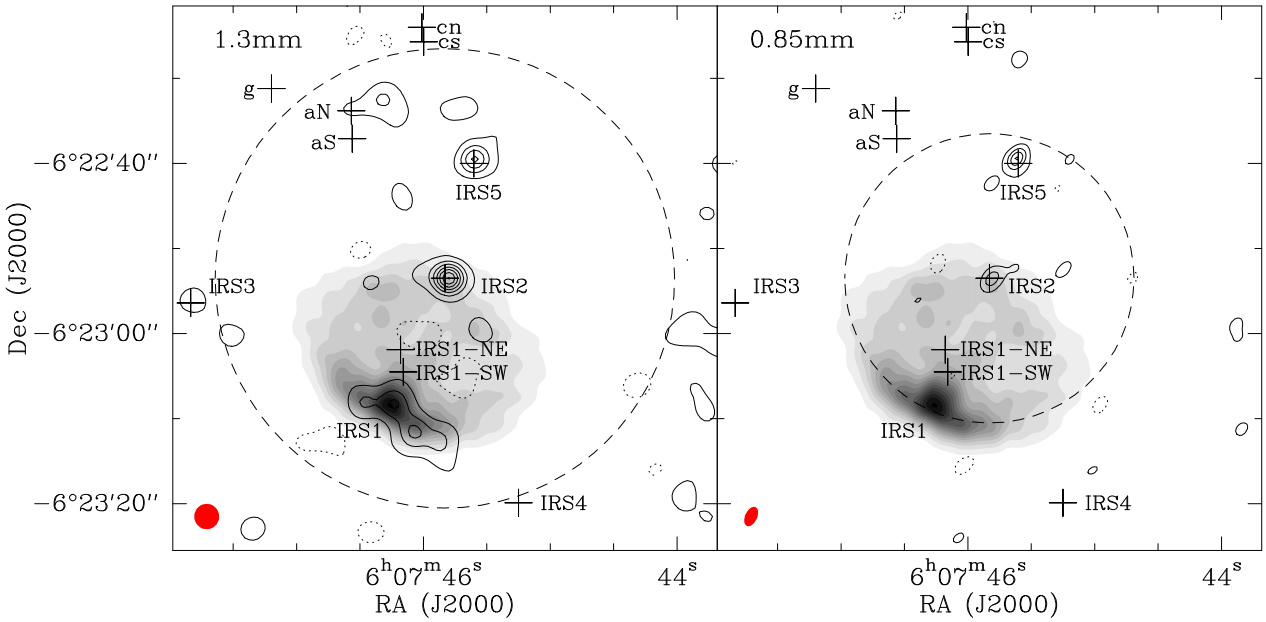

Figure 7.1: *Left:* Continuum emission detected at 1.3 mm in Compact configuration towards the MonR2 star-forming region (contours) overlaid on the 1.3 cm continuum image (from the dataset of Zapata et al., 2009). Contours start at 12 mJy beam^{-1} (3σ) and are spaced at 24 mJy beam^{-1} (6σ) intervals. Dotted contours correspond to the negative 3σ level. The beam size is shown as a red ellipse in the lower left corner. For the VLA data, the first contour is at 3 mJy beam^{-1} (3σ) and the step level is 17 mJy beam^{-1} (17σ). The dashed circle indicates the primary beam of the observations, ∼57" at 1.3 mm. *Right*: As for the left panel, but for the 0.85 mm continuum image. The first contour is at 30 mJy beam^{-1} (3σ) and the step level is 60 mJy beam^{-1} (6σ). At 0.85 mm the primary beam of the observations is ∼35" (dashed circle). The plus signs indicate the positions of the main sources in the region, including IRS2, IRS3, IRS4, IRS5 and the ionizing star of the HII region, IRS1 SW (note that this is different from IRS 1 NE, which is an unrelated non-embedded star detected in the optical; see Cohen and Frogel 1977. The maps were made using uniform weighting.

emission detected in the SMA images probes the innermost regions around IRS1 and therefore arises from ionized gas associated with the UC HII region. The comparison between the 1.3 cm and 1.3 mm flux for IRS1 yields a negative spectral index $\alpha \sim -0.5$ (with $S_\nu \propto \nu^\alpha$), consistent with free-free emission. By using this spectral index, we can extrapolate the expected flux for this source to 0.85 mm. This flux, at the half-power of the primary beam, is $\sim$20 mJy beam^{-1}, well below the 3σ noise level of 30 mJy beam^{-1} in the 0.85 mm image of Fig. 7.1. This explains why the IRS1 source has not been detected in our SMA continuum image at 0.85 mm.

From Fig. 7.1, we find that the brightest sources in our SMA images are IRS2 and IRS5. A qualitative comparison of the two maps at 1.3 mm and 0.85 mm reveals that these two sources are very different in nature. While IRS2 appears brighter at 1.3 mm than at 0.85 mm (as for IRS1 and as expected for an HII region), IRS5 shows the opposite behavior, indicating that its emission is mainly due to dust. In Table 7.2 we report parameters calculated from two-dimensional Gaussian fits to the continuum emission of these two sources. The derived coordinates are close to those obtained from previous infrared and X-ray measurements (e.g. Carpenter et al., 1997; Kohno et al., 2002; Nakajima et al., 2003). As IRS5 is offset from the phase center of the observations by approximately 15", primary-beam corrected maps were used to estimate its flux parameters. After smoothing the 0.85 mm images to the same angular resolution as that of the 1.3 mm data ($\sim$ 3"), we compare the peak flux values at 1.3 mm and 0.85 mm (see Table 7.2) to estimate the spectral index, α, of the two sources (with $S_\nu \propto \nu^\alpha$). We obtain $\alpha_{\rm IRS2} \sim -0.2$ and $\alpha_{\rm IRS5} \sim 3.0$. The decreasing spectral index of IRS2 is consistent with that previously reported by Jiménez-Serra et al. (2013), and indicates that this source is dominated by optically thin free-free emission. This source, with an estimated central mass of 13 $M_\odot$ (a B1-type star in the ZAMS) and a luminosity of 5000 $L_\odot$ (Howard et al., 1994), likely powers a dense and collimated ionized jet (Jiménez-Serra et al., 2013).

In contrast to IRS2, the spectral index of IRS5 steeply increases with frequency ($\alpha_{IRS5} = 3.0$), indicating that its emission at millimeter wavelengths is dominated by dust thermal emission. This suggests that IRS5 is at an earlier stage of evolution than IRS2. Since the emission from IRS5 is dominated by dust, we can estimate the envelope dust mass in the source following the method from Hildebrand (1983):

$$M_{\rm dust} = \frac{F(\nu) d^2}{B_\nu(T_{\rm dust}) \kappa_\nu} \tag{7.1}$$

where $F(\nu)$ is the continuum flux density at frequency ν, d is the distance to the source, $B_\nu(T_{\rm dust})$ is the Planck function for dust temperature $T_{\rm dust}$, and κ_ν is the dust opacity (Hildebrand, 1983). κ_ν is given by $10\left(\frac{\nu}{1.2{\rm THz}}\right)^\beta$, where β is the dust opacity index. Assuming a power law of the type $Q(\nu) \propto \nu^\beta$ for the emissivity $Q(\nu)$, in the Rayleigh-Jeans limit β and α are then related by $\beta = \alpha - 2$. Since $\alpha_{\rm IRS5} \sim 3.0$, we therefore obtain $\beta_{\rm IRS5} \sim 1$. Although this value is similar to those assumed by Qiu et al. (2007) for a sample of massive star-forming regions, we cannot rule out the possibility that our estimate of β for IRS5 is affected by a small contribution from free-free emission, especially at 1.3 mm (see Giannakopoulou et al., 1997). We have used as lower and upper limits for the dust temperature the gas excitation temperatures[3] (25 K and 230 K) derived from a 2-component fitting of the CH_3CN (12-11) $K = 0$ to $K = 6$ molecular lines detected towards IRS5 (see Sect. 7.3.3).

From the integrated flux reported in Table 7.2, and considering a constant gas-to-dust mass ratio of 100 (following e.g. Giannakopoulou et al., 1997; Beuther et al., 2007), we obtain estimates for the IRS5 envelope gas mass of ∼0.52-5.9 $M_\odot$, as reported in Table 7.3. The upper mass derived is similar to those reported by Giannakopoulou et al. (1997) (∼ 5 $M_\odot$, see clump C5 in their Table 4).

In Table 7.2, we also report the continuum flux measured at 1.3 mm towards IRS3 (after the primary-beam correction of the images). Since this source falls outside the primary beam of our observations, the measured 1.3 mm flux and derived dust continuum properties (Table 7.3) should be taken with caution.

Towards the northeast of IRS5 we also find some continuum emission in the SMA 1.3 mm continuum image at the 9σ level (Fig. 7.1). Although the bulk of the emission does not coincide with the location of any IR source, the elongated asymmetry towards the east of this emission is indeed associated with source a_N detected by Carpenter et al. (1997) and Andersen et al. (2006). As Fig. 7.2 shows, the SMA emission is resolved into several condensations and could therefore represent a cluster of deeply embedded protostars. Future high angular resolution observations covering this region will help to establish the origin of the 1.3 mm continuum emission towards the northeast of IRS5.

[3]If we consider Local Termodinamic Equilibrium (LTE) conditions, which is a reasonable assumption for this core, we can assume that the kinetic temperature of the region is approximately equal to the gas excitation temperature. Moreover, since the high densities in the hot cores couple the gas and the dust, the kinetic temperature of the gas is a good estimation of the dust temperature. Hence, we can approximate the dust temperature with the gas excitation temperature.

Table 7.4: IRS5 properties with combined COM and VEX data at 1.3 mm.

Source	Beam size ("×")	R.A. (J2000)	DEC (J2000)	F_{peak} (Jy/beam)	F_{int} (Jy)	Mass ($M_\odot$)	
						T= 25 K	T_{dust} = 230 K
IRS5A1	0.756×0.538	$06^h07^m45.61^s$	$-06°22'39.35''$	0.082 ± 0.003	0.16±0.02	1.6	0.14
IRS5A2	0.756×0.538	$06^h07^m45.65^s$	$-06°22'40.13''$	0.016 ± 0.003	0.021±0.005	0.2	0.02

The error in the peak flux corresponds to the 1σ noise level in the corresponding imag

★ VEX Observations of the Small-Scale Structure

Fig. 7.2 presents the 1.3 mm continuum map of the MonR2 cluster obtained by combining the SMA data at 1.3 mm in the COM and VEX configurations. The VEX data provide a much improved angular resolution of 0.5". Towards IRS1, the extended emission at 1.3 mm associated with this infrared source reveals at least two distinct bright peaks. These peaks, however, do not coincide with the IR sources IRS1 NE or IRS1 SW previously reported by Aspin and Walther (1990) and Howard et al. (1994) and shown by black crosses in Fig. 7.2; rather, they appear associated with the IR ring nebula related to the HII region (see Fig. 4.1 in chapter 4). This indicates that the 1.3 mm emission is likely associated with dense inhomogeneities in the ionized gas.

Fig. 7.2 also shows that IRS2 remains unresolved by our resolution of 0.76" × 0.54". The secondary continuum peak towards the southwest of IRS2 is not associated with a real source, but rather due to limited UV coverage. This implies that the source does not include substructure at scales of 0.5" (i.e. 400 AU). This compact morphology is consistent with the results of the high-spatial resolution (∼0.2") HST-NICMOS observations presented in chapter 4, and those from Alvarez et al. (2004) obtained by using near-IR Speckle imaging.

Further north, IRS5 shows hints of substructure not seen previously in the COM data alone. In particular, a secondary peak to the southeast of the main source appears as a 5σ detection. In addition, an elongation along the northeast-southwest axis is highlighted by the contours, suggesting the existence of a third source that remains unresolved at the current resolution. For the purpose of characterizing these sources, we refer to the main IRS5 peak as IRS5A1, and to the secondary source as IRS5A2. Flux parameters for these two sources are reported in Table 7.4. Following the method in Hildebrand (1983) and assuming a dust opacity index of $\beta \sim 1$, we estimate envelope dust masses of 0.14-1.6 $M_\odot$ for IRS5A1 and of 0.02-0.2 $M_\odot$ for IRS5A2 (see Table 7.4.) As expected, IRS5A1 is the dominant source, as it accounts

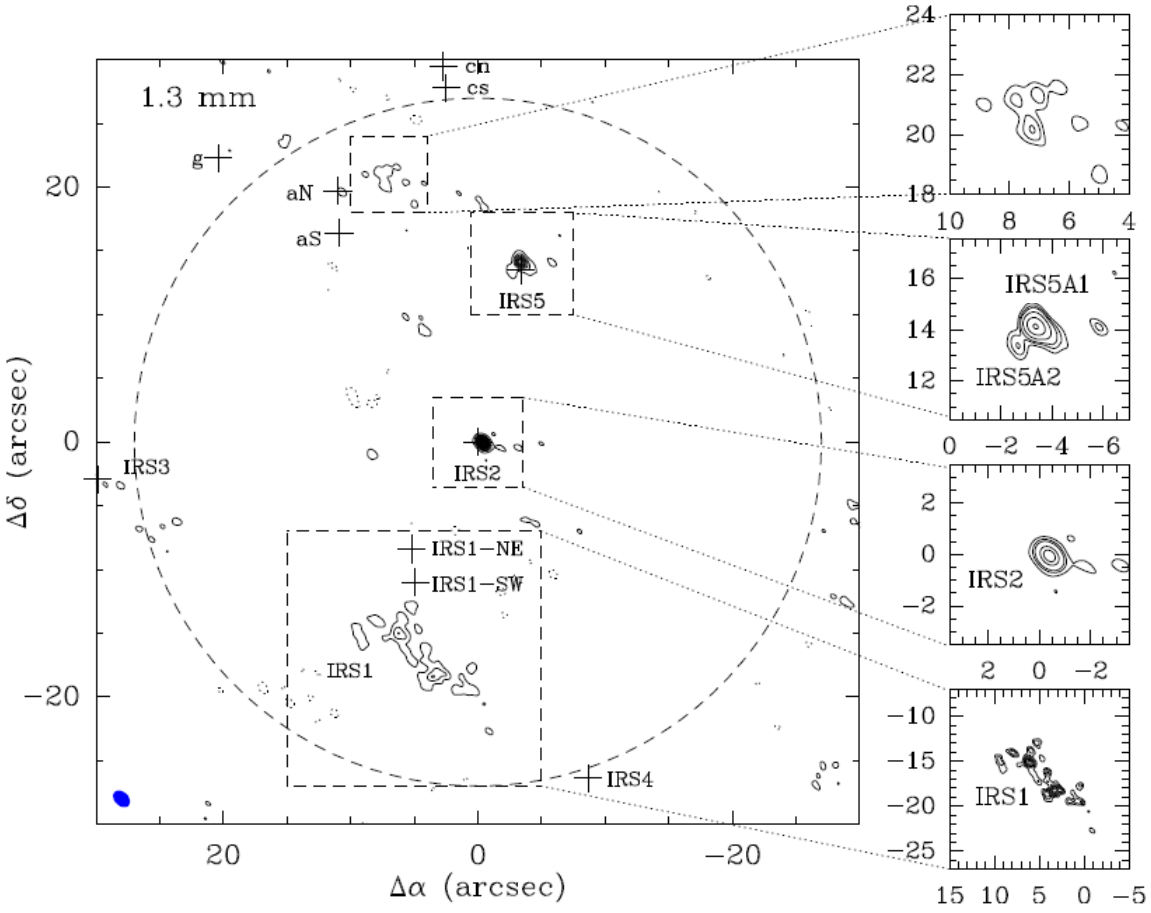

Figure 7.2: Combined VEX and COM data at 1.3 mm. In this map of the entire FoV, contours start at 3σ and are spaced at 3σ intervals, with $\sigma \sim 2.5$ mJy beam^{-1}. The beam size of the map is shown as a blue ellipse in the bottom left corner of the image. Large crosses indicate the position of the main sources in the region as in Fig. 7.1. For the top two zoom-in panels, we show the 3σ, 4σ, 5σ, 8σ, 15σ, and 25σ contours. For IRS2, we show the 3σ, 6σ, 10σ, 30σ, 50σ, and 70σ contours. Finally, for IRS1 we show contours starting at 3σ and spaced by 1σ. Dotted contours correspond to the negative 3σ level. The map was made using uniform weighting.

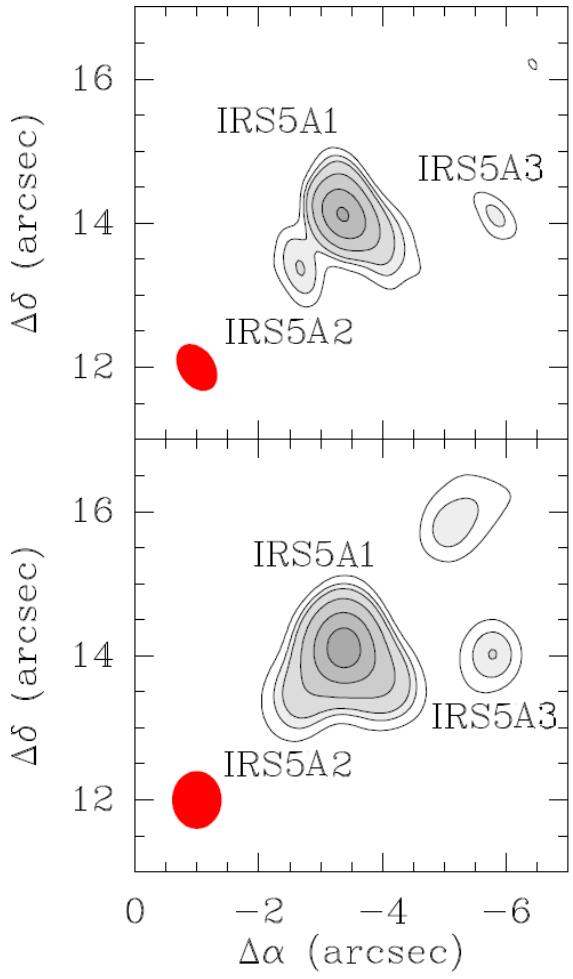

Figure 7.3: Maps of the combined VEX and COM 1.3 mm data for IRS5 produced with different beams. The beam size of the map is shown as a red ellipse in the bottom left corner of each panel. The elongation along the northeast-southwest axis of IRS5 remains when the image is convolved with a circular beam. We show the 3σ, 4σ, 5σ, 8σ, 15σ, and 25σ contours, with $\sigma \sim 2.5$ mJy beam^{-1}. The map was made using uniform weighting.

for ∼90% of the total envelope mass in IRS5. In addition, an elongation along the northeast-southwest axis is outlined by the contours. As shown in Fig. 7.3, this elongation is robust when the image is convolved with a circular beam. One possibility to explain this structure would be an unresolved third protostar. However, we will discuss in Sect. 7.3.2 that this millimeter emission, which perfectly match with the IR conical nebulosity towards SE observed by HST-NICMOS (see lower right panel of Fig. 4.10, chapter 4), likely arise from the dusty walls of the cavity of an outflow driven by IRS5-A.

7.3.2 ^{12}CO Emission: a new cluster of outflows in MonR2

★ Morphology

Fig. 7.4 presents the integrated intensity maps of the ^{12}CO(2-1) emission (at 230.538 GHz) measured towards MonR2 in COM configuration overlaid on the continuum emission at 1.3 mm. The chosen velocity ranges highlight at least four (labeled with letters in Fig. 7.4) and up to eleven previously unknown outflows in the central region of the MonR2 cluster. The orientation of the outflows are indicated by black arrows in Fig. 7.4. IRS3 and IRS5 are both associated with bright and highly collimated bipolar outflows (left panel of Fig. 7.4.) The CO emission around IRS5 is aligned along the northeast to southwest axis, exhibiting a large degree of collimation (outflow B). The redshifted component of the outflow appears between 26 and 40 km s^{-1} and exhibits two separate knots detected at 12σ and 15σ levels. These knots, or "bullets", are commonly observed in low-mass outflows such as e.g. L1448-mm and HH211 (see Guilloteau et al., 1992; Hirano et al., 2006; Palau et al., 2006; Lee et al., 2007; Hirano et al., 2010) and may represent outburst ejection due to disk variability caused by episodic, unsteady accretion (Qiu and Zhang, 2009; Lee et al., 2010). Another redshifted emission peak is detected further to the northeast (+13", +40") and appears more prominently in primary-beam corrected maps, where it is well-aligned with the rest of the redshifted lobe. On these grounds we calculate the physical parameters of the outflow in Sect. 7.3.2 assuming all three bullets belong to the redshifted lobe. Its blueshifted counterpart appears between -16 and -5 km s^{-1} and is less extended spatially. IRS5A1 is located at the geometric center of this outflow and is therefore likely its driving source (see Sect. 7.3.2). Similarly,

The IR source IRS3 (which harbors a subcluster, see chapter 4) is associated with the geometric center of a bipolar outflow along the northeast to southwest axis

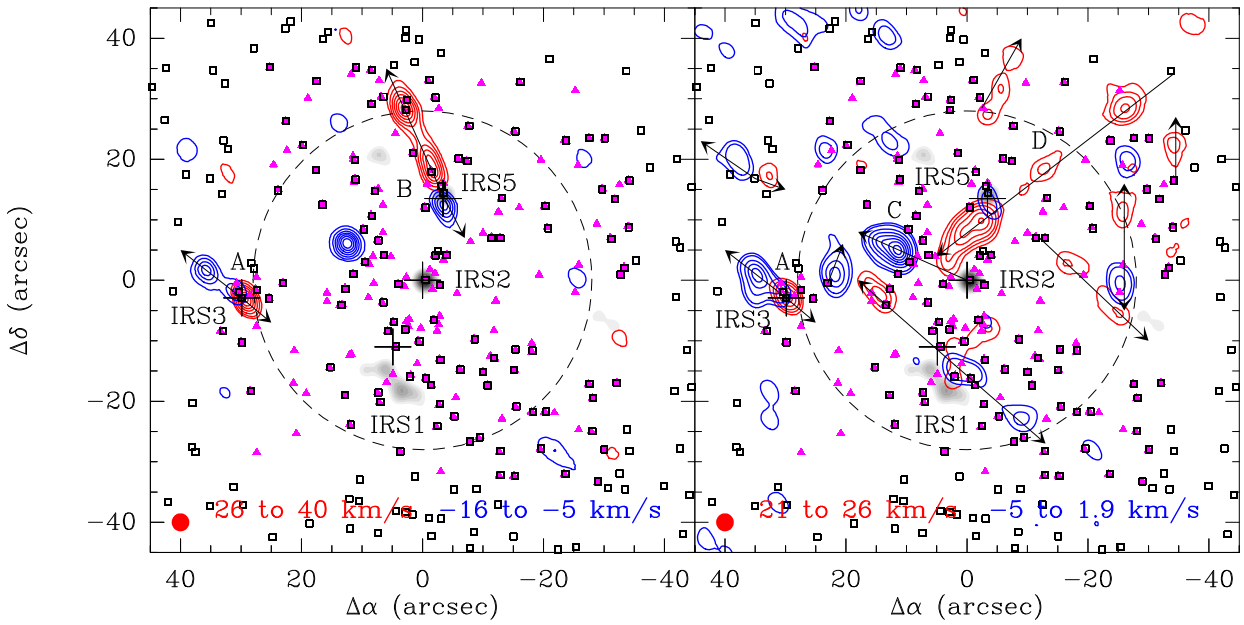

Figure 7.4: Moment-zero maps of the CO(2-1) transition in MonR2 (colored contours) overlaid on the 1.3 mm continuum (greyscale). *Left*: The redshifted emission has been integrated over the 26-40 km s^{-1} velocity range ($\sigma \sim 0.15$ Jy); the blueshifted gas appears between -16 and -5 km s^{-1} ($\sigma \sim 0.14$ Jy). The first contour and step levels are 4σ. *Right*: The redshifted gas appears for velocities comprised between 21 and 26 km s^{-1} ($\sigma \sim 0.60$ Jy). The 3σ, 5σ and 7σ contours are shown; contour spacing is 3σ thereafter. The blueshifted counterparts appear between -5 km s^{-1} and 1.9 km s^{-1} ($\sigma \sim 0.41$ Jy). Here the 3σ, 5σ and 10σ contours are shown; contour spacing is 5σ thereafter. Magenta triangles indicate the positions of the IR sources observed with NICMOS by Andersen et al. (2006), while black squares mark the coordinates of the IR sources identified by Carpenter et al. (1997). Black arrows indicate the conjectured orientation of the outflows. The beam size is shown as a red ellipse in the lower left corner, and the dashed circle indicates the primary beam of the observations, ∼57" at 1.3 mm. The maps were made using uniform weighting.

(outflow A). The red- and blueshifted components appear in the 26 to 40 km s^{-1} and -16 and 1.9 km s^{-1} velocity ranges and are shown in the left and right panels of Fig. 7.4. The blue lobe features two separate knots and is spatially more extended.

The right panel of Fig. 7.4 presents additional outflows identified in the 21 to 26 km s^{-1} and -5 to 1.9 km s^{-1} velocity ranges for redshifted and blueshifted emission, respectively. A prominent large scale redshifted lobe is present along the northwest-southeast direction in the vicinity of IRS5. This outflow lacks an obvious blueshifted counterpart; the corresponding blue lobe could be located outside the field of view of our observations. The extended redshifted lobe features three approximately equally-spaced peaks. The angular separation between the knots is roughly 20", giving a projected separation of approximately 1.5×10^4 AU $\simeq$ 0.08 pc. If these bullets are associated with periodic outbursts, this separation between knots implies time-scales of $\sim$5000 yrs between bursts, which are consistent with those predicted by episodic accretion models in low-mass protostars (see Baraffe and Chabrier, 2010; Zhu et al., 2010). We also detect one red and two blue lobes aligned on either side of IRS1. Between IRS3 and IRS5, the image reveals the presence of two bright blueshifted condensations. The emission is strong for a wide range of velocities, lacks of a well-defined axis and of a redshifted counterpart. This blueshifted lobe is also seen in the left panel of Fig. 7.4 for the velocity range from -16 to -5 km s^{-1}. Finally, we detect a number a relatively bright structures located beyond the edge of the primary beam, which we tentatively assign to outflows according to their association with sources detected in the near-IR across the cluster (Sect. 7.3.2). These outflows can be found towards the northern edge of the image, west of IRS5, and due north of IRS3 (right panel of Fig. 7.4).

★ Comparison with IR sources

The inner region of the MonR2 stellar cluster, approximately the FoV of our SMA observations, is known to harbor a centrally peaked gas density distribution where the H_2 volume density, $n(H_2)$, peaks towards the position of the IRS1 and IRS2 sources (see Figures 8 and 9 in Choi et al., 2000). In addition, surveys in the infrared (Carpenter et al. 1997, Andersen et al. 2006) and in the X-rays (Kohno et al. 2002, Nakajima et al. 2003, Preibisch et al. 2002) have also revealed a dense population of embedded low-mass stars (see detailed study of the stellar population in chapter 4). Here we compare the cluster of molecular outflows described in Sect. 7.3.2 with

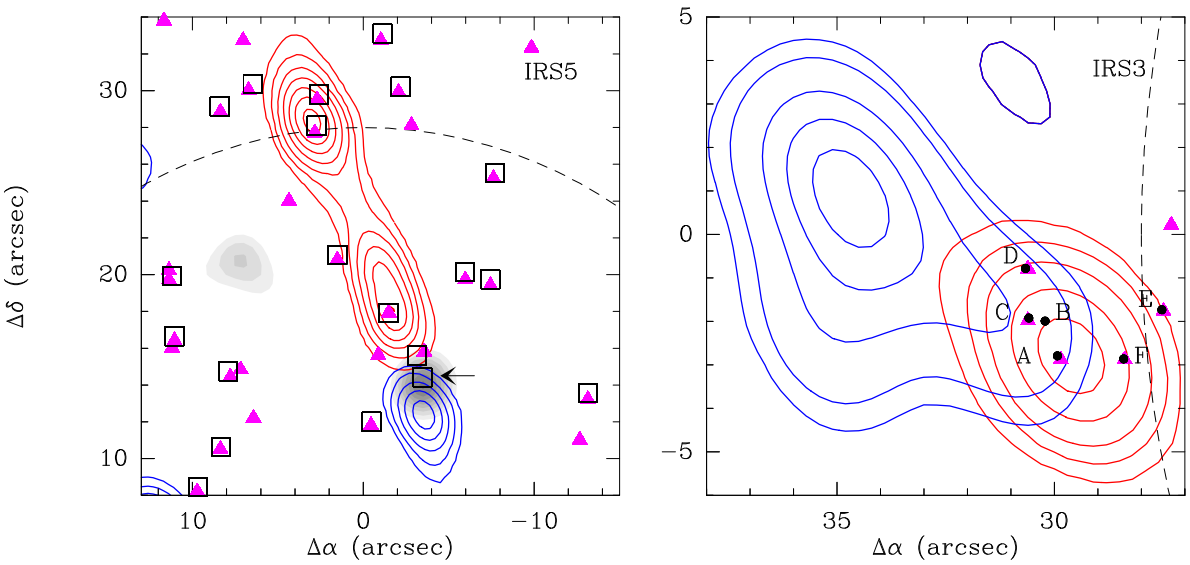

Figure 7.5: Zoom-in views of the moment-zero maps of the CO(2-1) transition in MonR2 (colored contours) overlaid on the 1.3 mm continuum (greyscale). First panel: A zoom-in on IRS5 where the redshifted emission has been integrated over the 26-40 km s^{-1} velocity range ($\sigma \sim 0.15$ Jy); the blueshifted gas appears between -16 and -5 km s^{-1} ($\sigma \sim 0.14$ Jy). The first contour and step levels are 4σ. Second panel: A zoom-in on IRS3 where the redshifted gas appears for velocities comprised between 21 and 26 km s^{-1} ($\sigma \sim 0.60$ Jy). The 3σ, 5σ and 7σ contours are shown; contour spacing is 3σ thereafter. The blueshifted counterparts appear between -5 km s^{-1} and 1.9 km s^{-1} ($\sigma \sim 0.41$ Jy). Here the 3σ, 5σ and 10σ contours are shown; contour spacing is 5σ thereafter. Magenta triangles indicate the positions of the IR sources observed with NICMOS by Andersen et al. (2006), black squares the stellar population described in Carpenter et al. (1997), and black dots and letters the IR sources identified by Preibisch et al. (2002). The dashed circle indicates the primary beam of the observations, ∼57" at 1.3 mm.

the IR sources found by Carpenter et al. (1997) and Andersen et al. (2006)[4] and the HST-NICMOS image of the region (see Fig. 4.10 in chapter 4), in order to identify the possible driving sources that power the CO outflows detected in MonR2.

In Fig. 7.5, we present zoom-in maps of the CO outflows detected towards IRS5 and IRS3 (outflows B and A in Fig. 7.4.) From the left panel of Fig. 7.5, we find that the collimated CO outflow towards IRS5 is likely associated with the star IRS5A detected in the near-IR by HST-NICMOS images and Carpenter et al. (1997) (indicated with an arrow in Fig. 7.4; see also lower right panel of Fig. 4.10 in chapter 4). In Fig. 7.3.2 we show a zoom-in view of the HST-NICMOS image (F160W band) of the region where the outflow is generated. As we have already discussed, the star with a more massive envelope is IRS5A1 (the mass of its envelope is the largest one measured in the cluster; see Fig. 7.2 and Table 7.4), and hence this is the best candidate to be the outflow driver. Fig. 7.3.2 shows that the elongated structure of IRSA1 observed at 1.3 mm by SMA is perfectly coincident with the IR nebulosity observed by HST-NICMOS. This is a strong indication that this conical emission, rather than an independent protostar, can be interpreted in terms of reflected light from the dusty walls of the cavity of the outflow arising from IRS5A1. Similarly, the relative positions of the IR sources IRS5B and IRS5C (Fig. 7.3.2) with respect to the lobe of the CO outflow suggest that they may be also reflected light related with the outflow cavity rather than other young stars.

The right panel of Fig. 7.5 shows the presence of a compact stellar subcluster in IRS3 with masses ranging 1-15 $M_{\odot}$ (sources IRS3 A-F) as detected from IR data (Preibisch et al. 2002). As revealed by their K-band image (Fig. 7.7), the massive star IRS3 B presents an elongated jet-like nebulous feature that points towards the north-east with P.A.$\sim$50°. This feature could be the near-IR counterpart of the blueshifted lobe of the IRS3 CO outflow. Since IRS3 B is located symmetrically with respect to the outflow lobes, this source is likely the best candidate for the IRS3 CO outflow. The stellar mass of the IRS3 B source is $\sim$8-12 $M_{\odot}$, as reported by Preibisch et al. (2002). On the other hand, IRS3 A has a more extended IR nebulosity in the south-west direction (Fig. 7.7). Although our CO data do not have sufficient spatial resolution to pinpoint whether IRS3 A or B is the driving source, the orientation of these nebulous features provides clues. Blueshifted lobes pointing in the observer's direction suffer less from extinction than the redshifted lobes and the former are typically detected in the IR. Since the direction of the IR nebulosity associated with

[4] We use the IR stellar catalogs because in the MonR2 region they detect more cluster members than the less sensitive X-ray observations (see chapter 4).

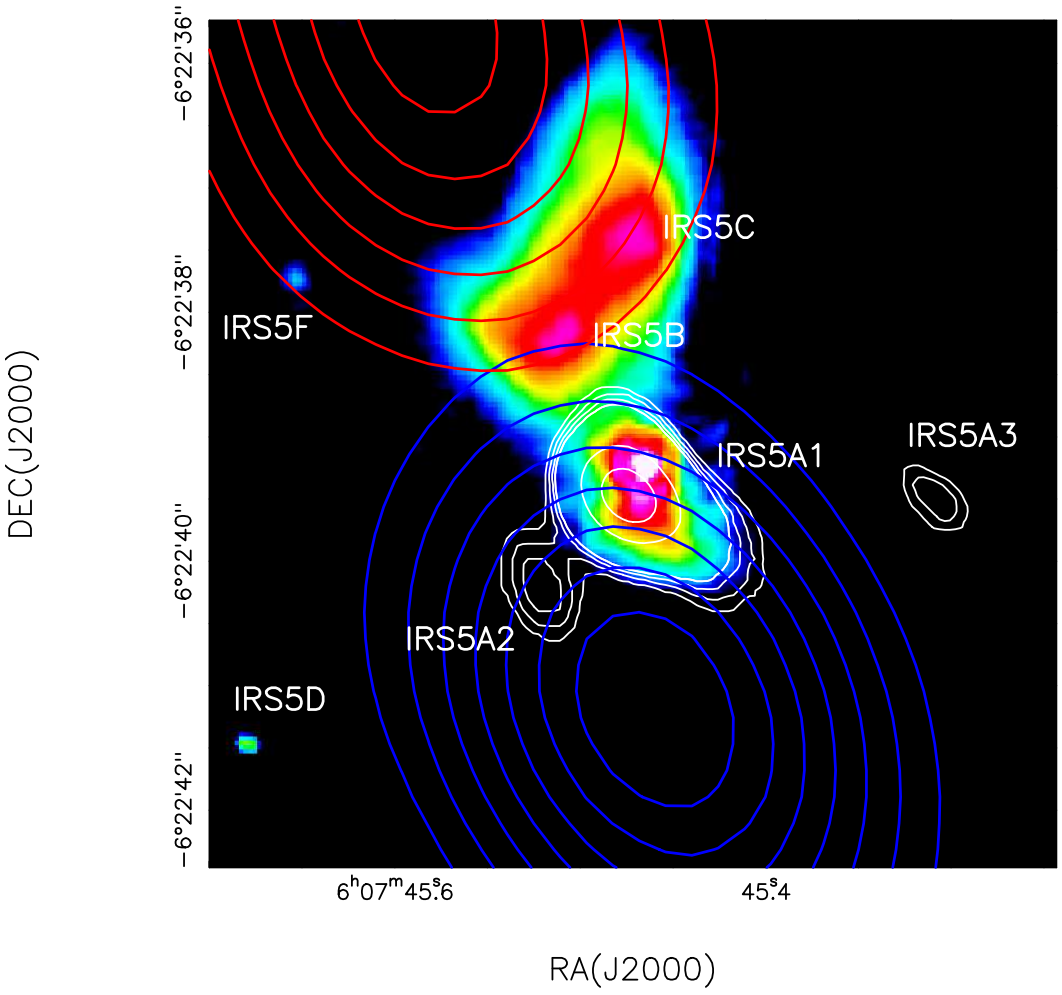

Figure 7.6: HST-NICMOS F160W band image of the IRS5 region (color scale). The solid blue and red contours show the blueshifted and redshifted lobes of the IRS5 outflow, respectively. The solid white contours indicate the VEX+COM SMA 1.3 mm emission.

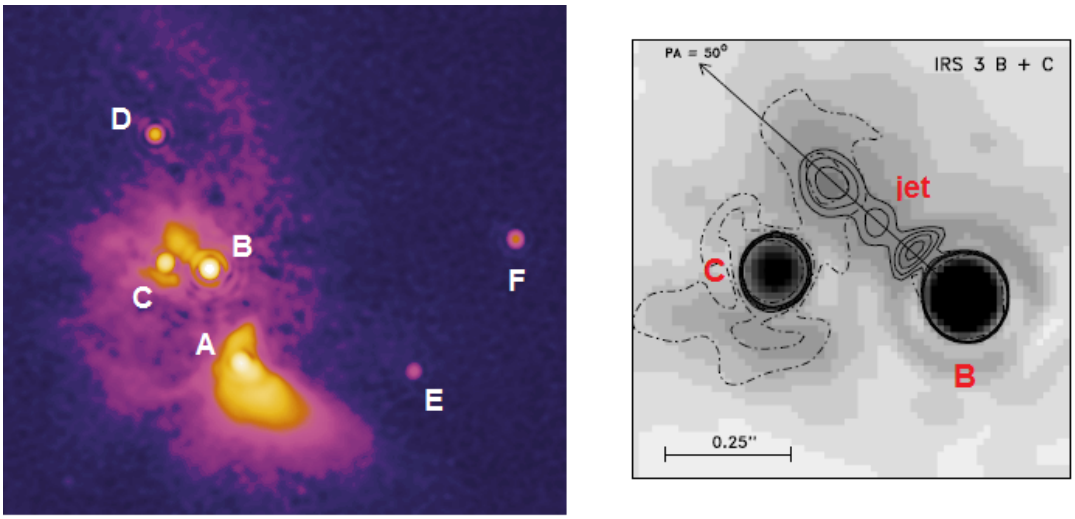

Figure 7.7: Near IR speckle interferometric images of the IRS3 subcluster (spatial resolution of 0.075"), adapted from Preibisch et al. (2002). *Left:* K-band speckle image with the different stars and the IRS3-B jet labelled. *Right:* K-band speckle image (greyscale and contours) with dashed contours of the H-band speckle image.

IRS3 B (i.e. the jet reported by Preibisch et al., 2002) matches the orientation of the blueshifted lobe observed with the SMA, IRS3 B is the more likely driving source of this outflow.

Besides the IRS5 and IRS3 CO outflows, the large-scale redshifted outflow visible in the right panel of Fig. 7.4 is closely aligned with an IR star detected in the NW corner of the image. This star is likely to be the outflow driver, consistent with the hypothesis that the blueshifted counterpart lies outside of the field of view to the northwest. The elongation of the knots on either side of IRS1 point to the location of the massive star IRS1 SW. Since this object is the exciting source of the MonR2 HII region (and it is thus at a late stage of evolution), it is possible that a low-mass companion is responsible for the CO molecular outflow. For the blueshifted condensation close to IRS3, IR observations reveal a nearby star aligned with the elongation axis, which could be its driving source. The exciting object of the blueshifted outflow C is less clear. The elongation axis suggests that one of the stars in the dense IRS2 subcluster could be the driving source of this high-velocity blueshifted condensation, as indicated by the arrow in Fig. 7.4. For the other five additional outflow candidates (most of them located outside of the primary beam of the observations), their emission peaks appear associated with IR sources. The presence of IR stars at approximately the outflow geometric centers suggests that

these outflows are true detections.

★ Physical properties

In this section, we estimate the physical properties of the brightest CO outflows detected in MonR2 with a robust identification (i.e. outflows A to D; Fig. 7.4). Except for the blueshifted lobes associated with IRS3 and IRS5 (outflows A and B), the physical parameters of the outflows are derived assuming the ^{12}CO emission is optically thin, as suggested by the non-detection of associated ^{13}CO emission. For the blue lobes of outflows A and B however, we detected ^{13}CO(2-1) emission for velocities between -16 km s^{-1} and 1.9 km s^{-1}, and hence a correction for optical depth is needed. The optical depths are derived by using Equation 1 from Roberts et al. (2010), assuming a ^{13}C/^{12}C isotopologue ratio of ∼1/69 (see Wilson, 1999), and are 3.7 for the blueshifted lobe of outflow A, and 11 for the blueshifted lobe of outflow B. From this, the masses of these two lobes are higher by a factor of ∼4 and 11, respectively, where the correction factor is calculated as $\tau/(1-\exp[-\tau])$ and τ is the optical depth.

We apply the method described in Garden et al. (1991) and Scoville et al. (1986) to the CO(2-1) transition:

$$N_{\rm CO} = 1.08 \times 10^{13}(T_{ex}+0.92)\exp\left(\frac{16.6}{T_{ex}}\right)\int T_B dv \;\; cm^{-2} \tag{7.2}$$

Here 16.6 K is the upper level energy of the transition, dv is the velocity interval in km s^{-1}, and T_{ex} and T_B are the excitation temperature and brightness temperature, respectively. The outflow mass, momentum, energy, dynamical age, outflow rate and momentum rate are then given by:

$$M = d^2 \left[\frac{\mathrm{H_2}}{\mathrm{CO}}\right] \mu_g m(H_2) \int_\Omega N_{\mathrm{CO}}(\Omega') d\Omega' \quad (7.3)$$

$$P = Mv \quad (7.4)$$

$$E = \frac{1}{2} Mv^2 \quad (7.5)$$

$$t_{dyn} = \frac{Length}{v_{max}} \quad (7.6)$$

$$\dot{M}_{out} = \frac{M}{t_{dyn}} \quad (7.7)$$

$$F_{\mathrm{out}} = \frac{P}{t_{\mathrm{dyn}}} \quad (7.8)$$

$$(7.9)$$

We assumed a CO to H_2 abundance of $[CO/H_2]=10^{-4}$ and a distance d of 830 pc (Herbst and Racine, 1976). μ_g is the mean atomic weight of the gas (μ_g=1.36) and m(H_2) is the mass of the hydrogen molecule. The physical parameters of the CO outflows are reported in Table 7.5. These results are sensitive to the temperature assumed for the CO gas. In Table 7.5, we present approximate ranges for the physical parameters of the outflows based on a temperature range of 30 K−60 K. The masses are in the 10^{-4} to 10^{-2} $M_\odot$ range. The momenta are of order 10^{-3} - 10^{-1} $M_\odot$ km s^{-1}, while the energies are of order ∼0.05-0.5 $M_\odot$ km ^{2} s^{-2}. From these parameters, the dynamical ages of the outflows are found to lie between ∼1000 and ∼6000 yr, with corresponding outflow mass loss rates lying between ∼0.1-10×10^{-6} $M_\odot$ yr^{-1}.

The outflow mass, momentum and energy are smaller than these from protostars of similar luminosities (Zhang et al., 2001, 2005; Beuther et al., 2002). However, besides the optical depth correction, we need to also consider other several effects: i) outflowing material at velocities near the ambient clump velocity (factor of 2; Arce et al. 2010); ii) projection effects (factors of 1.4 and 2 for the outflow momentum and kinetic energy, respectively; Arce et al. 2010); iii) 50% of the gas in an outflow could be in atomic form (there may be dissociative shocks; Reipurth and Bally 2001), and thus the outflow momentum would be a factor of 2 higher; and iv) the values presented here represent a lower limit since the spatially extended emission in the outflow may not be recovered in the SMA observations, which can be a large fraction of the total mass (e.g. Zhang et al., 2000; Qiu et al., 2009).

Table 7.5: Physical parameters of the CO outflows detected towards MonR2 with the SMA, assuming a temperature range of 30-60K.

Outflow	M (10^{-3} $M_\odot$)	P (10^{-2} $M_\odot$ km s^{-1})	E ($M_\odot$ km^2 s^{-2})	t_{dyn} ($\times 10^3$ yr)	$\dot{M}_{out}$ (10^{-6} $M_\odot$ yr^{-1})	$\dot{F}_{out}$ (10^{-5} $M_\odot$ yr^{-1} yr^{-1})
A - Blue	1.5-2.2	2.5-3.8	0.2-0.3	1.8	0.8-1.2	1.4-2.1
A - Red	0.7-1.0	1.5-2.2	0.2-0.3	2.0	0.35-0.5	0.8-1.1
B - Blue	0.19-0.28	0.4-0.5	0.04-0.05	1.2	0.16-0.23	0.3-0.4
B - Red[a]	1.6-2.4	3.4-5.1	0.4-0.6	4.9	0.33-0.49	0.7-1.0
C - Blue lobe between IRS3 and IRS5	2.3-3.5	2.5-3.8	0.14-0.21	2.7	0.88-1.3	1.0-1.5
D - W of IRS5	7.2-10.6	8.3-12.2	0.5-0.7	6.2	1.2-1.7	1.3-2.0

[a] For the red lobe of B (IRS5 outflow) the estimates include the knot up far to the northeast of IRS5 towards position (13", 40") in the left panel of Fig. 7.5 (best visible in the primary-beam corrected map). Without this additional bullet, the mass, momentum and energy estimates are smaller by about 10%.

★ Spectral Energy Distribution (SED) fitting of IRS5

We showed in chapter 4 that the high spatial resolution (∼0.2") HST-NICMOS near-IR observations confirm that the IRS5 region harbors a subcluster of stars (see Fig. 4.10 in chapter 4). Our COM+VEX 1.3mm SMA observations (see Fig. 7.3 or Fig. 7.3.2) have revealed dusty material concentrated in the sources IRS5A1 and IRS5A2, being the latter the more massive and likely the outflow driver. In Fig. 7.3.2 we show images of the region detected are different wavelengths, from near-IR to millimeter wavelengths. In the low resolution 2MASS H band image (1.65 μm) the emission the emission seems to arise mainly from IRS5B and IRS5C, which can be resolved with the higher spatial resolution HST-NICMOS images (Fig. 7.3.2). However, the emission at longer wavelengths (Spitzer-IRAC bands) is clearly concentrated in the southern region, around IRS5A1, indicating the presence of a large amounts of circumstellar material around a young star. Although the moderate spatial resolution of Spitzer is not able to resolve IRS5A and IRS5B, our 0.3" VEX observations at shows that the emission at 1.3 mm arises from IRS5A1 (lower right panel of Fig. 7.3.2), indicating that this is the dominant source (in the VEX+COM images IRS5A1 provides the ∼90% of the emission from IRS5A). Therefore, to obtain the physical properties and evolutionary state of IRS5A1 we have built its SED considering that it is responsible for the measured IRAC and SMA-COM fluxes. Moreover, we have used other fluxes from the literature (Hackwell et al., 1982; Kraemer et al., 2001; Mueller et al., 2002; Carpenter et al., 1997; Gutermuth et al., 2009; de Wit et al., 2009). These values have then been fitted by means of the radiative transfer models of Robitaille et al. (2006). These results are reported in Fig. 7.3.2. The best fit to the IRS5A1 SED

provides a stellar mass of $\sim$7 $M_\odot$ and a stellar luminosity of $\sim$300 $L_\odot$. This stellar luminosity is consistent with that previously detrived by hackwell82 from 10$-$20 μm colors.

This source presents a stellar age of $\lesssim 10^4$ yr, which is consistent with the idea of a young stellar object that it is still accreting mass. The IRS5A1 source is deeply embedded in the cloud with an estimated circumstellar extinction of A_v $\sim$50 mag, roughly consistent with the extinction inferred from the H_2 column densities measured towards IRS5 (i.e., $\sim$20$-$40 mag; see Sect. 7.3.3). The estimated disk mass is high ($\sim$0.2 $M_\odot$), supporting the idea that IRS5A1 is relatively young. This disk mass is only a fraction of the total envelope mass derived for IRS5 (see Table 7.3). The rich molecular line emission centered towards IRS5A1 (see Sect. 7.3.3) also indicates that this source is at an early stage of evolution characterized by a hot-core-like chemistry.

7.3.3 Molecular line emission from other molecules: hot cores

★ Morphology of the molecular gas

In addition to the continuum emission at 1.3 mm and 0.85 mm and to the ^{12}CO J=2$\rightarrow$1 rotational line, our SMA data report the detection of several molecular line transitions towards the MonR2 star-forming region. The detected rotational lines are shown in Table 7.6, and include lines from molecular species typical of hot core chemistry such as CH_3CN, CH_3OH and sulphur-bearing molecules such as SO_2, CS and OCS. The integrated intensity images of some representative lines are presented in Fig. 7.10.

From Fig. 7.10, we find that the molecular emission in the MonR2 region is concentrated towards the IRS3 and IRS5 sources. IRS3, with a luminosity of 1.5×10^4 $L_\odot$ (Henning et al., 1992; Giannakopoulou et al., 1997), is expected to show a rich chemistry as a consequence of the evaporation of the mantles of dust grains as revealed by the detection of warm H_2O, SO_2 and CH_3OH molecular gas (excitation temperatures of 110-125 K for SO_2 and CH_3OH and of 250 K for H_2O; see van der Tak et al., 2003; Boonman and van Dishoeck, 2003; Boonman et al., 2003). However, only lines from SO_2 and the K=0 to K=3 transitions of CH_3CN are measured towards this source. This is probably due to the fact that IRS3 falls outside of the primary beam of our observations, preventing the detection of fainter molecular lines. New high angular resolution observations centered on IRS3 are needed to study in detail the chemistry of the molecular gas towards this source.

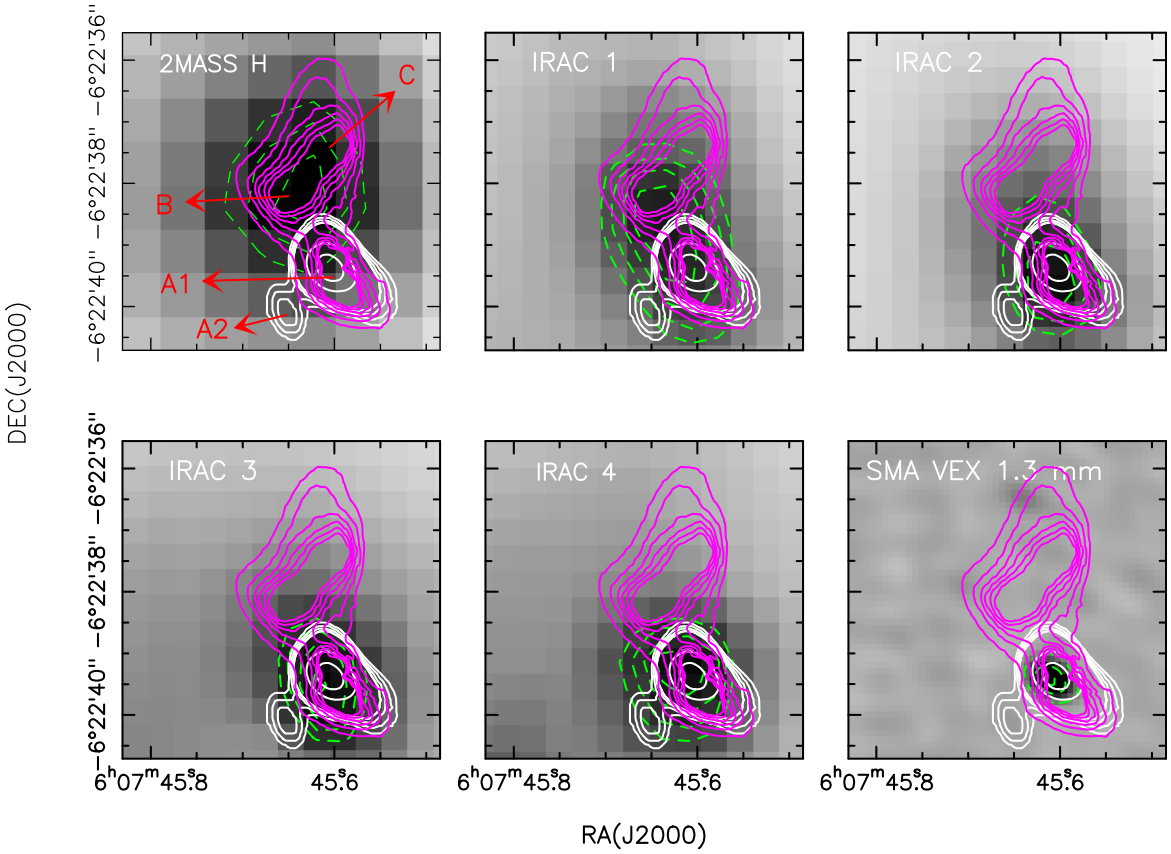

Figure 7.8: IRS5 region observed from shorter to longer wavelengths. The gray scale is emission observed with 2MASS H band (1.65 μm), Spitzer-IRAC1 (3.6 μm), Spitzer-IRAC2 (4.5 μm), Spitzer-IRAC3 (5.8 μm), Spitzer-IRAC4 (8.0 μm) and SMA VEX (1.3 mm). The dashed green contours indicate the emission of the backgrounf gray scale image. The superimposed magenta contours is the HST-NICMOS emission at F160W band (see chapter 4), and the solid white contours are the continuum VEX+COM 1.3 mm emission. In the upper right panel we have indicated with arrows the position of the sources IRS5A1, IRS5A2, IRS5B and IRS5C (see lower right panel of Fig. 4.10).

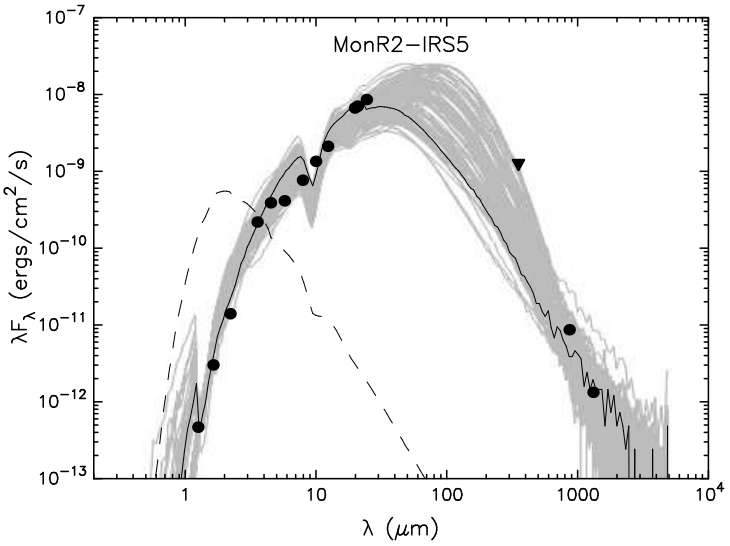

Figure 7.9: SED fitting of the IRS5A source. Filled circles show the fluxes measured with the SMA (Table 7.2) and those observed in the near- and mid-IR, which are available in the literature (see Hackwell et al., 1982; Kraemer et al., 2001; Mueller et al., 2002; Carpenter et al., 1997; Gutermuth et al., 2009; de Wit et al., 2009). Filled triangle indicates an upper limit to the measured flux. The black line shows the best fit to the data while the grey lines indicate the 100 best fits to the IRS5 SED. The dashed line shows the emission arising from the star's photosphere. The results of the SED fitting provide a stellar mass and luminosity of $\sim$7 $M_\odot$ and $\sim$300 $L_\odot$ respectively for the IRS5 source.

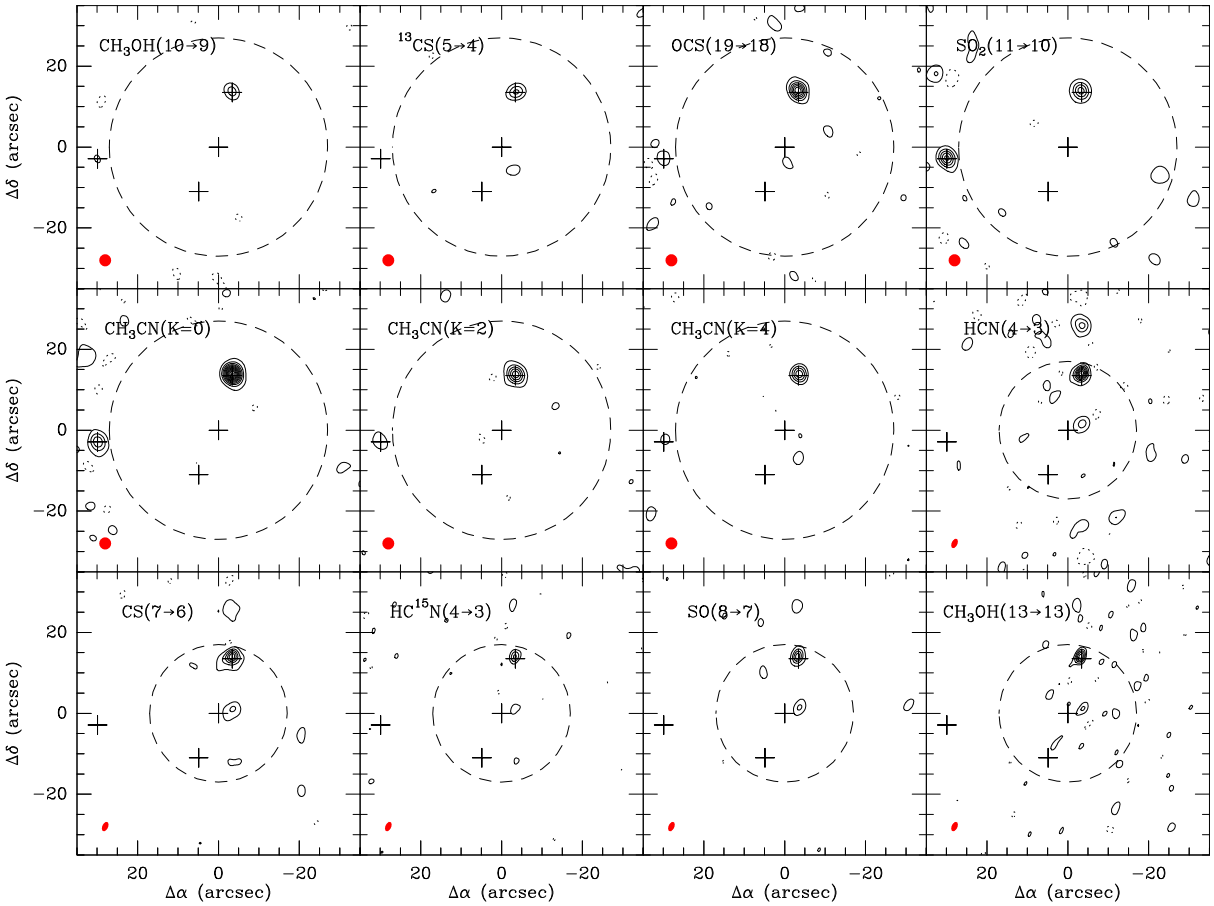

Figure 7.10: Images of the MonR2 region for different spectral lines, indicated in the upper left-hand corner of each panel. The maps show the integrated emission from 5 to 15 km s^{-1}, with each line's central velocity set at 10 km s^{-1}. As before, crosses mark the positions of the main IRS sources in the region and dotted contours indicate the negative 3σ level. The first contour and step level are 3σ, except for OCS($19 \rightarrow 18$), $SO_2(11 \rightarrow 10)$, CH_3CN ($K = 0$ and $K = 2$), HCN($4 \rightarrow 3$), CS($7 \rightarrow 6$) and SO($8 \rightarrow 7$), where the contour spacing is 6σ. The beam size is shown as a red ellipse in the lower left corner. The dashed circle indicates the primary beam of the observations, ∼57" at 1.3 mm, and ∼35" at 0.85 mm. The maps were made using natural weighting.

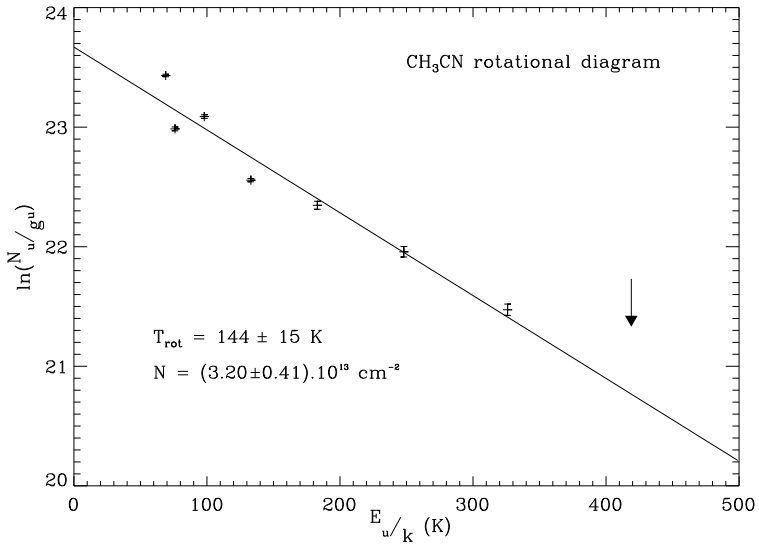

Figure 7.11: Methyl cyanide rotational diagram for the $K = 0$ to $K = 6$ ladder detected towards IRS5. The data are shown as black plus signs with corresponding 1σ error bars, and the linear fit as a black line. The upper limit derived for the $K = 7$ transition is shown as a black arrow.

Fig. 7.10 also shows that most of the molecular emission in our SMA images arises from IRS5 and thus, besides IRS3, this source appears as the most chemically active object in the region. This confirms IRS5's nature as a very young object with a chemically rich envelope. The molecular line emission towards IRS5 is very compact and its line profiles show a single Gaussian component with line widths ranging from 5 to 7 km s^{-1}, typical of a hot core (Kurtz et al. 2000). We do not detect any broader velocity component that could be associated with the high-velocity CO outflow reported in Sect. 7.3.2. This suggests that the molecular line emission detected towards IRS5 likely arises from the hot core surrounding this source, instead of from outflowing shocked gas.

We note that the other two molecular condensations seen towards the north and south of IRS5 in HCN, CS and SO, are artifacts generated by the limited UV plane coverage of our 0.85 mm observations.

★ Excitation Temperatures, Column Densities and Molecular Abundances towards MonR2 IRS5

- Methyl cyanide

Table 7.6: Derived parameters of the molecular line emission measured towards IRS5.

Line	ν (GHz)	E_u (K)	Area (Jy/beam km s^{-1})	v_{LSR} (km s^{-1})	Δv (km s^{-1})	I_{peak} (Jy/beam)
CH_3CN ($12 \rightarrow 11, K = 0$)	220.74726	69	6.21 ± 0.05	9.34 ± 0.08	7.3 ± 0.2	0.801 ± 0.018
CH_3CN ($12 \rightarrow 11, K = 1$)	220.74301	76	3.22 ± 0.05	9.4 ± 0.3	6.1 ± 0.4	0.492 ± 0.021
CH_3CN ($12 \rightarrow 11, K = 2$)	220.73026	98	4.28 ± 0.06	8.89 ± 0.18	6.9 ± 0.4	0.583 ± 0.020
CH_3CN ($12 \rightarrow 11, K = 3$)	220.70902	133	4.85 ± 0.06	8.75 ± 0.14	7.4 ± 0.3	0.619 ± 0.021
CH_3CN ($12 \rightarrow 11, K = 4$)	220.67929	183	1.87 ± 0.05	8.89 ± 0.21	6.5 ± 0.6	0.268 ± 0.020
CH_3CN ($12 \rightarrow 11, K = 5$)	220.64108	248	1.18 ± 0.04	9.20 ± 0.15	4.5 ± 0.4	0.247 ± 0.020
CH_3CN ($12 \rightarrow 11, K = 6$)	220.59442	326	1.31 ± 0.06	9.00 ± 0.30	6.5 ± 0.7	0.190 ± 0.022
CH_3CN ($12 \rightarrow 11, K = 7$)	220.53932	419	≤ 0.14	-	-	≤ 0.05
SO_2 ($11_{1,11} \rightarrow 10_{0,10}$)	221.96521	60	3.27 ± 0.05	9.09 ± 0.14	6.1 ± 0.3	0.646 ± 0.020
OCS ($19 \rightarrow 18$)	231.06098	111	5.35 ± 0.07	8.95 ± 0.09	6.5 ± 0.2	0.78 ± 0.03
^{13}CS ($5 \rightarrow 4$)	231.22099	33	3.14 ± 0.15	9.22 ± 0.23	6.2 ± 0.5	0.48 ± 0.06
CH_3OH ($10_{2,9} \rightarrow 9_{3,6}$ A$^-$)	231.28111	165	4.07 ± 0.07	8.76 ± 0.11	5.8 ± 0.2	0.66 ± 0.03
CH_3OH ($13_{1,12} \rightarrow 13_{0,13}$ A)	342.72980	228	20.6 ± 0.3	9.07 ± 0.12	6.1 ± 0.3	3.16 ± 0.16
CS ($7 \rightarrow 6$)	342.88300	66	42.8 ± 0.23	8.59 ± 0.01	6.30 ± 0.03	10.8 ± 0.1
$HC^{15}N$ ($4 \rightarrow 3$)	344.20032	41	6.8 ± 0.3	8.21 ± 0.24	5.2 ± 0.6	1.24 ± 0.16
SO ($8 \rightarrow 7$)	344.31061	88				
Component 1			15.8 ± 0.2	7.3 ± 0.7	6.4 ± 0.7	2.3 ± 0.1
Component 2			3.42 ± 0.18	9.7 ± 0.7	4.4 ± 0.7	0.7 ± 0.1
HCN ($4 \rightarrow 3$)	354.50548	43	60.2 ± 0.7	8.18 ± 0.03	5.4 ± 0.1	10.4 ± 0.4

The SO ($8 \rightarrow 7$) presented with a double Gaussian profile corresponding to two velocity components. Since the CH_3CN (K= 7) transition was not detected, the upper limit on the peak intensity is given by the 3σ level in the spectrum. The upper limit to the integrated intensity of the $K = 7$ line is estimated as $3\sigma \times \sqrt{\delta v \times \Delta v}$, with δv the velocity resolution in the spectrum and Δv the linewidth of the CH_3CN line (column 6 in this Table).

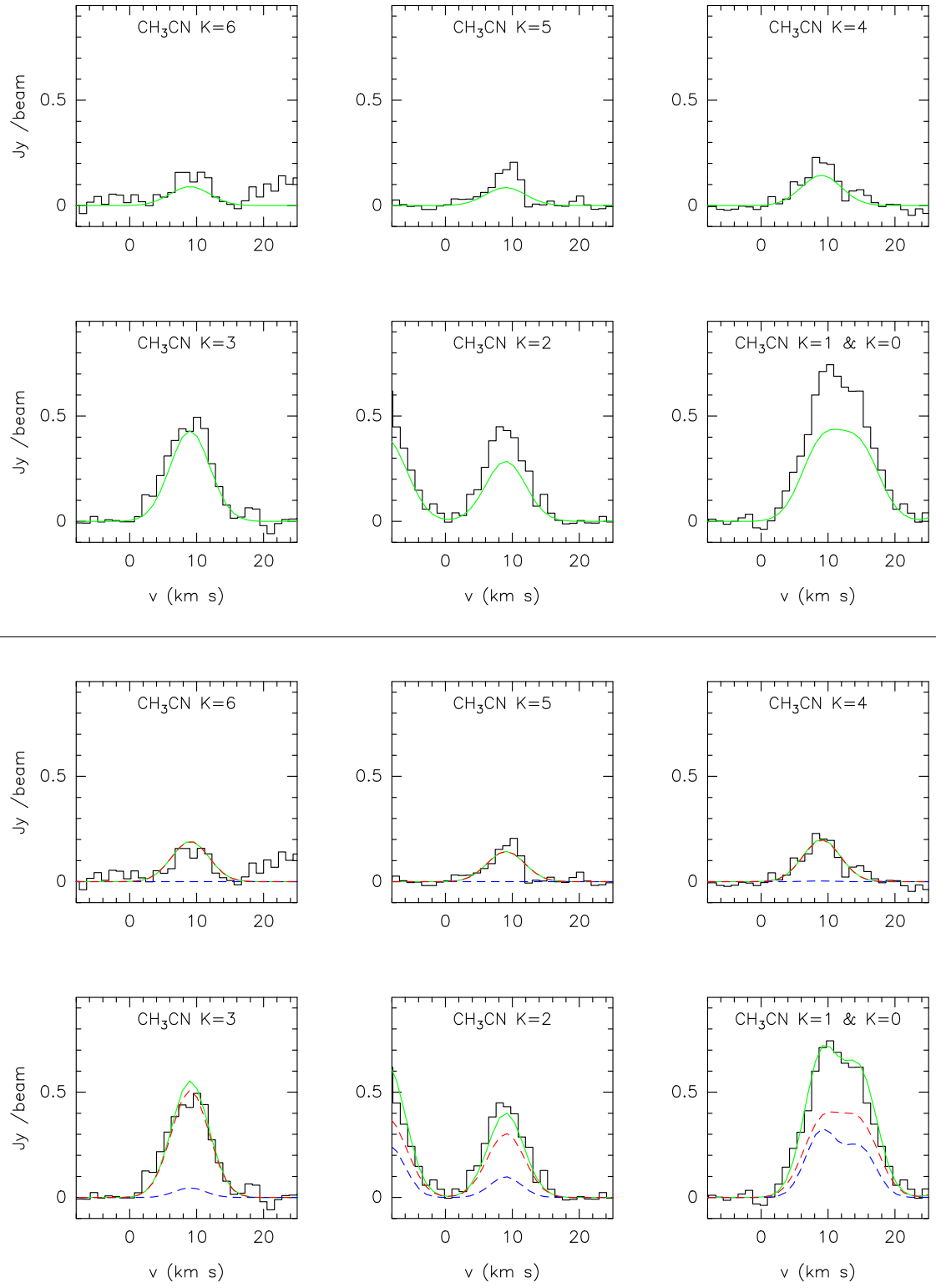

Figure 7.12: MADCUBAJ simulations of the CH_3CN spectra detected towards IRS5. In the first two rows we have simulated the spectra with the physical conditions derived from the rotational diagram analysis ($T_{\rm rot}$)=144 K and N=3.2×10^{13} cm^{-2}; green solid line). In the two last rows we have simulated the spectra with 2 components: i) hot and dense component ($T_{\rm rot}$)=230 K and N=5.8×10^{13} cm^{-2}; dashed red line); and iii) cold and less dense component ($T_{\rm rot}$)=25 K and N=1.4×10^{13} cm^{-2}; blue dashed line). The total contribution considering both components is shown with a green solid lines.

Within our dataset towards MonR2, we have detected seven rotational transitions of the methyl cyanide molecule (CH_3CN.) This molecule is commonly used to derive the excitation temperature of the warm/hot gas in star-forming regions. In Fig. 7.10, we show the images for the CH_3CN $K = 0$, $K = 2$ and $K = 4$ transitions detected with the SMA. The CH_3CN spectra at the position of the IRS5 continuum peak were extracted from the cube after primary-beam correction. The line parameters listed in Table 7.6 were derived from the fitting of the CH_3CN $K = 0$ to $K = 6$ transitions with single Gaussian line profiles. The $K = 0$ and $K = 1$ transitions are very close in frequency and hence the accuracy of the fitted parameters suffers from the overlap of the lines. The rotational diagram of the CH_3CN molecule, derived by following the method described in the Appendix B, is shown in Fig. 7.11. Considering a single-temperature component, from the slope of the linear least squares fit to the data, we estimate an excitation temperature for the CH_3CN gas of 144 ± 15 K. The derived total column density of CH_3CN towards IRS5 is $(3.2 \pm 0.4) \times 10^{13}$ cm^{-2}. The scatter in the rotational diagram for the lines with lower E_u suggests that a single-temperature component might not be fully adequate to fit all the observed spectra.

Alternatively to the rotational diagram, we have derived the physical properties of the IRS5 hot core using *MADCUBAJ* (Madrid Data Cube Analysis in ImageJ[5]). This software solves the equation of radiative transfer and simulate the line profiles considering as input parameters the excitation temperature (T_{rot}) and the molecular column density (N). In the first two rows of Fig. 7.12 we show the simulated lines profiles with the physical conditions derived from the rotational diagram analysis (T_{rot}=144 K and N=3.2×10^{13} cm^{-2}). It is clear that the simulation from the conditions derived from the rotational diagram does not reproduce well the observed line profiles, especially for the low-excitation lines K=0,1 and 2 transitions. This strongly indicates that a single-temperature component is not able to reproduce the observations.

Another evidence favoring the presence of 2 temperature components is the different intensities of the K=0 K=1 lines[6]. The *MADCUBAJ* simulator shows that for extinction temperatures above ∼120 K the intensity of these two lines is nearly equal (see e.g. the simulated spectra for T_{rot}=144 K in the second uppermost row of Fig. 7.12). However, the spectrum shows clearly that the intensity of the K=0 line is higher (see Fig. 7.12). To produce this difference a component with lower

[5] ImageJ is a public domain Java image processing program (http://imagej.nih.gov/ij/index.html).

[6] These lines are close in frequency and hence they appear partially overlapped.

temperature ($T_{\rm rot}$ <100 K) is needed. Since this cold component is not able to excite the levels with higher E_u, a second hotter component must be also present.

Then, we have fitted the spectra with 2 components. The results are shown in the two downmost rows of Fig. 7.12. We find that a model with 2 components is able to fit much better the observed spectra. We obtain a hot and dense component with $T_{\rm rot}$=230 K and N=5.8×10^{13} cm^{-2}, and a cold and less dense component with $T_{\rm rot}$=25 K and N=1.4×10^{13} cm^{-2}. The former is responsible for the excitation of the lines with upper E_u, while the latter component only contributes for the lower E_u lines.

The IRS3 molecular core falls outside the primary beam of our SMA observations, and hence the sensitivity of the images towards this position is significantly lower. We only detected the transitions from K=0 to K=3 ($E_{\rm u}$ < 133 K, Table 7.6) above 5σ level. This prevents an adequate 2-temperature fit of the line profiles. Therefore, we just provide an estimate for the excitation temperature of the gas derived from the rotational diagram using the four CH_3CN transitions detected. The derived excitation temperature is ∼125 K. This temperature is consistent with those measured by van der Tak et al. (2003) from single-dish observations of several SO_2 and CH_3OH lines (∼110 K to 125 K).

- Other molecular species

The column densities of the other molecular species detected towards IRS5 are estimated by assuming LTE and optically thin emission. In the case of HCN, the emission is not optically thin because HC^{15}N is detected (see Table 7.6). Therefore, we correct for optical depth effects (see the expression for the correction factor in Sect. 7.3.2) based on an $^{15}N/^{14}N$ isotopic ratio of 1/388 (Wilson, 1999). The derived optical depth for HCN is τ ∼47. We used Equation B.3 to determine the values of N_u/g_u for every rotational transition, and then calculate the total column density (N_{tot}) of the molecular species by reformulating B.2 into:

$$N_{\rm tot} = \frac{N_u}{g_u} Q(T_{\rm rot}) e^{E_u/kT_{\rm rot}}. \qquad (7.10)$$

The values of $S\mu^2$ and $Q(T_{\rm rot} \simeq 150$ K[7]) are taken from the Cologne Database

[7] We have found that the CH_3CN emission from the IRS5 molecular core is explained with a model with 2 different temperatures, 25 K and 230 K. To estimate average values for the column density of different molecules, we have used an average temperatures between these two values of

Table 7.7: Molecular column densities and abundances measured towards IRS5 with the SMA.

	CH_3CN	SO_2	OCS	^{13}CS	CH_3OH	CS	$HC^{15}N$	SO	HCN
N ($\times 10^{15}$cm^{-2})	0.032 ± 0.004	1.23 ± 0.11	1.31 ± 0.08	0.031 ± 0.003	24.5 ± 2.0	0.468 ± 0.004	0.027 ± 0.001	1.12 ± 0.02	10.000 ± 0.001
χ ($\times 10^{-8}$)	0.2	7.3	7.7	0.2	150	1.2	0.07	3.0	26.3

for Molecular Spectroscopy (CDMS; Müller et al., 2005). We estimate the molecular abundances, χ, by matching the beams of the 1.3 mm and 0.85 mm continuum maps with those of the line maps at 1.3 mm and 0.85 mm, respectively. The H_2 column density towards IRS5 is calculated from the measured 1.3 mm and 0.85 mm peak fluxes of IRS5 (Table 7.2) using the expression (Enoch et al. 2006):

$$N_{H_2} = \frac{F(\nu)}{\Omega\, \mu_{H_2}\, m_H\, \kappa_\nu\, B_\nu(T_{dust})}, \tag{7.11}$$

where Ω is the beam solid angle, m_H is the mass of hydrogen, κ_ν is the dust opacity, B_ν is the Planck function and T_{dust} is the dust temperature and μ_{H_2} is the mean molecular weight per H_2 molecule. We assume a gas-to-dust ratio of 100. The derived H_2 column densities towards this source are 1.7×10^{22} cm^{-2} at 1.3 mm and 3.8×10^{22} cm^{-2} at 0.85 mm. These values are derived from the peak fluxes at different angular resolutions to match the peak flux of the molecular lines. The resulting molecular column densities and abundances are reported in Table 7.7. When comparing the abundances of different molecules, note the different beam sizes at 1.3 and 0.85 mm (a small factor given the approximate nature of the estimates done here.)

7.4 Discussion

7.4.1 IRS5: An intermediate- to high-mass star in the hot-core phase

In Sect. 7.3.3, we report the detection of rich molecular line spectra towards the IR sources IRS3 and IRS5 in the MonR2 cluster. These spectra present several molecular line transitions from complex organic species, such as CH_3OH and CH_3CN, and from sulfur-bearing species, such as SO_2 or OCS. The high temperatures measured towards the innermost envelope regions around massive stars (of few 100 K) yield the thermal

150 K, which is approximately the one resulting from the rotational diagram.

evaporation of the icy mantles of dust grains, chemically enriching their molecular environment gas (these objects are commonly known as *hot cores*; see e.g. Charnley et al., 1992; Charnley, 1997; Viti et al., 2004; Wakelam et al., 2004). For IRS3, previous millimeter and infrared observations towards this source already noted the detection of a rich hot-core chemistry (Boonman and van Dishoeck, 2003; van der Tak et al., 2003). Although shocks are also expected to enhance the abundance of certain molecular species in star-forming regions, the radiative transfer modeling study carried out by van der Tak et al. (2003) showed that their contribution is likely small. As we show in chapter 4, the IRS3 region harbors a subcluster of young stars with three massive objects. The hot core molecular emission detected with COM data is centered on IRS3-C, and hence this is the best candidates for driving the hot-core chemistry. However, new sensitive and high angular resolution interferometric observations are needed to confirm this.

For IRS5, our SMA observations reveal that this object also presents a hot-core-like chemistry, indicative of its youth. The molecular abundances measured towards IRS5 indeed range from 2×10^{-9} for CH_3CN to 1.5×10^{-6} for CH_3OH, showing that they have been enhanced by several orders of magnitude with respect to the quiescent gas in molecular dark clouds as expected in hot cores (see e.g. van der Tak et al., 2000, 2003). Also, the derived excitation temperature for the hottest gas towards IRS5 is typical of hot cores ($\sim$230 K, see Sect. 7.3.3), and the derived mass of the IRS5 central star ($\sim$7 $M_\odot$, Sect. 7.3.2) is capable of warming up its surroundings yielding the observed rich chemistry.

Sulfur-bearing molecules are considered good chemical clocks since their abundance are predicted to vary by several orders of magnitude with time (e.g. Charnley, 1997; Viti et al., 2004). Sulfur chemistry in hot cores starts with the injection of H_2S into the gas phase after grain mantle evaporation (although H_2S is undetected in solid form in the ISM, this species is believed to be the most abundant carrier of atomic sulfur on the surface of dust grains; Smith, 1991). H_2S is destroyed by H and H_3O^+ to form S and H_3S^+, which then react with O and OH to form SO (Charnley, 1997). For temperatures $<$300 K, SO is destroyed in favour of SO_2 through the reaction O + SO $\rightarrow$ SO_2 + photon, which takes over for time-scales $\gtrsim10^4$ yr yielding abundance ratios $\chi(SO)/\chi(SO_2)\leq1$ (Wakelam et al., 2004). Towards IRS5, the abundance ratio $\chi(SO)/\chi(SO_2)\sim0.4$, which indicates that the age of the IRS5 source is $\gtrsim10^4$ yr, in reasonable agreement with the age estimated from the SED fitting of the source (Sect. 7.3.2). The H_2 densities are likely $\geq10^6$ cm^{-3}, since SO_2 is never found to be

more abundant than SO for lower H_2 densities (Wakelam et al., 2004). This density is consistent with the ratio between the derived hydrogen column density (N_{H_2}, Sect. 7.3.3) and the size of the core (radius of $R \sim$0.01 pc), which gives $N_{H_2}/R \sim 10^6$ cm^{-2}. The derived abundances of OCS and CS ($\sim 8\times10^{-8}$ and $\sim 10^{-8}$, respectively) are also similar to those predicted by chemical models for the same time-scales of $\gtrsim 10^4$ yr (see Charnley, 1997; Wakelam et al., 2004) .

7.4.2 Competitive accretion scenario in the MonR2 stellar cluster

Previous near-IR observations carried out by Hodapp (2007) towards the MonR2 star cluster reported a population of H_2 2.12 μm outflows (likely powered by young Class 0/I sources) located in the periphery of the MonR2 central region. This lead them to propose an *inside − out* scenario where star formation had been triggered by the interaction of the large-scale CO outflow with the surrounding ambient cloud. In contrast, our SMA observations towards the center of this cluster (inner 1′-region, i.e. $\sim$0.25 pc) revealed a population of 11 new CO outflows in the central region of the MonR2 cluster region. This population of CO outflows, which was not detected in near-IR or mid-IR surveys mainly due to the high extinction towards the cluster center (Carpenter et al., 1997; Gutermuth et al., 2005)[8], is likely associated with the youngest population of Class 0 sources in the cluster. Therefore, the presence of young stars in the center of the cluster suggest that an alternative mechanism different from external triggering must dominate the star formation process in the MonR2 cluster.

By inspecting the distribution of Class I and Class II sources in MonR2, Gutermuth et al. (2005) found that the Class I sources cluster around the MonR2 region along the north-south direction while the more evolved Class II objects are distributed across the cluster (see Fig. 13 in the review paper of Carpenter and Hodapp, 2008). In addition, the distribution of the H_2 molecular gas (as derived from multi-transition excitation analysis of CS lines; H_2 peak densities of $\sim 2\times10^7$ cm^{-3}; see Choi et al., 2000) and of dust (as estimated from CO; peak extinction of $A_v \sim$50 mag; see Carpenter et al., 1997) is found to peak towards the center of the cluster. These observational facts would be consistent with the competitive accretion scenario where the youngest (and the most deeply embedded) YSOs, probed by the CO outflows detected with the SMA, are located at the center of the MonR2 cluster as a consequence of gas

[8]The Spitzer data also suffer from saturation and crowding towards the inner region of MonR2 (see Gutermuth et al., 2005).

accretion by the potential well. This would explain not only the differences in the distribution of Class 0, I and II sources towards MonR2, but also the centrally-peaked distribution of H_2 gas and dust towards the cluster center.

If competitive accretion were the dominant mechanism for star formation in the MonR2 cluster, one would expect the most massive objects in the cluster (IRS 1, IRS 2, IRS 3 and IRS 5) to grow via gas accretion accompanied by a significant population of low mass stars (Bonnell and Bate, 2006). As seen from Fig. 7.4, the density of low-mass stars in MonR2 is found to be higher around the most massive objects in the cluster such as IRS1, IRS2 and IRS3. In particular, the peak value of the stellar density in MonR2 (of $>10^{5.5}$ stars pc^{-3}; see chapter 4) is found towards the IRS2 source, which is approximately located at the geometrical center of the cluster. As we will show in chapter 8, the presence of the CO outflows does not increase the velocity dispersion of the gas in the core, and hence it would not hinder any possible gas accretion to the cluster center as required by the competitive accretion scenario (Bonnell and Bate, 2006).

The competitive accretion scenario could also explain the large-scale CO outflow detected in MonR2, which emanates from the cluster but for which no powering source has been identified yet (Tafalla et al., 1997; Giannakopoulou et al., 1997). Since the stellar densities at the center of the MonR2 core are very high ($>10^6$ stars pc^{-3}), close dynamical encounters are likely to occur as proposed for the large-scale and powerful CO outflows detected in the Orion BN/KL and DR 21 high-mass star-forming regions (Zapata et al. 2009, 2013; see also chapters 2 and 3). A large-scale SMA or ALMA mosaic covering the extent of the MonR2 CO outflow is needed to verify this hypothesis.

7.4.3 Non-detenction of (sub)mm flares from the dense low-mass stellar population

It is still unclear if flares from young low-mass stars can be produced at higher frequencies, in the millimeter range, as occurred for instance in the Sun, where millimeter gyrosyncrhotron flares without radio counterparts have been observed (Kundu et al. 2000). New observations at higher frequencies could detect emission from highly-energetic electrons that might caused by different physical mechanisms.

In chapter 4 we have seen that the central part of MonR2 harbors a dense population of young low mass stars. The results of our radio continuum monitoring in the ONC/OMC cluster (chapter 5) have shown that young low-mass stars exhibit

non-thermal and variable radio emission, and we have detected several examples of radio flares. It is still not clear if similar phenomena can be produced at higher frequencies in the millimeter range, as have been observed in the Sun, where millimeter gyrosyncrhotron flares without radio counterparts have already been reported (Kundu et al. 2000). The observation presented in our SMA observations have not detected emission from any of the numerous low-mass stars in the FoV (see Fig. 7.4). One may wonder whether this is because (sub)millimeter flares from young stars are rare events, or because the sensitivity of the SMA observations is not enough to detect them. With the aim of answer this question, we use the equation 5.1 (chapter 5) to estimate the expected number of radio flares $N_{\rm RF}$ (flares day^{-1}), considering that the distance of MonR2 is approximately twice the distance to Orion. We obtain that our COM SMA continuum observations at 1.3 mm and 0.85 mm should detect $<<$ 1 flares/day, respectively, which is fully consistent with the non-detection of any flare in our images. Therefore, even if they exist, the limited sensitivity of SMA images would prevent their detection. To detect a 1.3 mm flare we would need a rms of $\sim$50 μJy, a sensitivity a factor of 80 better than our SMA observations. This sensitivity can be more easily reached with ALMA, whose future observations will confirm if young low-mass stars also produce (sub)millimeter flares.

7.5 Summary and conclusions

Our SMA study of the MonR2 core has characterized the thermal continuum and molecular line emission from the main sources in the region at (sub)millimeter wavelengths. The main conclusions of this study are:

- *Continuum observations*: IRS2 and IRS5 are the brightest continuum sources detected at 1.3 mm and 0.85 mm towards MonR2. IRS3 falls outside the primary beam of the observations, preventing us from accurately characterizing its physical properties. While IRS1 and IRS2 are dominated by free-free emission ($\alpha_{\rm IRS2} \sim -0.2$), towards IRS5 dust thermal emission prevails ($\alpha_{\rm IRS5} \sim 3.0$.) We obtain a gas mass estimate of $\sim$ 0.5-6 M$_\odot$ for IRS5, and a lower limit of $\sim$ 0.3-3 M$_\odot$ for IRS3, the most luminous source in the region. Higher-angular resolution observations with the SMA Very Extended configuration reveal the substructure of IRS5 and IRS1 at the 0.5" level, while IRS2 retains its compact morphology even at this angular resolution.

  The (sub)millimeter continum observations have not detected emission from any

of the numerous low-mass young stars located in the dense MonR2 stellar cluster. This do not necessarily imply that (sub)millimeter flares are rare events in young low-mass stars, but that the limited sensitivity of our SMA observations do not allow their detection. New deeper observations with ALMA are needed to confirm if (sub)millimeter flares are common events during the first phases of star formation.

- *Molecular outflows*: We detected 11 previously unknown young outflows in the ^{12}CO (2-1) transition. IRS5 and IRS3 are associated with bright collimated bipolar outflows, with masses in the 10^{-4}-10^{-2} $M_\odot$ range. Their momenta are of order 10^{-3} - 10^{-1} $M_\odot$ km s^{-1}, while the energies are of order $\sim$0.05-0.5 $M_\odot$ km ^{2} s^{-2}. A comparison with known IR sources indicates that the IRS5 outflow is likely associated with the IRS5-A source and that the IRS3 outflow is likely driven by the IRS3B massive source . The SED fitting for IRS5 yields a stellar mass and luminosity of $\sim$ 7 $M_\odot$ and $\sim$ 300 $L_\odot$, respectively, and further suggests that IRS5 is a deeply embedded young stellar object still accreting gas.

- *IRS5 physics and chemistry*: Our observations show that IRS5 is an intermediate- to high-mass star at an early stage of evolution, as shown by its rich hot-core-like chemistry and the bright, collimated molecular outflow originating from it. From the methyl cyanide K ladder transitions, we have fitted the emission arising from the core with a 2-component model: i) hot and dense component with $T_{\rm rot}$=230 K and N=5.8$\times$10^{13} cm^{-2}; and ii) cold and less dense component with $T_{\rm rot}$=25 K and N=1.4$\times$10^{13} cm^{-2}. We also provide estimates for the molecular column densities and abundances for the molecular species detected towards IRS5. We conclude that IRS5 is an intermediate- to high-mass star at an early stage of evolution, as shown by its rich hot-core-like chemistry and the bright, collimated molecular outflow originating from it.

CHAPTER 8

The impact of outflow-driven turbulence in massive star-forming regions

Abstract

The OMC1-S region and the central part of Monoceros R2 harbor clusters of molecular outflows driven by their dense and young stellar population. We have evaluated the impact of outflow feedback in these two massive star-forming regions. From the fraction of the stellar population driving outflows and we have estimated that star formation has been occurring during periods longer than the typical free-fall times, which indicates that some activity has been acting to prevent a rapid collapse of the parental clumps. We propose that this activity could be the turbulence injected by the molecular outflows arising from the young PMS stars. The presence of multiple molecular outflows in the two dense stellar clusters suggests that the outflow feedback may favor the fragmentation of the parental clump.

In the OMC1-S region, the injection of turbulence could explain the observed velocity dispersion of the gas and hence the observed linewidths of dense molecular tracers. If the outflow feedback in this region is maintained throughout the entire lifetime of the clump, it could potentially disrupt it, although a significant fraction of gas would be already accreted by the nascent cluster before suffering ejection by outflows.

In the MonR2 region, the known highly-energetic large-scale CO outflow may contribute to the gas dispersion of the clump and may be able to expel a fraction of the clump through the cavity observed in the molecular material. On the other hand, the newly discovered outflows (chapter 7) driven by young stars are expected to make negligible contributions to the velocity gas dispersion of the central region and do not have any impact in a possible disruption of the clump.

Our analysis shows that the outflow-driven turbulence arising from the young stars barely affect the overall star formation efficiency in these two regions, allowing the

formation of the observed dense stellar clusters. Only the high-energetic large-scale outflow in MonR2 has the potential to decrease the star formation efficiency.

Finally, we discuss the effects of outflow feedback in the formation of massive stars, concluding that the injected turbulence is compatible with the competitive accretion scenario proposed in previous chapters for these two massive star-forming regions, especially in the presence of outflow collisions (as observed in OMC1-S), which decrease the transfer of turbulence to the gas.

8.1 Introduction

We have seen in previous chapters that massive star cradles harbors dense cluster of PMS low-mass stars. These young stars drives molecular outflows during their early evolution, that inject energy into the natal environments. Randomly oriented outflows in these dense clusters could impact a significant fration of the surrounding gas, affecting or even hindering further star formation or the formation of massive stars (Stanke and Williams 2007).

The injection of momentum and energy into the ISM may have several consequences in: i) favoring the fragmentation of the parental clump (Knee and Sandell 2000, Li and Nakamura 2006, Shimajiri et al. 2009, Cunningham et al. 2011); ii) generating turbulence (Li and Nakamura 2006; Nakamura and Li 2007), which could affect the accretion rates onto the stars (Krumholz et al. 2005), the initial fragmentation (Fontani et al. 2012), and can give support against rapid collapse; iii) reducing the efficiency of radiation feedback in preventing accretion (Hansen et al. 2012); iv) triggering further star formation through compression of gas due to shock waves.

We evaluate in this chapter the role of outflow feedback in the two clusters of stars studied in this thesis, OMC1-S and MonR2, and compare our results with those for other stellar clusters. We discuss in detail the role of molecular outflows in: i) injecting turbulence in the surrounding gas; ii) providing support against rapid gravitational collapse; iii) increasing the the gas velocity dispersion and hence broadening the molecular linewidths; iv) disrupting the parental condensation; and v) regulating the star formation efficiency within the cluster. We also discuss how the outflow feedback can affect the formation of massive stars in these clusters, concluding that the injected turbulence is compatible with the competitive accretion scenario proposed in previous chapters.

8.2 On the impact of outflow feedback in massive star-forming regions

In this section we present the general background used to evaluate the impact of outflow feedback in the processes of star formation.

8.2.1 Timescales of outflows and star formation

Molecular outflows appear during earliest stages of star formation, and thus they provide a useful tool to probe the population of younger stars in clusters. Complementarily, the presence of young stars without outflows suggests that star formation has been occurring for longer than the typical duration of the outflow phase ([0.5−2] $\times 10^5$ yr, Arce et al. 2010 and Narayanan et al. 2012). We can estimate the time that star formation has been going on ($t_{\rm SF}$) using the expression:

$$\frac{N_{\rm outflow}}{N_{\rm tot}} = \frac{t_{\rm outflow}}{t_{\rm SF}}, \tag{8.1}$$

where $N_{\rm outflow}$ is the number of stars driving outflows at present time, $N_{\rm tot}$ is the total numbers of stars in the cluster, and $t_{\rm outflow}$ is the outflow lifetime. Therefore, if we know the fraction of stars that drive outflows at a given time in a young stellar cluster we can roughly infer the estimated time that the region has been forming stars ($t_{\rm SF}$), i.e., the cluster age. The comparison of this time with the typical free-fall time ($t_{\rm ff}$) of the parental clump will tell us whether the collapse occurs rapidly or alternatively the star formation is taken place during a longer time due to the presence of any kind of support.

8.2.2 Outflow-driven turbulence

Numerical simulations by Nakamura and Li (2007) and Carroll et al. (2009) revealed that the outflows from a cluster of young stars can sustain the turbulence in the cloud gas at pc scales. The detection of dense stellar subclusters and multiple molecular outflows in OMC1-S and MonR2 makes these regions excellent laboratories to study the effects of outflows at smaller scales (∼0.05−0.15 pc). We estimate whether the energy and momentum injected by the outflows can potentially replenish the turbulence in the regions, that it expected to decay on timescales comparable to the core free-fall time $t_{\rm ff}$. The rate at which energy is lost due to decay of turbulence is (Stanke

and Williams 2007):

$$L_{\rm turb} = E_{\rm turb}/t_{\rm ff}, \tag{8.2}$$

with

$$E_{\rm turb} = (3/2) M_{\rm reg}\, \sigma^2_{\rm 1D}, \tag{8.3}$$

where $\sigma_{\rm 1D}$ is the observed one dimensional velocity dispersion of the gas in the core and $M_{\rm reg}$ the mass of the region.

We will evaluate the 1D velocity dispersion using the linewidths of dense molecular tracers observed towards the regions. For a 1D Maxwellian distribution of velocities, the relation between the linewidth and the one dimensional velocity dispersion is:

$$\Delta v = 2\sqrt{2\, Ln2}\, \sigma_{\rm 1D}, \tag{8.4}$$

On the other hand, the rate at which the core gains energy, assuming that all of the outflow momentum is converted into turbulence in the core, and taking into account radiative losses, is given by (Stanke and Williams 2007):

$$L_{\rm gain} = \frac{1}{2} \dot{M}_{\rm reg}\, \sigma^2_{\rm 3D} = \frac{\sqrt{3}}{2} F_{\rm outflow}\, \sigma_{\rm 1D}, \tag{8.5}$$

where $\dot{M}_{\rm reg}$ is the mass set in motion by outflows per unit time and $F_{\rm outflow}$ is the outflow momentum rate.

8.2.3 Increase of gas velocity dispersion

The injection of momentum into the medium will lead to an increase of the velocity dispersion of the surrounding material, and hence the linewidths of the molecular lines observed towards these regions. The gas velocity dispersion provided by the presence of outflows can be estimated by assuming that the total momentum of the outflows ($p_{\rm outflows}$) is transferred to the medium:

$$\sigma_{\rm gain} = \frac{P_{\rm outflow}}{M_{\rm reg}}, \tag{8.6}$$

The value of $\sigma_{\rm gain}$ can be compared with the observed velocity dispersion $\sigma_{\rm 1D}$ with the aim of confirm whether the outflows could explain the observed linewidths in the regions, and therefore whether they may influence any future star formation,

including massive stars.

8.2.4 Disruption of the natal condensation

Several works (Myers and Goodman 1988, Arce et al. 2010, Narayanan et al. 2012) have evaluated the outflow impact on the disruption of the parental condensations. One way to evaluate this possibility is by comparing the measured total energy from outflows ($E_{\rm outflows}$) with the gravitational energy of the region ($E_{\rm grav}$), given by:

$$E_{\rm grav} = \frac{GM_{\rm reg}^2}{R_{\rm reg}}, \tag{8.7}$$

Another way to evaluate the disruptive effects of outflows is by using the escape velocity $v_{\rm esc}$ (or in terms of dispersion velocity, $\sigma_{\rm esc} = \frac{v_{\rm esc}}{2\sqrt{2Ln2}}$), which is defined as the velocity needed for the gas to escape from the gravitational potential well of the core. The comparison with the observed velocity dispersion $\sigma_{\rm 1D}$ could indicate whether it is possible that a fraction of the gas can be locally accelerated by outflows until it reaches $\sigma_{\rm esc}$, escaping from the region. To estimate an upper limit of the mass that can be expelled by the molecular outflows we use the "escape mass" parameter ($M_{\rm esc}$) defined as the mass that could potentially escape the region assuming that the current total outflow momentum is used to accelerate gas to reach the escape velocity (Arce et al. 2010):

$$M_{\rm esc} = \frac{p_{\rm outflow}}{v_{\rm esc}}. \tag{8.8}$$

8.2.5 Outflows regulating the star formation efficiency

Nakamura and Li (2007) showed that the outflow turbulence could lead to a delay of the gravitational collapse and, consequently, yields lower star formation efficiency (SFE), which is defined as:

$$SFE = \frac{M_*}{M_{\rm core} + M_* + f \times M_{outflow}}, \tag{8.9}$$

where M_* is the total mass of the stellar cluster, $M_{\rm reg}$ is the mass of the region, $M_{\rm outflow}$ is the total outflowing mass and f is a correction factor depending on the age of the star-forming region.

Given that the current star formation is dependent on the free-fall time of the

core (t_{ff}) and the period that the region has been forming stars[1] ($t_{\rm SF}$), we also use the "normalized" star formation efficiency[2] defined by Arce et al. (2010):

$$SFE_{\rm n} = SFE \times \frac{t_{\rm ff}}{t_{\rm SF}}, \tag{8.10}$$

8.3 Results

The outflow feedback depends on the outflow momentum as well as the mass and radius of the region which is being affected. The OMC1-S region has a mass, $M_{\rm region}$, of ∼100 $M_\odot$ (Mezger et al. 1990) and a radius of ∼25" (∼0.05 pc; Fig. 6.1 in chapter 6; see also Batrla et al. 1983; Mundy et al. 1986).

For the MonR2 region, Ridge et al. (2003) estimated a mass of ∼1800 $M_\odot$ for the gas within a radius of ∼0.7 pc. Walker et al. (1990) found that the inner ∼ 0.22 pc contains ∼ 180 $M_\odot$. These values are consistent with the density stellar profile of r^{-1} found in the region by Choi et al. (2000). The cluster of outflows detected by SMA (see Fig. 7.4 of chapter 7) is distributed within the inner ∼0.15 pc. Scaling the mass using the r^{-1} density profile, this region roughly contains a mass of ∼75 $M_\odot$. We will use $R_{\rm reg}$=0.15 pc and $M_{\rm reg}$=75 $M_\odot$ to evaluate the impact of the cluster of compact SMA outflows in the close enviroment. The CO large-scale outflow, whose size is much large (0.6−3.8 pc; Wolf et al. 1990), is expected to act over a larger and more massive region. We will use the values of the region studied by Ridge et al. (2003): $R_{\rm reg}$=0.7 pc and $M_{\rm reg}$=1800 $M_\odot$.

In Table 8.1 we summarized the physical properties of the OMC1-S and the MonR2 massive star-forming regions, along with the parameters of their respective clusters of outflows. For comparison, we also include in Table 8.1 other star-forming regions with active outflow acticity from the literature (Stanke and Williams 2007 and Arce et al. 2010). As commented in chapter 7, we note that the values of the outflow masses in OMC1-S and MonR2 have probably been underestimated because different effects: i) inclination effects (correction factor of 1.4 for the outflow momentum); ii) unaccounted missing flux due to short-spacings (we assume a correction factor of 2); and iii) 50% of the gas in an outflow could be in atomic form instead of molecular due

[1] A region with a constant star formation rate will have a higher SFE with increasing time because more of the gas will be transformed into stars.

[2] Magnetic fields may also have an effect on SFE, since Nakamura and Li (2007) found a trend where the SFE decreases with increasing the magnetic field strength. Unfortunately, the lack of measurements of the magnetic fields in these massive star-forming regions prevents the consideration of this contribution.

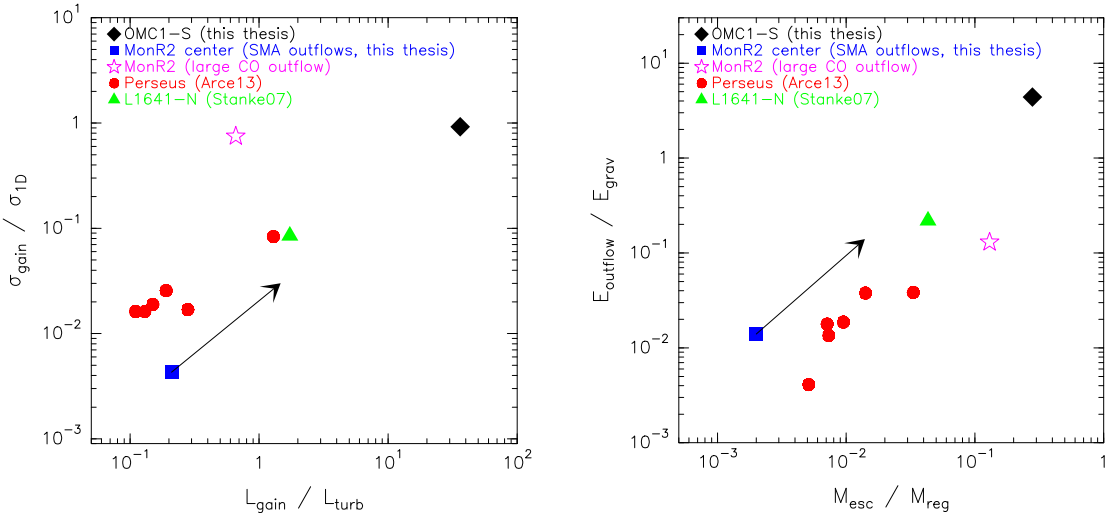

Figure 8.1: Outflow feedback from the MonR2 (blue filled square) and OMC1-S cluster of outflows (black diamond). We compare their feedback with the impact of the MonR2 larg-scale outflow (magenta filled star, Wolf et al. 1990) and several cluster of outflows from other star-forming regions (from Stanke and Williams 2007 and Arce et al. 2010). The black arrow indicates the correction of the different parameters ($L_{\rm gain}$, $\sigma_{\rm gain}$, $E_{\rm outflow}$ and $M_{\rm esc}$) to take into account the underestimation of outflow masses (Arce et al. 2010).

to dissipative shocks (correction factor of ∼2; Reipurth and Bally 2001). In addition, optical depth effects should be taken into account for the blueshifted lobes of the MonR2 outflows A and B, which imply correction factors of 4 and 11 for the masses, respectively. In Fig. 8.1 we included a "correction vector" that accounts for this effects[3].

8.3.1 Outflows and star formation timescales

The deeply embedded stellar clusters driving molecular outflows from OMC1-S and from MonR2 are expected to be in a early evolutionary stage. Carpenter et al. (1997); Andersen et al. (2006), based on the near-IR colors of the stars, estimated that the median age of the MonR2 cluster is ∼ 1 Myr. In chapter 7 we have shown that one of the drivers of molecular outflows, IRS5, shows a spectral energy distribution (SED) and a hot-core-like chemistry indicative of the very early stage of evolution, even $\gtrsim 10^4$ yr. In the case of OMC1-S, it is expected that the associated stellar cluster embedded in the Orion Molecular Cloud (OMC) is younger than the foregroun population of the Orion Nebula Cluster (ONC), whose approximate age is ∼1 Myr (Hillenbrand

[3] For comparison, the data from Arce et al. (2010) and Stanke and Williams (2007) are shown in Fig. 8.1 without being corrected by these factors.

1997). In chapter 6 we have fitted the SED of some of the outflow driving sources, and obtained ages in the range [0.5−4] × 10^5 yr, in agreements with the expected youth.

Furthermore, both regions show evidence of current massive star formation (chapters 2,4 and 6), suggesting also stellar ages ∼10^4-10^5 yr. In addition, it is known that the earlier the evolutionary stage of the star, the larger the extinction is. Prisinzano et al. (2008) and Ybarra et al. (2013) found that stars with log$N_{\rm H}$ >22.5 cm^{-2} (equivalent to $A_{\rm V}$ >15 mag) in Orion and the Rossette Nebulae, respectively, are associated with very young objects (Class 0/I with ages of ∼10^5 yr; André 1994, Evans et al. 2009). We have shown in chapters 2 and 4 that the members of these stellar clusters show high extinctions (generally log$N_{\rm H}$ >22.5 cm^{-2}), suggesting that they are very young stars.

The molecular outflows in the OMC1-S and the MonR2 clusters have a typical lengths of ∼0.03 pc and ∼0.03−0.15 pc, respectively, which are in the low limit of sizes observed in outflows (0.03−2 pc, Guenthner and Kauffmann 2009). This compact sizes yield small dynamical ages: 100−3×10^3 yr in the OMC1-S region, and 1−3.3×10^3 yr in MonR2 (see Table 8.1). Although several uncertainties are present in these age estimates, it seems that these outflows are in general younger than the ones found in other star-forming regions, like L1641-N (∼10^4 years, Stanke and Williams 2007) or Taurus (∼10^5 years, Narayanan et al. 2012). This further supports the youth of the stellar population in these two massive star-forming regions.

As shown in Sect. 8.2 we can use the fraction of stars that are driving molecular outflows ($N_{\rm outflow}/N_{\rm tot}$) to estimate the time that star formation occurs in the clusters, $t_{\rm SF}$, i.e., the cluster's age. In the OMC1-S region, up to six out of the 22 young stars are currently driving molecular outflows (chapter 6). In the case of the inner 0.15 pc of the MonR2 cluster, where 172 stars have been detected[4], our SMA observation detected up to 11 outflows. Therefore, we obtain that values for $N_{\rm outflow}/N_{\rm tot}$ of ∼0.27 and ∼0.064, respectively. This would imply, using Eq. 8.1, that the parental condensations has produced stars for a time ($t_{\rm SF}$) span ∼4−15 times longer than the outflow lifetimes, i.e., of the order a few 10^5 to 10^6 yr.[5] This is a strong indication that some agent has been acting to prevent the parental condensatino from collapsing at the very short expected freefall time, which is ∼10^4 Myr and ∼10^5 Myr for OMC1-S

[4] To count the number of stars within the inner 0.15 pc in the MonR2 stellar cluster, we have used the NICMOS observations by Andersen et al. (2006), which are the more sensitive available (see chapter 4).

[5] This estimate is an upper limit, if we consider a little contamination by non-cluster members and the fact that due to confusion probably only the most prominent outflows are detected.

and MonR2, respectively (Table 8.1). In the following sections we will show that the prime candidate for this effect is the outflow feedback, which is able to maintain the turbulence support of the region.

Table 8.1: Physical parameters of the OMC1-S and MonR2 regions and properties of the outflow feedback. We compare with other star-forming regions from the literature (Stanke and Williams 2007 and Arce et al. 2010).

Region	R_{reg} (pc)	M_{region} ($M_\odot$)	ρ (g cm^{-3})	t_{ff} (yr) (10^4 yr)	$p_{outflow}$ ($M_\odot$ km s^{-1})	t_{dyn} (10^3 yr)	L_{gain} ($L_\odot$)	L_{turb} ($L_\odot$)	σ_{1D} (km s^{-1})	σ_{gain} (km s^{-1})	$E_{outflow}$ (10^{46} erg)	E_{grav} (10^{46} erg)	M_{esc} ($M_\odot$)	t_{SF} (10^5 yr)	SFE_n (%)
OMC1-S	0.05	100	1.3e-17	2	116	0.1-3	78	2.2	1.3	1.2	7.5	1.7	28	2-8	0.3
MonR2 central (SMA outflows)	0.15	75	3.6e-19	10	0.31	1-3.3	0.03	0.15	1.0	0.004	4e-3	0.32	0.15	7.5-30	2.6
MonR2 (large-scale outflow)	0.7	1800	3.2e-20	20	1088	100	0.8	1.3	0.8	0.6	5.2	39	230	7.5-30	0.7
L1641-N	0.5	200	2.6e-20	40	16	2.7-58.5	0.18	0.11	0.9	0.08	0.15	0.68	8.7	-	-
B5	1.4	420	2.5e-21	100	22.3	50*	0.04	0.03	0.6	0.05	4e-2	1.1	14	10	0.3
L1448	0.6	150	1.1e-20	60	3.1	50*	0.007	0.04	0.8	0.02	1e-2	0.32	2	5	0.9
IC 348	0.9	620	1.4e-20	60	7.7	50*	0.02	0.16	0.8	0.01	2e-2	3.6	3	25	1.0
NGC 1333	2.0	1100	2.2e-21	100	17.4	50*	0.05	0.17	0.9	0.02	7e-2	5.1	8	10	3.4
B1 ridge	0.7	210	9.9e-21	70	3.2	50*	0.007	0.05	0.8	0.02	1e-2	0.53	2	10	0.8
B1	0.9	430	9.5e-21	70	6.2	50*	0.02	0.12	0.9	0.01	3e-2	1.7	3	10	0.7

8.3.2 Outflow-driven turbulence support

Since the star formation timescales are larger than the free-fall times of the parental condensations, it is expected that another mechanism may have prevented the rapid collapse, allowing the formation of the low-mass star cluster and the growth of more massive stars. In the case of MonR2, Wolf et al. (1990) already claimed that the large-scale CO outflow detected in the region could provide enough support to the whole clump. We estimate now whether the population of molecular outflows arising from young stars in the OMC1-S and the MonR2 clusters play a significant role in the turbulence support.

To compare the rate at which the initial turbulence decays ($L_{\rm turb}$) with the rate at which the region gains energy due to outflows ($L_{\rm gain}$), we need an estimation of the 1D gas velocity dispersions ($\sigma_{\rm 1D}$). FOr OMC1-S we use the linewidths of dense molecular tracers observed towards the region: $\Delta v \sim 3$ km s^{-1} (CN from Rodriguez-Franco et al. 1998 and NH_3 from Batrla et al. 1983). For MonR2 we use the CS linewidth observed by Tafalla et al. (1997). These authors showed that the linewidth decreases with the distance to the cluster center. From their Fig. 14 we consider an average value of linewidth of Δv ~2.3 km s^{-1} for radius < 0.15 pc and ~1.9 km s^{-1} for radius < 0.7 pc. Considering a 1D Maxwellian distribution of velocities (see Eq. 8.4), we obtain the values for $\sigma_{\rm 1D}$ shown in Table 8.1. Using Eq. 8.2 and Eq.8.3 we obtain the rate at which energy is lost due to decay of turbulence, $L_{\rm turb}$ (Table 8.1).

To estimate the rate at which the region gains energy, $L_{\rm gain}$, we use the measured values from the molecular outflows[6]. In the left panel of Fig. 8.1 we show the ratio $L_{\rm gain}/L_{\rm turb}$. In the OMC1-S region, $L_{\rm gain}/L_{\rm turb}$ ~36. This value suggests that the outflows are able to maintain the turbulence in the region, even if not all the outflow momentum is converted into turbulence in the region, and even without correcting by the underestimation of the outflow masses.

In MonR2, we obtain that a lower value, $L_{\rm gain}/L_{\rm turb}$ ~0.2. As shown in Fig. 8.1, this value is about the same order of magnitude than the ones found in several Perseus clumps (Arce et al. 2010). Considering the corrections due to underestimation of outflow masses, the ratio $L_{\rm gain}/L_{\rm turb}$ for the SMA outflows would reach a value ~1.4 (Fig. 8.1). This implies that, even if not all the energy of the compact outfows in transformed into turbulent energy, the SMA cluster of outflows could maintain the

[6] In OMC1-S we have considered the 136-359 CO outflow detected by Zapata et al. (2005) and all the SiO outflows from Zapata et al. (2006). We do not use the SO outflow and the southern CO outflow because Zapata et al. (2010) did not present its parameters. For the MonR2 outflows, we have used the values shown in Table 7.5.

turbulence in the center of the MonR2 clump whether a significant fraction of the outflow momentum is converted into turbulence. In the case of the large-scale CO outflow, we obtain that $L_{\rm gain}/L_{\rm turb}$ ~0.6.

8.3.3 Increase of gas velocity dispersion: broadening the linewidths

In OMC1-S, the gas velocity dispersion injected by the outflows is $\sigma_{\rm gain} \sim 1$ km s^{-1} (Eq. 8.6), which is approximatelly equal to the observed velocity dispersion $\sigma_{\rm 1D}$. Therefore, the outflows driven by the members of the dense OMC1-S cluster could explain the observed turbulence in the region, and therefore they may influence any future star formation, including massive stars (see Sect. 8.4).

In MonR2, Tafalla et al. (1997) found that the linewidths of the dense molecular tracer CS increase towards the center of the region. They suggested that this is due to a combination of the broadening produced by the giant CO outflow and an additional turbulence source in the inner region. Since we have detected a cluster of young molecular CO outflows at the center of the MonR2 clump, we evaluate whether this outflow feedback can contribute to the broadening of the molecular linewidths. We obtain that the ratio between the gas dispersion produced by outflows $\sigma_{\rm gain}$ and the observed velocity dispersion $\sigma_{\rm 1D}$ is << 1 (see Table 8.1 and Fig. 8.1). Even considering a correction factor of 7 for the momentum (Arce et al. 2010), and hence for $\sigma_{\rm gain}$, it is clear that the dispersion injected by the cluster of CO outflows detected by SMA ($\sigma^{corr}_{\rm gain}$ ~0.03 km s^{-1}) cannot be responsible for the observed gas velocity dispersion. In the case of the large-scale outflow, the ratio $\sigma_{\rm gain}/\sigma_{1D}$ is ~0.75 (Fig. 8.1), indicating that this agent may be able to contribute to the linewidths observed in the MonR2 clump.

The low dispersion injected by the compact SMA outflows do not explain either the difference of linewidth observed by Tafalla et al. (1997) between the center and the periphery of the region. This difference is $\Delta v_{\rm diff}$ ~0.5 km s^{-1} (Tafalla et al. 1997), which in terms of dispersion is equivalent to $\sigma_{\rm diff}$=0.21 km s^{-1}. This value is one order of magnitude higher than the corrected value for $\sigma^{corr}_{\rm gain} \sim$ (0.03 km s^{-1}) indicating that the contribution of the cluster of compact CO outflows to the broadening of the molecular linewidth is negligible.

8.3.4 Disruption of the natal condensation

The ratio $E_{\rm outflows}/E_{\rm grav}$ in OMC1-S is 4.6, which is significantly higher than the ones found by Arce et al. (2010) in Perseus (<0.40) (see Fig. 8.1) and of the order of the one found in the L1551 dark cloud in Taurus (Narayanan et al. 2012). This means that the outflows in OMC1-S could potentially disrupt the core. Table 8.1 shows that $\sigma_{\rm esc}$ is slightly higher than the observed velocity dispersion $\sigma_{\rm 1D}$. However, given that the values of the two velocities are close, it is possible that a fraction of the gas can be locally accelerated by outflows until it reaches $\sigma_{\rm esc}$, escaping from the clump. Therefore, the molecular outflow feedback could potentially expel out material from the clump. To estimate an upper limit of the mass that can be expelled by the molecular outflows we use the "escape mass" $M_{\rm esc}$. In OMC1-S $M_{\rm ecs}$ $\sim$28 $M_\odot$ (i.e., $\sim$28% of the current mass of the region). This suggest that if the outflow feedback is maintained throughout the entire lifetime of the core, it could potentially disrupt the clump. We note however that a fraction of the gas will be accreted by the nascent stellar cluster before suffering ejection by outflows. Matzner and McKee (2000) found that 50% − 70% of the mass of the parental clump of low-mass stellar clusters will be dispersed by outflows, while the rest (i.e., 30% − 50%) will be turned into stars. In Sect. 8.4 we evaluate the ability of Bondi-Hoyle accretion to transfer mass into the OMC1-S stellar cluster.

For MonR2, $E_{\rm outflows}/E_{\rm grav}$ is 0.014, similarly to the those obtained in Perseus clumps (Fig. 8.1). Even considering a correction factor of 10 (Arce et al. 2010), it seems that the outflows in MonR2 do not have the potential to disrupt the clump. The right panel of Fig. 8.1 shows that the fraction of mass of the MonR2 clump that can be ejected is only a $\sim$0.2%, consistently with the ideo of no disruption. However, the energy of the giant CO outflow is much closer to the gravitational binding energy, ($E_{\rm outflows}/E_{\rm grav}$=0.13), and therefore it may be able to expel a fraction of the whole clump ($\sim$13%) through the cavity previously observed in the molecular material (Tafalla et al. 1997; Choi et al. 2000).

8.3.5 Outflows regulating the star formation efficiency

Using Eq. 8.9 and 8.10, we assume a value f=2, typical of very young regions (Arce et al. 2010), a mean mass for the clusters members of 0.5 $M_\odot$ (as in Jørgensen et al. 2008, Evans et al. 2009, and Arce et al. 2010), and the upper limits to $t_{\rm SF}$ $\sim$8×10^5 yr and $\sim$3×10^6 yr for OMC1-S and MonR2, repectively (Sect. 8.3.1). We obtain

lower limits for $SFE_{\rm n}$ of ∼0.3% for OMC1-S, ∼2.6% for the central region of MonR2 affected by the SMA outflows, and ∼0.7% for the full clump affected by the large-scale outflow[7] (see Table 8.1). Arce et al. (2010) found similar values (0.3−3.4%) in a sample of 6 young star-forming regions with multiple molecular outflows.

As for the clumps considered by Arce et al. (2010), in OMC1-S and MonR2 the star formation efficiency is barely affected by the presence of molecular outflows driving by the young stars (due to the low ratio between the outflowing mass of the total mass of the clumps, even considering a the correction factors for the mass of the outflows). The values of $SFE_{\rm n}$ considering outflows compared with those expected without outflows are only lower in a factor of 0.96-0.99. Furthermore, the large-scale outflow in MonR2, which is very massive, could have a higher impact in the star formation efficiency, because it has the potential to expel a large fraction of the available gas in the clump (Sect. 8.3.4), and thus to decrease the $SFE_{\rm n}$ by a factor of ∼0.8.

In principle, one could think that regions with a high ratio between the energy rate injected by outflows and the turbulent dissipation rate ($L_{\rm gain}/L_{\rm turb}$) should have lower SFE_n (see Nakamura and Li 2007). However, Arce et al. (2010) detected no correlation between outflow strength and the $SFE_{\rm n}$. Our analysis have shown that the OMC1-S cluster of outflows is able to provide high levels of turbulence ($L_{\rm gain}/L_{\rm turb}$ ∼36, Table 8.1). However, despite this high outflow feedback, the $SFE_{\rm n}$ is similar to those found by Arce et al. (2010), where the impact of outflows is much lower than in OMC1-S (see Fig. 8.1). This suggests that the outflow-driven turbulence does not significantly prevent the star formation within the cluster, and may indicate that: i) although high levels of turbulence can prevent accretion in well defined directions (the polar axis of the outflows, Cunningham et al. 2006), other paths are still available to allow accretion; and ii) shocks associated with outflows compress the gas forming new dense cores that collapse and likely form new stars.

[7] For the OMC1-S region, we have counted the number of embedded stars revealed by *Chandra* in the OMC1-S region (see chapter 6). In MonR2 we have used the NICMOS observations from Andersen et al. (2006) for the inner 0.15 pc, completed by the *Chandra* observations from Nakajima et al. (2003) for distances 0.15 pc $< r <$ 0.7 pc (see chapter 4).

8.4 Discussion

8.4.1 The role of outflow feedback in massive star formation

The effects of outflow feedback on star formation could have important implications for the current theories of massive star formation: monolithic accretion (Yorke and Sonnhalter 2002; McKee and Tan 2002, 2003; Krumholz et al. 2005 and Krumholz et al. 2009) and competitive accretion in stellar clusters (Bonnell and Bate 2006). The monolithic-accretion theory needs the existence of a massive clum supported against self-gravity by its internal turbulence. This turbulence could be provided by the outflows, which would be able to keep the clump close to virial equilibrium (Li and Nakamura 2006). However, observations have shown that the molecular clumps where massive stars form usually exhibit gas dispersions that prevent the virialization of the clump (Martin-Pintado et al. 1985). On the other hand, the presence of outflows may favor the fragmentation, producing the formation of a cluster of low-mass stars (Knee and Sandell 2000; Li and Nakamura 2006; Li et al. 2010; Cunningham et al. 2011). The competitive accretion theory relies precisely in the existence of a low-mass star cluster in the massive star cradles.

The presence of multiple outflows in the dense stellar clusters in OMC1-S and MonR2 suggests that the outflow feedback may favor the fragmentation of the parental clump, as suggested by other works (Knee and Sandell 2000, Li and Nakamura 2006, Shimajiri et al. 2009, Cunningham et al. 2011). Along this line, we have proposed in chapter 2 a scenario for massive star formation where the parental clump fragments in multiple smaller cores that collapse and give birth to a low-mass stellar cluster, in agreement with the observations. Once the cluster is formed, the stars that win the competition for accretion can become massive.

The efficiency of this accretion mechanism has been questioned by Krumholz et al. (2005), who proposed that the turbulence of the clump – favored by the presence of outflows – could increase the velocity dispersion of the gas and hence decrease the accretion rates. However, Bonnell and Bate (2006) remarked that using the local properties of massive star-forming regions, Bondi-Hoyle accretion is indeed effective to form massive stars. In agreement with this, we have shown in chapter 2 that competitive accretion could be the possible mechanism for massive star formation in the Orion Hot Core.

A key parameter to determine if Bondi-Hoyle accretion is relevant for forming massive objects – besides the gas density ρ – is the relative velocity of the gas, $v_{\rm RMS}$

. In the case of MonR2, we have shown that the the increase of the velocity dispersion induced by the outflows arising from the stellar population is negligible, and therefore their presence do not hinder the subsequent Bondi-Hoyle accretion.

However, in the OMC1-S cluster the contribution to the gas dispersion is significantly higher. We evaluate here whether the impact of this outflow feedback will allow the growing of massive stars by Bondi-Hoyle accretion in this region. The relative velocity of the gas can be estimated from the measured linewidth of dense gas tracers using Eq. 2.3 from chapter 2, obtaining that $v_{\rm RMS}$ ∼2.2 km s^{-1}. Considering initial "stellar seeds" of $M = 1$ M$_\odot$ formed via core accretion, we show in Fig. 8.2 the timescale for Bondi-Hoyle accretion to form a massive star. In order to evaluate the timescale to form the stellar seeds (dotted line in Fig. 8.2) we have used the expression from Krumholz et al. (2012) for the mass accretion rate (with a surface stellar density of Σ=3.5 g cm^{-2}, obtained from the gas density ρ assuming a circular geometry). The Bondi-Hoyle accretion time has been calculated using Eq. 2.2 (chapter 2) and Bonnell and Bate (2006), who considered that the gas density has a radial profile of $\rho(r) \sim$ r^{-1} and $\rho(r) \sim$ r^{-2}, respectively (solid and dashed lines in Fig. 8.2). This range in the radial dependence of the gas density is usually measured in massive star-forming regions (Choi et al. 2000). In our calculations we considered the mean gas density[8] of the core, ρ ∼1.3×10^{-17} g cm^{-3}. Fig. 8.2 shows that the dispersion injected by outflows does not prevent that Bondi-Hoyle accretion could transfer a mass of ∼10 M$_\odot$ to the stellar cluster, allowing the formation of a massive star in a timescale of several 10^5 yr.

We also need to take into account the inability of the outflows to inject their momentum into the whole solid angle. Cunningham et al. (2006) claimed that the effect of the outflows is spatially limited to the outflow axis: only those regions of the that have been swept over by the outflow will be strongly affected. This means that the turbulence is mainly injected along the outflow axis, while the rest of the solid angle remains nearly unaffected by the energy injection, allowing the accretion in these directions. Li and Nakamura (2006) remarked that it may be difficult for collimated outflows to prevent material from falling towards the center of the potential well in all directions. Therefore, the accretion of mass to the star will be oriented through the plane perpendicular to the outflow axis, i.e., the plane of the circumstellar disk.

[8] The accretion timescale is inversely proportional to the gas density (Eq. 2.2, chapter 2). The density decays with time (due to accretion and ejection processes), and therefore it was higher at the very early evolution and it will be lower in the future. We consider here an average value equal to the current density, that provides an average mass accretion rate.

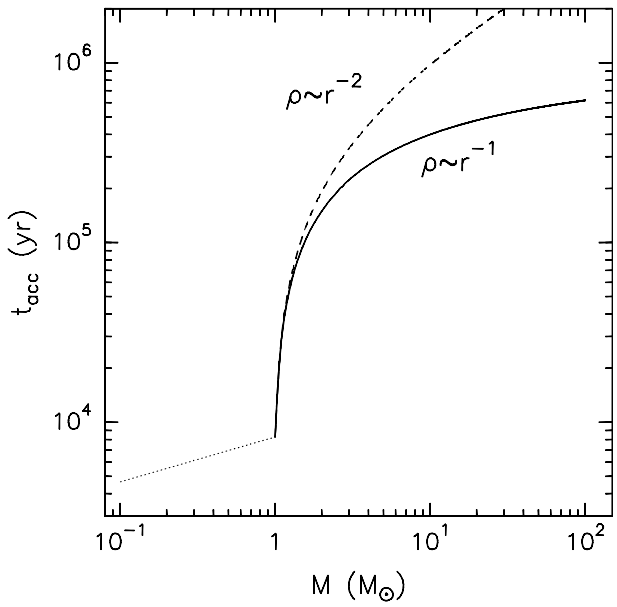

Figure 8.2: Accretion time to form a massive star in the OMC1-S region. The dotted line corresponds to the time needed to form the stellar seeds of 1 $M_\odot$ via subcore accretion, using the expression from Krumholz et al. (2012) for the mass accretion rate. The dashed and solid lines correspond to the accretion time needed to reach the final mass M, assuming that the gas density is $\rho \sim r^{-2}$ and $\rho \sim r^{-1}$, from the expression presented in Bonnell and Bate (2006) and Eq. 2.2 from chapter 2, respectively. We have used a value for the relative velocity of the gas of $v_{\rm RMS}$=2.2 km s^{-1}, using Eq. 2.3 of chapter 2 and the typical linewidth measured in OMC1-S, Δv ~3 km s^{-1}. The volume and surface densities used are ρ=1.3×10^{-17} g cm^{-3} and Σ=3.5 g cm^{-2}.

8.4.2 Effects of outflow collisions

It is worth considering the impact on the turbulence of a phenomena that is rarely explored: outflow collisions. In the dense stellar clusters where massive stars form the probability of an encounter between two outflows is non negligible. In this section we show that there is evidence of an outflow collision in OMC1-S, and we discuss its implications for the formation of massive stars.

Fig. 6.1 (chapter 6) shows that two molecular outflows arising from the very dense stellar cluster located in OMC1-S(S) (the SO and SiO 137-408 SE outflows) have likely collided. Given that the presence of outflows is ubiquitous in star-forming regions, and that it is believed that every star might power an outflow during their formation process, it seems likely that two outflows could encounter in dense clusters like the one found in OMC1-S.

We can estimate the probability of a collision between two coeval molecular outflows with the expression:

$$P = (\rho_* \, \pi R^2 L)^2, \tag{8.11}$$

where R and L are the radius and length of the outflow, respectively, and n_* the number density of stars.

Beltrán et al. (2012) already detected an encounter between two molecular outflows in the star-forming region IC 1396N. They calculated a probability of encounter of two outflows in this cluster of 5% (P ∼0.05). In OMC1-S(S), considering the dense concentration of stars of $\rho_* \sim 7.0{\times}10^5$ stars pc^{-3} and the mean sizescales of the outflows (L ∼15" and R ∼1.25"), we derived a probability of $P \sim 0.17$. This means that the effect of collisions is not negligible, which is consistent with our claimed collision of the SiO and SO outflows.

The lower right panel of Fig. 6.1 shows that the SO outflow knots do not follow a straight path, but they have a bending trajectory. We suggest that the SO outflow originates in COUP 594 and, when it reaches knot C, the outflow deviates leading to the formation of knot D. From knot C, both SO and SiO outflows share the same path, as if these two flows may have interacted. The SiO outflow could inject energy into the SO outflow, explaining the deflection in its trajectory. The initial orientation of the SO outflow could gradually change by the interaction with the SiO outflow. This is consistent with the fact that the SiO outflow is slowing down as it moves away from its driving source (Zapata et al. 2006). This energy loss would be used to deviate the SO outflow.

The interaction between both outflows might explain the rotation observed around the SO outflow axis. Zapata et al. (2007) found asymmetries (see their Fig. 3) in the velocities of the outer SO knots (C and D). However, they claimed that the rotation is much less evident or absent in the innermost knots A and B. This may indicate that the outflow initially does not exhibit rotation or a very slight rotation, until it encounters the SiO outflow, at knot C, where the tangential forces produced by the SiO outflow induce rotation in the gas traced by SO.

Murphy et al. (2008) studied the encounter of two outflows where the interference clearly affects their subsequent evolution. In their study one of the outflows is engulfed into the second one, as observed in OMC1-S[9]. Cunningham et al. (2006) simulated the collision of two outflows, finding that the interaction, contrary to generate more turbulence in the region, reduces the transfer of momentum into the region. This is because the gas compression produced by the radiative collision shock remains within a more spatially confined region than if the outflows would have collided. As a consequence, one would expect that the collision of outflows could decrease the level of turbulence with respect to that without encounters. This would favor the Bondi-Hoyle accretion from the distributed gas component, specially in the center of the cluster, where the higher stellar density facilitates the collisions and where the accretion is higher due to the gravitational attraction of the potential well. This would favor that the "privileged" low-mass stars could accrete enough mass to become massive. Obviously, only a fraction of the outflows in the cluster would collide, and the total impact on the clump turbulence and clump evolution is probably minor, although more theoretical efforts are needed to properly evaluate this effect.

8.5 Summary and conclusions

Since the massive star-forming regions OMC1-S and MonR2 harbors multiple young molecular outflows, we have evaluated in this chapter the impact of outflow feedback in star formation and particularly in massive star formation. Based on the fraction of stars driving outflows we have estimated that star formation has been ocurring during periods clearly longer than the typical free-fall times of the parental gas clumps, indicating that some agent has been acting to prevent a rapid collapse. We have confirmed that molecular outflows are good candidates to provide this required support,

[9] We note however that Murphy et al. (2008) considered a close binary in their simulations with a separation of 45 AU, while the separation of the driving sources of the SO and SiO outflows is ∼1300 AU.

because they are able to injects enough amount of energy to replenish the decay of initial turbulence.

The presence of multiple molecular outflows in the these two dense stellar clusters suggests that the outflow feedback do not seem to hinder fragmentation, but it may favor that the parental clump fragments into multiple smaller and denser cores, giving birth to the observed crowded clusters of PMS low-mass stars.

In OMC1-S, the expected injection of turbulence into the region is high, and could explain the observed gas velocity dispersion. If the outflow feedback observed now continues throughout the entire lifetime of the clump, it may finally disrupt it through the ejection of matter. However, a significant fraction of material would have been already converted into stars before suffering the ejection by outflows.

In the MonR2 region, the large-scale CO outflow may contribute to the gas velocity dispersion of the clump and may be able to expel a fraction of the material outside the clump. On the other hand, the small-scale outflows revealed by SMA provide a negligible contribution to the gas velocity dispersion of the central region.

The outflow-driven turbulence arising from the young stars in OMC1-S and the central region of MonR2 barely affect the overall star formation efficiency in these two regions, allowing the formation of the observed dense stellar clusters with star formation efficiencies in the typical range found for other star-forming regions. Only the very high-energetic large-scale outflow in MonR2 has the potential to decrease (in a factor of $\sim$0.8) the star formation efficiency due to expulsion of material.

We show that the injection of turbulence produced by the young stellar clusters is still compatible with the idea that Bondi-Hoyle accretion gather enough mass in a timescale of a few 10^5 yr to form massive stars. This agrees with the competitive accretion scenario proposed in previous chapters for the formation of the massive stars in these regions.

CHAPTER 9

Summary and Main Conclusions

The formation of massive stars (M>8 $M_{\odot}$) remains one of the most debated topic in modern Astrophysics. Indeed, although the formation of low-mass stars is quite well understood, the mechanisms involved in the formation of massive stars are still unclear. Their fast evolution along with the large amount of extinction which characterizes their birth regions, complicate their study. These stars need high accretion rates to become massive in short timescales (of severals 10^5 yr).

Two models have been proposed in order to explain how these objects gather mass: i) the monolithic gravitational collapse and core accretion; ii) the competitive accretion of material by low- and intermediate-mass stars. The first model implies low levels of fragmentation of the parental gas condensation, forming either a single isolated star or a system formed by a few objects. On the other hand, the competitive accretion scenario requires high levels of fragmentation resulting in a dense population of low-mass stars. According to this scenario, the stars located in the central potential wells generated by the cluster are able to accrete gas and then become massive objects.

For this reason, the study of the distribution of young PMS low-mass stars in massive star-forming regions is key to discriminate between the two proposed scenarios. This PMS population is deeply embedded in the parental molecular cloud where high amounts of gas and dust are present, which prevent their detection in the optical and even in the near-IR wavelengths. Only X-ray, radio/(sub)millimeter and very deep IR observations are able to penetrate into the massive star cradles, since they are barely affected by extinction.

This thesis is thus focused on the role of young PMS low-mass star clusters in three nearby regions of massive star formation ($d < 1.5$ kpc): Orion, DR21 and Monoceros R2. The main objectives of this work are the following:

i) The analysis of the distribution of the PMS low-mass star population in Orion, DR21 and Monoceros R2, using X-ray data obtained from the space telescope *Chandra* along with deep IR observations.

ii) The study of the radiocontinuum emission of young stars in the Orion Nebula Cluster and Molecular Cloud, using observations in 14 different epochs carried out with the Very Large Array (VLA) interferometer.

iii) The study of the molecular enviroment and the thermal emission of the most massive objects in Monoceros R2, from new (sub)millimeter observations carried out with the Submillimeter Array (SMA) interferometer.

iv) The evaluation of the role of the outflow-driven turbulence in two massive star-forming regions, such as the Orion OMC1-S and the central region of Monoceros R2.

The main results and conclusions of this thesis are the following:

★ Massive stars are born within dense low-mass star subclusters

The spatial distribution analysis of the PMS low-mass stellar populations in the Orion, DR21 and MonR2 clusters has been considered. Two methods have been used to this aim: i) the spatial gridding method; and ii) the close neighbours method. The results derived show that the close vicinity of massive stars (0.03−0.05 pc) contains a dense population of low-mass stars (>10^5-10^6 stars pc^{-3}). This suggests that the parental molecular condensations have suffered high levels of fragmentation, forming subclusters of stars with a typical mass similar to the Jeans mass ($\sim$ 1 M$_\odot$). This scenario is in agreement with the competitive accretion theory, rather than the monolithic collapse scenario.

Our analysis suggests that the formation of massive stars needs at least two ingredients: i) dense gas; and ii) the presence of a subcluster of low-mass stars, consistently with the competitive accretion scenario. Once the stellar cluster is formed, the regions with high stellar densities create local gravitational potential wells which are able to attract the remaining gas available after the fragmentation process. We have confirmed that objects located within dense stellar subclusters are able to accrete enough mass to become massive through the Bondi-Hoyle mechanism in timescales of several 10^5 yr.

The material can be funneled towards these dense subclusters through infalling filaments of gas and dust moving towards the potential gravitational wells. In the three clusters studied in this thesis there is evidence of dusty and molecular filaments going towards the region where massive star formation occurs. Furthermore, this process can feed new events of star formation, being able to explain the age segregation

found in the clusters. Indeed, the youngest objects - Class I objects - are generally found in the central regions while the most evolved objects are characterized by a more uniform distribution.

As a consequence of the competitive accretion, a large concentration of gas and dust (and thus high extinctions), is expected in regions with high stellar density, where massive stars form. The analysis of the extinction distribution in the three stellar clusters confirmed this trend. In particular, the stellar clusters DR21 and MonR2 show an extinction profile which peaks in the central regions. For what concerns the Trapezium Cluster (which harbors MS massive stars), we have found for the first time that the stars located close to the most massive object, θ^1 *Ori C*, are more extincted than the those found at larger distances.

The analysis of the cumulative stellar density radial profile in the the Orion Hot Core, DR21 and MonR2 has revealed that these young stellar clusters are characterized by a radial profile following the r^{-2} law, with the exception of the inner region, where the profile is shallower. The X-ray population deviates less from the r^{-2} profile than the IR population. This result can be explained as due to the extinction distribution, which is higher in the inner region and thus prevents the detection of a fraction of objects. The similarity of the radial profile found in the three clusters suggest that this could be a common feature of stellar clusters at the first stages of the evolution. If this profile is confirmed in a larger number of young regions, it will give us more clues about the cluster formation processes.

In both the Orion Trapezium and DR21 clusters a mass segregation has been found, with the most massive objects located close to the center. In the MonR2 region, although a mass segregation is not compelling, it is clear that the most massive objects have formed in the central region of the cluster. This is what we expect if the competitive accretion scenario takes place, in which the global potential gravitational well generated by the stellar cluster can accrete material towards the inner regions.

★ Role of outflow-driven turbulence in massive star formation

Since massive stars are born escorted by a dense population of PMS low-mass stars, we have studied how the outflow-driven turbulence can affect cluster and massive star formation. We have found that the injection of energy is able to replenish the decay of initial turbulence. As a consequence, the natal condensation do not collapse in its rapid free-fall time, as expected in absece of outflow-driven support. This allows star formation during a longer period. On one hand, the gas can form overdensities

which will collapse and form new stars. On the other hand, the stars located at the center of gravitational potential wells can accrete more material and became massive. The detection of multiple outflows in compact regions (r<0.15 pc) in OMC1-S and MonR2 massive star cradles confirms this scenario.

In the case of OMC1-S, the outflow-driven turbulence is able to produce the detected velocity dispersion of the gas. Whether the outflow feedback in this region is maintained throughout the entire lifetime of the clump, it could potentially disrupt it. However, a significant fraction of gas would be already accreted by the stellar cluster before suffering ejection by outflows.

In the case of the central region of MonR2, the multiple outflows we have detected have negligible impact in the velocity dispersion of the gas or in the disruption of the natal condensation. However, the highly-energetic large-scale CO outflows can contribute to the velocity dispersion of the gas and it could be able to eject a fraction of the natal material. In any case, the presence of a high-dense stellar cluster of low-mass stars in the center of the region, including several massive objects, clearly indicates that this kind of high-energetic outflows do not inhibit completely the star formation.

It is possible that a collision between outflows occur in very dense and young stellar clusters. We propose that two of the outflows detected in the OMC1-S regions have likely collided. According with theoretical models, this kind of interactions, instead of generating more turbulence, reduces the transfer of momentum into the region.

★ Short- and long-term radiovariability from young stars in the ONC/OMC region

Our multi-epoch radiocontinuum monitoring of the ONC/OMC region have revealed emission from 19 sources, mainly concentrated in the Trapezium Cluster and the Orion Hot Core . All the sources show clear variability on timescales of months, with the exception of the massive object Becklin-Neugebauer (BN) and the source C (associated with a proplyd). Moreover, we have confirmed shor-term radiovariability (timescales from hours to days) in 5 of the sources. One of them, OHC-E, has been detected for the first time. Furthermore, we have confirmed variability (in long- and short-term timescales) towards the massive source I.

Combining our radio sample with other radio and X-ray catalogs, we have studied the properties of the entire sample of radio/X-ray stars in the region (55 sources). We

have classified these objects cross-correlating them with optical and IR surveys, and comparing with the distribution of the dense molecular gas from the OMC. We obtain the following membership: 42 ONC stars, 11 stars still embedded in the OMC, one extragalactic object and one object with uncertain classification (embedded member of the OMC or extragalactic).

We conclude that the radio emission is due to two different mechanisms:

i) gyrosynchrotron non-thermal emission produced by accelerated electrons in the magnetosphere of PMS low-mass stars. This emission is highly variable, and sometimes flaring (timescales of hours to days).

ii) thermal emission due to free-free radiation from ionized gas and/or heated dust around embedded massive objects and proplyds.

We have detected a high radio flaring rate in the dense subcluster embedded in the OHC ($\sim$0.14 flares day^{-1}). This suggests that these events are more common than previously thought during the earliest phases of stellar evolution.

The comparison between the stars detected with radio and X-ray observations reveals that the radio wavelengths have mainly detected the brighter X-ray sources. This confirms a link between the X-ray activity and the origin of the radiocontinuum emission. Furthermore, it suggest that the improved sensitivity of the new VLA and ALMA will surely increase the number of young stars detected at radio wavelengths. Therefore, we will be able to better characterize the low-mass stellar densities in embedded massive star cradles through its emission at radio wavelengths; and we will improve our knowledge of the nature of this radio emission.

★ Massive stars, hot molecular cores and molecular outflows in Monoceros R2

The SMA ^{12}CO(2-1) image towards MonR2 reveal 11 previously unknown molecular outflows in the central region (r <0.15 pc) of this stellar cluster, which argues in favor of the competitive accretion scenario as origin of this stellar cluster. The (sub)millimeter continuum images have revealed thermal emission towards the massive objects IRS1, IRS2, IRS3 and IRS5. The emission from IRS1 and IRS2 is dominated by free-free radiation, while that from IRS3 and IRS5 appears to be dominated by dust emission. In addition, the images of molecular emission from species such as CH_3CN, CH_3OH or SO_2 show the presence of two hot molecular cores towards IRS3 and IRS5 (T >125-230 K). The IRS5 hot core is the most chemically active source in the region. The Spectral Energy Distribution (SED) analysis of IRS5 gives a mass

for the central source of $\sim$7 $M_{\odot}$ and a luminosity of $\sim$300 $L_{\odot}$.

★ Stellar collisions producing highly-energetic and large-scale outflows

We have proposed that the highly-energetic and large scale outflows detected towards these three massive star forming regions might be originated by violent stellar collisions. From a simple analysis of the physical mechanism involved in these processes, we consider likely a single stellar collision within these high density subclusters ($>10^5-10^6$ estrellas pc^{-3}). This coalescence can be favored by the presence of circumstellar disks, stellar binaries and accretion of material.

CHAPTER 10

Conclusiones

La formación de las estrellas masivas ($M>8M_{\odot}$) sigue siendo uno de los temas más debatidos de la Astrofísica moderna. Al contrario de lo que sucede con las estrellas de baja masa, todavía no se conocen bien los mecanismos que desembocan en el nacimiento de las estrellas masivas. Sus rápidos tiempos de evolución y las grandes extinciones de las regiones donde se forman complican mucho su estudio. Estas estrellas necesitan de altas tasas de acreción de material para llegar a alcanzar sus elevadas masas finales en tiempos de evolución muy cortos (del orden de 10^5 años).

Se han propuesto dos modelos principales para intentar explicar cómo estos objetos pueden acumular la suficiente masa para convertirse en estrellas masivas: i) el colapso gravitacional monolítico de la condensación de gas natal; ii) la acreción competitiva en el seno de un cúmulo de estrellas de baja masa. El primer modelo supone que la condensación natal apenas sufre fragmentación, formando una única estrella aislada o un sistema múltiple con pocos objetos. Por el contrario, el modelo de acreción competitiva requiere altos niveles de fragmentación de la condensación natal, dando como resultado un cúmulo de estrellas de baja masa. En este escenario, las estrellas situadas en el centro del potencial gravitacional creado por el cúmulo son aquellas que pueden seguir acretando gas (remanente del proceso de fragmentación), y convertirse en objetos masivos.

Por lo tanto, el estudio de la distribución de la población de estrellas de baja masa muy jóvenes (aún en la fase de pre-secuencia principal) en las regiones de formación estelar masiva es fundamental a la hora de discriminar entre los dos modelos planteados. Esta población se encuentra generalmente aún muy embebida en el gas y polvo natal, por lo que no se puede detectar con observaciones ópticas o incluso infrarrojas. Por ello, las longitudes de onda más adecuadas para observar estas regiones son las radio-ondas, las ondas (sub)milimétricas y los rayos X, que se ven poco afectadas por la extinción.

Esta tesis se ha centrado en el estudio del papel que juegan los cúmulos de estrellas de masa baja (en fase de pre-secuencia principal) en tres regiones de formación

estelar masiva cercanas (d <1.5 kpc): Orión, DR21 y Monoceros R2. Los principales objetivos de estudio han sido:

i) El análisis de la distribución de la población de baja masa en estos tres cúmulos, utilizando para ello catálogos de rayos X obtenidos a partir de observaciones del telescopio espacial *Chandra*, complementados con observaciones IR profundas.

ii) El estudio de la emisión del radiocontinuo de las estrellas jóvenes de la Nebulosa de Orión y de la Nube Molecular de Orión situada detrás, mediante observaciones en 14 épocas distintas con el interferómetro *Very Large Array* (VLA).

iii) El estudio del entorno molecular y de la emisión térmica de los objetos más masivos de Monoceros R2, a partir de nuevas observaciones (sub)milimétricas realizadas con el interferómetro *Submillimeter Array* (SMA).

iv) La evaluación del impacto de la turbulencia producida por múltiples *outflows* moleculares en las regiones de formación estelar masiva situadas en la region OMC1-S de Orión y en la parte central de cúmulo estelar de MonR2.

Los principales resultados y conclusiones de esta tesis se exponen a continuación:

★ Las estrellas masivas nacen en el seno de cúmulos de estrellas jovenes de baja masa

Hemos realizado el análisis de la distribución espacial de la población de baja masa en los cúmulos de Orión, DR21 y MonR2. Para ello hemos utilizado dos métodos: i) método *de malla*; y ii) método de vecinos cercanos. Los resultados obtenidos en los tres cúmulos estelares muestran que las estrellas masivas están acompañadas por estrellas de baja masa en su entorno más cercano ($\sim$0.03$-$0.05 pc). Es decir, las estrellas masivas nacen en el seno de densos subcúmulos de estrellas baja masa, con altas densidades estelares (>10^5-10^6 estrellas pc^{-3}). Esto implica que el grado de fragmentación de la condensación de gas natal ha sido elevado, formando un cúmulo de estrellas de masa en torno a la masa de Jeans ($\sim$ de 1 M$_\odot$). Este escenario concuerda con el modelo de acreción competitiva, en oposición al colapso monolítico.

Nuestro análisis sugiere que la formación de estrellas masivas se ve favorecida no sólo por la existencia de gas denso, sino también por la presencia de subcúmulos de estrellas de masa baja. Una vez formado el cúmulo estelar, las regiones de mayor densidad estelar crean potenciales gravitacionales que son capaces de atraer el gas circundante que ha quedado libre después del proceso de fragmentación. Hemos

comprobado que algunos de los objetos situados en el seno de densos subcúmulos estelares son capaces de acretar suficiente masa mediante el mecanismo de Bondi-Hoyle. Como consecuencia, estas estrellas se pueden convertir en masivas en escalas de tiempo del orden de 10^5 años.

Esta acreción puede realizarse mediante filamentos de gas y polvo que caen hacia los potenciales gravitacionales. En los tres cúmulos estelares estudiados hay evidencias de filamentos orientados hacia la región donde las estrellas masivas están formándose. Además, este proceso puede alimentar nueva formación estelar en estas regiones, lo que explicaría la segregación de edad observada en los cúmulos: estrellas con estados evolutivos más tempranos − objetos de Clase I − se encuentran en determinadas regiones (generalemente centrales), mientras que los objetos más evolucionados aparecen distribuidos de forma más uniforme.

Como consecuencia de la acreción competitiva, es de esperar que se produzca una concentración de gas y de polvo, y por tanto de la extinción, en las regiones con mayor densidad estelar (donde se forman los objetos masivos). Nuestro análisis de la distribución de la extinción ha mostrado que, en efecto, esto es así en los tres cúmulos estelares estudiados. Se ha encontrado que los cúmulos estelares de DR21 y MonR2 tienen un perfil de extinción con su máximo en el centro. En el cúmulo estelar del Trapezio de Orión (con estrellas masivas ya en fase de secuencia principal) se ha encontrado por primera vez que las estrellas situadas en torno al objeto más masivo, θ^1 *Ori C*, están más extinguidas que las situadas la region circundante.

El análisis del perfil radial de densidad estelar que hemos realizado en el *Hot Core* de Orión, DR21 y MonR2 ha revelado que estos cúmulos estelares jóvenes presentan un perfil radial que sigue aproximadamente r^{-2}, a excepción de las zonas más centrales, donde el perfil se hace más plano. La poblacion detectada con rayos X se aleja menos del perfil r^{-2} que la poblacion detectada con IR. Esto sugiere que este efecto es una consecuencia de la estructura de la extinción, que es mayor en el centro, y que no permite la detección de una fracción de los objetos situados en el centro de los cúmulos. El hecho de que hayamos encontrado un perfil radial muy similar en las tres regiones podría indicar que es una característica propia de cúmulos estelares jóvenes en sus primeras fases de evolución. Si este perfil se confirma en un número mayor de cúmulos, podría darnos pistas acerca de cómo es su proceso de formacíon.

Tanto en el Trapezio de Orión como en el cúmulo de DR21, se ha encontrado una segregación en masa, con objetos más masivos situados hacia las partes centrales. En el caso de MonR2, aunque no se ha confirmado una segregación en masa general, está

claro que los objetos más masivos se han formado en el centro del cúmulo. Este escenario es el esperable en un contexto donde la acreción competitiva ha permitido mayor acumulación de masa en las regiones centrales, por efecto del potencial gravitacional global del cúmulo estelar.

★ Impacto de la turbulencia inyectada por "outflows" moleculares en la formación de estrellas masivas

Dado que hemos encontrado que las estrellas masivas nacen acompañadas de una población densa de estrellas de baja masa muy jóvenes, hemos estudiado como la turbulencia inyectada por múltiples *outflows* moleculares puede afectar a la formación del cúmulo y de las estrellas más masivas. Hemos encontrado que esta inyección de energía puede ser capaz de compensar el decaimiento de la turbulencia inicial de la condensación natal. Por tanto, la condensación no colapsa rápidamente en su tiempo de *caída libre*, como se esperaría en ausencia de la turbulencia producida por los *outflows*. Esto permite que el proceso de formación estelar se prolonge en el tiempo. Por un lado, el gas puede formar subestructuras con núcleos de gas más denso que acaban fragmentándose y formando nuevas estrellas. Por otro lado, las estrellas favorecidas por el pozo de potencial pueden seguir acumulando masa hasta llegar a ser masivas. La detección de múltiples outflows en OMC1-S y en MonR2 en regiones compactas (r<0.15 pc) donde se produce formación estelar masiva confirma este escenario.

En el caso de la región de OMC1-S, la inyección de energía propocionada por el cúmulo de *outflows* podría ser capaz de producir la dispersión de velocidad del gas detectada a partir de observaciones moleculares de gas denso. Además, si el impacto de los *outflows* se mantuviera a lo largo de la vida de la condensación de gas natal, podría llegar a producirse su disgregación, interumpiendo así la formación estelar. Sin embargo, llegado ese momento, una fracción muy importante del gas inicial ya habría sido acretado por las estrellas.

En el caso de la región central del cúmulo de MonR2, los múltiples *outflows* que hemos detectado parecen tener poca influencia en la dispersión de velocidad del gas circundante o en una posible disgregación de la condensación de gas. Sin embargo, el *outflow* enérgetico de gran tamaño sí que puede contribuir a la dispersión de velocidad del gas y podría ser capaz de expulsar parte del gas de la región central. En todo caso, la presencia de un denso cúmulo estelar de baja masa en el centro de la región, incluyendo varios objetos masivos, indica que *outflows* de este tipo no son capaces de

inhibir completamente la formación estelar.

En el caso de cúmulos estelares jóvenes muy densos, donde múltiples *outflows* moleculares se generan al mismo tiempo en regiones muy compactas, es posible que algunos de ellos puedan colisionar. Hemos propuesto que dos de los *outflows* observados en OMC1-S pueden haber sufrido una interación. De acuerdo con modelos teóricos, estas interacciones, en lugar de aumentar la turbulencia inyectada en el entorno, reducirían el impacto de los *outflows*.

★ Radio-variabilidad en diferentes escalas temporales de las estrellas jóvenes de Orión

Nuestras observaciones multiépoca de la emisión del radiocontinuo han detectado emisión procedente de 19 fuentes, concentradas principalmente en el cúmulo del Trapecio y en el *Hot Core*. Con la excepción del objeto masivo Becklin-Neugebauer (BN) y de la fuente C (asociada a un *proplyd*) hemos detectado radiovariabilidad en todas las estrellas en escalas temporales de meses. En escalas de tiempo más cortas (de horas a días) hemos confirmado variabilidad en 5 de las estrellas. Una de estas radio-fuentes, OHC-E, ha sido detectada por primera vez. Además, hemos confirmado variabilidad (tanto en escalas de tiempo mensuales como de horas) en la protoestrella masiva conocida como fuente I.

Comparando nuestro catálogo de radio fuentes con otras observaciones de radio y con el catálogo proporcionado por *Chandra*, hemos elaborado la muestra de fuentes que emiten radio-ondas y rayos X en la region (55 fuentes). Hemos clasificado los objetos de esta muestra comparando con observaciones en el óptico y en el IR y con la distribución de gas molecular, y utilizando los valores de $N_{\rm H}$ obtenidos con los rayos X: 42 son estrellas de la Nebulosa de Orión; 11 son estrellas aún embebidas en la nube molecular situada detrás; una fuente es un objeto extragaláctico; y un objeto tiene clasificación incierta (miembro embebido en la nube molecular o extragaláctico).

Nuestro análisis concluye que la emisión de radio-ondas se debe a dos tipos de mecanismos:

i) radiación girosincrotrón (no térmica) debida a la aceleración de electrones en la magnetosfera de estrellas de baja masa en fase de pre-secuencia principal. Esta emisión es muy variable, y en ocasiones se presenta en forma de rápidas fulguraciones en escalas de tiempo cortas (horas o días).

ii) radiación térmica debida a emisión libre-libre de gas ionizado y/o a emisión de polvo caliente, situados en las inmediaciones de objetos masivos o *proplyds*.

Hemos detectado una alta tasa de radio-fulguraciones en el cúmulo estelar denso embebido en el *hot core* de Orión ($\sim$0.14 fulguraciones día^{-1}). Esto indica que estos eventos parecen ser más frecuentes durante las primeras fases de evolución estelar de lo que se pensaba anteriormente.

La comparación de las estrellas detectadas tanto en radio-ondas como en rayos X revela que las observaciones de radio-ondas han detectado principalmente sólo las fuentes más brillantes en rayos X. Esto confirma que existe una relación entre la actividad de rayos X y los mecanismos que producen la emisión de radio-ondas. Además, sugiere que la mejorada sensibilidad del nuevo VLA y de ALMA puede incrementar considerablemente el número de estrellas jóvenes detectadas con observaciones radio. Esto nos ayudará a entender mejor el origen de la emisión de radio-ondas procedente de estos objetos, y abre la posibilidad de detectar la población de estrellas de baja masa embebida en las regiones de formación estelar masiva.

★ Estrellas masivas, "hot molecular cores" y "outflows" en Monoceros R2

Nuestras observaciones moleculares de ^{12}CO(2-1) han revelado la presencia de de hasta 11 *outflows* moleculares no detectados anteriormente en la región central (r <0.15 pc) de este cúmulo estelar. Las imágenes del continuo (sub)milimétrico han detectado la emisión de los objetos más masivos de la región: IRS1, IRS2, IRS3 y IRS5. La emisión procedente de IRS1 y IRS2 está producida por radiación libre-libre del gas ionizado en torno a estos objetos, mientras que la emisión de IRS3 y IRS5 está dominada por emisión del polvo de sus envolturas. El análisis de la emisión molecular de especies como CH_3CN, CH_3OH o SO_2, ha confirmado la presencia de dos *hot cores* moleculares en torno a IRS3 y IRS5 (T >125-230 K), que indican estados evolutivos muy tempranos de formación estelar masiva. El *hot core* asociado a IRS5 es la región químicamente más activa de la region. El estudio de su distribución espectral de energía muestra que este *hot core* aloja en su interior una estrella en fase muy temprana de masa $\sim$7 $M_\odot$ y luminosidad $\sim$300 $L_\odot$

★ Colisiones estelares en densos subcúmulos como origen de "outflows" energéticos a gran escala

Proponemos que los *outflows* energéticos a gran escala que se han observado en los tres cúmulos estelares observados pueden tener su origen en violentas colisiones estelares. A partir de un análisis simple de la física involucrada en estos procesos, consideramos plausible que se haya producido una colisión estelar en estas regiones de

formación de estrellas masivas con densidades estelares muy altas ($>10^5-10^6$ estrellas pc^{-3}). Este proceso se vería favorecido por la existencia de discos circunestelares, binarias y procesos de acreción, todos ellos presentes en cúmulos estelares en fase de formación como los estudiados en esta tesis.

Publications

Accepted refereed publications related to this thesis

'The role of low-mass star clusters in forming the massive stars in DR 21', **V. M. Rivilla**, I. Jiménez-Serra, J. Martín-Pintado, J. Sanz-Forcada', MNRAS, 437:1561-1575, January 2014, doi:10.1093/mnras/stt1989; arXiv:1307.528, http://arxiv.org/abs/1310.4049.

'X-ray embedded stars as driving sources of outflow-driven turbulence in OMC1-S', **V. M. Rivilla**, J. Martín-Pintado, J. Sanz-Forcada, I. Jiménez-Serra, A. Rodríguez-Franco, MNRAS, 434:2313-2328, September 2013, doi: 10.1093/mnras/stt1173; arXiv:1307.528, http://arxiv.org/abs/1307.5283

'The role of low mass star clusters in massive star formation. The Orion case', **V. M. Rivilla**, J. Martín-Pintado, I. Jiménez-Serra, A. Rodríguez-Franco, A&A, 554: A48, June 2013, doi: 10.1051/0004-6361/201117487; arXiv:1302.2763, http://arxiv.org/abs/1302.2763

'A New Radio Recombination Line Maser Object toward the MonR2 H II Region', I. Jiménez-Serra, A. Baéz-Rubio, **V.M. Rivilla**, J. Martín-Pintado, Q. Zhang, M. Dierickx, N. Patel, ApJ, 764:L4, February 2013, doi: 10.1088/2041-8205/764/1/L4; arXiv:1212.0792, http://arxiv.org/abs/1212.0792

Submitted papers related to this thesis

'Short- and long-term radio variability of young stars in the Orion Nebula Cluster and Molecular Cloud', **V. M. Rivilla**, C.J. Chandler, J. Sanz-Forcada, I. Jiménez-Serra, J. Forbrich, J. Martín-Pintado, submitted to ApJ.

'Submillimeter Array high-angular resolution observations of the Monoceros R2 Star Forming Cluster', M. Dierickx, I. Jiménez-Serra, **V. M. Rivilla**, and Q. Zhang, submitted to ApJ.

Papers in preparation related to this thesis

'The role of low-mass star clusters in forming the massive stars in Monoceros R2', **V.M. Rivilla**, I. Jiménez-Serra, J. Martín-Pintado, J. Sanz-Forcada, in preparation to submit to MNRAS.

Other Accepted Publications

'SDC13 infrared dark clouds: Longitudinally collapsing filaments?', N. Peretto, G. A. Fuller, Ph. André, D. Arzoumanian, **V.M. Rivilla**, S. Bardeau, S. Duarte Puertas, J. P. Guzman, C. Lenfestey, G.-X. Li, F. A. Olguin, B. R. Röck, H. de Villiers, J. Williams, A&A, 561:A835, January 2014, doi:10.1051/0004-6361/201322172; arXiv:1311.0203 http://arxiv.org/abs/1311.0203

Bibliography

D. A. Allen and M. G. Burton. Explosive ejection of matter associated with star formation in the Orion nebula. *Nature*, 363:54–56, May 1993. doi: 10.1038/363054a0. URL http://adsabs.harvard.edu/abs/1993Natur.363...54A.

L. E. Allen, N. Calvet, P. D'Alessio, B. Merin, L. Hartmann, S. T. Megeath, R. A. Gutermuth, J. Muzerolle, J. L. Pipher, P. C. Myers, and G. G. Fazio. Infrared Array Camera (IRAC) Colors of Young Stellar Objects. *ApJS*, 154:363–366, September 2004. doi: 10.1086/422715. URL http://adsabs.harvard.edu/abs/2004ApJS..154..363A.

R. J. Allison, S. P. Goodwin, R. J. Parker, S. F. Portegies Zwart, R. de Grijs, and M. B. N. Kouwenhoven. Using the minimum spanning tree to trace mass segregation. *MNRAS*, 395:1449–1454, May 2009. doi: 10.1111/j.1365-2966.2009.14508.x. URL http://adsabs.harvard.edu/abs/2009MNRAS.395.1449A.

C. Alvarez, M. Hoare, A. Glindemann, and A. Richichi. Near-IR speckle imaging of massive young stellar objects. *Astron. Astrophys.*, 427:505–518, November 2004. doi: 10.1051/0004-6361:20034438. URL http://adsabs.harvard.edu/abs/2004A%26A...427..505A.

M. Andersen, M. R. Meyer, B. Oppenheimer, C. Dougados, and J. Carpenter. NICMOS2 Hubble Space Telescope Observations of the Embedded Cluster Associated with Mon R2: Constraining the Substellar Initial Mass Function. Astron. J., 132:2296–2308, December 2006. doi: 10.1086/508485. URL http://adsabs.harvard.edu/abs/2006AJ....132.2296A.

P. André. Observations of protostars and protostellar stages. In T. Montmerle, C. J. Lada, I. F. Mirabel, & J. Tran Thanh Van , editor, *The Cold Universe, Proceedings of the 28th Rencontre de Moriond, Les Arcs, France, March 13-20, 1993.*, page 179, 1994. URL http://adsabs.harvard.edu/abs/1994coun.conf..179A.

P. Andre. Radio Emission as a Probe of Large-Scale Magnetic Structures Around Young Stellar Objects. In A. R. Taylor & J. M. Paredes, editor, *Radio Emission from the Stars and the Sun*, volume 93 of *Astronomical Society of the Pacific Conference Series*, page 273, 1996. URL http://adsabs.harvard.edu/abs/1996ASPC...93..273A.

P. Andre, D. Ward-Thompson, and M. Barsony. Submillimeter continuum observations of Rho Ophiuchi A - The candidate protostar VLA 1623 and prestellar clumps. *Astrophys. J.*, 406:122–141, March 1993. doi: 10.1086/172425. URL http://adsabs.harvard.edu/abs/1993ApJ...406..122A.

P. André, A. Belloche, F. Motte, and N. Peretto. The initial conditions of star formation in the Ophiuchus main cloud: Kinematics of the protocluster condensations. *Astron. Astrophys.*, 472:519–535, September 2007. doi: 10.1051/0004-6361:20077422. URL http://adsabs.harvard.edu/abs/2007A%26A...472..519A.

E. D. Araya, S. Kurtz, P. Hofner, and H. Linz. Radio Continuum and Methanol Observations of DR21(OH). *ApJ*, 698:1321–1329, June 2009. doi: 10.1088/0004-637X/698/2/1321. URL http://adsabs.harvard.edu/abs/2009ApJ...698.1321A.

H. G. Arce, D. Shepherd, F. Gueth, C.-F. Lee, R. Bachiller, A. Rosen, and H. Beuther. Molecular Outflows in Low- and High-Mass Star-forming Regions. *Protostars and Planets V*, pages 245–260, 2007. URL http://adsabs.harvard.edu/abs/2007prpl.conf..245A.

H. G. Arce, M. A. Borkin, A. A. Goodman, J. E. Pineda, and M. W. Halle. The COMPLETE Survey of Outflows in Perseus. *ApJ*, 715:1170–1190, June 2010. doi: 10.1088/0004-637X/715/2/1170. URL http://adsabs.harvard.edu/abs/2010ApJ...715.1170A.

K. Arzner, M. Güdel, K. Briggs, A. Telleschi, and M. Audard. Statistics of superimposed flares in the Taurus molecular cloud. *Astron. Astrophys.*, 468:477–484, June 2007. doi: 10.1051/0004-6361:20066551. URL http://adsabs.harvard.edu/abs/2007A%26A...468..477A.

C. Aspin and D. M. Walther. Infrared imaging polarimetry of Monoceros R2 IRS. *Astron. Astrophys.*, 235:387–394, August 1990. URL http://adsabs.harvard.edu/abs/1990A%26A...235..387A.

J. Bally and H. Zinnecker. The Birth of High-Mass Stars: Accretion and/or Mergers? *AJ*, 129:2281–2293, May 2005. doi: 10.1086/429098. URL http://adsabs.harvard.edu/abs/2005AJ....129.2281B.

J. Bally, C. R. O'Dell, and M. J. McCaughrean. Disks, Microjets, Windblown Bubbles, and Outflows in the

Orion Nebula. *AJ*, 119:2919–2959, June 2000. doi: 10.1086/301385. URL http://adsabs.harvard.edu/abs/2000AJ....119.2919B.

I. Baraffe and G. Chabrier. Effect of episodic accretion on the structure and the lithium depletion of low-mass stars and planet-hosting stars. *Astron. Astrophys.*, 521:A44, October 2010. doi: 10.1051/0004-6361/201014979. URL http://adsabs.harvard.edu/abs/2010A%26A...521A..44B.

I. Baraffe, G. Chabrier, F. Allard, and P. H. Hauschildt. Evolutionary models for solar metallicity low-mass stars: mass-magnitude relationships and color-magnitude diagrams. *Astron. Astrophys.*, 337:403–412, September 1998. URL http://adsabs.harvard.edu/abs/1998A%26A...337..403B.

M. R. Bate. Stellar, brown dwarf and multiple star properties from a radiation hydrodynamical simulation of star cluster formation. *Mon. Not. R. astr. Soc.*, 419:3115–3146, February 2012. doi: 10.1111/j.1365-2966.2011.19955.x. URL http://adsabs.harvard.edu/abs/2012MNRAS.419.3115B.

M. R. Bate and I. A. Bonnell. Computer Simulations of Star Cluster Formation via Turbulent Fragmentation. In H. J. G. L. M. Lamers, L. J. Smith, and A. Nota, editors, *The Formation and Evolution of Massive Young Star Clusters*, volume 322 of *Astronomical Society of the Pacific Conference Series*, page 289, December 2004. URL http://adsabs.harvard.edu/abs/2004ASPC..322..289B.

M. R. Bate, I. A. Bonnell, and V. Bromm. The formation of close binary systems by dynamical interactions and orbital decay. *Mon. Not. R. astr. Soc.*, 336:705–713, November 2002. doi: 10.1046/j.1365-8711.2002.05775.x. URL http://adsabs.harvard.edu/abs/2002MNRAS.336..705B.

M. R. Bate, I. A. Bonnell, and V. Bromm. The formation of a star cluster: predicting the properties of stars and brown dwarfs. *MNRAS*, 339:577–599, March 2003. doi: 10.1046/j.1365-8711.2003.06210.x. URL http://adsabs.harvard.edu/abs/2003MNRAS.339..577B.

W. Batrla, T. L. Wilson, K. Ruf, and P. Bastien. Clumping in molecular clouds - The region between OMC 1 and 2. *A&A*, 128:279–290, December 1983. URL http://adsabs.harvard.edu/abs/1983A%26A...128..279B.

S. Beckwith, N. J. Evans, II, E. E. Becklin, and G. Neugebauer. Infrared observations of Monoceros R2. *Astrophys. J.*, 208:390–395, September 1976. doi: 10.1086/154618. URL http://adsabs.harvard.edu/abs/1976ApJ...208..390B.

I. M. Beerer, X. P. Koenig, J. L. Hora, R. A. Gutermuth, S. Bontemps, S. T. Megeath, and et al. Schneider. A Spitzer View of Star Formation in the Cygnus X North Complex. *ApJ*, 720:679–693, September 2010. doi: 10.1088/0004-637X/720/1/679. URL http://adsabs.harvard.edu/abs/2010ApJ...720..679B.

M. T. Beltrán, F. Massi, F. Fontani, C. Codella, and R. López. Close encounters of the protostellar kind in IC 1396N. *A&A*, 542:L26, June 2012. doi: 10.1051/0004-6361/201219166. URL http://adsabs.harvard.edu/abs/2012A%26A...542L..26B.

H. Beuther, P. Schilke, F. Gueth, M. McCaughrean, M. Andersen, T. K. Sridharan, and K. M. Menten. IRAS 05358+3543: Multiple outflows at the earliest stages of massive star formation. *A&A*, 387:931–943, June 2002. doi: 10.1051/0004-6361:20020319. URL http://adsabs.harvard.edu/abs/2002A%26A...387..931B.

H. Beuther, S. Leurini, P. Schilke, F. Wyrowski, K. M. Menten, and Q. Zhang. Interferometric multi-wavelength (sub)millimeter continuum study of the young high-mass protocluster IRAS 05358+3543. *A&A*, 466:1065–1076, May 2007. doi: 10.1051/0004-6361:20066742. URL http://adsabs.harvard.edu/abs/2007A%26A...466.1065B.

J. Binney and S. Tremaine. *Galactic dynamics*. 1987. URL http://adsabs.harvard.edu/abs/1987gady.book.....B.

G. A. Blake, E. C. Sutton, C. R. Masson, and T. G. Phillips. Molecular abundances in OMC-1 - The chemical composition of interstellar molecular clouds and the influence of massive star formation. *Astrophys. J.*, 315:621–645, April 1987. doi: 10.1086/165165. URL http://adsabs.harvard.edu/abs/1987ApJ...315..621B.

I. A. Bonnell and M. R. Bate. Accretion in stellar clusters and the collisional formation of massive stars. *Mon. Not. R. astr. Soc.*, 336:659–669, October 2002. doi: 10.1046/j.1365-8711.2002.05794.x. URL http://adsabs.harvard.edu/abs/2002MNRAS.336..659B.

I. A. Bonnell and M. R. Bate. Binary systems and stellar mergers in massive star formation. *MNRAS*, 362:915–920, September 2005. doi: 10.1111/j.1365-2966.2005.09360.x. URL http://adsabs.harvard.edu/abs/2005MNRAS.362..915B.

I. A. Bonnell and M. R. Bate. Star formation through gravitational collapse and competitive accretion. *MNRAS*, 370:488–494, July 2006. doi: 10.1111/j.1365-2966.2006.10495.x. URL http://adsabs.harvard.edu/abs/2006MNRAS.370..488B.

I. A. Bonnell, M. R. Bate, and H. Zinnecker. On the formation of massive stars. *MNRAS*, 298:93–102, July 1998. doi: 10.1046/j.1365-8711.1998.01590.x. URL http://adsabs.harvard.edu/abs/1998MNRAS.298...93B.

I. A. Bonnell, M. R. Bate, C. J. Clarke, and J. E. Pringle. Competitive accretion in embedded stellar clusters. *MNRAS*, 323:785–794, May 2001a. doi: 10.1046/j.1365-8711.2001.04270.x. URL http://adsabs.harvard.edu/abs/2001MNRAS.323..785B.

I. A. Bonnell, C. J. Clarke, M. R. Bate, and J. E. Pringle. Accretion in stellar clusters and the initial mass function. *Mon. Not. R. astr. Soc.*, 324:573–579, June 2001b. doi: 10.1046/j.1365-8711.2001.04311.x. URL http://adsabs.harvard.edu/abs/2001MNRAS.324..573B.

I. A. Bonnell, M. R. Bate, and S. G. Vine. The hierarchical formation of a stellar cluster. *Mon. Not. R. astr. Soc.*, 343:413–418, August 2003. doi: 10.1046/j.1365-8711.2003.06687.x. URL http://adsabs.harvard.edu/abs/2003MNRAS.343..413B.

I. A. Bonnell, S. G. Vine, and M. R. Bate. Massive star formation: nurture, not nature. *MNRAS*, 349:735–741, April 2004. doi: 10.1111/j.1365-2966.2004.07543.x. URL http://adsabs.harvard.edu/abs/2004MNRAS.349..735B.

I. A. Bonnell, R. B. Larson, and H. Zinnecker. The Origin of the Initial Mass Function. *Protostars and Planets V*, pages 149–164, 2007. URL http://adsabs.harvard.edu/abs/2007prpl.conf..149B.

S. Bontemps, P. Andre, S. Terebey, and S. Cabrit. Evolution of outflow activity around low-mass embedded young stellar objects. *A&A*, 311:858–872, July 1996. URL http://adsabs.harvard.edu/abs/1996A%26A...311..858B.

S. Bontemps, F. Motte, T. Csengeri, and N. Schneider. Fragmentation and mass segregation in the massive dense cores of Cygnus X. *A&A*, 524:A18, December 2010. doi: 10.1051/0004-6361/200913286. URL http://adsabs.harvard.edu/abs/2010A%26A...524A..18B.

A. M. S. Boonman and E. F. van Dishoeck. Abundant gas-phase H_2O in absorption toward massive protostars. *Astron. Astrophys.*, 403:1003–1010, June 2003. doi: 10.1051/0004-6361:20030364. URL http://adsabs.harvard.edu/abs/2003A%26A...403.1003B.

A. M. S. Boonman, S. D. Doty, E. F. van Dishoeck, E. A. Bergin, G. J. Melnick, C. M. Wright, and R. Stark. Modeling gas-phase H_2O between 5 μ m and 540 μ m toward massive protostars. *Astron. Astrophys.*, 406:937–955, August 2003. doi: 10.1051/0004-6361:20030765. URL http://adsabs.harvard.edu/abs/2003A%26A...406..937B.

A. P. Boss. Protostellar Fragmentation Enhanced by Magnetic Fields. *Astrophys. J. L.*, 545:L61–L64, December 2000. doi: 10.1086/317332. URL http://adsabs.harvard.edu/abs/2000ApJ...545L..61B.

A. P. Boss. Protostellar formation in rotating interstellar clouds. VI - Nonuniform initial conditions. *Astrophys. J.*, 319:149–161, August 1987. doi: 10.1086/165441. URL http://adsabs.harvard.edu/abs/1987ApJ...319..149B.

M. Bossi, A. Gaspani, M. Scardia, and M. Tadini. Orionis A - A pre-main sequence low Q binary system? *Astron. Astrophys.*, 222:117–120, September 1989. URL http://adsabs.harvard.edu/abs/1989A%26A...222..117B.

G. C. Bower, R. L. Plambeck, A. Bolatto, N. McCrady, J. R. Graham, I. de Pater, M. C. Liu, and F. K. Baganoff. A Giant Outburst at Millimeter Wavelengths in the Orion Nebula. *ApJ*, 598:1140–1150, December 2003. doi: 10.1086/379101. URL http://adsabs.harvard.edu/abs/2003ApJ...598.1140B.

J. M. Carpenter and K. W. Hodapp. *The Monoceros R2 Molecular Cloud*, page 899. December 2008. URL http://adsabs.harvard.edu/abs/2008hsf1.book..899C.

J. M. Carpenter, M. R. Meyer, C. Dougados, S. E. Strom, and L. A. Hillenbrand. Properties of the Monoceros R2 Stellar Cluster. Astron. J., 114:198–221, July 1997. doi: 10.1086/118465. URL http://adsabs.harvard.edu/abs/1997AJ....114..198C.

J. J. Carroll, A. Frank, E. G. Blackman, A. J. Cunningham, and A. C. Quillen. Outflow-Driven Turbulence in Molecular Clouds. *ApJ*, 695:1376–1381, April 2009. doi: 10.1088/0004-637X/695/2/1376. URL http://adsabs.harvard.edu/abs/2009ApJ...695.1376C.

R. Cesaroni, D. Galli, G. Lodato, M. Walmsley, and Q. Zhang. The critical role of disks in the formation of high-mass stars. *Nature*, 444:703–706, December 2006. doi: 10.1038/nature05344. URL http://adsabs.harvard.edu/abs/2006Natur.444..703C.

G. Chabrier. Galactic Stellar and Substellar Initial Mass Function. *PASP*, 115:763–795, July 2003. doi: 10.1086/376392. URL http://adsabs.harvard.edu/abs/2003PASP..115..763C.

C. J. Chandler, W. K. Gear, and R. Chini. Dust emission associated with DR21 (OH). *MNRAS*, 260:337–342, January 1993. URL http://adsabs.harvard.edu/abs/1993MNRAS.260..337C.

S. B. Charnley. Sulfuretted Molecules in Hot Cores. *Astrophys. J.*, 481:396, May 1997. doi: 10.1086/304011. URL http://adsabs.harvard.edu/abs/1997ApJ...481..396C.

S. B. Charnley, A. G. G. M. Tielens, and T. J. Millar. On the molecular complexity of the hot cores in Orion A - Grain surface chemistry as 'The last refuge of the scoundrel'. *Astrophys. J. L.*, 399:L71–L74, November 1992. doi: 10.1086/186609. URL http://adsabs.harvard.edu/abs/1992ApJ...399L..71C.

M. Choi, N. J. Evans, II, M. Tafalla, and R. Bachiller. The Structure of the Monoceros R2 Molecular Cloud Core. *ApJ*, 538:738–750, August 2000. doi: 10.1086/309156. URL http://adsabs.harvard.edu/abs/2000ApJ...538..738C.

E. Churchwell. Ultra-Compact HII Regions and Massive Star Formation. *Ann. Rev. Astron. Astr.*, 40:27–62, 2002. doi: 10.1146/annurev.astro.40.060401.093845. URL http://adsabs.harvard.edu/abs/2002ARA%26A..40...27C.

P. C. Clark and I. A. Bonnell. Clumpy shocks and the clump mass function. *MNRAS*, 368:1787–1795, June 2006. doi: 10.1111/j.1365-2966.2006.10251.x. URL http://adsabs.harvard.edu/abs/2006MNRAS.368.1787C.

C. J. Clarke, I. A. Bonnell, and L. A. Hillenbrand. The Formation of Stellar Clusters. *Protostars and Planets IV*, page 151, May 2000. URL http://adsabs.harvard.edu/abs/2000prpl.conf..151C.

M. J. Claussen, R. A. Gaume, K. J. Johnston, and T. L. Wilson. The W3 IRS 5 cluster: Radio continuum and water maser observations. *Astrophys. J. L.*, 424:L41–L44, March 1994. doi: 10.1086/187270. URL http://adsabs.harvard.edu/abs/1994ApJ...424L..41C.

L. M. Close, J. R. Males, K. Morzinski, D. Kopon, K. Follette, T. J. Rodigas, P. Hinz, Y.-L. Wu, A. Puglisi, S. Esposito, A. Riccardi, E. Pinna, M. Xompero, R. Briguglio, A. Uomoto, and T. Hare. Diffraction-limited Visible Light Images of Orion Trapezium Cluster with the Magellan Adaptive Secondary Adaptive Optics System (MagAO). *Astrophys. J.*, 774:94, September 2013. doi: 10.1088/0004-637X/774/2/94. URL http://adsabs.harvard.edu/abs/2013ApJ...774...94C.

J. G. Cohen and J. A. Frogel. Photography at 9400 A of infrared and molecular line sources. *Astrophys. J.*, 211:178–180, January 1977. doi: 10.1086/154916. URL http://adsabs.harvard.edu/abs/1977ApJ...211..178C.

B. Commerçon, P. Hennebelle, and T. Henning. Collapse of Massive Magnetized Dense Cores Using Radiation Magnetohydrodynamics: Early Fragmentation Inhibition. *Astrophys. J. L.*, 742:L9, November 2011. doi: 10.1088/2041-8205/742/1/L9. URL http://adsabs.harvard.edu/abs/2011ApJ...742L...9C.

J. J. Condon. Radio emission from normal galaxies. *Ann. Rev. Astron. Astr.*, 30:575–611, 1992. doi: 10.1146/annurev.aa.30.090192.003043. URL http://adsabs.harvard.edu/abs/1992ARA%26A..30..575C.

I. Cruz-González, L. Salas, and D. Hiriart. H_2 Velocity Structure in the Molecular Outflow DR 21. *RMXAA*, 43:337–351, October 2007. URL http://adsabs.harvard.edu/abs/2007RMxAA..43..337C.

T. Csengeri, S. Bontemps, N. Schneider, F. Motte, and S. Dib. Gas dynamics in massive dense cores in Cygnus-X. *A&A*, 527:A135, March 2011. doi: 10.1051/0004-6361/201014984. URL http://adsabs.harvard.edu/abs/2011A%26A...527A.135C.

A. J. Cunningham, A. Frank, and E. G. Blackman. Protostellar Jet Collisions Reduce the Efficiency of Outflow-Driven Turbulence in Molecular Clouds. *ApJ*, 646:1059–1069, August 2006. doi: 10.1086/505132. URL http://adsabs.harvard.edu/abs/2006ApJ...646.1059C.

A. J. Cunningham, R. I. Klein, M. R. Krumholz, and C. F. McKee. Radiation-hydrodynamic Simulations of Massive Star Formation with Protostellar Outflows. *ApJ*, 740:107, October 2011. doi: 10.1088/0004-637X/740/2/107. URL http://adsabs.harvard.edu/abs/2011ApJ...740..107C.

C. J. Cyganowski, M. J. Reid, V. L. Fish, and P. T. P. Ho. Dual Cometary H II Regions in DR 21: Bow Shocks or Champagne Flows? *ApJ*, 596:344–349, October 2003. doi: 10.1086/377688. URL http://adsabs.harvard.edu/abs/2003ApJ...596..344C.

M. B. Davies, M. R. Bate, I. A. Bonnell, V. C. Bailey, and C. A. Tout. Stellar encounters involving massive stars in young clusters. *MNRAS*, 370:2038–2046, August 2006. doi: 10.1111/j.1365-2966.2006.10644.x. URL http://adsabs.harvard.edu/abs/2006MNRAS.370.2038D.

C. J. Davis, M. S. N. Kumar, G. Sandell, D. Froebrich, M. D. Smith, and M. J. Currie. WFCAM, Spitzer/IRAC and SCUBA observations of the massive star-forming region DR21/W75 - I. The collimated molecular jets. *MNRAS*, 374:29–53, January 2007. doi: 10.1111/j.1365-2966.2006.11163.x. URL http://adsabs.harvard.edu/abs/2007MNRAS.374...29D.

C. G. De Pree, T. Peters, M.-M. Mac Low, D. J. Wilner, W. M. Goss, R. Galván-Madrid, E. R. Keto, R. S. Klessen, and A. Monsrud. Flickering of 1.3 cm Sources in Sgr B2: Toward a Solution to the Ultracompact H II Region Lifetime Problem. *Astrophys. J. L.*, 781: L36, February 2014. doi: 10.1088/2041-8205/781/2/L36. URL http://adsabs.harvard.edu/abs/2014ApJ...781L..36D.

P. de Vicente, J. Martín-Pintado, R. Neri, and P. Colom. A ridge of recent massive star formation between Sgr B2M and Sgr B2N. *Astron. Astrophys.*, 361:1058–1072, September 2000. URL http://adsabs.harvard.edu/abs/2000A%26A...361.1058D.

P. de Vicente, J. Martín-Pintado, R. Neri, and A. Rodríguez-Franco. On the Heating Source of the Orion KL Hot Core. *ApJL*, 574:L163–L166, August 2002. doi: 10.1086/342508. URL http://adsabs.harvard.edu/abs/2002ApJ...574L.163D.

W. J. de Wit, L. Testi, F. Palla, L. Vanzi, and H. Zinnecker. The origin of massive O-type field stars. I. A search for clusters. *Astron. Astrophys.*, 425:937–948, October 2004. doi: 10.1051/0004-6361:20040454. URL http://adsabs.harvard.edu/abs/2004A%26A...425..937D.

W. J. de Wit, L. Testi, F. Palla, and H. Zinnecker. The origin of massive O-type field stars: II. Field O stars as runaways. *Astron. Astrophys.*, 437:247–255, July 2005. doi: 10.1051/0004-6361:20042489. URL http://adsabs.harvard.edu/abs/2005A%26A...437..247D.

W. J. de Wit, M. G. Hoare, T. Fujiyoshi, R. D. Oudmaijer, M. Honda, H. Kataza, T. Miyata, Y. K. Okamoto, T. Onaka, S. Sako, and T. Yamashita. Resolved 24.5 micron emission from massive young stellar objects. *Astron. Astrophys.*, 494:157–178, January 2009. doi: 10.1051/0004-6361:200810771. URL http://adsabs.harvard.edu/abs/2009A%26A...494..157D.

J. Di Francesco, D. Johnstone, H. Kirk, T. MacKenzie, and E. Ledwosinska. The SCUBA Legacy Catalogues: Submillimeter-Continuum Objects Detected by SCUBA. *Astrophys. J. Suppl.*, 175:277–295, March 2008. doi: 10.1086/523645. URL http://adsabs.harvard.edu/abs/2008ApJS..175..277D.

C. L. Dobbs, I. A. Bonnell, and P. C. Clark. Centrally condensed turbulent cores: massive stars or fragmentation? *MNRAS*, 360:2–8, June 2005. doi: 10.1111/j.1365-2966.2005.08941.x. URL http://adsabs.harvard.edu/abs/2005MNRAS.360....2D.

S. A. Drake and J. L. Linsky. Radio-continuum emission from the ionized stellar winds of warm supergiants. Astron. J., 98:1831–1841, November 1989. doi: 10.1086/115262. URL http://adsabs.harvard.edu/abs/1989AJ.....98.1831D.

A. Duarte-Cabral, S. Bontemps, F. Motte, M. Hennemann, N. Schneider, and P. André. CO outflows from high-mass Class 0 protostars in Cygnus-X. *Astron. Astrophys.*, 558:A125, October 2013. doi: 10.1051/0004-6361/201321393. URL http://adsabs.harvard.edu/abs/2013A%26A...558A.125D.

M. L. Enoch, K. E. Young, J. Glenn, N. J. Evans, II, S. Golwala, A. I. Sargent, P. Harvey, J. Aguirre, A. Goldin, D. Haig, T. L. Huard, A. Lange, G. Laurent, P. Maloney, P. Mauskopf, P. Rossinot, and J. Sayers. Bolocam Survey for 1.1 mm Dust Continuum Emission in the c2d Legacy Clouds. I. Perseus. *Astrophys. J.*, 638:293–313, February 2006. doi: 10.1086/498678. URL http://adsabs.harvard.edu/abs/2006ApJ...638..293E.

N. J. Evans, II, M. M. Dunham, J. K. Jørgensen, M. L. Enoch, B. Merín, E. F. van Dishoeck, J. M. Alcalá, P. C. Myers, K. R. Stapelfeldt, T. L. Huard, and 8 coauthors. The Spitzer c2d Legacy Results: Star-Formation Rates and Efficiencies; Evolution and Lifetimes. *ApJS*, 181:321, April 2009. doi: 10.1088/0067-0049/181/2/321. URL http://adsabs.harvard.edu/abs/2009ApJS..181..321E.

F. Favata and G. Micela. Stellar Coronal Astronomy. *Space Science Reviews*, 108:577–708, October 2003. doi: 10.1023/B:SPAC.0000007491.

80144.21. URL http://cdsads.u-strasbg.fr/abs/2003SSRv..108..577F.

C. Federrath, R. Banerjee, P. C. Clark, and R. S. Klessen. Modeling Collapse and Accretion in Turbulent Gas Clouds: Implementation and Comparison of Sink Particles in AMR and SPH. *ApJ*, 713:269–290, April 2010. doi: 10.1088/0004-637X/713/1/269. URL http://adsabs.harvard.edu/abs/2010ApJ...713..269F.

E. D. Feigelson and T. Montmerle. High-Energy Processes in Young Stellar Objects. *Ann. Rev. Astron. Astr.*, 37: 363–408, 1999. doi: 10.1146/annurev.astro.37.1.363. URL http://adsabs.harvard.edu/abs/1999ARA%26A..37..363F.

E. D. Feigelson, K. Getman, L. Townsley, G. Garmire, T. Preibisch, N. Grosso, T. Montmerle, A. Muench, and M. McCaughrean. Global X-Ray Properties of the Orion Nebula Region. *ApJS*, 160:379–389, October 2005. doi: 10.1086/432512. URL http://adsabs.harvard.edu/abs/2005ApJS..160..379F.

M. Felli, M. Massi, and M. Catarzi. Intercontinental VLBI observations of Theta(1) Orionis A. *Astron. Astrophys.*, 248:453–457, August 1991. URL http://adsabs.harvard.edu/abs/1991A%26A...248..453F.

M. Felli, G. B. Taylor, M. Catarzi, E. Churchwell, and S. Kurtz. The Orion Radio Zoo Revisited - Source Variability. *A&AS*, 101:127, October 1993. URL http://adsabs.harvard.edu/abs/1993A%26AS..101..127F.

D. F. Figer, F. Najarro, D. Gilmore, M. Morris, S. S. Kim, E. Serabyn, I. S. McLean, A. M. Gilbert, J. R. Graham, J. E. Larkin, N. A. Levenson, and H. I. Teplitz. Massive Stars in the Arches Cluster. *Astrophys. J.*, 581:258–275, December 2002. doi: 10.1086/344154. URL http://adsabs.harvard.edu/abs/2002ApJ...581..258F.

E. Flaccomio, F. Damiani, G. Micela, S. Sciortino, F. R. Harnden, Jr., S. S. Murray, and S. J. Wolk. Chandra X-Ray Observation of the Orion Nebula Cluster. I. Detection, Identification, and Determination of X-Ray Luminosities. *ApJ*, 582:382–397, January 2003. doi: 10.1086/344535. URL http://adsabs.harvard.edu/abs/2003ApJ...582..382F.

K. M. Flaherty, J. L. Pipher, S. T. Megeath, E. M. Winston, R. A. Gutermuth, J. Muzerolle, L. E. Allen, and G. G. Fazio. Infrared Extinction toward Nearby Star-forming Regions. *ApJ*, 663:1069–1082, July 2007. doi: 10.1086/518411. URL http://adsabs.harvard.edu/abs/2007ApJ...663.1069F.

T. A. Fleming, J. H. M. M. Schmitt, and M. S. Giampapa. Correlations of Coronal X-Ray Emission with Activity, Mass, and Age of the Nearby K and M Dwarfs. *ApJ*, 450:401, September 1995. doi: 10.1086/176150. URL http://adsabs.harvard.edu/abs/1995ApJ...450..401F.

E. B. Fomalont, K. I. Kellermann, R. B. Partridge, R. A. Windhorst, and E. A. Richards. The Microjansky Sky at 8.4 GHz. Astron. J., 123:2402–2416, May 2002. doi: 10.1086/339308. URL http://adsabs.harvard.edu/abs/2002AJ....123.2402F.

F. Fontani, P. Caselli, Q. Zhang, J. Brand, G. Busquet, and A. Palau. Temperature and kinematics of protoclusters with intermediate and high-mass stars: the case of IRAS 05345+3157. *Astron. Astrophys.*, 541: A32, May 2012. doi: 10.1051/0004-6361/201118153. URL http://adsabs.harvard.edu/abs/2012A%26A...541A..32F.

J. Forbrich and S. J. Wolk. On the radio-X-ray connection in young stellar objects in the Orion nebula cluster. *Astron. Astrophys.*, 551:A56, March 2013. doi: 10.1051/0004-6361/201220579. URL http://adsabs.harvard.edu/abs/2013A%26A...551A..56F.

J. Forbrich, T. Preibisch, K. M. Menten, R. Neuhäuser, F. M. Walter, M. Tamura, N. Matsunaga, N. Kusakabe, Y. Nakajima, A. Brandeker, S. Fornasier, B. Posselt, K. Tachihara, and C. Broeg. Simultaneous X-ray, radio, near-infrared, and optical monitoring of young stellar objects in the Coronet cluster. *A&A*, 464:1003–1013, March 2007. doi: 10.1051/0004-6361:20066158. URL http://adsabs.harvard.edu/abs/2007A%26A...464.1003F.

J. Forbrich, K. M. Menten, and M. J. Reid. A 1.3 cm wavelength radio flare from a deeply embedded source in the Orion BN/KL region. *A&A*, 477:267–272, January 2008. doi: 10.1051/0004-6361:20078070. URL http://adsabs.harvard.edu/abs/2008A%26A...477..267F.

W. Frieswijk. *Early stages of clustered star formation: massive dark clouds throughout the Galaxy*. PhD thesis, Kapteyn Astronomical Institute <EMAIL>frieswyk@astro.rug.nl</EMAIL>, 2008. URL http://adsabs.harvard.edu/abs/2008PhDT.....108F.

R. Galván-Madrid, E. Keto, Q. Zhang, S. Kurtz, L. F. Rodríguez, and P. T. P. Ho. Formation of an O-Star Cluster by Hierarchical Accretion in G20.08-0.14 N. *Astrophys. J.*, 706:1036–1053, December 2009. doi: 10.1088/0004-637X/706/2/1036. URL http://adsabs.harvard.edu/abs/2009ApJ...706.1036G.

R. Galván-Madrid, T. Peters, E. R. Keto, M.-M. Mac Low, R. Banerjee, and R. S. Klessen. Time variability in simulated ultracompact and hypercompact H II regions. *Mon. Not. R. astr. Soc.*, 416:1033–1044, September 2011. doi: 10.1111/j.1365-2966.2011.19101.x. URL http://adsabs.harvard.edu/abs/2011MNRAS.416.1033G.

G. Garay. The Orion radio zoo - PIGS, DEERS and FOXES. *RMXAA*, 14:489–505, May 1987. URL http://adsabs.harvard.edu/abs/1987RMxAA..14..489G.

G. Garay and S. Lizano. Massive Stars: Their Environment and Formation. *Pub. Astron. Soc. Pac.*, 111:1049–1087, September 1999. doi: 10.1086/316416. URL http://adsabs.harvard.edu/abs/1999PASP..111.1049G.

R. P. Garden, M. Hayashi, T. Hasegawa, I. Gatley, and N. Kaifu. A spectroscopic study of the DR 21 outflow source. III - The CO line emission. *ApJ*, 374:540–554, June 1991. doi: 10.1086/170143. URL http://adsabs.harvard.edu/abs/1991ApJ...374..540G.

R. A. Gaume, T. L. Wilson, F. J. Vrba, K. J. Johnston, and J. Schmid-Burgk. Water Masers in Orion. *ApJ*, 493:940, January 1998. doi: 10.1086/305161. URL http://adsabs.harvard.edu/abs/1998ApJ...493..940G.

K. V. Getman, E. D. Feigelson, N. Grosso, M. J. McCaughrean, G. Micela, P. Broos, G. Garmire, and L. Townsley. Membership of the Orion Nebula Population from the Chandra Orion Ultradeep Project. *ApJS*, 160:353–378, October 2005a. doi: 10.1086/432097. URL http://adsabs.harvard.edu/abs/2005ApJS..160..353G.

K. V. Getman, E. Flaccomio, P. S. Broos, N. Grosso, M. Tsujimoto, L. Townsley, G. P. Garmire, J. Kastner, J. Li, and Harnden. Chandra Orion Ultradeep Project: Observations and Source Lists. *ApJS*, 160:319–352, October 2005b. doi: 10.1086/432092. URL http://adsabs.harvard.edu/abs/2005ApJS..160..319G.

K. V. Getman, E. Flaccomio, P. S. Broos, N. Grosso, M. Tsujimoto, L. Townsley, G. P. Garmire, J. Kastner, J. Li, and Harnden. Chandra Orion Ultradeep Project: Observations and Source Lists. *ApJS*, 160:319–352, October 2005c. doi: 10.1086/432092. URL http://adsabs.harvard.edu/abs/2005ApJS..160..319G.

K. V. Getman, E. D. Feigelson, P. S. Broos, G. Micela, and G. P. Garmire. X-Ray Flares in Orion Young Stars. I. Flare Characteristics. *Astrophys. J.*, 688:418–436, November 2008. doi: 10.1086/592033. URL http://adsabs.harvard.edu/abs/2008ApJ...688..418G.

K. V. Getman, E. D. Feigelson, and M. A. Kuhn. Core-Halo Age Gradients and Star Formation in the Orion Nebula and NGC˜2024 Young Stellar Clusters. *ArXiv e-prints*, March 2014. URL http://adsabs.harvard.edu/abs/2014arXiv1403.2742G.

J. Giannakopoulou, G. F. Mitchell, T. I. Hasegawa, H. E. Matthews, and J.-P. Maillard. The Star-forming Core of Monoceros R2. *Astrophys. J.*, 487:346, September 1997. doi: 10.1086/304574. URL http://adsabs.harvard.edu/abs/1997ApJ...487..346G.

P. Girichidis, C. Federrath, R. Banerjee, and R. S. Klessen. Importance of the initial conditions for star formation - I. Cloud evolution and morphology. *Mon. Not. R. astr. Soc.*, 413:2741–2759, June 2011. doi: 10.1111/j.1365-2966.2011.18348.x. URL http://adsabs.harvard.edu/abs/2011MNRAS.413.2741G.

C. Goddi, L. J. Greenhill, E. M. L. Humphreys, C. J. Chandler, and L. D. Matthews. Unveiling Sources of Heating in the Vicinity of the Orion BN/KL Hot Core as Traced by Highly Excited Inversion Transitions of Ammonia. *Astrophys. J. L.*, 739:L13, September 2011a. doi: 10.1088/2041-8205/739/1/L13. URL http://adsabs.harvard.edu/abs/2011ApJ...739L..13G.

C. Goddi, E. M. L. Humphreys, L. J. Greenhill, C. J. Chandler, and L. D. Matthews. A Multi-epoch Study of the Radio Continuum Emission of Orion Source. I. Constraints on the Disk Evolution of a Massive YSO and the Dynamical History of Orion BN/KL. *ApJ*, 728:15, February 2011b. doi: 10.1088/0004-637X/728/1/15. URL http://adsabs.harvard.edu/abs/2011ApJ...728...15G.

L. Gómez, L. F. Rodríguez, L. Loinard, S. Lizano, C. Allen, A. Poveda, and K. M. Menten. Monitoring the Large Proper Motions of Radio Sources in the Orion BN/KL Region. *ApJ*, 685:333–343, September 2008. doi: 10.1086/590229. URL http://adsabs.harvard.edu/abs/2008ApJ...685..333G.

C. P. Gonatas, P. Palmer, and G. Novak. High-resolution imaging of the galactic cloud Monoceros R2. *Astrophys. J.*, 398:118–127, October 1992. doi: 10.1086/171841. URL http://adsabs.harvard.edu/abs/1992ApJ...398..118G.

N. Grosso, E. D. Feigelson, K. V. Getman, L. Townsley, P. Broos, E. Flaccomio, M. J. McCaughrean, G. Micela, S. Sciortino, J. Bally, N. Smith, A. A. Muench, G. P. Garmire, and F. Palla. Chandra Orion Ultradeep Project Census of X-Ray Stars in the BN-KL and OMC-1S Regions. *ApJS*, 160:530–556, October 2005. doi: 10.1086/432101. URL http://adsabs.harvard.edu/abs/2005ApJS..160..530G.

M. Güdel. Stellar Radio Astronomy: Probing Stellar Atmospheres from Protostars to Giants. *Ann. Rev. Astron. Astr.*, 40:217–261, 2002. doi: 10.1146/annurev.astro.40.060401.093806. URL http://adsabs.harvard.edu/abs/2002ARA%26A..40..217G.

M. Güdel and Y. Nazé. X-ray spectroscopy of stars. *A&AR*, 17:309–408, September 2009. doi: 10.1007/s00159-009-0022-4. URL http://adsabs.harvard.edu/abs/2009A%26ARv..17..309G.

K. Guenthner and J. Kauffmann. Identification and Characterization of Protostellar Outflows in Spitzer c2d Images. In *American Astronomical Society Meeting Abstracts #213*, volume 41 of *Bulletin of the American Astronomical Society*, page 413.14, January 2009. URL http://adsabs.harvard.edu/abs/2009AAS...21341314G.

F. Gueth and S. Guilloteau. The jet-driven molecular outflow of HH 211. *Astron. Astrophys.*, 343:571–584, March 1999. URL http://adsabs.harvard.edu/abs/1999A%26A...343..571G.

S. Guilloteau, R. Bachiller, A. Fuente, and R. Lucas. First observations of young bipolar outflows with the IRAM interferometer - 2 arcsec resolution SiO images of the molecular jet in L 1448. *A&A*, 265:L49–L52, November 1992. URL http://adsabs.harvard.edu/abs/1992A%26A...265L..49G.

R. A. Gutermuth, S. T. Megeath, J. L. Pipher, J. P. Williams, L. E. Allen, P. C. Myers, and S. N. Raines. The Initial Configuration of Young Stellar Clusters: A K-Band Number Counts Analysis of the Surface Density of Stars. *Astrophys. J.*, 632:397–420, October 2005. doi: 10.1086/432460. URL http://adsabs.harvard.edu/abs/2005ApJ...632..397G.

R. A. Gutermuth, S. T. Megeath, P. C. Myers, L. E. Allen, J. L. Pipher, and G. G. Fazio. A Spitzer Survey of Young Stellar Clusters Within One Kiloparsec of the Sun: Cluster Core Extraction and Basic Structural Analysis. *Astrophys. J. Suppl.*, 184:18–83, September 2009. doi: 10.1088/0067-0049/184/1/18. URL http://adsabs.harvard.edu/abs/2009ApJS..184...18G.

J. A. Hackwell, G. L. Grasdalen, and R. D. Gehrz. 10 and 20 micron images of regions of star formation. *Astrophys. J.*, 252:250–268, January 1982. doi: 10.1086/159552. URL http://adsabs.harvard.edu/abs/1982ApJ...252..250H.

C. E. Hansen, R. I. Klein, C. F. McKee, and R. T. Fisher. Feedback Effects on Low-mass Star Formation. *Astrophys. J.*, 747:22, March 2012. doi: 10.1088/0004-637X/747/1/22. URL http://adsabs.harvard.edu/abs/2012ApJ...747...22H.

P. M. Harvey, M. F. Campbell, and W. F. Hoffmann. High-resolution far-infrared observations of H II regions - Sagittarius B2, W49, DR 21-W75. *ApJ*, 211:786–797, February 1977. doi: 10.1086/154988. URL http://adsabs.harvard.edu/abs/1977ApJ...211..786H.

P. M. Harvey, N. Chapman, S.-P. Lai, N. J. Evans, II, L. E. Allen, and J. K. et al. Jørgensen. The Spitzer c2d Survey of Large, Nearby, Insterstellar Clouds. II. Serpens Observed with IRAC. *ApJ*, 644:307–325, June 2006. doi: 10.1086/503520. URL http://adsabs.harvard.edu/abs/2006ApJ...644..307H.

J. Hashimoto, M. Tamura, R. Kandori, N. Nobuhiko Kusakabe, Y. Nakajima, S. Sato, C. Nagashima, M. Kurita, T. Nagata, T. Nagayama, and J. H. Hough. Near-Infrared Polarization Images of the Orion Molecular Cloud 1 South Region. *PASJ*, 59:481–486, June 2007. URL http://adsabs.harvard.edu/abs/2007PASJ...59..481H.

M. Hennemann, F. Motte, N. Schneider, P. Didelon, T. Hill, D. Arzoumanian, S. Bontemps, T. Csengeri, P. André, and V. et al. Konyves. The spine of the swan: a Herschel study of the DR21 ridge and filaments in Cygnus X. *A&A*, 543:L3, July 2012. doi: 10.1051/0004-6361/201219429. URL http://adsabs.harvard.edu/abs/2012A%26A...543L...3H.

W. J. Henney, C. R. O'Dell, L. A. Zapata, M. T. García-Díaz, L. F. Rodríguez, and M. Robberto. Large-Scale Flows from Orion South1,. *AJ*, 133:2192–2205, May 2007. doi: 10.1086/513074. URL http://adsabs.harvard.edu/abs/2007AJ....133.2192H.

T. Henning, R. Chini, and W. Pfau. Submm/mm observations of the Monoceros R2 cloud core. *Astron. Astrophys.*, 263:285–291, September 1992. URL http://adsabs.harvard.edu/abs/1992A%26A...263..285H.

W. Herbst and R. Racine. R-associations. V. Monoceros R2. Astron. J., 81:840–844, October 1976. doi: 10.1086/111963. URL http://adsabs.harvard.edu/abs/1976AJ.....81..840H.

M. H. Heyer and C. M. Brunt. The Universality of Turbulence in Galactic Molecular Clouds. *Astrophys. J. L.*, 615:L45–L48, November 2004. doi: 10.1086/425978. URL http://adsabs.harvard.edu/abs/2004ApJ...615L..45H.

R. H. Hildebrand. The Determination of Cloud Masses and Dust Characteristics from Submillimetre Thermal Emission. , 24:267, September 1983. URL http://adsabs.harvard.edu/abs/1983QJRAS..24..267H.

L. A. Hillenbrand. On the Stellar Population and Star-Forming History of the Orion Nebula Cluster. *AJ*, 113:1733–1768, May 1997. doi: 10.1086/118389. URL http://adsabs.harvard.edu/abs/1997AJ....113.1733H.

L. A. Hillenbrand and J. M. Carpenter. Constraints on the Stellar/Substellar Mass Function in the Inner Orion Nebula Cluster. *ApJ*, 540:236–254, September 2000. doi: 10.1086/309309. URL http://adsabs.harvard.edu/abs/2000ApJ...540..236H.

L. A. Hillenbrand and L. W. Hartmann. A Preliminary Study of the Orion Nebula Cluster Structure and Dynamics. *ApJ*, 492:540, January 1998. doi: 10.1086/305076. URL http://adsabs.harvard.edu/abs/1998ApJ...492..540H.

N. Hirano, S.-Y. Liu, H. Shang, P. T. P. Ho, H.-C. Huang, Y.-J. Kuan, M. J. McCaughrean, and Q. Zhang. SiO J = 5-4 in the HH 211 Protostellar Jet Imaged with the Submillimeter Array. *Astrophys. J. L.*, 636:L141–L144, January 2006. doi: 10.1086/500201. URL http://adsabs.harvard.edu/abs/2006ApJ...636L.141H.

N. Hirano, P. P. T. Ho, S.-Y. Liu, H. Shang, C.-F. Lee, and T. L. Bourke. Extreme Active Molecular Jets in L1448C. *Astrophys. J.*, 717:58–73, July 2010. doi: 10.1088/0004-637X/717/1/58. URL http://adsabs.harvard.edu/abs/2010ApJ...717...58H.

P. T. P. Ho, J. M. Moran, and K. Y. Lo. The Submillimeter Array. *Astrophys. J. L.*, 616:L1–L6, November 2004. doi: 10.1086/423245. URL http://adsabs.harvard.edu/abs/2004ApJ...616L...1H.

K. W. Hodapp. New H_2 Jets in Monoceros R2. Astron. J., 134:2020–2034, November 2007. doi: 10.1086/522784. URL http://adsabs.harvard.edu/abs/2007AJ....134.2020H.

P. Hofner, R. Cesaroni, L. Olmi, L. F. Rodríguez, J. Martí, and E. Araya. Sub-arcsecond resolution radio continuum observations of IRAS 20126+4104. *A&A*, 465:197–205, April 2007. doi: 10.1051/0004-6361:20065770. URL http://adsabs.harvard.edu/abs/2007A%26A...465..197H.

J. G. Hosking and A. P. Whitworth. Fragmentation of magnetized cloud cores. *Mon. Not. R. astr. Soc.*, 347:1001–1010, January 2004. doi: 10.1111/j.1365-2966.2004.07274.x. URL http://adsabs.harvard.edu/abs/2004MNRAS.347.1001H.

E. M. Howard, J. L. Pipher, and W. J. Forrest. A near-infrared study of the Monoceros R2 star formation region. *Astrophys. J.*, 425:707–719, April 1994. doi: 10.1086/174016. URL http://adsabs.harvard.edu/abs/1994ApJ...425..707H.

I. Jiménez-Serra, J. Martín-Pintado, P. Caselli, S. Martín, A. Rodríguez-Franco, C. Chandler, and J. M. Winters. Unveiling the Main Heating Sources in the Cepheus a HW2 Region. *Astrophys. J. L.*, 703:L157–L161, October 2009. doi: 10.1088/0004-637X/703/2/L157. URL http://adsabs.harvard.edu/abs/2009ApJ...703L.157J.

I. Jiménez-Serra, A. Báez-Rubio, V. M. Rivilla, J. Martín-Pintado, Q. Zhang, M. Dierickx, and N. Patel. A New Radio Recombination Line Maser Object toward the MonR2 H II Region. *Astrophys. J. L.*, 764:L4, February 2013. doi: 10.1088/2041-8205/764/1/L4. URL http://adsabs.harvard.edu/abs/2013ApJ...764L...4J.

D. Johnstone and J. Bally. JCMT/SCUBA Submillimeter Wavelength Imaging of the Integral-shaped Filament in Orion. *Astrophys. J. L.*, 510:L49–L53, January 1999. doi: 10.1086/311792. URL http://adsabs.harvard.edu/abs/1999ApJ...510L..49J.

J. K. Jørgensen, P. M. Harvey, N. J. Evans, II, T. L. Huard, and L. E. et al. Allen. The Spitzer c2d Survey of Large, Nearby, Interstellar Clouds. III. Perseus Observed with IRAC. *ApJ*, 645:1246–1263, July 2006. doi: 10.1086/504373. URL http://adsabs.harvard.edu/abs/2006ApJ...645.1246J.

J. K. Jørgensen, D. Johnstone, H. Kirk, P. C. Myers, L. E. Allen, and Y. L. Shirley. Current Star Formation in the Ophiuchus and Perseus Molecular Clouds: Constraints and Comparisons from Unbiased Submillimeter and Mid-Infrared Surveys. II. *ApJ*, 683:822–843, August 2008. doi: 10.1086/589956. URL http://adsabs.harvard.edu/abs/2008ApJ...683..822J.

J. H. Kastner, G. Franz, N. Grosso, J. Bally, M. J. McCaughrean, K. Getman, E. D. Feigelson, and N. S. Schulz. X-Ray Emission from Orion Nebula Cluster Stars with Circumstellar Disks and Jets. *ApJS*, 160:511–529, October 2005. doi: 10.1086/432096. URL http://adsabs.harvard.edu/abs/2005ApJS..160..511K.

J. Keene, R. H. Hildebrand, and S. E. Whitcomb. A high resolution submillimeter map of OMC-1. *ApJL*, 252:L11–L15, January 1982. doi: 10.1086/183709. URL http://adsabs.harvard.edu/abs/1982ApJ...252L..11K.

E. Keto. The Formation of Massive Stars by Accretion through Trapped Hypercompact H II Regions. *Astrophys. J.*, 599:1196–1206, December 2003. doi: 10.1086/379545. URL http://adsabs.harvard.edu/abs/2003ApJ...599.1196K.

R. S. Klessen, A. Burkert, and M. R. Bate. Fragmentation of Molecular Clouds: The Initial Phase of a Stellar Cluster. *Astrophys. J. L.*, 501:L205, July 1998. doi: 10.1086/311471. URL http://adsabs.harvard.edu/abs/1998ApJ...501L.205K.

L. B. G. Knee and G. Sandell. The molecular outflows in NGC 1333. *A&A*, 361:671–684, September 2000. URL http://adsabs.harvard.edu/abs/2000A%26A...361..671K.

M. Kohno, K. Koyama, and K. Hamaguchi. Chandra Observations of High-Mass Young Stellar Objects in the Monoceros R2 Molecular Cloud. *ApJ*, 567:423–433, March 2002. doi: 10.1086/338381. URL http://adsabs.harvard.edu/abs/2002ApJ...567..423K.

K. E. Kraemer, J. M. Jackson, L. K. Deutsch, M. Kassis, J. L. Hora, G. G. Fazio, W. F. Hoffmann, and A. Dayal. Dust Characteristics of Massive Star-forming Sites in the Mid-Infrared. *Astrophys. J.*, 561:282–298, November 2001. doi: 10.1086/323219. URL http://adsabs.harvard.edu/abs/2001ApJ...561..282K.

S. Kraus, G. Weigelt, Y. Y. Balega, J. A. Docobo, K.-H. Hofmann, T. Preibisch, D. Schertl, V. S. Tamazian, T. Driebe, K. Ohnaka, R. Petrov, M. Schöller, and M. Smith. Tracing the young massive high-eccentricity binary system Orionis C through periastron passage. *Astron. Astrophys.*, 497:195–207, April 2009. doi: 10.1051/0004-6361/200810368. URL http://adsabs.harvard.edu/abs/2009A%26A...497..195K.

P. Kroupa. On the variation of the initial mass function. *MNRAS*, 322:231–246, April 2001. doi: 10.1046/j.1365-8711.2001.04022.x. URL http://adsabs.harvard.edu/abs/2001MNRAS.322..231K.

M. R. Krumholz. Radiation Feedback and Fragmentation in Massive Protostellar Cores. *ApJL*, 641:L45–L48, April 2006. doi: 10.1086/503771. URL http://adsabs.harvard.edu/abs/2006ApJ...641L..45K.

M. R. Krumholz and I. A. Bonnell. Models for the Formation of Massive Stars. *ArXiv e-prints*, December 2007. URL http://adsabs.harvard.edu/abs/2007arXiv0712.0828K.

M. R. Krumholz, C. F. McKee, and R. I. Klein. The formation of stars by gravitational collapse rather than competitive accretion. *Nature*, 438:332–334, November 2005. doi: 10.1038/nature04280. URL http://adsabs.harvard.edu/abs/2005Natur.438..332K.

M. R. Krumholz, R. I. Klein, and C. F. McKee. Radiation-Hydrodynamic Simulations of Collapse and Fragmentation in Massive Protostellar Cores. *Astrophys. J.*, 656:959–979, February 2007. doi: 10.1086/510664. URL http://adsabs.harvard.edu/abs/2007ApJ...656..959K.

M. R. Krumholz, R. I. Klein, C. F. McKee, S. S. R. Offner, and A. J. Cunningham. The Formation of Massive Star Systems by Accretion. *Science*, 323:754–, February 2009. doi: 10.1126/science.1165857. URL http://adsabs.harvard.edu/abs/2009Sci...323..754K.

M. R. Krumholz, R. I. Klein, and C. F. McKee. Radiation-hydrodynamic Simulations of the Formation of Orion-like Star Clusters. I. Implications for the Origin of the Initial Mass Function. *Astrophys. J.*, 740:74, October 2011. doi: 10.1088/0004-637X/740/2/74. URL http://adsabs.harvard.edu/abs/2011ApJ...740...74K.

M. R. Krumholz, R. I. Klein, and C. F. McKee. Radiation-hydrodynamic Simulations of the Formation of Orion-like Star Clusters. II. The Initial Mass Function from Winds, Turbulence, and Radiation. *ApJ*, 754:71, July 2012. doi: 10.1088/0004-637X/754/1/71. URL http://adsabs.harvard.edu/abs/2012ApJ...754...71K.

M. S. N. Kumar, C. J. Davis, J. M. C. Grave, B. Ferreira, and D. Froebrich. WFCAM, Spitzer/IRAC and SCUBA observations of the massive star-forming region DR21/W75 - II. Stellar content and star formation. *MNRAS*, 374:54–62, January 2007. doi: 10.1111/j.1365-2966.2006.11145.x. URL http://adsabs.harvard.edu/abs/2007MNRAS.374...54K.

M. R. Kundu, S. M. White, K. Shibasaki, and T. Sakurai. Nonthermal Flare Emission from MEV-Energy Electrons at 17, 34, and 86 GHZ. *Astrophys. J.*, 545:1084–1088, December 2000. doi: 10.1086/317849. URL http://adsabs.harvard.edu/abs/2000ApJ...545.1084K.

R. Kurosawa, T. J. Harries, M. R. Bate, and N. H. Symington. Synthetic infrared images and spectral energy distributions of a young low-mass stellar cluster. *MNRAS*, 351:1134–1150, July 2004. doi: 10.1111/j.1365-2966.2004.07869.x. URL http://adsabs.harvard.edu/abs/2004MNRAS.351.1134K.

S. Kurtz, R. Cesaroni, E. Churchwell, P. Hofner, and C. M. Walmsley. Hot Molecular Cores and the Earliest Phases of High-Mass Star Formation. *Protostars and Planets IV*, pages 299–326, May 2000. URL http://adsabs.harvard.edu/abs/2000prpl.conf..299K.

J. Kwan and N. Scoville. The nature of the broad molecular line emission at the Kleinmann-Low nebula. *ApJL*, 210:L39–L43, November 1976. doi: 10.1086/182298. URL http://adsabs.harvard.edu/abs/1976ApJ...210L..39K.

C. J. Lada. Star formation - From OB associations to protostars. In M. Peimbert and J. Jugaku, editors, *Star Forming Regions*, volume 115 of *IAU Symposium*, pages 1–17, 1987. URL http://adsabs.harvard.edu/abs/1987IAUS..115....1L.

C. J. Lada and E. A. Lada. Embedded Clusters in Molecular Clouds. *ARAA*, 41:57–115, 2003a. doi: 10.1146/annurev.astro.41.011802.094844. URL http://adsabs.harvard.edu/abs/2003ARA%26A..41...57L.

C. J. Lada and E. A. Lada. Embedded Clusters in Molecular Clouds. *ARAA*, 41:57–115, 2003b. doi: 10.1146/annurev.astro.41.011802.094844. URL http://adsabs.harvard.edu/abs/2003ARA%26A..41...57L.

C. J. Lada, E. A. Lada, D. P. Clemens, and J. Bally. Dust extinction and molecular gas in the dark cloud IC 5146. *Astrophys. J.*, 429:694–709, July 1994. doi: 10.1086/174354. URL http://adsabs.harvard.edu/abs/1994ApJ...429..694L.

C. J. Lada, A. A. Muench, K. E. Haisch, Jr., E. A. Lada, J. F. Alves, E. V. Tollestrup, and S. P. Willner. Infrared L-Band Observations of the Trapezium Cluster: A Census of Circumstellar Disks and Candidate Protostars. *AJ*, 120:3162–3176, December 2000. doi: 10.1086/316848. URL http://adsabs.harvard.edu/abs/2000AJ....120.3162L.

C. J. Lada, A. A. Muench, E. A. Lada, and J. F. Alves. Deep 3.8 Micron Observations of the Trapezium Cluster. *AJ*, 128:1254–1264, September 2004. doi: 10.1086/423294. URL http://adsabs.harvard.edu/abs/2004AJ....128.1254L.

E. A. Lada, D. L. Depoy, N. J. Evans, II, and I. Gatley. A 2.2 micron survey in the L1630 molecular cloud. *Astrophys. J.*, 371:171–182, April 1991. doi: 10.1086/169881. URL http://adsabs.harvard.edu/abs/1991ApJ...371..171L.

R. B. Larson. Numerical calculations of the dynamics of collapsing proto-star. *Mon. Not. R. astr. Soc.*, 145: 271, 1969. URL http://adsabs.harvard.edu/abs/1969MNRAS.145..271L.

R. B. Larson. The evolution of spherical protostars with masses 0.25 M_solar to 10 M_solar. *Mon. Not. R. astr. Soc.*, 157:121, 1972. URL http://adsabs.harvard.edu/abs/1972MNRAS.157..121L.

R. B. Larson. Turbulence and star formation in molecular clouds. *MNRAS*, 194:809–826, March 1981. URL http://adsabs.harvard.edu/abs/1981MNRAS.194..809L.

A. Lawrence, S. J. Warren, O. Almaini, A. C. Edge, N. C. Hambly, R. F. Jameson, P. Lucas, M. Casali, and A. et al. Adamson. The UKIRT Infrared Deep Sky Survey (UKIDSS). *MNRAS*, 379:1599–1617, August 2007. doi: 10.1111/j.1365-2966.2007.12040.x. URL http://adsabs.harvard.edu/abs/2007MNRAS.379.1599L.

C.-F. Lee, P. T. P. Ho, N. Hirano, H. Beuther, T. L. Bourke, H. Shang, and Q. Zhang. HH 212: Submillimeter Array Observations of a Remarkable Protostellar Jet. *Astrophys. J.*, 659:499–511, April 2007. doi: 10.1086/512540. URL http://adsabs.harvard.edu/abs/2007ApJ...659..499L.

C.-F. Lee, T. I. Hasegawa, N. Hirano, A. Palau, H. Shang, P. T. P. Ho, and Q. Zhang. The Reflection-Symmetric Wiggle of the Young Protostellar Jet HH 211. *Astrophys. J.*, 713:731–737, April 2010. doi: 10.1088/0004-637X/713/2/731. URL http://adsabs.harvard.edu/abs/2010ApJ...713..731L.

Z.-Y. Li and F. Nakamura. Cluster Formation in Protostellar Outflow-driven Turbulence. *ApJL*, 640:L187–L190, April 2006. doi: 10.1086/503419. URL http://adsabs.harvard.edu/abs/2006ApJ...640L.187L.

Z.-Y. Li, P. Wang, T. Abel, and F. Nakamura. Lowering the Characteristic Mass of Cluster Stars by Magnetic Fields and Outflow Feedback. *ApJL*, 720:L26–L30, September 2010. doi: 10.1088/2041-8205/720/1/L26. URL http://adsabs.harvard.edu/abs/2010ApJ...720L..26L.

H. B. Liu, R. Galván-Madrid, J. Forbrich, L. F. Rodríguez, M. Takami, G. Costigan, C. Felice Manara, C.-H. Yan, J. Karr, M.-Y. Chou, P. T.-P. Ho, and Q. Zhang. Time Monitoring of Radio Jets and Magnetospheres in the Nearby Young Stellar Cluster R Coronae Australis. *Astrophys. J.*, 780:155, January 2014. doi: 10.1088/0004-637X/780/2/155. URL http://adsabs.harvard.edu/abs/2014ApJ...780..155L.

M. Lombardi and J. Alves. Mapping the interstellar dust with near-infrared observations: An optimized multi-band technique. *Astron. Astrophys.*, 377:1023–1034, October 2001. doi: 10.1051/0004-6361:20011099. URL http://adsabs.harvard.edu/abs/2001A%26A...377.1023L.

S. N. Longmore, T. Pillai, E. Keto, Q. Zhang, and K. Qiu. Is Protostellar Heating Sufficient to Halt Fragmentation? A Case Study of the Massive Protocluster G8.68-0.37. *Astrophys. J.*, 726:97, January 2011. doi: 10.1088/0004-637X/726/2/97. URL http://adsabs.harvard.edu/abs/2011ApJ...726...97L.

C. J. Lonsdale, E. E. Becklin, T. J. Lee, and J. M. Stewart. New members of the infrared cluster in the Orion Molecular Cloud. Astron. J., 87:1819–1827, December 1982. doi: 10.1086/113272. URL http://adsabs.harvard.edu/abs/1982AJ.....87.1819L.

R. B. Loren. The Monoceros R2 cloud - Near-infrared and molecular observations of a rotating collapsing cloud. *Astrophys. J.*, 215:129–150, July 1977. doi: 10.1086/155340. URL http://adsabs.harvard.edu/abs/1977ApJ...215..129L.

R. B. Loren. High-velocity CO wings and CO self-reversals. *Astrophys. J.*, 249:550–562, October 1981. doi: 10.1086/159314. URL http://adsabs.harvard.edu/abs/1981ApJ...249..550L.

J. Martin-Pintado, T. L. Wilson, K. J. Johnston, and C. Henkel. High-resolution maps of 6 centimeter formaldehyde - Clumping in molecular clouds. *ApJ*, 299:386–404, December 1985. doi: 10.1086/163708. URL http://adsabs.harvard.edu/abs/1985ApJ...299..386M.

J. Martin-Pintado, A. Rodriguez-Franco, and R. Bachiller. Large-scale interaction of the outflow and quiescent gas in Orion. *Astrophys. J. L.*, 357:L49–L52, July 1990. doi: 10.1086/185763. URL http://adsabs.harvard.edu/abs/1990ApJ...357L..49M.

J. Martín-Pintado, I. Jiménez-Serra, A. Rodríguez-Franco, S. Martín, and C. Thum. A New Intermediate-Mass Protostar in the Cepheus A HW2 Region. *Astrophys. J. L.*, 628:L61–L64, July 2005. doi: 10.1086/432684. URL http://adsabs.harvard.edu/abs/2005ApJ...628L..61M.

M. Massi, M. Felli, and M. Simon. Radio continuum observations of the blister type H II region in MON R2. *Astron. Astrophys.*, 152:387–392, November 1985. URL http://adsabs.harvard.edu/abs/1985A%26A...152..387M.

B. C. Matthews, C. A. McPhee, L. M. Fissel, and R. L. Curran. The Legacy of SCUPOL: 850 μm Imaging Polarimetry from 1997 to 2005. *ApJS*, 182:143–204, May 2009. doi: 10.1088/0067-0049/182/1/143. URL http://adsabs.harvard.edu/abs/2009ApJS..182..143M.

L. D. Matthews, L. J. Greenhill, C. Goddi, C. J. Chandler, E. M. L. Humphreys, and M. W. Kunz. A Feature Movie of SiO Emission 20-100 AU from the Massive Young Stellar Object Orion Source I. *ApJ*, 708:80–92, January 2010. doi: 10.1088/0004-637X/708/1/80. URL http://adsabs.harvard.edu/abs/2010ApJ...708...80M.

C. D. Matzner and C. F. McKee. Efficiencies of Low-Mass Star and Star Cluster Formation. *ApJ*, 545:364–378, December 2000. doi: 10.1086/317785. URL http://adsabs.harvard.edu/abs/2000ApJ...545..364M.

C. F. McKee and J. C. Tan. Massive star formation in 100,000 years from turbulent and pressurized molecular clouds. *Nature*, 416:59–61, March 2002. URL http://adsabs.harvard.edu/abs/2002Natur.416...59M.

C. F. McKee and J. C. Tan. The Formation of Massive Stars from Turbulent Cores. *ApJ*, 585:850–871, March 2003. doi: 10.1086/346149. URL http://adsabs.harvard.edu/abs/2003ApJ...585..850M.

K. M. Menten and M. J. Reid. What is powering the Orion Kleinmann-low infrared nebula. *ApJL*, 445:L157–L160, June 1995. doi: 10.1086/187913. URL http://adsabs.harvard.edu/abs/1995ApJ...445L.157M.

M. R. Meyer, N. Calvet, and L. A. Hillenbrand. Intrinsic Near-Infrared Excesses of T Tauri Stars: Understanding the Classical T Tauri Star Locus. *AJ*, 114:

288–300, July 1997. doi: 10.1086/118474. URL http://adsabs.harvard.edu/abs/1997AJ....114..288M.

P. G. Mezger, R. Zylka, and J. E. Wink. Lambda 1.3 MM dust emission from the star-forming cloud cores OMC 1 and 2. *A&A*, 228:95–107, February 1990. URL http://adsabs.harvard.edu/abs/1990A%26A...228...95M.

N. Moeckel and C. J. Clarke. Collisional formation of very massive stars in dense clusters. *Mon. Not. R. astr. Soc.*, 410:2799–2806, February 2011. doi: 10.1111/j.1365-2966.2010.17659.x. URL http://adsabs.harvard.edu/abs/2011MNRAS.410.2799M.

D. G. Monet, S. E. Levine, B. Canzian, H. D. Ables, A. R. Bird, C. C. Dahn, H. H. Guetter, H. C. Harris, A. A. Henden, S. K. Leggett, H. F. Levison, C. B. Luginbuhl, J. Martini, A. K. B. Monet, J. A. Munn, J. R. Pier, A. R. Rhodes, B. Riepe, S. Sell, R. C. Stone, F. J. Vrba, R. L. Walker, G. Westerhout, R. J. Brucato, I. N. Reid, W. Schoening, M. Hartley, M. A. Read, and S. B. Tritton. The USNO-B Catalog. Astron. J., 125:984–993, February 2003. doi: 10.1086/345888. URL http://adsabs.harvard.edu/abs/2003AJ....125..984M.

M. Morris, P. Palmer, and B. Zuckerman. Hot ammonia in Orion. *Astrophys. J.*, 237:1–8, April 1980. doi: 10.1086/157837. URL http://adsabs.harvard.edu/abs/1980ApJ...237....1M.

F. Motte, P. Andre, and R. Neri. The initial conditions of star formation in the rho Ophiuchi main cloud: wide-field millimeter continuum mapping. *Astron. Astrophys.*, 336:150–172, August 1998. URL http://adsabs.harvard.edu/abs/1998A%26A...336..150M.

F. Motte, S. Bontemps, P. Schilke, N. Schneider, K. M. Menten, and D. Broguière. The earliest phases of high-mass star formation: a 3 square degree millimeter continuum mapping of Cygnus X. *Astron. Astrophys.*, 476:1243–1260, December 2007. doi: 10.1051/0004-6361:20077843. URL http://adsabs.harvard.edu/abs/2007A%26A...476.1243M.

P. Mucciarelli, T. Preibisch, and H. Zinnecker. Revealing the "missing" low-mass stars in the S254-S258 star forming region by deep X-ray imaging. *A&A*, 533:A121, September 2011. doi: 10.1051/0004-6361/201117074. URL http://adsabs.harvard.edu/abs/2011A%26A...533A.121M.

K. E. Mueller, Y. L. Shirley, N. J. Evans, II, and H. R. Jacobson. The Physical Conditions for Massive Star Formation: Dust Continuum Maps and Modeling. *Astrophys. J. Suppl.*, 143:469–497, December 2002. doi: 10.1086/342881. URL http://adsabs.harvard.edu/abs/2002ApJS..143..469M.

A. A. Muench, E. A. Lada, C. J. Lada, and J. Alves. The Luminosity and Mass Function of the Trapezium Cluster: From B Stars to the Deuterium-burning Limit. *ApJ*, 573:366–393, July 2002. doi: 10.1086/340554. URL http://adsabs.harvard.edu/abs/2002ApJ...573..366M.

H. S. P. Müller, F. Schlöder, J. Stutzki, and G. Winnewisser. The Cologne Database for Molecular Spectroscopy, CDMS: a useful tool for astronomers and spectroscopists. *Journal of Molecular Structure*, 742:215–227, May 2005. doi: 10.1016/j.molstruc.2005.01.027. URL http://adsabs.harvard.edu/abs/2005JMoSt.742..215M.

L. G. Mundy, N. Z. Scoville, L. B. Baath, C. R. Masson, and D. P. Woody. Protostellar condensations within the Orion ridge. *ApJL*, 304:L51–L55, May 1986. doi: 10.1086/184669. URL http://adsabs.harvard.edu/abs/1986ApJ...304L..51M.

G. C. Murphy, T. Lery, S. O'Sullivan, D. Spicer, F. Bacciotti, and A. Rosen. Interacting jets from binary protostars. *A&A*, 478:453–460, February 2008. doi: 10.1051/0004-6361:20078609. URL http://adsabs.harvard.edu/abs/2008A%26A...478..453M.

P. C. Myers and A. A. Goodman. Evidence for magnetic and virial equilibrium in molecular clouds. *ApJL*, 326:L27–L30, March 1988. doi: 10.1086/185116. URL http://adsabs.harvard.edu/abs/1988ApJ...326L..27M.

H. Nakajima, K. Imanishi, S.-I. Takagi, K. Koyama, and M. Tsujimoto. X-Ray Observation on the Monoceros R2 Star-Forming Region with the Chandra ACIS-I Array. , 55:635–651, June 2003. URL http://adsabs.harvard.edu/abs/2003PASJ...55..635N.

F. Nakamura and Z.-Y. Li. Protostellar Turbulence Driven by Collimated Outflows. *ApJ*, 662:395–412, June 2007. doi: 10.1086/517515. URL http://adsabs.harvard.edu/abs/2007ApJ...662..395N.

G. Narayanan, R. Snell, and A. Bemis. Molecular outflows identified in the FCRAO CO survey of the Taurus Molecular Cloud. *MNRAS*, 425:2641–2667, October 2012. doi: 10.1111/j.1365-2966.2012.21579.

x. URL http://adsabs.harvard.edu/abs/2012MNRAS.425.2641N.

H. D. Nissen, M. Gustafsson, J. L. Lemaire, Y. Clénet, D. Rouan, and D. Field. Observations of spatial and velocity structure in the Orion molecular cloud. *Astron. Astrophys.*, 466:949–968, May 2007. doi: 10.1051/0004-6361:20054304. URL http://adsabs.harvard.edu/abs/2007A%26A...466..949N.

C. R. O'Dell and T. Doi. High Proper Motion Features in the Central Orion Nebula. *AJ*, 125:277–287, January 2003. doi: 10.1086/345512. URL http://adsabs.harvard.edu/abs/2003AJ....125..277O.

C. R. O'Dell, W. J. Henney, N. P. Abel, G. J. Ferland, and S. J. Arthur. The Three-Dimensional Dynamic Structure of the Inner Orion Nebula. *AJ*, 137:367–382, January 2009. doi: 10.1088/0004-6256/137/1/367. URL http://adsabs.harvard.edu/abs/2009AJ....137..367O.

S. S. R. Offner, J. Capodilupo, S. Schnee, and A. A. Goodman. Observing turbulent fragmentation in simulations: predictions for CARMA and ALMA. *Mon. Not. R. astr. Soc.*, 420:L53–L57, February 2012. doi: 10.1111/j.1745-3933.2011.01194.x. URL http://adsabs.harvard.edu/abs/2012MNRAS.420L..53O.

A. Palau, P. T. P. Ho, Q. Zhang, R. Estalella, N. Hirano, H. Shang, C.-F. Lee, T. L. Bourke, H. Beuther, and Y.-J. Kuan. Submillimeter Emission from the Hot Molecular Jet HH 211. *Astrophys. J. L.*, 636:L137–L140, January 2006. doi: 10.1086/500242. URL http://adsabs.harvard.edu/abs/2006ApJ...636L.137P.

A. Palau, A. Fuente, J. M. Girart, R. Estalella, P. T. P. Ho, Á. Sánchez-Monge, F. Fontani, G. Busquet, B. Commerçon, P. Hennebelle, J. Boissier, Q. Zhang, R. Cesaroni, and L. A. Zapata. Early Stages of Cluster Formation: Fragmentation of Massive Dense Cores down to 1000 AU. *Astrophys. J.*, 762:120, January 2013. doi: 10.1088/0004-637X/762/2/120. URL http://adsabs.harvard.edu/abs/2013ApJ...762..120P.

A. Palau, R. Estalella, J. M. Girart, A. Fuente, F. Fontani, B. Commercon, G. Busquet, S. Bontemps, A. Sanchez-Monge, L. A. Zapata, Q. Zhang, P. Hennebelle, and J. Di Francesco. Fragmentation of massive dense cores down to ˜1000 AU: Relation between fragmentation and density structure. *ArXiv e-prints*, January 2014. URL http://adsabs.harvard.edu/abs/2014arXiv1401.8292P.

F. Palla and S. W. Stahler. Star Formation in the Orion Nebula Cluster. *Astrophys. J.*, 525:772–783, November 1999. doi: 10.1086/307928. URL http://adsabs.harvard.edu/abs/1999ApJ...525..772P.

R. Pallavicini, L. Golub, R. Rosner, G. S. Vaiana, T. Ayres, and J. L. Linsky. Relations among stellar X-ray emission observed from Einstein, stellar rotation and bolometric luminosity. *ApJ*, 248:279–290, August 1981. doi: 10.1086/159152. URL http://adsabs.harvard.edu/abs/1981ApJ...248..279P.

N. Panagia. Some Physical parameters of early-type stars. *AJ*, 78:929–934, November 1973. doi: 10.1086/111498. URL http://adsabs.harvard.edu/abs/1973AJ.....78..929P.

T.-C. Peng, D. Despois, N. Brouillet, B. Parise, and A. Baudry. Deuterated methanol in Orion BN/KL. *Astron. Astrophys.*, 543:A152, July 2012. doi: 10.1051/0004-6361/201118310. URL http://adsabs.harvard.edu/abs/2012A%26A...543A.152P.

N. Peretto, P. André, and A. Belloche. Probing the formation of intermediate- to high-mass stars in protoclusters. A detailed millimeter study of the NGC 2264 clumps. *Astron. Astrophys.*, 445:979–998, January 2006. doi: 10.1051/0004-6361:20053324. URL http://adsabs.harvard.edu/abs/2006A%26A...445..979P.

N. Peretto, P. Hennebelle, and P. André. Probing the formation of intermediate- to high-mass stars in protoclusters. II. Comparison between millimeter interferometric observations of NGC 2264-C and SPH simulations of a collapsing clump. *Astron. Astrophys.*, 464:983–994, March 2007. doi: 10.1051/0004-6361:20065653. URL http://adsabs.harvard.edu/abs/2007A%26A...464..983P.

N. Peretto, G. A. Fuller, P. André, D. Arzoumanian, V. M. Rivilla, S. Bardeau, S. Duarte Puertas, J. P. Guzman Fernandez, C. Lenfestey, G.-X. Li, F. A. Olguin, B. R. Röck, H. de Villiers, and J. Williams. SDC13 infrared dark clouds: Longitudinally collapsing filaments? *Astron. Astrophys.*, 561:A83, January 2014. doi: 10.1051/0004-6361/201322172. URL http://adsabs.harvard.edu/abs/2014A%26A...561A..83P.

T. Peters, R. S. Klessen, M.-M. Mac Low, and R. Banerjee. Limiting Accretion onto Massive Stars by Fragmentation-induced Starvation. *ApJ*, 725:134–145, December 2010. doi: 10.1088/0004-637X/725/1/134. URL http://adsabs.harvard.edu/abs/2010ApJ...725..134P.

T. Pillai, J. Kauffmann, F. Wyrowski, J. Hatchell, A. G. Gibb, and M. A. Thompson. Probing the initial conditions of high-mass star formation. II. Fragmentation, stability, and chemistry towards high-mass star-forming regions G29.96-0.02 and G35.20-1.74. *Astron. Astrophys.*, 530:A118, June 2011. doi: 10.1051/0004-6361/201015899. URL http://adsabs.harvard.edu/abs/2011A%26A...530A.118P.

R. L. Plambeck, A. D. Bolatto, J. M. Carpenter, J. A. Eisner, J. W. Lamb, E. M. Leitch, D. P. Marrone, S. J. Muchovej, L. M. Pérez, M. W. Pound, P. J. Teuben, N. H. Volgenau, D. P. Woody, M. C. H. Wright, and B. A. Zauderer. The Ionized Circumstellar Envelopes of Orion Source I and the Becklin-Neugebauer Object. *Astrophys. J.*, 765:40, March 2013. doi: 10.1088/0004-637X/765/1/40. URL http://adsabs.harvard.edu/abs/2013ApJ...765...40P.

A. Pon, J. A. Toalá, D. Johnstone, E. Vázquez-Semadeni, F. Heitsch, and G. C. Gómez. Aspect Ratio Dependence of the Free-fall Time for Non-spherical Symmetries. *Astrophys. J.*, 756:145, September 2012. doi: 10.1088/0004-637X/756/2/145. URL http://adsabs.harvard.edu/abs/2012ApJ...756..145P.

T. Preibisch and E. D. Feigelson. The Evolution of X-Ray Emission in Young Stars. *ApJS*, 160:390–400, October 2005. doi: 10.1086/432094. URL http://adsabs.harvard.edu/abs/2005ApJS..160..390P.

T. Preibisch, Y. Y. Balega, D. Schertl, and G. Weigelt. High-resolution study of the young stellar objects in Mon R2 IRS 3. *Astron. Astrophys.*, 392:945–954, September 2002. doi: 10.1051/0004-6361:20021191. URL http://adsabs.harvard.edu/abs/2002A%26A...392..945P.

T. Preibisch, Y.-C. Kim, F. Favata, E. D. Feigelson, E. Flaccomio, K. Getman, G. Micela, S. Sciortino, K. Stassun, B. Stelzer, and H. Zinnecker. The Origin of T Tauri X-Ray Emission: New Insights from the Chandra Orion Ultradeep Project. *ApJS*, 160:401–422, October 2005. doi: 10.1086/432891. URL http://adsabs.harvard.edu/abs/2005ApJS..160..401P.

R. C. Prim. Shortest connection networks and some generalizations. 36(6):1389–1401, November 1957. ISSN 0005-8580. URL http://bstj.bell-labs.com/BSTJ/images/Vol36/bstj36-6-1389.pdf;http://www.alcatel-lucent.com/bstj/vol36-1957/articles/bstj36-6-1389.pdf.

L. Prisinzano, G. Micela, E. Flaccomio, J. R. Stauffer, T. Megeath, L. Rebull, M. Robberto, K. Smith, E. D. Feigelson, N. Grosso, and S. Wolk. X-Ray Properties of Protostars in the Orion Nebula. *ApJ*, 677:401–424, April 2008. doi: 10.1086/528842. URL http://adsabs.harvard.edu/abs/2008ApJ...677..401P.

A. Ptak and R. Griffiths. XAssist: A System for the Automation of X-ray Astrophysics Analysis. In H. E. Payne, R. I. Jedrzejewski, and R. N. Hook, editors, *Astronomical Data Analysis Software and Systems XII*, volume 295 of *Astronomical Society of the Pacific Conference Series*, page 465, 2003. URL http://adsabs.harvard.edu/abs/2003ASPC..295..465P.

K. Qiu and Q. Zhang. Discovery of Extremely High Velocity "Molecular Bullets" in the HH 80-81 High-Mass Star-Forming Region. *Astrophys. J. L.*, 702:L66–L71, September 2009. doi: 10.1088/0004-637X/702/1/L66. URL http://adsabs.harvard.edu/abs/2009ApJ...702L..66Q.

K. Qiu, Q. Zhang, H. Beuther, and J. Yang. High-Resolution Imaging of Molecular Outflows in Massive Young Stars. *Astrophys. J.*, 654:361–372, January 2007. doi: 10.1086/509069. URL http://adsabs.harvard.edu/abs/2007ApJ...654..361Q.

K. Qiu, Q. Zhang, J. Wu, and H.-R. Chen. Submillimeter Array Observations of the Molecular Outflow in High-Mass Star-Forming Region G240.31+0.07. *Astrophys. J.*, 696:66–74, May 2009. doi: 10.1088/0004-637X/696/1/66. URL http://adsabs.harvard.edu/abs/2009ApJ...696...66Q.

R. Racine. Stars in reflection nebulae. Astron. J., 73:233, May 1968. doi: 10.1086/110624. URL http://adsabs.harvard.edu/abs/1968AJ.....73..233R.

D. R. Rayburn. Accretion Onto Binary Systems: Effects on the Orbital Elements. *Pub. Astron. Soc. Pac.*, 88:238, June 1976. doi: 10.1086/129936. URL http://adsabs.harvard.edu/abs/1976PASP...88..238R.

M. Reggiani, M. Robberto, N. Da Rio, M. R. Meyer, D. R. Soderblom, and L. Ricci. Quantitative evidence of an intrinsic luminosity spread in the Orion nebula cluster. *Astron. Astrophys.*, 534:A83, October 2011. doi: 10.1051/0004-6361/201116946. URL http://adsabs.harvard.edu/abs/2011A%26A...534A..83R.

M. J. Reid, K. M. Menten, L. J. Greenhill, and C. J. Chandler. Imaging the Ionized Disk of the High-Mass Protostar Orion I. *ApJ*, 664:950–955, August 2007. doi: 10.1086/518929. URL http://adsabs.harvard.edu/abs/2007ApJ...664..950R.

B. Reipurth and J. Bally. Herbig-Haro Flows: Probes of Early Stellar Evolution. *Ann. Rev. Astron. Astr.*, 39: 403–455, 2001. doi: 10.1146/annurev.astro.39.1.403. URL http://adsabs.harvard.edu/abs/2001ARA%26A..39..403R.

K. J. Richardson, G. J. White, T. S. Monteiro, and S. S. Hayashi. Submillimetre HCO(+) observations of warm cloud cores - The excitation of molecular lines in dense star formation regions. *Astron. Astrophys.*, 198:237–248, June 1988. URL http://adsabs.harvard.edu/abs/1988A%26A...198..237R.

N. A. Ridge, T. L. Wilson, S. T. Megeath, L. E. Allen, and P. C. Myers. A ^{13}CO and C^{18}O Survey of the Molecular Gas Around Young Stellar Clusters within 1 Kiloparsec of the Sun. Astron. J., 126:286–310, July 2003. doi: 10.1086/375455. URL http://adsabs.harvard.edu/abs/2003AJ....126..286R.

G. H. Rieke and M. J. Lebofsky. The interstellar extinction law from 1 to 13 microns. *ApJ*, 288:618–621, January 1985. doi: 10.1086/162827. URL http://adsabs.harvard.edu/abs/1985ApJ...288..618R.

V. M. Rivilla, J. Martín-Pintado, I. Jiménez-Serra, and A. Rodríguez-Franco. The role of low-mass star clusters in massive star formation. The Orion case. *A&A*, 554:A48, June 2013a. doi: 10.1051/0004-6361/201117487. URL http://adsabs.harvard.edu/abs/2013A%26A...554A..48R.

V. M. Rivilla, J. Martín-Pintado, J. Sanz-Forcada, I. Jiménez-Serra, and A. Rodríguez-Franco. X-ray embedded stars as driving sources of outflow-driven turbulence in OMC1-S. *Mon. Not. R. astr. Soc.*, 434:2313–2328, September 2013b. doi: 10.1093/mnras/stt1173. URL http://adsabs.harvard.edu/abs/2013MNRAS.434.2313R.

V. M. Rivilla, J. Martin-Pintado, J. Sanz-Forcada, I. Jimenez-Serra, and A. Rodriguez-Franco. The role of low-mass star clusters in forming the massive stars in DR 21. *ArXiv e-prints*, October 2013c. URL http://adsabs.harvard.edu/abs/2013arXiv1310.4049R.

M. Robberto, S. V. W. Beckwith, N. Panagia, S. G. Patel, T. M. Herbst, S. Ligori, A. Custo, P. Boccacci, and M. Bertero. The Orion Nebula in the Mid-Infrared. *AJ*, 129:1534–1563, March 2005. doi: 10.1086/428000. URL http://adsabs.harvard.edu/abs/2005AJ....129.1534R.

J. F. Roberts, I. Jiménez-Serra, J. Martín-Pintado, S. Viti, A. Rodríguez-Franco, A. Faure, and J. Tennyson. The magnetic precursor of L1448-mm: excitation differences between ion and neutral fluids. *Astron. Astrophys.*, 513:A64, April 2010. doi: 10.1051/0004-6361/200913086. URL http://adsabs.harvard.edu/abs/2010A%26A...513A..64R.

A. C. Robin, C. Reylé, S. Derrière, and S. Picaud. A synthetic view on structure and evolution of the Milky Way. *Astron. Astrophys.*, 409:523–540, October 2003. doi: 10.1051/0004-6361:20031117. URL http://adsabs.harvard.edu/abs/2003A%26A...409..523R.

T. P. Robitaille, B. A. Whitney, R. Indebetouw, K. Wood, and P. Denzmore. Interpreting Spectral Energy Distributions from Young Stellar Objects. I. A Grid of 200,000 YSO Model SEDs. *ApJS*, 167:256–285, December 2006. doi: 10.1086/508424. URL http://adsabs.harvard.edu/abs/2006ApJS..167..256R.

T. P. Robitaille, B. A. Whitney, R. Indebetouw, and K. Wood. Interpreting Spectral Energy Distributions from Young Stellar Objects. II. Fitting Observed SEDs Using a Large Grid of Precomputed Models. *ApJS*, 169:328–352, April 2007. doi: 10.1086/512039. URL http://adsabs.harvard.edu/abs/2007ApJS..169..328R.

L. F. Rodríguez, A. Poveda, S. Lizano, and C. Allen. Proper Motions of the BN Object and the Radio Source I in Orion: Where and When Did the BN Object Become a Runaway Star? *ApJL*, 627:L65–L68, July 2005. doi: 10.1086/432052. URL http://adsabs.harvard.edu/abs/2005ApJ...627L..65R.

A. Rodriguez-Franco, J. Martin-Pintado, J. Gomez-Gonzalez, and P. Planesas. Large-scale interaction of the H II region and the quiescent gas in Orion A. *Astron. Astrophys.*, 264:592–609, October 1992. URL http://adsabs.harvard.edu/abs/1992A%26A...264..592R.

A. Rodriguez-Franco, J. Martin-Pintado, and A. Fuente. CN emission in Orion. The high density interface between the H II region and the molecular cloud. *A&A*, 329:1097–1110, January 1998. URL http://adsabs.harvard.edu/abs/1998A%26A...329.1097R.

A. Rodríguez-Franco, J. Martín-Pintado, and T. L. Wilson. Jets and high-velocity bullets in the Orion A outflows. Is the IRc2 outflow powered by a variable jet? *A&A*, 344:L57–L61, April 1999a. URL http://adsabs.harvard.edu/abs/1999A%26A...344L..57R.

A. Rodríguez-Franco, J. Martín-Pintado, and T. L. Wilson. Jet driven molecular outflows in Orion. *A&A*, 351: 1103–1114, November 1999b. URL http://adsabs.harvard.edu/abs/1999A%26A...351.1103R.

K. L. J. Rygl, A. Brunthaler, A. Sanna, K. M. Menten, M. J. Reid, H. J. van Langevelde, M. Honma, K. J. E. Torstensson, and K. Fujisawa. Parallaxes and proper motions of interstellar masers toward the Cygnus X star-forming complex. I. Membership of the Cygnus X region. *A&A*, 539:A79, March 2012. doi: 10.1051/0004-6361/201118211. URL http://adsabs.harvard.edu/abs/2012A%26A...539A..79R.

C. E. Ryter. Interstellar Extinction from Infrared to X-Rays: an Overview. *ApSS*, 236:285–291, February 1996. doi: 10.1007/BF00645150. URL http://adsabs.harvard.edu/abs/1996Ap%26SS.236..285R.

H. Saito, M. Saito, K. Sunada, and Y. Yonekura. Dense Molecular Clumps Associated with Young Clusters in Massive Star-forming Regions. *ApJ*, 659:459–478, April 2007. doi: 10.1086/512058. URL http://adsabs.harvard.edu/abs/2007ApJ...659..459S.

H. Saito, M. Saito, Y. Yonekura, and F. Nakamura. High-Resolution Studies of the Multiple-Core Systems toward Cluster-forming Regions Including Massive Stars. *Astrophys. J. Suppl.*, 178:302–329, October 2008. doi: 10.1086/590146. URL http://adsabs.harvard.edu/abs/2008ApJS..178..302S.

J. D. Scargle. Studies in Astronomical Time Series Analysis. V. Bayesian Blocks, a New Method to Analyze Structure in Photon Counting Data. *ApJ*, 504:405, September 1998. doi: 10.1086/306064. URL http://adsabs.harvard.edu/abs/1998ApJ...504..405S.

J. Schmid-Burgk, R. Densing, E. Krugel, H. Nett, H. P. Roser, F. Schafer, G. Schwaab, P. van der Wal, and R. Wattenbach. Extended CO (J = 7-6) emission from Orion molecular cloud 1 - Hot ambient gas, two hot-outflow sources. *A&A*, 215:150–164, May 1989. URL http://adsabs.harvard.edu/abs/1989A%26A...215..150S.

J. Schmid-Burgk, R. Guesten, R. Mauersberger, A. Schulz, and T. L. Wilson. A highly collimated outflow in the core of OMC-1. *ApJL*, 362:L25–L28, October 1990. doi: 10.1086/185839. URL http://adsabs.harvard.edu/abs/1990ApJ...362L..25S.

N. Schneider, S. Bontemps, R. Simon, H. Jakob, F. Motte, M. Miller, C. Kramer, and J. Stutzki. A new view of the Cygnus X region. KOSMA ^{13}CO 2 to 1, 3 to 2, and ^{12}CO 3 to 2 imaging. *A&A*, 458:855–871, November 2006. doi: 10.1051/0004-6361:20065088. URL http://adsabs.harvard.edu/abs/2006A%26A...458..855S.

N. Schneider, T. Csengeri, S. Bontemps, F. Motte, R. Simon, P. Hennebelle, C. Federrath, and R. Klessen. Dynamic star formation in the massive DR21 filament. *A&A*, 520:A49, September 2010. doi: 10.1051/0004-6361/201014481. URL http://adsabs.harvard.edu/abs/2010A%26A...520A..49S.

N. Z. Scoville, A. I. Sargent, D. B. Sanders, M. J. Claussen, C. R. Masson, K. Y. Lo, and T. G. Phillips. High-resolution mapping of molecular outflows in NGC 2071, W49, and NGC 7538. *Astrophys. J.*, 303:416–432, April 1986. doi: 10.1086/164086. URL http://adsabs.harvard.edu/abs/1986ApJ...303..416S.

Y. Shimajiri, S. Takahashi, S. Takakuwa, M. Saito, and R. Kawabe. Millimeter- and Submillimeter-Wave Observations of the OMC-2/3 Region. IV Interaction between the Outflow and the Dense Gas in the Cluster Forming Region of OMC-2 FIR 6. , 61:1055–, October 2009. URL http://adsabs.harvard.edu/abs/2009PASJ...61.1055S.

F. H. Shu. Self-similar collapse of isothermal spheres and star formation. *Astrophys. J.*, 214:488–497, June 1977. doi: 10.1086/155274. URL http://adsabs.harvard.edu/abs/1977ApJ...214..488S.

F. H. Shu, F. C. Adams, and S. Lizano. Star formation in molecular clouds - Observation and theory. *Ann. Rev. Astron. Astr.*, 25:23–81, 1987. doi: 10.1146/annurev.aa.25.090187.000323. URL http://adsabs.harvard.edu/abs/1987ARA%26A..25...23S.

R. Y. Shuping, M. Morris, and J. Bally. A New Mid-Infrared Map of the BN/KL Region Using the Keck Telescope. Astron. J., 128:363–374, July 2004. doi: 10.1086/421373. URL http://adsabs.harvard.edu/abs/2004AJ....128..363S.

L. Siess, E. Dufour, and M. Forestini. An internet server for pre-main sequence tracks of low- and intermediate-mass stars. *A&A*, 358:593–599, June 2000. URL http://adsabs.harvard.edu/abs/2000A%26A...358..593S.

J. P. Simpson, S. W. J. Colgan, E. F. Erickson, M. G. Burton, and A. S. B. Schultz. Hubble Space Telescope NICMOS Polarization Measurements of OMC-1. *Astrophys. J.*, 642:339–353, May 2006. doi: 10.1086/500656. URL http://adsabs.harvard.edu/abs/2006ApJ...642..339S.

H. A. Smith, J. L. Hora, M. Marengo, and J. L. Pipher. Outflows from Massive Young Stellar Objects as Seen with the Infrared Array Camera. *ApJ*, 645:1264–1271, July 2006. doi: 10.1086/504370. URL http://adsabs.harvard.edu/abs/2006ApJ...645.1264S.

N. Smith, J. Bally, R. Y. Shuping, M. Morris, and T. L. Hayward. Thermal-Infrared Detection of Optical Outflow Sources in OMC-1 South. *ApJL*, 610:L117–L120, August 2004. doi: 10.1086/423318. URL http://adsabs.harvard.edu/abs/2004ApJ...610L.117S.

R. G. Smith. A search for solid H2S in dense clouds. *Mon. Not. R. astr. Soc.*, 249:172–176, March 1991. URL http://adsabs.harvard.edu/abs/1991MNRAS.249..172S.

R. J. Smith, P. C. Clark, and I. A. Bonnell. Fragmentation in molecular clouds and its connection to the IMF. *Mon. Not. R. astr. Soc.*, 396:830–841, June 2009a. doi: 10.1111/j.1365-2966.2009.14794.x. URL http://adsabs.harvard.edu/abs/2009MNRAS.396..830S.

R. J. Smith, S. Longmore, and I. Bonnell. The simultaneous formation of massive stars and stellar clusters. *MNRAS*, 400:1775–1784, December 2009b. doi: 10.1111/j.1365-2966.2009.15621.x. URL http://adsabs.harvard.edu/abs/2009MNRAS.400.1775S.

D. P. Smits, R. J. Cohen, and B. Hutawarakorn. OH 4765-MHz maser flares in MON R2. *Mon. Not. R. astr. Soc.*, 296:L11, May 1998. doi: 10.1046/j.1365-8711.1998.01515.x. URL http://adsabs.harvard.edu/abs/1998MNRAS.296L..11S.

S. W. Stahler, F. Palla, and P. T. P. Ho. The Formation of Massive Stars. *Protostars and Planets IV*, page 327, May 2000. URL http://adsabs.harvard.edu/abs/2000prpl.conf..327S.

T. Stanke and J. P. Williams. Molecular CO Outflows in the L1641-N Cluster: Kneading a Cloud Core. *AJ*, 133:1307–1320, April 2007. doi: 10.1086/510619. URL http://adsabs.harvard.edu/abs/2007AJ....133.1307S.

B. Stelzer, E. Flaccomio, T. Montmerle, G. Micela, S. Sciortino, F. Favata, T. Preibisch, and E. D. Feigelson. X-Ray Emission from Early-Type Stars in the Orion Nebula Cluster. *Astrophys. J. Suppl.*, 160:557–581, October 2005. doi: 10.1086/432375. URL http://adsabs.harvard.edu/abs/2005ApJS..160..557S.

I. M. Stewart, D. M. Fenech, and T. W. B. Muxlow. A multiple-beam CLEAN for imaging intra-day variable radio sources. *Astron. Astrophys.*, 535:A81, November 2011. doi: 10.1051/0004-6361/201016010. URL http://adsabs.harvard.edu/abs/2011A%26A...535A..81S.

S. R. Stolovy, M. G. Burton, E. F. Erickson, M. J. Kaufman, A. Chrysostomou, E. T. Young, S. W. J. Colgan, D. J. Axon, R. I. Thompson, M. J. Rieke, and G. Schneider. NICMOS 2 Micron Continuum and H 2 Images of OMC-1. *ApJL*, 492:L151, January 1998. doi: 10.1086/311111. URL http://adsabs.harvard.edu/abs/1998ApJ...492L.151S.

M. Tafalla, R. Bachiller, M. C. H. Wright, and W. J. Welch. A Study of the Mutual Interaction between the Monoceros R2 Outflow and Its Surrounding Core. *Astrophys. J.*, 474:329, January 1997. doi: 10.1086/303447. URL http://adsabs.harvard.edu/abs/1997ApJ...474..329T.

S. Takahashi, P. T. P. Ho, P. S. Teixeira, L. A. Zapata, and Y.-N. Su. Hierarchical Fragmentation of the Orion Molecular Filaments. *Astrophys. J.*, 763:57, January 2013. doi: 10.1088/0004-637X/763/1/57. URL http://adsabs.harvard.edu/abs/2013ApJ...763...57T.

J. C. Tan, M. R. Krumholz, and C. F. McKee. Equilibrium Star Cluster Formation. *Astrophys. J. L.*, 641:L121–L124, April 2006. doi: 10.1086/504150. URL http://adsabs.harvard.edu/abs/2006ApJ...641L.121T.

K. N. R. Taylor, J. W. V. Storey, G. Sandell, P. M. Williams, and W. J. Zealey. Molecular hydrogen jets from the Orion nebula. *Nature*, 311:236, September 1984. doi: 10.1038/311236a0. URL http://adsabs.harvard.edu/abs/1984Natur.311..236T.

P. S. Teixeira, C. J. Lada, E. T. Young, M. Marengo, A. Muench, J. Muzerolle, N. Siegler, G. Rieke, L. Hartmann, S. T. Megeath, and G. Fazio. Identifying Primordial Substructure in NGC 2264. *ApJL*, 636:L45–L48, January 2006. doi: 10.1086/500009. URL http://adsabs.harvard.edu/abs/2006ApJ...636L..45T.

L. Testi and A. I. Sargent. Star Formation in Clusters: A Survey of Compact Millimeter-Wave Sources in the Serpens Core. *Astrophys. J. L.*, 508:L91–L94, November 1998. doi: 10.1086/311724. URL http://adsabs.harvard.edu/abs/1998ApJ...508L..91T.

L. Testi, F. Palla, T. Prusti, A. Natta, and S. Maltagliati. A search for clustering around Herbig Ae/Be stars. *Astron. Astrophys.*, 320:159–166, April 1997. URL http://adsabs.harvard.edu/abs/1997A%26A...320..159T.

J. M. Torrelles, L. F. Rodríguez, J. Canto, P. Carral, J. Marcaide, J. M. Moran, and P. T. P. Ho. Are interstellar toroids the focusing agent of the bipolar molecular outflows? *Astrophys. J.*, 274:214–230, November 1983. doi: 10.1086/161439. URL http://adsabs.harvard.edu/abs/1983ApJ...274..214T.

L. K. Townsley, P. S. Broos, Y.-H. Chu, M. Gagné, G. P. Garmire, R. A. Gruendl, K. Hamaguchi, M.-M. Mac Low, T. Montmerle, Y. Nazé, M. S. Oey, S. Park, R. Petre, and J. M. Pittard. The Chandra Carina Complex Project: Deciphering the Enigma of Carina's Diffuse X-ray Emission. *ApJS*, 194:15, May 2011. doi: 10.1088/0067-0049/194/1/15. URL http://adsabs.harvard.edu/abs/2011ApJS..194...15T.

C. Ukidss. UKIDSS-DR6 Galactic Plane Survey (Lucas+ 2012). *VizieR Online Data Catalog*, 2316:0, July 2012. URL http://adsabs.harvard.edu/abs/2012yCat.2316....0U.

W. F. van Altena, J. T. Lee, J.-F. Lee, P. K. Lu, and A. R. Upgren. The velocity dispersion of the Orion Nebula cluster. *AJ*, 95:1744–1754, June 1988. doi: 10.1086/114772. URL http://adsabs.harvard.edu/abs/1988AJ.....95.1744V.

F. F. S. van der Tak, E. F. van Dishoeck, and P. Caselli. Abundance profiles of CH_3OH and H_2CO toward massive young stars as tests of gas-grain chemical models. *Astron. Astrophys.*, 361:327–339, September 2000. URL http://adsabs.harvard.edu/abs/2000A%26A...361..327V.

F. F. S. van der Tak, A. M. S. Boonman, R. Braakman, and E. F. van Dishoeck. Sulphur chemistry in the envelopes of massive young stars. *Astron. Astrophys.*, 412:133–145, December 2003. doi: 10.1051/0004-6361:20031409. URL http://adsabs.harvard.edu/abs/2003A%26A...412..133V.

E. F. van Dishoeck and G. A. Blake. Chemical Evolution of Star-Forming Regions. *Ann. Rev. Astron. Astr.*, 36: 317–368, 1998. doi: 10.1146/annurev.astro.36.1.317. URL http://adsabs.harvard.edu/abs/1998ARA%26A..36..317V.

S. Viti, M. P. Collings, J. W. Dever, M. R. S. McCoustra, and D. A. Williams. Evaporation of ices near massive stars: models based on laboratory temperature programmed desorption data. *Mon. Not. R. astr. Soc.*, 354:1141–1145, November 2004. doi: 10.1111/j.1365-2966.2004.08273.x. URL http://adsabs.harvard.edu/abs/2004MNRAS.354.1141V.

M. H. Vuong, T. Montmerle, N. Grosso, E. D. Feigelson, L. Verstraete, and H. Ozawa. Determination of the gas-to-dust ratio in nearby dense clouds using X-ray absorption measurements. *A&A*, 408:581–599, September 2003. doi: 10.1051/0004-6361:20030942. URL http://adsabs.harvard.edu/abs/2003A%26A...408..581V.

V. Wakelam, P. Caselli, C. Ceccarelli, E. Herbst, and A. Castets. Resetting chemical clocks of hot cores based on S-bearing molecules. *Astron. Astrophys.*, 422:159–169, July 2004. doi: 10.1051/0004-6361:20047186. URL http://adsabs.harvard.edu/abs/2004A%26A...422..159W.

C. K. Walker, F. C. Adams, and C. J. Lada. 1.3 millimeter continuum observations of cold molecular cloud cores. *Astrophys. J.*, 349:515–528, February 1990. doi: 10.1086/168338. URL http://adsabs.harvard.edu/abs/1990ApJ...349..515W.

J. Wang, L. K. Townsley, E. D. Feigelson, K. V. Getman, P. S. Broos, G. P. Garmire, and M. Tsujimoto. An X-Ray Census of Young Stars in the Massive Southern Star-forming Complex NGC 6357. *ApJS*, 168:100–127, January 2007. doi: 10.1086/509147. URL http://adsabs.harvard.edu/abs/2007ApJS..168..100W.

K.-S. Wang, T. L. Bourke, M. R. Hogerheijde, F. F. S. van der Tak, A. O. Benz, S. T. Megeath, and T. L. Wilson. Dense molecular cocoons in the massive protocluster W3 IRS5: a test case for models of massive star formation. *Astron. Astrophys.*, 558:A69, October 2013. doi: 10.1051/0004-6361/201322087. URL http://adsabs.harvard.edu/abs/2013A%26A...558A..69W.

P. Wang, Z.-Y. Li, T. Abel, and F. Nakamura. Outflow Feedback Regulated Massive Star Formation in Parsec-Scale Cluster-Forming Clumps. *ApJ*, 709:27–41, January 2010. doi: 10.1088/0004-637X/709/1/27. URL http://adsabs.harvard.edu/abs/2010ApJ...709...27W.

B. A. Whitney, K. Wood, J. E. Bjorkman, and M. Cohen. Two-dimensional Radiative Transfer in Protostellar Envelopes. II. An Evolutionary Sequence. *ApJ*, 598:1079–1099, December 2003. doi: 10.1086/379068. URL http://adsabs.harvard.edu/abs/2003ApJ...598.1079W.

B. A. Wilking and C. J. Lada. The discovery of new embedded sources in the centrally condensed core of the Rho Ophiuchi dark cloud - The formation of a bound cluster. *ApJ*, 274:698–716, November 1983. doi: 10.1086/161482. URL http://adsabs.harvard.edu/abs/1983ApJ...274..698W.

J. P. Williams, L. Blitz, and C. F. McKee. The Structure and Evolution of Molecular Clouds: from Clumps to Cores to the IMF. *Protostars and Planets IV*, page 97, May 2000. URL http://adsabs.harvard.edu/abs/2000prpl.conf...97W.

P. M. Williams, K. A. van der Hucht, A. M. T. Pollock, D. R. Florkowski, H. van der Woerd, and W. M. Wamsteker. Multi-frequency variations of the Wolf-Rayet system HD 193793. I - Infrared, X-ray and radio observations. *Mon. Not. R. astr. Soc.*, 243:662–684, April 1990. URL http://adsabs.harvard.edu/abs/1990MNRAS.243..662W.

T. L. Wilson. Isotopes in the interstellar medium and circumstellar envelopes. *Reports on Progress in Physics*, 62:143–185, February 1999. doi: 10.1088/0034-4885/62/2/002. URL http://adsabs.harvard.edu/abs/1999RPPh...62..143W.

G. A. Wolf, C. J. Lada, and J. Bally. The giant molecular outflow in MON R2. Astron. J., 100:1892–1902, December 1990. doi: 10.1086/115645. URL http://adsabs.harvard.edu/abs/1990AJ....100.1892W.

M. G. Wolfire and J. P. Cassinelli. Conditions for the formation of massive stars. *Astrophys. J.*, 319:850–867, August 1987. doi: 10.1086/165503. URL http://adsabs.harvard.edu/abs/1987ApJ...319..850W.

S. J. Wolk, F. R. Harnden, Jr., E. Flaccomio, G. Micela, F. Favata, H. Shang, and E. D. Feigelson. Stellar Activity on the Young Suns of Orion: COUP Observations of K5-7 Pre-Main-Sequence Stars. *Astrophys. J. Suppl.*, 160:423–449, October 2005. doi: 10.1086/432099. URL http://adsabs.harvard.edu/abs/2005ApJS..160..423W.

M. C. H. Wright, R. L. Plambeck, and D. J. Wilner. A Multiline Aperture Synthesis Study of Orion-KL. *ApJ*, 469:216, September 1996. doi: 10.1086/177773. URL http://adsabs.harvard.edu/abs/1996ApJ...469..216W.

Y. Wu, Y. Wei, M. Zhao, Y. Shi, W. Yu, S. Qin, and M. Huang. A study of high velocity molecular outflows with an up-to-date sample. *A&A*, 426:503–515, November 2004. doi: 10.1051/0004-6361:20035767. URL http://adsabs.harvard.edu/abs/2004A%26A...426..503W.

F. Wyrowski, P. Schilke, and C. M. Walmsley. Vibrationally excited HC_3N toward hot cores. *Astron. Astrophys.*, 341:882–895, January 1999. URL http://adsabs.harvard.edu/abs/1999A%26A...341..882W.

T. Xie and P. F. Goldsmith. The giant molecular cloud Monoceros R2. 1: Shell structure. *Astrophys. J.*, 430:252–255, July 1994. doi: 10.1086/174399. URL http://adsabs.harvard.edu/abs/1994ApJ...430..252X.

J. E. Ybarra, E. A. Lada, C. G. Román-Zúñiga, Z. Balog, J. Wang, and E. D. Feigelson. The Progression of Star Formation in the Rosette Molecular Cloud. *ApJ*, 769:140, June 2013. doi: 10.1088/0004-637X/769/2/140. URL http://adsabs.harvard.edu/abs/2013ApJ...769..140Y.

H. W. Yorke and C. Sonnhalter. On the Formation of Massive Stars. *ApJ*, 569:846–862, April 2002. doi: 10.1086/339264. URL http://adsabs.harvard.edu/abs/2002ApJ...569..846Y.

L. A. Zapata, L. F. Rodríguez, S. E. Kurtz, and C. R. O'Dell. Compact Radio Sources in Orion: New Detections, Time Variability, and Objects in OMC-1S. *AJ*, 127:2252–2261, April 2004a. doi: 10.1086/382715. URL http://adsabs.harvard.edu/abs/2004AJ....127.2252Z.

L. A. Zapata, L. F. Rodríguez, S. E. Kurtz, C. R. O'Dell, and P. T. P. Ho. A Cluster of 1.3 Centimeter Continuum Sources in OMC-1 South. *ApJL*, 610:L121–L124, August 2004b. doi: 10.1086/423428. URL http://adsabs.harvard.edu/abs/2004ApJ...610L.121Z.

L. A. Zapata, L. F. Rodríguez, P. T. P. Ho, Q. Zhang, C. Qi, and S. E. Kurtz. A Highly Collimated, Young, and Fast CO Outflow in OMC-1 South. *ApJL*, 630:L85–L88, September 2005. doi: 10.1086/491470. URL http://adsabs.harvard.edu/abs/2005ApJ...630L..85Z.

L. A. Zapata, P. T. P. Ho, L. F. Rodríguez, C. R. O'Dell, Q. Zhang, and A. Muench. Silicon Monoxide Observations Reveal a Cluster of Hidden Compact Outflows in the OMC 1 South Region. *ApJ*, 653:398–408, December 2006. doi: 10.1086/508319. URL http://adsabs.harvard.edu/abs/2006ApJ...653..398Z.

L. A. Zapata, P. T. P. Ho, L. F. Rodríguez, P. Schilke, and S. Kurtz. Circumbinary molecular rings around young stars in Orion. *A&A*, 471:L59–L62, September 2007. doi: 10.1051/0004-6361:20077782. URL http://adsabs.harvard.edu/abs/2007A%26A...471L..59Z.

L. A. Zapata, J. Schmid-Burgk, P. T. P. Ho, L. F. Rodríguez, and K. M. Menten. Explosive Disintegration of a Massive Young Stellar System in Orion. *ApJL*, 704:L45–L48, October 2009. doi: 10.1088/0004-637X/704/1/L45. URL http://adsabs.harvard.edu/abs/2009ApJ...704L..45Z.

L. A. Zapata, J. Schmid-Burgk, D. Muders, P. Schilke, K. Menten, and R. Guesten. A rotating molecular jet in Orion. *A&A*, 510:A2, January 2010. doi: 10.1051/0004-6361/200810245. URL http://adsabs.harvard.edu/abs/2010A%26A...510A...2Z.

L. A. Zapata, J. Schmid-Burgk, and K. M. Menten. Orion KL: the hot core that is not a "hot core". *A&A*, 529: A24, May 2011. doi: 10.1051/0004-6361/201014423. URL http://adsabs.harvard.edu/abs/2011A%26A...529A..24Z.

L. A. Zapata, J. Schmid-Burgk, N. Pérez-Goytia, P. T. P. Ho, L. F. Rodríguez, L. Loinard, and I. Cruz-González. A 10,000 Year Old Explosion in DR21. *ApJL*, 765: L29, March 2013. doi: 10.1088/2041-8205/765/2/L29. URL http://adsabs.harvard.edu/abs/2013ApJ...765L..29Z.

Q. Zhang, P. T. P. Ho, and N. Ohashi. Dynamical Collapse in W51 Massive Cores: CS (3–2) and CH 3CN Observations. *Astrophys. J.*, 494:636, February 1998. doi: 10.1086/305243. URL http://adsabs.harvard.edu/abs/1998ApJ...494..636Z.

Q. Zhang, P. T. P. Ho, and M. C. H. Wright. The SIO and CS Emission in the Molecular Outflow toward L1157. Astron. J., 119:1345–1351, March 2000. doi: 10.1086/301274. URL http://adsabs.harvard.edu/abs/2000AJ....119.1345Z.

Q. Zhang, T. R. Hunter, J. Brand, T. K. Sridharan, S. Molinari, M. A. Kramer, and R. Cesaroni. Search for CO Outflows toward a Sample of 69 High-Mass Protostellar Candidates: Frequency of Occurrence. *Astrophys. J. L.*, 552:L167–L170, May 2001. doi: 10.1086/320345. URL http://adsabs.harvard.edu/abs/2001ApJ...552L.167Z.

Q. Zhang, T. R. Hunter, J. Brand, T. K. Sridharan, R. Cesaroni, S. Molinari, J. Wang, and M. Kramer. Search for CO Outflows toward a Sample of 69 High-Mass Protostellar Candidates. II. Outflow Properties. *Astrophys. J.*, 625:864–882, June 2005. doi: 10.1086/429660. URL http://adsabs.harvard.edu/abs/2005ApJ...625..864Z.

Z. Zhu, L. Hartmann, C. F. Gammie, L. G. Book, J. B. Simon, and E. Engelhard. Long-term Evolution of Protostellar and Protoplanetary Disks. I. Outbursts. *Astrophys. J.*, 713:1134–1142, April 2010. doi: 10.1088/0004-637X/713/2/1134. URL http://adsabs.harvard.edu/abs/2010ApJ...713.1134Z.

H. Zinnecker and H. W. Yorke. Toward Understanding Massive Star Formation. *ARAA*, 45:481–563, September 2007. doi: 10.1146/annurev.astro.44.051905.092549. URL http://adsabs.harvard.edu/abs/2007ARA%26A..45..481Z.

L. M. Ziurys, R. N. Martin, T. A. Pauls, and T. L. Wilson. Ammonia in Orion. II - The gas in and around OMC-1. *A&A*, 104:288–295, December 1981. URL http://adsabs.harvard.edu/abs/1981A%26A...104..288Z.

L. M. Ziurys, T. L. Wilson, and R. Mauersberger. A new bipolar outflow source in OMC-1. *ApJL*, 356: L25–L29, June 1990. doi: 10.1086/185742. URL http://adsabs.harvard.edu/abs/1990ApJ...356L..25Z.

B. Zuckerman, M. Morris, and P. Palmer. The location of the hot molecular core in Orion. *Astrophys. J. L.*, 250:L39–L42, November 1981. doi: 10.1086/183670. URL http://adsabs.harvard.edu/abs/1981ApJ...250L..39Z.

List of Tables

List of Figures

-

List of Acronyms

2MASS ..... *Two Microns All Sky Survey*

ACIS ..... *Advanced CCD Imaging Spectrometer*

CCD ..... *Charge-coupled device*

CIAO ..... *Chandra Interactive Analysis of Observations*

COUP ..... *Chandra Orion Ultradeep Project*

CXOXASSIST *Chandra XAssist Source List archive*

FIR ..... *Far Infrared*

GPS ..... *Galactic Plane Survey*

HH ..... *Herbig-Haro*

IMF ..... *Initial Mass Function*

IR ..... *Infrared*

IRAF ..... *Image Reduction and Analysis Facility*

IRDC ..... *Infrared Dark Cloud*

ISM ..... *Interstellar Medium*

MF ..... *Molecular Filament*

MS ..... *Main Sequence*

MST ..... *Minimum Spanning Tree*

NE ..... *North East*

NICMOS ..... *Near Infrared Camera and Multi-Object Spectrometer*

OHC ..... *Orion Hot Core*

OMC ..... *Orion Molecular Cloud*

ONC ..... *Orion Nebula Cluster*

PAH ..... *Polycyclic aromatic hydrocarbons*

PMS ..... *Pre-main Sequence*

RRL ..... *Radio Recombination Lines*

SCUBA ..... *Submillimetre Common-User Bolometer Array*

SDSS ..... *Sloan Digital Sky Survey*

SED ..... *Spectral Energy Distribution*

SFE ..... *Star Formation Efficiency*

SMA ..... *Submillimeter Array*

TC ..... *Trapezium Cluster*

UKIDSS ..... *United Kingdom Infrared Telescope Infrared Deep Sky Survey*

UKIRT ..... *United Kingdom Infrared Telescope*

UV ..... *Ultraviolet*

VLA ..... *Very Large Array*

WFCAM ..... *Wide Field Camera*

ZAMS ..... *Zero Age Main Sequence*

Appendices

APPENDIX A

Stellar collisions in dense clusters

The coalescence of low- and intermediate-mass stars has been proposed as one of the mechanisms that may form massive stars (Bonnell et al. 1998; Stahler et al. 2000; Bonnell and Bate 2002; Bally and Zinnecker 2005). Observations have shown that stars are almost never born in isolation but favor formation in clusters (Lada and Lada 2003b). Bonnell et al. (1998) and Stahler et al. (2000) argued that high stellar densities may exist for a brief period of time during the very embedded early evolution of stellar clusters in molecular cores, making stellar collisions more likely. Therefore, interactions could occur among members of a protostellar cluster, especially at the early stages of cluster evolution. These interactions could play a role in the formation of high-mass stars.

Coalescence requires stellar densities in the order of 10^6-10^8 stars pc^{-3} (Bonnell and Bate 2005, Bally and Zinnecker 2005) that are higher than the highest densities (of $\sim 10^5$ stars pc^{-3}) found observationally (e.g., Claussen et al. 1994 or Figer et al. 2002). However, we have detected in this work a very high stellar density in the OHC region of 10^6 stars pc^{-3}, a range where stellar collisions may occur. This indicates that a collision could be possible in the OHC. This idea is also supported by some observational evidence that suggests that a violent event occurred in the OHC in the past: a large-scale CO outflow (Kwan and Scoville 1976), the H_2 fingers (Taylor et al. 1984; Allen and Burton 1993), the CO filaments (Zapata et al. 2009), and the proper motions measured for the massive objects BN, I and n (Rodríguez et al. 2005; Gómez et al. 2008; Goddi et al. 2011b), all of them pointing towards approximately the same central position within the OHC region (see Fig. 1 in Zapata et al. 2011). Rodríguez et al. (2005) and Zapata et al. (2009) suggested that this violent event could have been triggered by an interaction among several stars in the protostellar cluster. This interaction is consistent with a close encounter that would induce stars to coalescence in this particular high-density cluster revealed by X-ray observations.

In this appendix, we derive some expressions to describe stellar collisions in a cluster and apply them to the properties of the OHC with the aim to determine if a

stellar collision was possible in the region. We also compare our results with other works that include dynamical simulations of stellar encounters.

We follow Binney and Tremaine (1987) to study the case where two naked stars encounter (A.1) and extend this case to a encounter between a star and a star with a circumstellar disk (A.2). In section A.3 we present the possibility of disk-induced stellar capture in an encounter forming a binary, and finally in A.4, we give a simple analysis of the orbital decay of a binary trigger by accretion onto the system, which may produce a collision between the two stars.

A.1 Direct star-star encounter

We consider an encounter between two stars with mass M. Applying conservation of momentum and energy in the system, it is possible to obtain the collision rate (essentially the inverse of the time needed to produce a collision, $t_{\rm coll}$):

$$\frac{1}{t_{\rm coll}}\ [yr^{-1}] = 4\sqrt{\pi}\rho_* \sigma_* r_{\rm coll}^2 \left(1 + \frac{GM}{\sigma_*^2 r_{coll}}\right), \tag{A.1}$$

where ρ_* is the volume stellar density and σ_* is the velocity dispersion of the cluster. The first term corresponds to the geometrical cross section of the stars, and the second is due to gravitational focusing. The two stars collide when the collision distance $r_{\rm coll}$ is equal to the distance between the centers of mass of the stars, i.e., the sum of their radii: $r_{\rm coll} = R_1 + R_2$.

A.2 Star-(star+disk) encounter

In this section, we extend the previous case by adding the presence of a circumstellar disk. Calculating the gravitational potential generated by a disk is difficult in general (Binney and Tremaine 1987). For this reason, we made a reasonable approximation to characterize the disk, so that the calculation of its potential is rather simple. We consider the disk to be an infinitesimal thin surface, with surface density

$$\Sigma(r) = \beta \frac{r_d M_d}{2\pi \left(r^2 + r_d^2\right)^{3/2}}, \tag{A.2}$$

where $\beta = (1 - 1/\sqrt{2})^{-1}$, r_d and M_d are the radius and mass of the disk, and r is the radial distance to the disk center. Applying the Gauss theorem, one can obtain

the gravitational potential created by the disk as

$$\Phi = -\beta \frac{GM_d}{\sqrt{r^2 + r_d^2}}. \tag{A.3}$$

This potential generated by the disk adds one term to the expression of the stellar collision rate τ_{coll}^{-1}:

$$\frac{1}{\tau_{coll}}[yr^{-1}] = 4\sqrt{\pi}\rho_* \sigma_* r_{coll}^2 \left(1 + \frac{GM}{\sigma_*^2 r_{coll}} + \frac{\beta G M_d}{\sigma_*^2 \sqrt{r_{coll}^2 + r_d^2}}\right) \tag{A.4}$$

In this case, a collision in the system would occur when $r_{coll} = r_{disk}$, considerably increasing the probability of collision.

A.3 Capture of the incident star by the system star+disk

When a collision as described in A.2. is produced, the disk may capture the incident star. The condition for a star to be captured by the disk is that the energy of the incident star is lower than the potential energy created by the star+disk system:

$$\frac{1}{2} m \sigma_*^2 < \frac{\beta G M_d m}{\sqrt{r_{coll}^2 + r_d^2}} + \frac{GMm}{r_{coll}}, \tag{A.5}$$

This gives a maximum value of r_{coll} for a star to be disk-captured in the collision:

$$r_{\max} = \frac{2G}{\sigma_*^2}\left(\frac{\beta M_d}{\sqrt{2}} + M\right). \tag{A.6}$$

Then, if $r_{coll} < r_{max}$, a binary could be formed as a consequence of the collision.

A.4 Orbital decay in the binary system induced by accretion

The subsequent accretion onto a binary system will harden the binary, moving the orbit closer. This produces an orbital decay (Bate et al. 2002) and eventually could end in a collision between the two stars. The evolution of the semi-mayor axis of the

binary orbit (a) due to accretion can be described as (Rayburn 1976)

$$\dot{a} = -3\, a \frac{\dot{M}}{M}, \tag{A.7}$$

where we considered that the two binaries have the same mass M. Integrating this expression from the moment when both stars have initial masses M_i and an initial semi-major orbit a_i, to the moment when the stars have accreted mass to form stars with mass M_f, we obtain the value of the final semi-major axis:

$$a_f = a_i \left(\frac{M_i}{M_f} \right)^3 < a_i. \tag{A.8}$$

APPENDIX B

Rotational Diagram Method for the CH_3CN rotational lines

In chapter 7 we have shown seven CH_3CN rotational transitions arising from thr MonR2-IRS5 molecular core. This molecule is commonly used to derive the kinetic temperature in star-forming regions. Images for the CH_3CN $K = 0$, $K = 2$ and $K = 4$ transitions are presented in Fig. 7.10. In Table 7.6 we present the parameters extracted from fitting each $K = 0$ to $K = 6$ transition to a Gaussian emission line, as well as upper limits on the integrated area and peak intensities for the undetected $K = 7$ transition. The $K = 0$ (220.74726 GHz) and $K = 1$ (220.74301 GHz) transitions are very close in frequency and hence the fits suffer from partial merging of the lines.

We apply the rotational diagram method to CH_3CN in order to estimate the gas excitation temperature of the source IRS5 in MonR2. To this end we assume the emission is optically thin, and that the medium is in Local Thermodynamic Equilibrium (LTE). This implies that the level populations are described by the Maxwell-Boltzmann distribution with temperature $T_{\rm rot}$, such that:

$$\frac{N_u}{N_l} = \frac{g_u}{g_l} e^{-h\nu/kT_{\rm rot}} \tag{B.1}$$

where g_u and g_l designate the statistical weights of the upper and lower levels respectively, and ν is the transition frequency. Rewriting the expression after assuming LTE gives:

$$\frac{N_u}{g_u} = \frac{N_{\rm tot}}{Q(T_{\rm rot})} e^{-E_u/kT_{\rm rot}} \tag{B.2}$$

where $Q(T)$ is the partition function, E_u is the upper level energy, and $N_{\rm tot}$ is the total column density. The quantity $\frac{N_u}{g_u}$ is calculated following Zhang et al. (1998):

$$\frac{N_{JK}}{g_{JK}} = 1.669 \times 10^{17} \frac{\int T_B dv (\text{K km s}^{-1})}{S_{JK}\mu(\text{D})^2 \nu(\text{MHz})}\ cm^{-2} \tag{B.3}$$

where μ is the dipole moment and equals 3.92 Debye (Blake et al., 1987); S_{JK} is the line strength and is given by $S_{JK} = (J^2 - K^2)/J$ ($J = 12$, K = 0 to K = 6 here); and T_B is the brightness temperature. The velocity-integrated brightness temperature can be obtained from the line areas though the Rayleigh-Jeans law:

$$\int T_B dv = 1.224 \times 10^6 \quad \frac{S_\nu}{\nu(\mathrm{GHz})^2 \theta_B(")^2} \; K\, km\, s^{-1} \tag{B.4}$$

where S_ν is the line area in Jy/beam km s^{-1} as in Table 7.6, and θ_B is the beam size in arcseconds. The statistical weights are given by $g_{JK} = (2J + 1)g_K$ where $g_K = 4$ for K = 0 or K $\neq 3n$, and $g_K = 8$ for K = $3n$, where n is a nonzero integer.

The resulting rotational diagram is shown in Fig. 7.11. Extracting the slope from a linear fit to the data following Equation B.2 gives an estimate of the gas excitation temperature of 144 ± 15 K. The error of T_{ex} has been derived by propagating errors. This value is consistent with typical temperatures of hot cores (e.g. Jiménez-Serra et al., 2009). The total column density can easily be estimated from the y-intercept of the fit. To this end the CH_3CN partition function is given by Blake et al. (1987):

$$Q(T_{\mathrm{rot}}) = \frac{2}{3}\sqrt{\left(\frac{k}{h}\right)^3 \frac{\pi}{AB^2}} \quad T_{\mathrm{rot}}^{3/2} \tag{B.5}$$

This yields an estimate for the column density of $(3.2 \pm 0.4) \times 10^{13}$ cm^{-2}.